

**Proceedings of the
21st Annual Symposium
Imaging Network Ontario
March 23 – 24, 2023
DoubleTree by Hilton
London, Ontario**

Table of Contents

ImNO 2023 Co-Chairs	4
Welcome Letter	5
Imaging Network Ontario Code of Conduct	6
Supporting Consortia	7
Machine Learning in Medical Imaging Consortium (MaLMIC)	7
Ontario Institute for Cancer Research Imaging Program	7
Ontario Network of Excellence for Translation of Hyperpolarized MRI Technologies Consortium	7
Corporate Sponsors	8
Scintica	8
NDI	8
GE HealthCare	8
Keynote Speakers	9
Karen Yeates	9
Lena Maier-Hein	10
Panel Session	11
How Can Medical Imaging Contribute to Solving the Canadian Healthcare Crisis?	11
Innovation Think Tank Certification Program	13
Organizing Committee	14
Scientific Committee	14
Student Committee	14
Planning Committee	14
Abstract Reviewers	14
Oral and Pitch/Poster Judges	15
Program	16
Program at a Glance	16
Thursday, March 23, 2023	17
Friday, March 24, 2023	23
Oral and Pitch/Poster Abstracts	29
Oral Session 1: Ultrasound Imaging	30
Oral Session 2: Neuroimaging I	35

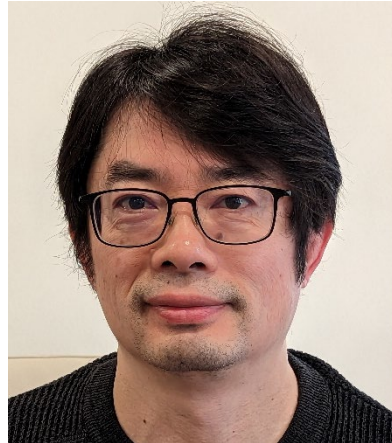
Pitch/Poster Session 1: Ultrasound and Optical Imaging	40
Pitch/Poster Session 2: Neuroimaging	49
Oral Session 3: Hyperpolarized MR Imaging	59
Oral Session 4: Image Guidance	64
Pitch/Poster Session 3: Hyperpolarized MR and Lung Imaging	69
Pitch/Poster Session 4: Image Guidance	79
Oral Session 5: Hardware Development	89
Oral Session 6: MR Imaging	94
Pitch/Poster Session 5: Image Processing and Machine Learning	99
Pitch/Poster Session 6: MR Imaging	109
Oral Session 7: Cancer Imaging	119
Oral Session 8: Cardiac and Lung Imaging	124
Pitch/Poster Session 7: Cancer Imaging	129
Pitch/Poster Session 8: Musculoskeletal and Vascular Imaging	139
Oral Session 9: MR and Magnetic Particle Imaging	149
Oral Session 10: Device Development	154
Pitch/Poster Session 9: Contrast Agents and Radiopharmaceuticals	159
Pitch/Poster Session 10: Device, Hardware and Software Development	169
Oral Session 11: Deep Learning	179
Oral Session 12: Neuroimaging II	184
Pitch/Poster Session 11: Deep Learning	189
Pitch/Poster Session 12: Cellular and Molecular/Image Guidance	199
Author Index	209

ImNO 2023 Co-Chairs



[Jessica Rodgers](#)

University of Manitoba



[Elvis Chen](#)

Robarts Research Institute

Welcome Letter

Dear ImNO 2023 Attendees:

On behalf of the 2023 Organizing Committee, we are excited to welcome you to the 21st annual Imaging Network Ontario (ImNO) Symposium. We are delighted to be returning to an in-person event this year and are looking forward to reconnecting with this exceptional community as we come together once again.

The annual two-day ImNO symposium features world-class scientists and showcases multidisciplinary presentations from Ontario and across the country. This rendezvous of researchers promotes collaborations, broadcasts career opportunities, informs trainees on diverse imaging applications, and fosters a greater understanding of the commercialization process. The symposium features world-renowned keynote speakers and sessions that bring our trainees together with imaging scientists, clinicians, patient groups, and industry representatives.

Highlights for this year's program include two keynote speakers, Karen Yeates and Lena Maier-Hein, as well as a lunch-and-learn panel session on medical imaging for times of urgent need in the Canadian healthcare system. The symposium will feature 155 accepted presentations split between 48 oral presentations and 107 pitch-and-poster presentations. There will also be plenty of opportunities for you to network with your imaging colleagues, including a reception and ImNO Jeopardy event.

We are pleased to thank the following groups for their support of the 2023 symposium:

- Machine Learning in Medical Imaging Consortium (MaLMIC)
- Ontario Institute of Cancer Research (OICR) Imaging Program
- Ontario Network of Excellence for Translation of Hyperpolarized MRI Technologies Consortium
- Scintica Instrumentation, Inc.
- GE Healthcare
- Northern Digital Inc. (NDI)

We are also pleased to work with Siemens, Western University, and Robarts Research Institute this year to host an Innovation Think Tank (ITT) Certification Program, allowing our trainees to learn innovation management methodologies and co-implementation approaches by working on real-life healthcare challenges. Top teams from the ITT will be sharing their presentations with the ImNO community, highlighting themes of Cost Containment within Healthcare Systems and Clinical Translation.

In closing, we would like to thank our reviewers who provided feedback on the proffered abstracts and acknowledge the significant contributions made by members of the Scientific, Student, and Planning Committees. These teams have worked very hard to bring us this year's meeting. We hope you enjoy this year's program of keynotes, discussion, oral talks, and pitch-and-poster presentations.

Sincerely,

Jessica Rodgers and Elvis Chen

Imaging Network Ontario Code of Conduct

All attendees, speakers, sponsors and volunteers at the ImNO symposium are required to agree with the following code of conduct. Organisers will enforce this code throughout the event. We expect cooperation from all participants to help ensure a safe environment for everybody.

Need Help?

If you are being harassed, notice that someone else is being harassed, or have any other concerns, contact the Symposium Manager at imno@imno.ca or send an email to ombudsperson@ImNO.ca or chairs@ImNO.ca.

Overview

Imaging Network Ontario is committed to providing a harassment-free symposium experience for everyone, regardless of gender, gender identity and expression, age, sexual orientation, disability, physical appearance, body size, race, ethnicity, religion (or lack thereof), or technology choices. We do not tolerate harassment of symposium participants in any form. Use of sexualised language and imagery that does not convey a scientific message is not appropriate. We expect participants and sponsors to follow these rules for the duration of the symposium in any symposium venue or platform, including talks, social events, Twitter and other online media. Symposium participants violating these rules may be sanctioned or expelled from the symposium without a refund at the discretion of the symposium organisers.

Details

All attendees, speakers, sponsors and volunteers at ImNO are subject to the anti-harassment policy.

Harassment includes offensive verbal comments related to gender, gender identity and expression, age, sexual orientation, disability, physical appearance, body size, race, ethnicity, religion, technology choices, sexual images in public spaces, deliberate intimidation, stalking, following, harassing photography or recording, sustained disruption of talks or other events, inappropriate contact, and unwelcome sexual attention. Use of images, activities, uniforms/costumes or other materials that create a sexualised environment will not be tolerated.

Anyone asked to stop any harassing behaviour is expected to comply immediately.

If anyone engages in harassing behaviour, the symposium organisers may take any action they deem appropriate, including warning the offender or expulsion from the symposium with no refund.

If you are being harassed, notice that someone else is being harassed, or have any other concerns, please contact a member of conference staff immediately. Conference staff can be identified as they'll be wearing clearly marked badges saying "ImNO staff". You can also send an email to the ImNO ombudsperson, Dr. Amir Moslemi, at ombudsperson@ImNO.ca or the ImNO 2023 Chairs, Drs. Jessica Rodgers and Elvis Chen, at chairs@ImNO.ca.

We expect everyone to follow these rules for the duration of the symposium within and outside symposium venues and platforms, including but not limited to symposium-related talks, workshops, and social events involving ImNO attendees, and in all symposium-related communications, including social media.

Supporting Consortia

The Annual Meeting of Imaging Network Ontario (ImNO) promotes Canada's role as a leader in medical imaging innovation by cultivating synergy among consortia and partnerships between Ontario and other Canadian imaging entities.

The following consortia and programs supported the 2023 ImNO Symposium financially.

Machine Learning in Medical Imaging Consortium (MaLMIC)

Machine Learning for Medical Imaging Working Group: Aaron Fenster, Anne Martel, Julia Publicover, Amber L. Simpson, Lincoln Stein, Aaron Ward, Martin Yaffe



The Consortium was launched to accelerate research and development of machine learning solutions for unmet needs in medical imaging through collaborations between academic and clinical researchers, and with Canadian industry. It hosts monthly forums on machine learning in medical imaging and promotes collaboration through its website at <https://malmic.ca/>.

Ontario Institute for Cancer Research Imaging Program

Directors: Aaron Fenster and Martin Yaffe

Ontario Institute for Cancer Research



The OICR Imaging Program accelerates the translation of research into the development of new imaging innovations for earlier cancer detection, diagnosis and treatment through four major projects: probe development and commercialization, medical imaging instrumentation and software, pathology validation, and imaging for clinical trials. The Imaging Program facilitates improved screening and treatment options for cancer patients by streamlining advances in medical imaging through the complex pipeline from discovery to clinical translation and ultimately to clinical use.

Ontario Network of Excellence for Translation of Hyperpolarized MRI Technologies Consortium

Lead Researcher: Charles Cunningham

Ontario Research Fund



Ontario is home to five major research groups developing new forms of MRI based on Hyperpolarized (HP) contrast agents, with the aim of transforming patient care for conditions such as cancer, heart failure and lung disease. Just as an injection of dye prior to an x-ray exam can reveal important new information, the introduction of HP contrast agents, which are magnetized to be directly detectable in an MRI scan, can open up many new applications of MRI. Several HP agents have been developed in the past 20 years for MR imaging, and Ontario is uniquely positioned to take a leadership role in the development of the next generation of agents and technologies, with expertise and activity in all of the related technology development areas. The overall objective of this program is to integrate and develop this substantial expertise, creating an Ontario Network of Excellence, bringing these technologies forward to commercialization and, ultimately, application in the health system. Each of the related technologies is being developed in

partnership with MRI hardware vendors and pharmaceutical companies for application in targeted disease areas.

There are five major centres of activity in HP-MRI in Ontario led by: Mitchell Albert at Lakehead University in Thunder Bay, Andrea Kassner and Giles Santyr at the Hospital for Sick Children in Toronto, Charles Cunningham at Sunnybrook Health Sciences Centre in Toronto, Charles McKenzie, Grace Parraga and Timothy Scholl at the Robarts Research Institute in London, and Michael Noseworthy at McMaster University in Hamilton.

Corporate Sponsors

Gold Sponsors

Scintica:

[Scintica](#)'s mission is to link scientists with the right precision tools to further research by providing high-value instrumentation and research solutions to scientists and the preclinical research community. We are a leading supplier of medical research solutions and provide elite applications, technical support, and a platform for today's scientists to share their scientific findings.

We carry a diverse portfolio of products, ranging from imaging systems (PET, CT, MRI, optical, DEXA, intravital microscopy, photoacoustic and high-frequency ultrasound systems), lab equipment, instruments, workstations, incubators, tissue culture analysis, and much more.



[GE HealthCare](#) is a leading global medical technology innovator dedicated to providing integrated solutions to make clinicians more effective, therapies more precise, and patients healthier.

Silver Sponsor



[NDI](#) is the world's leading innovator of optical and electromagnetic navigation technology. For 40+ years, we've helped medical device OEMs bring new surgical navigation applications—and clinical breakthroughs—to market.

Keynote Speakers

Thursday, March 23 at 8:45

Using Implementation Science and AI Approaches to Radically Improve Cervical Cancer Prevention Globally: Can the Outputs of a Global Effort Be Protected as a Global Public Good?

[Karen Yeates](#), Queen's University

Dr. Karen Yeates MD, FRCPC, MPH is a nephrologist at Queen's University and is a graduate of McGill University (BSc 1993) and Queen's University School of Medicine (1997). She is a Professor of Medicine and Clinician-Scientist in the Department of Medicine at Queen's University. She co-founded (2012) and co-directed the Office of Global Health (ending in 2016) within the Faculty of Health Sciences and developed the first Global Health curriculum within the Undergraduate curriculum within the School of Medicine in 2013.



Dr. Yeates currently directs a program of global health implementation science research in low-resource settings in Tanzania with collaborative projects in Rwanda and Kenya. Dr. Yeates is considered a global leader in the development of mobile health interventions (mHealth) to improve detection and management of non-communicable diseases. Her work to improve training, scaling, quality assurance and cervical cancer screening outcomes in Tanzania has been recognized by the WHO and the program has been integrated into the national Tanzanian Ministry of Health Cervical Cancer Prevention Program (CECAP). She and her team are part of a 10-country consortium led by the National Institutes of Health and the National Cancer Institute in the United States that is working on developing a global AI solution for cervical cancer prevention in low and middle income countries called Automated Visual Evaluation. Dr. Yeates has 140 peer-reviewed publications. Since 2012, her research program has been funded with over \$8 million in grants from peer-review agencies including the Canadian Institutes for Health Research, Grand Challenges Canada, Grand Challenges Africa, International Development Agency of Canada, and the Wellcome Trust.

Friday, March 24 at 15:50

Embracing Failure

[Lena Maier-Hein](#), German Cancer Research Centre

Dr. Maier-Hein is a full professor at Heidelberg University (Germany) and managing director of the National Center for Tumor Diseases Heidelberg. At the German Cancer Research Center she is head of the division Intelligent Medical Systems and managing director of the "Data Science and Digital Oncology" cross-topic program. Her research concentrates on machine learning-based biomedical image analysis with a specific focus on surgical data science, computational biophotonics and validation of machine learning algorithms. She is a fellow of the Medical Image Computing and Computer Assisted Intervention (MICCAI) society and of the European Laboratory for Learning and Intelligent Systems, president of the MICCAI special interest group on challenges and chair of the international surgical data science initiative.



Dr. Maier-Hein serves on the editorial board of the journals Nature Scientific Data, IEEE Transactions on Pattern Analysis and Machine Intelligence and Medical Image Analysis. During her academic career, she has been distinguished with several science awards including the 2013 Heinz Maier Leibnitz Award of the German Research Foundation and the 2017/18 Berlin-Brandenburg Academy Prize. She has received a European Research Council starting grant (2015-2020) and consolidator grant (2021-2026).

Panel Session

Thursday, March 23 at 11:45

How Can Medical Imaging Contribute to Solving the Canadian Healthcare Crisis?

Moderator: [Terry Peters](#)

Medical Imaging is a cornerstone in medical decision-making and treatment. It is used for diagnosis, tracking a patient's progress during treatment, and guiding surgical maneuvers during minimally invasive surgeries. However, Canadians are now facing a prolonged backlog for medical imaging, one that has been further exacerbated by the COVID-19 pandemic. In this session, 4 panel members will present what they see as some of the urgent needs in the Canadian healthcare system and how medical imaging can be better utilized to address these needs. The presentations will be followed by questions and open discussion with symposium participants.

Panel Members

[Karen Yeates](#), Queen's University

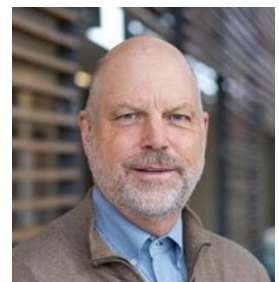
Dr. Karen Yeates MD, FRCPC, MPH is a nephrologist at Queen's University and is a graduate of McGill University (BSc 1993) and Queen's University School of Medicine (1997). She is a Professor of Medicine and Clinician-Scientist in the Department of Medicine at Queen's University. She co-founded (2012) and co-directed the Office of Global Health (ending in 2016) within the Faculty of Health Sciences and developed the first Global Health curriculum within the Undergraduate curriculum within the School of Medicine in 2013.



Dr. Yeates currently directs a program of global health implementation science research in low-resource settings in Tanzania with collaborative projects in Rwanda and Kenya. Dr. Yeates is considered a global leader in the development of mobile health interventions (mHealth) to improve detection and management of non-communicable diseases. Her work to improve training, scaling, quality assurance and cervical cancer screening outcomes in Tanzania has been recognized by the WHO and the program has been integrated into the national Tanzanian Ministry of Health Cervical Cancer Prevention Program (CECAP). She and her team are part of a 10-country consortium led by the National Institutes of Health and the National Cancer Institute in the United States that is working on developing a global AI solution for cervical cancer prevention in low and middle income countries called Automated Visual Evaluation. Dr. Yeates has 140 peer-reviewed publications. Since 2012, her research program has been funded with over \$8 million in grants from peer-review agencies including the Canadian Institutes for Health Research, Grand Challenges Canada, Grand Challenges Africa, International Development Agency of Canada, and the Wellcome Trust.

[John Rudan](#), Queen's University

Dr. John Rudan joined the Department of Surgery at Queen's in 1988 and was appointed to the role of Head, Department of Surgery in 2009. He was later cross-appointed as Professor, School of Computing, in 2014. He has held an appointment as Attending Staff in Orthopedic Surgery at the previous Kingston General and Hotel Dieu Hospitals, which recently integrated to Kingston Health Sciences Centre, since 1988. In 2021, he was appointed Chair in Surgical Innovation and Research and Director of Research, Department of Surgery.



Dr. Rudan is a prolific and respected researcher. He has over 300 peer-reviewed journal and conference publications focused on excellence in Orthopaedic education and advances in technology-assisted surgical techniques. He held an appointment as Senior Principal Investigator, Clinical Mechanics Group, Queen's University, from 1988 to 2000, and has been in his current appointment as Senior Principal Investigator, Human Mobility Research Centre, for over 20 years. His research grant funding over the past 10 years exceeds \$6.7 million, and through his research, Dr. Rudan has been granted eight international patents and developed technology licensed by DePuy, Johnson & Johnson, Zimmer corp and Smith, Nephew and IGO Technologies.

Dr. Rudan's research expertise and contributions have been widely acknowledged. In 2020, his research achievements earned awards from the Imaging Network of Ontario Symposium, the Annual Congress in Clinical Mass Spectrometry, and Computer Assisted Radiology and Surgery. He has previously been acknowledged by the International Society of Computer Assisted Orthopaedic Surgery, Canadian Surgery Forum, and Canadian Orthopaedic Foundation, and he has received a Founders Medal from Canadian Orthopaedic Research Society (1990) and a McLaughlin Fellowship (1987).

[Golafsoun Ameri](#), Cosm Medical

Dr. Golafsoun Ameri received her PhD in Biomedical Engineering in the field of image-guided therapy from Robarts Research Institute at Western University in 2018. Shortly after graduation, she joined Cosm Medical as the first employee and helped start the company. As Head of Research, Dr. Ameri leads Cosm's research and scientific affairs. Cosm is a medical device start-up in Toronto, developing a data-driven platform to create personalized treatment for female pelvic floor disorders, which affect up to 50% of the female population. Cosm's platform leverages novel medical imaging techniques based on ultrasound imaging, as well as machine learning and 3D printing to address the needs of this underserved patient population. Dr. Ameri has been part of Cosm's growth from 2 to 18 full-time employees to date.



[Parvin Mousavi](#), Queen's University

Dr. Parvin Mousavi is a Professor of Computer Science, Medicine, Pathology and Biomedical and Molecular Sciences at Queen's University, and a member of the Royal Society of Canada, College of New Scholars. She received her PhD from the University of British Columbia, Canada and her MSc from Imperial College, UK. She has previously held a Senior Scientist position at Brigham and Women's Hospital in Boston and visiting professorships at Harvard Medical School and the University of British Columbia. Her research focus is on developing and leveraging machine learning in computer assisted medical interventions and precision medicine, contributing to the societal impact of AI on the global community. She also leads training of the next generation of AI talent through a multi-institutional NSERC CREATE Training program in Medical Informatics at the intersection of machine learning and digital health.



Innovation Think Tank Certification Program

Friday, March 24 at 12:35

ImNO is pleased to join Siemens Healthineers, Western University and Robarts Research Institute in hosting an Innovation Think Tank Certification Program with a theme of cost containment for healthcare systems and clinical translation. The training program took place over the two weeks before the symposium and the top teams will present at lunch on the second day of the symposium.



Organizing Committee

Chairs: Jessica Rodgers and Elvis Chen

Scientific Committee

Michael Daly	Amoon Jamzad	Amir Moslemi	Eran Ukwatta
Gabor Fichtinger	Miranda Kirby	Sarah Svenningsen	Jill Weyers
Nancy Ford	Elodie Lugez	Jean Théberge	Dan Xiao
Justin Hicks	Sarah Mattonen	Rebecca Thornhill	

Student Committee

Fateen Basharat	Farah Kamar	Stefanie Markevich	Jaykumar Patel
Melissa Chasse	Kalysta Makimoto	Fatou Ndiaye	Zachary Szentimrey
Miriam Hewlett			

Planning Committee

Carol Richardson	Kitty Wong
------------------	------------

Abstract Reviewers

Coordinators: Sarah Mattonen, Nancy Ford, Michael Daly and Amoon Jamzad

Faranak Akbarifar	Michael Hardisty	Anne Martel	Tales Santini
Corey Baron	Justin Hicks	Sarah Mattonen	Giles Santyr
Jeffrey Carson	Matthew Holden	Charles McKenzie	Dafna Sussman
Elvis Chen	Eno Hysi	Amir Moslemi	Sarah Svenningsen
Jianan Chen	Amoon Jamzad	Jamie Near	Ali Tavallaei
Michael Daly	Ivan Kosik	Michael Noseworthy	Jonathan Thiessen
Maria Drangova	Andras Lasso	Laurentius Osapoetra	Rebecca Thornhill
Razieh Enjilela	Angus Lau	Alexei Ouriadov	Eranga Ukwatta
Aaron Fenster	M Louis Lauzon	Terry Peters	Tamas Ungi
Nancy Ford	Ting-Yim Lee	Thomas Purdie	Gabriel Varela-Mattatall
Neil Gelman	Daniel Lorusso	Jessica Rodgers	Justin Wan
Donna Goldhawk	Elodie Lugez	John Ronald	Jill Weyers
Wenchao Han	Chris Macgowan	Benjamin Rotstein	Dan Xiao

Oral and Pitch/Poster Judges

Coordinators: Elodie Lugez and Sarah Svenningsen

Sarah Aubert	Wenchao Han	Maryam Mozaffari	Kelly Smart
Corey Baron	Michael Hardisty	Lucas Narciso	Qin (Daisy) Sun
Jeff Bax	Miriam Hewlett	Elizabeth Norman	Sarah Svenningsen
Dana Broberg	Justin Hicks	Claire Park	Ali Tavallaei
Elvis Chen	Emily Lalone	Anna Pees	David Tessier
Alicia Cronin	Angus Lau	Terry Peters	Jean Théberge
Michael Daly	Liam Lawrence	Fatemeh Rastegar Jooybari	Tamas Ungi
Aneesh Dhar	Ting-Yim Lee	Jessica Rodgers	Edward Wang
Xi Feng	Sarah Mattonen	John Ronald	Jill Weyers
Aaron Fenster	Daniel Milej	Giles Santyr	Benjamin Wilk
Gabor Fichtinger	Amir Moslemi	Timothy Scholl	Shuwei Xing
Amanda Hamilton			

Program at a Glance

March 23, 2023	
Ballroom Centre	Ballroom East
08:30 - 08:45 Opening Remarks	
08:45 - 09:30 Keynote Session I — Using Implementation Science and AI approaches to Radically Improve Cervical Cancer Prevention Globally: Can the Outputs of a Global Effort be Protected as a Global Public Good? Karen Yeates, Queen's University	
09:30 - 09:45 Coffee Break	
09:45 - 10:45 Oral 1 Ultrasound Imaging	09:45 - 10:45 Oral 2 Neuroimaging I
10:45 - 11:15 Pitch 1 Ultrasound and Optical Imaging	10:45 - 11:15 Pitch 2 Neuroimaging
11:15 - 11:45 Meet-and-Greet Poster Viewing (Pitch Sessions 1 & 2 presenting) Lunch Pickup	
11:45 - 12:45 Panel Session — How Can Medical Imaging Contribute to Solving the Canadian Healthcare Crisis?	
12:45 - 13:00 Break	
13:00 - 14:00 Oral 3 Hyperpolarized MR Imaging	13:00 - 14:00 Oral 4 Image Guidance
14:00 - 14:30 Pitch 3 Hyperpolarized MR and Lung Imaging	14:00 - 14:30 Pitch 4 Image Guidance
14:30 - 15:00 Meet-and-Greet Poster Viewing (Pitch Sessions 3 & 4 presenting) Coffee Break	
15:00 - 16:00 Oral 5 Hardware Development	15:00 - 16:00 Oral 6 MR Imaging
16:00 - 16:30 Pitch 5 Image Processing and Machine Learning	16:00 - 16:30 Pitch 6 MR Imaging
16:30 - 17:00 Meet-and-Greet Poster Viewing (Pitch Sessions 5 & 6 presenting)	
17:00 - 19:00 Reception and ImNO Jeopardy	

March 24, 2023	
Ballroom Centre	Ballroom East
08:30 - 08:35 Opening Remarks	
08:35 - 09:35 Oral 7 Cancer Imaging	08:35 - 09:35 Oral 8 Cardiac and Lung Imaging
09:35 - 10:05 Pitch 7 Cancer Imaging	09:35 - 10:05 Pitch 8 Musculoskeletal and Vascular Imaging
10:05 - 10:35 Meet-and-Greet Poster Viewing (Pitch Sessions 7 & 8 presenting) Coffee Break	
10:35 - 11:35 Oral 9 MR and Magnetic Particle Imaging	10:35 - 11:35 Oral 10 Device Development
11:35 - 12:05 Pitch 9 Contrast Agents and Radiopharmaceuticals	11:35 - 12:05 Pitch 10 Device, Hardware and Software Development
12:05 - 12:35 Meet-and-Greet Poster Viewing (Pitch Sessions 9 & 10 presenting) Lunch Pickup	
12:35 - 13:35 Siemens Innovation Think Tank Presentations on Cost Containment for Healthcare Systems and Clinical Translation	
13:35 - 13:50 Break	
13:50 - 14:50 Oral 11 Deep Learning	13:50 - 14:50 Oral 12 Neuroimaging II
14:50 - 15:20 Pitch 11 Deep Learning	14:50 - 15:20 Pitch 12 Cellular and Molecular / Image Guidance
15:20 - 15:50 Meet-and-Greet Poster Viewing (Pitch Sessions 11 & 12 presenting) Coffee Break	
15:50 - 16:35 Keynote Session II — Embracing Failure Lena Maier-Hein, German Cancer Research Center	
16:35 - 17:00 Closing and Awards	

ImNO 2023 Program
March 23, 2023

08:30 - 08:45	Opening Remarks		Ballroom Centre and East
	Elvis Chen and Jessica Rodgers, ImNO 2023 Chairs		
08:45 - 09:30	Keynote Session I		Ballroom Centre and East
	Chairs: Gabor Fichtinger and Dilakshan Srikanthan		
	Using Implementation Science and AI approaches to Radically Improve Cervical Cancer Prevention Globally: Can the Outputs of a Global Effort be Protected as a Global Public Good?		
	Karen Yeates, Queen's University		
09:30 - 09:45	Coffee Break		
09:45 - 10:45	Oral 1	Oral 2	
	Ultrasound Imaging	Neuroimaging I	
	Ballroom Centre	Ballroom East	
	Chairs: Kalysta Makimoto and Daniel Milej	Chairs: Dana Broberg and Lucas Narciso	
	O1-1: Endobronchial Ultrasound (EBUS)-Enhanced Drug Delivery for Treatment of Lung Cancer	O2-1: Structure-Function Coupling and Connectivity in Newly Diagnosed Pediatric Focal Epilepsy Patients	
	Sean McGrath, University of Toronto	Mary Taylor, Western University	
	O1-2: Predicting Head & Neck Cancer Treatment Outcomes with Pre-Treatment Quantitative Ultrasound Texture Features & Optimizing Machine Learning Classifiers with Texture-of-Texture Features	O2-2: Investigating Long-Term Microstructural Changes Following Repeated Mild Traumatic Brain Injury in Mice Using Advanced Diffusion MRI	
	Aryan Safakish, Toronto Metropolitan University	Jake Hamilton, Robarts Research Institute	
	O1-3: Identification of Lung Sliding in a Clinical Ultrasound Dataset using Deep Learning	O2-3: Imaging Dementia in African Populations: Closing the Gap on Challenges - A perspective	
	Chris Yeung, Queen's University	Olujide Oyeniran, Western University	
	O1-4: Three-Dimensional Ultrasound for Investigating Synovial Blood Flow in Thumb Osteoarthritis	O2-4: Non-invasive Quantification of [18F]SynVesT-1 for PET Studies of Synaptic Density in Parkinson's Disease	
	Megan Hutter, Western University	Kelly Smart, Centre for Addiction and Mental Health	

Imaging Network Ontario Symposium 2023 Proceedings

10:45 - 11:15

Pitch 1
Ultrasound and Optical Imaging
Ballroom Centre

Chairs: Kalysta Makimoto and Karen Yeates

P1-1: A Hand-held Photoacoustic Imaging Probe for Breast Cancer Margin Assessment

Elina Rascevska, Lawson Health Research Institute

P1-2: Quantitative Spatial-Frequency Fluorescence Imaging for Surgical Guidance: Pre-Clinical Nanoparticle Experiment

Josephine La Macchia, University Health Network

P1-3: Double Exposure ESPI Method for Non-Contact Dynamic Photoacoustic Wave Detection

Hui Wang, Western University

P1-4: The Ideal Composition of Tissue-Mimicking Phantoms for Near-Infrared Spectroscopy

Rasa Eskandari, Western University

P1-5: Extended Views for Gynecological Brachytherapy Using Three-Dimensional Ultrasound Fusion

Tiana Trumpour, Western University

P1-6: Investigating Ultrasound Stimulated Microbubble Mediated Microvascular Disruption

Xiaoxiao Zhao, University of Toronto

P1-7: Self-Supervised Enhanced Ultrasound Thyroid Nodule Detection and Evaluation

Ningtao Liu, Robarts Research Institute

P1-8: Three-Dimensional Complementary Breast Ultrasound (CBUS) with Orthogonal Images to Improve Resolution

Claire Park, Robarts Research Institute

Pitch 2
Neuroimaging
Ballroom East

Chairs: Farah Kamar and Benjamin Wilk

P2-1: Optimizing [11C]Butanol Radiosynthesis and Positron Emission Tomography Image Analysis for Assessing the Blood-Brain Barrier Integrity in Alzheimer's Disease

Olujide Oyeniran, Western University

P2-2: An Interpretable Alzheimer's Disease Dementia Risk Prediction Model

Mason Kadem, McMaster University

P2-3: Simultaneous Estimation of a Model-Derived Input Function for Quantifying Cerebral Glucose Metabolism with [18F]FDG Positron Emission Tomography

Lucas Narciso, Lawson Health Research Institute

P2-4: CT Perfusion Monitored Selective Brain Cooling for Acute Brain Injuries

Olivia Tong, Western University

P2-5: Anatomical Features Predicting Outcome from Stereotactic Laser Amygdalohippocampotomy

Chris Zajner, Western University

P2-6: Imaging Ocular Dominance Columns in Human Brain At High Magnetic Field

Atena Akbari, Western University

P2-7: Diffusion Tensor Imaging of Glioma Patients During Radiotherapy on a 1.5T MRI-Linear Accelerator

Liam Lawrence, University of Toronto

P2-8: Sensitivity of Cerebral Blood Flow and Oxygenation to High-Intracranial Pressure

Sule Karagulleoglu-Kunduraci, Western University

P2-9: Effects of Drug Efflux and Sex Differences on the Novel p38 MAPK Radiotracer [11C]SCIO-469

Melissa Chassé, University of Toronto

11:15 - 11:45

Meet-and-Greet
Poster Viewing (Pitch Sessions 1 & 2 presenting)
Lunch Pickup

Ballroom West

11:45 - 12:45	Panel Session — How Can Medical Imaging Contribute to Solving the Canadian Healthcare Crisis?		Ballroom Centre and East
	Chairs: Liam Lawrence and Terry Peters		
	Panel Members:		
	Golafsoun (Goli) Ameri, Cosm Medical		
	Parvin Mousavi, Queen's University		
	John Rudan, Queen's University		
	Karen Yeates, Queen's University		
12:45 - 13:00	Break		
13:00 - 14:00	Oral 3	Oral 4	
	Hyperpolarized MR Imaging	Image Guidance	
	Ballroom Centre	Ballroom East	
	Chairs: Fatemeh Rastegar Jooybari and Sarah Svenningsen		
	O3-1: Hyperpolarized Chemical Exchange Saturation Transfer (HyperCEST) Maximization of Cucurbit[6]uril Imaging Biosensor in Blood for 3.0 T Clinical MRI	O4-1: Learning-assisted 3D US-CT/MRI Registration for Liver Tumour Ablation	
	Viktoriiia Batarchuk, Lakehead University	Shuwei Xing, Robarts Research Institute	
	O3-2: Hyperpolarized ¹²⁹Xe MRI Ventilation Textures Predict Short- and Long-term Response to Anti-IL-5Rα Biologic Therapy in Eosinophilic Asthma	O4-2: Deep Learning-Enabled Fluorescence Imaging for Surgical Guidance: In Silico Tumour Models	
	Marrissa McIntosh, Robarts Research Institute	Natalie Won, University Health Network	
	O3-3: ¹²⁹Xe Gas-Exchange MRI and CT Pulmonary Vascular Abnormalities in GINA 4-5 Asthma	O4-3: Automated Catheter Localization in Transrectal Ultrasound Images for High-Dose-Rate Prostate Brachytherapy	
	Alexander Matheson, Robarts Research Institute	Nicole Kitner, Queen's University	
	O3-4: Accelerated 3D MRI with Inhaled Hyperpolarized ¹²⁹Xe in Human Lungs: Troubleshooting	O4-4: A Hybrid Augmented Multi-Baseline and Near-Referenceless MR Thermometry Pipeline to Reduce Motion Artifacts during Magnetic Resonance Guided High-Intensity Focused Ultrasound	
	Samuel Perron, Western University	Arthur Akbulatov, The Hospital for Sick Children	

14:00 - 14:30

Pitch 3
Hyperpolarized MR and Lung Imaging
 Ballroom Centre

Chairs: Corey Baron and Fatemeh Rastegar Jooybari

P3-1: CT and MRI Measurements Uniquely Explain All-cause Mortality in Ex-smokers

Maksym Sharma, Western University

P3-2: Minimal Clinically Important Difference for 129Xe MRI Ventilation Defect Percent in Patients with Asthma

Alexander Biancaniello, Western University

P3-3: Deep-Learning Based Segmentation of 3D Hyperpolarized 129Xe Lung MRI for Generating vADC for a Large Patient Population Studied with The Use of Transfer Learning

Ramtin Babaeipour, Western University

P3-4: Feasibility Study of in-Vivo Simultaneous Hyperpolarized 129Xe MRI and [15O]-water PET Measurements

Ramanpreet Sembhi, Western University

P3-5: CT Imaging Measurements with Machine Learning for Predicting Progression to Chronic Obstructive Pulmonary Disease in At-Risk Smokers

Kalysta Makimoto, Toronto Metropolitan University

P3-6: Serial Two-Photon Tomography of Fluorescently-Labelled Alveolar-Like Macrophages Instilled in Rat Lungs

Melanie Posiewko, The Hospital for Sick Children

P3-7: Pulmonary Small Vessel Worsening in Ex-smokers with COPD

Vedanth Desaigoudar, Western University

P3-8: Sex Differences in CT Airway Measurements and their Relationship to Post-Acute COVID-19 Syndrome

Harkiran Kooner, Robarts Research Institute

P3-9: Radiomics Analysis of Ultrashort Echo-Time Lung MRI in Pediatric Cystic Fibrosis

Daniel Genkin, Toronto Metropolitan University

Pitch 4
Image Guidance
 Ballroom East

Chairs: Rasa Eskandari and Tamas Ungi

P4-1: Analysis of Cautery Trajectory for Evaluation of Resection Margins in Breast-Conserving Surgery

Chris Yeung, Queen's University

P4-2: The CathPilot: First Preclinical Safety and Feasibility Assessment

Mahdi Tahmasebi, Toronto Metropolitan University

P4-3: Electromagnetic Navigation for Residual Tumor Localization in Breast-Conserving Surgery

Olivia Radcliffe, Queen's University

P4-4: Development and Evaluation of an Open-Source Virtual Reality C-Arm Simulator

Daniel Allen, Western University

P4-5: Surgical Tool Detection in Open Hernia Repair Surgery Using Deep Neural Networks

Rebecca Hisey, Queen's University

P4-6: Point-Of-Care Ultrasound Carotid Artery Volume Reconstruction Using Deep-Learning

Michellie Choi, Robarts Research Institute

P4-7: Evaluation of Tracked Optical Tissue Sensing for Tumor Bed Inspection

David Morton, Queen's University

P4-8: Anthropomorphic Liver Phantom Development for Training and Validation of Surgical Navigation Systems

Joeana Cambranis-Romero, Robarts Research Institute

P4-9: The Development of an AI-based System for Training Percutaneous Nephrostomy in Senegal

Rebecca Hisey, Queen's University

14:30 - 15:00

Meet-and-Greet
Poster Viewing (Pitch Sessions 3 & 4 presenting)
Coffee Break

Ballroom West

15:00 - 16:00

Oral 5
Hardware Development
Ballroom Centre

Chairs: Sarah Aubert and Ali Tavallaei

O5-1: Evaluation of a Custom Scintillation Detector for a Focussed Gamma Probe

Sydney Wilson, Western University

O5-2: Quantification of Mechanical Characteristics of Conventional Steerable Ablation Catheters for Treatment of Atrial Fibrillation Using a Heart Phantom

Jacob Miller, Toronto Metropolitan University

O5-3: Integrated MRI Coils and Restraints for Simultaneous fMRI and Fibre Photometry in Awake Mice

Sam Laxer, Western University

O5-4: The Design and Construction of a Tx/Rx 31P Birdcage Head Coil and Feed Network at 3 Tesla

Peter Truong, Sunnybrook Research Institute

Oral 6
MR Imaging
Ballroom East

Chairs: Angus Lau and Peyman Tahghighi

O6-1: pH-Weighted Chemical Exchange Saturation Transfer (CEST) MRI Reproducibility in the Spinal Cord

Alicia Cronin, Western University

O6-2: High-resolution μ FA of the hippocampus at 3T

Farah Mushtaha, Robarts Research Institute

O6-3: Wave-MP2RAGE at Ultra-High Field

Gabriel Varela-Mattatall, Robarts Research Institute

O6-4: Iterative Point Spread Function Correction for T2 Mapping with Fast Spin Echo MRI

Tristhal Parasram, University of Windsor

Imaging Network Ontario Symposium 2023 Proceedings

16:00 - 16:30

Pitch 5
Image Processing and Machine Learning
 Ballroom Centre

Chairs: Michael Hardisty and Suzy Wong

P5-1: Vessel Bifurcation-Based Rigid-Registration: A Preliminary Accuracy Assessment

Joeana Cambranis-Romero, Robarts Research Institute

P5-2: Deep Learning for Placenta Accreta Spectrum Classification of Ultrasound Images

Dylan Young, Toronto Metropolitan University

P5-3: Cautery Tool State Detection in Basal Cell Carcinoma Excision Surgery Videos

Lucas March, Queen's University

P5-4: Direct Continuous Optimization of Displacement Fields for Medical Image Registration

Teodora Vujovic, University of Waterloo

P5-5: Machine Learning Based Automated Canine Radiography Quality Control Tool

Peyman Tahghighi, University of Guelph

P5-6: Feasibility of Computational Realistic-Textured XCAT Phantoms for Assessing Radiomic Feature Stability

Jaryd Christie, Western University

P5-7: Anatomical Measuring of the Entire Cochlea at a Sub-Millimeter Resolution Using Synchrotron-Radiation Phase-Contrast Imaging

Ashley Micuda, Western University

P5-8: Thickness and Design Features of Clinical Cranial Implants – What Should Automated Methods Strive to Replicate?

Zachary Fishman, Sunnybrook Research Institute

P5-9: Finite Element Modelling of the Human Middle Ear Using Synchrotron-Radiation Phase-Contrast Imaging

Caleb Thompson, Western University

Pitch 6
MR Imaging
 Ballroom East

Chairs: Sule Karagulleoglu Kunduraci and Heeseung Lim

P6-1: Decoupling CEST Solute Exchange Rate from Pool Size

Siddharth Sadanand, Toronto Metropolitan University

P6-2: Low-Heating B1+-Mapping of Subjects with Deep Brain Stimulation (DBS) Implants Using Optimized Radiofrequency (RF) Shimming Parallel Transmission (PTX)

Maryam Arianpouya, University of Toronto

P6-3: Correction of Motion and Resulting Field Offsets for Susceptibility Weighted MRI Using Navigators

Miriam Hewlett, Western University

P6-4: Characterising Magnetic Field Drift in Rosette-MRSI Data In-Vivo

Sneha Senthil, Sunnybrook Research Institute

P6-5: PLA2 Inhibition Using Mepacrine Reduces MR Spectroscopy Measures of Total Choline in a Rat Model of Alzheimer's Disease

Colleen Bailey, Sunnybrook Research Institute

P6-6: Multimodal Connectivity Gradients of the Human Basal Forebrain

Sudesna Chakraborty, Western University

P6-7: Examining the Impact of Pediatric Arterial Ischemic Stroke on Cerebral Blood Flow within the Hippocampus and its Relationship with Observed Neurological Deficits

Ethan Luk, The Hospital for Sick Children

P6-8: MRI Biomarkers of Neuroinflammation Across Neurodegenerative Diseases

Vishaal Sumra, University of Toronto

P6-9: Cortical Network Disruption in First-Episode Psychosis

Peter Van Dyken, Western University

16:30 - 17:00

Meet-and-Greet
Poster Viewing (Pitch Sessions 5 & 6 presenting)

Ballroom West

17:00 - 19:00

Reception and ImNO Jeopardy

Ballroom Centre and East

March 24, 2023

08:30 - 08:35

Opening Remarks

Ballroom Centre and East

Elvis Chen and Jessica Rodgers, ImNO 2023 Chairs

08:35 - 09:35

Oral 7

Cancer Imaging

Ballroom Centre

Chairs: Elina Rascevska and Timothy Scholl

O7-1: Identification of Glioblastoma Using Rapid Evaporative Ionization Mass Spectrometry

Dilakshan Srikanthan, Queen's University

O7-2: Predicting the Dose Distribution of Multi-Lesion Lung Stereotactic Body Radiotherapy Plans using Generative Adversarial Networks

Edward Wang, Western University

O7-3: Deep-Learning-Based Auto-segmentation in Prostate Brachytherapy, with Implanted Needles

Prakash Hampole, Robarts Research Institute

O7-4: Prostate Cancer Detection using Multi-Scale Analysis of Micro-Ultrasound Imaging

Paul Wilson, Queen's University

Oral 8

Cardiac and Lung Imaging

Ballroom East

Chairs: Elizabeth Norman and Frank Prato

O8-1: Real Time Mitral Annulus Segmentation from 4D Transesophageal Echocardiography Using Deep Learning Regression

Patrick Carnahan, Robarts Research Institute

O8-2: Accelerated 4D Flow MRI in Pediatric Patients with Congenital Heart Disease Using an Undersampled 3D Radial Acquisition, Double Golden Angle Sampling, and Compressed Sensing Reconstruction

Fatemeh Rastegar Jooybari, University of Toronto

O8-3: Progressive Airway Wall Thinning and Loss of Total Airway Count after Three-Years in COPD

Paulina Wyszkiwicz, Robarts Research Institute

O8-4: Novel COPD Classification/Staging Technique Using Lung CT Data and Neural Network

Halimah Alsurayhi, Western University

Imaging Network Ontario Symposium 2023 Proceedings

09:35 - 10:05

Pitch 7 **Cancer Imaging** Ballroom Centre

Chairs: Sarah Mattonen and Elina Rascevska

P7-1: Radiomics to Predict Local Progression of Non-Spine Bone Metastases Following Stereotactic Radiotherapy

Lauren Zelko, Western University

P7-2: Predicting the Need for a Replan in Oropharyngeal Cancer: A Radiomic, Clinical, and Dosimetric Model

Tricia Chinnery, Western University

P7-3: Prostate Stereotactic Body Radiation Therapy – Using 18 Fluorine Prostate Specific Membrane Antigen-1007 Positron Emission Tomography and Multiparametric Magnetic Resonance Imaging to Escalate the Dose to Dominant Intraprostatic Lesions – ARGOS-CLIMBER: A Phase I/II clinical Trial

Aneesh Dhar, London Health Sciences Centre

P7-4: Quantitative Nuclear Grading to Improve Risk Stratification for Patients with Noninvasive Bladder Cancer

Katherine Lindale, Queen's University

P7-5: Prediction Risk of Breast Cancer Development Using Breast Bilateral Asymmetry Analysis within a Machine Learning Framework

Xi Feng, Western University

P7-6: Radiomics-based Approach to Classify Benign and Malignant Solid Renal Masses on MRI

Rohini Gaikar, University of Guelph

P7-7: Automatic Classification of Endometrial Pathology Slides

Daniel Sherman, Toronto Metropolitan University

P7-8: Horizontal Federated Learning in Kidney Cancer Disease Classification on Histopathology Images

Timothy Wong, A.I. VALI Inc.

P7-9: Deep Learning Method for Detection of Cancerous Lung Nodules from High-Dose and Low-Dose Computed Tomography Images

Jenita Manokaran, University of Guelph

Pitch 8 **Musculoskeletal and Vascular Imaging** Ballroom East

Chairs: Emily Lalone and Elizabeth Norman

P8-1: Best Fit Sphere to Determine Femoral Head Centre and Radius from 3D CT Data

Kenna Bartlett, Queen's University

P8-2: Four-dimensional Computed Tomography and Ultrasonography for Assessing Thumb Biomechanics in Thumb Osteoarthritis Patients

Randa Mudathir, Robarts Research Institute

P8-3: The Relationship Between Kinematic Joint Loading and Depth-Specific Volumetric Bone Mineral Density

Lauren Straatman, Western University

P8-4: The Sensitivity of Bony Landmarks and the Scapholunate Interval to Wrist Malrotation in the Posteroanterior Radiograph

Maxwell Campbell, Western University

P8-5: Remote Telemetry System for Monitoring Arthritis Rehabilitation

Kyle Wilson, Western University

P8-6: Synthetic-Mask x-ray Energy-Subtraction Angiography for Improved Cardiac-Stent Visualization

Lisa Garland, Robarts Research Institute

P8-7: Dual-Energy X-ray Angiography with a Photon-Counting X-ray Detector

Sarah Aubert, Toronto Metropolitan University

P8-8: A Polyacrylamide (PAA) Gel Phantom for Studying Catheter Ablation

Victor Chu, Western University

P8-9: 2D/3D Image Registration for Guidance of Endovascular Interventions in Tibial Vessels

Moujan Sadari, University of Toronto

10:05 - 10:35

Meet-and-Greet
Poster Viewing (Pitch Sessions 7 & 8 presenting)
Coffee Break

Ballroom West

10:35 - 11:35

Oral 9
MR and Magnetic Particle Imaging
Ballroom Centre

Chairs: Alicia Cronin and John Ronald

O9-1: Sodium (²³Na) MRI of the Prostate using an External Butterfly Coil

Josephine Tan, Western University

O9-2: Quantitative Magnetization Transfer Imaging in Glioblastoma Patients using Balanced Steady-state Free Precession on a 1.5 T MR-Linac

Brandon Tran, University of Toronto

O9-3: Imaging the Liver Uptake of Nanoparticles Tailored for Magnetic Particle Imaging

Nitara Fernando, Robarts Research Institute

O9-4: Deep Brain Stimulation Targeting Using an Open-Access Anatomical Fiducial Framework

Alaa Taha, Robarts Research Institute

Oral 10
Device Development
Ballroom East

Chairs: Joeana Cambranis and Gabor Fichtinger

O10-1: Monitoring Cerebral Oxygenation and Metabolism with Time-Resolved Compressive Sensing Spectroscopy

Natalie Li, Western University

O10-2: A Photothermal Therapy Guidance Platform Based on Photoacoustic Thermometry, Diffuse Optical Tomography, and Nanotechnology

Ivan Kosik, University Health Network

O10-3: Assessing the Sensitivity of a Full-Head Coverage Near-Infrared Spectroscopy Device (NIRS) to Regional Cerebral Oxygenation Changes

Farah Kamar, Western University

O10-4: Three-Dimensional Automated Breast Ultrasound (ABUS) System Toward Point-of-care Breast Cancer Screening

Claire Park, Robarts Research Institute

Imaging Network Ontario Symposium 2023 Proceedings

11:35 - 12:05

Pitch 9

Contrast Agents and Radiopharmaceuticals

Ballroom Centre

Chairs: Tricia Chinnery and Kelly Smart

P9-1: PET/MRI of Microbial Therapy in the Pig: Autoradiography of 89Zr-Labelled Bacteria in the Gut

Enzo Rabbath, Lawson Health Research Institute

P9-2: SPAAC Incorporation of Fluorine into FC131 Analogues Towards Discovery of CXCR4 Radiopharmaceuticals

Julia Mason, Western University

P9-3: A Monte Carlo Voxel Dose Calculation Method for Cancer Radiotheranostics

Thanh-Tai Duong, Western University

P9-4: Radiometallation of Monoclonal Antibodies Relevant to Immune Checkpoint Therapy

Mojmír Suchý, Lawson Health Research Institute

P9-5: Automated Radiosynthesis of the L-isomer of Fluorodeoxyglucose (FDG)

Ghazaleh Takalloobanafshi, Western University

P9-6: Integrating Tc-99m in Small Molecules for Improving Access to Alzheimer's Disease Imaging

Ghazaleh Takalloobanafshi, Western University

P9-7: Radiotracer Development for Imaging the Endocannabinoid System with PET

Anna Pees, Centre for Addiction and Mental Health

P9-8: Solid-supported Preparation of [18F]tetrafluoroborate ([18F]TFB) for Reporter Gene PET

John Diemert, Western University

P9-9: Comparison of [18F]FEOBV and [3H]VAT for Imaging VACHT in Neurodegenerative Diseases

Faustine d'Orchymont, Centre for Addiction and Mental Health

Pitch 10

Device, Hardware and Software Development

Ballroom East

Chairs: Michael Daly and Mohammad Khoobani

P10-1: Image Quizzer: A Versatile and Customizable Tool for Education and Standardized Data Collection in Imaging Research

Carol Johnson, London Regional Cancer Program

P10-2: End-To-End Mass Spectrometry Imaging Analysis Software

Hanad Elmi, Queen's University

P10-3: Comprehensive Review of Biomedical Software Tools for 3D Segmentation and Registration

Ashley Mathialagan, Toronto Metropolitan University

P10-4: SlicerTrack: an Open-source Research Toolkit for Target Tracking Verification in 3D Slicer

Ha Phan Tran, Toronto Metropolitan University

P10-5: A "Smart" Brain Retraction System Utilizing Photoplethysmography: Development of a Prototype System to Measure Applied Pressure with Optical Signals

Lee Sikstrom, Western University

P10-6: Adapting Electromagnetic Tool Tracking for Ultrasound-Guided Oral Cavity Cancer Resection

Pavel-Dumitru Cernelev, Queen's University

P10-7: Optical Position Tracking Fiducial Marker for High Performance Rigid Body Motion Parameter Estimation

Marina Silic, University of Toronto

P10-8: Low-Cost Fourier Ptychographic Microscope for Malaria Diagnosis

Justin Yang, Robarts Research Institute

P10-9: Inducing Cavitation Within Hollow Cylindrical Transducers for Use in Intravascular Thrombolysis

Li Gong, University of Toronto

12:05 - 12:35

Meet-and-Greet

Poster Viewing (Pitch Sessions 9 & 10 presenting)

Lunch Pickup

Ballroom West

Imaging Network Ontario Symposium 2023 Proceedings

12:35 - 13:35	Siemens Innovation Think Tank Presentations on Cost Containment for Healthcare Systems and Clinical Translation Chairs: Elvis Chen and Farah Kamar	Ballroom Centre and East
13:35 - 13:50	Break	
13:50 - 14:50	Oral 11 Deep Learning Ballroom Centre Chairs: Ryan Au and Amir Moslemi	Oral 12 Neuroimaging II Ballroom East Chairs: Maryam Mozaffari and Jill Weyers
	O11-1: Predicting Tumour Mutational Burden from H&E Slides of Lung Squamous Cell Carcinoma: Observers vs a Neural Network Salma Dammak, Western University	O12-1: Development of a Brain-Penetrating PET Radiotracer for Imaging 4R-Tauopathies Anton Lindberg, Centre for Addiction and Mental Health
	O11-2: Improved Surgical Margin Detection in Mass Spectrometry Data Using Uncertainty Estimation Ayesha Syeda, Queen's University	O12-2: Multiphase CT Angiography-based Prediction of Favourable Infarct-Penumbra Mismatch for Acute Ischemic Stroke Treatment Triage Ting-Yim Lee, Robarts Research Institute
	O11-3: Deep Learning for Prostate Cancer Recurrence Prediction on T2W MR Images Negin Piran Nanekaran, University of Guelph	O12-3: Choline Changes in the Primary Motor Cortex of People with Mild Cognitive Impairment are Predicted by Dual Task Gait Performance Jack Elkas, Western University
	O11-4: Deep Learning-Enabled Fluorescence Imaging for Surgical Guidance: Optical Phantoms from Patient Imaging Stefanie Markevich, University Health Network	O12-4: Metabolite Abnormalities in Epilepsy Patients with Malformations of Cortical Development Observed with 3T Magnetic Resonance Spectroscopy Pierre Ibrahim, Robarts Research Institute

Imaging Network Ontario Symposium 2023 Proceedings

14:50 - 15:20

Pitch 11
Deep Learning
 Ballroom Centre

Chairs: Ryan Au and Wenchao Han

P11-1: Federated Learning for Kidney Tumor Segmentation: Preliminary Findings

Zachary Szentimrey, University of Guelph

P11-2: MRI-degad: Conversion of Gadolinium-Enhanced T1w MRIs to Non-Contrast-Enhanced MRIs Using a Convolutional Neural Network

Feyifoluwa Ogunsanya, Western University

P11-3: Artifact Detection Algorithm Using Deep Learning in Fetal MRI

Adam Lim, Toronto Metropolitan University

P11-4: Background Parenchymal Enhancement Estimation on DCE Breast MRI using a Siamese Network

Grey Kuling, University of Toronto

P11-5: Placental MRI Segmentation Using a Novel Convolutional Neural Network

Alejo Costanzo, Toronto Metropolitan University

P11-6: Intracranial Hemorrhage Detection Using Machine Learning

Navkiran Sohal, Western University

P11-7: Creating Better Whole Slide Image Datasets: Quality Control Detection of Out-Of-Focus Patches in Digital Pathology

Phoenix Wilkie, University of Toronto

P11-8: Classifying Points of Interest in FAST Ultrasound Videos Using Neural Networks

Ilan Gofman, University of Toronto

P11-9: Improving the Reliability of Video-Based Skill Assessment Metrics with Uncertainty Quantification

Catherine Austin, Queen's University

Pitch 12

Cellular and Molecular / Image Guidance
 Ballroom East

Chairs: Amanda Hamilton and Maryam Mozaffari

P12-1: Tracking 89Zr-labelled Escherichia Coli Nissle 1917 Post-ingestion Using PET/MRI

Moayyad Nassar, Lawson Health Research Institute

P12-2: Activatable Reporter Imaging Systems for Visualization of New Genomic Medicines Called Adenine Base Editors

Shirley Liu, Western University

P12-3: Detecting in Vivo Cell-Cell Communication Using an Inducible Antigen-Dependent Synthetic Blood Biomarker

Yanghao Fu, Robarts Research Institute

P12-4: Visualizing Cytosine Base Editor Activity following Minicircle Delivery using an Activatable Reporter Gene System

Melissa Evans, Robarts Research Institute

P12-5: Magnetic Resonance Relaxation Rates of Bacteria: Magnetospirillum Magneticum AMB-1 Versus Lactobacillus Crispatus ATCC33820

Jonathan Yohans, Lawson Health Research Institute

P12-6: Elucidating Factors That Contribute to Changes in Magnetic Particle Imaging (MPI) Signal for the Longitudinal Tracking of Iron-Labeled Therapeutic Cells

Samantha Flood, Robarts Research Institute

P12-7: Margin Detection in Skin Cancer Surgery via 2D Representation of Mass Spectrometry Data

Laura Connolly, Queen's University

P12-8: Open Source Video-Based Hand-Eye Calibration

Daniel Allen, Western University

P12-9: Comparing Methods of Identifying Tissues for Workflow Recognition of Simulated Open Hernia Repair

Elizabeth Klosa, Queen's University

15:20 - 15:30

Meet-and-Greet
Poster Viewing (Pitch Sessions 11 & 12 presenting)
Coffee Break

Ballroom West

15:50 - 16:35

Keynote Session II
 Chairs: Sule Karagulleoglu Kunduraci and Jessica Rodgers
Embracing Failure
 Lena Maier-Hein, German Cancer Research Center

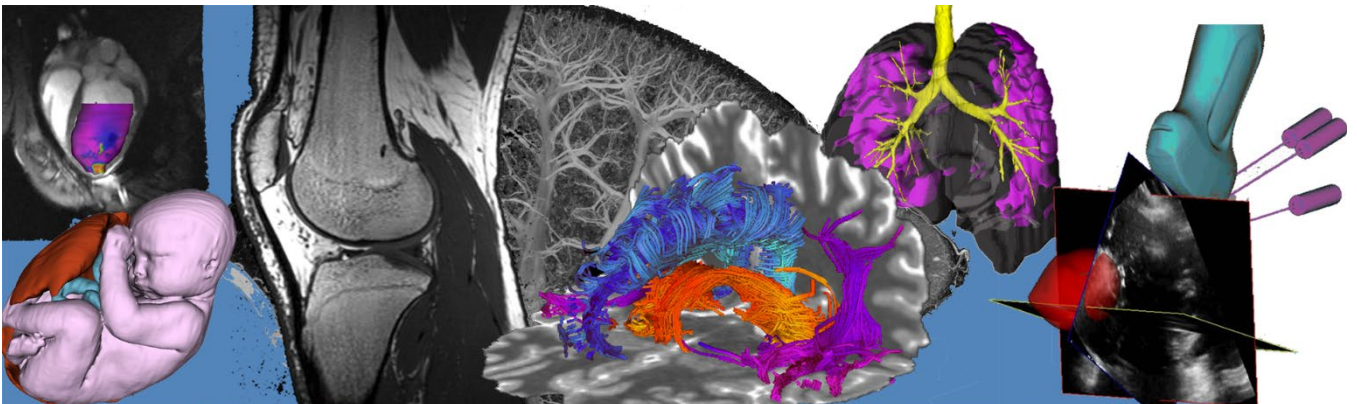
Ballroom Centre and East

16:35 - 17:00

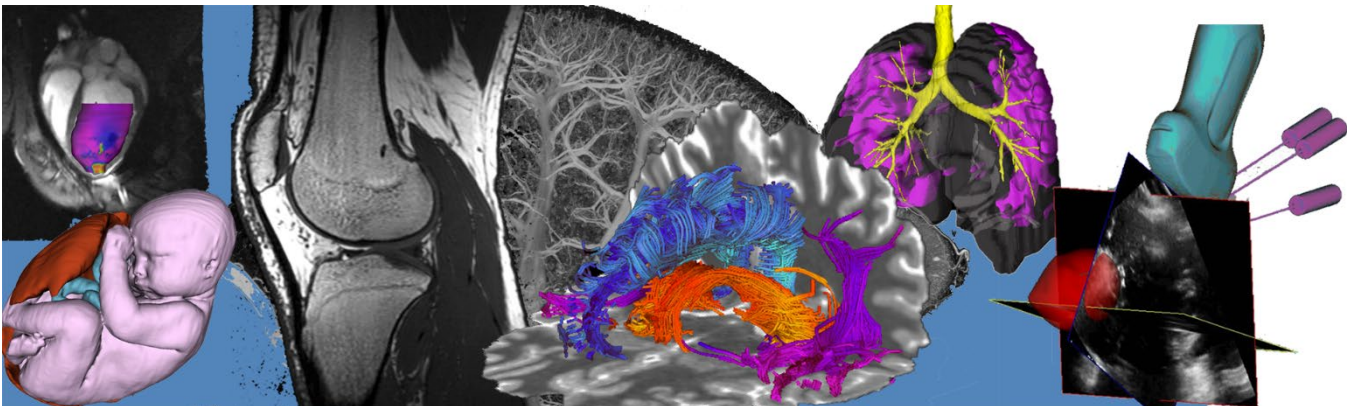
Closing and Awards

Ballroom Centre and East

Oral and Pitch/Poster Abstracts (in order of the talks)



Oral Session 1: Ultrasound Imaging Abstracts



Endobronchial Ultrasound (EBUS)-enhanced drug delivery for treatment of lung cancer

Sean McGrath^{1*}, Yu-Jack Shen^{1*}, Masato Aragaki², Yamato Motooka², Takamasa Koga², Alexander Gregor², Nicholas Bernards², Kazuhiro Yasufuku³ and Naomi Matsuura^{1,3,4}

¹*Institute of Biomaterials and Biomedical Engineering, University of Toronto,* ²*Division of Thoracic Surgery, Toronto General Hospital, University Health Network, Toronto,* ³*Department of Material Science and Engineering, University of Toronto,* ⁴*Department of Medical Imaging, University of Toronto*

**These authors contributed equally to this work*

Introduction: Lung cancer is responsible for approximately 18% of all cancer-related deaths [1,2]. Early discovery of lung cancer allows for surgical resection with curative intent [2]. However, many lung cancers are only discovered when the disease has progressed to distant metastases, greatly reducing average survival [2,3]. It has previously been shown that before cancers progress to distant metastases, many first metastasize to the local lymph nodes [4], thus making them a target for treatment. However current treatments of nodal lung cancers remain inadequate [3], in part due to low lymph node uptake of systemically delivered drugs [5]. Endobronchial ultrasound (EBUS) is a clinical modality used to diagnose and stage lymphatic lung cancer. EBUS has direct and local access to the lung-adjacent lymph nodes, which presents a unique opportunity for ultrasound-potentiated cancer treatment inside of the lung. Previous work has been conducted using therapeutic ultrasound combined with microbubbles for improved systemically injected chemotherapeutic uptake in non-lung targets [6]. Recently, our group has shown that contrast-enhanced EBUS (CE-EBUS) can cavitate microbubbles (MBs) in situ, similar to standard non-EBUS ultrasound systems. In this work, we investigate if systemically injected cisplatin in combination with EBUS exposure and MBs can increase cisplatin uptake in tumours in mouse models of lung cancer in comparison to controls, towards improving drug delivery to lymph nodes in the clinic.

Methods: Lipid shelled MBs were synthesized in-house, with a peak diameter of $1.1 \pm 0.1 \mu\text{m}$. In-vivo mouse AE17-OVA mesothelioma tumours (subcutaneous) in C57Bl/6 mice (Taconic Bioscience, NY) were used as proxies for lymphatic tumours. Mice were anesthetized with 2-5% isoflurane. To ensure tumour vascularization, $10 \mu\text{L}$ of MBs ($1.1 \times 10^8 \text{ MB/mL}$) were injected and the tumour was imaged with CE-EBUS. Following an injection of 1 mg/kg cisplatin, a series of 4, $20 \mu\text{L}$ injections of $1.1 \times 10^8 \text{ MBs/mL}$ were administered 4 minutes apart, with EBUS being flashed repeatedly for 7 seconds at high mechanical index ($\text{MI} = 1.2$) and 3 seconds at low mechanical index ($\text{MI} = 0.06$) for MB cavitation and reperfusion, respectively. The mice were recovered, and 1 hour after the initial cisplatin injection they were sacrificed and samples of the tumours, livers, kidneys, lungs, spleens, hearts, and muscle were taken and frozen in liquid nitrogen for nitric acid digestion and platinum quantification via inductively coupled plasma mass spectrometry (ICP-MS).

Results: Mice treated with cisplatin alone resulted in $0.3 \pm 0.1 \text{ mg Pt/kg}$ in tumour tissue, similar to what has been observed previously in the literature [7]. As expected, untreated mice had very low platinum signal in the tumour (i.e., $0.003 \pm 0.004 \text{ mg Pt/kg tissue}$). In contrast, cisplatin with MBs and EBUS exposure resulted in a significant increase in Pt levels of $0.5 \pm 0.1 \text{ Pt/kg}$ in tumour tissue ($p < 0.05$, Figure 1). Cisplatin treatment with either EBUS exposure or MB injection resulted in a slight decrease and a slight increase in Pt levels in the tumours, respectively, when compared to controls, however, this was not significant. These results indicate that EBUS exposure and MBs with cisplatin is required to obtain a significant increase in Pt in mouse tumours. Future work will include a longitudinal study to assess improvement in survival due to increased cisplatin uptake using EBUS and MBs.

Conclusion: This study showed that EBUS and MBs can successfully lead to increased tumour uptake of cisplatin *in vivo*. The use of common clinically used agents (MBs and cisplatin) with a clinical transducer (EBUS) may facilitate the study results to be easily translated to clinical trials.

References: [1] H. Sung et al., CA Cancer J Clin. 2021;71(3):209-249. [2] C. Zappa et al., Transl Lung Cancer Res. 2016;5(3):288-300. [3] F. Couñago et al., World J Clin Oncol. 2019;10(10):318-339. [4] H.H. Popper et al., Cancer Metastasis Rev. 2016;35(1):75-91. [5] Kodama et al., Sci Rep. 2016;6:32506. [6] K. Yamaguchi et al., Cancer Sci. 2021;112(6):2493-2503. [7] H. Yu et al., J Control Release. 2015:205:89-97.

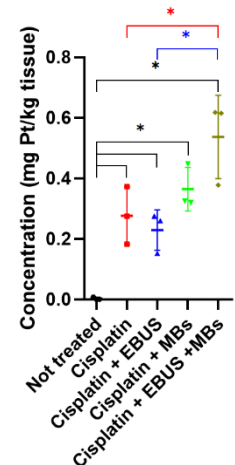


Figure 1: Tumour platinum levels 1 hour after cisplatin injection.

Predicting Head & Neck Cancer Treatment Outcomes with Pre-Treatment Quantitative Ultrasound Texture Features & Optimizing Machine Learning Classifiers with Texture-of-Texture Features.

Safakish, A.^{1,2,4}, Sannachi, L.^{1,2,3}, DiCenzo D.^{1,2,3}, Kolios, C.^{1,2,3,4}, Czarnota, G.J.^{1,2,3,4}, Pejović-Milić, A.⁴

¹ Physical Sciences, Sunnybrook Research Institute, Sunnybrook Health Sciences Centre, Toronto, Canada

² Department of Radiation Oncology, Sunnybrook Health Sciences Centre, Toronto, Canada

³ Department of Medical Biophysics, University of Toronto, Toronto, Canada

⁴ Department of Physics, Toronto Metropolitan University (Formerly Ryerson), Toronto, Canada

Introduction: Quantitative ultrasound spectroscopic (QUS) parameters like mid-band fit (MBF), spectral slope (SS), spectral intercept (SI), average scatter diameter (ASD), and average acoustic concentration (AAC) have been shown to characterize tissue microstructure [1]. Radiomics features were developed to quantify characteristics of an image and used to investigate phenotypic properties of biological conditions [2]. We hypothesize that prior to treatment, index lymph nodes (LN) (targeted in treatment plan) of Head & Neck (H&N) cancer patients contain acoustic phenotypic information that can be used to train ML-classifiers to predict treatment response as complete responders (CR) or partial responders (RP), and that higher order texture-of-texture features (TOT) can be used to optimize ML-classifiers performance.

Methods: H&N cancer patients (n = 72, 26 CR, 46 PR) with metastatic lymph node involvement were recruited and US RF data were collected from the index LN. After manual segmentation on B-mode US (Fig.1(a)), 7 QUS parameters (MBF, SS, SI, ASD_Anderson, ASD_Gaussian, AAC_Anderson, AAC_Gaussian) are made into parametric maps for the LN region of interest (ROI) using a sliding window technique with a 2x2 mm window size and 94.1% overlap between adjacent windows (Fig.1(b)) [3]. For each QUS parametric map, 68 texture features were determined with Python package PyRadiomics (476 total features). SMOTE technique was used to account for unbalanced data. Two classifiers (*k*-Nearest Neighbour (*k*-NN) & Support Vector Machines (SVM)) were used to evaluate models with 1-7 features.



Figure 1 – (a) H&N cancer patient B-mode US with lymph node ROI in red. (b) QUS SS parametric map (dBr/MHz). (c) TOT parametric map (SS - GLSZM - small area low gray level emphasis (arbitrary units)).

Features identified in the 5-feature multivariate model were used to create new QUS texture parametric maps as shown in Fig.1(c), from which texture features are determined. TOT features and original 5 best features were concatenated to create a new dataset used to optimize ML classifiers.

Results: Both classifiers were trained to predict binary treatment outcomes. SVM outperformed *k*-NN but both classifiers improved after implementing higher order TOT features. Results comparing 5-feature and

Table 1. Results comparing 5-feature and 7-feature multivariate models of QUS texture vs QUS texture + TOT dataset for SVM and *k*-NN classifiers. Performance evaluated on sensitivity (%Sens), specificity (%Spec), accuracy (%Acc) and area under the curve (AUC).

# of Feats	SVM Classifier					<i>k</i> -NN Classifier				
	% Sens	% Spec	% Acc	% Prec	AUC	% Sens	% Spec	% Acc	% Prec	AUC
5	78.7	76.0	77.7	86.0	0.817	72.3	72.0	72.2	82.9	0.717
TOT-5	78.7	80.0	79.2	88.1	0.854	78.7	64.0	73.6	80.4	0.751
7	80.9	76.0	79.2	86.4	0.824	61.7	68.0	63.4	78.4	0.655
TOT-7	85.1	80.0	83.3	88.9	0.851	74.4	68.0	72.2	81.4	0.769

7-feature multivariate models for both QUS texture features and QUS texture +TOT features can be seen in the Table 1.

Conclusion: H&N cancer treatment outcomes can be predicted with texture features determined from QUS parametric maps based on US RF data of metastatic index LN used to train machine learning algorithms. These algorithms can be optimized by implementing TOT features after preliminary analysis. Future work should consider larger sample sizes and testing on previously unseen set of patients to improve generalizability, as well as comparing efficacy of QUS features to CT and MRI features determined from images acquired for treatment planning.

References [1] M.C. Kolios, G.J. Czarnota, M. Lee, J.W. Hunt, & M.D. Sherar, *Ultrasound Med. Biol.*, vol. 28, no.5, pp. 589-597, 2002

[2] R. M. Haralick, I. Dinstein, and K. Shanmugam, *IEEE Trans. Syst. Man Cybern.*, vol. SMC-3, no. 6, pp. 610-621, 1973

[3] F. L. Lizzi, M. Ostromogilsky, E. J. Feleppa, M. C. Rorke, and M. M. Yaremko, *IEEE Trans. Ultrason. Ferroelectr. Freq. Control*, vol. 34, no. 3, pp. 319-329, 1987

Identification of Lung Sliding in a Clinical Ultrasound Dataset using Deep Learning

Colton Barr¹, Roland Incze², Róbert Zsolt Szabó², Chris Yeung¹, Gabor Fichtinger¹, Tamás Haidegger², Tamas Ungi¹ and Gábor Orosz^{2,3}

¹Queen's University, Canada. ²Óbuda University, Hungary. ³Semmelweis University, Hungary.

INTRODUCTION: Lung ultrasound (LU) has gained interest as a rapid means of assessing lung function in a critical care setting. Clinical signs such as the relative motion of the visceral and parietal pleura, referred to as lung sliding, can be detected in a sequence of LU images based on motion artifacts. These signs can be combined into a decision tree to facilitate rapid diagnosis of acute lung conditions. One such diagnostic tool is the Bedside Lung Ultrasound in Emergency (BLUE) protocol, an established clinical decision tree for identifying several acute lung conditions [1]. The BLUE protocol includes a unique LU artifact profile for pneumothorax, a potentially life-threatening condition defined by the partial or full collapse of the lung. While the diagnostic utility of LU has been well studied in the literature, a lack of clinician training and experience with ultrasound has limited its adoption [2]. The use of artificial intelligence methods has been proposed as a method to help identify LU signs and support both the training and clinical decision making of physicians. Previous studies have explored this concept for a variety of different LU signs, including lung sliding, however they often suffer from limited datasets and rely on non-clinical models [3]. The objective of this study is to demonstrate automated identification of lung sliding using deep learning on a large, custom built clinical dataset.

METHODS: The data for this study was obtained at Semmelweis University in Hungary on a combination of critically ill patients, a cadaver model, and healthy volunteers, for a total of 51 subjects and over 800 m-mode ultrasound loops [2]. The ultrasound images were captured according to the BLUE protocol in distinct locations bilaterally. A custom 3D Slicer module was developed to convert b-mode image sequences to m-mode images, with the m-mode sample lines selected by trained annotators as shown in Figure 1 (a). The resulting m-mode images were verified and labelled as either “lung sliding” or “no lung sliding” by four critical care physicians, each with at least 8+ years of experience using LU. Based on the framerate of each sequence, m-mode images corresponding to 3 seconds of ultrasound data were extracted from the raw m-mode data. These images were generated using a sliding window as shown in Figure 1 (b). A shallow convolutional neural network (CNN) architecture was built, trained, and validated on this dataset. A hyperparameter sweep was performed to optimize for classification accuracy on the training set. All networks were validated on a set of 4 patients that did not appear in the training set with a total of 100 no lung sliding and 215 lung sliding images.

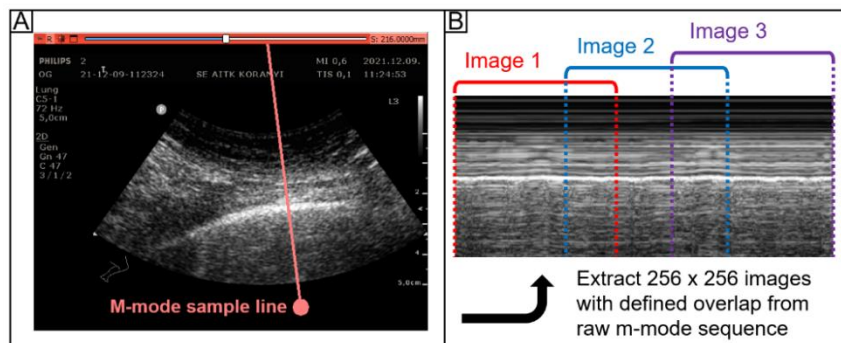


Fig. 1: a) Demonstration of 3D Slicer module for generating m-mode images; b)

Illustration of a raw m-mode image and the method used to extract 256x256 images. These images were generated using a sliding window as shown in Figure 1 (b). A shallow convolutional neural network (CNN) architecture was built, trained, and validated on this dataset. A hyperparameter sweep was performed to optimize for classification accuracy on the training set. All networks were validated on a set of 4 patients that did not appear in the training set with a total of 100 no lung sliding and 215 lung sliding images.

RESULTS: A total of 200 CNNs were generated. The best performing CNN achieved a classification accuracy of 93.0%, with a sensitivity of 85.0% and a specificity of 96.3% on the validation set.

CONCLUSIONS: These are encouraging initial results to obtain on this dataset and are comparable to published method for identification of lung sliding in LU [3]. A major challenge in generating this dataset has been obtaining sufficient examples of less common lung pathologies. Our clinical partners have compensated for this by using healthy volunteers performing breath holds and the construction of a pneumothorax cadaver model. Future work will include the incorporation of new data simulating pneumothorax as well as further hyperparameter tuning. Finally, improving our validation method using a leave-n-patients-out scheme and the addition of a dedicated test set are necessary steps to ensure robust results. This project is ongoing and has not been published in any venue.

ACKNOWLEDGEMENTS: C. Barr is supported by an NSERC CGS-D. G. Fichtinger is supported as an NSERC Canada Research Chair.

REFERENCES: [1] Lichtenstein, D. A. (2014). Lung ultrasound in the critically ill. *Annals of intensive care*, 4(1), 1-12. [2] Orosz, G., Gyombolai, P., Tóth, J. T., & Szabó, M. (2022). Reliability and clinical correlations of semi-quantitative lung ultrasound on BLUE points in COVID-19 mechanically ventilated patients: The ‘BLUE-LUSS’—A feasibility clinical study. *PLoS One*, 17(10), e0276213. [3] Jaščur, M., Bundzel, M., Malík, M., Dzian, A., Ferenčík, N., & Babič, F. (2021). Detecting the Absence of Lung Sliding in Lung Ultrasounds Using Deep Learning. *Applied Sciences*, 11(15), 6976.

Three-Dimensional Ultrasound for Investigating Synovial Blood Flow in Thumb OsteoarthritisMegan Hutter^{1,2,3}, Randa Mudathir^{1,2,3}, Carla du Toit³, Aaron Fenster^{1,2,3}, Emily Lalone^{2,4}¹Department of Medical Biophysics, Western University, London, Canada, ²Bone and Joint Institute, Western University, London, Canada, ³Robarts Research Institute, Western University, London, Canada, ⁴Department of Mechanical and Materials Engineering, Western University, London, Canada

Introduction: The first carpometacarpal (CMC-1) joint is the most important joint in the thumb and is a common site of osteoarthritis (OA).¹ Synovial inflammation is recognized as a characteristic of OA and plays a role in disease progression and pain. In recent decades, there has been an improved understanding of the role of inflammation in OA progression, with inflammation and synovial vascularization being related processes.² However, the role of synovial vascularization in CMC-1 OA progression is not well understood. Ultrasound (US) imaging visualizes the soft tissue structures of the joint and is used to diagnose and assess synovial inflammation.³ Additionally, US Doppler technologies such as Power Doppler (PD) and superb microvascular imaging (SMI), can visualize blood flow by detecting motion.³ 2D Doppler US signal is used in musculoskeletal imaging to indicate active joint inflammation and is graded semi-quantitatively.⁴ Previous studies have shown that SMI detects more blood flow signals compared to PD and has better detection of low-grade inflammation. 2DUS is limited to visualizing 3D anatomy and vasculature in 2D, is operator dependent and unable to quantify the synovial blood flow. The purpose of this research project is to develop a 3DUS system with PD and SMI technologies to image, visualize and quantify synovial blood flow in CMC-1 OA patients.

Methods: A 3DUS device was developed with the capability to acquire images with PD and SMI technology. 3DUS images were acquired using a Canon Aplio i800 US machine and a 14L5 linear transducer with the device. Five CMC-1 OA patients were imaged with PD and SMI. Synovial volumes were manually segmented in the 3DUS images and the region-of-interest incorporating the synovial volumes was determined for quantification of the Doppler signals. PD and SMI coloured voxels were then quantified using software to determine the number of coloured voxels within the segmented volumes. Blood flow quantities will be evaluated with respect to patient-reported pain measures and synovial volumes.

Results: 3DUS PD and SMI images demonstrated the ability of the 3DUS system to visualize Doppler signals within the synovial volume. Acquired images of a patient with CMC-1 OA showed Doppler signals in 3D PD (Fig. 1A) and SMI (Fig. 1B) images. Synovial PD and SMI coloured voxels were identified and automatically counted within the segmented region-of-interest. A voxel count was determined and provided quantification of the Doppler signals present in the 3D images. Anticipated results include investigating synovial blood flow quantities with patient-reported pain measures and segmented volumes of synovitis.

Conclusion: The novel 3DUS device was developed and demonstrated the ability to acquire 3DUS images with PD and SMI technology and quantify blood flow signals in CMC-1 OA patients. Through blood flow quantification of 3DUS images, this application showed a novel method of assessing synovial blood flow that is otherwise limited in 2DUS. This application has the potential to be a novel method of imaging and monitoring synovial blood flow and can further the understanding of the role of synovial vascularization in OA progression.

References: [1] Neumann DA, et al. (2003) J Orthop Sports Phys Ther. 33. [2] Ashraf S, et al. (2008) Curr Opin Rheumatol. 20. [3] Koski JM, et al. (2006) Ann Rheum Dis. 65. [4] Oo WM, et al. (2020) Ultrasound Med Biol. 46.

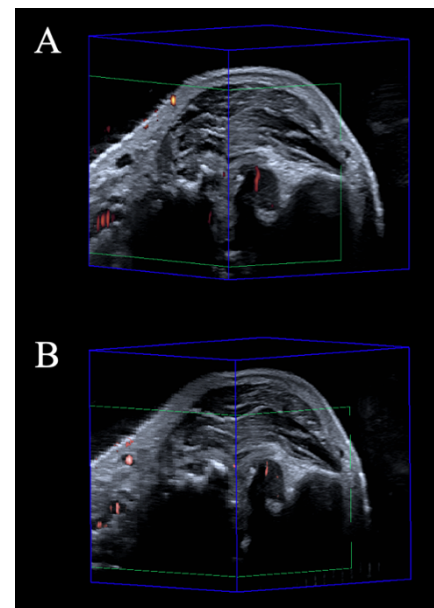
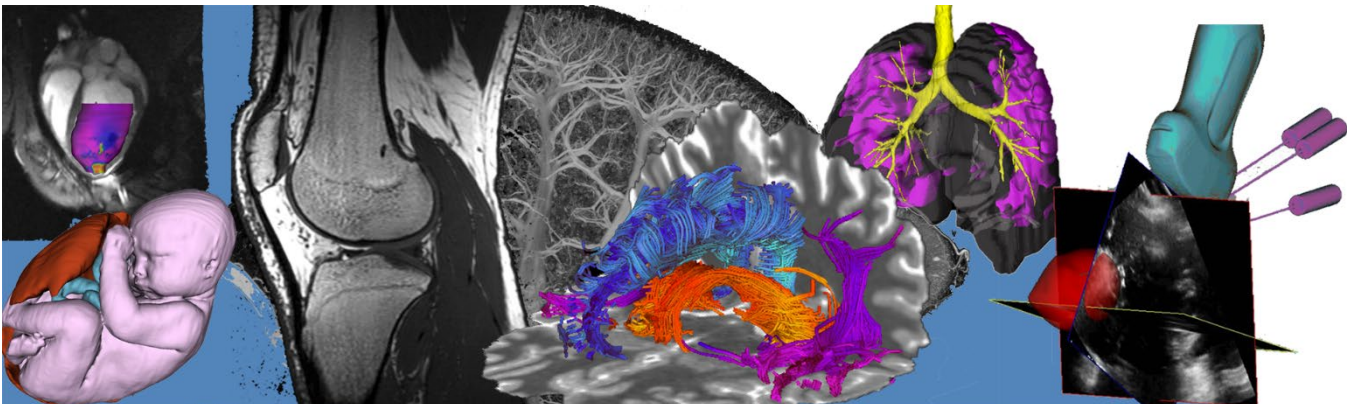


Figure 1. 3DUS images of a CMC-1 OA patient acquired with (A) PD and (B) SMI.

Oral Session 2: Neuroimaging I

Abstracts



Structure-Function Coupling and Connectivity in Newly Diagnosed Pediatric Focal Epilepsy Patients

Mary G Taylor^{1,2}, Jason Kai^{1,2}, Sabrina Freund³, Roy A Haast⁴, Rochelle Sorzano³, Denait Haile³, Andrea Andrade³, Egidio Spinelli³, Michael Jurkiewicz³, Ali R Khan^{1,2}, Maryam N Nouri^{1,3}

¹Schulich School of Medicine & Dentistry, ²Robarts Research Institute, ³London Health Sciences Centre, ⁴Aix-Marseille University

Introduction: Epilepsy is a network disorder which affects how brain regions communicate (Diessen, 2013). Network communication, or connectivity, is investigated through magnetic resonance imaging (MRI). Structural connectivity (SC) is examined through diffusion MRI (dMRI), which estimates how many physical connections exist between regions. Functional connectivity (FC) is examined through resting-state functional MRI (rs-fMRI) and uses the correlation of haemodynamic activity to estimate how regions communicate regardless of their anatomical connections. Structure-function coupling (SFC) examines the interplay between SC and FC, and has the ability to uncover additional information compared to either modality individually (Chiang, 2015), but has not been studied in pediatric focal epilepsy. The objective of this preliminary work is to investigate the ability of SFC to identify network alterations compared to SC and FC individually.

Methods: We plan to enroll 50 patients (aged 7-18) within 5 years of focal epilepsy diagnosis. Healthy control data (n=348) was age matched from the Lifespan Human Connectome Project-Development (HCP-D) study. Participants were scanned with a protocol (matched to HCP-D) on a 3 Tesla Siemens Prisma MRI with a 32-channel head coil including high-resolution 0.8mm T1w and T2w images with prospective motion correction, 2mm rs-fMRI, and 1.5mm multi-shell dMRI sequences. rs-fMRI was preprocessed, denoised, and warped to a standard Montreal Neurological Institute template. dMRI was denoised, corrected for artefacts, susceptibility, motion and distortions. Probabilistic tractography was derived from dMRI within a white matter mask. The Schaefer parcellation (300 regions) was applied to identify regional SC and FC, performing Spearman correlations on corresponding columns of respective connectivity matrices to calculate SFC. SC, FC and SFC were averaged for each of the Yeo-7 networks (visual, default, somatomotor, dorsal attention, ventral attention, limbic and frontoparietal control) to obtain network-specific SC, FC and SFC (Figure 1).

Results: Preliminary results are presented on the first six subjects recruited. SC, FC and SFC of patients were normalized to controls in each network (Figure 2). Independent t-tests were used to compare average SC, FC and SFC of patients to controls in each network. Significant differences (p<0.05, uncorrected) were identified in the left visual SFC and right limbic SFC networks. No significant differences were identified in SC or FC.

Conclusions: SFC has not been studied extensively in pediatric epilepsy. In this preliminary analysis SFC identified network alterations not detectable by SC or FC alone, warranting further investigation of SFC as a biomarker to determine network alterations in pediatric focal epilepsy. Patients will be analyzed longitudinally to improve understanding of how networks change over time, as well as before and after surgery to determine how networks relate to outcome, in order to improve the lives of individuals with epilepsy.

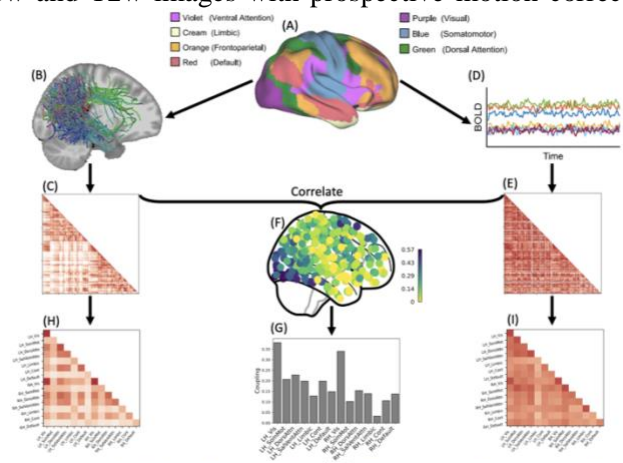


Figure 1. Image analysis. (A) The Schaefer parcellation was applied to images with each parcel corresponding to one of the Yeo 7 networks. (B) Tractography was determined by measuring how many white matter connections exist between voxels and is viewed as a (C) structural connectivity matrix. (D) Functional connections were determined by measuring the presence of oxygen over time, also called the blood oxygen level dependent (BOLD) signal, where correlated activation over time indicates connectivity. (E) viewed as a matrix. (F) Spearman correlations were performed on corresponding columns of the structural and functional matrices to determine SFC. (G) SFC. (H) structural, and (I) functional connectivity were averaged for each of the Yeo 7 networks (left hemisphere (LH) and right hemisphere (RH)) to obtain aggregate network-specific measures.

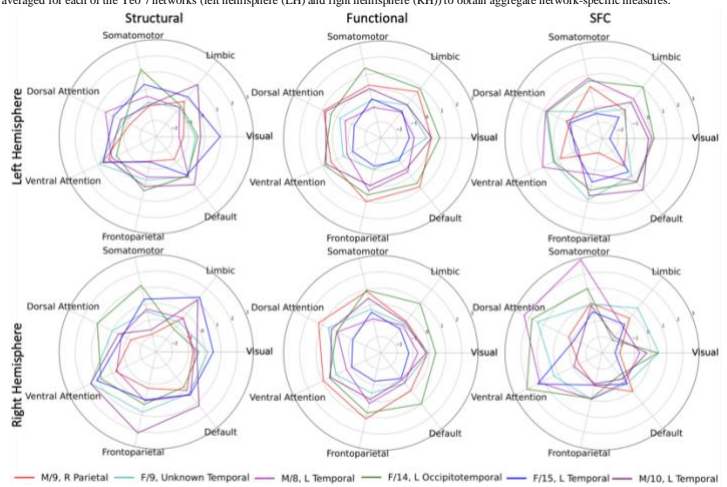


Figure 2. Connectivity in patients normalized to controls. Z-scores for (first column) structural, (second column) functional, and (third column) SFC in (top row) left and (bottom row) right hemisphere networks. Sex (M=male, F=female), age, lateralization (R=right, L=left) and localization are shown for each patient (represented by colours).

Chiang, S., *et al.* Brain Research, 10.1016/j.brainres.2015.04.052. Diessen, E., *et al.* Epilepsia, 10.1111/epi.12350.

Investigating long-term microstructural changes following repeated mild traumatic brain injury in mice using advanced diffusion MRI

Jake Hamilton, Kathy Xu, Arthur Brown, Corey A. Baron

Robarts Research Institute, University of Western Ontario, London, Ontario, Canada.

Introduction: The long-term consequences of mild traumatic brain injury (mTBI or concussion) remain understudied primarily because current neuroimaging techniques are unable to probe the spatial scales at which the resultant pathological changes occur. The advanced diffusion MRI (dMRI) technique oscillating gradient spin echo (OGSE) dMRI may provide additional sensitivity in detecting these microstructural changes as it allows us to probe spatial scales unattainable by conventional pulsed gradient spin echo (PGSE) dMRI. Previous work has shown OGSE dMRI is sensitive to microstructural changes weeks after a single concussive impact¹, however, whether this technique is sensitive to long-term changes after repeated concussive impact is unknown. We aim to use OGSE dMRI to quantify differences in mean kurtosis (MK) as well as traditional metrics, mean diffusivity (MD) and fractional anisotropy (FA), between sham and repetitively concussed mice several months post-injury.

Methods: Both concussed and sham groups consisted of 4 mice (3 males, aged 5-6 months at baseline), with those in the concussed group undergoing mTBI using a controlled cortical impactor on 3 consecutive days. Baseline imaging was performed ~1 week prior to injury and again 6 months post-injury. The dMRI protocol was implemented on a 9.4 T scanner and included both PGSE (i.e., 0 Hz) and OGSE at 60 and 120 Hz using single-shot echo planar imaging (EPI) with parameters: in-plane resolution 200x200 μm^2 , slice thickness 500 μm , total scan time of 66 minutes. Image post-processing included denoising² and eddy current correction³. A manually drawn ROI over the hippocampus was used for analysis.

Results: Figure 1 shows parameter maps from one representative mouse brain at baseline. Within the hippocampus, we see a trend of decreased change in MK and FA and a subtle increase in MD in the concussion group relative to sham at all examined frequencies (Figure 2). No statistically significant changes were found in this study.

Conclusions: This preliminary study, despite small sample sizes, shows a trend of differences in dMRI metrics between concussed and sham groups 6 months post-injury. We anticipate decreased MK in the concussed group may be due to neuron loss and/or impaired myelination formation based on previous work^{4,5}, while decreased FA and increased MD are known to be general indicators of microstructural damage and neurodegeneration⁶. We show here there are long-lasting microstructural changes present at least 6 months after repeated mTBI in mice. In conclusion, we demonstrate that OGSE dMRI metrics reveal differences in concussed and sham groups, illustrating the technique's value for studying long-term microstructural pathologies following brain injury.

References: ¹Rahman et al. *IMNO* (2022). ²Veraart et al. *Neuroimage* (2016). ³Andersson JLR et al. *Neuroimage* (2016). ⁴Aggarwal et al. *MRM* (2020). ⁵Wang et al. *Acta Radiologica* (2022). ⁶Zhang et al. *BMJ Open* (2012).

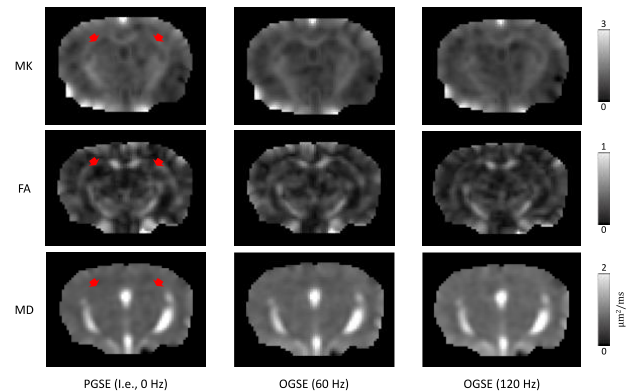


Figure 1. Parameter maps from a representative mouse brain in the sham group at baseline across PGSE- and OGSE-based dMRI sequences (Top – mean kurtosis, middle – fractional anisotropy, bottom – mean diffusivity). Arrowheads indicate the location of the hippocampus.

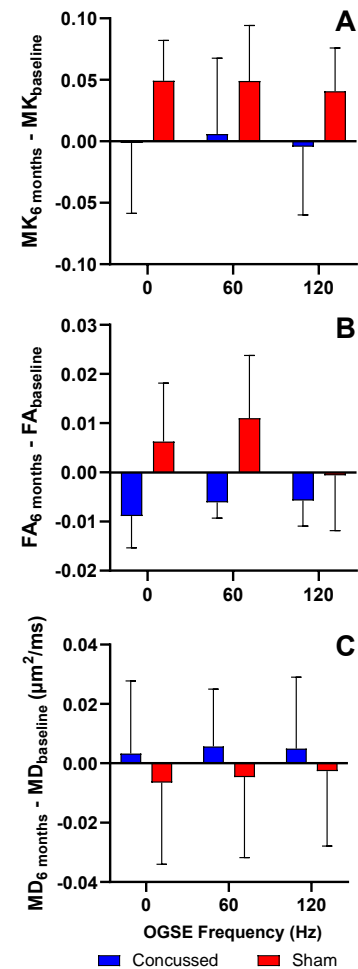


Figure 2. Comparison of changes in dMRI metrics between concussed (n=4) and sham (n=4) groups at 6 months relative to baseline (A – mean kurtosis, B – fractional anisotropy, C – mean diffusivity). Group averages were obtained in each group at each frequency and timepoint. Error bars = standard error of the mean.

Title: Imaging Dementia in African Populations: Closing the Gap on Challenges - A perspective**Author list:** Olujide Oyeniran^{1,2}, Akintunde Orunmuyi³, Rufus Akinyemi⁶, Pedro-Rosa Neto^{4,5}, Ozioma Okonkwo⁷, Udunda C Anazodo^{1,2,5}¹ Lawson Health Research Institute, London, Ontario, Canada, ² Department of Medical Biophysics, Western University, London, Ontario, ³ Integrated Molecular Imaging Centre, Kenyatta University Teaching Research and Referral Hospital, Nairobi, Kenya, ⁴ Douglas Research Centre, Department of Psychiatry, McGill University, Montreal, Quebec, Canada, ⁵ Montreal Neurological Institute, McGill University, Montreal, Quebec, Canada, ⁶ Neuroscience and Aging Research Unit, College of Medicine, University of Ibadan, Nigeria, ⁷ Department of Medicine, University of Wisconsin, Madison, WI, USA.**Background:** Globally, population aging is increasing and consequently, non-communicable diseases (NCDs) including Alzheimer's Disease and Related Dementia (ADRD) are on the rise (*WHO 2021*). In the next two decades, low-and-middle-income countries (LMICs) such as Sub-Saharan Africa (SSA) are projected to have the highest number of people living with dementia (*WHO 2017*). Neuroimaging, particularly Magnetic Resonance Imaging (MRI) and Positron Emission Tomography (PET) are established diagnostic tools of significant importance in characterizing ADRD. Though significant, the use of these imaging tools in dementia research is not well known globally, particularly in SSA.**Methods:** We reviewed clinical studies on ADRD neuroimaging including registered ongoing trials to present a global dementia imaging research landscape based on the total number of study sites, trial participants, and capacity (participants/site). Within SSA, we conducted Medline and Embase keyword searches ('Alzheimer's disease', 'Cognitive impairment', 'Dementia') to identify MRI or PET studies performed across the region. Finally, we provide our perspective on the dementia resources (infrastructure and competencies) required to conduct comparable ADRD research in African populations.**Results:** Only 30 countries (~15% of all countries in the world) account for global ADRD neuroimaging research. While the US has the highest number of study sites, the capacity for ADRD was highest in India. (Figure 1). Overall SSA had the lowest capacity for ADRD research with only 39 original studies, of which 9 used MRI only and none used PET. These imaging studies evaluated Human Immunodeficiency Virus Associated Neurocognitive Disorder (6/9) or investigated Post Stroke Cognitive Impairment (3/9). The overwhelming majority of dementia research in SSA were non-imaging epidemiology or dementia care studies (28/39). The composition of resources required to achieve comparable global ADRD research in SSA is also highlighted.**Figure 1:** Global ADRD Neuroimaging Research Landscape summarizing clinical studies and trials including ongoing registered studies conducted in each country around the world based on the total number of reported study sites per country (A), the total number of reported participants per site (B) including the completed and projected, and the capacity for neuroimaging (C). Although the US had the greatest number of sites (342) and participants (18,393), it had a moderate level of capacity (53.78) compared to Peru which has the capacity (350) to scan 700 participants at just two sites, demonstrating the potential of equipping 1-2 LMICs sites with neuroimaging resources.**Conclusion:** The current global ADRD research landscape mirrors neuroimaging capacity and is dominated by the Global North. The moderate to high ADRD neuroimaging capacity in LMICs such as India and Peru demonstrate the impact of capacity building in low-resourced settings though a subset of the study population was scanned. Within SSA, the composition of resources required for valuable ADRD research suggests priorities for developing neuroimaging capacity should be central to ongoing efforts to promote global ADRD research.

This work was presented at the Alzheimer's Association International Conference (AAIC) December 2022.

Title: Non-invasive quantification of [^{18}F]SynVesT-1 for PET studies of synaptic density in Parkinson's Disease

Authors: Kelly Smart^{1,2}, Carme Uribe¹, Kimberly L. Desmond^{1,2}, Neil Vasdev^{1,2,3} and Antonio P. Strafella^{1,3,4}

Affiliations: 1. Brain Health Imaging Centre, Centre for Addiction and Mental Health; 2. Department of Psychiatry, University of Toronto; 3. Institute for Medical Sciences, University of Toronto, 4. Edmond J. Safra Parkinson Disease Program Neurology Division, Toronto Western Hospital & Krembil Brain Institute, UHN, University of Toronto.

Introduction: Brain synaptic density can be measured in living people using PET with radiotracers selective for the synaptic vesicle glycoprotein 2A (SV2A), such as [^{18}F]SynVesT-1. This is a uniquely specific and sensitive tool to identify molecular alterations in neurodegenerative disorders. Existing quantification methods for [^{18}F]SynVesT-1 require arterial catheterization for blood sampling during scans, a procedure that can be particularly challenging in older people and those with movement disorders. The objective of this work was to validate a non-invasive quantification method for [^{18}F]SynVesT-1 in people with Parkinson's disease (PD) using a reference tissue approach.

Methods: [^{18}F]SynVesT-1 scans have been acquired in 2 patients with PD and 3 healthy control (HC) subjects to date. 120-min scans were collected on a GE Discovery 5-ring PET/CT scanner after injection of ~ 185 MBq [^{18}F]SynVesT-1. Arterial blood sampling was completed throughout each scan to generate a metabolite-corrected arterial input function. Kinetic modeling was performed to estimate [^{18}F]SynVesT-1 binding potential (BP_{ND}), a measure of specific target availability in regions of interest (ROI). The one-tissue compartment model (1TCM) was fitted to time-activity curves from brain and arterial input function to estimate BP_{ND} in each ROI, using distribution volume in centrum semiovale (CS) as a measure of free and non-specifically bound radiotracer.

Non-invasive quantification was evaluated using the simplified reference tissue model-2 (SRTM2) with CS reference region. The SRTM2 was fitted in two ways: (1) fixing the reference region efflux rate constant k_2' to a population value based on group average k_2 in CS ($\text{CS-}k_2$) from 1TCM fits (see Results); or (2) a two-step procedure in which the k_2' parameter is first determined in a coupled fit across grey matter regions, then fixed to estimate BP_{ND} . Absolute agreement and bias were assessed between BP_{ND} values derived from SRTM2 using each method or 1TCM across 22 brain ROIs.

Results: V_T in CS was similar between PD ($n=2$, 3.0 and 3.7 mL/cm³) and HC ($n=3$, 3.6 ± 0.9 mL/cm³) groups, supporting the validity of CS as a reference region in this population. $\text{CS-}k_2$ was also similar in PD (0.035 min⁻¹ and 0.045 min⁻¹) and HC (0.037 ± 0.006 min⁻¹) groups. Across all participants, average $\text{CS-}k_2$ value was 0.038 min⁻¹, consistent with a recently reported population k_2 value of 0.032 min⁻¹ ($n=8$ HCs; Naganawa et al. 2022 J Nucl Med). Using the fixed k_2' value of 0.038 min⁻¹ (i.e., $\text{CS-}k_2$; method 1), agreement between BP_{ND} values from SRTM2 versus 1TCM was excellent for every participant (R^2 values >0.99 ; $BP_{\text{ND}}^{\text{SRTM}} = 0.99 * BP_{\text{ND}}^{\text{1TCM}} - 0.11$) and bias was low ($+4.5\% \pm 3.1\%$). Results were comparable using fixed $k_2' = 0.032$ min⁻¹ (R^2 's >0.99 , $BP_{\text{ND}}^{\text{SRTM}} = 1.03 * BP_{\text{ND}}^{\text{1TCM}} - 0.15$, bias $+1.9\% \pm 2.1\%$). Using a coupled fit (method 2), agreement was also excellent for each participant (R^2 's > 0.99 ; $BP_{\text{ND}}^{\text{SRTM}} = 0.97 * BP_{\text{ND}}^{\text{1TCM}} - 0.075$) and bias was similarly low ($+5.4\% \pm 3.5\%$).

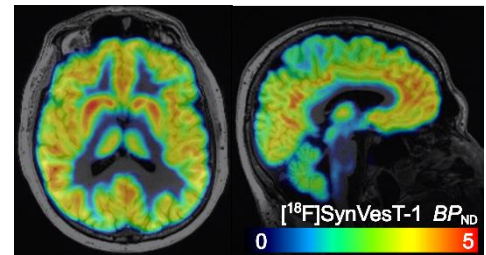
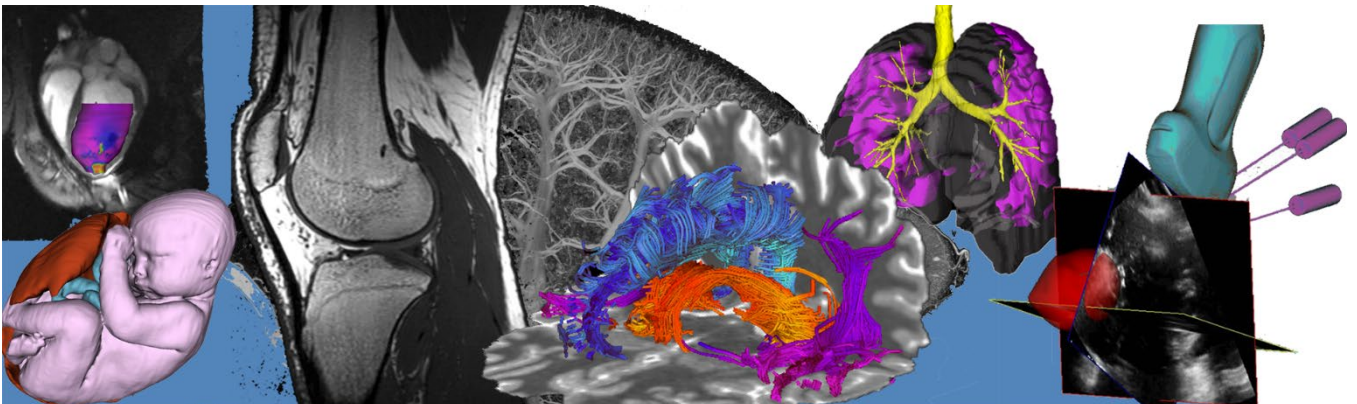


Figure. Non-invasive synaptic density PET imaging in a patient with PD.

Conclusions: Non-invasive quantification produced BP_{ND} values in excellent agreement with those derived from 1TCM with arterial sampling for both HCs and patients with PD. For the population k_2' method, studies are ongoing to determine if the optimal k_2' value will differ in people with PD. Notably, values from the coupled fitting method were also in excellent agreement with 1TCM results. Coupled fitting may therefore be a valuable method that avoids the need for prior population estimates by estimating k_2' at the individual level in a two-step procedure, which can be applied at the ROI or voxel level (**Figure**). Our preliminary results suggest that accurate [^{18}F]SynVesT-1 quantification can be performed without arterial blood sampling in individuals with PD, which could greatly improve patient comfort and throughput in studies of brain synaptic density.

Pitch/Poster Session 1: Ultrasound and Optical Imaging Abstracts



A hand-held photoacoustic imaging probe for breast cancer margin assessment

E. Rascevska^{a,b}, L.C.M. Yip^{a,c}, P. Omid^{a,b}, M. Brackstone^{d,e}, J.J.L. Carson^{a,b,c,d}

^aImaging Program, Lawson Health Research Institute, London, Canada

^bSchool of Biomedical Engineering, Western University, London, Canada

^cDepartment of Medical Biophysics, Schulich School of Medicine & Dentistry, Western University, London, Canada

^dDepartment of Surgery, Schulich School of Medicine & Dentistry, Western University, London, Canada

^eDepartment of Oncology, Schulich School of Medicine & Dentistry, Western University, London, Canada

Introduction: Standard of care procedure for patients diagnosed with stage I or stage II breast cancer is breast conserving surgery (BCS). During BCS all tumour tissue is excised together with a continuous margin of healthy tissue. In approximately 20% of cases, pathology reports cancerous cells found on the excised specimen margins, requiring patient to return for a re-excision surgery to remove the cells and reduce the change of local recurrence. X-ray and ultrasound imaging are available for intraoperative margin assessment but are not always reliable (*Maloney et al., 2018, J. Biomed. Opt.*). Many have proposed that a method sensitive to the molecular characteristics of tissue may lead to a more precise intraoperative margin assessment.

Our group has developed a hand-held photoacoustic imaging (PAI) probe for detection of residual cancer tissue during BCS and prior to sending the specimen to pathology. In PAI, short laser pulses are used to generate acoustic waves resulting in images of optical contrast with ultrasonic resolution. In previous work, we have (i) successfully differentiated cancerous and healthy breast tissue with PAI based on lipid content (*Kosik et al., 2020, Photoacoustics*) and (ii) demonstrated feasibility of a prototype hand-held PAI probe (*Rascevska et al., 2022, Photoacoustics*). As a follow-up, we have developed a miniature hand-held PAI probe compatible for use in a surgical environment.

Methods: Photoacoustic (PA) image data was collected with a miniature hand-held PAI probe connected to a tunable pulsed laser and high-speed data acquisition system. The probe was scanned using an industrial robot with 6 degrees of freedom. A line source phantom consisting of two rows of $\text{\O}400\ \mu\text{m}$ nylon string with varying spacing and an active PA signal source made of $\text{\O}400\ \mu\text{m}$ multimode fiber with a coated black tip was imaged. Point spread function analysis of the string features in the image was used to estimate the resolution of the integrated imaging system. The bandwidth of the sensor was obtained through Fourier analysis of the signal from the PA signal source.

Results: Figure 1a shows the miniature hand-held PAI probe. The probe consists of an acoustic detection and illumination device. The acoustic sensor ($\text{\O}13\ \text{mm}$) consisting of a single layer of polyvinylidene fluoride, and an integrated preamplifier was positioned in the central opening of the illumination device. Illumination device ($\text{\O}20\ \text{mm}$) consists of an axicon lens in front of a ring of 72 $\text{\O}200\ \mu\text{m}$ multimode fibers. Through analysis of the image in Figure 1b, the resolution of the probe in the axial and lateral directions was found to be 0.62 mm and 1.72 mm, respectively. The frequency bandwidth at -3dB was estimated to be 133% from 317 kHz to 1.58 MHz.

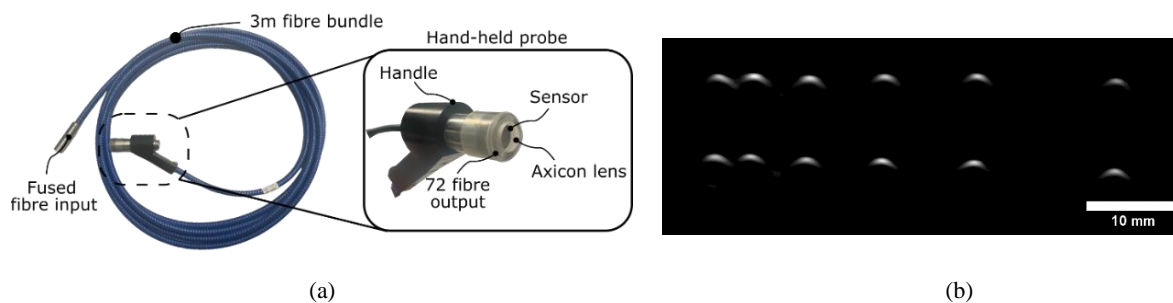


Figure 1. (a) Illustration of the miniature hand-held PAI probe. (b) Cross-sectional PA image of a string phantom obtained with robotic scanning of the miniature hand-held PAI probe.

Conclusion: We report on the resolution and bandwidth of a miniature hand-held PAI probe compatible for use in a surgical environment. The relatively low resolution aims to optimize imaging of bulk tissue, while identification of closer margins might prove to be challenging, we believe this probe will enable detection of most residual cancerous cells. This will be investigated in future clinical studies. Future work will include integration of a positional tracking system into the probe, which would enable free-hand photoacoustic imaging. Free-hand imaging would enable the surgeon to build up a 3D photoacoustic image of the surgical cavity in real-time potentially improving the intraoperative detection of tumour tissue leading to a greater number of successful BCS.

Quantitative Spatial-Frequency Fluorescence Imaging for Surgical Guidance: Pre-Clinical Nanoparticle Experiment

Josephine La Macchia,¹ Anjola Adewale,¹ Esmat Najjar,² Sharon Tzelnick,² Alessandra Ruaro,² Harley Chan,¹ Jason Townson,¹ Brian C. Wilson,^{1,3} Jonathan C. Irish¹⁻³ and Michael J. Daly¹

¹TECHNA Institute, University Health Network, Toronto ON

²Department of Otolaryngology – Head & Neck Surgery, University of Toronto

³Ontario Cancer Institute, Princess Margaret Cancer Centre, Toronto ON

Introduction: Spatial-frequency domain imaging (SFDI) uses structured illumination patterns to quantify optical properties and fluorescence concentration from light interaction with complex tissue (like tumors). We are investigating the abilities and limitations of our SFDI prototype (Fig. a) to quantify fluorescence during nanoparticle-guided oral cancer surgery.¹ Here, we investigate estimation performance in pre-clinical animal tumor models.

Methods: Mouse oral squamous cell carcinoma cells were subcutaneously injected in the right leg of immunocompetent mice (N=10). After tumor growth (3-10 mm), we injected a fluorescent nanoparticle (porphyrinsomes) 24-hours prior to surgery.² Fluorescence images were processed to compensate for absorption and scattering, based on optical property maps computed from reflectance SFDI images. We used the compensated fluorescence images to evaluate pre-resection fluorescence concentration (Fig. b), and post-resection fluorescence in residual tumor. After tumor resection, we took biopsies in areas of high and low fluorescent uptake to characterize residual fluorescence of the tumor margins (Fig. c).

Results: In vivo fluorescence concentrations were observed in the range 3-6 $\mu\text{g}/\text{mL}$ for pre-resected tumors. Biopsy locations selected in fluorescence images were projected onto the surgical field using phase-shift profilometry and camera-projector stereo calibration (0.8 mm accuracy). The histology of our high and low fluorescent uptake biopsies confirmed that areas of high uptake (5×10^{-4} fluorescence re-emission) were malignant, and low uptake areas (2.5×10^{-4} % fluorescence re-emission) were normal.

Conclusions: Initial comparisons of fluorescence images with pathology show agreement, but future work is required in a larger population to understand the sensitivity and specificity of fluorescence throughout the surgical field. This study is establishing baseline values for tissue optical properties and nanoparticle accumulation in a mouse cancer model, and this data will be used in future to compare different therapeutic approaches (e.g., photodynamic therapy) and optimize a deep learning algorithm for 3D fluorescence.

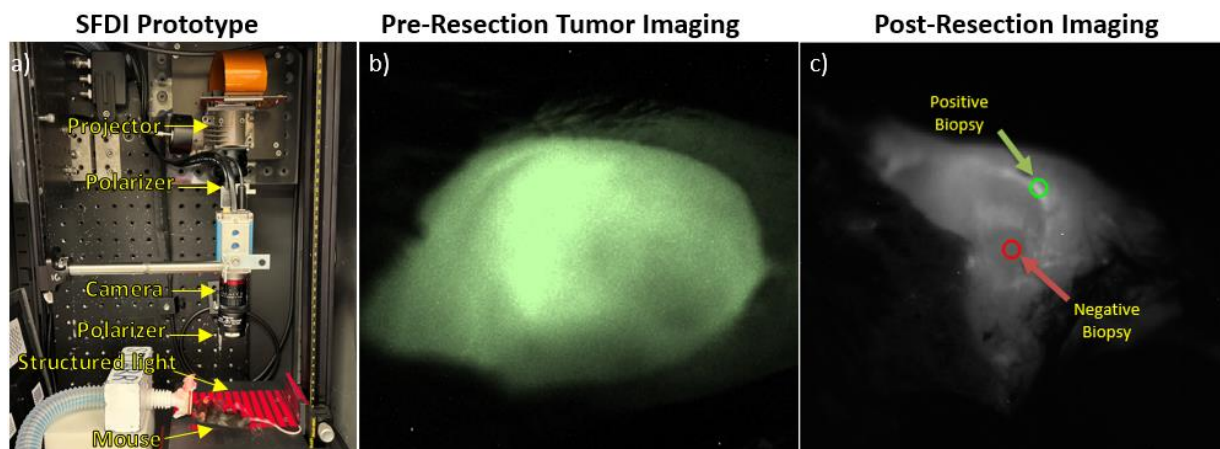


Figure. (a) SFDI fluorescence prototype. (b) Pre-resected fluorescence image of tumor (c) Post-resection fluorescence image of surgical bed with biopsy locations marked.

References:

1. Daly MJ et. al., SPIE Photonics West 2021, Vol 11625.
2. Tzelnick et. al., Terry Fox Research Institute Scientific Meeting, 2022.

Double exposure ESPI method for non-contact dynamic photoacoustic wave detectionHui Wang^{1,2}, Mamadou Diop^{1,2,3}, and Jeffrey Carson^{*1,2,3}¹Imaging Program, Lawson Health Research Institute, London, Ontario, Canada²School of Biomedical Engineering, Western University, London, Ontario, Canada³Department of Medical Biophysics, Western University, London, Ontario, Canada

Introduction: Photoacoustic tomography (PAT) is a well-established imaging modality that has grown in importance for applications in breast cancer, dermatology, and vascular studies^{1,2,3}. Photoacoustic signals are generated when tissue absorbs short pulses of light. Because of the acoustic impedance mismatch between tissue and air, photoacoustic sensors must be coupled to tissue with water or gel. This approach is suboptimal in many application scenarios, such as image-guided biopsy applications needing sterility, or rapid breast cancer screening methods. Here, we present an innovative electronic speckle pattern interferometry (ESPI) method for non-contact estimation of photoacoustic signals as a first step toward fully non-contact PAT.

Methods: In contrast to water-coupled photoacoustic sensors, double exposure ESPI records the surface deformation due to a photoacoustic wave over time. We implemented the method with an off-axis Mach-Zehnder interferometer. After reflection from the tissue (phantom) surface, the object beam combined with the reference beam to produce a speckle pattern that was captured with a 50MP digital camera. High speed video recording of the speckle pattern combined with a phase reconstruction technique resulted in a dynamic surface displacement measurement. For testing, we used a two-layer phantom consisting of an Intralipid™ doped first layer to mimic the optical scattering of tissue and an agarose second layer containing a 9-mm diameter spherical absorber (India Ink) embedded approximately 3.5 cm below the detection surface. The second layer was exposed repeatedly to a pulsed laser at 1064 nm (5 ns, 10 Hz repetition rate). The speckle pattern was recorded immediately prior to each pulse and at a controlled delay after each pulse (double exposure, 1-110 μ s in 1 μ s increment). The images were processed with phase reconstruction software.

Results: Figure 1 presents the reconstructed phase amplitude representative of the surface displacement changes over 110 μ s. The phantom was exposed to the pulsed laser at $t = 0$. Due to the depth of the absorber, the front-end of the photoacoustic signal appeared approximately 24-26 μ s into the recording as expected. The duration of the photoacoustic waveform was observed approximately 8 μ s on the phantom surface. This is consistent with the expected result of 6 μ s, calculated from the 9 mm spherical absorber propagating at a speed of 1.5 mm/ μ s in an isotropic medium. Following the initial peak, the waveform showed some ringing before settling into a relatively calm state beyond 70 μ s. Through comparison of the phase (in radians) of the surface tomography overtime, the SNR of the system was evaluated to be 15.

Conclusions: Double exposure ESPI detected a photoacoustic signal at an effective sampling rate of 1 MHz. The photoacoustic signal was resolved from the surface of the phantom with tissue-mimicking characteristics at a distance of more than 30 cm from the camera. Future research will examine the bandwidth of this technique and ascertain its applicability in translational PAT studies involving real tissue.

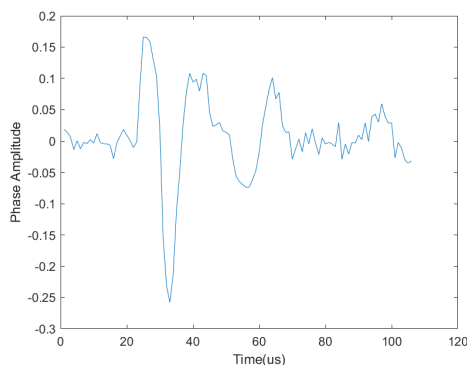


Figure 1. Phase amplitude as a function of time measured at the surface of a tissue-mimicking phantom during photoacoustic excitation.

References:

- [1] Attia, et al. *Photoacoustics* **16**, 100144 (2019).
- [2] Steinberg, et al. *Photoacoustics* **14**, 77–98 (2019).
- [3] Beard, P. *Interface Focus* **1**(4), 602–631 (2011).

The ideal composition of Tissue-Mimicking Phantoms for Near-Infrared Spectroscopy Rasa Eskandari¹ and Mamadou Diop^{1,3}

¹Department of Medical Biophysics, Western University, London, ON, Canada

²School of Biomedical Engineering, Western University, London, ON, Canada

³Imaging Program, Lawson Health Research Institute, London, ON, Canada

Introduction: Near-infrared spectroscopy (NIRS) is now widely used as a non-invasive approach to real-time monitoring of tissue blood content and oxygenation at the point-of-care. Tissue-mimicking phantoms are used to test and validate NIRS devices and algorithms. Phantoms are media prepared with accessible resources to mimic the optical properties of a biological tissue. Tissue-mimicking phantoms typically contain a light scatterer, which is commonly a lipid emulsion (e.g., Intralipid),¹ and one or multiple light-absorbing dyes, with the most widely used being indocyanine green (ICG). This dye, which is harmless to patients, plays a crucial universal role as a contrast agent in medical imaging and diagnostics. Current evidence, however, suggests that the optical properties of ICG can change as a function of the phantom composition;² two different concentrations of ICG in a consistent concentration of the same light scatterer may have different absorption spectra. This behaviour is not ideal as it hinders the ability to accurately estimate the dye concentration. In an ideal phantom, there would be minimal interaction between the scatterer and dye, thereby preserving the absorption spectrum of the dye for any combination of scatterer and dye concentrations. The objective of this study is to identify the ideal light scatterer from Intralipid, glass microspheres, and titanium oxide for NIRS tissue-mimicking phantoms with ICG as the light absorber. We hypothesize that Intralipid will alter the absorption spectra of the dye while the inorganic light scatterers (i.e., glass microspheres and titanium oxide) will not.

Methods: A custom-made spectrometer and a 20-W halogen lamp were used to measure the attenuated light transmitted through phantoms based on each of the three light scatterers (Intralipid, glass microspheres, and titanium oxide) in combination with ICG. For each acquisition, the concentration of the light scatterer was kept constant while the concentration of the dye was increased linearly. Lamp intensity, spectrometer slit width (10 μm), and sampling rate (100 ms/spectrum) were kept constant across all measurements. Each combination was repeated five times, preparing a new phantom each time. The signal count for the five trials were averaged, normalized with the area under the curve, and plotted collectively for each set of measurements using MATLAB 2021b.

Results: Fig. 1 shows the normalized spectra of phantoms with constant concentrations of glass microspheres, titanium oxide, and Intralipid as ICG concentration was increased from 0.04 μM to 0.2 μM in steps of 0.04 μM . In Intralipid, the spectra shifted to longer wavelengths as the concentration of ICG was increased. In contrast, the spectral shape and position did not change in phantoms made of glass microspheres and titanium oxide when the concentration of ICG was increased.

Conclusions: Despite the wide use of Intralipid as a light scatterer in NIRS phantoms, the findings of this study suggest that Intralipid is not ideal since it alters the absorption spectra of ICG in tissue-mimicking phantoms. The spectral shifts observed when Intralipid concentration was fixed suggest that there is interaction between Intralipid and the dyes. Notably, when scattering is constant, the change in light attenuation is equal to the product of the absorption coefficient and optical pathlength. Because of the unchanging light scattering when Intralipid concentration is fixed, the pathlength can be assumed to be constant, and the spectral shifts are therefore likely due to changes in the molar extinction coefficients of the dyes due to interaction with Intralipid. The absorption spectra of the dye did not change when Intralipid was substituted with glass microspheres and titanium oxide. NIRS tissue mimicking phantoms continues to rely on ICG as a chromophore; therefore, glass microspheres and titanium oxide should be used to replace Intralipid, which has traditionally served as the standard light scatterer for liquid phantoms. Among the two inorganic light scatterers, titanium oxide is a more convenient choice, because suspensions of glass microspheres require constant stirring to avoid settlement. Future work will investigate the absorption properties of ICG when its concentration is constant while scatterer concentrations increase linearly.

References: [1] Pogue B. W., et al. *Journal of Biomedical Optics* **11**(4), 041102 (2006). [2] Yuan B., et al. *Journal of Biomedical Optics* **9**(3), 497-503 (2004).

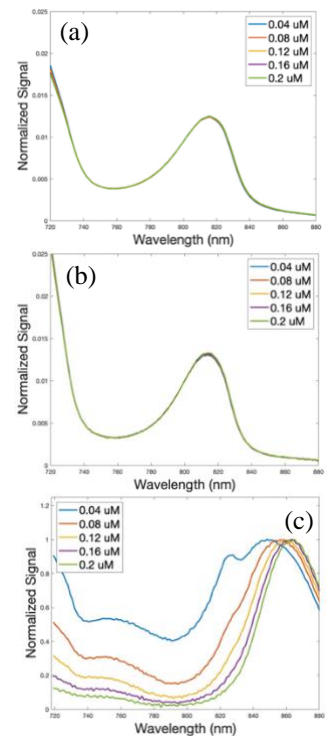


Figure 1 Normalized spectra for linearly increasing ICG concentrations in phantoms based (a) glass microspheres, (b) titanium oxide, and (c) Intralipid.

Extended views for gynecological brachytherapy using three-dimensional ultrasound fusionTiana Trumpour^{1,2}, Claire K. Park^{1,2}, Jessica Rodgers³, Lucas Mendez⁴, Kathleen Surry^{1,4,5}, Aaron Fenster^{1,2,4}¹ Department of Medical Biophysics, Western University, Canada ² Robarts Research Institute, Western University, Canada ³ Department of Physics and Astronomy, University of Manitoba, Canada ⁴ London Regional Cancer Program, Canada ⁵ Department of Oncology, Western University, Canada

Introduction: During high dose-rate gynecological brachytherapy procedures, radioactive sources are placed internally using specialized applicators and/or interstitial needles. For positive treatment outcomes, accurate placement of these devices is vital. As an alternative to magnetic resonance (MR) or computed tomography (CT) imaging, three-dimensional (3D) ultrasound (US) has previously been investigated to assess applicator placement, but only using either 3D trans-abdominal (TAUS) or 3D trans-rectal (TRUS) views, which presents shadowing artifacts [1]. Previously, we performed proof-of-concept experiments showing the feasibility of a 3D TAUS-TRUS fusion technique and now aim to extend that work to a greater suite of brachytherapy applicators while improving our fusion algorithm. We hypothesize that the updated 3D US fusion will improve visualization of the region of interest and potentially aid clinical brachytherapy procedures [2].

Methods: A multi-modal female pelvic phantom with anatomical structures and an embedded applicator was created for both an intracavitary Fletcher applicator and a hybrid Vienna applicator. For 3D US registration analysis, fiducials (N=4) were embedded within the Fletcher phantom and needles (N=4) were added to the Vienna phantom. We acquired 3D TAUS and 3D TRUS images with our custom mechatronic system that integrates any commercial US transducer. Computational image reconstruction took ≈ 45 seconds. A 3D rendered model of the applicator was manually aligned to each of the 3D US images based on visible applicator landmarks and anatomy, and a TAUS-TRUS registration was completed based on the model positions. Fusion of the 3D US images was then performed using a voxel-based algorithm with a nonlinear-weighted combination of overlapping voxel intensities. Target registration error (TRE) and fiducial localization error (FLE) were calculated using the fiducial spheres or needle tips to assess the registration accuracy of the 3D TAUS-TRUS images. The fused image was compared to gold-standard CT and MR images of the same phantom.

Results: Image examples are depicted in Fig. 1. Registration analysis of the 3D TAUS-TRUS images of the Fletcher applicator case found TRE values of 3.6 ± 0.3 (3.3-3.9) mm and FLE values of 0.6 ± 0.3 (0.3-1.0) mm. The same analysis for the Vienna applicator phantom resulted in TRE mean, standard deviation, and range values of 2.9 ± 0.2 (2.6-3.1) mm and FLE values of 0.7 ± 0.7 (0.1-1.8) mm. Qualitative comparison with CT and MR saw the applicator, needles, and surrounding anatomy fully visualized by a trained observer in the fused 3D US image.

Conclusions: This study shows the generalizability of our 3D US fusion technique to a variety of applicators, with an extended field-of-view when compared with 2D US images or a single 3D US view. The results suggest that manual registration has < 4 mm error and that fiducials are being localized with sub-mm Euclidean distance error. We attribute some registration errors to the manual alignment technique, which should be mitigated by automating our process. We plan to automate this procedure by mechanically linking the TAUS and TRUS systems such that registration is completed in real time and fusion is completed in < 1 minute. We also aim to perform numerous experiments and multiple imaging sessions in a clinical study.

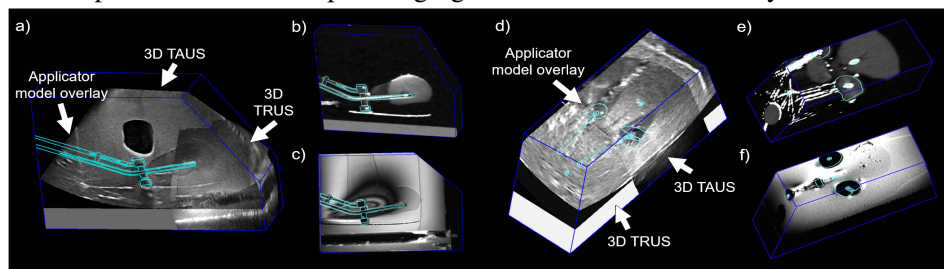


Figure 1: Multi-modal phantom with brachytherapy applicators imaged with a) fused 3D TAUS-TRUS of Vienna applicator compared with b) CT and c) MR; d) fused 3D TAUS-TRUS of Fletcher applicator compared with e) CT and f) MR.

References: [1] Rodgers et al. *Med. Phys.* 2017. 44(5); [2] Mendez et al. *Rad. Oncol.* 2020. 15(1)

Investigating ultrasound stimulated microbubble mediated microvascular disruptionXiaoxiao Zhao^{1,2}, Carly Pellow¹, Alex Wright¹, David Goertz^{1,2}¹Sunnybrook Research Institute, Toronto, Canada, ²University of Toronto, Toronto, Canada

Introduction: Microbubbles (MBs) can induce microvascular damage and shut down blood flow when stimulated by sufficiently high ultrasound pressures. This approach has been termed mechanical ablation or antivasular ultrasound (AVUS) and has been shown to synergistically enhance the antitumour effects of conventional cancer therapies. However, the underlying mechanisms remain unclear, and treatment and control protocols remain to be optimized. Here we investigate AVUS *in vivo* and in benchtop experiments with cavitation monitoring and microscopy, with implications for establishing an AVUS-specific treatment protocol and control platform.

Methods: For *in vivo* experiments, ultrasound transmitters and receivers were integrated into a murine dorsal window chamber tumour model (Green fluorescent protein tagged human squamous cell carcinoma (GFP-FaDu) cell line) for intravital multiphoton microscopy studies capable of real-time (~ 1 Hz) visual and acoustic monitoring during AVUS. Vessel type (normal and tumour-affected), caliber, and viability were assessed under higher pressure conditions (1.05 MHz, 5 ms pulse, P=1, 2, 3 MPa), cavitation signatures were analyzed and linked to vessel biological effects. For benchtop experiments, acoustic emission detection and high-speed microscopy (10kframes/s; 1 μ s shutter speed) were employed to examine the evolution of MB behaviour in wall-less channels from 1200 to 15 μ m in diameter over millisecond timescales (1.4 MHz, 5 ms pulse, P=0.5-3 MPa). The cavitation signals were analyzed and linked to the size of the channels.

Results: *In vivo*, vessel calibre changes, spasms, flow directionality changes, permeabilization and vessel shutdown were visualized during AVUS. Those vascular events and sustained microvascular shutdown occurred preferentially in tumor-affected vessels with greater incidence in smaller vessels and with more severity as a function of increasing pressure (Fig. 1A). The same trends applied to the normal mice, but with overall lower incidence suggesting a self-targeting effect on tumors. Cavitation monitored indicated association broadband emissions from violent inertial cavitation (IC), with sub- and ultra-harmonics (SHs and UHs) as well as 1/3 and 2/3 SHs and UHs appearing with increasing pressure (Fig. 1B). In benchtop experiments, MBs in channels of the size that were disrupted by AVUS exhibited IC spectral characteristics along with distinct spectral peaks (1/2 and 1/3 order SHs and UHs) that were associated with clustering in smaller channels $\leq 50 \mu$ m (Fig. 1C).

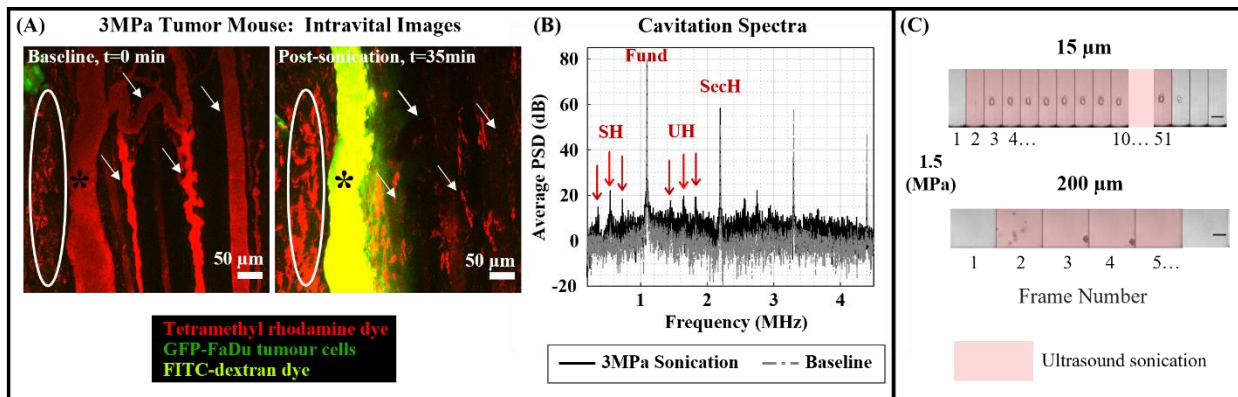


Figure 1. (A) Example intravital images of vessels perfused with red fluorescent dye prior to MB injection and sonication, and 30 min after AVUS-relevant exposure (3 MPa) of MBs with injection of a second green dye. Viable vessels perfuse and appear yellow while shut-down vessels remain red (circled section) or appear dark (indicated with an arrow). (B) Representative cavitation spectra recorded during AVUS at 3 MPa compared to baseline, demonstrating IC, as well as distinct elevated SH and UH peaks. (C) Example optical data for the 15 and 200 μ m channels reveal distinct bubble and cluster behaviors in different calibers.

Conclusions: The observed vascular events taken collectively with identified cavitation signatures provide an improved mechanistic understanding of AVUS at the microscale; benchtop results provide new insights into the behavior of MBs in small vessels at higher pressures. These results have implications for establishing a specific treatment protocol and control platform for AVUS.

Self-supervised enhanced ultrasound thyroid nodule detection and evaluation

Ningtao Liu^{1,2}, Aaron Fenster^{1,3,4}, David Tessier¹, Shuiping Gou², Jaron Chong⁴

¹Robarts Research Institute, Western University, London, ON, Canada, ²School of artificial intelligence, Xidian University, Xi'an 710071, Shaanxi, China, ³Department of Medical Biophysics, Western University, London, ON, Canada, ⁴Department of Medical Imaging, Western University, London, ON, Canada

Abstract

Introduction. Thyroid nodules are very common, and ultrasound (US) is the primary method used to detect and classify them. In the clinical workflow of Computer-Aided Diagnosis (CAD), the determination of the location and contours of the thyroid nodule is critical. Although deep learning methods have achieved good performance on US thyroid nodule detection tasks, these methods are based on single-frame images and ignore the significance of temporal contextual information in ultrasound videos for detection accuracy. Therefore, a video-scale thyroid nodule detection method was used in this study. In addition, considering the cost of annotating ultrasound videos, we also improved the performance of detection with a self-supervised model trained on the unlabeled dataset. The performance was evaluated at multiple scales, respectively.

Methods. In this study, a dataset containing 69 thyroid US videos obtained from 51 subjects was used for a five-fold cross-validation. The training and test sets in each fold were divided by subject because there were some videos collected from the same subject. The mean value of the length of the videos is 262 frames. Each video contains an average of 1.21 nodes. The nodule sizes varied greatly from 14 to 1445 frames, with an average of 526.71 frames. The video object detection model SELSA¹ was used for the detection of thyroid nodules. In PASS, features of nodule objects in adjacent frames are aggregated to endow the model with awareness of video context information. In addition, we proposed a patch scale self-supervised (PASS) pre-training model based on SimCLR². Unlike augmentation methods that apply on image scales, such as random flip and zoom, US images were also augmented by shuffling randomly selected patch pairs in PASS, which allows the PASS to extract image features accurately without label information employing contrastive learning. The weight of PASS was then used as the initialization parameter of SELSA to enhance its ability to extract nodule-distinguishing features. The pipeline and the augmented image are shown in fig. 1a.

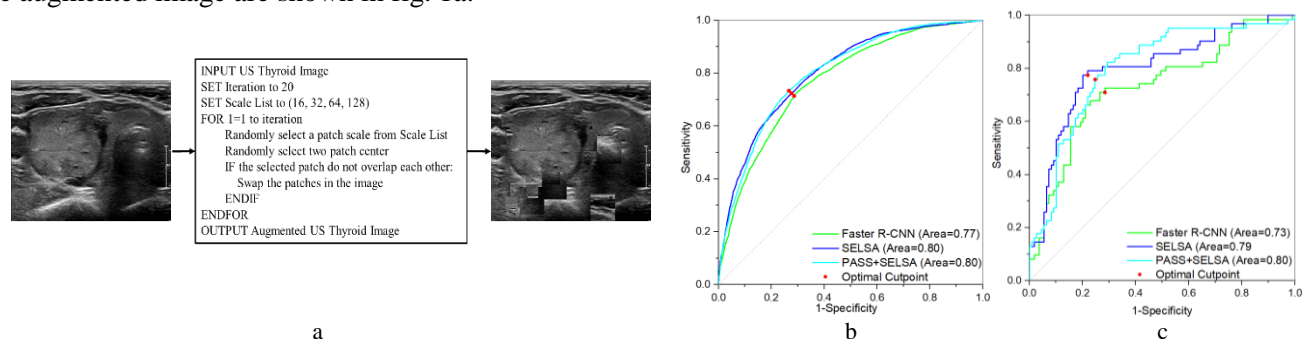


Figure Patch shuffling augmentation process (a), ROC curves for frame image (b) and video clip scale (c) classification.

Results. We performed ablation experiments with Faster R-CNN³, SELSA with random initialization, and SELSA with PASS initialization to verify the improvement of detection performance by temporal context information and pre-trained models. In addition, we evaluate the model performance on the scales of the bounding box, frame image, and video clip, respectively. The mean average precision with 50% intersection over union (mAP@50) of the three models was 0.256, 0.335 and 0.39 respectively. As shown in fig. b and c, the AUC-ROC of the three models on the frame binary classification task was 0.77, 0.80 and 0.80 respectively, and the AUC-ROC on the video segment binary classification task was 0.73, 0.79 and 0.80 respectively.

Conclusion. We proposed a video-scale thyroid nodule detection method enhanced by a pre-trained model. Experimental results show that both ultrasound video temporal context information and the pre-trained model can improve detection accuracy.

Reference

1. Lee, Jayoung, et al. "Benchmarking video object detection systems on embedded devices under resource contention." *Proceedings of the 5th International Workshop on Embedded and Mobile Deep Learning*. 2021.
2. Chen, Ting, et al. "A simple framework for contrastive learning of visual representations." *International conference on machine learning*. PMLR, 2020.
3. Girshick, Ross. "Fast r-cnn." *Proceedings of the IEEE international conference on computer vision*. 2015.

Three-dimensional complementary breast ultrasound (CBUS) with orthogonal images to improve resolution

Claire K. Park^{1,2}, Tiana Trumpour^{1,2}, Igor Gyacskov², Lori Gardi², Jeff Bax², David Tessier², Aaron Fenster^{1,2}

¹Department of Medical Biophysics, Schulich School of Medicine and Dentistry, ²Center for Advanced Medical Imaging Technology, Robarts Research Institute, Western University, London, Ontario, Canada

Introduction: With increasing evidence toward three-dimensional (3D) automated breast ultrasound (ABUS) for supplemental screening of breast cancer in intermediate to high-risk women, including those with dense breasts, there is an interest in developing more cost-effective, robust, and high-resolution techniques. [1] Compared with commercially available 3D ABUS systems that use specialized high-frequency US transducers, hybrid approaches integrate conventional linear array US transducers, which are more cost-effective and widely available in clinical practice. However, 3D ABUS image resolution may be limited due to the poor intrinsic elevational resolution of linear array US transducers. Specifically, in any oblique view to the US scan plane in the 3DUS image will include intensity information from the high in-plane and poor out-of-plane resolution, which will diminish the overall 3D voxel resolution and result in blurred structures. We hypothesize that combining orthogonal 3DUS images can improve resolution by recovering out-of-plane resolution from the acquisition direction. This work describes and experimentally validates an orthogonal 3DUS image acquisition and spherical-weighted combination approach to improve resolution uniformity in the 3D complementary breast ultrasound (CBUS) image.

Methods: We developed a dedicated 3D ABUS device that contains a wearable 3D-printed dam, adjustable compression assembly, and removable motorized linear scanner for 3DUS image acquisition, which is adaptable to any conventional US system and linear array transducer. [2] Orthogonal 3DUS images were acquired in an angular wire phantom (with wires positioned in-plane at various oblique angles) with linear scanning geometries in the craniocaudal (V_A) and mediolateral (V_B) directions. To recover the out-of-plane resolution, any view plane slicing the 3D CBUS (V_{CBUS}) image can be obtained from the spherical-weighted combination of the intensity values at any 3D voxel, given the complementary resolution of the orthogonal 3DUS images. [3]

The spatial resolution in the original orthogonal 3DUS and CBUS images were evaluated with cross-sectional 2DUS image slices ($N=3$) acquired for each wire, [Fig. 1(a)] which depicts the 2D intensity distribution [Fig. 1(b)]. The full width at half maximum (FWHM) was measured from the line spread profiles of the wires as a function of wire angle, which corresponds to the view angle from entirely in-plane (0° or parallel to the scan plane) to out-of-plane (90° or orthogonal to the scan plane) scan directions. The mean FWHM and range were determined and regression analysis was performed to evaluate the relationship between FWHM and wire angle.

Results: The measured FWHM resolution across all wires resulted in a mean and range of 1.05 (0.68–1.39) mm, 1.07 (0.58–1.54) mm, and 0.90 (0.79–0.98) mm for V_A , V_B , and V_{CBUS} 3DUS images, respectively. In comparison with the original orthogonal 3DUS images, the range in the CBUS image was more constrained, which demonstrates that the CBUS image recovers out-of-plane resolution, from its complementary in-plane resolution. Linear regression analysis resulted in R^2 values of 0.80 and 0.99 for V_A and V_B 3DUS images, showing a high correlation between FWHM and wire angle across original orthogonal 3DUS images.

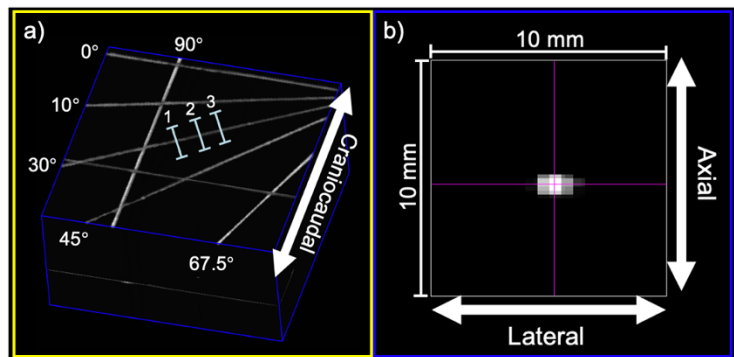
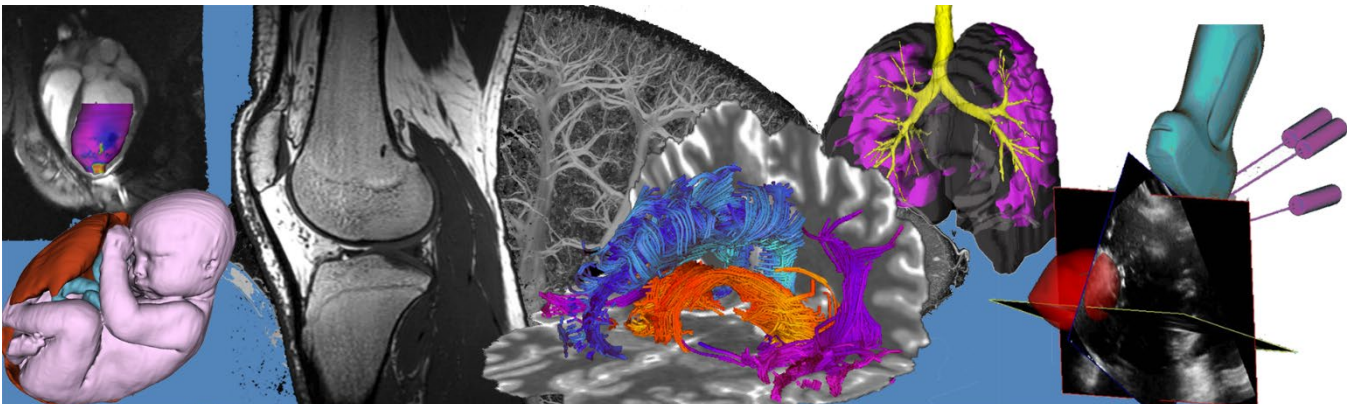


Fig. 1: a) Orthogonal 3DUS image with a craniocaudal acquisition direction. Blue lines show the location of cross-section 2D US image slices ($N=3$) for one wire. b) Cross-section 2D US image slice for resolution analysis.

Conclusions: Our results show that 3D CBUS with orthogonally acquired 3DUS images improves resolution uniformity by recovering some out-of-plane resolution in the US elevational direction. Our orthogonal 3DUS acquisition and CBUS combination approach shows potential to enable high-resolution whole breast 3DUS imaging with any linear array US transducer in clinical practice.

[1] S. H. Kim, H. H. Kim, W. K. Moon. Korean J. Radiol., 21(4) 15–24, 2020. [2] A. Fenster, J. Bax, D. Tessier, and C. Park, US Provisional Patent: 63/335,857, 2022. [3] C. K. Park, T. Trumpour, et al. Medical Imaging 2022: Ultrasonic Imaging and Tomography. 12470–3, 2022.

Pitch/Poster Session 2: Neuroimaging Abstracts



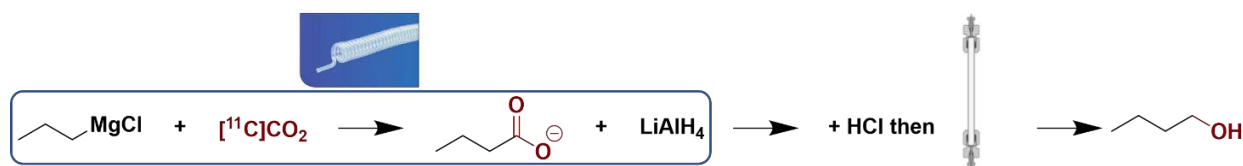
Optimizing [^{11}C]butanol radiosynthesis and positron emission tomography image analysis for assessing the blood-brain barrier integrity in Alzheimer's disease

Olujide Oyeniran^{a,b}, Michael S. Kovacs^{a,b}, Udunna Anazodo^{a,c} and Justin W. Hicks^{a,b}

^aLawson Health Research Institute Cyclotron and Radiochemistry Facility, ^bMedical Biophysics, Western University and ^cMontreal Neurological Institute, McGill University, Montreal, QC, Canada,

Introduction: Alzheimer's disease (AD), the most common cause of dementia, is a progressive neurodegenerative disorder and in Canada, 1 in 14 adults aged 65 and above are diagnosed with AD. Definitive diagnosis of AD is limited, and studies have shown its pathology starts decades before clinical manifestation. Alteration in the blood-brain barrier (BBB) integrity has been identified as one of the earliest pathological processes in AD. Positron emission tomography (PET) using [^{11}C]butanol and [^{15}O]water radiotracers is the gold standard quantifiable imaging modality for assessing the BBB integrity in living humans by measuring its permeability through cerebral blood flow (CBF) changes. [^{15}O]water has been synthesized and Health Canada approved for production at the Lawson facility and has been used to study BBB permeability and cerebral blood flow¹. However, the best available method for [^{11}C]butanol radiosynthesis² is difficult to automate on commercially available and widely used automated synthesizers. Therefore, the objective of this study is to optimize [^{11}C]butanol radiosynthesis and validate for Health Canada approval for routine production.

Method: [^{11}C]butanol radiosynthesis from [^{11}C]CO₂ and propylmagnesium chloride is dated back to the 1980s. The process has been modified using a solid-phase extraction (SPE) batch procedure in 2020 by Waterhouse et al.² Considering the short half-life of carbon-11 (20.4 min), the synthesis time needs to be shortened which is not usually obtained in the batch approach. We employed a flow chemistry approach to reduce synthesis time and increase efficiency. The synthesis was done using a GE TRACERlab Fx C synthesizer. [^{11}C]CO₂ generated from the ¹⁴N(p, α)¹¹C nuclear reaction was passed through a polyethylene tube impregnated with propylmagnesium chloride. The resultant butanoic acid was reduced using LiAlH₄ while simultaneously flushing the tube's contents into the reaction vessel to quench the reaction. [^{11}C]butanol was isolated from the reaction mixture using high-performance liquid chromatography (HPLC) with phosphate-buffered saline, ready for injection without further modification. Quality control was performed following conventional methods.



Results: [^{11}C]CO₂ activity was well captured on the loop and there is sufficient time for carboxylation as it flowed through the loop. Also, the loop provided a large surface area for further reduction by LiAlH₄ and allowed for a shorter reaction time (25+2min vs 37±5min) with about 10% yield. Analytical HPLC reveals [^{11}C]butanol was produced in sufficient time with a purity of about 95% which is within specifications. Purification by HPLC took as long as the SPE approach but had the added benefit of reducing ethanol content of the final formulation.

Conclusion: [^{11}C]Butanol has been prepared in yield and quality sufficient for preclinical imaging using a widely available commercial automated synthesizer. Further optimization to increase yield and prepare for clinical use is underway. Using HPLC for purification rather than an SPE cartridge is counter to current trends in radiochemistry but the reduction of ethanol from the final product is advantageous as ethanol will confound the [^{11}C]butanol image interpretation. Future work will use the optimized [^{11}C]butanol to evaluate BBB permeability using the dual tracer in a porcine model where BBB changes are effected by aquaporin inhibition and implementing a non-invasive technique for analysis of BBB PET using image-derived input functions (IDIF)³.

References: 1) Cockburn et al. *Nucl Med Commun*, 2020, 41, 1100 – 5. 2)Waterhouse et al. *Applied Radiation and Isotopes*. 2020;159:109078. 3) Dassanayake et al. *Neuroimage*. 2022;256:119261.

An interpretable Alzheimer's disease dementia risk prediction model

Mason Kadem¹, Thomas E. Doyle^{1,2}, and Michael D Noseworthy^{1,2,3}

¹School of Biomedical Engineering, McMaster University, Hamilton, ON, Canada; ²Electrical and Computer Engineering, McMaster University, Hamilton ON Canada; ³Department of Radiology, McMaster University, Hamilton, ON, Canada.

Introduction: Differentiating mild cognitive impairment (MCI_{stable}) from preclinical Alzheimer's disease (MCI_{AD}) that eventually progresses to Alzheimer's disease dementia (ADD) is vital worldwide. Despite genetic markers, such as APOE, we have yet to identify patients at the highest risk of developing ADD¹, which could reduce the onset and burden of the disease³. To assess the landscape of existing ADD prediction models, we searched PubMed for "(Alzheimer's Disease Dementia) AND (prediction OR predict) published between Jan. 1, 2012 and Nov.1, 2022. Based on this search, we have identified three key limitations in existing ADD prediction models: 1) models are based on traditional statistics, 2) ML models are based on difficult to acquire, invasive and costly data⁴, and 3) ML models often lack interpretability^{5,6}. In summary, rapid, accurate, low-cost, easily accessible, non-invasive, interpretable and early clinical evaluation of ADD is critical at this time. To support healthcare decision-making and planning, this research leverages the Alzheimer's Disease Neuroimaging Initiative database and a mathematical modelling approach based on supervised machine learning to identify predictive markers of ADD and patients at the highest risk of developing ADD.

Methods: Data for model development included non-invasive biomarkers, imaging, genetic, cognitive testing, lifestyle and health history tabular data (43 features). Experiment 1 classified controls (n=121) vs ADD (n = 53), while Experiment 2 classified MCI_{stable} (n = 41) vs MCI_{AD} (n = 25) using an additional independent test set with MCI_{stable} (n = 26) vs MCI_{AD} (n = 17). Each experiment had two models (complex and interpretable). For both experiments, we ranked the top 10 features according to their average feature importance accumulated from the XGBoost model, using random splits in a ratio of 7:3, over 100 repetitions with varied number seeds (0-99). The complex model performances, for both experiments, were evaluated with fivefold stratified cross-validation for 100 iterations. The interpretable models were created using a single 7:3 split and evaluated on the validation set (Exp 1; ADNI 3) and an independent test set (Exp 2; ADNI 2) .

Results: We implemented a supervised XGBoost classifier with the objective of identifying high risk factors and patients at the highest risk of ADD. Machine learning tools selected two features (i.e., Modified Preclinical Alzheimer Cognitive Composite and Functional Assessment Questionnaire (Exp 1); Delayed Total Recall Alzheimer's Disease Assessment Scale (Exp 2). Using the selected features, the XGBoost complex model achieved cross-validation accuracy of 98% and 80%, for Exp1 and Exp2, respectively. The interpretable models for each experiment maintained performance (sensitivity and specificity above 90%) while improving their interpretability. The models can reliably predict patient diagnosis (Exp 1) and prognosis (Exp 2). Interestingly, in Exp 2, the test set's performance (see table) was comparable to the validation set, suggesting the algorithm identifies the major indicators of MCI-to-ADD progression.

Performance metrics of the interpretable model on an independent test set (ADNI 2)				
	Precision	Recall	F1 score	Support
MCI _{stable}	96	88	92	26
MCI _{AD}	84	94	89	17
Accuracy			98	43
Macro avg	90	91	90	43
Weighted avg	90	91	91	43

Conclusion: Our work extends beyond the identification of high-risk factors for ADD risk, providing an intuitive explanation of the decision process behind assessing risk. We identified data-driven decision routes with absolute thresholds for key clinical features with performances above 90%. Finally, the most prominent predictors are non-invasive and easily collected. This study highlights the performance and interpretability advantages of gradient boosted ensembles over linear models for heterogeneous tabular data, notably in predicting ADD risk.

References: ¹Palmqvist, S. *et al. Nat. Med* (2021), ²Kivipelto, M. *et al. Lancet Neurol* (2006); ³World Health Organization (2021); ⁴Palmqvist, S. *et al. JAMA Neurol* (2014); ⁵Lundberg *et al. Nat Biomed Eng* (2018); ⁶Lundberg *et al. Nat Mach Intell* (2020);

Simultaneous estimation of a model-derived input function for quantifying cerebral glucose metabolism with [^{18}F]FDG positron emission tomography

Lucas Narciso¹, Praveen Dassanayake^{1,2}, Linshan Liu¹, Samara Pinto³, Uduinna Anazodo^{1,4}, Andrea Soddu⁵, Keith St Lawrence^{1,2}

¹Lawson Health Research Institute, London, Ontario; ²Department of Medical Biophysics, Western University, London, Ontario; ³PUCRS, Porto Alegre, Brazil; ⁴Neurology and Neurosurgery, MNI, McGill University, Montreal, Quebec; ⁵Department of Physics and Astronomy, Western University, London, Ontario

Introduction: Measuring the cerebral metabolic rate of glucose (CMRGlu) by dynamic PET imaging with 2-deoxy-2- ^{18}F fluoro-D-glucose (^{18}F]FDG) has proven valuable for assessing cerebral energy metabolism in neurological diseases [1]. Additionally, quantifying the kinetics of ^{18}F]FDG has been stimulated by a growing interest in understanding how CMRGlu is potentially affected by disease-related alterations in glucose delivery and phosphorylation [2]. Efforts to avoid invasive arterial sampling required for quantification include the simultaneous estimation (SIME) approach, which models the image-derived input function (IDIF) by a series of exponentials with coefficients obtained by fitting time activity curves (TACs) from multiple volumes-of-interest (VOI) [3]. Alternatively, we propose a SIME approach based on the irreversible two-tissue compartment model (2TCM) to extract a high signal-to-noise ratio model-derived input function (MDIF) from the whole-brain TAC. The purpose of this study is to implement the MDIF SIME approach in the analysis of human data. **Methods:** Retrospective data from neurologically healthy volunteers ($n = 18$) were used to extract kinetic parameters from dynamic ^{18}F]FDG PET data. VOIs were generated by means of clustering voxel TACs based on similarity by implementing a k -means clustering algorithm (Fig. 1A). Two venous samples collected during dynamic PET imaging (20-30-min and 45-60-min post-injection) were used as anchors. For comparison, an IDIF was extracted using the conventional SIME approach (i.e., series of exponentials). Voxelwise rate constants were estimated by including the net clearance rate constant of ^{18}F]FDG (i.e., K_i) from Patlak graphical analysis to simplify the fitting routine. **Results:** The MDIF method was superior in characterizing the first pass of ^{18}F]FDG (Fig 1B). The MDIF-to-IDIF area under the curve ratio was 1.05 ± 0.11 , resulting in good MDIF-IDIF agreement in CMRGlu (Fig. 1C). Fig. 1D shows average K_i images ($n = 18$) obtained by Patlak analysis using the MDIFs, as well as corresponding images of rate constants. Groupwise parametric images obtained with the MDIF showed the expected patterns. **Conclusions:** In this study we presented a SIME method based on the irreversible 2TCM to derive a high-quality input function. We showed that the MDIF approach can properly model the shape of the input function and requires fewer fitting parameters than the conventional IDIF.

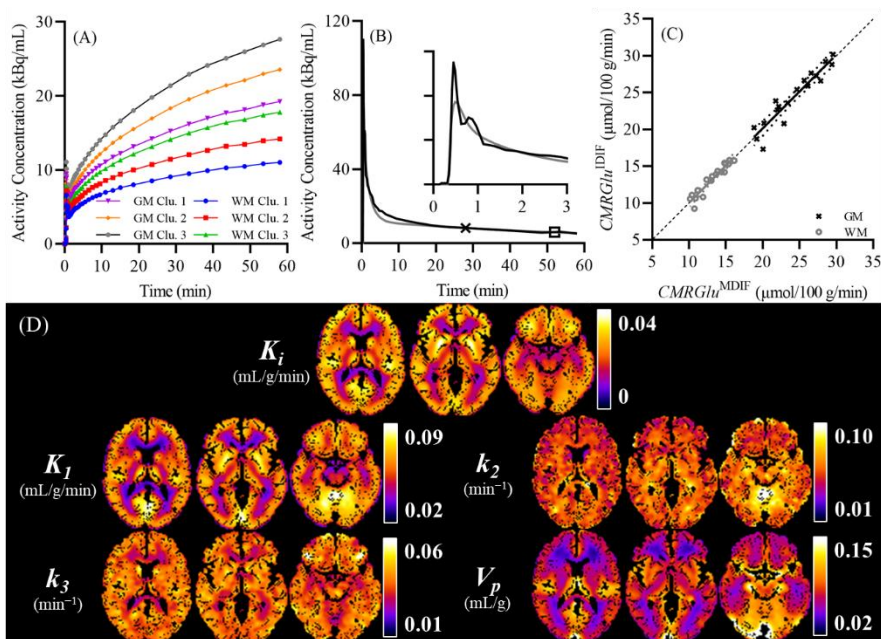


Figure 1. (A) TACs from the six clusters used to obtain the MDIF and IDIF from one representative subject. (B) SIME MDIF (black line) and IDIF (grey line) from the same subject shown in (A). The inset presents the first 3 min of the input functions. Venous samples are shown as the symbols. (C) Linear regression comparing CMRGlu estimates from IDIF and MDIF for total grey matter (GM; exes) and white matter (WM; circles) TACs extracted from healthy individuals ($n = 18$). Line-of-best fit is shown as a solid line alongside the 95% confidence interval (dotted lines). Average regression for GM had a slope of 1.00 ± 0.09 and an intercept of $0.1 \pm 2.1 \mu\text{mol}/100 \text{ g}/\text{min}$ ($R^2 = 0.89$, Pearson correlation coefficient $[\rho]$ of 0.94 , $p < 0.01$), respectively. Average regression for WM had a slope 1.01 ± 0.08 and an intercept of $-0.2 \pm 1.1 \mu\text{mol}/100 \text{ g}/\text{min}$ ($R^2 = 0.91$, $\rho = 0.95$, $p < 0.01$), respectively. The identity line is represented by the dashed line. (D) Groupwise ($n = 18$) K_i images obtained from the Patlak graphical analysis, alongside K_1 , k_2 , k_3 , and V_p images from the fitting routine. All images were normalized to the MNI space.

References: [1] Johnson et al. Brain imaging in Alzheimer disease. Cold Spring Harb. Perspect. Med., v2(4), a006213–a006213. 2012. [2] Hermanides et al. Metabolic derangements are associated with impaired glucose delivery following traumatic brain injury. Brain. v144(11), 3492–3504. 2021. [3] Feng et al. Noninvasive input function acquisition and simultaneous estimations with physiological parameters for PET quantification: a brief review. IEEE Trans. Radiat. Plasma Med. Sci. v4(6). 676–683. 2020.

CT Perfusion Monitored Selective Brain Cooling for Acute Brain Injuries

Olivia L.H. Tong^{1,2,3}, Kevin J. Chung^{1,2,3}, Jennifer Hadway¹, Laura Morrison¹, Lise Desjardins¹, Susan Tyler¹, Marcus Flamminio¹, Lynn Keenlside¹, Ting-Yim Lee^{1,2,3}

¹Imaging Program, Lawson Health Research Institute, London, ON, Canada; ²Robarts Research Institute, London, ON, Canada; ³Department of Medical Biophysics, The University of Western Ontario, London, ON, Canada

INTRODUCTION: Severe brain injuries from stroke and traumatic brain injury (TBI) pose a substantial public health burden. These injuries are not only acute conditions but also chronic diseases with long-term consequences such as late-onset neurodegeneration.¹ To minimize long-term consequences, therapeutic hypothermia has been proposed to prevent secondary brain injuries after the initial insult.² While conventional whole-body cooling has severe adverse effects (e.g., coagulopathy, cardiac problems, and lung infection)², selective brain cooling could limit these complications. However, clinical application is limited by the lack of optimal delivery methods and unknown treatment parameters. Survival after large vessel occlusion stroke and severe head traumas is critically dependent on cerebral blood flow (CBF).^{1,3} We aim to determine the relationship between CBF as determined by CT Perfusion (CTP) and brain cooling in acute brain injuries. We hypothesized that CTP could guide brain cooling, delivered by our in-house developed Vortex tube IntraNasal Cooling Instrument (VINCI), to provide a personalized treatment plan for maximal benefit in severe stroke and TBI.

METHODS: Severe stroke (n = 12) or severe TBI (n = 12) were induced in pigs which were then assigned to treatment (n = 16) and normothermia/control groups (n = 8). The treatment group had brain cooling with VINCI at target temperature (2-5°C from normothermia) for 17-h before rewarming at 0.5°C/h to normothermia, as suggested by small animal hypothermia studies.² Throughout the study, the vitals including intracranial pressure (ICP) and CBF were recorded. To assess the utility of CTP, CBF was compared to vitals, blood biomarker (neurofilament light chain, NfL, at 4-hour intervals to evaluate neuronal damage), and histology at sacrifice (TTC infarct staining for stroke only).

RESULTS: Independent of the mode of injury, severe global hyperemia (high CBF) before rewarming was associated with either abnormal vitals (i.e., high ICP and low blood pressure) or severe neuronal damage. Global hyperemia preceded significant changes in physiological variables from baseline. When severe hyperemia was absent, subacute injuries were averted suggesting hyperemia could be a marker of effective neuroprotection from cooling. This was further corroborated by (1) predicted lesion volume by CTP at target temperature matched the true infarct by histology (severe stroke), and (2) NfL levels remained constant (severe TBI).

CONCLUSIONS: Our findings support the utility of CTP for selective brain cooling. Global hyperemia during cooling could be an early manifestation of poor treatment outcomes in acute brain injuries. In future, VINCI-enabled brain cooling could be guided by CTP imaging as a neuroprotective therapy for brain injuries. This work lays the groundwork toward individualized selective brain cooling.

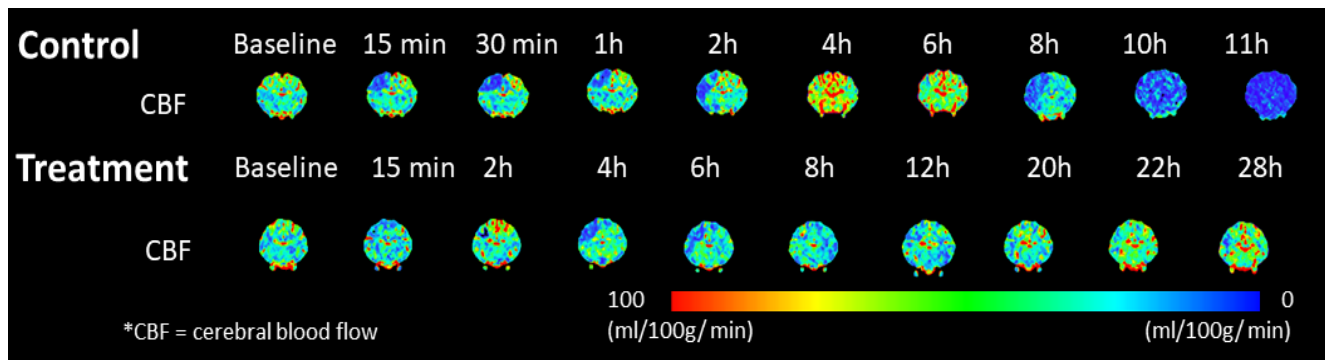


Figure 1. Examples of CBF imaging by CTP at different time points following stroke. The brain was not viable by 11h in control, but the animal survived throughout the 28-hour study in the treatment group.

¹Mass et al. (2022) *Lancet Neurology*. ²Yenari et al. (2012) *Nat. Neurosci*. ³Lyden et al. (2021) *Stroke*.

Anatomical features predicting outcome from stereotactic laser amygdalohippocampotomy

Chris Zajner¹, Facial Isbaine², Nealen Naxpati², Robert E. Gross², Jonathan Lau^{1,3}

¹ Imaging Research Laboratories, Robarts Research Institute, Western University, London, Canada.

² Departments of Neurosurgery and Neurology, Emory University School of Medicine, Atlanta, Georgia.

³ Department of Neuroscience, Schulich School of Medicine and Dentistry, Western University, London, Canada.

Introduction: Temporal lobe epilepsy (TLE) is the most common adult form of epilepsy, and Mesial Temporal Sclerosis (MTS) is its most common subtype. Stereotactic laser amygdalohippocampotomy (SLAH) is a novel procedure which has recently been shown to be comparable in effectiveness in the treatment of TLE to traditional temporal lobectomy procedures (Youngerman et., 2020). Optimal operative ablation location and extent is uncertain, as are the neuroanatomical features guiding successful ablations. The lateral mesencephalic sulcus (LMS) is one such landmark that is frequently used during SLAH. To date, the volume of ablation has been found to correlate with functional outcome (Satzner et., 2021), yet other characteristics remain unknown. SLAH technology has recently been approved for use in Canada, although experience across the country remains overall limited. The objective of this retrospective study was to advance the understanding of the potential role of SLAH for MTS, by investigating the morphometric features of pre and post surgical MRI scans in relation to post-surgical epilepsy freedom.

Methods: Patients treated with SLAH for MTS at Emory University between 2011 and 2019 were considered in this retrospective study. Post-procedure T1 MRI scans of patients were used to create manual segmentations of the ablation region of each patient. This was performed by two independent raters who then determine ablation volumes, location, and characteristics. Ablations were assessed in relation to 1) whether they crossed the coronal plane of the lateral mesencephalic sulcus (LMS) as defined in a T1-MRI validated anatomical fiducials protocol (Lau et al. 2019), 2) the extent to which the ablation extended posterior to the LMS, and 3) the extent of ablation of the uncus. SLAH patients were analyzed with reference to their categorization with 12-month Engel classification score. Wilcoxon ranked-sign test was performed for each variable of interest between groups of patients with Engel score 1 versus Engel score 2-4.

Results: The cohort consisted of 65 patients (36 female, 29 male) who underwent SLAH for MTS, 59 of whom were followed up at 12 months for Engel classification. Distance of ablation past the coronal plane of the LMS was weakly associated with better surgical outcome, with Engel class 1 patients having an average of $6.32 \pm 4.16\text{mm}$, and Engel class 2-4 with $7.93 \pm 3.75\text{mm}$ ($p = 0.099$). Ratio of ablations extending posterior to the LMS was 0.82 (SD = 0.39) in Engel 1 patients, and 0.90 (SD = 0.30) in Engel 2-4 patients ($p = 0.370$). Volume of ablation showed little correlation with 12-month seizure freedom average ablation of Engel class 1 = $6064 \pm 2128\text{mm}^3$, Engel class 2-4 = $5828 \pm 3031\text{mm}^3$, and no significant difference with Wilcoxon ranked-sign test ($p = 0.239$). Ablation of the uncus showed a strong association with better surgical outcome, with ratio of uncus ablation for Engel class 1 at 0.71 (SD = 0.31), and Engel class 2-4 at 0.37 (SD = 0.36); $p < 0.001$.

Conclusions: Larger ablation alone was not associated with better surgical outcomes. Ablation of the uncus was shown to result in better outcomes. Contrary to current practice, extension of SLAH ablation posterior to the lateral mesencephalic sulcus did not demonstrate improved post-operative outcomes.

References:

Lau, J. C., Parrent, A. G., Demarco, J., Gupta, G., Kai, J., Stanley, O. W., Kuehn, T., Park, P. J., Ferko, Satzer, D., Tao, J. X., & Warnke, P. C. (2021). Extent of parahippocampal ablation is associated with seizure freedom after laser amygdalohippocampotomy. *Journal of Neurosurgery*, 135(6), 1742-1751.
Youngerman, B. E., Save, A. V., & McKhann, G. M. (2020). Magnetic resonance imaging-guided laser interstitial thermal therapy for epilepsy: systematic review of technique, indications, and outcomes. *Neurosurgery*, 86(4), E366-E382.

Imaging ocular dominance columns in human brain at high magnetic fieldAtena Akbari ^{a,b}, Joseph S Gati ^a, Peter Zeman ^a, Brett Liem ^a, and Ravi S Menon ^{a,b}^a Centre for Functional and Metabolic Mapping, Robarts Research institute, The University of Western Ontario, London, ON, Canada ^b Department of Medical Biophysics, The University of Western Ontario, London, ON, Canada**Introduction**

The neurons located in the striate cortex preferentially respond to the input from one eye or another, forming a stripy pattern (columns) called the ocular dominance columns (ODCs) [1]. These structures have been imaged previously in-vivo using functional magnetic resonance imaging (fMRI) [2]. Most of these studies have relied on oxygenation-level-dependent (BOLD) contrast, however, BOLD fMRI suffers from low signal spatial specificity. In this study we examined the feasibility of employing a fMRI contrast with higher signal spatial specificity called vascular space occupancy (VASO) [3].

Method

VASO and BOLD fMRI images were acquired on a head-only 7T scanner (MAGNETOM 7T Plus, Siemens) with the following parameters: $TR_2/TE/TI_2 = 3294/21.8/2379$ ms, and 0.8 mm isotropic resolution. Five participants with normal or corrected-to-normal vision participated in this study after giving written consent form approved by the Human Subjects Research Ethics Board at the University of Western Ontario. A house-made MR compatible LCD goggles with the ability of viewing the visual stimulus monocularly and binocularly was used to present the stimulus to participants eyes. The visual stimulus was a flickering checkerboard interleaved with a grey screen presented in 22 blocks of each 30 second long. Motion correction and GLM statistics were performed using SPM12. Voxels with t-values above 3.1 corresponding to an uncorrected significance level of $p < 0.001$ were identified as the activated regions in both BOLD and VASO contrasts. A region-of-interest (ROI) was manually defined on V1, and ten equidistance layers were created in the ROI using LAYNII [4]. To identify the monocular columns, voxels from the right eye and left eye t-maps with t-value > 2.3 were identified as the right-eye-dominated and left-eye-dominated columns respectively. These binary masks were used to determine the response of the unstimulated eye to the stimulation of the other eye.

Results and Conclusion

Figure 1A shows the VASO and BOLD fMRI maps of ODCs overlaid on the inflated left hemisphere of one participant. Hot (cool) colour represents image voxels whose fMRI response was greater in magnitude during right (left) eye stimulation than during left (right) eye stimulation. Figure 1B and 1C depicts the fMRI responses to a monocular stimulation as a function of cortical depth. With VASO, the response of the unstimulated eye is smaller than that of the stimulated eye during monocular stimulation. However, with BOLD, both responses are similar in amplitude and trend across the cortical depths and columns. In summary, our results show that VASO better distinguishes the ODCs monocular responses compared to BOLD, likely due to its smaller cortical point spread.

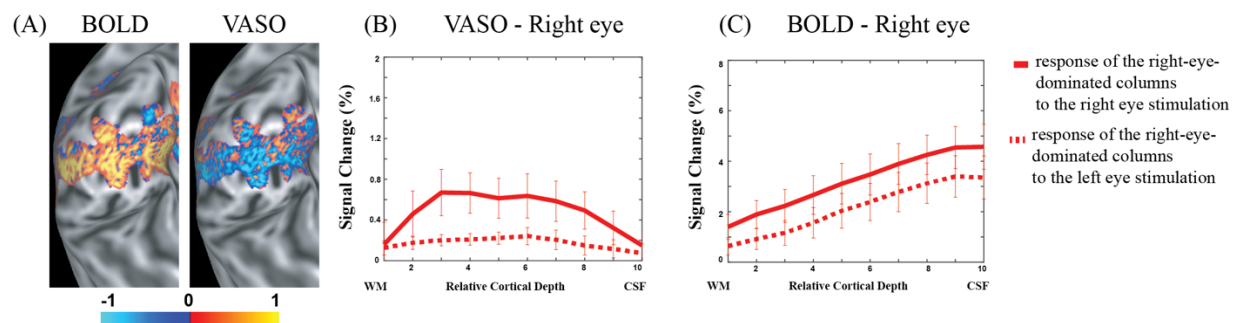


Figure 1. (A) BOLD and VASO ODCs maps overlaid on an inflated left hemisphere of one representative participant. (B) and (C) VASO and BOLD responses to a monocular stimulation as a function of cortical depth.

References

- [1] Hubel DH, Wiesel TN., 1968; 195:215–43. [2] Goodyear BG, Menon RS., 2001; 14:210–7. [3] Lu, Hanzhang, et al., 50.2 (2003): 263-274. [4] Huber, Laurentius Renzo, et al., 237 (2021): 118091.

Diffusion tensor imaging of glioma patients during radiotherapy on a 1.5T MRI-linear accelerator

Liam S. P. Lawrence,^a Rachel W. Chan,^b James Stewart,^b Mark Ruschin,^b Aimee Theriault,^b Sten Myrehaug,^b Jay Detsky,^b Pejman J. Maralani,^b Chia-Lin Tseng,^b Hany Soliman,^b Mary Jane Lim-Fat,^b Sunit Das,^c Greg J. Stanisiz,^{a,b} Arjun Sahgal,^b Angus Z. Lau^{a,b}

a. Medical Biophysics, University of Toronto, Toronto, Ontario. b. Sunnybrook Health Sciences Centre, Toronto, Ontario. c. St. Michael's Hospital, Toronto, Ontario.

Introduction: Diffusion tensor imaging (DTI) is potentially sensitive to the effects of the infiltrative brain cancer glioma on white matter.¹ Detection of infiltration could be used to inform radiotherapy targeting and adaptation on MRI-linear accelerators (MR-Linacs). We provide the first report of DTI in the brain on an MR-Linac. Our objective was to characterize the DTI parameter fractional anisotropy (FA) by comparing MR-Linac FA values to those of a 3T diagnostic MRI scanner and literature values at 1.5T and 3T.² Additionally, we sought to replicate previous studies which used DTI to detect tumour infiltration by comparing high- and low-grade tumours.¹

Methods: Forty-five patients with gliomas (grades 2-4) were treated with fractionated radiotherapy (40-60 Gy, 15-33 fractions). Ten patients were treated and imaged on 1.5T Elekta Unity MR-Linac and DTI was acquired weekly. On a 3T Philips Achieva ("MR-sim"), thirty-five patients were scanned at treatment planning, and weeks 2, 4, and 10 after radiotherapy start. MR-Linac DTI: TRSE EPI, 30 directions at $b=500$ s/mm², 3 $b=0$ images, TR/TE=5750/93 ms, voxel size=3.0×3.0×3.0 mm³, FOV=240×240×132 mm³, $\Delta/\delta=68.5/14.8$ ms, $G_{max}=15$ mT/m). MR-sim DTI: PGSE EPI (10 directions at $b=1000$ s/mm², 1 $b=0$ image, TR/TE=9145/108 ms, voxel size=1.5×1.5×3.0 mm³, FOV=240×192×177 mm³, $\Delta/\delta=53.0/17.6$ ms, $G_{max}=40$ mT/m). The ICBM-DTI-81 atlas was warped to subject space to create white matter (WM) regions. The peritumoural zone (PTZ) was defined as the clinical target volume excluding the gross tumour volume. Segmentation with ANTs was used to create contralateral "whole WM". Cerebrospinal fluid was excluded from all regions. Only voxels receiving <20 Gy based on the radiation treatment plan were included in the white matter regions to ensure FA changes did not result from radiation effects. Mean FA values over regions (**Figure 1A**) were compared with a linear model (effects: cohort, region). Within-subject coefficients of variation (wCVs) were calculated from repeated measures of mean FA. Changes in FA were evaluated by comparing with the repeatability coefficient $\%RC=2.77 \times wCV$.

Results: Compared to the MR-sim, MR-Linac FA values were lower ($p = .007$), possibly because of the lower b-value; the wCVs were comparable (**Figure 1B**). In 7 of 16 (44%) high-grade MR-sim patients, FA changed within the PTZ at week 4 relative to treatment planning (**Figure 1C**). Five high-grade patients had repeated scans on the MR-Linac; 1 of 5 (20%) showed significant change, at week five relative to week one. The low-grade glioma patients did not show changes except for one, due to changes in edema.

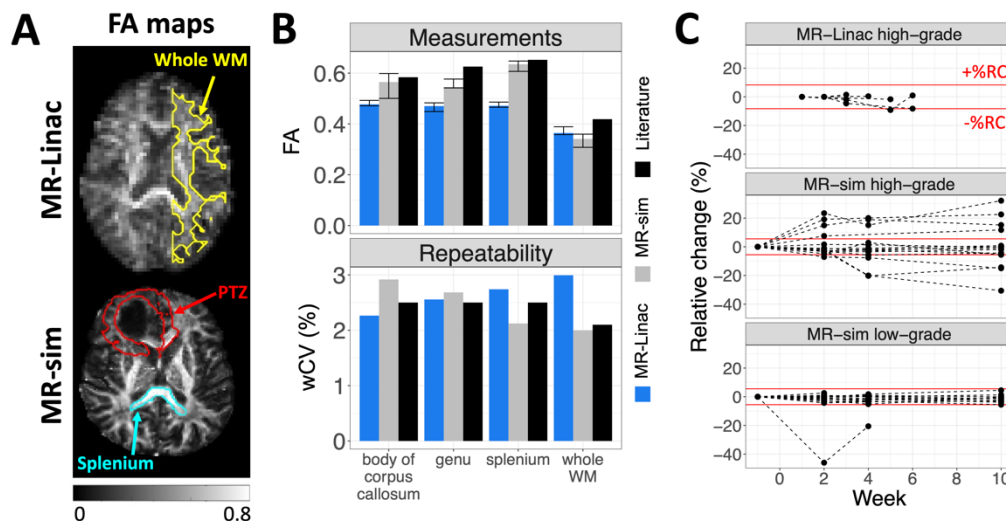


Figure 1. (A) MR-Linac and MR-sim FA maps. (B) FA values and repeatability. (C) Relative FA changes.

Conclusions: Compared to a 3T scanner, 1.5T MR-Linac DTI showed comparable repeatability but lower FA. MR-Linac DTI is sensitive to peritumoural changes that may reflect tumour infiltration. Future work will include investigating potential relationships between DTI changes and patterns of tumour recurrence.

References: 1. Price et al., *Clin Radiol*, 2003. 2. Grech-Sollars et al., *NMR Biomed*, 2015.

Sensitivity of Cerebral Blood Flow and Oxygenation to High-Intracranial Pressure

S. Karagulleoglu-Kunduraci*, M. Diop

Department of Medical Biophysics, Western University, Canada

Presenting Author Email Address: skaragul@uwo.ca

Introduction: Premature infants born with extremely low birth weights are at a high risk of intraventricular hemorrhage (IVH), partly because the premature brain is prone to hemodynamic instabilities and poor cerebral autoregulation. The incidence of IVH is 15-20 percent in preterm infants born with very low birth weights (VLBW, 1500 g) and typically occurs within the first 72 hours of life, often leading to hydrocephalus which is an abnormal accumulation of cerebral spinal fluid (CSF) in the brain and can lead to high intracranial pressure (ICP) and subsequent brain injuries. Although methods such as Ultrasonography can be used to follow the progression of hydrocephalus, they only identify injuries that have already occurred rather than pathophysiological processes that suggest impending harm. This highlights the need for prognostic techniques to identify indicators of brain injury. Animal studies investigating the effect of rising ICP on cerebral perfusion have shown that cerebral blood flow (CBF) decreases when ICP increases. Further, it has been shown in neonates that CBF and oxygenation are reduced before CSF drainage but improve afterward. Therefore, the objective of the current study is to establish that CBF and brain oxygenation are sensitive to elevated ICP.

Methods: CBF and oxygenation were measured using a hybrid optical device that combines hyperspectral near-infrared spectroscopy (h-NIRS) and diffuse correlation spectroscopy (DCS). Preliminary experiments were conducted in five neonatal piglets (less than 8 days old), including an experimental (n = 3) and a control group (n = 2). Piglets were anesthetized. The h-NIRS and DCS probes were placed on the piglets' scalps, and ICP was increased in the experimental group by the continuous infusion of saline into the lumbar CSF region. Saline was infused with a syringe pump, ICP was monitored using a catheter connected to a fluid pressure line and, ICP was continuously recorded. In the experimental group, ICP was increased from baseline (normal ICP level: 10–15 mmHg) in 5 mmHg increments until it reached 25–40 mmHg. CBF and oxygenation measurements were continuously acquired with the DCS and h-NIRS, respectively. Measurements were used to compute changes in CBF and deoxy- and oxy-hemoglobin by applying approaches described in our previous reports. The time course of the mean changes in Hb and HbO₂ were calculated for each ICP level and compared to the measured changes in ICP. Linear regression and Pearson correlation were used to determine if HbO₂, Hb, and ICP are correlated. The same approach was also applied to investigate the correlation between CBF and ICP.

Results: As expected, there was no change in Hb, HbO₂, and CBF in the absence of changes in ICP (i.e., at the baseline ICP [5-7 mmHg]) for the control group. When ICP increases, Hb increases while HbO₂ and CBF decreases. Figure 1 shows that ICP and Hb have a strong positive correlation ($p < 0.05$, $r > 0.9$), while HbO₂ and CBF have a strong negative correlation with ICP ($p < 0.05$, $r < -0.9$).

Conclusion: The goal of this work was to establish that CBF and brain oxygenation are sensitive to elevated ICP. Our preliminary results suggest that CBF, Hb, and HbO₂ are sensitive to increased ICP. Here we observed that by increasing ICP, Hb increases while HbO₂ and CBF decrease. Notably, increased ICP also correlated significantly with the shape of Hb, HbO₂, and CBF changes trace. This trend could be explained by compress the brain due to the high ICP, which leads to compromised CBF and reduced cerebral oxygenation.

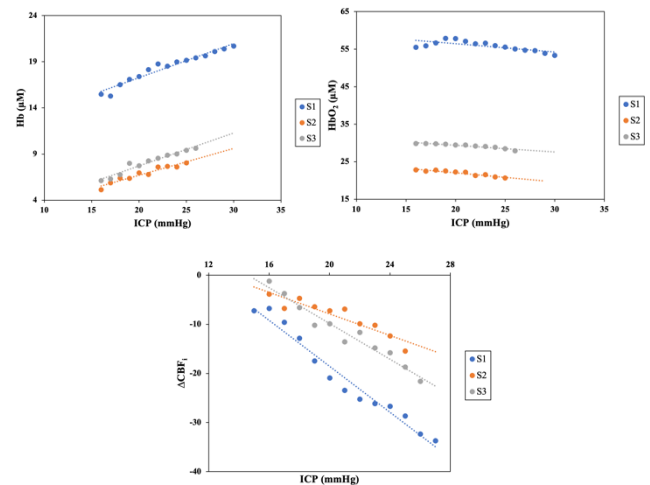
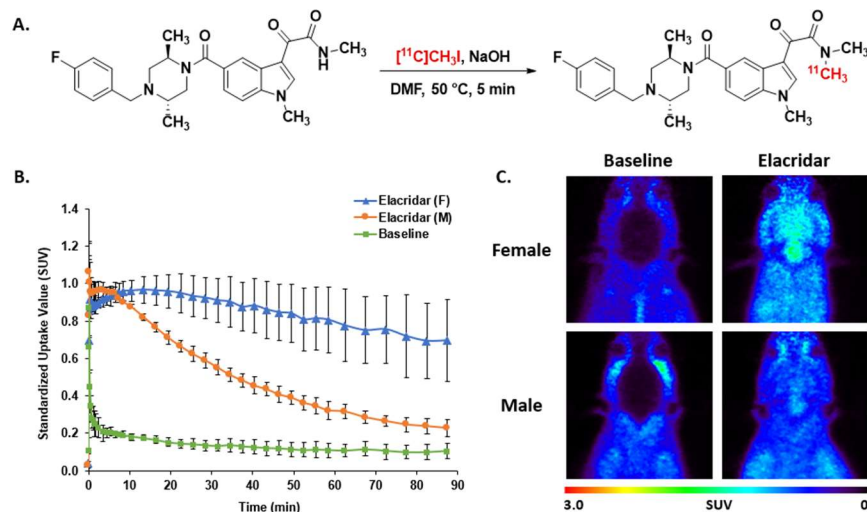


Figure 1: ICP correlation with Hb, HbO₂, and ΔCBFi for the experimental group (Subjects: S1, S2 and S3). Dash lines are linear regressions; $R^2 > 0.9$ and $p < 0.05$.

Effects of Drug Efflux and Sex Differences on the Novel p38 MAPK Radiotracer [¹¹C]SCIO-469Melissa Chassé^{a,b} and Neil Vasdev^{a,b,c}^aInstitute of Medical Science, University of Toronto. ^bAzrieli Centre for Neuro-Radiochemistry, Centre for Addiction and Mental Health. ^cDepartment of Psychiatry, University of Toronto.

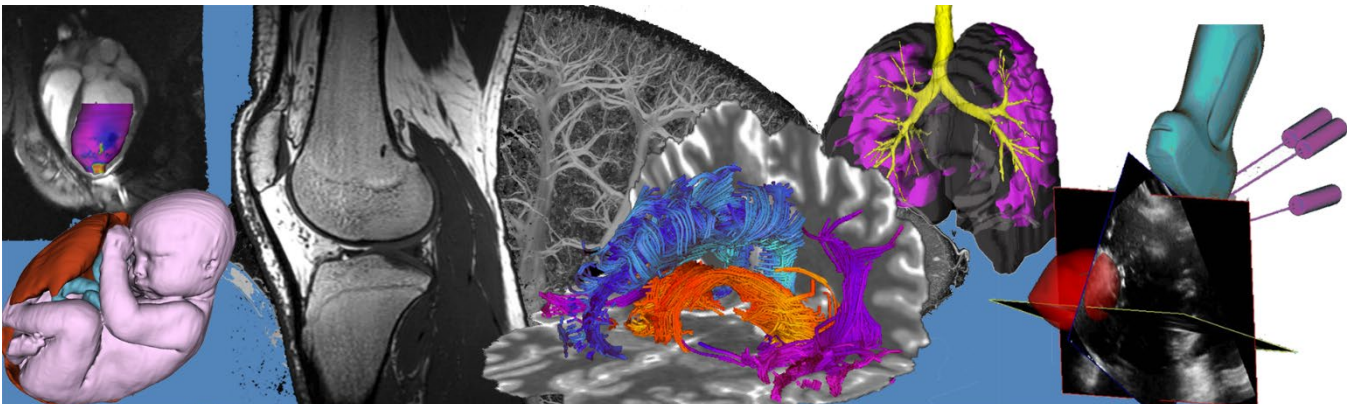
Introduction. Stress activated kinases are of interest for treating neurodegenerative disease due to their involvement in pro-inflammatory signaling and synaptic dysfunction. Clinical and preclinical evidence suggest that the p38 mitogen-activated protein kinase (MAPK) is a druggable target for several neurodegenerative conditions, including Alzheimer's disease, Parkinson's disease, and amyotrophic lateral sclerosis. Positron emission tomography (PET) imaging is a useful tool to guide drug discovery efforts through the *in vivo* evaluation of biodistribution, pharmacokinetics, metabolism, and target engagement of biologically active molecules. In this study, we report the first attempt to develop a PET radiotracer for imaging p38 MAPK through the synthesis and biological characterization of a carbon-11 labeled p38 α/β inhibitor, SCIO-469 (**Figure 1A**). **Methods.** [¹¹C]SCIO-469 was synthesized through reaction of the desmethyl precursor with [¹¹C]CH₃I in a solution of 300 μ L anhydrous dimethylformamide and 10 μ L 3 M sodium hydroxide, which was heated to 50 °C for 5 min. Preclinical PET studies were performed in healthy adult Sprague-Dawley rats at baseline ($n = 4$) and after pre-treatment with 5 mg/kg elacridar 30 min prior to radiotracer injection ($n = 6$). An MDCK-MDR1 assay was performed to evaluate human P-glycoprotein (P-gp) drug efflux substrate status. Further imaging studies in elacridar pre-treated rodents included blocking studies with \sim 7.5 mg/kg VX-745 ($n = 4$), and displacement studies with \sim 0.3 mg/kg SCIO-469 administered 20 minutes into the scan ($n = 4$). *In vitro* digital autoradiography (ARG) was performed at K_d concentration (9 nM) at baseline, self-block (10 μ M), or VX-745 block (10 μ M) in 10 μ m thick fresh-frozen rodent brain tissue. Radiometabolites in rodent plasma and brain homogenate at 40 min post-injection will be analyzed by column-switching HPLC. **Results.** [¹¹C]SCIO-469 was reliably synthesized by methylation with non-decay corrected radiochemical yields of $3.1 \pm 0.7\%$, molar activities of 39 ± 13 GBq/ μ mol, and $>99\%$ radiochemical purity. Preclinical PET imaging in rodents revealed a low baseline brain retention of \sim 0.2 standardized uptake values (SUV) (**Figure 1B, 1C**). Pre-treatment with the P-gp inhibitor elacridar enabled [¹¹C]SCIO-469 to pass the blood-brain barrier (>1.0 SUV), with distinct sex differences in washout kinetics. An MDCK-MDR1 assay suggests that SCIO-469 is likely to be a substrate for human P-gp, in addition to the rodent isoform. Neither blocking studies with VX-745, nor displacement studies with SCIO-469 were able to displace the observed brain uptake in elacridar-pretreated rodents. ARG confirmed the non-displaceable nature of [¹¹C]SCIO-469, with self-blocking and VX-745 blocking only decreasing the total signal by $12.9 \pm 8.8\%$ and $2.66 \pm 2.1\%$ in healthy controls (C57bl/6), and $29.3 \pm 2.7\%$ and $26.7 \pm 12\%$ in amyloid positive transgenic mouse (Tg2576) tissue. **Conclusions.** This study is the first reported attempt to develop a PET tracer for imaging p38 MAPK. While [¹¹C]SCIO-469 exhibits significant non-displaceable binding, it remains an interesting case study on the effects of drug efflux transporters and sex differences in radiotracer development. Further efforts to develop radiotracers for p38 MAPK should explore different structural classes of p38 inhibitors to assess binding properties and P-gp affinity.



sex differences in radiotracer development. Further efforts to develop radiotracers for p38 MAPK should explore different structural classes of p38 inhibitors to assess binding properties and P-gp affinity.

Figure 1. A) Radiolabeling of [¹¹C]SCIO-469. B) Whole brain time-activity curves after [¹¹C]SCIO-469 injection comparing male and female brain uptake at baseline ($n = 3$) and in elacridar pre-treated rats (5 mg/kg, $n = 3$). C) Representative PET summation images (0-60 min).

Oral Session 3: Hyperpolarized MR Imaging Abstracts



Hyperpolarized Chemical Exchange Saturation Transfer (HyperCEST) Maximization of Cucurbit[6]uril Imaging Biosensor in Blood for 3.0 T Clinical MRI

Viktoriia Bataruchuk^{1,2}, Vira Grynko^{2,3}, Yurii Shepelytskyi^{1,2}, Hannah Aalto⁴, Joseph Deschamps⁴, Iulian C. Ruset⁵, Mitchell S. Albert^{1,2,6}

¹Chemistry Department, Lakehead University, Thunder Bay, ON, Canada, ²Thunder Bay Regional Health Research Institute, Thunder Bay, ON, Canada, ³Chemistry and Materials Science Program, Lakehead University, Thunder Bay, ON, Canada, ⁴Applied Life Science Program, Lakehead University, Thunder Bay, ON, Canada, ⁵Xemed LCC, Durham, New Hampshire, USA, ⁶Northern Ontario School of Medicine, Thunder Bay, ON, Canada

Introduction: Hyperpolarized (HP) ^{129}Xe chemical exchange saturation transfer (HyperCEST) MRI is a promising technique that may potentially be used for high-resolution molecular imaging of specific biosensors^{1,2}. A biosensor is a molecular agent which enables investigation of biological and pathological processes in living systems. Cucurbit[6]uril (CB6) is a supramolecular cage molecule that reversibly encapsulates HP ^{129}Xe atoms and has been previously studied as a potential biosensor imaging agent³. There were no previous studies, however, for maximization of the HyperCEST effect by optimization of the saturation pre-pulse trains, albeit *in vivo* detection of the CB6 within the vasculature of a living rat, has been investigated^{4,5}. In the present work, we

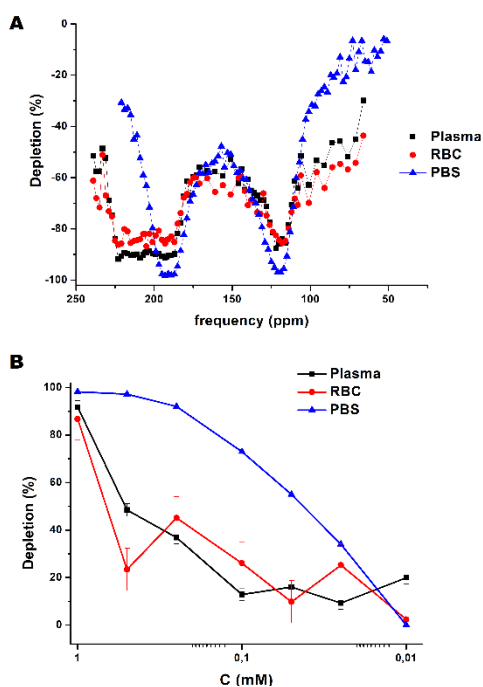


Figure 1. (A) HyperCEST depletion spectra for 1mM CB6 and (B) its dependence on the CB6 concentration after application of block pulses.

demonstrate the optimum saturation conditions and studied the effect of different depolarization (or saturation) pulses for maximization of the HyperCEST effect for CB6 in bovine blood.

Methods: The study was conducted using a clinical Philips Achieva 3.0T MRI scanner, equipped with a custom-built quadrature coil tuned to the ^{129}Xe resonance frequency (35.33 MHz). Naturally abundant ^{129}Xe (~26%) was polarized up to 56% using a XeBox-10E polarizer (Xemed LCC). Spectral data were acquired *in vitro* using a set-up similar to that used by Norquay et al⁶. 10 mL of sterile bovine blood was manually pumped through an exchange module perpendicular to the ^{129}Xe flow for ~3 sec. Samples of CB6 (1mM, 0.5mM, 0.25mM, 0.1mM, 0.05mM, 25uM, and 10uM) were prepared by adding a constant volume (1.33 mL) of CB6 in phosphate-buffered saline (PBS) solutions (0.075mM, 0.1875mM, 0.375mM, 0.75mM, 1.875mM, 3.75mM, 7.5mM) to blood (8.67 mL) in order to obtain 10mL samples. The various radiofrequency saturation pulses were used as in Grynko et.al⁷ along with a block pulse. Dynamic HyperCEST MRS was performed using the following parameters: TR/TE=10s/0.25ms, bandwidth (BW)=32kHz, 90° excitation pulse, 2048 sampling points.

Results: The HyperCEST effect in bovine blood was observed at approximately +118 ppm for both the plasma and red blood cell (RBC) resonances (Fig.1.A). The HyperCEST change with CB6 concentration for block saturation pulses in both the PBS and blood is shown in Fig.1.B. Similar dynamics were observed for all studied

pulses. The strongest HyperCEST effect of 0.1 mM CB6 in blood was 30% (plasma) and 25% (RBC) for the block depolarization pulse. The 3-lobe-sinc pulse shape demonstrated a slightly lower (~28%) HyperCEST effect, while the other two pulse shapes (sine and hyperbolic secant) showed only a ~14% HyperCEST effect.

Conclusions: For the first time, we observed a HyperCEST effect for the ^{129}Xe -RBC pool for all concentrations. The HyperCEST detectability limit was found to be 0.1 mM of CB6 in blood for all depolarization pulses, which is 4 times lower than previously reported⁵.

Acknowledgments: This study was funded by a Natural Science Engineering Research Council (NSERC) Discovery grant (RGPIN-2017-05359). VB and VG were supported by a MITACS Accelerate grant (IT31144). YS was supported by a MITACS Elevate postdoctoral fellowship (IT25574).

References: ¹Schroder L, et. al. Science (2006); ²Kim SJ, Lee HY. Lab Anim Res (2022); ³Newman, CJ, et al. in Proc. ISMRM (2020); ⁴Hane FT, et.al. Sci Rep. (2017); ⁵Hane FT, Contrast Media Mol Imaging (2016); ⁶Norquay G, et.al. Magn Reson Med. (2017); ⁷Grynko V, et.al. In Proc. ISMRM (2022).

Hyperpolarized ¹²⁹Xe MRI ventilation textures predict short- and long-term response to Anti-IL-5Rα Biologic Therapy in Eosinophilic Asthma

Marrissa J McIntosh,^{1,2} Maksym Sharma,^{1,2} Harkiran K Kooner,^{1,2} Hana Serajeddini,^{1,3} Anurag Bhalla,³ Cory Yamashita³ and Grace Parraga^{1,4}

¹Robarts Research Institute, ²Department of Medical Biophysics, ³Division of Respiriology, Department of Medicine, ⁴School of Biomedical Engineering, Western University, London, Canada.

INTRODUCTION: Airway inflammation, eosinophilia and mucus-plugs are important pathophysiologic features of eosinophilic-asthma. Ventilation abnormalities related to these may be non-invasively evaluated using hyperpolarized noble gas MRI ventilation-defect-percent (VDP),¹⁻³ while signal intensity differences, or ventilation heterogeneity, may be quantified as texture features.⁴ We previously showed that hyperpolarized gas MRI-VDP and MRI texture features could help identify eosinophilic-asthma patients who would experience early, within 28-days of treatment initiation, responses to anti-IL-5Rα biologic therapy.⁵ Here we hypothesized that hyperpolarized MRI texture features would significantly predict eosinophilic-asthma patients with early and late responses to such therapy, and that these features would outperform standard clinical measurements.

METHODS: We retrospectively analyzed 29 participants with poorly-controlled eosinophilic-asthma, who completed MRI,⁶ spirometry⁷ and the Asthma Control Questionnaire (ACQ-6)⁸ just prior to anti-IL-5Rα treatment initiation (Day-0) and at Day-28 and 1-year (n=16) following continuous anti-IL-5Rα therapy. Participants were dichotomized as responders if the reduction in ACQ-6 score at Day-28 or 1-year as compared to Day-0 was greater than the minimal-clinically-important-difference (0.5).⁹ MRI analysis was performed using a semi-automated segmentation algorithm.¹⁰ Texture features were extracted using PyRadiomics.⁴ Feature selection (10 participants/feature¹¹) was performed using area-under the receiver-operating-characteristic curve (AUC-ROC). Logistic regression models were generated and performance was evaluated using accuracy, sensitivity and specificity.

RESULTS: Using AUC, we identified five features for Day-28, three features for 1-year and one feature for both Day-28 and 1-year to identify anti-IL-5Rα response. VDP was not identified as a significant feature for either time-point (rank: 10/107 and 13/107, respectively), but did outperform all clinical variables (VDP: Day-28 AUC=0.756; 1-year AUC=0.771; highest ranked clinical features: Day-28, blood eosinophils AUC=0.703; 1-year, mucus count AUC=0.646). The highest model accuracy was achieved with MRI texture features for Day-28 (accuracy=76%, sensitivity=67%, specificity=80%) and 1-year response (accuracy=81%, sensitivity=50%, specificity=92%).

CONCLUSIONS: There are currently six biologic therapies for the treatment of eosinophilic-asthma, however it is difficult to predict which patients may benefit prior to this high-cost (\$30,000 annually) therapy initiation. Here, we developed accurate logistic regression models, using pre-treatment MRI texture features that describe ventilation “patchiness” and large regions of similar signal intensities, to identify patients who experienced early and late responses to anti-IL-5Rα biologic therapy.

REFERENCES: 1. Svenningsen, S. *AJRCCM* (2018); 2. Mummy, D.G. *Radiology* (2021); 3. Svenningsen, S. *Chest* (2019); 4. van Griethuysen, J.J.M. *CancerRes* (2017); 5. McIntosh, M.J. *ISMRM* (2020); 6. Svenningsen, S. *JMRI* (2013); 7. Miller, M.R. *ERJ* (2005); 8. Juniper, E.F. *ERJ* (1999); 9. Juniper, E.F. *RespirMed* (2005); 10. Kirby, M. *AcadRadiol* (2012); 11. Harrell, F.E. *StatMed* (1984).

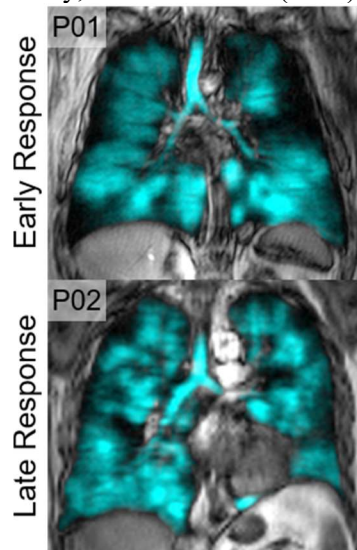


Table 1. Logistic Regression Models

Parameter	Accuracy	Sensitivity	Specificity
Day-28 Response			
MRI-based	75.9%	66.7%	80.0%
Clinical-based	72.0%	33.3%	93.8%
1-year Response			
MRI-based	81.3%	50.0%	91.7%
Clinical*	73.3%	0.0%	100.0%

Day-28 Models: MRI-based features= GLSZM Small area low gray level emphasis, GLSZM low gray level zone emphasis, GLDM small dependence low gray level emphasis, GLCM cluster shade, GLRLM Long run low gray level emphasis, GLRLM Short run low gray level emphasis; Clinical features= Blood eosinophils, mucus count, pre-BD FVC, pre-BD FEV₁, FeNO
 1-year Models: MRI-based features= GLCM Correlation, NGTDM Strength, GLSZM low gray level zone emphasis, FO Skewness; Clinical features= Mucus count, FeNO, BMI, Pre-BD FVC

Figure 1: Qualitative results of early responders (P01) vs. late responders (P02) pre-treatment and regression models for response prediction. P01: 65 year old female, VDP=18%, low gray-level zone emphasis=0.0018, P02: 71 year old female, VDP=8%, low gray-level zone emphasis=0.0008.

*= indicates classifier that predicted all

participants as responders; VDP= ventilation defect percent; GLSZM= gray level size zone matrix; GLDM= gray level dependence matrix; GLCM= gray level co-occurrence matrix; GLRLM= gray level run length matrix; FO= first order; BD= bronchodilator; FVC= forced vital capacity; FEV₁= forced expiratory volume in 1 second; FeNO= fractional exhaled nitric oxide; NGTDM= neighbouring gray tone difference matrix.

^{129}Xe Gas-Exchange MRI and CT Pulmonary Vascular Abnormalities in GINA 4-5 AsthmaAlexander M Matheson^{1,2}, Marrison J McIntosh^{1,2}, Narinder Paul,³ Anurag Bhalla⁴, Cory Yamashita,⁴ and Grace Parraga¹⁻⁴¹Robarts Research Institute, ²Department of Medical Biophysics, ³Department of Medical Imaging, ⁴Division of Respiriology, Department of Medicine, Western University London, Canada

PURPOSE: In asthma, inflammatory abnormalities including airway wall thickening,^{1,2} luminal occlusion³ and airway loss⁴ were related to symptoms² and in some cases, improved post-therapy.¹ Inflammatory processes may also affect the pulmonary vasculature and parenchyma. Abnormal alveolar collagen deposits have been described in poorly controlled asthma.⁵ The Severe Asthma Research Program has also suggested pulmonary vascular pruning in patients with severe, eosinophilic asthma.⁶ Hyperpolarized ^{129}Xe MRI can provide measurements of airway function and notably, the function of alveolar-capillary interface as ^{129}Xe diffuses into the alveolar membrane and binds to red-blood-cells (RBC).⁷ ^{129}Xe gas-exchange MRI has suggested gas-exchange abnormalities in ILD and COPD⁸, but until now, patients with asthma have not been investigated. Hence our goal was to measure ^{129}Xe gas-exchange and CT pulmonary vascular tree density in participants with severe asthma and compare these with healthy volunteers.

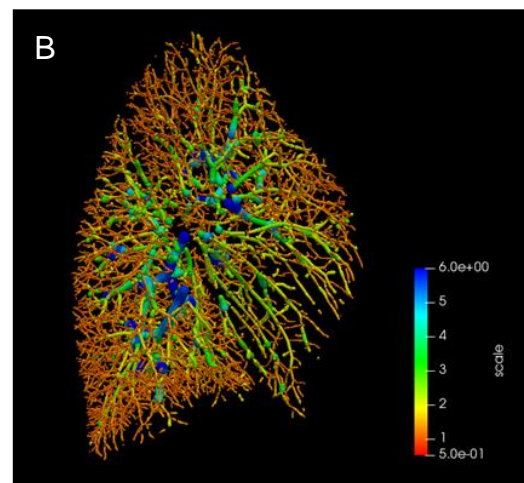
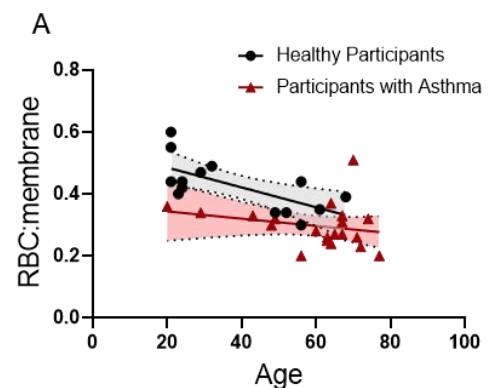
METHODS: Participants enrolled from a quaternary-care asthma centre, provided written informed consent to an approved protocol (NCT02351141 or NCT03733535) and underwent pulmonary function tests, thoracic CT, and ^{129}Xe MRI. Healthy volunteers underwent MRI only. CT pulmonary vessel volumes were measured using Chest Imaging Platform and reported as the blood-volume in vessels with cross-sectional-area<5mm² normalized to total-blood-volume (BV5/TBV).⁹ MRI data were fit to a three-peak (gas, membrane, and RBC) model and reported as membrane and RBC signal normalized to gas signal (membrane:gas; RBC:gas). Intergroup differences were measured using Student's t-tests and relationships using Pearson correlations.

RESULTS: 19 participants with GINA4-5 asthma (age=59±15, 16/19 females) and 16 healthy volunteers (age=37±17, 5/16 females) were enrolled. RBC:membrane (asthma: 0.30±0.07, healthy: 0.42±0.10, p<.001) and RBC:gas (asthma:0.28±0.08, healthy:0.41±0.12, p<.001) were significantly different. Shown in Figure 1A, RBC:membrane correlated with age in healthy (r=.67, p=.008) but not asthma (r=.24, p=.29) groups and healthy values were greater across ages. CT vessel tree measurements were significantly lower in participants with asthma (BV5/TBV=57±4%) compared to published healthy values (BV5/TBV=62±4%)⁶ – an example participant with abnormally large vessels extending to the periphery is shown in Figure 1B.

CONCLUSIONS: A diminished RBC:membrane ratio in asthma appears to be driven by abnormal RBC signal. This may have been driven by pulmonary capillary abnormalities, as supported by CT results. To our knowledge, this is the first observation of abnormal gas-exchange in GINA4-5 asthma which suggests current inflammatory airways disease treatments may not be sufficiently targeting pulmonary vascular abnormalities in patients.

REFERENCES:Niimi et al. *AmJMed* 2004; Park et al. *JInvestAllergolClinImmunol* 1997; Dunican et al. *JClinInvest* 2018; Eddy et al. *AJRCCM* 2020; Weitoft et al. *RespirRes* 2014; Ash et al. *AJRCCM* 2018; Kaushik et al. *JApplPhysiol* 2013; Wang et al. *ERJ* 2019; Estepar et al. *IEEE IBSI* 2012.

Figure 1: A) There was a negative correlation between RBC:membrane and age for healthy participants (r=.67, p=.008) but not participants with asthma (r=.24, p=.29). B) A participant with asthma with abnormal vessels (29-year-old female, FEV₁=79%_{pred}, BV5/TBV=48%).



Accelerated 3D MRI with Inhaled Hyperpolarized ^{129}Xe in Human Lungs: TroubleshootingSamuel Perron¹, Matthew S. Fox^{1,2}, and Alexei Ouriadov^{1,2,3}¹Department of Physics and Astronomy; ²Lawson Health Research Institute, London, Canada;³School of Biomedical Engineering, The University of Western Ontario, London Canada

Introduction: Lung MR imaging using hyperpolarized (HP) gases, such as $^3\text{He}^1$ and $^{129}\text{Xe}^2$, is highly sensitive to diseased or damaged lung morphology, and is well suited to the low field regime ($<1\text{T}$)³. It has recently been shown that accelerated MRI via Compressed-Sensing, combined with fitting to the Stretched-Exponential-Model, is able to significantly improve imaging efficiency (SNR/time) for low field and hyperpolarized ^{129}Xe lung imaging.^{4,5} This method uses a decaying signal trend across the dataset to reconstruct the accelerated images: this signal decay, assumed to represent the decaying density of resonant nuclei in the lungs as it gets replaced with each wash-out breath, can be (a) fitted to the Stretched-Exponential-Model (SEM) equation⁶⁻⁹, and (b) induced or replaced by another mechanism causing this signal decay across the set of images. In previous work^{4,5}, this was done by applying a specific averaging pattern to the undersampled images (average for every unique combination of images without overlap); in single-pass acquisitions, all images are acquired without refilling the phantom or inhaling fresh xenon gas, and as such the resulting SNR of this set of images should also follow the SEM equation as the ^{129}Xe hyperpolarization is further destroyed with each scan. Using HP ^{129}Xe , we have acquired undersampled single-pass datasets of xenon-filled phantom at low field to verify this signal decay condition, and undersampled human lung images within a single breath-hold.

Methods: In-vitro MR was performed at 74mT (Litz wire¹⁰ nested T/R saddle RF coil) on a resolution phantom filled with 45mL of HP ^{129}Xe (35% polarization), using the Fast-Gradient-Recalled-Echo (FGRE) pulse sequence modified for centric-out acquisition (phase-encoding lines acquired from centre to edges), ensuring adequate sampling of the k-space centre. Three sets of 9 undersampled images were acquired at an acceleration factor (AF) of 7, each followed by a zero/dead-signal image for fitting purposes (900ms/image, 9s total scan time). One healthy volunteer underwent inhaled ^{129}Xe MRI: seven 30mm coronal slices of 9 undersampled (AF=7) human lung scans each were acquired at 3T (MR750, GEHC) using a commercial xenon-quadrature-flex human RF-coil¹¹ (MR Solutions). All images were acquired in one breath-hold (7s total, 1s/slice) after inspiration of 1L of hyperpolarized ^{129}Xe gas (33% polarization, 30/70 $^{129}\text{Xe}/^4\text{He}$ mix) obtained from a turn-key, spin-exchange-polarizer system (Polarean-9820 ^{129}Xe polarizer).¹² The SNR decay of both in-vitro and in-vivo datasets was assumed to represent the decreasing gas density of ^{129}Xe after each wash-out oxygen breath, and fitted to the SEM.^{13,14} The averaging pattern^{4,5} was applied to lung data as the clinical scanner orders the k-space lines to yield consistent SNR across all images, overwriting the intended signal decay.

Results: Fig.1 shows the signal decay from decreasing ^{129}Xe polarization in three single-pass sets of 10 phantom images each, following the expected exponential decay trend.

Fig.2 depicts reconstructions of three central-slice undersampled images of human lungs showing considerable SNR benefits (5-6 times) compared to the fully-sampled acquisitions.⁵

Conclusion: Due to the low resonant frequency of xenon at 74mT, severe artefacting caused by external low-frequency RF interference prevented adequate reconstruction of the phantom data. Still, the observed signal decay of this set of images agreed with predictions and should allow for direct reconstruction once hardware issues are sorted. The undersampled human lung images exhibit expected degrees and types of artefacting: future work involves building a neural network⁵ training dataset for undersampled human lung images to remove these reconstruction artefacts.

We acknowledge the support of NSERC, R5942A04.

References: 1. Komlosi, P. et al. MRM. (2017); 2. Eddy, R.L. et al. ERJ. (2020); 3. Parra-Robles, J. et al. Med Phys. (2005); 4. Perron, S. et al. ISMRM (2021); 5. Perron, S. et al. ISMRM (2022); 6. Westcott, A. et al. JMRI. (2019); 7. Abascal, J. et al. IEEE Trans Med Imaging. (2018); 8. Berberan-Santos, M.N. et al. Chemical Physics. (2005); 9. Parra-Robles, J. et al. ISMRM (2013); 10. Dominguez-Viqueira, W. et al. CMR.B. (2010); 11. Kaushik, S.S. et al. MRM. (2016); 12. Kaushik, S.S. et al. MRM. (2011); 13. Ouriadov, A.V. et al. MRM. (2015); 14. Santyr, G.E. et al. MRM. (2008).

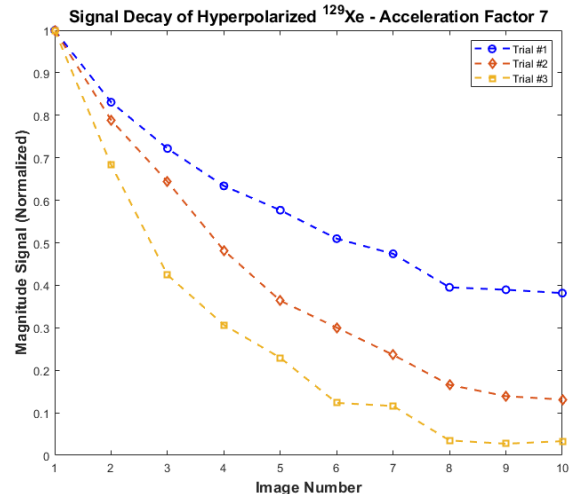


Figure 1. Phantom ^{129}Xe Signal Decay of 3 sets of 10 scans.

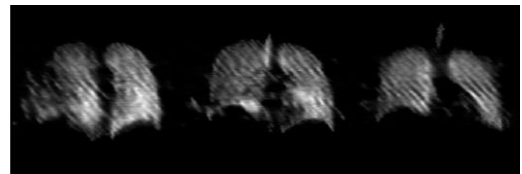
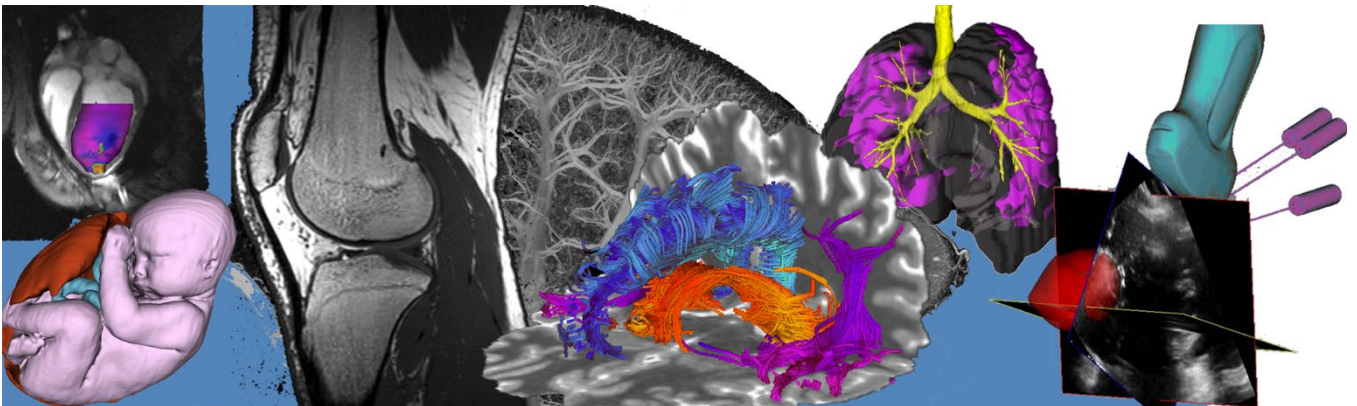


Figure 2. Undersampled (AF=7) central-slice human lung images using inhaled ^{129}Xe .

Oral Session 4: Image Guidance Abstracts



Learning-assisted 3D US-CT/MRI Registration for Liver Tumour Ablation

Shuwei Xing^{1,2}, Joeana Cambranis Romero^{1,2}, Priyanka Roy¹, Derek W. Cool⁴, David Tessier¹, Elvis C.S. Chen^{1,2,3,4}, Terry M. Peters^{1,2,3,4}, Aaron Fenster^{1,2,3,4}

¹Robarts Research Institute, Western University, London, ON, Canada

²School of Biomedical Engineering, Western University, London, ON, Canada

³Department of Medical Biophysics, Western University, London, ON, Canada

⁴Department of Medical Imaging, Western University, London, ON, Canada

Introduction. Ultrasound (US)-guided percutaneous liver ablations have been considered promising curative treatment techniques for focal liver tumours. However, for some cases, the conspicuity of liver tumours under the US may be low or even completely invisible, due to the similar tissue acoustic impedances between the tumour and surrounding healthy tissue, and the locality of the tumour being imaged (e.g., high in the liver dome). To address this issue, the registration of US images and corresponding diagnostic computed tomography (CT) or magnetic resonance imaging (MRI) has been considered one of the most critical steps in US-guided interventional systems. In this work, by taking advantage of deep learning techniques to efficiently detect representative features in both modalities, we aim to develop a 3D US-CT/MRI registration approach for liver tumour ablations.

Methods. The liver vasculature, such as hepatic vessels and portal veins, is first segmented using the deep learning technique based upon nnUNet. For 3D US, 95 images acquired from 16 healthy volunteers and 13 patients with hepatocellular carcinoma or liver metastases were divided into training, validation, and test partitions with 64, 16 and 15 images, respectively. For MRI images with spacings of $1.641 \times 1.641 \times 1.5$ mm³, we manually segmented the vessel due to lack of data for training. Then, we propose a coarse-to-fine 3D US-CT/MRI image registration pipeline based on segmented vessels from nnUNet. Our coarse registration step-Bayesian Coherent Point Drift, which relies on the extracted surface points of vessels, aims to provide a robust initial alignment with the fine step-Iterative Closet Point-further improving the registration accuracy using the vessels' centerlines. Lastly, phantom, healthy volunteer and patient studies were performed to demonstrate the effectiveness of our proposed registration approach.

Results. Our nnUNet-based vessel segmentation approach achieved a Dice score of 0.83. In a healthy volunteer study, 11 out of 12 3D US-MRI image pairs were successfully registered with an overall centerline distance of 4.03 ± 2.68 mm. In two patient cases, we achieved target registration errors (TRE), denoting the Euclidean distance between tumour centroids, of 4.16 mm and 5.22 mm, respectively. The qualitative registration results are shown in Figure 1.

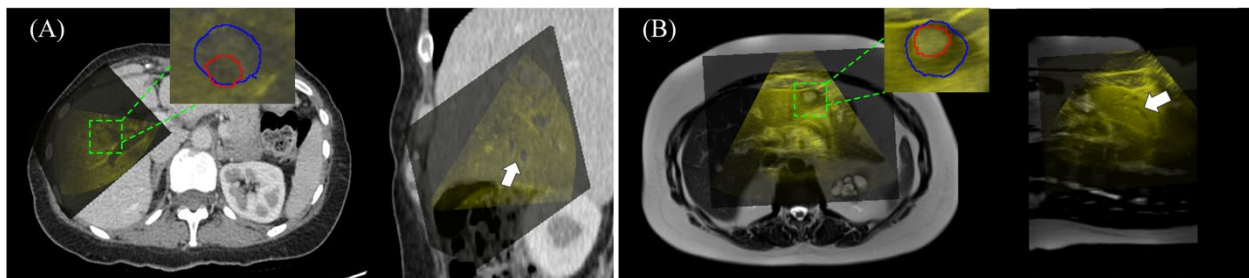


Figure 1. (A) Registration of 3D US with CT; (B) Registration of 3D US with MRI. US image are presented as overlays in yellow. The blue and red contours represent the tumour boundary in US and CT/MRI, respectively.

Conclusions. We proposed a coarse-to-fine 3D US-CT/MRI registration pipeline based on nnUNet vessel segmentation models. Experiments based on phantom, healthy volunteers, and patients demonstrated the effectiveness of our registration workflow for the clinical.

Deep Learning-Enabled Fluorescence Imaging for Surgical Guidance: In Silico Tumour Models

Natalie Won,¹ Scott Holtshousen,¹ Stefanie Markevich,¹ Arjun Jagota,¹ Josephine La Macchia,¹
Mandolin Bartling,² Brian C. Wilson,^{1,3} Jonathan C. Irish¹⁻³ and Michael J. Daly¹

¹TECHNA Institute, University Health Network, Toronto ON

²Department of Otolaryngology – Head & Neck Surgery, University of Toronto

³Ontario Cancer Institute, Princess Margaret Cancer Centre, Toronto ON

Introduction: Accurately assessing tumour depth of invasion remains a critical challenge in many surgical specialties¹. Fluorescence-guided surgery systems can help tumour visualization; however, current 2D fluorescence systems are unable to quantify depth. To overcome this limitation, our group is developing a deep learning (DL) model based on spatial frequency domain images to measure tumour depth and fluorescence concentration. Here, we investigate the capabilities of a DL model trained with *in silico* tumour shapes of increasing complexity.

Methods: An adapted deep convolutional neural network (CNN),² previously trained with cylinders of varying width and depth,³ was retrained with a sequence of more complex shape models. The Siamese CNN architecture uses optical properties and spatial-frequency fluorescent images as inputs, followed by a series of convolutions to learn the 6,000,000 parameters required for predicting depth and concentration maps. This model was trained (~4 hours) with 10,000 composite spherical harmonics (CSH): multiple spherical harmonics of randomly generated order, degree, and radius were combined, rotated, translated, scaled, and cut to create diverse representations of tumour shapes. A numerical diffusion theory-based light propagation model was then used to generate synthetic images for DL training. The new training set included irregular edges, asymmetric depths (1-5mm), buried regions of tumours, and variable optical properties ($\mu_a=0.0015-0.015$, $\mu_s'=0.75-2$ mm⁻¹, fluorescence concentration 1–10 $\mu\text{g/mL}$). DL models were tested (<1 sec) with 10 clinically-inspired oral cancer tumours drawn by a head and neck surgeon.

Results: (Fig. a) The model trained with cylinders had concentration and depth mean squared errors (MSE) of 0.74 ± 0.33 $\mu\text{g/mL}$ and 0.16 ± 0.16 mm. (Fig. b) In contrast, training with CSH had lower ($p=0.005$ and $p=0.04$) concentration and depth MSE of 0.30 ± 0.10 $\mu\text{g/mL}$ and 0.05 ± 0.04 mm.

Conclusions: The DL model yields depth accuracy of <0.1 mm when trained with *in silico* tumour shapes based on CSH. Future experimental studies in animal models and patient-derived optical phantoms will evaluate performance in larger tumours after upscaling the DL model.

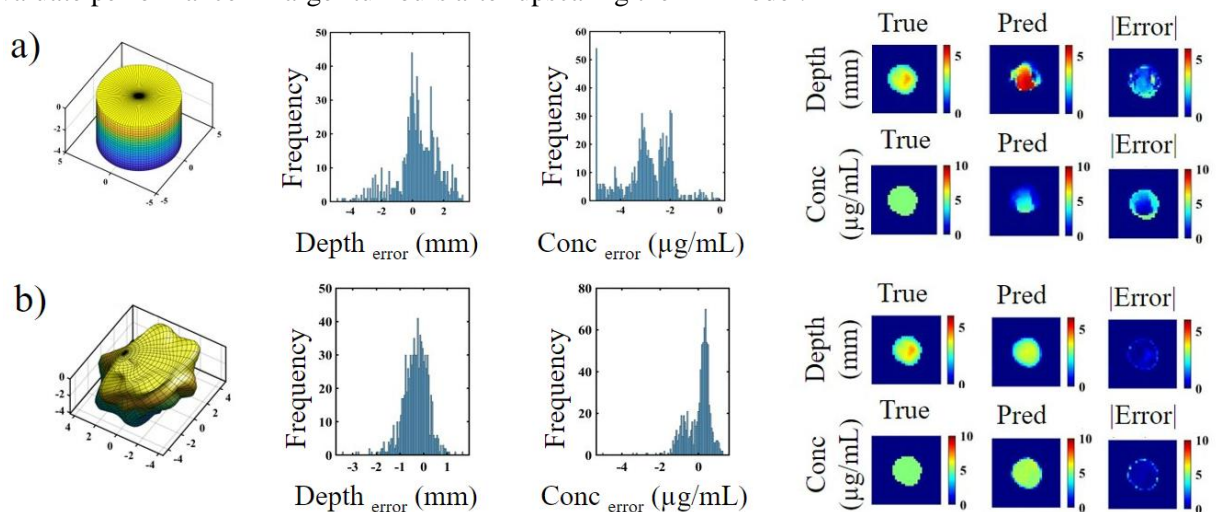


Figure. Testing DL models with digital tumour meshes. (a) Cylinder DL model. (b) *In silico* tumour DL model.

References: 1. Baddour HM et. Al., J. Surg. Oncol: The Importance of Margins in Head and Neck Cancer. 2016
2. Smith JT et. al., Opt Lett. 2020 45(15):4232-4235.
3. Daly MJ et. al., Biophotonics Congress: Biomedical Optics. 2022 OTS-2022 OW4D.4.

Automated catheter localization in transrectal ultrasound images for high-dose-rate prostate brachytherapy

N. Kitner¹, J.R. Rodgers³, T. Ungi¹, M. Korzeniowski², T. Olding², C.P. Joshi², P. Mousavi,¹ G. Fichtinger¹
¹School of Computing, Queen's University; ²Kingston Health Sciences Center, Kingston, Ontario;
³University of Manitoba, Winnipeg, Manitoba

Introduction: High-dose-rate brachytherapy (HDR-BT) is an internal radiotherapy technique in which catheters are guided through the perineum and into the prostate using three-dimensional (3D) transrectal ultrasound (TRUS) image guidance. Medical physicists must manually localize catheter positions on the TRUS images before radiation is administered. This process can be laborious and is subject to human variability, which can affect radiation dosimetry and clinical outcomes [1]. Approaches for catheter tracking have been proposed that utilize deep learning architectures [2], while others use classical feature extraction [3]. To our knowledge, none use the combination of deep learning and 3D Hough transform, which can rectify poor results for partially shadowed catheters, as was a problem when using the Hough transform alone. This will also better localize tips, something deep-learning approaches have trouble with. We propose a two-step pipeline involving a deep learning approach to localize catheters in HDR-BT using a 3D U-Net architecture, followed by fitting catheter models to the segmentation output of the 3D U-Net to remove excess noise, and model catheter shapes to better resemble ground truth predictions compared to previous works.

Methods: The 3D TRUS images and their corresponding ground truth catheter positions were obtained for 97 prostate HDR-BT patients treated at Kingston Health Sciences Centre between 2017 and 2021. The ground truth catheters were manually tracked by medical physicists during the implant procedures. In preparation for model training, the 3D TRUS images were cropped and resized to $128 \times 128 \times 128$. The manual contours were converted to binary segmentations and resized to the same dimensionality as their corresponding TRUS images. These segmentations were then used as the ground truth for training the deep learning model. After pre-processing, the data was exported for training on the 3D U-Net architecture (Fig. 1). Training made use of 67 images and their corresponding ground truths, while 10 were used for validation and 20 for testing. The model used the focal loss function and the Adam optimizer was used with a maximum learning rate (LR) of 0.01, a minimum LR of 0.00001, and a LR decay of 4.995×10^{-5} . This model was trained for 200 epochs with early stopping and a batch size of 5. Individual catheters were then extracted from the resulting segmentation using the 3D Hough transform. A least square fit was used to fit a second-degree polynomial to all points belonging to one catheter, and this polynomial represents the final catheter structure.

Results: Of the 343 catheters present in the testing data, the pipeline correctly identified 320 with 7 false positives (2.04%) and 13 false negatives (3.79%). The pipeline has an overall accuracy of 0.95 and precision of 0.98. The average distance \pm one standard deviation (SD) between the ground truth and predictions for each catheter shaft was 1.9 ± 0.3 mm, while the average distance \pm SD of each catheter tip was 3.0 ± 0.4 mm. Fig. 2 depicts a visual comparison of the methods relative to the ground truth segmentation.

Conclusion: The average distance between ground truth and predictions of catheter shafts are within the clinically relevant range of 2 mm [4], although average difference in tip position is larger than 2 mm. Further work to refine tip position localization is necessary, and work is underway to reduce the tip end tracking variability and assess complex catheter paths and reconstruction between slices. One limitation of this work is the small dataset size.

Data augmentation will be performed in the future to supplement dataset size and enhance deep learning outcomes. The proposed pipeline provides the clinical team with a method of reducing time spent on verification of catheter positions and equips the medical physics team with a way of reducing uncertainties and improving clinical workflow during the procedure. Reducing human variability in catheter placement predictions increases accuracy of tracking and radiation dose distribution.

References: [1] Chicas-Sett et al. *Brachy* 2018. [2] Zhang et al. *Phys in Med & Bio* 2020. [3] Hrinivich et al. *Med Phys* 2017. [4] Park et al. *Med Phys* 2013.

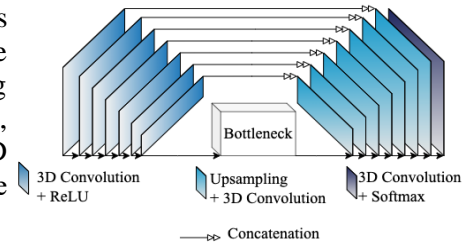


Figure 1: 3D U-Net structure used to train

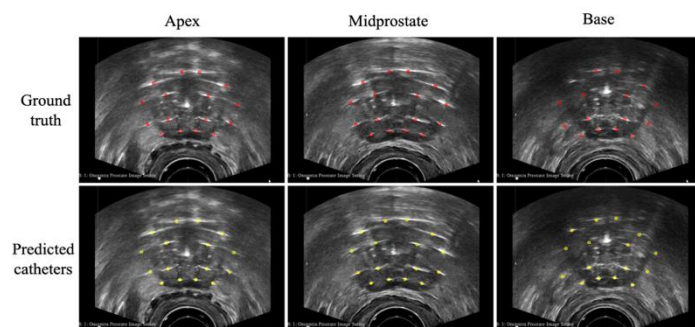


Figure 2: Images of the ground truth and predicted catheter positions at the apex, mid, and base regions of the prostate.

A Hybrid Augmented Multi-Baseline and Near-Referenceless MR Thermometry Pipeline to Reduce Motion Artifacts during Magnetic Resonance Guided High-Intensity Focused Ultrasound

Arthur Akbulatov¹, Suzanne M. Wong^{1,2}, Craig A. Macsemchuk^{1,2}, Andrew Headrick¹, James M. Drake^{1,2}, Adam C. Waspe^{1,3}

¹Posluns Centre for Image Guided Innovation & Therapeutic Intervention, The Hospital for Sick Children, Toronto, ON, Canada;

²Institute of Biomedical Engineering, University of Toronto, Toronto, ON, Canada; ³Department of Medical Imaging, University of Toronto, Toronto, ON, Canada.

Introduction: Magnetic resonance guided high-intensity focused ultrasound (MRgHIFU) is a non-invasive technique used to administer hyperthermia. MRgHIFU leverages MRI for treatment planning and monitors temperature changes within tissue in real time with MR thermometry. Maintaining accurate thermometry measurements is essential to provide precise and accurate heating to target tissue and avoid damaging tissue outside of the treatment area. Involuntary sporadic motions such as muscle twitching and sternutation can introduce large motion artifacts that severely impact the accuracy of MR thermometry. The objective of this work is to improve upon a hybrid principal component analysis (PCA) and projection onto dipole fields (PDF) motion compensation algorithm¹ to minimize thermometry artifacts caused by large unpredictable motions.

Methods: A PCA-PDF algorithm¹ was expanded upon to incorporate predicted motion into the PCA atlas using image augmentation techniques. Prior to treatment, an atlas of MR images is acquired to create the PCA reference. Each phase image acquired is augmented to create several new images that are added to the PCA atlas (Figure 1). These images are horizontally and vertically translated by a random number of pixels drawn from a Gaussian distribution centered at 0 with a specified pixel standard distribution. To assess the efficacy of the algorithm, MR images of a gelatin phantom undergoing lateral displacement, with and without HIFU hyperthermia, were retrospectively processed. In each retrospective processing, the atlas size and displacement standard deviation of displacement was varied. The gelatin phantom was translated by a robot positioner by approximately 2.25 cm, then moved back to its original position. As a measure of the severity of artifacts, the temperature standard deviation was calculated in each MR image without heating when the phantom was in the displaced position and averaged across five trials.

Results: With no motion compensation, the temperature standard deviation was 5.0 °C. The unmodified PCA-PDF algorithm, with no augmentation, yielded a temperature standard deviation of 4.1 °C. A 128-image atlas with a displacement standard deviation of 10 px yielded the lowest temperature standard deviation of 0.4 ± 0.1 °C over the five trials, significantly lower than the unmodified PCA-PDF approach ($p < 0.0001$). The visual difference in severity of motion artifacts is shown in Figure 2, where the augmented PCA-PDF approach yielded far fewer artifacts than no motion compensation and unmodified PCA-PDF. When hyperthermia was administered, accurate temperature measurements in the treatment area were maintained (Figure 2F).

Conclusions: Results indicate that supplementing the PCA-PDF method with an augmented atlas of predicted motion images was able to reduce artifacts created by sporadic motion in MR thermometry, while maintaining accurate measurements of HIFU heating. This may allow hyperthermia treatments using MRgHIFU to continue despite a large patient movement rather than being forced to stop and resume due to thermometry artifacts.

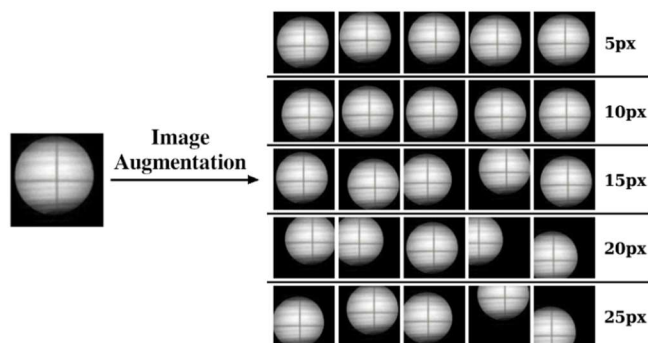


Figure 1: Examples of augmented atlas images with varying pixel standard deviation of displacement indicated on the right.

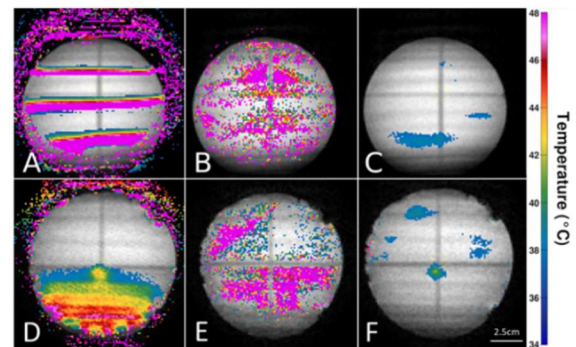
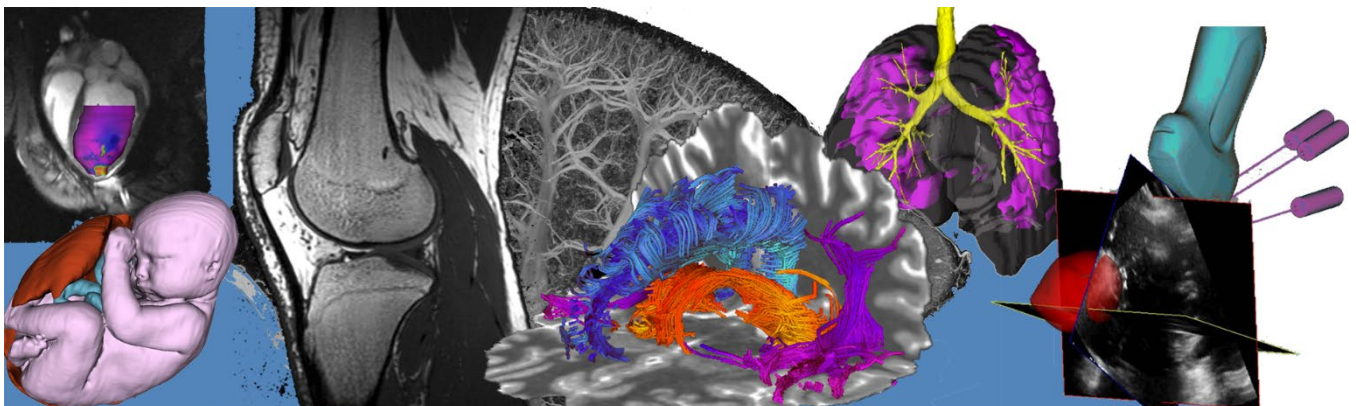


Figure 2: MR thermometry images of phantoms after 2.25 cm displacement. A-C: No heating. D-F: 40.5 °C hyperthermia. A, D: No motion compensation. B, E: Unmodified PCA-PDF. C, F: Augmented PCA-PDF.

1. J. Tan, C. Mougnot, S. Pichardo, J. M. Drake, and A. C. Waspe, "Motion compensation using principal component analysis and projection onto dipole fields for abdominal magnetic resonance thermometry," *Magnetic resonance in medicine*, vol. 81, no. 1, pp. 195–207, 2019, doi: [10.1002/mrm.27368](https://doi.org/10.1002/mrm.27368).

Pitch/Poster Session 3: Hyperpolarized MR and Lung Imaging Abstracts



CT and MRI Measurements Uniquely Explain All-cause Mortality in Ex-smokersMaksym Sharma,^{1,2} Paulina Wyszkiwicz,^{1,2} Marrissa J McIntosh,^{1,2} Harkiran K Kooner,^{1,2} Alexander M Matheson,^{1,2} David G McCormack³ and Grace Parraga¹⁻⁴¹Robarts Research Institute, ²Department of Medical Biophysics, ³Division of Respiriology, Department of Medicine, ⁴School of Biomedical Engineering, Western University, London, Canada

RATIONALE: In patients with chronic obstructive pulmonary disease (COPD), recent CT imaging studies have shown that emphysema progression over 5-years is associated with all-cause mortality.¹ Importantly, it is believed that small airway abnormalities typically precede the development of emphysema and airflow obstruction in such patients.² CT airway measurements are independently associated with lung function decline,³ predictive of COPD incidence,⁴ and are related to terminal bronchioles on micro-CT.⁵ In addition, MRI apparent-diffusion-coefficients (ADC) provide a highly sensitive measurement of terminal airspace enlargement and alveolar geometry, which may be indicative of early emphysematous destruction⁶ and/or small airways disease,⁷ where COPD is believed to initiate. We wondered if together, quantitative MRI and CT airway and vessel measurements would be associated with, or predict all-cause mortality in ex-smokers with and without COPD.

METHODS: Ex-smokers with and without COPD provided informed consent to the Thoracic Imaging Network of Canada (TINCan) study (NCT02279329) and completed pulmonary function tests [forced expiratory volume in 1-sec (FEV₁), forced vital capacity (FVC), and diffusing capacity for carbon-monoxide (DL_{CO})], ³He MRI and thoracic CT, all previously described.⁸ VIDAvision was used to quantify total airway count (TAC), as well as anatomically equivalent segmental, subsegmental and sub-subsegmental airway wall area (WA), lumen area (LA) and wall thickness (WT). CT emphysema was measured and defined as the relative-area-of-the-lung-with-attenuation <-950 Hounsfield Units (RA₉₅₀)>6.8%.⁹ Independent samples t-tests and multivariable logistic regression models were generated to evaluate the relationship between imaging and 10-year all-cause mortality.

RESULTS: We evaluated 87 participants (28 female/59 male, 71±10 years), 11 of whom [6/47(13%) ex-smokers with and 5/40(12.5%) without COPD] died over the TINCan study duration of 10-years. Deceased ex-smokers had a significantly lower DL_{CO} %_{pred} (70±21 vs 53±16, p=.01) and 6MWD (407±81m vs 352±97m, p=.04) compared to ex-smokers who remained alive at follow-up. All-cause mortality was associated with (Figure 1) abnormal DL_{CO} (<75%_{pred} hazard ratio [HR]=3.951, 95% CI=1.026-14.919, p=.046) and greater MRI ADC (HR=1.283, 95% CI=1.050-2.507, p=.047). Survival was associated with greater 6MWD (HR=0.834, 95% CI=0.705-0.981, p=.03), and CT lumen area (HR=0.887, 95% CI=0.836-0.965, p=.02). In a multivariable regression model, CT lumen area was a significant predictor (p=.001) of all-cause mortality.

CONCLUSIONS: In ex-smokers with and without COPD, abnormal DL_{CO}, worse 6MWD, MRI-ADC and airway lumen area provide unique information for mortality risk assessments.

REFERENCES: ¹Ash SY. *Radiology* (2021); ²Casio M. *NEngJMed* (1978); ³Kirby M. *AJRCCM* (2018); ⁴Kirby M. *EurRespirJ* (2021); ⁵Kirby M. *AJRCCM* (2020); ⁶Swift AJ. *EurJRadiol* (2005); ⁷Wang C. *JMRI* (2008); ⁸Kirby M. *ChronicObstrPulmDis* (2014); ⁹Lynch DA. *Radiology* (2018).

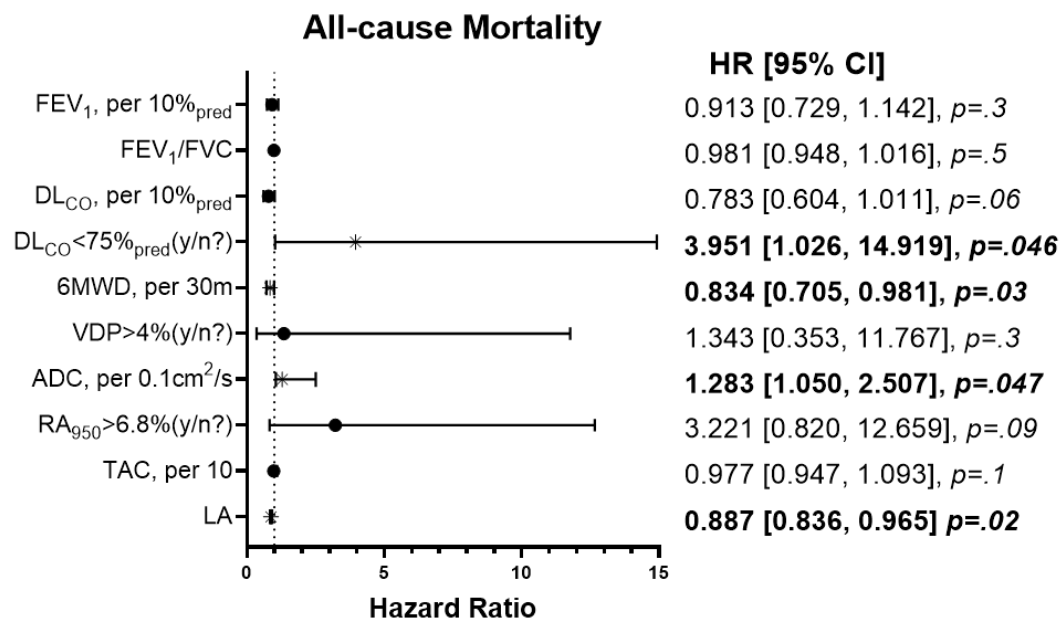


Figure 1: Logistic regression models for associations between 10-year all-cause mortality with clinical and imaging measurements. All hazard ratios were adjusted for age, sex, pack-years, and BMI.

Minimal Clinically Important Difference for ^{129}Xe MRI Ventilation Defect Percent in Patients with Asthma

Alexander Biancianiello,^{1,2} Hana Serajeddini,^{1,3} Marriisa J McIntosh,^{1,2} Harkiran K Kooner,^{1,2} Anurag Bhalla,³ Cory Yamashita,³ Rachel L Eddy,⁴ and Grace Parraga¹⁻³

¹Robarts Research Institute, ²Department of Medical Biophysics; ³Division of Respiriology, Department of Medicine, Western University, London, Canada, ⁴Centre for Heart Lung Innovation, St. Paul's Hospital and University of British Columbia, Vancouver, Canada

INTRODUCTION: Inhaled hyperpolarized gas MRI ventilation abnormalities are typically quantified as ventilation defect percent (VDP),¹ which has been shown to be sensitive to various components of asthma pathology.² Although hyperpolarized helium (^3He) gas has been well-established as an inhaled contrast agent for MRI, worldwide shortages have prompted a shift to the more readily available and affordable xenon (^{129}Xe) gas.¹ As with any health measurement, future research and clinical application of ^{129}Xe VDP requires estimation of the minimal-clinically-important-difference (MCID), which describes the smallest perceivable change in VDP that results in a clinically relevant difference of a patient-centred measurement.³ Whilst the MCID of hyperpolarized ^3He VDP was previously reported,⁴ the transition to ^{129}Xe MRI has necessitated a determination of the MCID for ^{129}Xe VDP. We aimed to determine ^{129}Xe MCID using anchor- and distribution-based approaches.

METHODS: Patients with asthma were enrolled in one of three approved protocols (www.clinicaltrials.gov, NCT02351141/NCT02263794/NCT03733535) and provided written informed consent to ^{129}Xe MRI (52±13-years, 34 female; n=2 GINA2, n=10 GINA3, n=17 GINA4 and n=26 GINA5). MRI was acquired using a 3T scanner as previously described.⁵ For the anchor-based approach,⁴ one observer quantified VDP in 55 participants using a previously described semi-automated algorithm,⁶ then estimated the ^{129}Xe MCID by relating VDP to Asthma Control Questionnaire (ACQ-6) score (a patient-reported metric based on the severity of asthma symptoms experienced throughout the past week),⁷ through linear regression modelling as previously described.⁴ For the distribution-based approach,⁸ two independent observers of differing training level quantified VDP in 10 participants over 3 rounds (10 participants x 3 rounds x 2 observers), then estimated the ^{129}Xe MCID using the standard deviation (SD), standard error of the mean (SEM; $SEM=SD/\sqrt{n}$),⁸ and the smallest detectable difference (SDD; $SDD=SEM*1.96*\sqrt{2}$, $\alpha=0.05$)⁹. These results for ^{129}Xe VDP were compared to the previously determined distribution- and anchor-based MCID for ^3He VDP.

RESULTS: For the anchor-based approach, ACQ and ^{129}Xe VDP were correlated (Figure 1: $r=0.37$, $p=0.006$) with a linear regression equation of $VDP=3.5 \cdot ACQ+4.9$. Using this equation and the MCID for ACQ score units (ACQ MCID=0.5)⁷ resulted in a Δ VDP and MCID of 1.75% for ^{129}Xe VDP. For the distribution-based approach, the average SEM was 1.0% (Observer 1, 1.0%; Observer 2, 0.9%) and the average SDD was 2.7% (Observer 1, 2.9%; Observer 2, 2.5%), resulting in an MCID of 2.7% for ^{129}Xe VDP. The previously determined MCID for ^3He VDP was estimated at 4% (anchor-based) and 2% (distribution-based).⁴

CONCLUSIONS: The ^{129}Xe VDP MCID was similar to that of ^3He when considering measurement precision (^{129}Xe MCID=2.7%, ^3He MCID=2%)⁴ but was more sensitive when considering patient-reported symptoms (^{129}Xe MCID=1.75%, ^3He MCID=4%).⁴ These differences can be explained by the potentially increased sensitivity of ^{129}Xe to airway abnormalities compared with ^3He ,¹⁰ and by considering multiple observers for a smaller population size (distribution-based: ^{129}Xe n=10, ^3He n=15) and broader disease severity (mild, moderate, and severe asthma) compared with previous ^3He MCID work.

REFERENCES: 1) Fain S, *JMagnResonImaging*, 2007. 2) Svenningsen S, *AmJRespirCritCareMed*, 2018. 3) Wells G, *JRheumatol*, 2001. 4) Eddy R, *EurRespirJ*, 2018. 5) Svenningsen S, *JMRI*, 2013. 6) Svenningsen S, *AcadRadiol*, 2021. 7) Juniper E, *RespirMed*, 2005. 8) Wyrwich K, *MedCare*, 1999. 9) Kirby M, *AcadRadiol*, 2012. 10) Kirby M, *Radiology*, 2012.

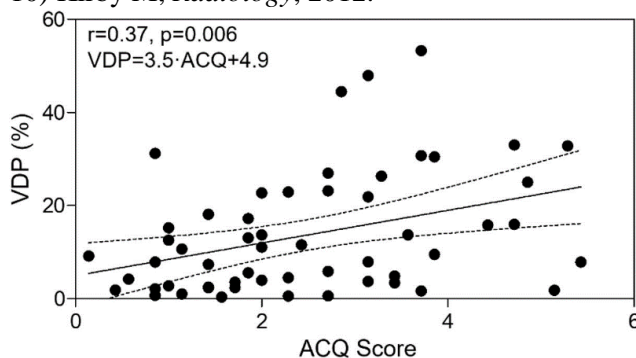


Figure 1. ^{129}Xe MRI VDP Minimal Clinically Important Difference Based on Asthma Control.

Asthma control questionnaire (ACQ) score was significantly related ($p=0.006$) to ^{129}Xe MRI ventilation defect percent (VDP) in a positive linear relationship ($r=0.37$), with a linear regression equation of $VDP=3.5 \cdot ACQ+4.9$.

Deep-Learning Based segmentation of 3D Hyperpolarized ^{129}Xe Lung MRI for Generating $v\text{ADC}$ for a Large Patient Population Studied with The Use of Transfer learning

Ramtin Babaeipour¹, Maria Mihele², Keeirah Raguram², Matthew S Fox^{2,3} and Alexei Ouriadov^{1,2,3}

¹School of Biomedical Engineering, Faculty of Engineering; ²Department of Physics and Astronomy; ³Lawson Health Research Institute, London, Canada, The University of Western Ontario, London, ON, Canada

Introduction: Hyperpolarized ^{129}Xe lung MRI is an efficient technique used to investigate and assess pulmonary diseases. However, the longitudinal observation of the emphysema progression using hyperpolarized gas MRI-based Apparent Diffusion Coefficient (ADC) can be problematic, as the disease-progression can lead to increasing unventilated-lung areas, which likely excludes the largest ADC estimates. One solution to this problem is to combine static-ventilation and ADC measurements following the idea of ^3He MRI ventilatory ADC ($v\text{ADC}$). We have demonstrated this method adapted for ^{129}Xe MRI to help overcome the above-mentioned shortcomings and provide an accurate assessment of the emphysema progression.

Methods: Ten study-subjects with written informed consent provided to an ethics-board-approved study protocol, underwent spirometry and $^3\text{He}/^{129}\text{Xe}$ MRI scanning. ^{129}Xe imaging was performed at 3.0T (MR750, GEHC, WI) using whole-body gradients (5G/cm maximum) and a commercial ^{129}Xe quadrature-flex RF coil (MR Solutions, USA).¹ Hyperpolarized ^{129}Xe gas (polarization=35%) was obtained from a turn-key, spin-exchange polarizer system (Polarean-9820 ^{129}Xe polarizer).² VDP was generated using the DL. We used 2-D U-Net³ architecture for segmentation and ResNet-152⁴ as the backbone network that was trained on the ImageNet⁵ and a low-resolution MRI dataset. The segmentation masks were compared to ground truths using dice similarity coefficient.

Results: Fig.1 shows the acquired static-ventilation images (top-panel), matched voxel-size unweighted ($b=0$,) images (middle-panel) and correspondent ADC maps (bottom-panel) in coronal view for a representative study-subject demonstrating a good-match between static-ventilation and matched resolution unweighted-slices. Table 1 shows the demographic, PFTs, mean VDP, ADC, and $v\text{ADC}$ estimations for all study-subjects.

Discussion and Conclusion: In this proof-of-concept-study, we showed that the emphysema-progression can be potentially quantified with using the pulmonary static-ventilation and diffusion-weighted images of hyperpolarized ^{129}Xe utilizing the ventilatory ADC approach powered by the DL-segmentation. The study results suggest that the matched resolution diffusion data had sufficient SNR to generate reliable ADC maps and reasonable matching with the static-ventilation data.

References:

- 1) Svenningsen et al. *JMRI*, 2013, 38(6), p. 1521. 2) Kaushik et al., *ISMRM*, 2011, 65(4), p. 1154. 3) Ronneberger et al., *MICCAI*, 2015, p.234. 4) He et al., *CVPR*, 2015. 5) Russakovsky et al., *CVPR*, 2014.

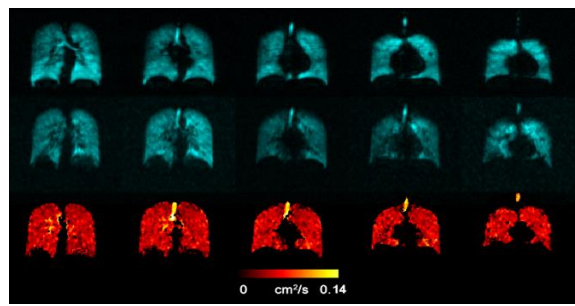


Table 1: Study Subject demographics and ^{129}Xe MRI results

	SS1	SS2	SS3	SS4	SS5	SS6	SS7	SS8	SS9	SS10
Age	74F	76M	69M	29F	47F	61F	63F	52F	36M	55M
BMI (kg/m ²)	33.6	36.6	41.1	19.2	20.8	38.4	33.4	28.4	32.0	29.0
FEV ₁ %	71	78	70	67	75	117	89	61	76	82
FVC %	91	73	66	92	60	111	88	66	73	94
RV %				73	116	73	95	95	116	115
DLco%				83	91	83	66	90	91	63
VDP %	26	8	3	11	7	16	5	12	13	9
ADC (SD), s/cm ²	0.035 (0.018)	0.041 (0.018)	0.037 (0.017)	0.041 (0.017)	0.049 (0.018)	0.041 (0.016)	0.036 (0.015)	0.035 (0.014)	0.035 (0.015)	0.039 (0.015)
$v\text{ADC}$, s/cm ²	0.042	0.043	0.038	0.047	0.048	0.049	0.038	0.040	0.040	0.042
SV SNR	15.0	14.0	24.0	29.0	40.0	26	34	27	42	21
UW SNR	13.0	16.0	20.0	18.0	21.5	18	20	20	27	14

Figure 1: Representative ^{129}Xe static-ventilation images (top-panel), matched voxel-size unweighted ($b=0$,) images (middle-panel) and correspondent ADC maps (bottom-panel) in coronal view obtained for Participant-4. Images demonstrating a good match between static-ventilation and key-hole-based unweighted slices. ADC=apparent diffusion coefficient.

Table 1 shows the demographic, PFTs, mean VDP, ADC, and $v\text{ADC}$ estimations for all study-subjects.

Feasibility study of *in-Vivo* Simultaneous Hyperpolarized ^{129}Xe MRI and ^{15}O -water PET Measurements

Ramanpreet K. Sembhi¹, Matthew S. Fox^{1,2}, Heeseung Lim², Justin W. Hicks^{2,3}, Shawn N. Whitehead⁴, Jonathan D. Thiessen^{2,3}, Grace Parraga^{3,5} and Alexei V. Ouriadov^{1,2,6}

¹Department of Physics and Astronomy; ²Lawson Health Research Institute; ³Department of Medical Biophysics; ⁴Department of Anatomy and Cell Biology; ⁵Robarts Research Institute; ⁶Department of Biomedical Engineering, The University of Western Ontario, London, Ontario, Canada

INTRODUCTION

Inhaled hyperpolarized (HP) ^{129}Xe magnetic resonance imaging (MRI) is a non-invasive imaging method, which is currently used to measure lung structure and function.^{1,2} This MRI approach provides a way to obtain simultaneous ventilation/perfusion (V/P) lung measurements. Due to various physical properties of the ^{129}Xe isotope, it can serve as a new probe for brain blood flow, grey and white matter mapping^{3,4} and functional measurements. ^{15}O -water positron emission tomography (PET) is the gold standard imaging method for determining cerebral perfusion^{5,6}. In this study, simultaneous *in-vivo* ^{129}Xe -based MRI and ^{15}O -water PET images were collected and compared.

METHODS

We used the ^{15}O -water solution (30mL) contained in a 60mL plastic syringe to dissolve 30mL of the hyperpolarized ^{129}Xe gas. Anesthesia was induced in rats with 5% isoflurane and oxygen and maintained at 2%. A 24g tail vein catheter was inserted for delivery of the ^{15}O -water / ^{129}Xe mixture. Hyperpolarized ^{129}Xe gas was obtained from a turn-key, spin-exchange polarizer system (Polarean 9800 ^{129}Xe polarizer). *In-vivo* PET imaging was obtained using a small animal MRI compatible PET insert (Cubresa Inc.) ^{15}O -water PET data was acquired simultaneously with ^{129}Xe MRI using the integrated PET system in the 3T PET/MRI.

RESULTS

Fig.1 shows 2D axial ^{129}Xe MRI images and ^{15}O -water PET images acquired simultaneously. ^{129}Xe /PET images indicate that the diameter of the phantom from both PET and MRI images are similar. The ^{129}Xe image demonstrates a sufficient SNR level (80) suggesting that 3D ^{129}Xe imaging is possible. Fig. 2 shows the anatomical-proton and ^{15}O -water-PET-perfusion images of rat-brain.

DISCUSSION AND CONCLUSIONS

The results of this study clearly indicate the feasibility of simultaneous hyperpolarized ^{129}Xe MRI and ^{15}O -water PET measurements. We have demonstrated that hyperpolarized ^{129}Xe dissolved in ^{15}O -water can be used in multi-modal imaging. The *in-vivo* demonstration did not bring the desired ^{129}Xe image quality because of various reasons like decay in polarization, difficulty in synchronizing the usage of both tracers. By increasing initial xenon polarization and reducing xenon-waiting time, we should be able to use ^{129}Xe as a non-radioactive tracer, providing similar and complementary information as ^{15}O PET which may be a much more cost-effective alternative to PET for imaging stroke, brain cancer and other brain diseases and will significantly increase the number of ^{129}Xe MRI clinical applications as our method is a potential non-radioactive and high-resolution imaging tool.



Figure 1. 2D axial A) ^{129}Xe MRI image and B) ^{15}O -water PET image obtained for xenon dissolved in ^{15}O -water inside the syringe phantom.

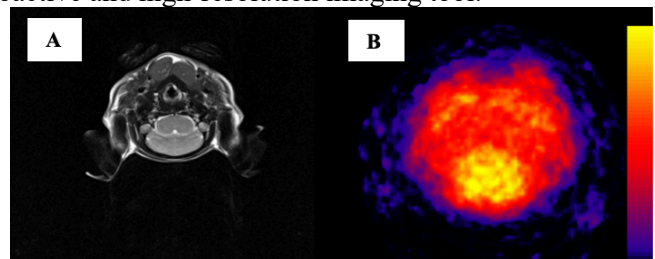


Figure 2. A) ^1H image and B) ^{15}O -water PET perfusion image obtained from rat brain.

References

1. Kaushik, S. S. et al. MRM (2016).
2. Kaushik, S. S. et al. J Appl Physiol (2013).
3. Kershaw, J. et al. MRM (2007).
4. Wakai, A., et. al. ICS (2004).
5. Fan, A., et. al. JCBFM (2016).
6. Ssali, T., et. al. JNM (2018).

Acknowledgements

Research and financial supports received from BrainsCAN-Accelerator-Program, R5942A02 and the Natural-Sciences-and-Engineering-Research-Council of Canada, R5942A04

CT Imaging Measurements with Machine Learning for Predicting Progression to Chronic Obstructive Pulmonary Disease in At-Risk Smokers

Authors and Institutions: Kalysta Makimoto BSc¹, James C. Hogg MD, PhD², Jean Bourbeau MD^{3,4}, Wan C. Tan MD² and Miranda Kirby PhD¹

¹Toronto Metropolitan University, Ontario, Canada; ²Center for Heart, Lung Innovation, University of British Columbia, Vancouver, Canada; ³Montreal Chest Institute of the Royal Victoria Hospital, McGill University Health Centre, Montreal, QC, Canada; ⁴Respiratory Epidemiology and Clinical Research Unit, Research Institute of McGill University Health Centre, Montreal, QC, Canada.

Introduction: Chronic obstructive pulmonary disease (COPD) is a major leading cause of death, with the primary risk factor being tobacco smoking. However, only around 20% of smokers progress to clinically defined COPD (Vestbo, 2002, *Am J Respir Crit Care Med*). Predicting who among the at-risk smokers will progress to COPD is an important goal of COPD management to enable early intervention. In this regard, previous studies have shown conventional risk factors, including demographic characteristics and lung function measurements, with machine learning, can predict at-risk smokers that will progress to COPD (Muro, 2021, *JMIR Med Inform*). However, conventional risk factors do not capture the early pathological changes that occur in the lungs. Quantitative computed tomography (qCT) features are established measurements that are able to detect structural changes occurring in the early stages of COPD in at-risk smokers. Additionally, texture-based radiomics is an emerging area in image analysis that involves converting medical images into numerical features based on voxel distributions of the various grey-level intensity values. Compared to qCT which provides a single global measurement, texture-based radiomics provides information about the distribution of disease. The objective of this study was to evaluate whether the addition of CT imaging features, texture-based radiomic features and qCT features, to conventional risk factors improves predicting progression to COPD in at-risk smokers with the use of the machine learning.

Methods: Smokers, current or former, with normal lung function (at-risk) from the Canadian Cohort Obstructive Lung Disease (CanCOLD) study underwent CT and spirometry at baseline; spirometry was repeated at a follow-up visit. A total of 111 features were used: 95 texture-based CT radiomics (Rad), 8 qCT (low-attenuation-areas-below -950HU (LAA₉₅₀), 15th-percentile-of-the-CT-density-histogram (HU₁₅), low-attenuation-cluster (LAC), normalized-join-count (NJC), theoretic-airway-wall-thickness-for-10mm-lumen-perimeter(Pi10), total-airway-count (TAC), lumen-area (LA), wall-area-percent (WA%)), 5 demographic (Demo) (Age, Sex, BMI, Pack-years, and Smoking Status) and 3 spirometry measurements (forced-expiratory-volume-in-1s, (FEV₁), forced-vital-capacity (FVC), and FEV₁/FVC). Combinations of 8 feature selection and 9 machine learning classification methods were evaluated for the various combinations of feature sets: conventional features only, CT imaging features only, and all features. Models were compared using the area under the receiver operating characteristic curve (AUC), F1-score, and accuracy. The machine learning model with the highest AUC performance was selected for each feature set.

Results: A total of 294 at-risk participants were evaluated. The average time to follow-up was 2.5±0.9years. There were 69 (20%) at-risk smokers that developed COPD at follow-up. The addition of CT imaging features to conventional risk factor features improved the model performance compared to the conventional features alone (All Features: AUC=0.88, F1-Score=0.79, Accuracy=0.85 vs. Demo+Spirometry: AUC=0.85, F1-Score=0.81, Accuracy=0.81), shown in Table 1. For the model with all features, 3 out of the 5 features selected for the machine learning model were CT imaging features, including 2 qCT features and 1 texture-based radiomic features.

Table 1: Performance metrics and top features selected for the various models with different feature sets.

	AUC	F1-Score	Accuracy	Features
<i>Demo+Spirometry</i>	0.85	0.79	0.81	FEV ₁ /FVC, Age, FEV ₁ , Smoke Status, Sex
<i>Rad+qCT</i>	0.71*	0.67	0.77	LA, NJC, GLDZM _{lgze} , GLDZM _{sdlge} , GLCM _{jointvar}
<i>All Features</i>	0.88	0.84	0.85	FEV ₁ /FVC, LA, Age, NJC, GLCM _{jointvar}

GLDZM = grey level distance zone matrix; GLCM = grey level co-occurrence matrix. * = statistically different from All Features (p<.05).

Conclusion: The addition of CT imaging features, texture-based radiomics and qCT features, to conventional risk factors improved the prediction of progression to COPD in at-risk smokers. CT imaging features may be able to detect the early structural changes occurring in the lungs, which is not identified by spirometry measurements. Specifically, CT imaging feature may be able to provide complementary information about COPD, which may allow for earlier diagnosis and improved disease monitoring.

Serial Two-Photon Tomography of Fluorescently-Labelled Alveolar-Like Macrophages Instilled in Rat Lungs

Melanie Posiewko¹, Daniel Li¹, Janny Kim^{1,2}, Michael Litvack¹, Sheena Bouch¹, Irene Tseu¹, Martin Post^{1,3}, Giles Santyr^{1,2}

¹The Hospital for Sick Children, Translational Medicine Program, Toronto, Ontario, Canada

²Department of Medical Biophysics, University of Toronto, Toronto, Ontario, Canada

³Department of Laboratory Medicine and Pathobiology, University of Toronto, Toronto, Ontario, Canada

Introduction: It is hypothesized that functional alveolar-like macrophages (ALMs) derived from pluripotent stem cells, when instilled into the airways of affected lung tissue, can mimic resident alveolar macrophages for treatment of chronic respiratory infections and disorders such as bronchopulmonary dysplasia, asthma, or cystic fibrosis (1,2). While ALMs have the potential to treat lung disease, the accuracy of instillation, end destination, and function of these cells has yet to be examined. This proof-of-concept project investigates the feasibility of using a novel serial two-photon tomography (STPT) system for *ex vivo* 3D localization and longitudinal tracking of ALMs instilled in the rat lung.

Methods: Fluorescently labelled ALMs were cultured, quantified, and instilled into the left lungs of intubated rats via guide tubing (3). After using a cell counter, the ~7 million ALMs were allowed to engraft in the lungs for varying lengths of time (15 minutes, 1 hour and 1 week) for three different rats respectively. Out of the 10 rats used in this project, 4 were PBS controls (no ALMs), and 6 were instilled with ALMs; of the 6 instilled rats, 3 were subjected to the time trials (one rat per trial) and the other 3 were sacrificed immediately following instillation. The entire lungs were extracted, separated into right and left lobes, embedded in agarose, and imaged by an STPT system (TissueCyte™, TissueVision). The resulting images from each full lung were assembled into a 3D data set and analyzed using commercial software (Volocity Quantification, Volocity) to localize the cells, confirm the instillation process, monitor cell migration, and quantify fluorescence. The fluorescence (rfu) was quantitated by comparing the brightest patch on each scan as well as comparing it with the constant value of the background.

Results: Imaging of the excised lung tissue confirmed the location of ALMs in the basal region of the left lung, consistent with previous results seen in our lab using this instillation procedure (3). Furthermore, the varying time trials revealed that the ALMs resided in regions distal from the main airways which became increasingly more distal and dispersed as a function of time (i.e., 1 week was more distal than 1 hour). The level of fluorescence was found to be higher in tissue instilled with tagged ALMs vs PBS controls [the right lung] (137 rfu), with the highest level found in the 1-hour cohort (3283 rfu).

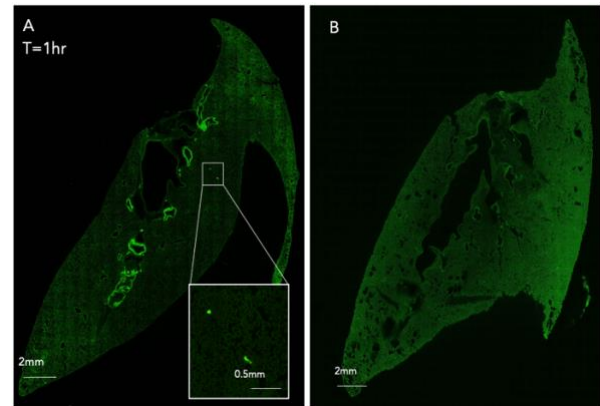


Figure 1: A) ALMs left for 1 hour, B) PBS control

Conclusions: Detection of fluorescently labelled ALMs instilled in the rat lung is feasible using two-photon serial microscopy (STPT). STPT confirmed that instilled ALMs migrate more distally and basally in the rat lung as a function of time, while the magnitude of fluorescence diminishes. This suggests that ALMs are relatively mobile in the rat lung and likely disperse following instillation, probably due to breathing forces.

Future work is required to understand the quantity and functionality of instilled ALMs in the lung to maximize therapeutic benefit.

References: [1] Bouch, S. et al, *Journal of Cellular and Molecular Medicine*, 2022. [2] Litvack, M. et al, *American journal of respiratory and critical care medicine* vol. 193,11, 2016 [3] Riberdy, V. et al, *Magnetic resonance in medicine* vol. 83,4, 2020

Pulmonary Small Vessel Worsening in Ex-smokers With COPDVedanth Desai^{1,2}, Paulina V Wyszkiwicz^{1,2}, Alexander M Matheson^{1,2}, Maksym Sharma^{1,2}, Marrison J McIntosh^{1,2}, Harkiran K Kooner^{1,2}, David G McCormack³ and Grace Parraga¹⁻⁴¹Robarts Research Institute, ²Department of Medical Biophysics, ³Division of Respiriology, Department of Medicine, ⁴School of Biomedical Engineering, Western University, London, Canada

INTRODUCTION: Pulmonary hypertension (PH) is characterized by increased pressure in the pulmonary artery, generally greater than 25 mmHg.¹ Previous studies suggest PH may contribute to worsening symptoms in individuals with chronic obstructive pulmonary disease (COPD).² Thoracic computed tomography (CT) pulmonary artery to aorta diameter ratio (PA:Ao) may serve as a biomarker for PH.² Furthermore, worse pulmonary small vessel remodeling may reflect more severe PH in COPD participants.³ However, it remains unclear how small vessel volume and PA:Ao persist or change over time in ex-smokers. In this study, we aim to investigate longitudinal changes in small vessel volumes and PA:Ao in both ex-smokers with and without COPD. We hypothesized that small vessel volume would decrease whereas PA:Ao would increase after three-years, together indicating subclinical PH.

METHODS: Ninety ex-smokers with (n=50) and without (n=40) COPD and no clinical diagnosis of PH, provided informed written consent (NCT02279329) to complete CT, pulmonary function tests (forced expiratory volume in one second and forced vital capacity) and a six minute walk distance (6MWD) test at baseline and at a three-year follow-up (2.6±0.6 years).⁴ PA:Ao was measured using custom-built software (Shift-64 Workstation). Chest Imaging Platform (Brigham and Women's Hospital) was used to generate total blood volume (TBV), blood volume in vessels with cross-sectional area less than 5 mm² (BV₅), between 5 and 10 mm² (BV₅₋₁₀) and greater than 10 mm² (BV₁₀). Paired samples t-tests were used to evaluate longitudinal differences.

RESULTS: Table 1 shows that in 40 ex-smokers without COPD, BV₅₋₁₀/TBV (p=.02) was significantly greater after three-years; however, BV₅/TBV, BV₁₀/TBV and PA:Ao were not. In 50 ex-smokers with COPD, BV₅/TBV (p=.02) significantly decreased after three-years, BV₅₋₁₀/TBV (p=.008) significantly increased after three-years; however, BV₁₀/TBV and PA:Ao did not.

CONCLUSIONS: After three-years, we observed small vessel worsening in ex-smokers with COPD. Our study revealed a significant decrease in small vessel volume and a significant increase in blood volume in vessels between 5 and 10 mm². Together, these findings may suggest vessel remodeling and potential blood redistribution from small vessels. In ex-smokers without COPD, small vessel volume did not change over time. This may indicate that the degree of pulmonary vessel changes are associated with COPD severity. In both ex-smokers with and without COPD, PA:Ao did not change significantly over three-years. Participant data at subsequent follow-up visits is required to investigate how PA:Ao may change or persist over extended periods of time.

REFERENCES: ¹Galie et al. *Eur Respir J* 2015; ²Wells et al. *N Engl J Med* 2012; ³Matsuoka et al. *AJRCCM* 2010; ⁴Kirby et al. *ChronicObstrPulmDis* 2014.

Parameter Mean (SD)	Ex-smokers without COPD (n=40)			Ex-smokers with COPD (n=50)		
	Baseline	Follow-up	p	Baseline	Follow-up	p
Age [yrs]	69 (10)	72 (10)	-	70 (9)	73 (9)	-
Female [n] %	17 (43)	17 (43)	-	16 (32)	16 (32)	-
BMI [kg/m ²]	30 (4)	30 (4)	.8	27 (4)	27 (4)	.7
Pack-years	30 (17)	30 (17)	-	44 (26)	44 (26)	-
FEV ₁ [%pred]	103 (18)	104 (20)	.5	69 (23)	68 (26)	.7
FEV ₁ /FVC [%]	81 (6)	79 (7)	.01	52 (13)	53 (12)	.4
6MWD [m]	421 (82)	409 (77)	.1	402 (72)	384 (90)	.07
PA:Ao	0.76 (0.1)	0.73 (0.1)	.1	0.74 (0.1)	0.74 (0.1)	.8
TBV [mL]	253 (40)	251 (41)	.9	269 (59)	265 (59)	.7
BV ₅ /TBV [%]	45 (6)	43 (5)	.1	43 (7)	40 (8)	.02
BV ₅₋₁₀ /TBV [%]	23 (3)	24 (2)	.02	22 (3)	24 (3)	.008
BV ₁₀ /TBV [%]	31 (5)	32 (4)	.3	34 (6)	35 (6)	.2

Table 1. Demographic data, pulmonary function tests, exercise-capacity and pulmonary vessel measurements for ex-smokers with and without COPD. BMI=body mass index; FEV₁=forced expiratory volume in 1 second; %pred=percent of predicted value; FVC=forced vital capacity; 6MWD=6 minute walk distance; PA:Ao=pulmonary artery to aorta diameter ratio; TBV=total blood volume in pulmonary vasculature; BV₅=blood volume in vessels <5 mm² cross-sectional area; BV₅₋₁₀=blood volume in vessels between 5-10 mm² cross-sectional area; BV₁₀=blood volume in vessels >10 mm² cross-sectional area; p=significant difference between time-points; bolded values=indicate statistically significant difference between baseline and follow-up.

Sex Differences in CT Airway Measurements and their Relationship to Post-Acute COVID-19 Syndrome

Harkiran K Kooner^{1,2}, Muhammad Faran³, Marrison J McIntosh^{1,2}, Alexander M Matheson^{1,2}, Paulina V Wyszkiwicz^{1,2}, Inderdeep Dhaliwal⁴, Mohammed Abdelrazek⁵, J Michael Nicholson⁴, and Grace Parraga^{1,2,4,5}

¹Robarts Research Institute; ²Department of Medical Biophysics; ³Department of Physiology and Pharmacology; ⁴Division of Respiriology, Department of Medicine; ⁵Department of Medical Imaging; Western University, London, Canada

RATIONALE: Post-acute COVID-19 syndrome (PACS) is defined by persistent symptoms and poor quality-of-life four-weeks beyond post-acute COVID-infection,¹ affecting ~6-30% of COVID-19 patients.² The mechanisms and pathologies responsible are not well-understood, although female sex was shown relevant in PACS development and/or persistence.²⁻⁴ There are well-documented CT airway measurement sex-differences, which in females with COPD are associated with worse outcomes.⁵ Based on these previous findings, we evaluated sex-differences in CT airway and pulmonary vascular measurements to determine relationships with longitudinal PACS outcomes.

METHODS: Participants were recruited three-months after COVID-19 infection⁶ and completed pulmonary function tests and six-minute walk test at two time points: 3- and 15-months post-infection. CT images were acquired only 3-months post-infection and were analyzed using VIDAvision to generate total airway count (TAC), wall area (WA), wall thickness percent (WT%), and lumen area (LA). Chest Imaging Platform⁷ was used to generate total blood volume (TBV), blood volume for vessels with cross-sectional area <5mm² (BV₅), between 5–10mm² (BV₅₋₁₀), and >10mm² (BV₁₀). Differences between males and females were evaluated using independent-samples t-tests and univariate linear-models adjusted for age, height, body mass index (BMI), lung volume, and chronic lung disease. Univariate relationships were evaluated using Spearman (ρ) correlations.

RESULTS: Of 76 participants with PACS recruited,⁶ 44 participants (n=23 males, 57±14yr; n=21 females, 50±12yr) consented to baseline CT and were evaluated 3±2 months following a positive COVID-19 test, of whom 33 returned for follow-up at 15±2 months. There was significantly different TAC ($p=.002$), WA ($p<.001$), WT% ($p=.007$), and LA ($p<.001$) in females. CT pulmonary vascular measurements were not different. Figure

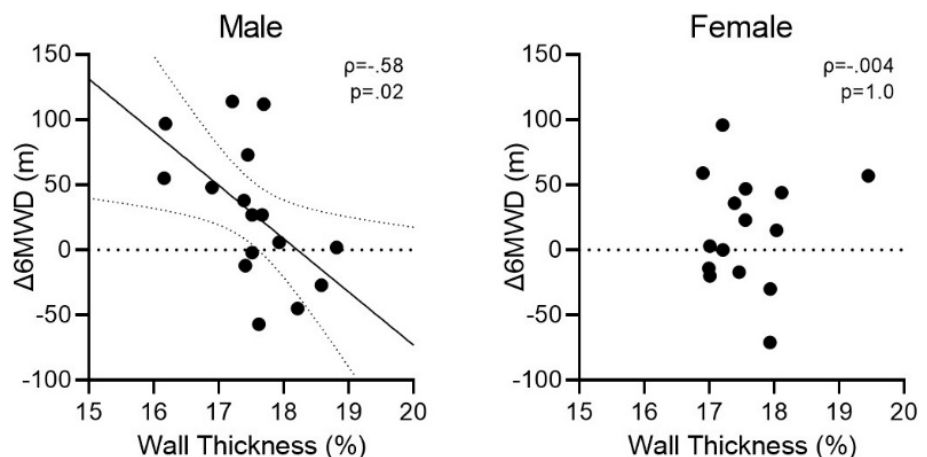


Figure 1. In males with PACS, CT wall thickness percent relates to the change in six-minute walk distance (6MWD) from 3- to 15-months post-infection, but not in females with PACS.

1 shows baseline CT WT% was related to improved six-minute walk distance 15-months post-infection in males ($\rho=-.58$, $p=.02$) but not females ($\rho=-.004$, $p=1.0$). There were no significant concordant relationships in males and females between CT airways measurements and clinical measurements.

CONCLUSIONS: While there were no differences in pulmonary vascular measurements, female participants with PACS reported significantly greater (worse) airway WA and WT% and lower (worse) TAC and LA, compared to males 3-months post-COVID infection. In agreement with previous observations of increased risk of PACS for females,^{3,4} our results suggest that sex-differences in airway, but not pulmonary vascular structure may play a role. The fact that improved exercise-capacity, 15-months post-infection, was related to airway wall thickness in males but not females may provide a link between airway sex-differences and longitudinal outcomes in PACS.

REFERENCES: ¹Nalbandian *NatMed*(2021); ²Global Burden of Disease Long COVID Collaborators *JAMA* (2022); ³Fernandez-de-Las-Penas *J Clin Med* (2022); ⁴Fumagalli *Eur J Intern Med* (2022); ⁵Bhatt *Radiology* (2022); ⁶Kooner & McIntosh *BMJ Open Respir Res* (2022); ⁷Estepar *Proc IEEE Int Symp Biomed Imaging* (2012).

Radiomics Analysis of Ultrashort Echo-Time Lung MRI in Pediatric Cystic FibrosisDaniel Genkin BEng¹, Brandon Zanette PhD², Thomas Benkert PhD³, Felix Ratjen MD^{2,4}, Giles Santyr PhD^{2,5}, and Miranda Kirby PhD⁶

Introduction: Cystic Fibrosis (CF) is a disease that results in pulmonary abnormalities such as airway inflammation (i.e. bronchiectasis), mucus plugging, and gas trapping.¹ Conventional measures such as a sweat-chloride test or spirometry, lack the ability to quantify local disease progression. Assessing these subtle structural changes can be achieved through visual scoring on computed tomography (CT)² and magnetic resonance imaging (MRI)³. However, visual scoring is laborious and introduces observer variability. Texture-based radiomics is an automated analysis technique that provides textural information by extracting the spatial distribution of signal intensities. Radiomics features have been shown to capture morphological changes in diseased lungs, and correlate with both CT visual score and pulmonary function in adult CF patients.^{4,5} Nevertheless, performing repeated CT imaging on the pediatric population to monitor progression is not ideal due to radiation exposure. To our knowledge, lung radiomics analysis has not been investigated in pediatric participants using MRI. We hypothesize that in pediatric CF participants, regions of pulmonary abnormalities reflecting signal heterogeneity will be detected using radiomics analysis. Therefore, our objective was to develop an automated method to extract lung MRI radiomics measurements and determine if they differentiate pediatric CF and healthy participants and correlate with pulmonary function.

Methods: CF (n=9) and age-matched healthy participants (n=4) had demographics, pulmonary function, and MRI collected at The Hospital for Sick Children (TO, Canada). Ultra-short echo time (UTE) images were acquired at 3T using a research application isotropic 1.5mm³ stack-of-spirals volumetric interpolated breath-hold examination, and reconstructed to end-expiration.⁶ Thereafter, image processing was performed using MATLAB. The lungs were automatically segmented using a deep learning model,⁷ and the MR lung volume (MR-LV) was extracted. Next, gray-level co-occurrence matrices (GLCM) were calculated, and 19 textural radiomics features were quantified.⁸⁻¹⁰ An ensemble-tree classification model selected the most relevant GLCM features (predictor importance>0.2). The Mann-Whitney U test was used to compare demographics, lung function, and radiomic measurements between groups. Spearman correlations were used to determine the relationships between radiomics and lung function measurements (forced expiratory volume in 1s (FEV₁), FEV₁/forced vital capacity (FEV₁/FVC)).

Results: There were no significant differences (p>0.05) between the groups for age (CF: 15.3±2.0yrs, Healthy: 14.5±1.7yrs), sex, or MR-LV. Compared to healthy participants, CF participants had reduced FEV_{1pp} (CF: 77.6±18.3%, Healthy: 98.5±8.6%; p=0.03), but no significant difference in FEV₁/FVC (CF: 86.3±10.4%, Healthy: 98.1±12.2; p=0.08). Contrast, entropy, and energy were the most important GLCM features selected by the ensemble-tree classification model. The groups were significantly different for energy and entropy (p<0.01), and on the threshold for contrast (p=0.05). All 3 radiomics measurements were significantly correlated (p<0.05) with pulmonary function: contrast (FEV_{1pp}: ρ=-0.62; FEV₁/FVC: ρ=-0.59), energy (FEV_{1pp}: ρ=0.71; FEV₁/FVC: ρ=0.66), and entropy (FEV_{1pp}: ρ=-0.74; FEV₁/FVC: ρ=-0.69).

Conclusion: In this proof-of-principle study with a small number of pediatric CF and healthy participants, we demonstrated that radiomics measurements automatically extracted from UTE MRI were significantly different between the two groups and significantly correlated with lung function. The findings of this study motivate further exploration of a wider set of UTE MRI radiomics through larger pediatric cohorts, and validation against established CT-based radiomics and visual scoring.

Author Affiliations

¹Department of Electrical, Computer, and Biomedical Engineering, Toronto Metropolitan University, Canada; ²Department of Translational Medicine, The Hospital for Sick Children, Toronto, Canada; ³MR Application Predevelopment, Siemens Healthcare GmbH, Germany; ⁴Department of Paediatrics, University of Toronto, Canada; ⁵Department of Medical Biophysics, University of Toronto, Canada; ⁶Department of Physics, Toronto Metropolitan University, Canada.

References

¹Turcios NL. *Respir Care*, 2020. ²Brody AS, et al. *Pediatr Radiol*, 1999. ³Roach DJ, et al. *Ann Am Thorac Soc*, 2016. ⁴Chassagnon G, et al. *Radiol Cardiothorac Imaging*, 2020. ⁵Wang T, et al. *Radiology*, 2022. ⁶Mugler J, et al. *Proc Intl Soc Mag Reson Med*, 2017. ⁷Weng AM, et al. *BMJ Med Imaging*, 2021. ⁸Haralick et al, *IEEE Trans. Syst*, 1973. ⁹Soh LK, et al. *IEEE Trans Geosci Remote Sens*, 1999. ¹⁰Uppuluri. *MATLAB Cent File Exch*, 2008.

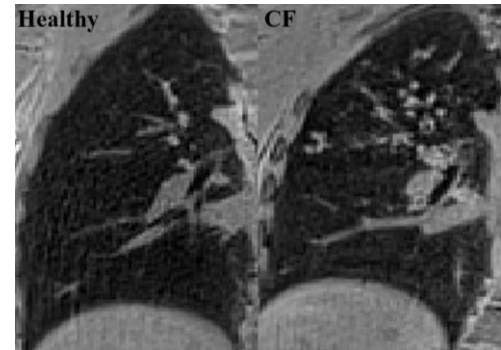
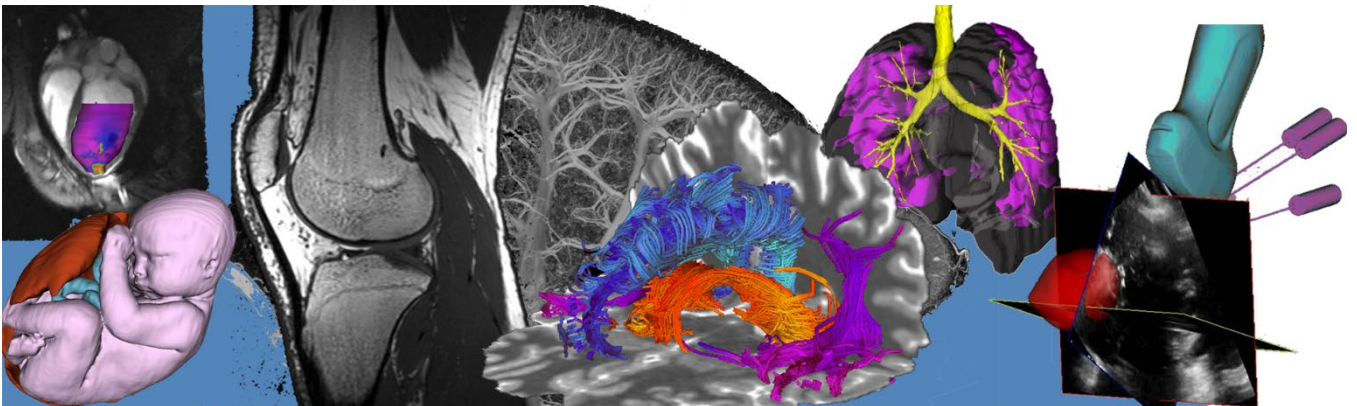


Figure 1. UTE MRI of the right lung in a Healthy (left) and CF (right) participant. The CF participant's right upper lobe has visible textural abnormalities (mucus plugging/bronchiectasis).

Pitch/Poster Session 4: Image Guidance Abstracts



Analysis of cautery trajectory for evaluation of resection margins in breast-conserving surgery

Chris Yeung^a, Josh Ehrlich^a, Amoon Jamzad^a, Martin Kaufmann^b, John Rudan^b, Cecil Jay Engel^b, Parvin Mousavi^a, Tamas Ungi^a, Gabor Fichtinger^a

^aSchool of Computing, Queen's University, Kingston, ON, Canada;

^bDepartment of Surgery, Kingston Health Sciences Centre, Kingston, ON, Canada

INTRODUCTION: Breast cancer is the most common cancer in women worldwide. Most often breast-conserving surgery (BCS) is performed to remove the tumor from the breast. However, positive margins can occur if the tumor specimen that was removed is not completely surrounded by healthy tissue, increasing the chance that some cancer was left behind. To address this, a surgical navigation system (NaviKnife) has been developed which uses electromagnetic tracking to visualize the locations of the surgical tools and tumor in real-time¹ (Fig. 1). This study aims to perform a gross evaluation of the NaviKnife and its application intraoperatively with respect to resection margins. The trajectory of the cautery used during BCS will be analyzed to determine whether the location of positive margins can be identified using the navigation system.

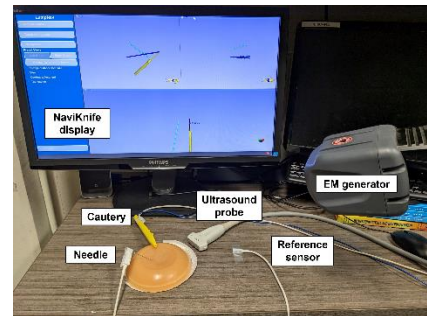


Figure 1. NaviKnife setup. Surgical tools are tracked and displayed to the user in real-time.

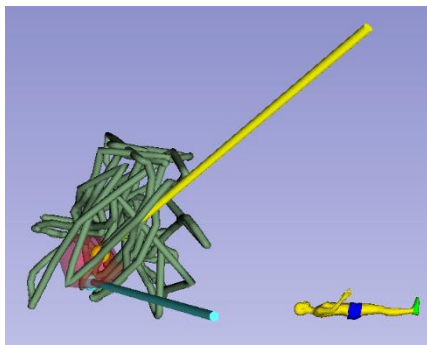


Figure 2. Trajectory of the surgical cautery when nearest the tumor model. Cautery (yellow), tumor (red), green (trajectory), blue (needle).

METHODS: The data used in this study was collected from six non-palpable BCS cases that were deemed margin-positive following the procedure. A 3D model of the tumor was generated in 3D Slicer via a radiologist marking points around the lesion on the ultrasound image, and the position of this tumor model along with the surgical cautery was recorded throughout the surgery. Following removal of the tumor, each anatomical direction of the tumor was inked with a separate color to report the location of the positive margin following pathological analysis. For every frame in the recording, the shortest Euclidean distance between the tumor model and the cautery tip was calculated. From these, the time interval of the procedure during which the smallest shortest distance occurred was determined. The path of the cautery tip during this time interval was visualized and its anatomical direction, hereon referred to as the side, relative to the tumor model was determined visually.

RESULTS: In two out of the six cases, the side where the cautery came the closest to the tumor model coincided with the anatomical location where positive margins were reported from pathology (Table 1). However, only one out of these two cases showed a direct breach in the ultrasound-based tumor margin (Fig. 2). For the four other cases, the cautery breached or came close to the tumor model, but at locations that were on an adjacent (a non-opposite anatomical direction; e.g. anterior and lateral) side compared to that reported from pathology.

Table 1. Location of the cautery when closest to the tumor model for 6 lumpectomy cases, compared with pathology reports.

Case	Breast	Side (pathology report)	Side (navigation)	Closest distance (mm)
1	Right	Deep inferior	Deep lateral	0
2	Right	Lateral	Inferior	0
3	Right	Anterior	Anterior	0
4	Right	Lateral	Lateral	2.2
5	Left	Medial	Superior	1.4
6	Left	Lateral	Anterior	0

CONCLUSIONS: Depending on the size of the breast and the position of the patient, the location of the cautery shown in the navigation may differ from its true anatomical location. Also, some breast cancers are not visible from ultrasound imaging, such as ductal carcinoma in situ. Thus, re-excision surgeries should also target margins adjacent to the location reported by pathology to ensure complete tumor removal. Future work will need to involve other methods, such as intraoperative mass spectrometry, to predict the location of positive margins.

REFERENCES:

1. Gauvin, G. *et al.* Real-time electromagnetic navigation for breast-conserving surgery using NaviKnife technology: A matched case-control study. *Breast Journal* **26**, 399–405 (2020).

The CathPilot: First preclinical safety and feasibility assessmentMohammadmahdi (Sina) Keshavarz,^{1,2} Graham Wright,² Andrew Dueck,² M. Ali Tavallaei^{1,2}¹Toronto Metropolitan University, Toronto, Canada²Sunnybrook Health Sciences Centre, Toronto, Canada

Introduction: Precise navigation and control of catheters and guidewires is a great challenge in various cardiovascular interventions. To address this need, J. Zhou et al.[1] developed the CathPilot, a novel steerable catheter that allows accurate device steering and control for various interventional procedures with an initial indication of use for peripheral revascularization [1], which is depicted in Fig.1-2. In this study, we assess the CathPilot's safety and feasibility *in vivo* using a swine model. The study's goal was to test the following: the feasibility of using the device in a conventional interventional procedure and its reliable functionality *in vivo*, potential damage to the arterial wall, and the device's thrombogenicity.

Methods: For our experiments, a male pig (56.6 Kg) was used. Heparin anticoagulant (100IU/Kg direct injection and 2000IU in IV) was administered. Procedures were performed by an experienced vascular interventionalist with more than 15 years of experience. To create blood flow dynamics similar to that of an arterial occlusion, a balloon catheter (7mm OD, Abbott Armada 35 PTA) was advanced from the carotid artery and deployed midway through the aorta. Using a right-side femoral artery access, a non-steerable 12 Fr sheath (Cook Medical G56279) was advanced with standard methods and positioned inferior to the balloon. The CathPilot was advanced through this delivery sheath and deployed at the target site inferior to the renal arteries (Fig. 2). With the frame of the CathPilot anchored onto the anatomy, it was steered and moved for 15 minutes with its motion confirmed via fluoroscopy. Every 5 minutes the system was flushed with saline (~10ml each time). Immediately after the procedure, the CathPilot was withdrawn and inspected visually for signs of coagulation. The pig was euthanized, and the artery was excised and cut open to observe for any visual signs of damage or trauma to the endothelial layer at the site of CathPilot deployment.

Results: The CathPilot was introduced and retracted with standard procedural flows and was fully functional throughout the experiment. It was able to successfully steer the device within its full workspace (as validated by fluoroscopy) without any mechanical issues. There were no visible signs of coagulation on the device frame or on its cables after its retraction. Also, the visual inspection of the harvested aorta showed no visible signs of damage or bruises to the endothelial layer and walls of the aorta.

Conclusion: This study was the first preclinical *in vivo* assessment of the CathPilot. We demonstrated that the CathPilot could be introduced, deployed, and retracted using standard practices and fluent procedural steps. Our results indicate that the operation of the CathPilot is feasible within an *in vivo* model, and there were no signs of coagulation or damage to the vessel wall.

Reference: J. J. Zhou et al., IEEE/ASME TMECH, 2021, doi: 10.1109/TMECH.2022.3188955.

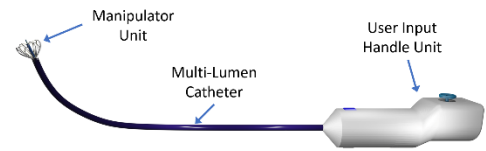


Fig. 1. The CathPilot system is shown [1].

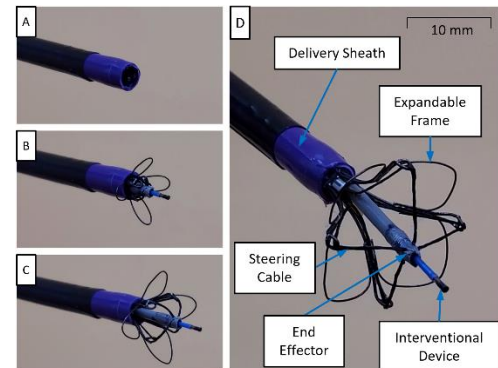


Fig 2. The CathPilot frame (manipulator unit) and its sequential steps of deployment (A-D) are shown [1].

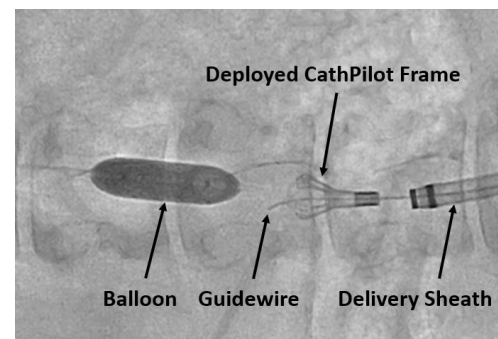


Fig. 3. X-ray images of CathPilot as deployed in the aorta in front of the balloon is shown.

Electromagnetic navigation for residual tumor localization in breast-conserving surgery
 Olivia Radcliffe¹, Laura Connolly¹, Tamas Ungi¹, Caitlin Yeo², John F. Rudan¹, Gabor Fichtinger¹,
 Parvin Mousavi¹

1. Queen's University, Kingston, ON, Canada,
2. University of Calgary, Calgary, AB, Canada

INTRODUCTION: As of 2021, breast cancer is the most common cancer worldwide [1]. A standard treatment option for breast cancer patients is breast conserving surgery (BCS). In these procedures, the tumor is removed from the breast while the surrounding healthy tissue is intentionally preserved. Currently, up to 40% of BCS patients must undergo repeat surgery because cancer is left behind in the tumor bed [1, 2]. Determining the completeness of the resection relies on pathological examination of the resected tumor. One of the challenges with this process is that the resection cavity in the breast is highly deformable making it difficult to map these pathological findings back to their original location on the tumor bed. Therefore, we hypothesize that performing a navigated imaging sweep of the tumor bed in BCS procedures will help localize residual cancer intraoperatively.

METHODS: To test this hypothesis we developed a navigation system for performing tumor bed inspection using the flexible, open-source medical imaging software, 3D slicer. The proposed surgical approach uses electromagnetic (EM) tracking, any intraoperative imaging device capable of detecting residual cancer and compatible with the Plus server application (www.plustoolkit.org), and our navigation system developed in 3D slicer. The process we propose involves i) scanning the tumor bed with a tracked imaging device; ii) marking detected cancer with the imaging device in our navigation system; iii) using our software to navigate a tracked cautery to the marked location and iv) performing resection. EM tracking was chosen as it has previously been incorporated into BCS [3]. To evaluate the accuracy of our approach, we simulated tumor bed inspection in BCS (Figure 1) and had users test our system. Our simulated setup included a breast implant with a portion removed to mimic the deformation of a breast tumor bed. We propped open the cavity with a custom 3D-printed retractor and attached an EM sensor to track the breast's movement. Since this study focused on localization, we used a non-functional 3D-printed endocavity ultrasound (US) probe with another EM sensor. The probe was used to simulate an US scan of the walls and to register the location of residual cancer on our display. A 5 mm sphere of red silicon plastic was placed inside the breast implant to visually mark residual cancer in our phantom. Lastly, in place of a cautery device, we used a tracked needle to determine the accuracy of localizing the marked residual cancer in the phantom and navigation display. To test our system, 7 students with varying experience levels with 3D Slicer performed our simulated workflow. We then recorded the distance between the needle and marked residual cancer in both our navigation display and in the physical breast phantom.

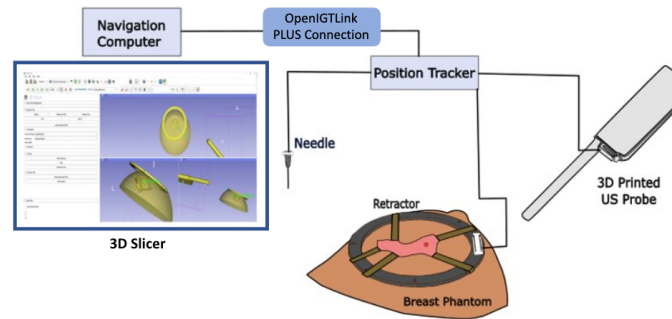


Figure 1: Simulated breast tumor bed inspection using our system.

RESULTS: Users placed their needle tip an average of 0.6 ± 0.9 mm to the target point in our navigation system visualization. In the physical breast phantom, all users inserted their needle within 4 mm of the silicon residual cancer model.

CONCLUSIONS: We demonstrated the feasibility of our developed platform which uses EM navigation to accurately target residual cancer for resection in a breast cavity phantom. Our method can potentially help reduce the volume of unnecessary resected healthy tissue in tumor bed inspection and decrease reoperation rates. Our developed 3D slicer module can further be adapted for use in other soft tissue tumor resection cavities.

References

- [1] World Health Organization. (2021, February). *Breast cancer now most common form of cancer: WHO taking action*. World Health Organization. Retrieved November 30, 2022, from <https://www.who.int/news/item/03-02-2021-breast-cancer-now-most-common-form-of-cancer-who-taking-action>
- [2] Intraoperative tissue identification using rapid evaporative ionization mass spectrometry. (2013). *Journal of Clinical Engineering*, 38(4), 153–154.
- [3] Gauvin, G et al. (2020). Real-time electromagnetic navigation for breast-conserving surgery using NaviKnife technology: A matched case-control study. *The Breast Journal*, 26(3), 399–405.

Development and Evaluation of an Open-Source Virtual Reality C-Arm Simulator

D.R.Allen^{1,2}, C. Clarke⁴, T.Peters^{1,2,3}, E.C.S.Chen^{1,2,3}

¹School of Biomedical Engineering, Western University, London, Ontario, Canada

²Robarts Research Institute, Western University, London, Ontario, Canada,

³Department of Medical Biophysics, Western University, London, Ontario, Canada

⁴Department of Anaesthesia, London Health Sciences Centre, London, Ontario, Canada

Purpose:

C-Arm positioning for interventional spine procedures is often associated with a steep learning curve. This task requires mentally reconstructing 3D surgical tools and patient anatomy from a 2D X-ray image, which is non-trivial and usually acquired through years of experience. Furthermore, standard training via apprenticeship-based programs must be limited due to the unnecessary exposure to ionizing radiation. To this end, we propose a radiation-free, Virtual Reality (VR) C-Arm simulator for interventional spine procedure training.

Methods:

We implemented the simulator as an open-source module in 3D Slicer, built on top of SlicerVR, to enable stereoscopic visualization of the scene through a VR Head-mounted-display (HMD). Based on the position of the virtual X-ray source and patient, Digitally Reconstructed Radiographs (DRR's) were generated using GPU ray-tracing and a 1D transfer function. We evaluated the efficacy of the simulator as a training tool through a user study, recruiting medical residents (N=12) and expert clinicians (N=2). The evaluation consisted of two rounds of C-Arm placement tasks in the simulator, in which the user aimed to achieve the optimal X-ray projection, for three standard views commonly employed in spinal procedures. The two rounds occurred consecutively in the same session, with a 7 minute training component in the middle in which they were allowed to use the real-time DRR functionality of the system to see how the DRR changes with respect to changes in the virtual C-Arm pose.

Results:

After completing the training component, the users showed an overall significant improvement in C-Arm placement capabilities with regards to angular accuracy (mean 2 degree improvement) and total procedure time (mean 11 minutes less time). The users also acquired on average approximately 16 fewer virtual X-ray images, however this change was not significant. The face and content validity was evaluated positively through a Likert scale questionnaire, with a mean score of 4 (out of 5) or higher for each of the questions.

Conclusions:

We have built an open-source VR C-Arm simulator and evaluated its efficacy as a training tool for C-Arm placement in fluoroscopy-guided interventional spine procedures. The quantitative results show the simulator provides effective training for C-Arm positioning, while eliminating the exposure to ionizing radiation associated with the current training standard. Although this work is catered towards spinal procedures, the system is extendable to other fields, such as cardiac and orthopaedic, and will be explored in future works.

Link to Github: <https://github.com/dallen-28/CarmSimulatorSlicer>

Surgical tool detection in open hernia repair surgery using deep neural networksKian Hashtrudi-Zaad^a, Rebecca Hisey^a, Elizabeth Klosa^a, Boris Zevin^b, Tamas Ungi^a, Gabor Fichtinger^a^aLaboratory for Percutaneous Surgery, School of Computing, Queen's University, Kingston, Ontario^bDepartment of Surgery, Queen's University, Kingston, Ontario

Introduction: Competency-based medical education demands more time from instructors and physicians to perform the necessary checks and assessments of trainees. To address the increased time demand, previous projects, such as the PerkTutor, have created computer-assisted skill assessment platforms for surgical procedures and interventions that rely on tool tracking [1]. As a result, there are limitations to the platforms, namely the added cost and complexity of attaching sensors to surgical tools, and modifications to the surgical field. To address these limitations, the current study aims to develop an object detection network to recognize surgical tools from low-cost webcam recordings of the procedure without the use of tracking sensors. This network provides the foundation for the computation of competence metrics and enables workflow recognition, aiding the development of a computer-assisted skill assessment platform for open inguinal hernia repair surgery.

Methods: To train the object detection network, three experts performed open inguinal hernia repairs on phantoms previously developed by Nazari et al. [2]. Recordings were recorded by two RGB webcams mounted on the table. This yielded six videos in total. Using DeepLearnLive, a 3D Slicer extension for medical imaging, the videos were broken into individual frames, yielding 51,442 images. VGG Image Annotator, a web-based annotation software, was used to manually label the dataset. As shown in Figure 1, each surgical tool was annotated with a rectangular bounding box and labelled with its corresponding class name. Due to time constraints posed by the annotation, a preliminary set of data using one video was used for this preliminary study. We hope

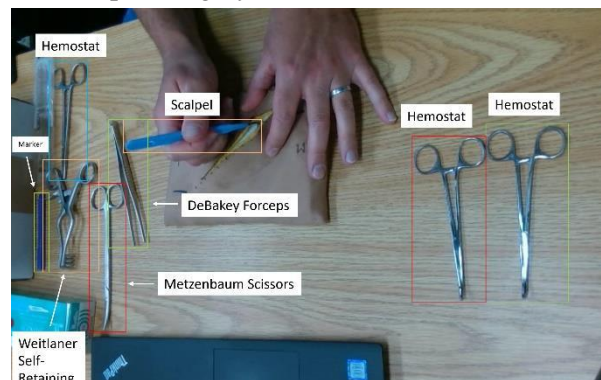


Figure 1. Bounding box annotations for the tools.

to use all six videos with cross-fold validation as the research progresses. Images obtained from the first video were randomly grouped into non-overlapping sets. 70 percent were assigned to train, 15 percent to validation, and 15 percent to test. We used a YOLOV3 model for the tool detection in our study, a convolutional network which performs well in object detection. It will divide an image into regions and predict bounding boxes and associate class probabilities. As opposed to other methods, YOLO will perform this with the entire image in one shot. YOLO will predict an “objectness” score for each bounding box and the class associated with it. The model then evaluates the scores and yields a final bounding box and confidence scores. The model’s ability to detect a specific tool class was quantitatively evaluated using mean average precision (mAP), which is calculated as the area under the precision-recall curve. This evaluates the model’s performance across all tool classes, while precision was also calculated for specific tool classes.

Results: Precision scores for the tool classes ranged from 0.22 to 0.98. Tool classes such as the Hemostat, Weitlaner retractor and Marker, had high scores of 0.87, 0.98, and 0.95, respectively. In contrast, other classes such as the Mesh, Debakey Forceps, Metzenbaum Scissors, and Scalpel had lower precisions of 0.22, 0.34, 0.36, and 0.53, respectively. The overall performance of the network was a 0.61 mAP.

Conclusion: Through object detection, surgical tools were identified successfully in videos of open inguinal hernia repair. Tools that were present frequently and not occluded performed especially well. Tools that physically resembled others such as the scissors or those with similar background as the tissue (mesh) were detected with low precision. Following tool recognition through object detection, future research will focus on integrating the model into a computer-assisted training platform.

[1] Ungi T, Sargent D, Moulton E, Lasso A, Pinter C, McGraw RC, Fichtinger G. Perk Tutor: an open-source training platform for ultrasound-guided needle insertions. *IEEE Trans Biomed Eng.* 2012 Dec;59(12):3475-81.

[2] Nazari, T., Simons, M. P., Zeb, M. H., van Merriënboer, J. J., et al “Validity of a low-cost Lichtenstein open inguinal hernia repair simulation model for surgical training,” *Hernia* 24(4), 895–901 (2019).

Point-Of-Care Ultrasound Carotid Artery Volume Reconstruction Using Deep-Learning

Michellie Choi, Shuwei Xing, M. Reza Azarpazhooh, Terry M. Peters, and Elvis C. S. Chen
 Robarts Research Institute, Schulich School of Medicine and Dentistry, Western University

Introduction: The volumetric assessment of plaque and carotid anatomy in atherosclerotic patients continues to be a challenging task using two-dimensional B-mode ultrasound [1]. Due to the superficial location of the carotid artery, ultrasound provides excellent visualization. In this work, we propose a method to combine AI assisted segmentation and tracked freehand ultrasound to create 3D volumes from 2D carotid ultrasound.

Methods: 3000 3D Ultrasound volumes containing manual segmentations were divided into batch sizes of 30 and run for 500 epochs. Training was performed using nnU-Net in Python (PyTorch) with GPU acceleration (NVIDIA Quadro RTX 6000) using Dice and cross-entropy as a cost function. Data was augmented by rotations scaling, Gaussian noise, Gaussian blur, brightness, contrast, simulation of low resolution, gamma correction and mirroring. Poly learning rate was scheduled with an initial value of 0.01 with learning reduced gradually. Volume reconstruction was conducted using webcam-tracked 2D ultrasound using the Clarius © HD3 wireless probe and Aruco markers.

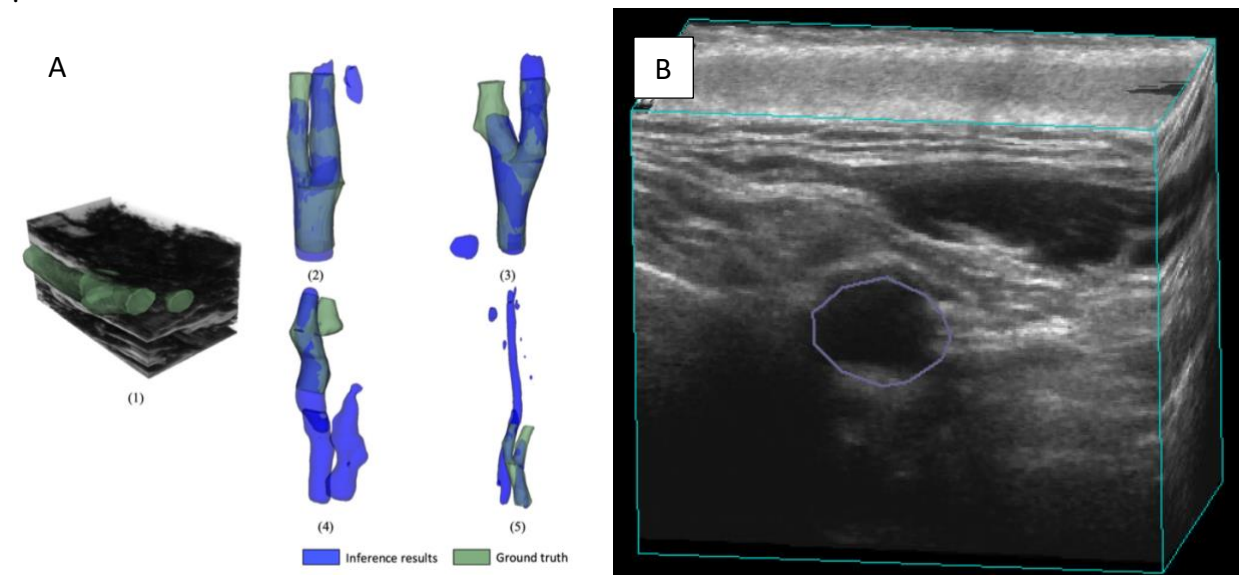


Fig 1. A) Ground truth 3D US segmentation (1) and inference results using our trained model (2-5). B) Sample carotid artery volume from the CAIN dataset.

Results: Preliminary results were obtained from training the network using a small (n=31) subset of data. While cases 2-3 have considerable overlap between the output inference (blue) and ground truth (green), cases 4-5 display over-segmentation. Accuracy of this method is to be assessed using Dice coefficient score and volumetric analysis using a carotid artery phantom obtained using CT.

Conclusions: In this work, we have presented a preliminary model for deep-learning based segmentation of the carotid artery and atherosclerotic plaque to be applied to reconstructed volumes using 2D linear-array point-of-care ultrasound with camera-based tracking.

References: [1] Design, . D. S. . I., Lukanova, D. V., Nikolov, N. D., Genova, K. Z., Stankev, M. D., and Georgieva, E. V., “The accuracy of noninvasive imaging techniques in diagnosis of carotid plaque morphology,” *Open Access Macedonian Journal of Medical Sciences* 3, 224–230 (2012).

Evaluation of tracked optical tissue sensing for tumor bed inspection

David Morton, Laura Connolly, Leah Groves, Kyle Sunderland, Amoon Jamzad,

John F. Rudan, Gabor Fichtinger, Tamas Ungi, Parvin Mousavi

Queen's University, Kingston, Canada

INTRODUCTION: Up to 30% of breast-conserving surgery patients require secondary surgery to remove cancerous tissue missed in the initial intervention [1]. This can lead to postoperative complications, impaired cosmesis, increased psychological distress, and increased cost [2]. The visual ambiguity of healthy and cancerous breast tissue is a factor contributing to high rates of revision surgeries. We hypothesize that tracked spectroscopy for tissue sensing can help mitigate this issue by allowing for intraoperative classification and localization of the tissue. In this work, we develop a modular research testbed for tracked spectrometry tissue classification. We present the experimental workflow to characterize the performance of our testbed in terms of localized classification accuracy, Dice similarity coefficient and testbed latencies on a tissue phantom.

METHODS: We develop a testbed consisting of a spectroscope, an electromagnetic tracker, and a custom-built 3D Slicer module (www.slicer.org). The spectroscope characterizes tissue in the near ultraviolet to infrared range. The tracker localizes the tip of the spectroscopy probe. The resultant spectra and position data are sent to the 3D Slicer module. We use PLUS (www.PlusToolkit.org) and OpenIGTLink (openigtlink.org) to allow any compatible devices to be used with the testbed. The 3D Slicer module classifies the incoming spectra using a machine-learning classifier. The classifications are combined with their corresponding position data to produce a colour-coded point cloud. The result is superimposed on an image of the scanned location [Figure 1]. This depicts the predicted tissue type overlaid on the sample.

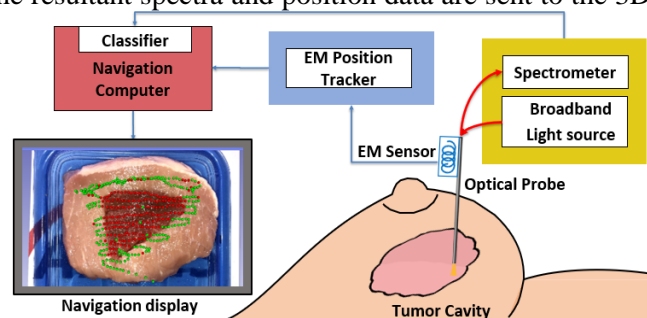


Figure 1: Diagram of proposed tracked optical tissue classification testbed.

A preliminary trial was conducted with a k-Nearest-Neighbours classifier. The classifier was trained and evaluated on biological ex vivo tissue. To validate model parameters, 72 spectra were recorded in two 6x6 grids, one bovine and one porcine. Each spectrum was normalized between 0 and 1. Binary labels were assigned to each class. Leave-one-out cross-validation was conducted. Each 6x6 grid was divided into 4 quadrants, 3 for training, and 1 for validation. After confirming the effectiveness of the classifier, a new model was trained on 100 spectra of bovine and porcine tissue for use in the live testbed evaluation. To evaluate the full testbed, a tissue phantom was created consisting of bovine tissue inserted into porcine tissue to simulate a tumor in benign tissue. The phantom was then scanned in a grid pattern to cover the entire simulated tumor and surrounding tissues. The resulting point cloud of classifications was colour-coded by class and registered to an image of the phantom. The number of correctly and incorrectly classified points were counted. Classification and position latencies were determined via visual inspection of a 240 Hz recording of the 60 Hz testbed display.

Results: In our preliminary trials we successfully classified biological ex vivo tissue samples with an accuracy of 0.94 and a Dice similarity coefficient of 0.93. We also achieved latencies of 167 ms and 125 ms for classification and tracking, respectively. Our confidence at tissue boundaries is notably limited due to errors in tracking. The error ranged from 1-2 mm based on proximity to the source. This study will continue with the further evaluation of classifiers such as the support vector machine, random forest, and 1D convolutional neural network. Preprocessing techniques such as data augmentation and calibration will also be conducted.

Conclusion: The modular research testbed presented in this study demonstrates the potential of tracked spectrometry for intraoperative tissue classification and localization. This research provides a basis for further development and evaluation of this technology.

REFERENCES: [1] D. M. Black, K. K. Hunt, and E. A. Mittendorf, "Long term outcomes reporting the safety of breast conserving therapy compared to mastectomy: 20-year results of EORTC 10801," *Gland Surg.* (2013).

[2] J. L. Oh, "Multifocal or Multicentric Breast Cancer: Understanding Its Impact on Management and Treatment Outcomes," *Methods Cancer Diagnosis, Ther. Progn.* (2008).

Anthropomorphic liver phantom development for training and validation of surgical navigation systemsJoeana Cambranis Romero^a, Terry M. Peters^{a,b,c}, and Elvis C. S. Chen^{a,b,c}^aSchool of Biomedical Engineering, ^bRobarts Research Institute, ^cDepartment of Medical Biophysics, Western University, London, Ontario, Canada

Introduction: While a variety of phantoms compatible with various imaging modalities are available commercially for training purposes, most of them contain simplified anatomy and are expensive.¹ Many also have blood vessel structures present but lack a closed-loop vasculature through which a blood-mimicking fluid can flow.² Additionally, the most prominent problem associated with commercial phantoms is their short lifetime when talking of needle insertions, which can be extended with specific additives, but it is still not comparable to other more sustainable materials.¹ This work presents the development of an anthropomorphic, multi-modality liver phantom with simulated tumour and vascular flow. The final goal of the phantom is to serve as a sandbox environment for training and validation of surgical navigation systems in the clinical context of focal liver tumour ablation.

Methods: The phantom consists of five different parts: the left and right lobes, internal and external vasculature (part of the Inferior Vena Cava), and simulated tumours. The geometry of these anatomical features is based on patient-specific CT data. Our anthropomorphic liver phantom is made with PolyVinyl Alcohol cryogel (PVA-c) to serve as an Ultrasound (US), Magnetic Resonance Imaging (MRI), and Computer Tomography (CT) compatible tissue-mimicking material.³ Talcum powder was added to the PVA-c to provide realistic speckle under US imaging. To create the closed-loop vasculature flow, positive silicone vasculature moulds were inserted into the liver body mould prior to PVA-c filling. After the freeze-thaw cycles, the silicone vasculature moulds are extracted from the liver body creating an internal network of canals. To recreate the blood flow, a water pump was connected to the liver phantom vasculature to allow the flowing through the internal canals.

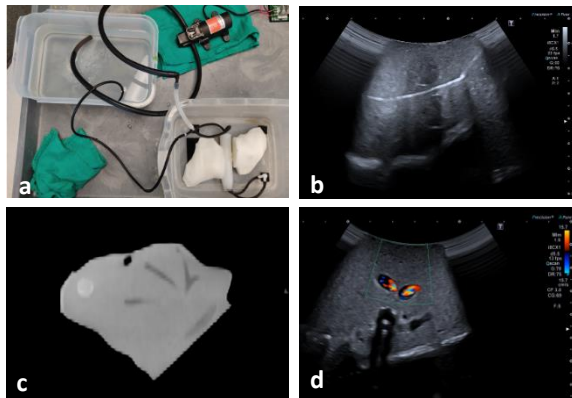


Figure 1. Liver phantom

Results: The phantom presented a semi-firm consistency, Figure 1.a show the resultant liver body (i.e., connected to a water pump). The imaging results show compatibility with CT and US, with tumours being visible in both imaging modalities. MRI imaging has been proven in other works.³ The anthropomorphic features, liver body edge (in US) and vessels (branches and bifurcations), can be appreciated with highly realistic characteristics in both imaging modalities. Figures 1.b and 1.c show the CT and US scans taken, where tumours, vessels and liver body can be appreciated in the volumes. The water pump could produce small bubbles on the circulating water allowing us to visualize some motion in the

vessels (Figure 1.d shows the US Doppler acquired). A proper blood mimic fluid will be used to test the doppler imaging properly and the “heat sink” effect during heat ablation procedures in the future.

Conclusion: The key advantage of our phantom is that it can be customized depending on the necessities (e.g., number of tumours, localization, size, etc.). The phantom can be imaged using CT, US and MRI. The anthropomorphic characteristics and the manufacturing technique make our liver phantom a good tool to function as a sandbox environment for needle puncture procedures (e.g., focal ablation or biopsies), where the vessels are not intended to be punctured. Future experiments should be performed to assess the lifespan of the vessels if suffering punctures, and ensure the overall phantom lifetime when talking of needle insertions. Other possible applications include training and validation of surgical navigation systems for these types of interventions.

References: [1] Pacioni A., et al., “Patient-specific ultrasound liver phantom: materials and fabrication method”. *International Journal of Computer Assisted Radiology and Surgery*, 10(7):1065– 1075, Jul 2015. [2] Rethy A., et al., “Anthropomorphic liver phantom with flow for multimodal image-guided liver therapy research and training”. *International Journal of Computer Assisted Radiology and Surgery*, Jan 2018. [3] Surry, K. J. M., et al., “Poly(vinyl alcohol) cryogel phantoms for use in ultrasound and MR imaging,” *Physics in Medicine & Biology*, Dec 2004.

The development of an AI-based system for training percutaneous nephrostomy in Senegal

R. Hisey¹, K. Sunderland¹, I. Seck², L. Groves¹, M. Camara², T. Ungi¹, P. Mousavi¹, G. Fichtinger¹, B. Diao³

¹School of Computing, Queen's University, Kingston, Canada

²Department Génie Informatique, École Supérieur Polytechnique, Dakar, Senegal

³Department of Urology, Ouakam Military Hospital, Dakar, Senegal

Introduction: Globally one of the most common urological emergencies is obstructive renal failure. In developed countries with well-funded health care systems these cases are typically caught early, and the problem can often be treated by removing the source of the blockage. This is not the case in sub-Saharan African countries such as Senegal. Due to the low prevalence of trained urologists, the cases obstructive renal failure due to cancer or schistosomiasis, are not seen until they are far more severe than would typically be seen here in Ontario, Canada. As such, one of the most common treatment approaches for obstructive renal failure in Senegal is to insert a nephrostomy tube into the calyces of the kidney to drain the urine to prevent further damage until the source of the blockage can be treated.

Computerized training platforms are a promising tool in the training of new physicians; especially those that provide feedback necessary for independent learning. These platforms often use trained deep neural networks to provide this feedback. Unfortunately, the datasets used to train deep learning models have historically been widely shown to under-represent individuals of African descent. In this paper, we propose a preliminary system for training percutaneous nephrostomy in Senegal, that simultaneously serves as a pipeline for creating a large dataset for training deep learning models that is representative of their population.

Methods: The system is composed of 2 RGB-D cameras, an ultrasound (US) probe, laptop, and a low-cost kidney phantom (Figure 1). An electromagnetic (EM) tracking system is also used to capture the motion of the US probe and needle with respect to the phantom. The user interface and main core of the system is built using the platform 3D Slicer, which is an open-source medical imaging platform (www.slicer.org). Data streamed from the US, cameras and EM tracking system is synchronized and sent to 3D Slicer using Plus Toolkit (www.plustoolkit.org).

The system is designed to be used independently by clinicians without needing a technical researcher to be present. It features provides a simplified overlay over the traditional 3D Slicer user interface. The module and all hardware connections can be started with the click of a single icon. The user interface provides clinicians with a suite of educational aides such as interactive workflow checklists and tracked 3D models of the anatomy, US probe and needle. Each time a user practices the procedure on the system; the video, US and tracking streams are recorded and saved to a directory that is synchronized with secure cloud storage. This provides clinicians with more convenient opportunities to practice the procedure, while still allowing collaborating researchers easy access to the data.

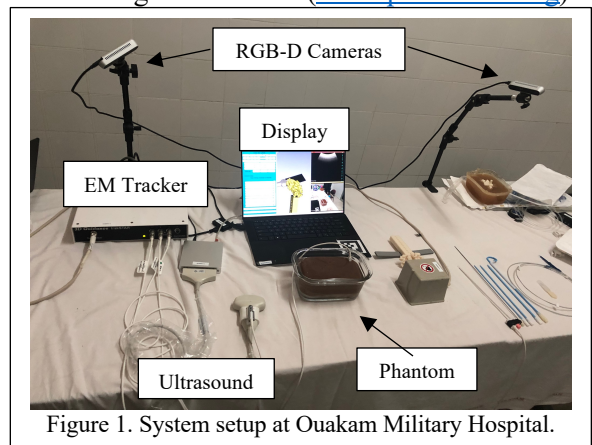
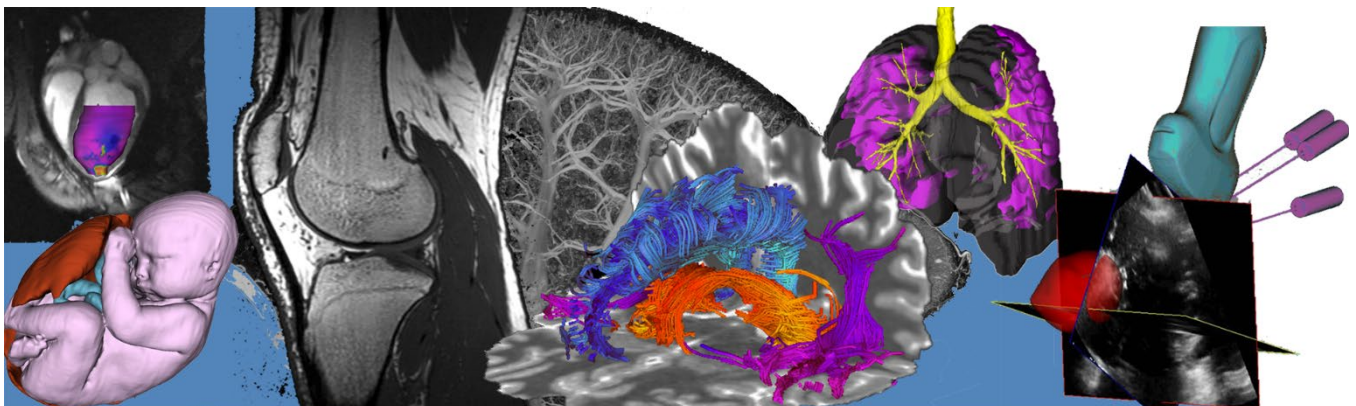


Figure 1. System setup at Ouakam Military Hospital.

Results: The proposed system was successfully installed in the urology department at Ouakam Military Hospital in Dakar, Senegal. The response to the system from clinicians was positive overall. During the first two-week period recordings were obtained from 7 Urology Residents and 6 Senior Urologists. Each user recorded a minimum of 4 trials which yielded a total of 52 recordings of the nephrostomy procedure. The recordings range in length from 3 to 10 minutes. Each recording contains 5 synchronized video streams (2 RGB video, 2 Depth video, and 1 US video) that can be used to train AI models. The cameras record only the phantom and hands of the participants to preserve anonymity.

Conclusions: A system for training percutaneous nephrostomy was designed and implemented in Ouakam Military Hospital. This system not only provides clinicians and trainees with opportunity to practice and learn the procedure with additional 3D guidance but also allows for the creation of a large dataset from users that have historically been under-represented. This data will be used to train AI models that provide improvements to the system such as additional feedback on workflow compliance, overall skill assessment, and removing the need for a costly tracking system. After processing we plan to release this dataset to encourage further research in this area.

Oral Session 5: Hardware Development Abstracts



Evaluation of a Custom Scintillation Detector for a Focussed Gamma Probe

Sydney Wilson^{1,2}, David W. Holdsworth^{1,2,3,4}

¹School of Biomedical Engineering, ²Robarts Research Institute, ³Dept. of Medical Biophysics, Schulich School of Medicine and Dentistry, ⁴Dept. of Surgery, Schulich School of Medicine and Dentistry, Western University

Introduction: Radioguided surgery using a gamma probe is common for intraoperative localization of radiolabeled lesions, however, currently available probes can lack sensitivity and resolution [1]. We previously proposed a new focussed gamma probe that provided high resolution detection of gamma photons in a remote focal region [2]. Our preliminary prototype utilized a traditional photomultiplier tube (PMT) based scintillation detector (Ludlum 44-2). While PMTs have been the gold-standard for amplification of low-light optical signals, they tend to be bulky and heavy. Silicon photomultipliers (SiPM) are a newer, solid-state alternative with a significantly smaller form factor. The objective of this study was to compare the performance of a SiPM and PMT based scintillation detector and examine the effects of energy discrimination on the performance of the detector.

Methods: A custom SiPM based scintillation detector was acquired from Berkeley Nucleonics Corporation. This detector features a thallium-doped cesium iodide (CsI(Tl)) crystal (20x20x20 mm) coupled to a SiPM with a built-in bias generator and preamplifier. The signal is then read-out by a Topaz-SiPM multichannel analyzer (MCA, BrightSpec). The PMT based detector used for the comparison contains a 25 mm thick, 25 mm diameter thallium-doped sodium iodide (NaI(Tl)) crystal. For consistency, the same 25 mm diameter, highly focussed tungsten collimator with a 35 mm focal length was used in all experiments [2]. The new SiPM based prototype is shown in Figure 1b.

Using a precision 3-axis stage, the detector was moved laterally across a sealed Cobalt-57 (122 keV) radioactive source that was placed at an axial depth of 35 mm (nominal focal length) and photons were counted for 100 seconds at each location. The energy spectrum was collected at each position for the SiPM detector, and a 20% energy window was centred around the spectrum peak. These experiments were repeated both in air and with a 2 cm polymethyl methacrylate (PMMA) tissue-mimicking phantom placed between the source and the probe.

Results: As shown in Figure 1a, the SiPM detector has a significantly smaller form factor with a 70% and 60% reduction in cross sectional area and length of the housing, respectively, and an 80% reduction in weight. In open air, the full width half maximum (FWHM) resolution was 3.6 mm and 3.9 mm for the SiPM and PMT detectors, respectively. The sensitivity was also similar for each detector, with the SiPM measuring 4.6 cps/kBq and 5 cps/kBq for the PMT. The FWHM resolution for the SiPM with PMMA was slightly poorer, measuring 4 mm. Applying a 20% energy window improved the FWHM by 0.06 mm in open-air and 0.16 mm in PMMA.

Conclusions: The custom-designed scintillation detector with SiPM readout electronics had comparable performance to the PMT prototype, but with a significantly reduced form factor, making it ideal for hand-held gamma detection. Applying energy discrimination provided no significant improvement in resolution, indicating that the collimator effectively blocks photons that have originated outside of the focal zone. It is expected that energy discrimination may have more impact at higher photon energies, or in clinical situations where multiple radioisotopes are utilized. Overall, the focussed gamma probe offers up to a 10-fold improvement in resolution compared to existing gamma probes [1], and the SiPM detector enabled the design of a prototype that is suitable for intraoperative assessment. This work is a significant milestone in a larger project where the focussed gamma probe will be incorporated with an ultrasound transducer for improved dual-modality surgical guidance during breast cancer surgery [3], with the goal of reducing the rates of revision surgeries.

References: 1. Radnia *et al.*, "Development and characterization of an all-in-one gamma probe with auto-peak detection for sentinel lymph node biopsy based on NEMA NU3-2004 standard," *Ann Nucl Med*, 2021. 2. Wilson *et al.*, "Highly Focussed Collimators for Increased Resolution of Hand-Held Gamma Probes," in *19th Annual ImNO Symposium*, 2021. 3. Wilson *et al.*, "Development of a novel, dual-modality image guidance system by combining a focussed gamma probe with ultrasound imaging," *Proc. SPIE* 12034, 2022.

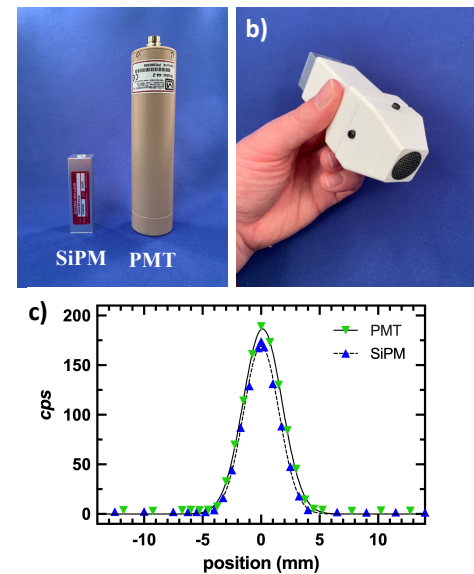


Figure 1: (a) SiPM vs PMT scintillation detector, (b) gamma probe prototype using SiPM detector, and (c) line profile comparing detector performance.

Quantification of Mechanical Characteristics of Conventional Steerable Ablation Catheters For Treatment of Atrial Fibrillation Using a Heart Phantom

^{1,2}Jacob Miller, ^{1,2}Alykhan Sewani, ^{1,2}Jeffery Rezazada, ^{1,2}Yara Alawneh, ³Pedram Kazemian, ¹Maria Terricabras, ¹Graham Wright, ^{1,2}M. Ali Tavallaei

¹Sunnybrook Health Sciences Centre, ²Toronto Metropolitan University, ³Deborah Heart and Lung Center

Introduction: The acute success rate for catheter ablation procedures of atrial fibrillation (AF) is high (97%) [1]. However, as with most ablation procedures, there is a high recurrence rate for AF, exceeding 40% within three years [1]. The long-term success of the treatment is understood to be correlated to the ability to create durable lesions during Pulmonary Vein Isolation (PVI) [2]. If a lesion is not sufficiently transmural, the result is the prevalence of gaps which, over time, allow electrical reconnections of the pulmonary veins (PV)[4]. Optimal lesion formation in PVI is proven to be correlated to optimal contact force between tissue and the catheter as well as inter lesion distance [2][3]. These parameters primarily depend on mechanical performance metrics, including the catheter's ability to accurately reach the target, its orientation at the target, and its deliverable forces. In this study, our aim is to provide objective measurements of these metrics in the left atrium (LA) using a heart phantom model to provide further insight into their potential contribution to successful ablation and recurrence of AF.

Methods: For the experimental setup, a 3D printed clear resin heart phantom was printed (Form 3, Formlabs). A pair of camera endoscopes (Wireless Endoscope, Taope) were placed in a 3D printed fixture to provide stereo vision feedback for the operator and to eliminate

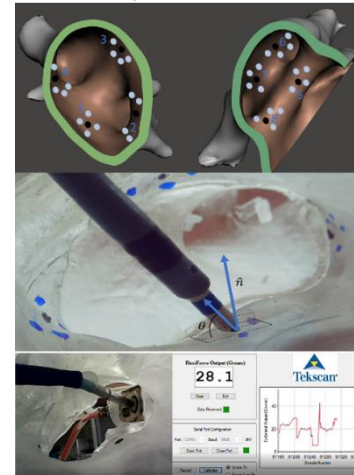


Figure 1. Endocardial view of RPV (left), LPV (right) black – target, blue – fiducial marker; demonstration of angle to surface characterization (middle); catheter characterizing force sensor with GUI

limitations due to poor visualization or device tracking. In the first experiment, four targets around the common ostium (inferior, superior, left, right) of each left and right pulmonary vein (LPV and RPV) were marked. Using a 7Fr catheter (J&J) and a steerable 8.5Fr sheath (Agilis, Abbott), the participants (including an electrophysiologist and three students) (n=4) were given 15

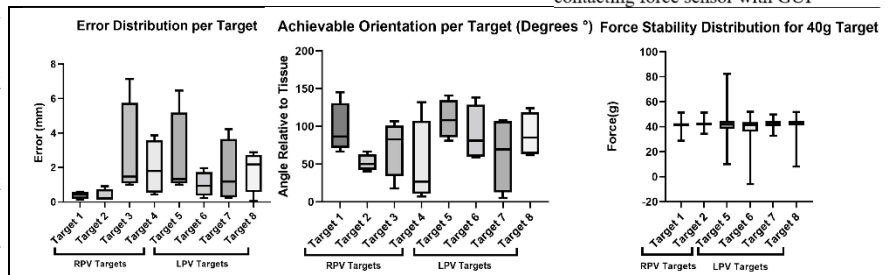


Figure 2. Error distribution comparison between targets (left); orientation distribution comparison between targets (middle); force stability comparison between targets for a 40g target force stabilization¹ (right)

¹ Targets 3 and 4 are not shown as operators were unable to reach targets and transmit a suitable force due to radial bend from catheter

minutes to navigate as close as they could to all the targets with the catheter tip. The position of the catheter relative to the target was measured using the Euclidean distance of the two points (target and catheter tip) obtained from the stereovision camera stream. The orientation was determined by triangulating the position of the catheter tip to the normal plane fitted to 4 fiducial markers on the surface (Figure 1). This surface was fitted using a least squares minimization approach. In the second experiment, force sensors (A101 flexiforce, Tekscan) were mounted at each of the targets. Operators were instructed to navigate the catheter, contact the force sensor and stabilize the catheter to achieve a 40g force for a duration of 60 seconds. Operators used a force sensor GUI as a visual aid to know the amount of force exerted against the sensor. **Results:** An overall positioning accuracy of 1.53 ± 0.72 mm was achieved for all targets. Given the size of an average ablation catheter (3mm), we believe this accuracy is acceptable for tracking and navigation. No statistical significance was observed in position accuracy between the right and left pulmonary veins (1.36 ± 0.94 mm vs. $1.77.36 \pm 0.62$ mm, $p = 0.4131$). The orientation of the catheter relative to tissue surface was $41 \pm 21^\circ$ with no statistical significance between targets. The overall force stability was 41 ± 6 g with higher difficulty in force stabilization in the right compared to the left pulmonary vein (40 ± 8 g vs. 43 ± 2 g, $p < 0.0001$). **Conclusions:** In conclusion, navigational parameters for a conventional catheter steering system for PVI were obtained. In this study we created a system in which we can objectively assess accuracy, orientation and stability of the catheter in an anatomical left atrium during PVI. **References** [1] F. Holmqvist et al., *Eur. Heart J.*, vol. 40, no. 10,, 2019, doi: 10.1093/eurheartj/ehy709. [2] P. Neuzil et al., *Circulation: Arrhythmia and Electrophysiology*, doi:10.1161/CIRCEP.113.000374 .

Integrated MRI Coils and Restraints for Simultaneous fMRI and Fibre Photometry in Awake Mice

Sam Laxer^{1,2}, Amr Eed¹, Kyle Gilbert^{1,2}, Peter Zeman¹, Miranda Bellyou¹, and Ravi Menon^{1,2}

¹Centre for Functional and Metabolic Mapping, Western University, London, Ontario, Canada

²Department of Medical Biophysics, Western University, London, Ontario, Canada

Introduction

Awake rodent imaging is an emerging strategy being implemented in functional Magnetic Resonance Imaging (fMRI) to investigate the neural basis of brain function. Without anesthesia, the undesirable side effects of long-term cognitive decline and altered neurovascular dynamics are avoided [1]. However, alternative means of alleviating motion must be implemented. Additionally, achieving the high resolution required for rodent fMRI often results in compromising sensitivity, especially when single-channel coils are implemented [2]. The objective of this study was 2-fold: 1) to analyze the performance of an in-house developed 4-channel coil with an integrated 3D-printed non-invasive animal restraint (namely body cast coil), and 2) compare it with a more conventional in-house developed single-loop coil with a headpost-style restraint (namely single-loop coil).

Methods

All animal protocols were approved by the Animal Care Committee at Western University. An awake imaging protocol was developed and used to compare the performance of the two coils (1 animal/coil). All imaging was done on a 9.4 T Varian magnet with a Bruker AV3HD console at the Centre for Functional and Metabolic Mapping at Western University. Image SNR, temporal SNR (tSNR), and motion were compared. Image SNR maps were calculated by dividing a typical gradient echo image with the standard deviation of the same gradient echo image without RF transmission (i.e. noise image). tSNR maps were calculated as the average pixel-wise value over 600 volumes of an echo-planar imaging (EPI) based fMRI run divided by the respective standard deviation of that voxel over the course of the run. Motion was calculated using rigid body analysis (AFNI) and finding the displacements and rotations of each volume in the functional run relative to the first volume [3].

Results

Table 1. Comparison of SNR and motion parameters between the single-loop and body cast coils.

Parameter	Single-Loop Coil	Body Cast Coil
Mean SNR	119	97
Mean tSNR	11	12
Max x-displacement	49.7 $\mu\text{m} \pm 6.43 \mu\text{m}$	62.4 $\mu\text{m} \pm 9.81 \mu\text{m}$
Max y-displacement	44.5 $\mu\text{m} \pm 18.3 \mu\text{m}$	33.1 $\mu\text{m} \pm 11.0 \mu\text{m}$
Max z-displacement	30.2 $\mu\text{m} \pm 11.5 \mu\text{m}$	79.5 $\mu\text{m} \pm 33.1 \mu\text{m}$
Max pitch	0.823° $\pm 0.208^\circ$	0.635° $\pm 0.248^\circ$
Max roll	1.56° $\pm 0.264^\circ$	1.06° $\pm 0.303^\circ$
Max yaw	0.591° $\pm 0.100^\circ$	0.462° $\pm 0.123^\circ$

With a voxel size of 300x300x500 μm , both forms of restraint effectively maintained motion within one voxel. Notably, motion was generally worse in the body cast coil. However, it produced minimal EPI distortions and accurate subject positioning of the coil over the brain due to the fully integrated restraint and coil.

Conclusions

The body cast coil provides many benefits over the conventional single-channel surface-coil. Despite the increased motion and worse image SNR, tSNR values are comparable. Further, considering the minimal distortions, better inter-subject alignment, and non-invasiveness, the body cast coil serves as an elegant solution for longitudinal fMRI studies, particularly those where maintaining brain and skull integrity is paramount (does not require the invasive implantation of a headpost as required for headpost-style restraints).

Motion can be expected to improve by customizing the body cast coil restraint to better match the curvature of the mouse head. Performance will be further evaluated with more subjects, and when implemented for various applications including longitudinal Alzheimer's studies and multi-modal fMRI experiments.

References: [1] Gutierrez-Barragan, et al. *Curr Biol* (2022). [2] Gilbert, K. M. et al. *J Neurosci Meth* (2019). [3] Cox, *Comput. Biomed. Res.* (1996).

The design and construction of a Tx/Rx ^{31}P birdcage head coil and feed network at 3 TeslaPeter Truong¹, Helmut Stark², Agessandro Abrahao^{1,3}, Lorne Zinman^{1,4}, Jamie Near^{1,5}

1 Hurvitz Brain Sciences Research Program, Sunnybrook Research Institute, Toronto, Canada; **2** Stark Contrast, Erlangen, Germany; **3** Consulting – Contact: helmutstark007@web.de; **3** Department of Medicine (Neurology), Sunnybrook Health Sciences Centre and University of Toronto, Toronto, Canada; **4** Institute of Medical Science and Rehabilitation Sciences Institute, University of Toronto, Toronto, Canada; **5** Department of Medical Biophysics, University of Toronto, Toronto, Canada

Introduction: Phosphorus (^{31}P) magnetic resonance spectroscopy (MRS) offers a non-invasive way to observe important metabolites involved in energy metabolism *in-vivo*¹. However, ^{31}P specific hardware is needed to acquire this data. Therefore, we designed and constructed a Tx/Rx ^{31}P birdcage head coil² and feed network for use on a 3T Siemens Prisma-XR (Erlangen, Germany) MRI system.

Methods: Birdcage Coil – We opted for a low-

pass coil design with 12 rungs and two capacitor gaps on every rung (**Figure 1a**). The network was designed using the dip-trace software (diptrace.com) and printed on flexible printed circuit board. Initial estimates for the capacitor values were obtained using the Birdcage Builder web application

(<https://research.med.psu.edu/departments/center-for-nmr-research/software/birdcage-builder-web-app/>). Non-magnetic ceramic capacitors rated for 2.5 kV (Knowles Syfer) were used, and further fine tuning was done using variable capacitors (Voltronics) at the drive ports to reach the desired resonance frequency (49.87 MHz). Proton (^1H) trap circuits were placed in the middle of each rung, tuned to 123.24 MHz, to isolate the ^{31}P birdcage from the proton body coil during ^1H imaging. A ^{31}P balun followed by a ^1H balun was placed at each drive port, formed by winding semi-rigid coaxial cable into inductors and bridging with a parallel capacitor.

Feed Network – The feed network³ consisted of a commercial grade quadrature hybrid (Anaren 10230-3), a 50 ohm preamplifier, and a pair of ^1H baluns, and two transmit-receive (TR) switches - one connected to the receive port of the scanner (to protect the scanner against high voltage transmit pulses), and the other to the transmit port (to prevent noise from the transmitter amplifier from coupling into the signal during receive) (**Figure 1b**).

Data Acquisition– We scanned a healthy

participant using a 3T Siemens Prisma-XR. A T1 weighted sagittal scan (1mm isotropic; FOV: 192 mm x 192 mm) was performed using the scanner's body coil, followed by a ^{31}P FID-CSI sequence using the ^{31}P coil with the following parameters: TR=2s; TE=2.3ms; 2 averages acquired; spectral width = 3000 Hz; 2048 points acquired; CSI FOV = 300mm x 300mm; CSI slice thickness = 40 mm; CSI dimensions = 12x12, CSI slice placed on coronal plane; total scan time = ~9min.

Results: The data were processed and visualized using FID-A ([GitHub.com/CIC-methods/FID-A](https://github.com/CIC-methods/FID-A)) and LCModel⁴ was used for analysis using a simulated basis set⁵. A coronal slice overlaid with MRSI colour map for PCr and a processed spectrum from one voxel is seen in **Figure 2**.

Conclusions: We successfully designed and constructed a ^{31}P birdcage coil and feed network for ^{31}P MRSI of the brain at 3 Tesla. Future work will focus on the optimization of pulse sequences and scan parameters for ^{31}P detection. Moreover, the processing and analysis pipeline is still under development and will be optimized.

References: [1] Rietzler et al. Journal of Neuroradiology 2022. [2] Hayes et al. Journal of Magnetic Resonance (1969) 1985. [3] Thapa et al. Concepts in Magnetic Resonance Part B: Magnetic Resonance Engineering 2016. [3] Provencher NMR in biomedicine 2001. [4] Deelshand et al. NMR Biomed 2015.

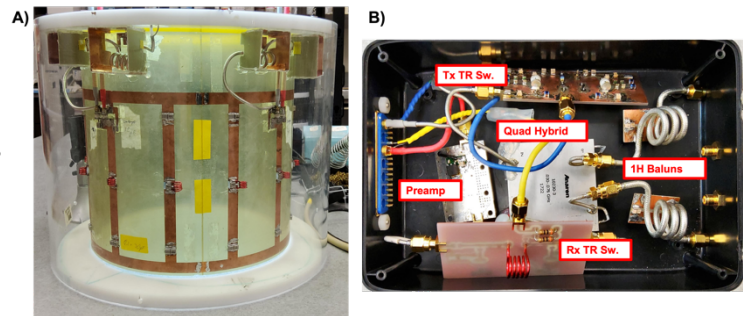


Figure 1 - A) ^{31}P Birdcage Coil; B) Feed Network

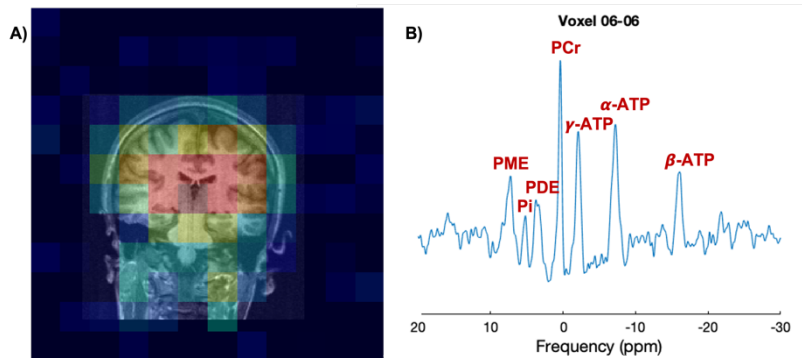
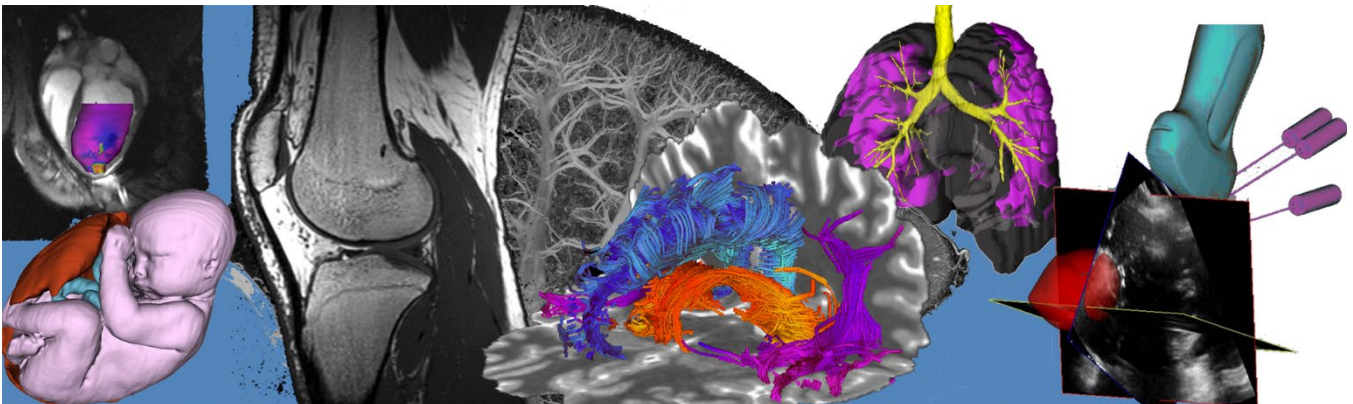


Figure 2 - A) Overlaid MRSI colour map of PCr; B) Processed spectrum from a single voxel

Oral Session 6: MR Imaging Abstracts



pH-Weighted Chemical Exchange Saturation Transfer (CEST) MRI Reproducibility in the Spinal CordAlicia Cronin*,^{1,2} Patrick Liebig,³ Sarah Detombe,⁴ Neil Duggal^{1,4} and Robert Bartha^{1,2}¹Department of Medical Biophysics; ²Centre for Functional and Metabolic Mapping, Robarts Research Institute, The University of Western Ontario; ³Siemens Healthcare GmbH, Erlangen Germany; and ⁴Department of Clinical Neurological Sciences, University Hospital, London Health Sciences Centre

Introduction: Several factors, including compression, injury, and vascular alterations, can cause ischemia and hypoxia in the spinal cord. Unfortunately, ischemia is challenging to measure non-invasively using MRI. Chemical Exchange Saturation Transfer (CEST) is an MRI contrast derived from the transfer of magnetic saturation from selectively excited endogenous protons to bulk water protons, causing a reduction in the observed water signal. pH-weighted CEST contrasts are produced by exploiting the pH dependence of the proton exchange rate. Since hypoxia alters tissue pH, pH-weighted CEST images could indirectly detect tissue hypoxia. Previously, it has been shown that pH-weighted CEST contrast can be generated in the brain using a ratiometric method called amine/amide concentration-independent detection (AACID).¹ The objective of this study was to evaluate the reproducibility of the AACID measurement at 3T along different healthy spinal cord levels using a 3D CEST sequence and evaluate the effectiveness of a respiratory correction because the spinal cord is close to the lungs and can cause signal fluctuations.

Methods: On a 3T Siemens MAGNETOM Prisma Fit MRI scanner, a prototype CEST sequence was used that consisted of a pre-saturation scheme followed by a 3D gradient-echo readout using centric spiral reordering. Saturation was performed using 30 Gaussian-shaped radiofrequency (RF) pulses with amplitude 0.5 μ T (total saturation time= 3.03 s), applied at 62 offsets from -6.5 to 6.5 ppm (total scan time = 8 min, 14 s). Other relevant imaging parameters included: TR/TE = 3.35/1.16 ms, matrix size = 96 \times 96 \times 14, resolution = 2.0 \times 2.0 \times 5.0 mm³. To evaluate the reproducibility of CEST contrast in the spinal cord, 12 healthy participants (7 females, mean age (\pm SD) 26 \pm 4 years) were scanned at two different time points (mean repeat time (\pm SD) 10 \pm 4 days) with the CEST acquisition centred at level C4 in the cord. T₂-weighted anatomical cervical spine images were acquired and semi-automatically segmented and labelled (C3-C6) using the Spinal Cord Toolbox (SCT).² Retrospectively, the acquired CEST data were corrected for any respiratory motion using the collected respiratory cycle, previously implemented by By *et al.*³ For both respiratory-corrected and non-corrected analysis, the scan-rescan reproducibility of the AACID measurements at levels C3-C6 were quantified. The absolute difference in AACID value between scans was calculated to quantify within-subject reproducibility for both techniques and compared (paired t-test, $p < 0.05$). The average AACID values for each level of the cervical spinal cord were calculated and compared for the non-corrected technique (repeated one-way ANOVA, corrected for multiple comparisons (Tukey), $p < 0.05$).

Results: The difference in absolute AACID measurements was most reliable at the C4 level (Figure 1A), demonstrated by the lowest absolute AACID difference between scans. There was no significant difference between the respiratory-corrected and non-corrected analysis techniques along the spinal cord ($p = 0.305$). There was also no significant difference in the average AACID values for the non-corrected analysis between spinal cord levels C3-C6 (Figure 1B).

Conclusion: This is the first study to utilize a 3D CEST sequence to evaluate AACID reproducibility in the healthy cervical spinal cord. There was no significant difference in AACID values between spinal cord levels, suggesting that AACID does not significantly change throughout the healthy cervical spinal cord. Level C4 had the best agreement between scans, indicating that the centre slices of the 3D sequence produce the most consistent measurements due to the blur on the outer slices. No difference was found when incorporating respiratory correction, indicating that the respiratory correction method utilized did not significantly improve CEST image reproducibility. In the future, patients with spinal cord injury or compression will be studied to determine if pH-weighted AACID measurements can detect pH heterogeneity in the spinal cord in these conditions.

References: [1] McVicar, N. et al. J. Cereb. Blood Flow Metab. 2014; [2] De Leener, B. et al. Neuroimage. 2017; [3] By, S. et al. Magn. Reson. Med. 2018

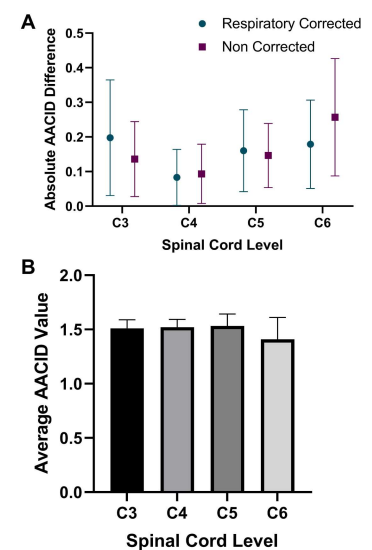


Figure 1: A: AACID difference between scans for both analysis techniques. B: Average AACID values for both time points at different spinal cord levels for the non-corrected technique.

High-resolution μ FA of the hippocampus at 3T

Farah N. Mushtaha, Nico J. J. Arezza, Ali R Khan, Corey A. Baron

Robarts Research Institute, Western University, London, Canada

Introduction: Neuron atrophy and reduced axon density in the hippocampus are common abnormalities in temporal lobe epilepsy (TLE)¹. Therefore, measuring and detecting a decrease in axon density can be a marker of TLE seizure foci. Diffusion magnetic resonance imaging (dMRI) is a promising imaging technique that sensitizes MRI contrast to the diffusion of water molecules. The diffusive motion of water is inhibited by cellular microstructure and, accordingly, dMRI is a promising method to characterize axon density. Fractional anisotropy is a dMRI parameter that is sensitive to axon density, but it is reduced when axons having different directions are present in the same voxel (“orientation dispersion”). Microscopic fractional anisotropy (μ FA) is a recently developed diffusion MRI (dMRI) parameter² that is sensitive to axon density while being insensitive to orientation dispersion, making it potentially more specific to axon losses that may occur in neurological disease. However, for the same scan time, the resolution μ FA is lower than traditional dMRI, and it is unclear if it can resolve individual hippocampal subfields. Further, it is susceptible to cerebrospinal fluid (CSF) partial volume effects that can confound measurements. Free water elimination (FWE) is an approach to measuring μ FA without the confounding of CSF³. In this study, we acquire high-resolution μ FA images with and without FWE at two resolutions to evaluate the feasibility of FWE μ FA in the hippocampus.

Methods: dMRI was implemented at 3T field strength using an echo planar imaging (EPI) sequence with linear tensor encoding (LTE) and spherical tensor encoding (STE; novel diffusion weighted required for μ FA) at variable b-values (Table 1) with a field of view (FOV) of 230.4mm. One healthy human control was scanned with 1.8 mm, and 1.6mm isotropic resolution with 14.65 minutes, and 14.82 minutes of scan time, respectively. The different resolutions were used to test the feasibility of the acquisition.

Results: Qualitatively, μ FA appears reduced in tissue adjacent to CSF in the images without FWE, which is likely due to CSF partial volume effects (Fig1). Few qualitative differences were observed between scans at 1.6mm, and 1.8mm resolution at 3T.

Conclusion: FWE may be a feasible approach to measure μ FA without CSF partial volume effects. FWE μ FA at 1.6mm and 1.8 mm resolution were comparable in quality, and acquiring high-resolution μ FA images at 3T was shown to be feasible.

Acknowledgements. This work was supported by the Canada First Research Excellence Fund, Brain Canada, and Discovery Grants from the Natural Sciences and Engineering Research Council (NSERC).

References: [1] Blümcke et al. *Epilepsia* (2013) [2] Lawrenz et al. *NeuroImage* (2015) [3] Arezza et al. *Medrxiv* (2022)

	B0 s/mm ²	B150s/mm ²	B1000s/mm ²	B2000 s/mm ²
LTE	6	6	26	26
STE	0	0	0	30

Table1. Number of acquisitions per tensor encoding per b-value.

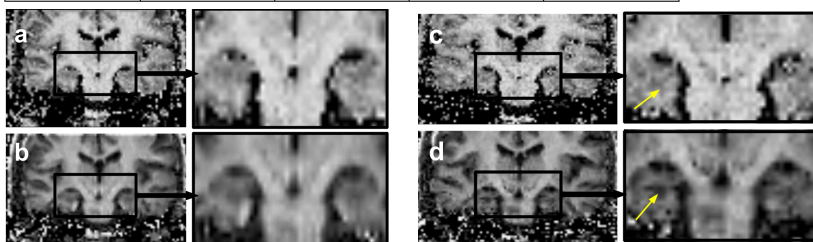


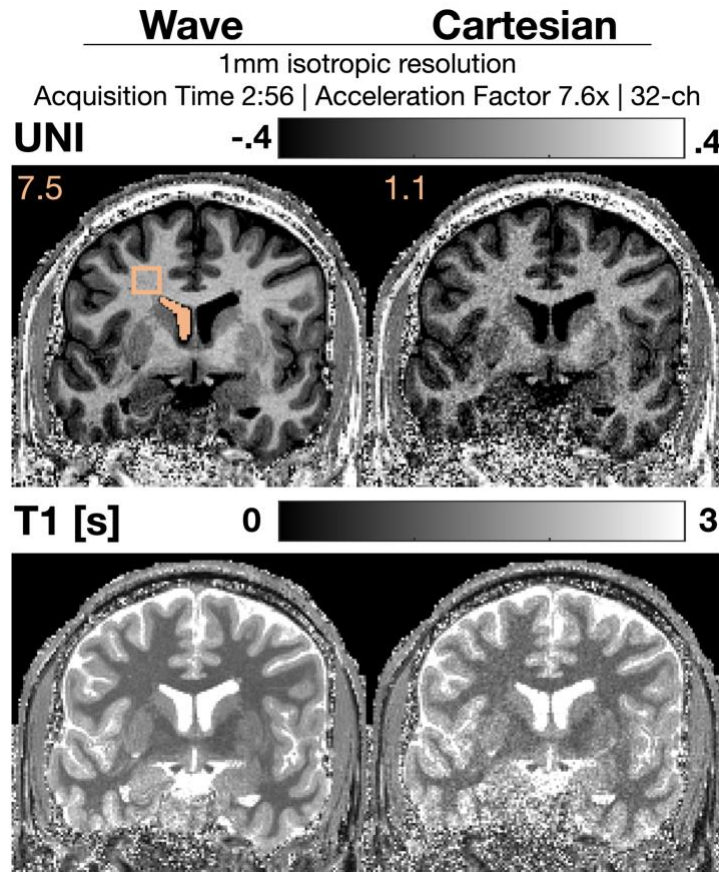
Fig 1. a) FWE μ FA image at 1.8 mm resolution. b) μ FA without FWE image at 1.8mm resolution. c) FWE μ FA image at 1.6 mm resolution. d) μ FA image without FWE at 1.6mm resolution. The yellow arrow shows areas affected by CSF partial volume effects in the hippocampus before and after FWE approach.

Wave-MP2RAGE at Ultra-High Field

Gabriel Varela-Mattatal^{1,2}, Wei-Ching Lo³, Omer Oran⁴, Ravi S. Menon^{1,2}, Berkin Bilgic^{5,6}

¹Centre for Functional and Metabolic Mapping (CFMM), London, Canada; ²Department of Medical Biophysics, London, Canada; ³Siemens Medical Solutions USA, Boston, United States; ⁴Siemens Healthcare Limited, Oakville, Canada; ⁵Athinoula A. Martinos Center for Biomedical Imaging, Massachusetts General Hospital & Harvard Medical School, Charlestown, United States; ⁶Harvard-MIT Division of Health Sciences and Technology, Massachusetts Institute of Technology, United States

Introduction: MP2RAGE¹ is considered the workhorse sequence at ultra-high field as it provides high-contrast and bias-free structural imaging. However, MP2RAGE imaging is hampered by both lengthy acquisitions and reduced SNR. In this work, we show preliminary results on our wave-MP2RAGE sequence that reduces the g-factor penalty to enable highly accelerated acquisitions². Wave encoding replaces the



conventional cartesian trajectory with corkscrews to mitigate g-factor penalization and to facilitate faster acquisitions.

Methods: This study was approved by the Institutional Review Board from Western University and informed consent was obtained prior to scanning. Acquisition was performed on a 7T MRI scanner (Magnetom Terra plus, Siemens, Erlangen, Germany) using a 32-channel receive and 8-channel transmit head-coil. Wave and Cartesian data at 1 mm isotropic resolutions were acquired with acceleration factor of 3x2 in PE/PAR directions with Elliptical Scanning (net acceleration 7.6x).

Additional sequence parameters:

FOV 256x256x192mm;

TE-Wave(Cartesian) /T₁/T₂/TR
3.27(3.18)/900/2500/5000ms;

FA₁/FA₂ 4°/5°;

echo spacing = 7.7/7.9ms;

Bandwidth = 200 Hz/Px. Wave parameters were G_{\max} 40 mT/m; 14 Cycles; $G_{\text{slew-rate}}$ 180.0 mT/m/ms.

Both sequences have a total acquisition time of 2:56.

The reference scan was used to estimate sensitivity coil maps using ESPIRIT after coil-compression to 21 virtual coils. The point-spread-function from wave encoding was estimated using autoPSF³, and the actual reconstructions were performed using Wave-CAIPI² and SENSE. From the reconstructions, we computed uniform (UNI) images and T₁ maps (<https://github.com/JosePMarques/MP2RAGE-related-scripts>).¹

Results: Wave encoding largely mitigated the noise amplification present in the Cartesian encoded data and led to high quality UNI imaging. Corresponding T₁ maps also show the gain from g-factor noise mitigation. Wave-UNI's SNR ($\mu_{\text{ROI}}/\sigma_{\text{CSF}}$) is 6-fold higher than the Cartesian-UNI's SNR.

Conclusion: our new Wave-MP2RAGE sequence at 7T enables fast and robust imaging over Cartesian acquisitions.

References: [1] Marques, 2010, NI; [2] Bilgic, 2015, MRM; [3] Cauley, 2017, MRM.

Iterative Point Spread Function Correction for T₂ Mapping with Fast Spin Echo MRITristhal Parasram¹, Mark Armstrong¹, Jonathan MacNeil¹, Dan Xiao¹¹Physics Department, University of Windsor, ON, Canada

Introduction: In MRI, the T₂ relaxation time reveals microscopic properties and interactions within a tissue. T₂ maps have been applied to study the brain and heart. Multi echo spin echo (MESE) is commonly used for T₂ mapping, but it requires long scan times. Multiple T₂ weighted images can be acquired with fast spin echo (FSE) for T₂ mapping with reduced scan time. However, the point spread function (PSF) depends on the image echo time as well as the voxel T₂ value, leading to artifacts in the T₂ map such as blurring and edge enhancement. A simple FSE PSF correction method based on the average T₂ [1] can be applied, but it is not very effective when a large range of T₂ values are present in the image and can amplify noise. We propose an iterative correction algorithm for accurate T₂ mapping with minimal noise amplification.

Methods: The average correction result and image with the shortest echo time are used as an initial guess for the T₂ and proton density (ρ), respectively. The T₂ and ρ maps are iteratively updated to minimize the difference between predicted images with various T₂ weighting and the acquired data. The minimization was performed using the Bound Optimization BY Quadratic Approximation (BOBYQA) method [2]. The cost function is

$$cost = \sum_i \| \mathbf{X}_i - \sum_j \rho_j \hat{\mathcal{T}}(j) \mathbf{PSF}(T_{2j}, i) \|_2^2$$

where { \mathbf{X}_i } is the set of images with i different echo times, and $\hat{\mathcal{T}}(j)$ is the translation operator. ρ_j and T_{2j} are the proton density and transverse relaxation time at position j , respectively. $\mathbf{PSF}(T_{2j}, i)$ is the PSF for a given T₂ determined by the gradient table of the i th image.

The method was tested on a simulated phantom with 100 SNR. A 2D T₂ mapping experiment was performed by acquiring 14 FSE images (17-minute total scan time) with TE varying from 13.7 ms to 823 ms on a tomato. The matrix size was 120x120, and FOV was 60x60 mm².

Results and Discussion: The simulation results are shown in Fig. 1. Severe edge enhancement was observed in the uncorrected T₂ map profile in Fig. 1a in orange. The correction using an average T₂ value, in blue, largely removed this artifact, but the resulting profile appeared noisier. The long T₂ points were overcorrected, while the short T₂ points were under corrected, leading to blurring and remaining edge enhancement. The proposed method yielded an accurate result (red in Fig. 1b) without noise amplification.

An FSE T₂ mapping measurement was performed on a tomato. Example T₂ and ρ maps are shown in Fig. 2. The uncorrected T₂ map had severe edge enhancement on the surface of the tomato, around the core and around the seeds, where discontinuities in either T₂ or ρ occurred. The solid seeds did not contribute to the FSE signal because of the extremely short T₂. Due to partial volume effect, these voxels should have T₂ values equal to the surrounding locular gel and a low intensity in the ρ map. The average correction resulted in a higher T₂ for the seeds compared to the locular gel and a noisier and more blurred T₂ map. The iterative method produced more reasonable T₂ and ρ maps with the highest spatial resolution, as the blurring visible in both the 1st and 2nd columns were largely removed.

Conclusion: An iterative PSF correction method for FSE T₂ mapping has been demonstrated. Blurring and edge enhancement in the T₂ map and ρ map have been effectively reduced in simulation and MRI experiments. These improvements could enable fast and accurate FSE based T₂ mapping.

References:[1] Zhou et al. JMRI vol. 3, no. 5, pp. 803–807 (1993) [2] Powell, DAMTP 2009/NA06 (2009)

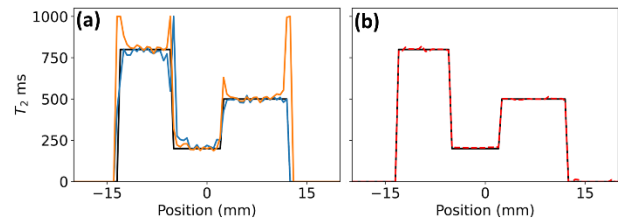


Figure 1. A single line from a simulated FSE T₂ map. The proton densities in the three regions were 1, 0.3, and 0.7. (a) The uncorrected T₂ map profile (orange) with significant artifacts were improved with the correction utilizing an average T₂ value (blue). (b) The proposed method yielded a T₂ profile (red) almost identical to the true profile (black).

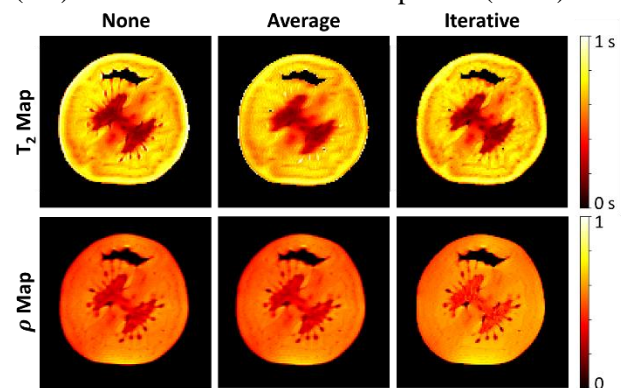
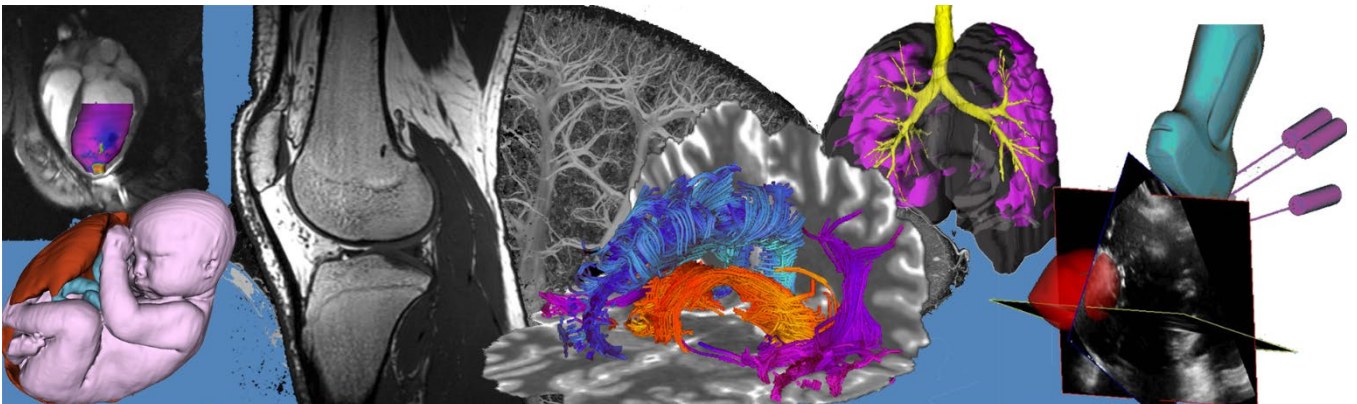


Figure 2. FSE T₂ maps (1st row) and proton density maps (2nd row) of a tomato without any PSF correction (1st column), with the average T₂ correction (2nd column) and with the proposed iterative correction (3rd column).

Pitch/Poster Session 5: Image Processing and Machine Learning Abstracts



Vessel bifurcation-based rigid-registration: A preliminary accuracy assessment.

Joeana Cambranis Romero^a, Shuwei Xing^a, Derek W. Cool^b, David Hocking^c, Terry M. Peters^{a,b,d,e}, Aaron Fenster^{a,b,d,e} and Elvis C. S. Chen^{a,b,d,e}

^aSchool of Biomedical Engineering, ^bDepartment of Medical Imaging and Oncology, ^cLondon Health Sciences Centre, ^dRobarts Research Institute, ^eDepartment of Medical Biophysics, Western University, London, Ontario, Canada

Introduction: Employing image-to-image registration in percutaneous procedures helps to improve the targeting of the lesion (i.e., tumour), the needle guidance and visualization of important structures, such as vessels.^{1,2} There are multiple approaches to perform registrations, and in our lab, we explore these solutions aiming to provide the best solution possible. In this work, the preliminary results of our rigid-registration approach, based on automatically selected vessel bifurcations are presented. Vessel bifurcations were chosen to perform the registration with the hypothesis that the deformation of the vessels could be minimal on those points.

Methods: Manual segmentation of the vessels and tumours of a commercial phantom (ground truth – 2 sets) and patient liver data (with pre and intraoperative volumes – 6 patients), was performed for each volume and reviewed by two expert interventional radiologists. Centerline extraction was obtained from the vessel segmentation models. Preoperative vessel information was discarded using a Region of Interest (ROI) depending on the liver segment scanned intraoperative with ultrasound (US). A bifurcation extraction algorithm that uses the information of each centerline section was developed. The bifurcation extraction compares the final and start point of each centerline section, and if both are the same the code detects it as a bifurcation point. The bifurcations were used to calculate a rigid registration between pre and intraprocedural volumes, using the 3D Slicer “Fiducial Registration” module based on an iterative-closest-point (ICP) algorithm. A minimum of 3 fiducials was required to perform the registration. For each experiment, the registration was applied and the Fiducial Registration Error (FRE), root-mean-square error of the fiducial points, and Target Registration Error (TRE), Euclidean distance between tumours centers, were obtained. TRE was used to assess the error between the segmentations, being the tumour’s center the primary target during an ablation procedure.

Results: For the ground truth experiment an FRE of 2.21 ± 1.03 mm and TREs of 1.66 ± 0.72 mm and 2.26 ± 0.56 mm were obtained (for each set). For the patient trial, an FRE of 2.35 ± 1.40 mm was obtained for the six patients included in the evaluation. For the patients with tumour visibility (4) in both volumes, the TRE acquired yielded an accuracy of 7.23 ± 3.45 mm. Figure 1 shows an example of the registration results for both experiments. After the registration, it is noticeable the alignment of the structures in the liver, such as vessels, gallbladder and liver edges, when visible.

Conclusion: The preliminary results ($TRE \approx 10$ mm) are similar to other work results.^{3,4} Some major causes for the TRE results could be due to breathing motion and deformation when scanning using with US (i.e., pressure applied with the probe). The results obtained with this method, even if global optimum is not ensured, suggest that this rigid registration method can be used as initialization to use in a deformable registration. To analyze the robustness of our algorithm a comparison between the results obtained in our work with those of other registration methods is yet to be performed. Other future work includes developing an automatic vessel segmentation and using patient volumes acquired with freehand ultrasound scans obtained with electromagnetic tracking.

References: [1] Puijk, R. S, et al., “Percutaneous Liver Tumour Ablation: Image Guidance, Endpoint Assessment, and Quality Control,” Canadian Association of Radiologists Journal, Feb 2018. [2] Carriero, S., et al., “Role of Fusion Imaging in Image-Guided Thermal Ablations,” Diagnostics, Mar 2021. [3] Smit, JN, et al “Technical note: Validation of 3D ultrasound for image registration during oncological liver surgery”. Med. Phys. 2021. [4] Fusaglia, M., et al. “A Novel Ultrasound-Based Registration for Image-Guided Laparoscopic Liver Ablation.” Surgical innovation, Mar 2016.

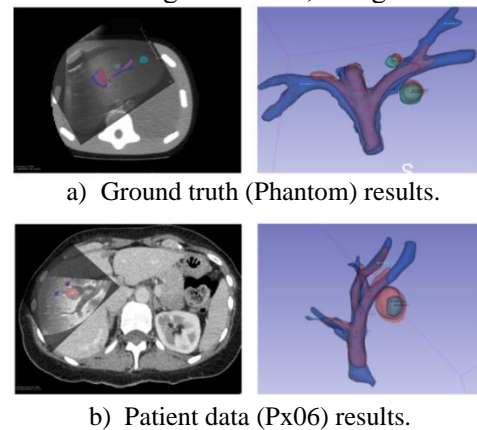


Figure 1. US-to-CT registration and 3D-models

Deep Learning for Placenta Accreta Spectrum Classification of Ultrasound Images

Dylan Young¹, Sebastian R. Hobson^{2,3}, Dilkash Kagal^{4,5}, Dafna Sussman^{1,2,4,6}

¹Department of Electrical, Computer and Biomedical Engineering, Toronto Metropolitan University, Toronto, Canada. ²Department of Obstetrics and Gynaecology, Mount Sinai Hospital. ³Department of Obstetrics and Gynaecology, Faculty of Medicine, University of Toronto, Toronto, Canada. ⁴Institute for Biomedical Engineering, Science and Technology (iBEST) at Toronto Metropolitan University & St. Michael's Hospital, Toronto, Canada. ⁵Keenan Research Centre for Biomedical Science, St. Michael's Hospital. ⁶Department of Obstetrics and Gynaecology, St. Michael's Hospital.

Introduction: Placenta accreta spectrum (PAS) is a placental abnormality that occurs as a result of abnormal implantation and attachment of the placenta to the myometrium or beyond¹. It is a complex, life-threatening pregnancy complication that has been becoming more prevalent worldwide due to the increase in intrauterine surgeries, such as cesarean sections and myomectomies. A 2021 meta-analysis showed that at least a third of cases go undiagnosed prior to delivery, leaving many pregnant patients at risk of serious complications during delivery and carrying a heavy biopsychosocial and public health burden^{2,3}. Ultrasound imaging is used as the first-line imaging modality for the diagnosis of PAS, frequently with adjunct magnetic resonance imaging (MRI). Ultrasound imaging has the advantages of being lower cost and more broadly available than MRI but suffers from low intra-operator variability. Given that the incidence of PAS is projected to continue increasing steadily, more reliable methodologies for diagnosing PAS prior to delivery are necessary. We aim to create a fully automated Deep Learning (DL) algorithm for the diagnosis of PAS from B-Mode ultrasound images.

Methods: We acquired B-mode trans-abdominal ultrasound images for 174 patients from a center in Toronto, Canada, each displaying the midsagittal view of the placenta and its myometrial interface. Images were preprocessed by applying filtering, cropping, and using image inpainting to remove all clinical annotations.

Each image was classified as either disease or control, wherein we had 97 PAS cases and 77 non-PAS cases. Random oversampling through image augmentation resampling was used to balance the datasets, achieving a total of 202 images for training and validation. Overfitting was a major obstacle during model development, therefore steps such as adding dropout layers, reducing model complexity, and applying optimized learning rate step decay and Nadam gradient descent optimization were integrated in order to avoid this. These dataset was used for training and validation of an in-house developed convolutional neural network (CNN) architecture that used the original ConvNet (LeNet5) as a backbone. This architecture was modified to implement ReLU activation and add the dropout layers to achieve higher performance.

Results: Preliminary modeling on the existing ultrasound images resulted in training and validation accuracies above 80% using an 80:20 training-validation split. Given the smallness of the dataset, a 20% test set in addition to the validation set was not feasible. Therefore, although these accuracies are a vast improvement over the projected 50-66% prenatal diagnosis rate of PAS using ultrasound, they will be further improved in parallel to a separate test set through ensuing dataset expansion and model architecture improvement.

Conclusion: The auspicious performance of the CNN model for PAS detection yields promise that this algorithm could serve as an adjunct method to clinicians in the diagnosis of PAS disorders. This could be done using easily acquired ultrasound images at the routine mid-trimester scan and be used in conjunction with known clinical risk factors such as placenta previa and the presence of prior intrauterine surgeries.

References: [1] Jauniaux E, Collins S, Burton GJ. Placenta accreta spectrum: Pathophysiology and evidence-based anatomy for prenatal ultrasound imaging. *American Journal of Obstetrics and Gynecology*. 2018;218(1):75–87. [2] Tinari S, Buca D, Cali G, Timor-Tritsch I, Palacios-Jaraquemada J, Rizzo G, et al. Risk factors, histopathology and diagnostic accuracy in posterior placenta accreta spectrum disorders: Systematic review and meta-analysis. *Ultrasound in Obstetrics & Gynecology*. 2021;57(6):903–9. [3] Soyer P, Morel O, Tsatsaris V, Bourgioti C, Barat M. Placenta accreta spectrum: A continuously evolving challenge for Radiologists. *Canadian Association of Radiologists Journal*. 2020;72(4):597–8.

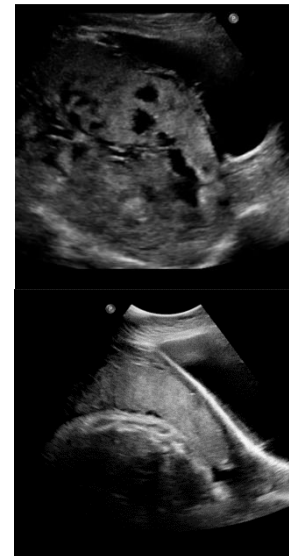


Fig. 1. Sample ultrasound for patient with PAS (top) and no PAS (bottom).

Cautery Tool State Detection in Basal Cell Carcinoma Excision Surgery VideosL March¹, R Hisey¹, A Jamzad¹, JR Rodgers², AML Santilli¹, D McKay¹, JF Rudan¹,
M Kaufmann¹, KYM Ren¹, G Fichtinger¹, P Mousavi¹¹Queen's University, Kingston, Ontario; ²University of Manitoba, Winnipeg, Manitoba

Introduction: Basal cell carcinoma (BCC) is an increasingly common cancer among Canadians. Standard treatment is an excisional surgery, where a cautery device is used to make cuts along the skin by generating electric burns. One of the main challenges of this surgery are positive margins—the presence of cancer cells on the skin after the tumour has been removed. This requires repeat surgery if cancerous cells are detected and further places strain on the hospitals and medical staff¹. iKnife technology can detect cancerous tissue through the extraction and analysis of smoke from the cautery tool burns. One limitation is that it does not provide spatial information of

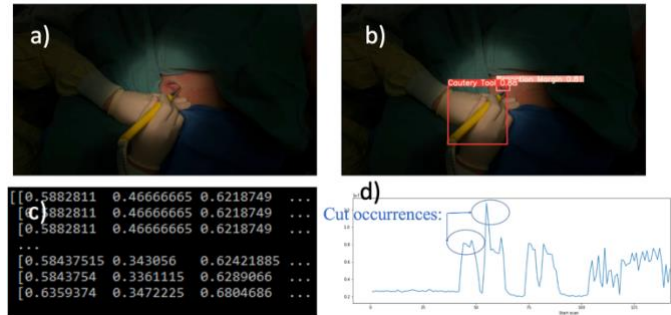


Figure 1. Workflow diagram of model pipeline. Surgery images from a CNN (a) are passed to an object detection network (b) followed by a bounding box sequence LSTM(c) to predict contact occurrences and match with iKnife MS data (d).

cautery tool location at the time cancerous tissue is detected. Additionally, a time delay from cut occurrence to mass spectra (MS) display makes it difficult to relocate potential positive margins². This project investigates the use of neural networks on video data to match frames of cautery tool cut occurrences with the iKnife MS data to allow surgeons to relocate suspicious sites of positive margins, potentially reducing the need for repeat surgeries. **Methods:** GoPro recordings of 14 BCC surgeries were collected and frames were extracted resulting in a dataset of 55,227 images. Workflow for cautery tool state detection was divided into three subtasks to facilitate the classification task due to a highly variable dataset. A summary of the workflow pipeline is shown in Figure 1. First, surgical workflow recognition was achieved by designing a convolutional neural network (CNN) to predict surgery occurrences, along with iKnife display frames to identify MS data acquisition start times to eliminate unimportant frames and reduce processing time. Next, object detection was achieved using the YOLOv5 model architecture to detect cautery tool and resection margin. Finally, using the identified surgery frames and bounding box annotations of the cautery tool and resection margin, a deep learning approach using a long short-term memory network (LSTM) was trained using sequence inputs of size 60×8 with a batch size of 64. A baseline computational approach was established by calculating the average resection margin position across the video, then finding the shortest cautery tool corner to resection margin center distance across each frame to quantify cautery tool tracking distance over time. Optimal distance threshold to classify contact or non-contact was found using a receiver operating characteristic curve. Networks were evaluated using accuracy and a 4-fold cross validation.

Results: Accuracies for the baseline and deep learning approach are summarized in Table 1. One limitation of the dataset is the high variability in camera positions and exposure, making it more difficult to view where the cautery tool is located on the resection margin, potentially causing mislabeled frames. Specifically, in fold 2 the training data had instances of unclear cautery tool tracking as shown in Figure 2. However, the deep learning approach generalizes better than the baseline in these types of scenarios.

Table 1. Shows accuracy over a 4-fold cross-validation for the baseline and LSTM approach

Fold	1	2	3	4
Baseline	0.73	0.49	0.80	0.77
LSTM	0.70	0.61	0.81	0.74



Figure 2. Example of unclear view of the surgical scene.

Conclusions: The deep learning LSTM approach was able to match the performance of the baseline approach and shows

promise for identifying cautery tool contact occurrences. Ongoing work investigates the improvement of the LSTM model and continue with matching identified contact frames with the iKnife MS data.

References: [1] Santilli et al. *IJCARS*. 887–896 (2020). [2] Ehrlich et al. *Sensors* 22(15). (2022).

Direct Continuous Optimization of Displacement Fields for Medical Image Registration

Teodora Vujovic
Vignesh Sivan
Stewart McLachlin
Michael Hardisty

Sunnybrook Research Institute
University of Waterloo
University of Waterloo
Sunnybrook Research Institute

Introduction

Medical image registration (MIR) is the task of spatially aligning a pair of medical images. It has many clinical applications including treatment planning and quantitative disease assessment. Deformable, non-rigid, registration methods align images by finding a displacement field (ϕ) that maps a moving image (m) to a fixed image (f) by optimizing a loss function, L . L are typically composed of image similarity and displacement field smoothness terms. MIR methods optimise L by variational approaches that iteratively directly update ϕ , or more recently by using deep learning networks to predict ϕ based on input images. In this work, we investigated a simple optimization formulation combined with strategies for escaping local minima to optimize performance by using large initial learning rates to escape local minima and then subsequently refining prediction with slowly decreasing learning rates. We demonstrated that this simply formulated method is: fast, with state-of-the-art performance, matched the prediction speeds of DL approaches, and has the possibility to generalize to multiple clinical applications.

Methods

We implemented a 3-dimensional direct continuous-domain optimization of ϕ using the ADAM optimizer [1]. L was minimized and composed of the similarity function (MIND feature loss) and regularization (magnitude of ϕ). Generally, L is non-convex and as such ADAM will converge to a local optimum. This investigation focused on the importance of the Learning Rate (LR) in determining the optima found. The following LR schedules were considered: constant LR of 1 (LR1), constant LR of 15 (LR15) and PieceWiseDecay (PWD) as described by Eq (1) where

$$LR(s) = \begin{cases} 15 & 0 \leq s < 70 \\ 7 \times \cos\left(\frac{2\pi}{200} \times (s - 70)\right) + 8 & 70 \leq s < 180 \\ \frac{-1.209}{70} \times (s - 180) + 1.343 & 180 \leq s \leq 250 \end{cases} \quad (1)$$

s represents the iteration number. The registration framework was implemented with PyTorch and run on Graphical Processing Units (RTX Titan). All ϕ were initialized with zeros.

The registration framework was applied to two open datasets: NLST (N=100 pairs of intra-patient chest Computed Tomography) and OASIS (N=414 T1 interpatient Magnetic Resonance Imaging). Each f, m

pair was affine-aligned using rigid transformations during pre-processing prior to deformable registration.

Results

Schedule	NLST (mm)	OASIS (DSC)
Unregistered	7.49	56.5
LR 1	1.38	75.2
LR 15	2.44	69.2
PWD	0.89	76.1

Table 1: Compares average keypoint error (NLST) and Dice Similarity Coefficient (OASIS), using the schedules listed. Results converged for all images in ~3 seconds.

The learning rate schedules showed consistent differences in performance in both datasets, with the PWD showing superior performance. The large initial LR enables the optimizer to escape local minima and the subsequent tapering of LR facilitates finer refinements to achieve consistent sub-voxel performance (Figure 1). This method succeeds in maintaining or exceeding performance over the most basic optimizer in 100% of NLST images with sub-voxel accuracy on 99/100 cases.

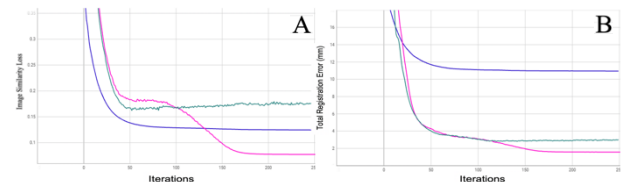


Figure 1: Compares Image Loss (A) and TRE (B) when using LR1 (Blue), LR15 (Green), and PWD (pink) over 250 iterations using an NLST image.

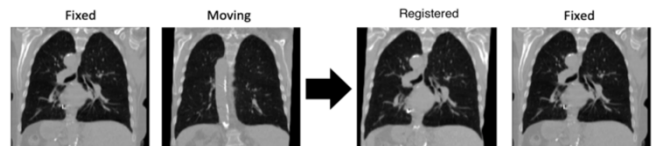


Figure 2: Compares 2D slices in the Coronal Plane at 187.50mm from an NLST sample in the following volumes: Fixed and (initial) Moving vs Registered (Moving) and Fixed.

Conclusion

By adjusting the learning rate of the ADAM optimizer using PieceWise Decay (PWD), Eq (1), the optimization effectively escapes local optima and consistently outperforms other methods. This investigation demonstrates the importance of the optimizer for image registration applications and that a simply formulated image registration approach with the appropriate optimizer can produce superior performance to other methods.

References:

- Kingma D & Ba J. Int Conf Learning Rep. 2014

Acknowledgments: CIHR BioTalent INOVAIT

Machine Learning Based Automated Canine Radiography Quality Control Tool

Peyman Tahghighi¹, Eranga Ukwatta¹, Ryan Appleby² and Amin Komeili³

¹School of Engineering, University of Guelph, Guelph, Ontario ²Ontario Veterinary College, Guelph, Ontario,

³Department of Mechanical and Manufacturing Engineering, University of Calgary, Calgary, Alberta

Introduction: Thoracic radiography is one of the most widely used modalities in veterinary clinics due to its diagnostic ability at a low cost. An informal survey of three radiologists at the Ontario Veterinary College (OVC) identified 20-25% of referral canine thoracic radiographic studies should be repeated to ensure appropriate diagnostic quality before proceeding with patient treatment. Poor radiographic positioning can cause misdiagnosis and is one of the primary sources of poor quality radiographs [1,2]. In this research, we have developed an automatic canine radiography quality assessment tool to predict the quality of radiographs right after acquisition.

Methods: Improper collimation can be detected by focusing on sternum bones or symmetry as indications for orientation and cranial edges and caudal edges as indications for coverage. First, we segmented the ribs, spine, abdomen, and sternum from radiographs. We utilized UNETR [3] as the segmentation model which is a combination of ViT [4] as the encoder and U-Net[5] architecture as the decoder. To detect the symmetry of hemithoraces, we fitted an active contour to the segmented ribs to find the whole thorax region. Then, we used the spine as a symmetry line to divide the thorax into left and right hemithoraces. Finally, we extracted features from both sides and used an ensemble of Support Vector Machine (SVM), Multi-Layer Perceptron and Gradient Boost to make the classification decision. In proper collimation, sternum bones overlap with the spine. Hence, we trained our segmentation model to only segment those sternum bones that fall outside of the spine boundary by removing the spine from the input radiograph. We then thresholded the outputted sternum pixels for the classification. To check for coverage on top, we looked for the isolated part of the spine (spine with no ribs connected), which happens on top of the thorax. We subtracted the segmented thorax and spine from each other to achieve this aim. Then, we extracted features from the residual part and passed them to an SVM for classification. Finally, to check for coverage at the bottom, we utilized the segmented abdomen and extracted features from the contour. Then we utilized these features to train an SVM.

Results: In total, 900 radiographs were obtained from OVC and labelled by a veterinary radiologist. Two example radiographs are shown in Figure 1. Table 1 represents the F1 metric for each component of our system and its overall score achieved by five-fold cross-validation. Our proposed method takes approximately 5 seconds to process a radiograph. The proposed method for segmenting the thorax and classifying symmetry can work under any exposure condition or even when part of the ribs is wholly obscured. As shown in Figure 2, we artificially obscured part of both lungs, and a direct segmentation which directly outputs masks for both hemithoraces missed parts of the ribs. However, since we only consider the edges of the ribs during active contour fitting and control the degree of elasticity, we can recover shape even when parts of the spine are missing. This feature is primarily applicable when parts of the lungs are obscured due to certain diseases or imaging artifacts.



Figure 1: Example images from our dataset.

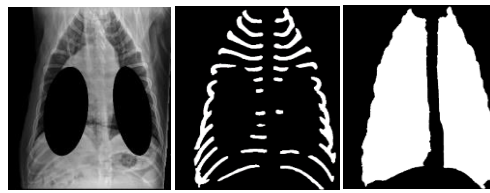


Figure 2: Results of our thorax segmentation method when parts of both lungs are obscured.

	Type	F1
Feature-wise	Sternum	81%
	Symmetry	83%
	Coverage	91%
Overall		80%

Table 1: Results on each component and overall model.

Conclusions: Evaluating the quality of canine thoracic radiographs can be broken down to four criteria, and we proposed a specialized method to automatically classify each. Further work can focus on expanding veterinary datasets to improve model performance. Additionally, we believe it is likely that the proposed method for thorax symmetry detection and thorax segmentation can be applied to human chest radiography with minimal changes.

References: [1] Reed et al., 2017 NAVTA Journal [2] Alexander et al., 2010 Pubmed PMID: PMC2857438 [3] Hatamizadeh et al., 2022 WACV [4] Dosovitskiy et al. CVPR 2020 [5] Ronneberger et al. MICCAI 2015

Feasibility of computational realistic-textured XCAT phantoms for assessing radiomic feature stabilityJaryd R. Christie^{1,2} and Sarah A. Mattonen^{1,2,3}.¹ *Department of Medical Biophysics, Western University, London, Ontario*² *Baines Imaging Research Laboratory, London Regional Cancer Program, London, Ontario*³ *Department of Oncology, Western University, London, Ontario*

Introduction: Radiomic models, which use features extracted from medical images such as computed tomography (CT) scans, are often used for outcome prediction in oncology. [1] In CT imaging, studies have shown that radiomic features can be affected by acquisition parameters such as slice thickness, tube current, reconstruction kernel, radiation dose, and noise. [2] This can result in radiomic features and models that are unstable and lack reproducibility across different scanners and acquisition protocols, which presents a barrier to clinical translation. [3] Studies have utilized physical phantoms to assess radiomic feature stability, however, few studies have attempted to use computational phantoms in these assessments. Recently, deep learning methods have been used to add heterogeneous textures onto computer-simulated phantoms to overcome the limitation of the lack of intra-organ anatomical details and textures. [4] Therefore, we aimed to assess the feasibility of using a deep learning network to synthesize realistic textures on 4D extended cardiac-torso (XCAT) phantoms to analyze the impact of acquisition parameters on radiomic features.

Methods: Three XCAT phantoms were generated each with a unique tumour inserted inside the lungs. A dual-discriminator conditional-generative adversarial network (D-CGAN) was then created to synthesize realistic textures in the XCAT phantoms. A dataset of 70 diagnostic CT scans (training: n=50, validation: n=20) from patients with early-stage non-small cell lung cancer was used to train and validate the model. [5] The validated network was then used to generate CT-realistic textures on the three XCAT phantoms which were acquired using three different protocols by varying the slice thickness (0.75 mm, 1.5 mm, and 3 mm). Slice thickness was chosen due to previous studies demonstrating its impact on radiomic features as well as to demonstrate proof of concept. Pyradiomics was used to extract 107 radiomic features (shape, first-order, and texture) from the tumour of each XCAT phantom. The intraclass correlation coefficient (ICC) was used to assess feature stability across the three slice thicknesses, with an ICC of greater than 0.80 representing excellent reliability.

Results: The validated D-CGAN model was able to successfully generate realistic CT anatomical textures on the XCAT phantoms as seen in **Figure 1**. [4] Additionally, the phantoms were successfully generated using different acquisition protocols for use in 2D or 3D radiomic analysis. Qualitatively, the generated images had similar textures to that of the real CT images (**Figure 2**). Previous studies quantified the similarity of these images to real CT textures. The ICC analysis between different protocols demonstrated that changing the slice thickness may not significantly affect extracted shape, first-order, and texture radiomic features. Gray level co-occurrence matrix (GLCM) texture features were most impacted by the slice thickness with an average ICC of 0.77.

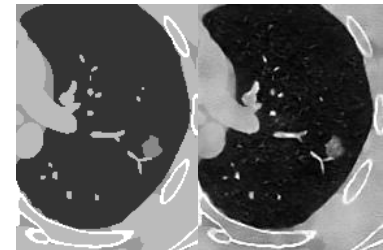


Figure 1. Input XCAT phantom (left) and generated CT-textured XCAT phantom (right).

Conclusions: This study assessed the feasibility of using computational phantoms to examine the impact on varying acquisition parameters on radiomic features extracted from lung nodules. Realistic CT anatomical textures were generated using a deep learning network. This study may provide an efficient, cost-effective pipeline to study radiomic feature robustness. Ongoing work involves assessing the impact of other acquisition parameters such as the tube current, noise, and reconstruction kernel.

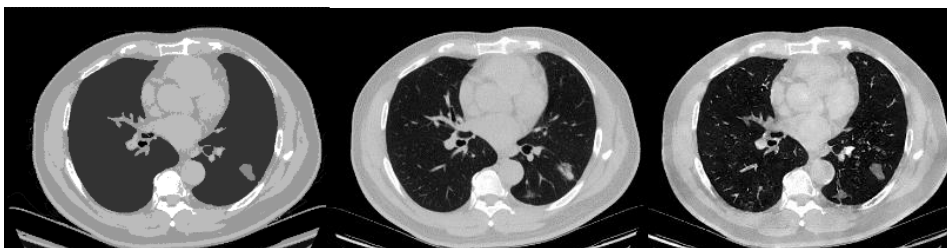


Figure 2. Input image (left), real CT image (middle), and model output (right) for D-CGAN model validation.

References:

- [1] Gillies, R. J., et al. 2016
- [2] Zhao, B., et al. 2021
- [3] Berenguer, R., et al. 2018
- [4] Chang, Y., et al. 2020
- [5] Bakr, S, et al. 2018

Title: Anatomical measuring of the entire cochlea at a sub-millimeter resolution using synchrotron-radiation phase-contrast imaging

Authors: Ashley Micuda¹, Seyed Alireza Rohani², Luke Helpard³, Sumit Agrawal^{1,4} & Hanif M Ladak^{1,4}

¹Department of Medical Biophysics, ²Department of Otolaryngology - Head and Neck Surgery, ³School of Biomedical Engineering, ⁴Department of Electrical and Computer Engineering, Western University, London, Ontario, Canada

Introduction: Cochlear implants are surgically implanted neural-prosthetic devices which directly stimulate sensory hair cells and auditory nerve fibers to restore sound perception in cases of sensorineural hearing loss. However, cochlear implants have highly variable outcomes and limitations due to the lack of anatomical knowledge on the fine cochlear structures. Synchrotron-radiation phase-contrast imaging (SR-PCI) has been proven as an effective alternative to histology and conventional imaging by providing three-dimensional visualization of the entire cochlea (figure 1). SR-PCI uses synchrotron X-rays and combines phase contrast techniques with computed tomography to produce images. These images provide detailed discernment of both bone and soft tissue in intact cadaveric cochlea. The objective of this work is to use SR-PCI to quantify the morphology of the human cochlea, from base to apex.

Methods: Nineteen fixed human cadaveric cochleae were scanned using SR-PCI. Imaging was conducted with the 42 keV monochromatic X-ray Bio-Medical Imaging and Therapy beamline at the Canadian Light Source Inc. The images were reconstructed using phase-retrieval to improve the discernment of cochlear soft tissues. Image processing techniques, such as the segmentation (outlining) and registration (alignment), were implemented. For each three-dimensional image, the two main cochlear ducts, the scala tympani and scala vestibuli, were semi-automatically segmented and aligned along the cochlea's virtual spiral axis of rotation. To allow for visualization and measuring of the cochleae, the images were radially sliced about the axis of rotation. The radial cross-sections were then converted to a binary label map and cross-sections at 5° increments were quantitatively analyzed to obtain anatomical measurements.

Results: Multiple cochlear ultrastructure measurements were made in the cochlea, including the maximum inscribed circle (figure 2) and the cross-sectional area. Additionally, the average overall cochlear axis height was 4.41 ± 0.3 mm.

Conclusions: A novel imaging technique, SR-PCI, was used to image 20 human cochleae with significantly improved contrast and resolution. This technique allowed for the first high resolution measurements of the entire cochleae to be conducted. These preliminary measurements of the cochlear apex will extend the current anatomical knowledge of the cochlea to inform safe implementation of longer electrode arrays to restore low-frequency ranges, not otherwise possible with current electrodes.

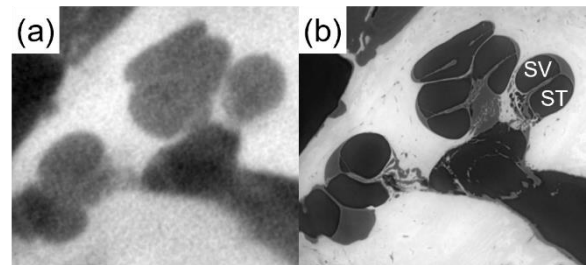


Figure 1: Comparison of (a) μ CT and (b) synchrotron-radiation phase-contrast imaged cochlea.

ST: scala tympani, SV: scala vestibuli

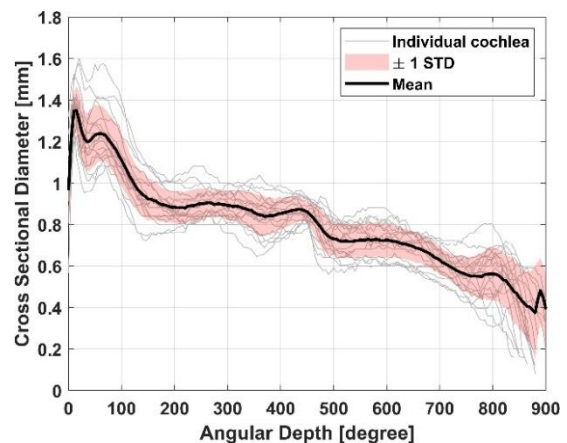


Figure 2: The largest inscribed circle fitting inside the scala tympani cross-sections, incremented every 5°.

Thickness and design features of clinical cranial implants – what should automated methods strive to replicate?

Z. Fishman (1), James G. Mainprize (2), Glenn Edwards (2), Oleh Antonyshyn (2,3), Michael Hardisty (1,4), C.M. Whyne (1,4,5)

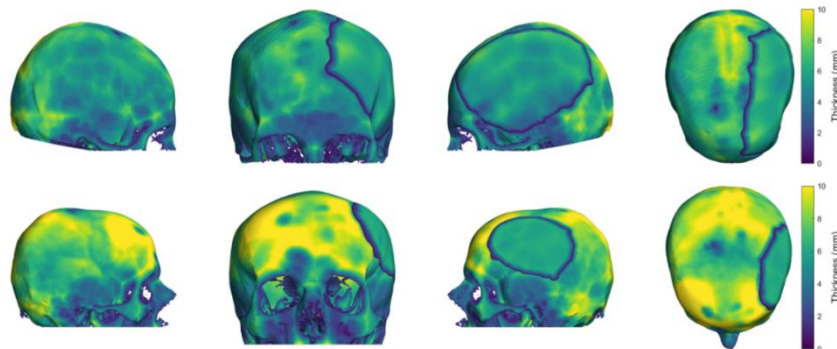
1. Orthopaedic Biomechanics Laboratory, Sunnybrook Research Institute; 2. Calavera Surgical Design Inc.; 3. Division of Plastic Surgery, Sunnybrook Health Sciences Centre; 4. Department of Surgery, University of Toronto; 5. Institute of Biomedical Engineering, University of Toronto.

Introduction: Following a craniotomy, a patient-specific cranial implant is required to reconstruct the skull geometry with a customized design dependent on the defect size and shape. New machine learning (ML) and statistical shape modelling (SSM) approaches aim to automate the cranial implant design process, as highlighted by the MICCAI AutoImplant Challenges. Such challenges often use simulated data to represent clinical cases for training validation and testing purposes, with implants designed solely for research use. If simulated data is used in this context, it is important to determine if these datasets represent the geometric features inherent in implants designed for clinical use, to ensure clinical usability of implants designed by new automated methods. This analysis aims to quantify design features of clinical cranial implants and compare to simulated craniotomy implant datasets used in ML and SSM applications.

Methods: Calavera Surgical Design provided a dataset of 206 anonymized post-craniotomy skulls and their associated implants (used clinically). In this data set, 162 unilateral cases enable direct comparison with the contra-lateral side of the skull. The MUG500+ dataset [1] (implants designed solely for cranial AutoImplant training) includes 29 craniotomy skulls and associated implants, with 26 unilateral cases. Implant and skull shapes (STL mesh format) from both datasets were segmented to separate the inner and outer cortical surfaces by calculating the angle between the surfaces' normal vectors and the skull centroid. Implant and skull thicknesses were measured with the Euclidean distance between the surfaces and mapped onto the outer cortical layer. The clinical implants were further segmented by a 3.5 mm thickness threshold to define a 'rim' that transitions to the skull from the middle section, which was not seen in the simulated data. For unilateral cases, each implant was mirrored to the contra-lateral side skull and the average thickness difference was evaluated.

Results: The average thickness of the Calavera implants was 6.0 ± 0.4 mm, which approximates the thickness on the contra-lateral side of the skull, with a relative difference between the implant and skull of -0.3 ± 1.4 mm (range: -3.6 mm, 4.4 mm). The average thickness of the MUG500+ implants was 2.8 ± 1.1 mm, significantly thinner than the contra-lateral side skull thickness (relative difference between the implant and skull thicknesses 2.9 ± 1.2 mm, range: -0.5 mm, 5.7 mm). Rim transitions were only found in the clinical data set (average width of 7.4 ± 2.7 mm), where they were used to create a smooth boundary between the implants and the skull.

Conclusions: Differences between clinical and simulated implants highlights the importance of capturing clinical features in simulated datasets in training for clinical tasks such as cranial implant design. The Calavera dataset illustrates a design approach where the average implant thickness reflects mirroring the contra-lateral skull and includes a rim feature to transition the curvature between implant and the skull defect. This shape analysis aims to help guide automated design approaches for future clinically acceptable cranial implants.



Craniotomy skulls and implants within the Calavera dataset with the thickness color-mapped to 10 mm (side, front, & top views). An implant thickness approximately equal to (top) and thinner than (bottom) the contra-lateral side skull.

1. Li J, Krall M, Trummer F, et al (2021) MUG500+: Database of 500 high-resolution healthy human skulls and 29 craniotomy skulls and implants. Data Br 39:0–5. <https://doi.org/10.1016/j.dib.2021.107524>

Finite Element Modelling of the Human Middle Ear Using Synchrotron-Radiation Phase-Contrast Imaging

Caleb W. Thompson^{1,2}; Seyed A. Rohani³; Hanif M. Ladak^{1,2,3}; Sumit K. Agrawal³

1. Department of Electrical and Computer Engineering, Western University, London, Ontario, Canada

2. Department of Medical Biophysics, Western University, London, Ontario, Canada

3. Department of Otolaryngology – Head and Neck Surgery, Western University, London, Ontario, Canada

Introduction Finite element (FE) models of the middle ear allow for measurement of stapes vibrations, which form the input to the cochlea where auditory transduction occurs. FE models often lack accurate geometry of soft tissue structures, such as the suspensory ligaments, as they can be difficult to discern using conventional imaging modalities, such as computed tomography. Synchrotron-radiation phase-contrast imaging (SR-PCI) is a non-destructive imaging modality that has been shown to produce excellent visualization of soft tissue structures without the need for extensive sample preparation. This study uses SR-PCI to create and evaluate an FE model of the human middle ear that includes all soft tissue structures, and secondly, investigates how modelling assumptions and simplifications of ligaments affect the simulated acoustic response of the FE model.

Methods Phase-retrieved SR-PCI with 9 μm isotropic voxel dimensions of a cadaveric human temporal bone was used to create the middle ear model (Figure 1). The FE model included the suspensory ligaments, ossicular chain, tympanic membrane, the incudostapedial and incudomalleal joints. Additionally, the ear canal was included in the model, derived from micro-CT with 20 μm isotropic voxel size.

Results Frequency responses obtained from the SR-PCI-based FE model agreed well with published laser doppler vibrometer measurements on separate cadaveric samples

(Figure 2). Revised models with exclusion of the superior malleal ligament (SML), simplification of the SML, and modification of the stapedial annular ligament (SAL) were studied, as these revised models represented modelling assumptions that have been made in literature. Ultimately, SML and SAL modelling decisions influenced the simulated acoustic response of the middle ear model.

Conclusions This study presents the first use of SR-PCI to create an FE model of the human middle ear. SR-PCI allowed for clear discernment of bony and soft tissue. The FE model agreed with laser doppler vibrometer data and revealed implications of modelling decisions on the suspensory ligaments. Future investigations in this field may benefit from the use of SR-PCI as an imaging modality to model full middle ear morphology. The exquisite detail produced by SR-PCI will benefit future biomechanical investigations of middle ear function through FE modelling.

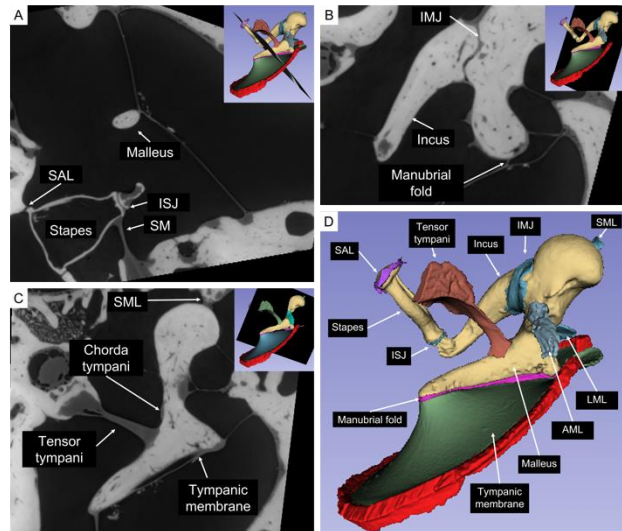


Figure 1: Visualization and segmentation of human middle ear structures using SR-PCI. A) Axial slice. B) Coronal slice. C) Sagittal slice. D) Segmentation of middle ear structures used for modelling. IMJ: Incudomalleal joint; ISJ: Incudostapedial joint; SAL: Stapes annular ligament; SML: Superior malleal ligament; SM: stapedius muscle; AML: anterior malleal ligament; LML: lateral malleal ligament.

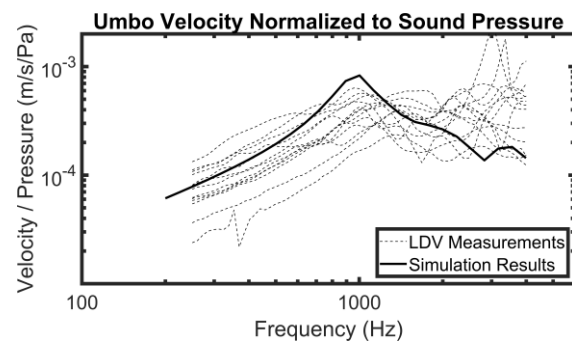
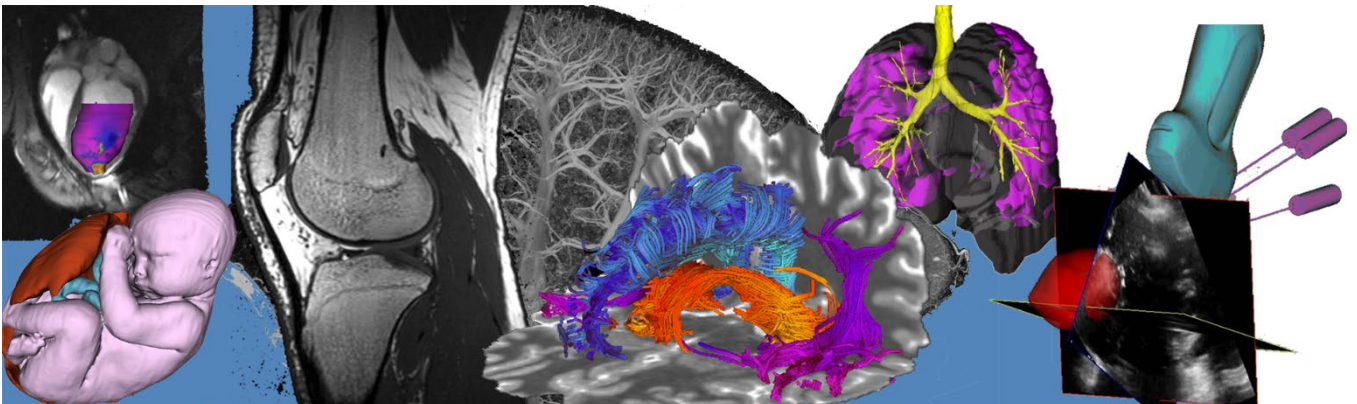


Figure 2: Simulated umbo velocity, normalized to a sound pressure of 90 dB, compared against experimental laser doppler vibrometer measurements on thirteen samples.

Pitch/Poster Session 6: MR Imaging Abstracts



DECOUPLING CEST SOLUTE EXCHANGE RATE FROM POOL SIZE

Sid Sadanand^{1,2}, Wilfred Lam³, Greg Stanisz^{3,4}, Dafna Sussman^{1,2,5}

¹Departments of Biomedical Physics and of Biomedical Engineering, Toronto Metropolitan University, ²Institute for Biomedical Engineering, Science and Technology (iBEST) at Toronto Metropolitan University and St. Michael's Hospital, ³Sunnybrook Research Institute, ⁴Department of Medical Biophysics, University of Toronto, ⁵Department of Obstetrics and Gynecology, University of Toronto

INTRODUCTION: Chemical exchange saturation transfer (CEST) is a powerful MR imaging tool for measuring signal from dilute analytes^[1], and is used preclinically in brain, tumour, and joint metabolic imaging. CEST signal is derived from measuring the magnetization of the water pool of protons before and after RF saturation of exchangeable analyte protons. The amount of saturation transfer (ST) to the water pool is affected by the rate of analyte proton chemical exchange (R_{CEST})^[2]. Characterisation of R_{CEST} is thus necessary for using CEST to quantify analyte concentration ($M_{0,CEST}$)^[3] in vivo. One way to measure $M_{0,CEST}$ using the Bloch-McConnell equations (BM) with exchange is through ST experiments in which long duration saturation (t_{sat}) and measurement are repeated until saturation and exchange reach steady state (SS)^[3]. Yet, this approach assumes that R_{CEST} is known a priori^[4], allowing the decoupling of $M_{0,CEST}$ from R_{CEST} . This is not necessarily the case, which prevents analyte quantification from SS ST CEST signal. Earlier work^[4] demonstrates this coupling of $M_{0,CEST}$ and R_{CEST} through Markov chain Monte Carlo (MCMC) sampling of the BM solution space fitted to SS ST data with varied $M_{0,CEST}$ and saturation power (B_1). Alternatively, in non-SS ($t_{sat} \ll TR$), Z-spectrum peak height is limited by saturation rather than R_{CEST} , potentially allowing for the decoupling of $M_{0,CEST}$ from R_{CEST} . We hypothesize that R_{CEST} and $M_{0,CEST}$ are not decoupled in non-SS ST experiments with varied B_1 and t_{sat} . We aim to develop methods to determine R_{CEST} to facilitate translation of CEST to clinical quantification of metabolites.

METHODS: A non-SS ST experiment was conducted using a similar 1M NH_4Cl solution to the prior study, with 1mM $CuSO_4$ added to reduce T_1 . The 1M NH_4Cl + 1mM $CuSO_4$ solution was imaged with a 2D ST EPI sequence on a 7T vertical bore Bruker Ascend at ambient temperature with block saturation $B_1 = \{0.5, 1.0, 1.5 \mu T\}$ and $t_{sat} = \{0.5, 1, 5, 9.95s\}$ for $TR = 10s$, with Z-spectrum sampling $\Delta\omega = \{-4 : 0.05 : 4ppm\}$. T_1 , B_1 , and B_0 maps were also collected and corrected for in the voxelwise fitting^[5]. Regions of interest (ROI) were drawn, and the non-SS BM model was fit voxelwise (Fig. 2). The non-SS BM step solver was validated with this collected non-SS ST data against the prior ambient temperature SS 1M NH_4Cl SS data^[4], shown in Table 1.

RESULTS:

Parameter	SS 1M NH_4Cl	non-SS 1M NH_4Cl + 1mM $CuSO_4$
$T_{1,Water}$	$3300 \pm 110ms$	$1200 \pm 39ms$
$T_{2,Water}$	$1010 \pm 10ms$	$1000 \pm 49ms$
$T_{2,CEST}$	$40 \pm 1ms$	$41 \pm 3ms$
R_{CEST}	$92 \pm 2Hz$	$56 \pm 3Hz$
$M_{0,CEST}$	$6 \pm 0.1\%$	$6 \pm 0.4\%$

Table 1: BM ROI average fitted parameters

Figure 1: non-SS MCMC parameter plot

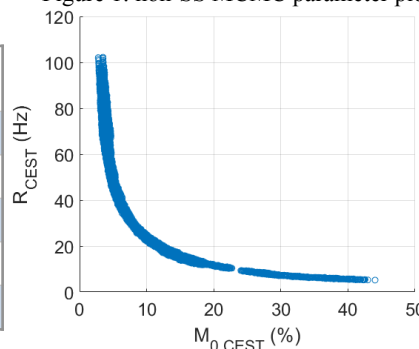


Figure 2: non-SS BM Z-spectrum fitting

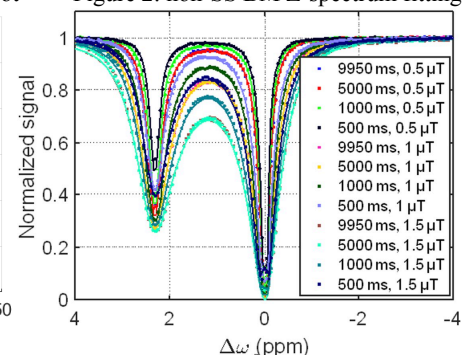


Table 1 shows BM fitted parameters for both SS and non-SS models agree for $T_{2,water}$, $T_{2,CEST}$, and $M_{0,CEST}$, validating the non-SS step solver. $T_{1,water}$ differs with the addition of 1mM $CuSO_4$, while the difference in R_{CEST} minima illustrates the ongoing challenge to quantify R_{CEST} . Fig. 1 shows a continued coupling of R_{CEST} and $M_{0,CEST}$ MCMC parameters in the non-SS fitting of the non-SS ST data, despite a good Z-spectrum fit of the voxelwise data, as shown in Fig. 2. Fig. 1 shows several disjointed local minima, indicating a smaller step size and differing cost function weighting are necessary for the non-SS case. Ongoing work will expand non-SS exchange rate fitting to multiple $M_{0,CEST}$ and MT confounds while varying B_1 , pH, slice thickness, and t_{sat} . Future work may include variable delay multi-pulse (VDMP) sequence or $T_{1\rho}$ determination of R_{CEST} .

CONCLUSIONS: The work here demonstrates that non-SS ST experiments cannot be used to determine R_{CEST} decoupled from $M_{0,CEST}$. Further investigation will be needed to determine R_{CEST} in order to facilitate the translation of quantitative CEST metabolic imaging to a clinical setting.

REFERENCES: [1] Zaiß et al., NMR in Biomed (2019) 32(9), e4113. [2] van Zijl et al., NeuroIm (2018) 168, 222–241. [3] McConnell, H.M. J Chem Phys 28: 430 (1958). [4] Lam, W. et al. Music City CEST (2017). [5] Henkelman, R.M. Med Phys 12: 232 (1985). [6] Kim, M. et al. Magn Reson Med 61:1441 (2009). [7] Zaiß et al., NMR in Biomed (2015) 28(2), 217-230.

Low-Heating B_1^+ -Mapping of Subjects with Deep Brain Stimulation (DBS) Implants Using Optimized Radiofrequency (RF) Shimming Parallel Transmission (PTX)

Maryam Arianpouya^{a,*} and Simon Graham^a; ^a Department of Medical Biophysics, University of Toronto, Toronto, ON, Canada

Introduction. This study focuses on RF shimming PTX for safe MRI of DBS patients. In PTX, multiple decoupled RF coils are driven by a common input signal, $V(t)$, with independent amplitudes and phase shifts. The total transmitted magnetic and electric fields ($B_{1,tot}^+, E_{tot}$) are the sum of individual weighted field “maps”. DBS MRI is restricted due to heating along the implant lead with maximum effect at the tip. Heating, caused by RF E-field interaction with the implant, is characterized by the specific absorption rate (SAR). By selecting optimized amplitudes and phase shifts to each PTX channel (i.e. “RF Shim”), SAR suppression can be achieved together with uniform B_1^+ (and thus good MR image quality). Here a two-step optimization algorithm is explored to enable 1) low-SAR B_1^+ mapping, and 2) RF shimming PTX with adequate B_1^+ homogeneity.

Methods. For proof-of-concept, the two-step optimization algorithm was performed for a simulation modelling of a uniform cylindrical phantom with an implanted copper wire surrounded by a 4-channel PTX system (Figure 1).

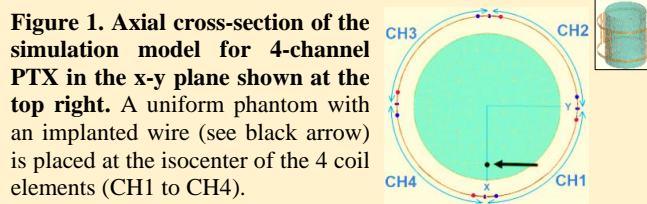


Figure 1. Axial cross-section of the simulation model for 4-channel PTX in the x-y plane shown at the top right. A uniform phantom with an implanted wire (see black arrow) is placed at the isocenter of the 4 coil elements (CH1 to CH4).

First, initial B_1^+ maps were simulated by applying a weighting factor of 1 to the input of individual RF coil elements, successively (i.e. $V(t) \times ([1,0,0,0], [0,1,0,0], [0,0,1,0], [0,0,0,1])$). Using the initial B_1^+ maps, an alternative low-SAR basis set of B_1^+ maps was determined via simulations and a constrained optimization algorithm to minimize local SAR surrounding the wire tip. **Second**, with the low SAR B_1^+ maps determined, a more complex optimization was performed for RF shimming including terms to minimize RF coupling artifact magnitude, as a surrogate of local SAR surrounding the wire tip, and B_1^+ field inhomogeneity. A simple matrix transformation was then applied to the amplitude and phase shifts for safe mode in the low SAR basis set, producing the actual RF shimming settings at the coil inputs.

Results. Simulated initial and low SAR E-field maps with their corresponding local SAR surrounding the wire tip are shown in Figure 2. Using the set of four low SAR B_1^+ maps (Figure 3A), the RF shimming B_1^+ map was then generated using the second optimization. Simulation results (Figure 3B) showed a substantial decrease in median local SAR of 96%, and a reasonable B_1^+ homogeneity of 78% for this specific PTX solution.

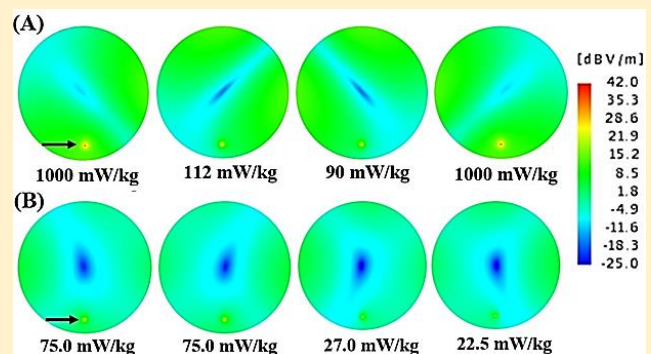


Figure 2. Simulated E-field maps (on a logarithmic scale) obtained by the initial vectors (A) and implementing a low SAR optimization (B) for the simulation model shown in figure 1. SAR at the tip of the wire is shown below each map.

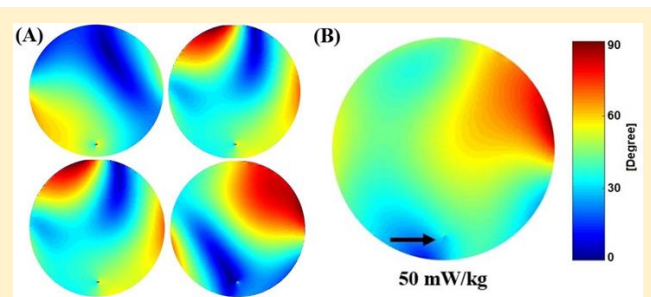


Figure 3. B_1^+ maps obtained by implementing a low SAR optimization (A), and the corresponding flip angle map (proportional to B_1^+) obtained from the 2-step optimization, providing minimal local SAR surrounding the wire tip (B).

Conclusion. The initial results of the RF shimming PTX with low SAR B_1^+ mapping are promising. Robustness of the proposed method can be investigated using realistic simulation models. In addition, the present simulation results require experimental validation which will be performed with a custom-built PTX platform developed in our laboratory.

Correction of motion and resulting field offsets for susceptibility weighted MRI using navigatorsMiriam Hewlett^{1,2}, Junmin Liu², and Maria Drangova^{1,2}¹Medical Biophysics, Western University, London ON²Robarts Research Institute, London ON

Introduction: Long scan times make motion artifacts more common in magnetic resonance imaging (MRI) than other imaging modalities [1]. Knowing the motion occurring during a scan enables correction of such artifacts, but residual artifacts may persist due to motion-induced magnetic field offsets. Susceptibility weighted imaging (SWI) is particularly sensitive to such effects as it exploits field distortions between anatomical structures for contrast enhancement [2]. However, motion-induced field offsets can be corrected if temporal changes in field are known. Navigator-based motion and field measurement is advantageous as data is acquired using the MRI itself (no additional hardware). The goal of this work was to combine spherical navigators (SNAVs) [3] with a free induction decay (FID) for simultaneous motion and zeroth order field measurement and correction in a SWI protocol.

Methods: The combined FID-SNAVs were interleaved in a 3D gradient echo sequence and tested on a 3T Siemens Prisma using a 32-channel head coil with imaging parameters matched to a typical SWI protocol. Navigators were acquired every 400 ms, requiring an additional minute of scan time (original acquisition 6:33, navigated acquisition 7:43). The SNAV portion of the navigator was processed in real-time within the scanner reconstruction to calculate motion estimates and prospectively update image acquisition. The FID portion of the navigator was processed offline to perform channel-wise correction of zeroth order field offsets prior to image reconstruction. Image quality was compared between acquisitions with no motion, motion but no correction, and motion with prospective motion correction (processed with and without retrospective correction of field offsets). To produce repeatable motion for scans with and without correction, participants were guided using a visual indicator (crosshair moving in a random, stepwise manner). A total of five trajectories were tested among three volunteers. Image quality was quantified using structural similarity index (SSIM) and compared with an analysis of variance (ANOVA).

Results: Measured rotations, translations, and field offsets ranged up to 6°, 5 mm, and 30 Hz, respectively, though varied between scans (depending on the subject, motion prompt). Prospective motion correction alone provided a notable improvement in image quality over uncorrected images, quantified by an increase in SSIM from 0.895 ± 0.014 to 0.920 ± 0.005 ($p < 0.05$). Retrospective correction of field offsets provided an incremental but significant improvement in image quality compared to prospective motion correction alone (SSIM 0.923 ± 0.005 , $p < 0.0001$). Sample images (Figure 1) show residual artifacts limit the visibility of small vessels compared to the reference.

Conclusions: Simultaneous correction of motion and resulting field offsets using combined FID-SNAVs showed significant improvement in image quality without the need for external hardware. Further improvement is expected with fine-tuning of motion and field estimation. Improved methods for motion correction would reduce the need for repeat scans, which increase costs and can delay diagnosis in a clinical setting.

References: [1] Andre et al. *J Am Coll Radiol.* 2015;**12**:689-695. [2] Berglund et al. *Magn Reson Med.* 2021;**86**:1970-1982. [3] Johnson et al. *Magn Reson Imaging.* 2016;**34**:1274-1282.

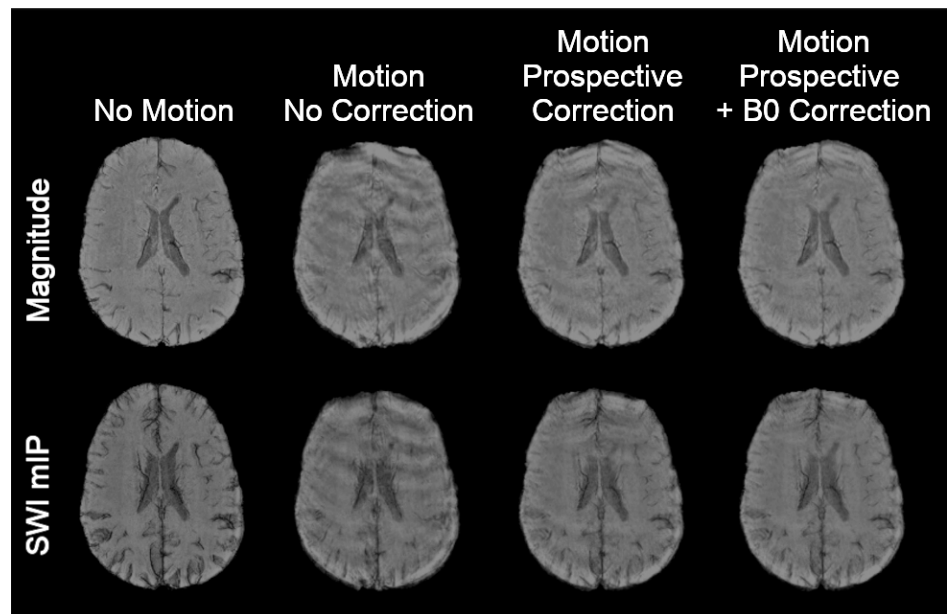


Figure 1. Sample images (magnitude and SWI, the latter displayed as a minimum intensity projection) acquired with no motion no correction, motion with no correction, motion with prospective motion correction (with and without retrospective correction of field offsets, denoted B0 correction).

Characterising magnetic field drift in Rosette-MRSI data *in-vivo***Sneha Senthil^{1,2}, Brenden Kadota¹, Peter Truong¹, Jamie Near^{1,2}***1. Sunnybrook Research Institute, Toronto, Ontario; 2. McGill University, Montreal, Quebec*

Introduction: Field drift correction is an important post-processing step in Magnetic Resonance Spectroscopic Imaging (MRSI) that considerably improves spectral quality and metabolite quantification. While several drift correction methods have been proposed in single-voxel MRS, drift correction in MRSI is more challenging due to the application of phase encoding gradients. In such cases, separately acquired navigator echoes are needed. Here, we demonstrate the use of self-navigating Rosette-MRSI trajectories for characterising scanner magnetic field drift using time-domain spectral registration *in-vivo*.

Methods: A two-dimensional (2D) PRESS-localised Rosette-MRSI sequence was implemented on a 3T Siemens Prisma MR scanner with a 20-channel head coil and, the following scan parameters: spectral width=1587Hz, FOV=240mm, FA (flip angle) =72°, 8 averages, TR/TE=1200/30ms, nominal voxel size 5x5x15mm³, and total scan time ~9min. Data was acquired in 5 healthy volunteers (4 males, 1 female; age: 29±6 years). Prior to the Rosette-MRSI scan, a 3D T1-weighted, MP-RAGE (Magnetization Prepared Rapid Gradient Echo) image was acquired for localisation purposes [1]. Data processing and reconstruction were performed using the FID-A toolkit [2]. To correct for field drift, FIDs from the centre of k-space were isolated from each repetition. Next, using the first k=0 FID as reference, frequency and phase offsets for each subsequent repetition were estimated using spectral registration [3], which uses non-linear least squares minimization to optimally align each FID signal to the reference spectrum. After estimating the frequency and phase offsets for each k=0 FID, the corresponding corrections were applied to full ADC signals, to achieve field drift correction across the entire k-space. SNR (amplitude of the NAA peak divided by the standard deviation of the noise) and NAA linewidths of the water suppressed spectra were compared before and after drift correction to assess improvements in spectral quality.

Results: Results of the frequency drift measurement are shown in Figure 1(A). The resonant frequency drifted approximately linearly by 5.7Hz (0.63Hz/min) for the representative

dataset. The mean frequency drift measured across all datasets was 5.8Hz (0.64Hz/min). This high rate of drift suggests that spatio-spectral MRSI sequences are likely associated with more gradient heating and greater frequency drift compared with single voxel MRS. Spectral registration resulted in a noticeable improvement in SNR, spectral linewidths and the lineshape of metabolite peaks. Figure 1(B) shows NAA SNR and NAA linewidth maps measured before and after drift correction in a representative subject. Across all voxels in all subjects, the average values of SNR increased by ~12.92% [t(528)=-16.05, p<0.001] and the NAA linewidths decreased by ~18.51% [t(530)=29.99, p<0.001]. Figure 2 shows spectra before (blue) and after (red) drift correction. Future work should aim to characterise typical field drift across multiple scanners and its impact on MRSI spectral quality.

Conclusion: This study demonstrated the use of the self-navigating Rosette-MRSI trajectories to retrospectively eliminate the adverse effect of frequency and phase drifts in the acquired *in-vivo* MRSI data. Since rapid high-resolution MRSI sequences are gradient-intensive, correction of gradient-induced field drift is an important consideration, and the proposed method allows these drifts to be easily measured and corrected.

References: 1. Marques JP et al. (2010) *Neuroimage*. 2. Simpson R, et al. (2017) *Magn Reson Med*. 3. Near J, et al. (2015) *Magn Reson Med*.

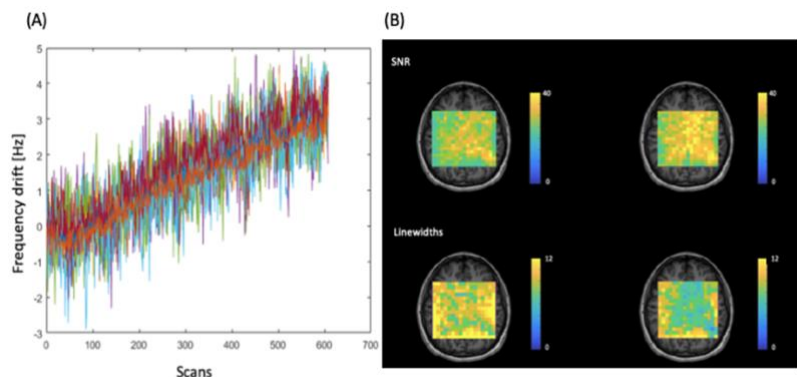


Figure 1: (A) Frequency drift measured for each coil and shot over 608 scans. (B) Illustration of NAA-SNR and NAA linewidth maps generated using FID-A, before and after field drift correction

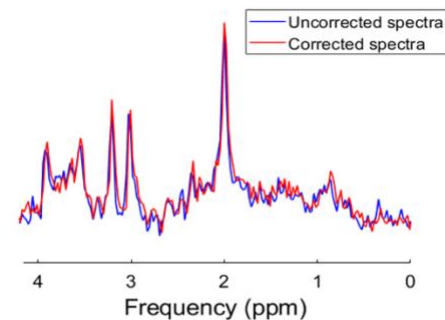


Figure 2: Spectra before and after drift correction

PLA2 inhibition using mepacrine reduces MR spectroscopy measures of total choline in a rat model of Alzheimer's disease

Colleen Bailey*¹, Ved Hatolkar*¹, Wendy Oakden^{1,2}, Margaret Koletar¹, JoAnne McLaurin^{1,2}, Jamie Near^{1,4}
¹Sunnybrook Research Institute, Toronto, ON; ²Synaptive Medical, Toronto, ON; ³Department of Laboratory Medicine and Pathobiology, University of Toronto; ⁴Department of Medical Biophysics, University of Toronto

Introduction

Magnetic resonance spectroscopy (MRS) studies have demonstrated elevated levels of brain cholines in Alzheimer's disease (AD)^{1,2}. This is believed to be associated with increased activity of the phospholipase A2 (PLA2) enzyme that breaks down membrane-bound phosphatidylcholine. In this study, we examine brain cholines and other metabolites in a transgenic rat model of AD. We hypothesize that inhibition of PLA2 with mepacrine will result in a decrease in total choline (tCho) levels observed by MRS.

Methods

Eleven Fischer 344 rats - 5 wildtype (WT; 3F, 2M), 6 transgenic (TgF344-AD, 6F) - aged 13 months were imaged at baseline, treated with 30 mg/kg mepacrine intraperitoneally each day for 7 days, then imaged post-treatment on day 8. One animal died before post-treatment MRS and was excluded from analysis. MRI was conducted under 1-4% isoflurane on a 7 T Bruker Avance BioSpec (Bruker BioSpin, Billerica, USA) with a 4-channel rat brain array for receive. For MRS, a 3.5 x 3.5 x 2 mm³ voxel was placed in the left dorsal hippocampus on a T2-weighted image and a Point RESolved Spectroscopy sequence with water suppression (TE=8.77 ms, TR=2500 ms, 2048 data points, spectral width 4000 Hz, 250 averages) was acquired. Spectra were analyzed using LCModel (Stephen Provencher Inc., Oakville, ON). The simulated basis set contained 18 metabolites and 9 macromolecule basis functions. Quantification used the unsuppressed water signal for reference. A decrease in choline levels between pre- and post-mepacrine treatment groups was tested using a one-sided t-test. All other metabolite comparisons used two-sided t-tests.

Results

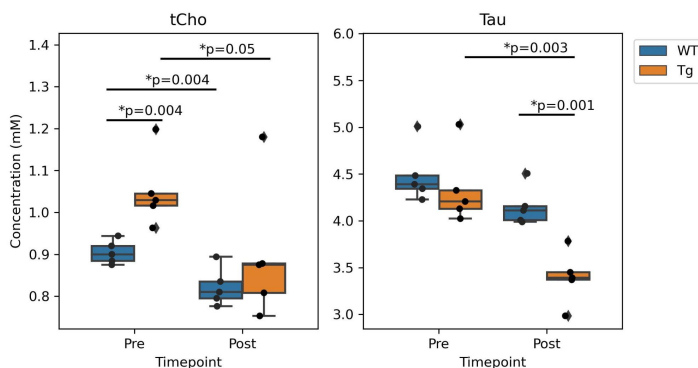


Figure 1 Absolute brain concentrations of total Choline (left) and Taurine (right) before and after mepacrine treatment in wildtype (WT) and TgF344-AD (Tg) rats.

Figure 1 shows the concentrations of total Choline (tCho) and Taurine (Tau) for animals in each group before and after treatment with mepacrine. tCho was higher in transgenic animals at baseline, but decreased following mepacrine treatment. Wildtype animals also showed a decrease in tCho following treatment. The only other metabolite that showed a significant change with treatment was taurine, which decreased significantly in TgF344-AD animals following mepacrine treatment.

Conclusions

Elevated pre-treatment brain tCho levels in the TgF344-AD rat model relative to wildtype at 13 months of age are consistent with previous work in this model¹ and human studies². The decrease in choline levels following mepacrine treatment is consistent with the hypothesis that mepacrine reduces PLA2-mediated membrane turnover and free cholines, but the drug has broad systemic effects so physiological changes (eg. perfusion) cannot be ruled out. In addition, outliers make it difficult to draw conclusions from the small group size. These findings motivate further investigation into total choline measures as a biomarker of PLA2 activity and use of PLA2 inhibitors to target neuroinflammatory pathways associated with AD pathophysiology.

¹Fowler CF, et al. Brain Commun. 2022; 4: fcac072. ²Marjańska M, et al. J Alzheimers Dis. 2019; 68: 559.

*These authors contributed equally to this work.

Multimodal connectivity gradients of the human basal forebrainSudesna Chakraborty^{1,2,5}, Roy A.M. Haast^{2,7}, Ali R. Khan^{1,2,5,6}, Taylor W. Schmitz^{1,2,3,4,5}

¹Neuroscience Graduate Program; ²Robarts Research Institute; ³Physiology and Pharmacology; ⁴Lawson Health Research Institute; ⁵Western Institute for Neuroscience; ⁶Medical Biophysics, Western University; ⁷CNRS CRMBM Aix-Marseille University

Introduction: The cholinergic innervation of the cortex predominantly originates from neuronal populations in the basal forebrain. Structurally, the ascending basal forebrain (BF) cholinergic projections are highly branched, with individual cells targeting multiple different cortical regions. The organization of ascending BF cholinergic projections may reflect complex spatial topographies of connectivity with the cortex. Within the BF, subregional structural changes in gray matter and white matter integrity are associated with distinct patterns of cortical degeneration and cognitive dysfunction. However, it is not known whether the structural organization of basal forebrain projections reflects their functional integration with the cortex.

Methods: We combined high-resolution 7T diffusion (DWI) and resting state functional MRI (rs-fMRI) data (n=173) from the Human Connectome Project ¹ with an existing stereotactic atlas of the BF ² to build structural and functional connectomes based on the number of connecting streamlines and time-wise correlation of signal fluctuations, respectively. This resulted in subject-wise 2-dimensional n -by- m matrices of connectivity strengths between BF voxels, n , and cortical targets, m ³. To capture gradients of connectivity differences between BF voxels, we used diffusion embedding, a nonlinear dimension reduction approach that identifies multiple axes of for the group-averaged structural and functional connectomes separately. Gradient-weighted cortical maps were then created by multiplying each row of the BF-cortical connectivity matrix with the corresponding gradient value of that BF voxel to examine how the BF functional and structural connectivity gradients are expressed in the

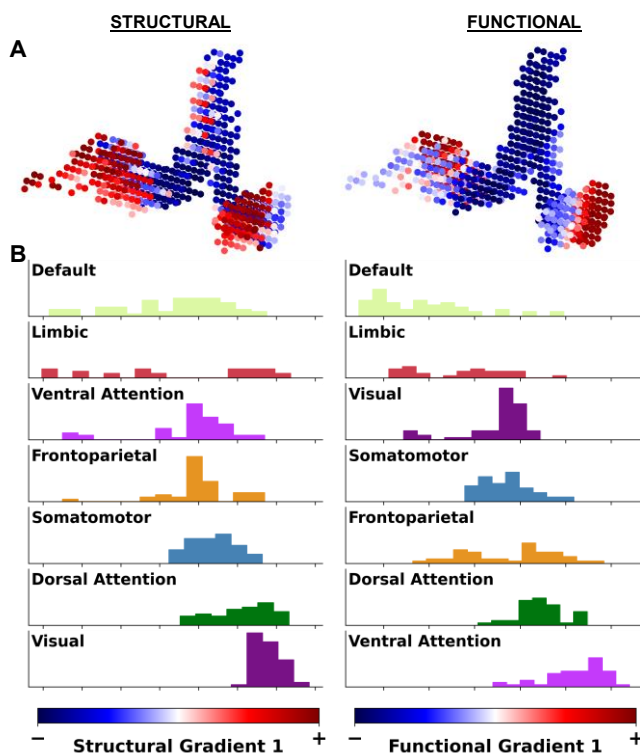


Figure: (A) The first principal gradient of the BF based on structural (sG1; left) and functional (fG1; right) connectivity both revealed an anteromedial to posterolateral axis. (B) G1-weighted maps were projected to the cortical surface; the histogram plots show the distribution of G1-weighted gradient values separately for each of the 7 networks⁴ (color-coded).

neocortex. **Results:** The first gradient for both structural (sG1) and functional (fG1) connectivity data explained ~30% of variance between BF voxels. For both sG1 and fG1, we observed a smooth gradient transition from anteromedial to posterolateral BF (Fig. A). The gradient-weighted cortical map for both sG1 and fG1 revealed stronger anteromedial BF connectivity with midline cortical structures, and stronger posterolateral BF connectivity with lateral cortical structures. We then examined whether the gradient values of the weighted cortical maps are preferably connected to the intrinsic cortico-cortical networks defined by Yeo ⁴. In the anteromedial BF, both gradients exhibited high similarity in overlap with the default mode and limbic networks. This structure-function overlap diverged moving posterolaterally, as the gradients exhibited more distinct connectivity patterns in the lateral cortex. These intermodal differences were most pronounced for the ventral attention network (Fig. B).

Conclusion: Our findings reveal that, moving from an anteromedial to posterolateral axis, spatial topographies of structural and functional connectivity within the BF become progressively detethered from one another.

References:

1. Glasser MF, et al. *Neuroimage*. 2013.
2. Zaborszky L, et al. *Neuroimage*. 2008.
3. Glasser MF, et al. *Nature Publishing Group*. 2016.
4. Yeo BTT, et al. *J Neurophysiol*. 2011.

Examining the Impact of Pediatric Arterial Ischemic Stroke on Cerebral Blood Flow within the Hippocampus and its Relationship with Observed Neurological Deficits

Ethan Luk¹, Kirstin Walker¹, Hannah Bernstein¹, Andrea Kassner², Amanda Robertson¹, Trish Domi¹, Pradeep Krishnan³, Prakash Muthusami³, Manohar Shroff³, Nicholas Stence⁴, Timothy Bernard⁵, Gabrielle deVeber⁶, Adam Kirton⁷, Helen Carlson⁷, Andrea Andrade⁸, Mubeen Rafay⁹, Bruce Bjornson¹⁰, Danny Kim¹¹, Max Wintermark¹², Nomazulu Dlamini^{1,6}

¹Program in Neurosciences and Mental Health, The Hospital for Sick Children, Toronto, Ontario, Canada, ²Translational Medicine, The Hospital for Sick Children, Toronto, Ontario, Canada, ³Department of Diagnostic Imaging, The Hospital for Sick Children, Toronto, Ontario, Canada, ⁴Pediatric Neuroradiology, Children's Hospital Colorado, Aurora, Colorado, United States of America, ⁵Child Neurology, Children's Hospital Colorado, Aurora, Colorado, United States of America, ⁶Division of Neurology, The Hospital for Sick Children, Toronto, Ontario, Canada, ⁷Alberta Health Services, Edmonton, Alberta, Canada, ⁸London Health Sciences Centre, London, United Kingdom, ⁹Health Sciences Centre Winnipeg, Winnipeg, Manitoba, Canada, ¹⁰The University of British Columbia, Vancouver, British Columbia, Canada, ¹¹BC Children's Hospital Research Institute, Vancouver, British Columbia, Canada, ¹²The University of Texas, Austin, Texas, United States of America

Introduction: Arterial ischemic stroke (AIS) is characterized by occlusion of an artery that leads to disruption of cerebral blood flow (CBF) to the neurons (brain cells), causing cell death. CBF can be captured using diffusion MRI and decreases in CBF are well-known markers of ischemic injury. However, holistic approaches that involve the impact of CBF on brain regions outside of the ischemic area, or stroke lesion, are not as well understood. We seek to analyze the hippocampus, a complex brain structure located within the temporal lobe that plays a significant role in learning, memory and spatial navigation; it is also known to be particularly vulnerable to deviations from homeostatic equilibrium. Monitoring hippocampal CBF after AIS may help in understanding its role in childhood development, determining appropriate treatment options, and allowing for predictions in stroke outcome. This study assesses CBF within the ipsilesional (stroke hemisphere) and contralesional (non-stroke hemisphere) hippocampi and associations to neurological and sensorimotor deficits observed at acute, subacute (3-7 days post-stroke) and chronic (3 months post-stroke) phases of stroke recovery.

Methods: Nine pediatric stroke patients (mean age 14.89 ± 2.85 , 4 Male) with unilateral, non-hippocampal stroke lesions were scanned using arterial spin labelling MRI in a 3T Siemens MRI scanner with a 2D pulsed labeling scheme. Neurological outcome was evaluated with the Pediatric Stroke Outcome Measure (PSOM) at 3-7 days and at 3 months post-stroke in all patients. One subject was excluded due to a recurrent stroke within three months of the initial stroke. Mean CBF at the hippocampi were compared to seven healthy controls (mean age 14.53 ± 1.43 , 2 Male). Differences between group means were identified using ANOVA, then Students' t-tests. CBF ratios between ipsilesional and contralesional hippocampi were plotted against PSOM scores at the acute and chronic timepoints; correlations were examined using the Spearman's rank (ρ) coefficient.

Results: Mean CBF (mL/100g/min) in the ipsilesional and contralesional hippocampi were 52.77 ± 10.98 and 54.69 ± 14.24 respectively. Mean CBF in the control group was found to be higher than both the ipsilesional and contralesional hippocampi at 61.14 ± 12.30 . ANOVA between groups revealed an F-statistic of $F=1.24$ ($p=0.30$) and a post hoc one tailed t-test between the ipsilesional and control group yielded a t-statistic of $t=1.55$ ($p=.067$). A negative correlation of $\rho = -0.77$ ($p=.025$) was observed between CBF ratios in intrasubject hippocampi and the PSOM score observed at the acute timepoint. Comparing the CBF ratio with PSOM score at three months post-stroke shows a greater negative correlation with a Spearman correlation coefficient of $\rho = -0.96$ ($p \ll .001$).

Conclusion: Comparing intrasubject CBF between hippocampi at the acute timepoint was found to be a strong indicator of neurological and sensorimotor deficits at three months post-stroke. We found evidence that PSOM score at the chronic stage and the CBF ratio at the acute stage can be modeled with a monotonic decreasing function. As in, we may be able to model an arbitrary function of CBF that never increases with PSOM score. A larger sample size is required to determine validity and consistency of the results found in this study.

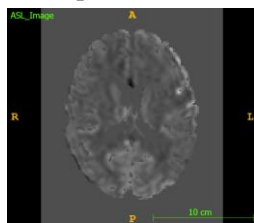


Figure 1: Sample ASL image at slice $z = 18$ (world units)

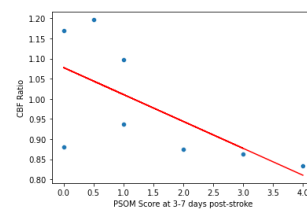


Figure 2: PSOM score at 3-7 days post-stroke vs CBF ratio between ipsilesional and contralesional hippocampi

MRI BIOMARKERS OF NEUROINFLAMMATION ACROSS NEURODEGENERATIVE DISEASES

V. Sumra¹, A. Ann Dillio², A. Frank³, A. Lang⁴, A. Roberts⁵, A. Troyer⁶, B. Levine⁷, S. Arnott⁷, B. Tan⁷, C. Fischer⁸, C. Marras⁹, D. Kwan¹⁰, D. Munoz¹⁰, D. Tang-Wai⁴, E. Finger¹¹, E. Rogaeva¹², J. Orange⁵, J. Ramirez¹³, K. Sunderland⁷, L. Zinman¹³, M. Binns⁷, M. Borrie², M. Masellis¹⁴, M. Freedman⁶, M. MonteroOdasso¹¹, M. Ozzoude¹³, R. Bartha², R. Hegle², R. Swartz¹³, A. Abrahao¹³, M. Strong¹¹, C. Tartaglia¹

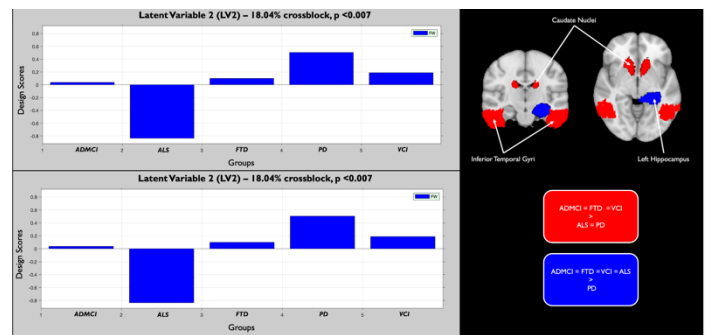
¹University of Toronto, Institute of Medical Science, Toronto, ON, Canada, ²Western University, Robarts Research Institute, London, ON, Canada, ³University of Ottawa, Bruyère Memory Program, Ottawa, ON, Canada, ⁴University Health Network, Krembil Research Institute, Toronto, ON, Canada, ⁵Western University, School of Communication Sciences and Disorders, London, ON, Canada, ⁶Baycrest Health Sciences, Neuropsychology and Cognitive Health, Toronto, ON, Canada, ⁷Baycrest Health Sciences, Rotman Research Institute, Toronto, ON, Canada, ⁸St. Michael's Hospital, Geriatric Psychiatry, Toronto, ON, Canada, ⁹Toronto Western Hospital, Movement Disorders Clinic, Toronto, ON, Canada, ¹⁰Queen's University, Center for Neuroscience Studies, Kingston, ON, Canada, ¹¹Western University, Schulich School of Medicine and Dentistry, London, ON, Canada, ¹²University of Toronto, Tanz Centre for Research in Neurodegenerative Disease, Toronto, ON, Canada, ¹³Sunnybrook Health Sciences Centre, Sunnybrook Research Institute, Toronto, ON, Canada, ¹⁴University of Toronto, Sunnybrook Health Sciences Centre, Sunnybrook Research Institute, Toronto, AB, Canada, ¹⁵University of Waterloo, Department of Kinesiology, Waterloo, ON, Canada,

Introduction: Although normal aging of the brain is associated with increases in neuroinflammation (Sparkman & Johnson, 2008), neurodegenerative diseases are also often associated with changes in blood and cerebrospinal fluid (CSF) biomarkers of neuroinflammation (Psenicka et al., 2021). Free-water diffusion (FWD), a diffusion MRI metric, is proposed to be a non-specific marker of neuroinflammation (Pasternack et al., 2009), where signal intensity (from 0 to 1) is related to volume of water within each voxel. Given previous research implicating neuroinflammation in the pathogenesis of neurodegenerative disorders, we examined FWD across neurodegenerative diseases in the Ontario Neurodegenerative Disease Research Initiative (ONDRI) Cohort.

Methods: Diffusion and structural MRI data from the ONDRI cohort was used to generate FWD maps in a dataset of 392 subjects (115 Alzheimer's Disease (AD)/Mild cognitive impairment (MCI), 37 Amyotrophic Lateral Sclerosis (ALS), 45 Frontotemporal Dementia (FTD), 129 Parkinson's Disease (PD), 66 Vascular Cognitive Impairment (VCI). FWD maps were generated according to Pasternack et al., (2009) using MATLAB, prior to partial least squares (PLS) analysis using 1000 permutations and 1000 bootstraps (McIntosh & Lobaugh, 2004). Post-hoc one-way ANOVA and Tukey's highest significant difference (HSD) tests were conducted in significant ROIs determined through PLS.

Results: PLS revealed three significant latent variables (LV1, LV2 and LV3). LV1 explained 66% of the sample variance and separated ALS and PD from ADMCI, FTD and VCI. LV2 explained 18% of the sample variance and separated ALS and FTD from ADMCI, PD and VCI. LV3 explained 9% of the sample variance and separated ADMCI and PD from ALS, FTD and VCI. Significant clusters were identified through PLS in the hippocampi, caudate nuclei, thalami, hypothalamus, putamen, insula, temporal cortex, frontal cortex, medial occipital cortex and superior cerebellum,. In all included ROI's but the thalami, insula, temporal pole and middle frontal gyrus, there was a significant effect of group (p <0.05) as identified through ANOVA. Tukey's HSD revealed two patterns in the dataset i) ROIs where ALS and PD had significantly lower FWD compared to ADMCI, FTD and VCI within the caudate nuclei, hypothalamus, putamen, inferior temporal gyrus and superior cerebellum and ii) ROIs where ALS has significantly lower FWD compared to PD, ADMCI, FTD and VCI in the medial occipital cortex.

Conclusions: In this preliminary dataset, regionally specific differences in FWD were observed across neurodegenerative diseases. Regional inflammation may play a role in selective neuronal and region-specific vulnerability across these diseases.



References

Sparkman, N. L., & Johnson, R. W. (2008). The Effects of Infection or Stress. *NeuroImmunoModulation*, 15(4–6), 323–330.

Psenicka, M. W., Smith, B. C., Tinkey, R. A., & Williams, J. L. (2021). Connecting Neuroinflammation and Neurodegeneration in Multiple Sclerosis: Are Oligodendrocyte Precursor Cells a Nexus of Disease? *Frontiers in Cellular Neuroscience*, 15(June), 1–29. <https://doi.org/10.3389/fncel.2021.654284>

Pasternak O, Sochen N, Gur Y, Intrator N, Assaf Y. Free water elimination and mapping from diffusion MRI. *Magn Reson Med*. 2009 Sep;62(3):717-30.

McIntosh AR, Lobaugh NJ. Partial least squares analysis of neuroimaging data: applications and advances. *Neuroimage*. 2004;23 Suppl 1:S250-63.

Cortical Network Disruption in First-Episode Psychosis

Peter Van Dyken¹, Ali R. Khan², Lena Palaniyappan³

¹Schulich School of Medicine and Dentistry; ²Robarts Research Institute, Western University; ³Department of Psychology, McGill University

INTRODUCTION

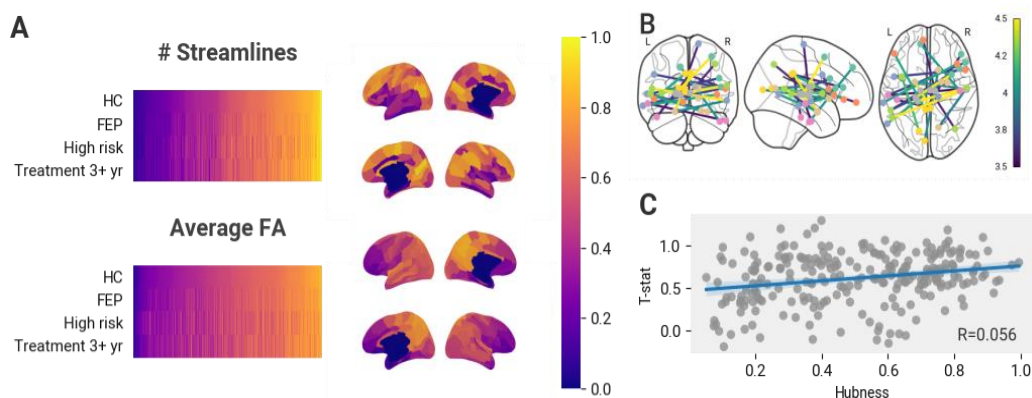
Current models of schizophrenia describe a degradation of the cortical architecture, suggesting cortical dysconnectivity as an explanation for schizophrenia symptoms. Previous reports have implicated central cortical nodes as key impact sites (Klauser et al, 2017). Most such studies have looked at chronic, treated schizophrenia; few have looked specifically at first-episode psychosis (FEP) patients. We explored the relation between connectivity disruption and hubness in data collected from FEP patients using a recently developed composite metric of node hubness.

METHODS

N=40 first-episode psychosis (FEP) patients and N=30 healthy controls were recruited from a cohort enrolled in the Prevention and Early Intervention Program for Psychoses (PEPP) in London, Ontario. Data was acquired with 7T MRI using diffusion-weighted (b=0,1000; 64 directions; 2mm res) and T1-weighted (MP2RAGE; 0.75mm res) protocols. Diffusion data was preprocessed with an FSL pipeline (TOPUP, EDDY), and tractography was generated using iFOD2, implemented in MRTrax. Structural connectivity matrices, weighted with average fractional anisotropy (FA) and streamline count, were found using the Brainnetome atlas. Node hubness was calculated using a composite score (Hanilioglu et al, 2021) based on four graph theory metrics: degree, betweenness, clustering coefficient, and path length, all of which have been previously used to capture hubness (van den Heuvel et al, 2010). The differences in edge weight between healthy controls and FEP patients was calculated using the Network Based Statistic, a family-wise method of error correction. The T-statistic of all edges connected to each node were averaged to get a nodal disruption score, which was correlated with hubness.

RESULTS

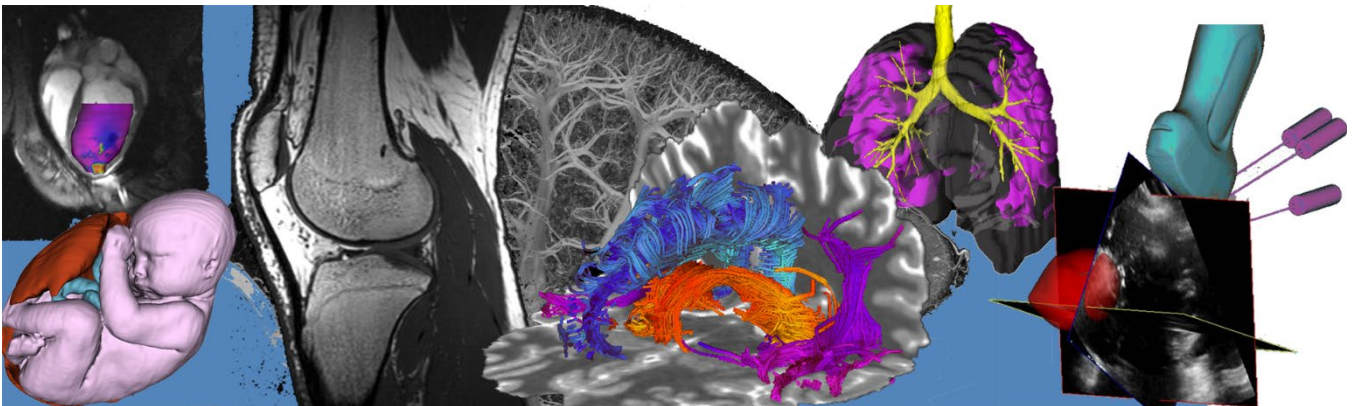
Hubs were found in the frontal, parietal, and cingulate cortices and the cuneus/precuneus, but varied greatly depending on the edge weight. Hub identity remained stable across disease conditions (Figure 1A). 282 connections (0.46% of total) in FEP had significantly reduced average FA according to NBS (Figure 1B). The nodal disruption score showed no significant association with node hubness (Figure 1C).



CONCLUSIONS

The structural disruption observed in our patients was much milder than that previously observed. Unlike previous reports, we did not observe a predilection toward disruption among high hubness nodes. This may reflect an absence of structural change in first episode patients, due either to the relatively shorter time course of psychotic symptoms or lack of exposure to antipsychotic medication.

Oral Session 7: Cancer Imaging Abstracts

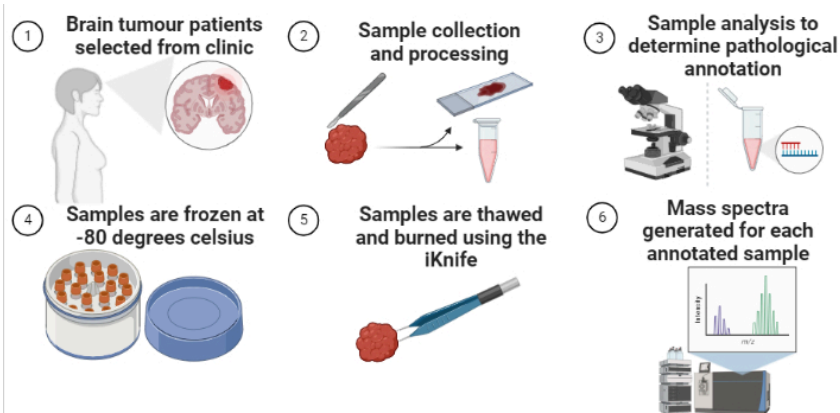


Identification of glioblastoma using rapid evaporative ionization mass spectrometry

D. Srikanthan¹, M. Kaufmann², A. Jamzad³, G. Fichtinger^{2,3}, J. Purzner², J. Rudan^{1,2}, P. Mousavi^{1,3}, T. Purzner^{1,2}

¹Department of Translational Medicine, Queen's University; ²Department of Surgery, Queen's University; ³School of Computing, Queen's University

INTRODUCTION: Glioblastoma (GBM) is the most common malignant brain tumour. Unfortunately, despite some improvement in the 2-year survival over time [1], the long-term prognosis has not significantly improved for the past 40 years, with 5-year survival rate of around 5% and overall mortality close to 100% [1]. Standard therapy, including surgery, radiation, and chemotherapy, yields a median overall survival of 12-18 months [1].



One factor that significantly affects survival outcomes is extent of surgical resection. Patients who undergo gross total resection (GTR) or supramarginal resection have delayed time to recurrence and improved overall survival [1]. Every millimeter of the brain has a unique function, thus resection of brain tissue can have significant consequences for the patient. By identifying areas with high and low risk of recurrence outside the tumour cavity, we can carry out supramarginal resection, benefiting

the patient while avoiding the cost of removing unnecessary brain tissue. A promising intraoperative technology for tumour margin detection is the intelligent knife (iKnife). iKnife uses rapid evaporative ionisation mass spectrometry (REIMS) which is capable of analyzing unprocessed solid tissue [2,3]. The ability to offer real-time information on the type of tissue being analyzed allows for the iKnife operator to correlate physical location and molecular profile. We curated a database of ex-vivo GBM and normal brain tissue that was used to train and validate a machine-learning model for preliminary results to demonstrate feasibility of GBM detection.

METHODS: According to a protocol sanctioned by the research ethics board at our institution, patients were selected from the neurosurgical clinic with a confirmed the GBM diagnosis. The surgeon marked the likely tumour spot on radiography and then removed it through standard-of-care navigated neurosurgery. Samples underwent gross cutting within the operating room and several samples from each tumour was selected for collection. Where possible, samples that represented several regions of the tumor were selected to promote reproducibility across regions within a tumor, and between tumors. When normal appearing brain tissue remote from the tumor site was resected during the initial exposure, these samples were also kept as controls. A neuropathologist confirmed final pathological diagnosis. All samples were collected on dry ice and frozen until the time of experiment where the resected specimen was thawed, and point burns were performed. Each spectrum was processed using the Online Model Builder (OMB), which normalized, lock mass corrected, and binned the intensity measurements. Each burn had one representative spectrum. Our dataset had 7 patients consisting of 3 normal brain samples and 4 GBM samples. To classify GBM tissue we employed two machine-learning models: PCA/LDA and a KNN. We employed a three-fold cross validation method whereby the three folds had a total of 316 normal brain spectra and 321 GBM spectra.

RESULTS: We found that we could detect GBM tissue with a PCA/LDA model with an accuracy of 93.7% with an AUC of 0.94. Our KNN model did slightly better with an accuracy of 94.4% and an AUC of 0.95. The sensitivity and specificity of our PCA/LDA model is 0.93 and 0.95 respectively. The sensitivity and specificity of our KNN model is 0.97 and 0.93 respectively.

DISCUSSION & CONCLUSION: The iKnife combined with machine learning can accurately differentiate GBM and normal brain tissue in real-time, offering clinical benefits such as reducing recurrence and improving outcomes. However, this study was ex vivo with homogenous tissue and point burns and future research with intraoperative data is needed to confirm its tissue differentiation ability. Additionally, the limited sample size of 7 patients in this dataset could pose a constraint. To overcome this, incorporating multiple spectra from each burn through data augmentation may prove beneficial. This study only utilizes 900 features of the spectra, but further research has the potential to uncover more significant information by utilizing all 9000 features.

References: [1] Weller, M., Wick, W., Aldape, K. et al. *Nat Rev Dis Primers* (2015); [2] Jamzad A, Sedghi A, Santilli A, et al., *MICCAI* (2020); [3] Tzafetas M, et al., *PNAS* (2020).

Predicting the Dose Distribution of Multi-Lesion Lung Stereotactic Body Radiotherapy Plans using Generative Adversarial Networks

Edward Wang,^{1,2} Jonatan Snir,³ Jaron Chong,⁴ Pencilla Lang,^{*,3} Sarah A. Mattonen^{*,1,2,3}

¹ Department of Medical Biophysics, Western University, London, Ontario, Canada

² Baines Imaging Research Laboratory, London Regional Cancer Program, London, Ontario, Canada

³ Department of Oncology, Western University, London, Ontario, Canada

⁴ Department of Medical Imaging, Western University, London, Ontario, Canada

Introduction: The lung is the second most common site of cancer metastasis. Stereotactic body radiotherapy (SBRT) is a radiation technique that allows for high doses to be delivered accurately to tumor sites and has been shown to increase survival in patients with metastatic disease. Over-irradiating healthy lung tissue can lead to radiation toxicity, while under-irradiating cancer increases the risk of recurrence. Determining whether a treatment plan will be both safe and effective is resource intensive and relies on a dosimetrist fully planning the prescription via specialized software. When a prescription does not meet dose constraints, another must be selected and re-planned, potentially leading to treatment delays. In extreme cases, it may be that a suitable prescription is not possible, requiring the patient to undergo alternate treatment options, causing further delays and distress. Physicians do not know at the time of prescription whether a plan is suitable. In this study, we present the first machine learning approach for dose prediction of SBRT for multiple lesions. Using a generative adversarial network (GAN), we model the radiation dose received by healthy lung tissue in multi-lesion SBRT without utilizing the full planning workflow, thereby allowing physicians to quickly estimate radiation toxicities when prescribing treatment.

Methods: A retrospective review of patients who received SBRT treatment for two or more lung lesions between January 2014 and May 2020 was conducted at a single tertiary academic center in Canada. All prescriptions were converted to their equivalent doses in two Gray fractions (EQD2). The CT scan, ground truth dose in EQD2, and contours of the tumour volumes and organs at risk (OARs) were all exported in DICOM format. An initial dose estimation (IDE) was created for each prescription using an exponential model. Eighty percent of the patient data was used to train each of the GAN models, with 20% reserved for testing. To allow the models to focus on clinically relevant locations, the standard conditional GAN loss function was modified to include a component of distance loss that is only calculated over the locations of the tumours and OARs. The models were evaluated by the mean squared error (MSE) between the synthetic dose distribution and ground truth dose distribution taken over a binary mask of the OARs, and the difference the percent volume of lung receiving greater than 20 Gray. GAN models were trained on the IDE and OAR contours, CT and OAR contours, and IDE, CT and OAR contours and compared. To determine the value of using the custom loss function, the best performing GAN configuration was retrained with a standard conditional loss function.

Results: In total, plans from 67 multi-lesion patients were collected (47 two-lesion plans, 20 plans with greater than 2 lesions). The GAN conditioned on the planning CT, IDE and OARs was the most accurate with a masked MSE of 5.21 Gray², and a difference in V20 of 1.33 absolute % percent averaged across all patients in the test set. The GAN conditioned on the IDE and OARs was the least accurate with a masked MSE of 9.27 Gray² and a difference in V20 of 2.04 absolute percent. All models were more accurate for two lesion plans compared to plans with greater than two lesions. When the best performing GAN configuration was retrained with the non-custom loss function, the difference in V20 increased to 1.75 absolute percent.

Conclusions: The model created in this study is the first ever for dose prediction of multiple lesions treated with SBRT. Two additional novel aspects of the work are providing the model with an initial estimation of dose, and using custom loss function during training, both of which improved model performance. We show that a GAN can accurately estimate the radiation delivered by a multi-lesion lung SBRT treatment in real-time. This work builds the foundation for the creation of a clinical tool that physicians can use in clinic to quickly determine the feasibility of SBRT treatment for a given patient, and to compare different treatment regimens.

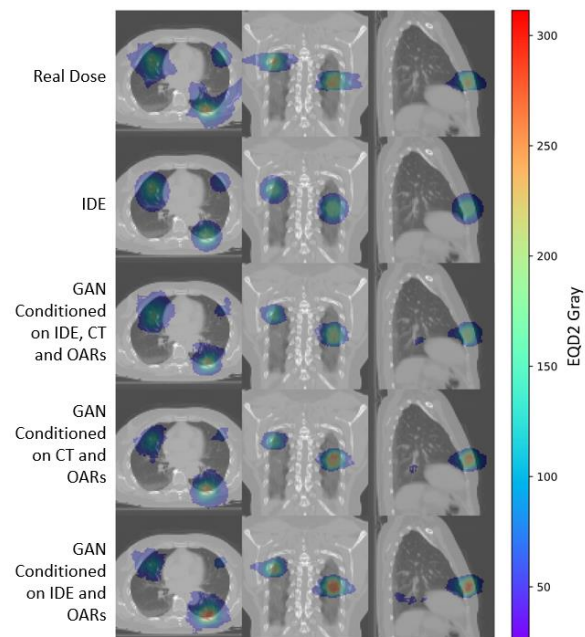


Figure 1: Axial, coronal, and sagittal slices from the distributions of the ground truth dose, initial dose estimation (IDE), and the three GAN doses are shown for a single patient in the testing set. The colour bar represents Gray in EQD2.

Deep-Learning-Based Auto-segmentation in Prostate Brachytherapy, with Implanted Needles

Prakash Hampole^{1,4,5}, Thomas Harding⁵, Derek Gillies⁵, Nathan Orlando^{1,4}, Chandima Edirisinghe⁴, Lucas Mendez^{3,5}, David D'Souza^{3,5}, Vikram Velker^{3,5}, Rohann Correa^{3,5}, Aaron Fenster^{1,2,4} & Douglas Hoover^{1,3,5}

Departments of ¹Medical Biophysics and ²Medical Imaging and ³Oncology, Western University, London, Canada; ⁴Robarts Research Institute, Western University, London, Canada; ⁵Department of Oncology, London Health Sciences Centre, London, Canada

Introduction: Brachytherapy is a common treatment modality for prostate cancer, which will directly impact 1 in 9 Canadian men. [1] Accurate segmentation of the prostate target on transrectal ultrasound (TRUS) is critical for treatment success; however, this can be time-consuming and challenging due to significant image artifacts from implanted needles. Previous work examining automatic algorithms for prostate segmentation has focused on the simpler problem of segmentation before needles have been implanted. [2] Here, we sought to utilize improvements made in auto-segmentation using convolutional neural networks (CNNs), which have demonstrated promising results in medical image segmentation. [3] Specifically, we have adapted and validated a CNN segmentation algorithm, initially developed for prostate biopsy and pre-implant brachytherapy, for use in prostate brachytherapy with implanted needles. [2] This previous work demonstrated that a 2D CNN could outperform a fully 3D CNN in the task of 3D prostate segmentation, and that the results of this approach are robust even in the presence of relatively sparse datasets. [4]

Methods: A retrospective dataset of 144 brachytherapy plans, which included 3D TRUS images and associated clinical prostate segmentations, was used to train a modified 2D U-Net CNN using a Dice Similarity Coefficient (DSC)-based loss function. 2D images for training were created by re-slicing the 3D TRUS image at various radial (around the anterior-posterior axis) and oblique angles cut through the 3D image centre, as well as axial, coronal, and sagittal planes. Datasets were split by patient, with approximately 80% of the data used for training and 20% held back for testing. 2D predictions were made on radially sliced images, 15° apart, and then reconstructed into a 3D image as shown in Figure 1. Algorithm performance was evaluated through metrics of accuracy, including precision, recall, DSC, volume percent differences (VPD), mean surface distance (MSD) and Hausdorff distance (HD). To assess segmentation agreement between physicians and benchmark algorithm performance, three physicians segmented a subset of five patients in the test dataset, repeating this at least one week later.

Results: Comparing results between the clinical and automated segmentations, the precision, recall, DSC and VPD after 3D reconstruction were $84.0 \pm 8.6\%$, $89.0 \pm 4.7\%$, $86.0 \pm 4.6\%$, and $12.3 \pm 10.6\%$, respectively; while the mean 2D MSD and 2D HD for the radial predictions were 1.9 ± 0.8 mm and 5.6 ± 2.8 mm, respectively. The time required to segment a set of 12 2D radial images was 2.47 ± 0.07 s. The mean DSC among same observers and between different observers were $87.0 \pm 6.1\%$ and $82.5 \pm 6.3\%$, respectively ($N_{\text{obs}} = 3$, $N_{\text{patient}} = 5$).

Conclusion: The CNN performed at a level consistent with an expert physician observer and in a fraction of the time taken for manual segmentation (approximately 5 minutes). Future work will involve a dosimetric evaluation to further assess clinical acceptability.

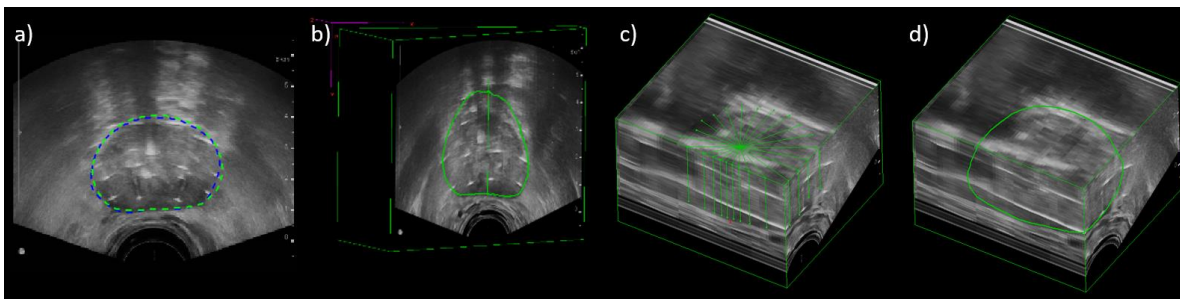


Figure 1. a) Radial slice showing predicted (green) versus clinical (blue) segmentation. b) 1 of 12 radial predictions for 3D reconstruction. c) 12 predicted radial slices. d) Predictions combined into a 3D volume.

[1] Canadian Cancer Statistics 2019. Canadian Cancer Society. Published 2019.

[2] Orlando N et al. *Phys Med Biol.* 2020;47(6):2413-2426.

[3] Yan W et al. *2021 13th International Conference on WCSP.* October 2021.

[4] Orlando N et al. *Phys Med Biol.* 2022;67(7)

Prostate Cancer Detection using Multi-Scale Analysis of Micro-Ultrasound Imaging

Paul Wilson¹, Mahdi Gilany¹, Andrea Perera-Ortega¹, Amoon Jamzad¹, Brian Wodlinger³, Fahimeh Fooladgar², M. N. Nhat To², Purang Abolmaesumi², Parvin Mousavi¹

¹Queen’s University, Kingston, Ontario, Canada, ² University of British Columbia, Vancouver, British Columbia, Canada,

³Exact Imaging, Markham, Ontario, Canada

INTRODUCTION: The standard method for prostate cancer (PCa) diagnosis and grading is histopathological analysis of tissue samples of the prostate, typically obtained via trans-rectal ultrasound (TRUS)-guided biopsy. This method has a high false-negative rate, and carries considerable risks of biopsy-related adverse effects. To improve ultrasound-based PCa detection, we propose a multi-scale approach to PCa detection using deep learning which analyzes ultrasound data at the scale of small ultrasound patches *and* whole biopsy cores.

METHODS: We use a private dataset captured via new micro-ultrasound technology (29 MHz center frequency) from 578 patients who underwent systematic TRUS-guided biopsy as part of a clinical trial (NCT02079025). ROIs corresponding to 5mm by 5mm areas of tissue are selected from the needle trace region (Fig 1, part 1) and matched with histopathology labels. Our proposed method consists of two main parts. First, we use self-supervised learning (SSL) to train a convolutional neural network to extract informative feature representations for RF ultrasound ROIs. To train this network, we adopted Variance-Invariance-Covariance Regularization (VICReg) method [1] (Fig 1, part 2). Second, we train a self-attention network which receives the feature representations from all ROIs within a core and the histopathology label of that core to distinguish cancerous from benign cores (Fig 1, part 3).

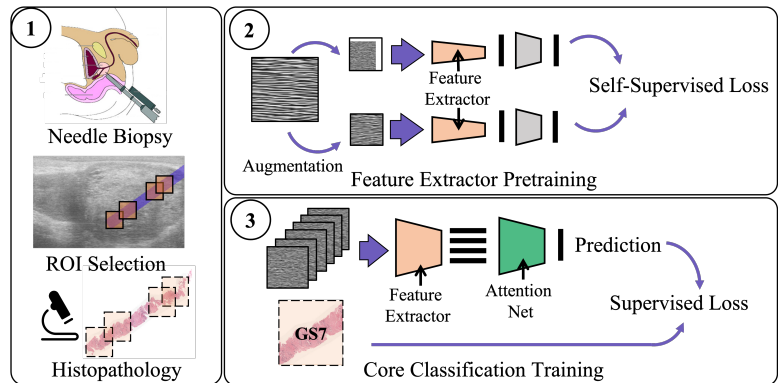


Figure 1: Summary of the proposed method: data collection and preprocessing (1), self-supervised pre-training (2), and core classification training using the self-attention network (3)

This network uses attention to gather context from the various input ROIs, allowing it to identify cancer more robustly than looking at individual ROIs in isolation.

RESULTS: Our proposed method (Row 2) has significantly improved performance compared to the baseline approach from our previous work [3] (i.e not using self-supervised learning or multi-scale analysis), as evidenced by the 4% improvement in AUROC. The model has a very high sensitivity in identifying cancerous from benign prostate cores, but relatively lower specificity. We found a larger number of false positives in cases where the needle region contained many ROIs *outside* of the prostate. These lowered sensitivity, but could potentially be corrected by applying prostate segmentations to remove out-of-prostate ROIs.

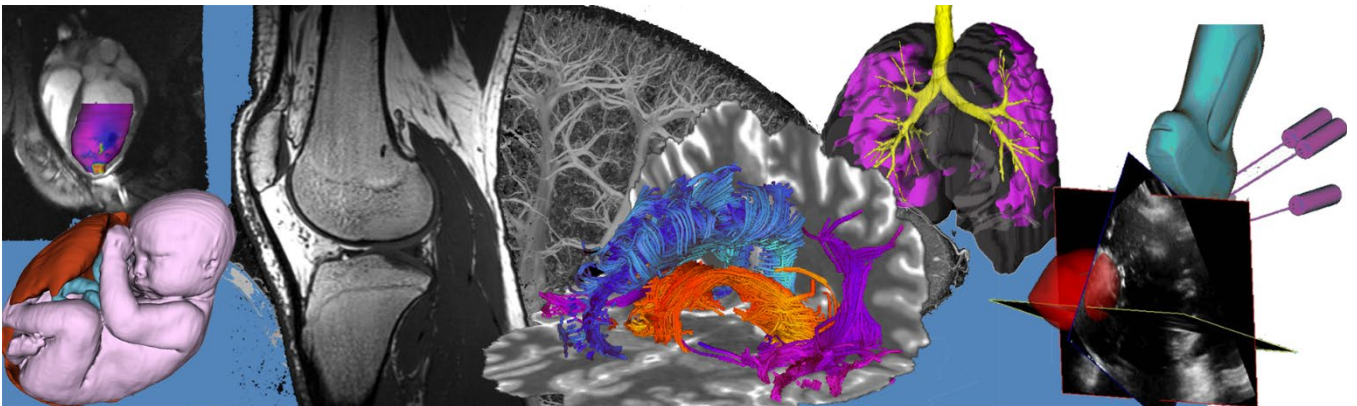
CONCLUSIONS: We proposed a multi-scale and context-aware method for PCa detection from TRUS. It improves performance by allowing the model to analyze multiple ROIs together. Due to its accuracy, the model is potentially a useful clinical tool for biopsy targeting. Future work should aim to generalize the architecture to an automatic grading model, improve accuracy, and further test the generalization performance via prospective studies.

REFERENCES: [1] Bardes A et al., ICLR 2022 [2] Ahmed H et al., The Lancet 2017 [3] Gilany M et al., MICCAI 2022

Table 1: Comparison of the proposed method to baseline methods. Metrics are based on core classification performance.

Method	AUROC	Sens	Spec
Supervised [3]	76.3±1.7	63.6±12.9	71.1±7.7
SSL + Attention (ours)	80.3±2.0	88.0±11.6	51.2±14.6

Oral Session 8: Cardiac and Lung Imaging Abstracts



Real time mitral annulus segmentation from 4D transesophageal echocardiography using deep learning regression

Patrick Carnahan^{1,2}, Apurva Bharucha³, Daniel Bainbridge⁴, Elvis C.S. Chen^{1,2,5}, and Terry M. Peters^{1,2,5}

¹Imaging, Robarts Research Institute, London, CA, ³King's College Hospital, Denmark Hill, London, UK

²School of Biomedical Engineering, ⁴Department of Anesthesiology, London Health Sciences Centre, ⁵Department of Medical Biophysics Western University, London, CA

Introduction: Segmentation of the mitral annulus is an important step in many cardiac applications including identifying pathologies, surgical planning and implant design¹. Additionally, mitral annulus tracking has been demonstrated to greatly improve procedure accuracy during trans-catheter mitral valve procedures². Several methods have been proposed to automate mitral annulus segmentation, including both annulus tracking from a manually defined initial state, and direct detection of the annulus from volumetric data. Existing direct detection methods achieve accuracy around 2mm annulus-to-annulus distance error; however, they suffer from poor runtime ranging from 10-60 seconds³. Tracking-based approaches can be applied in real time, however are susceptible to drift and require manual initialization. We propose a novel deep learning based mitral annulus detection algorithm structured as a regression predicting a set of Fourier coefficients that define the mitral annulus using convolutional neural networks (CNN), with a runtime supporting real-time applications.

Methods: We have acquired a dataset of 90 cases with 4D transesophageal echocardiography and segmented annuli from patients undergoing diagnostic imaging in preparation for mitral valve procedures, with appropriate ethics approval. From the 90 cases, we have a total of 2,190 volumes, split into training, validation and testing sets. Our network architecture uses a regressor approach based on the downsampling path of a Residual UNet with 5 layers of 16, 32, 64, 128, and 256 channels respectively, followed by two fully connected layers of size 256 and 60 which is then reshaped to output a prediction in the shape of (B, 10, 3, 2) where B is the batch size. This corresponds to 10 complex-valued Fourier coefficients for each of the 3 axes. Following prediction the full mitral annulus shape is sampled by zero-padding the coefficients to a size of 200, and taking the inverse Fourier transform to produce a set of 200 3D coordinates. Our model was trained for 500 epochs on 74 cases with 1862 volumes, utilizing data augmentation of random rotations of up to 15°, and random translations up to 10 voxels. The runtime of our method is 26ms per frame, or 40 frames per second.

Results: On our test set of 10 patient cases and 142 volumes, our method achieves a mean absolute curve-to-curve error of 5.5 ± 2.2 mm. On the validation set, the curve-to-curve was 5.4 ± 1.8 mm. As we see in Figure 1, the accuracy has large variability between cases, with examples (d) and (e) showing much better agreement between the prediction and ground-truth. The training error of our model reaches 0.28 ± 0.21 mm, indicating our model is at present over-fitting the training data, and we believe a larger dataset is still required to enable generalization.

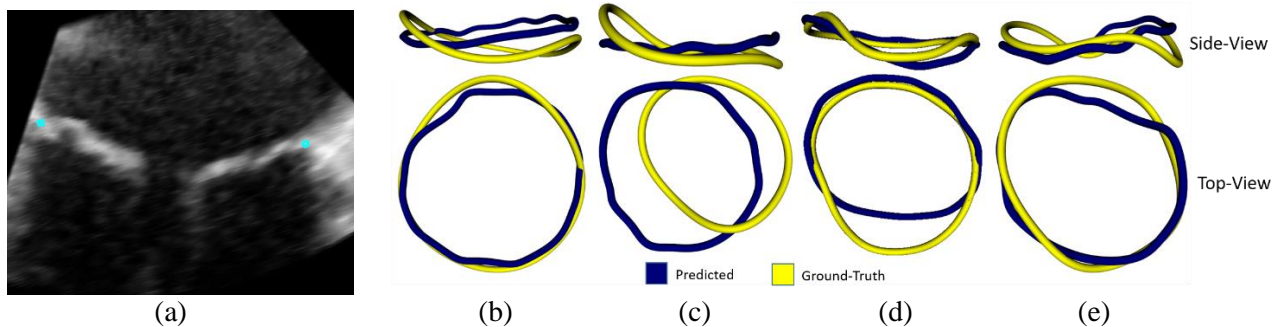


Figure 1: AP slice from TEE volume of mitral valve with annulus intersection shown in blue (a). Predicted (blue) and ground-truth (yellow) annuli for four test set cases with curve-to-curve errors of 6.1mm (b), 8.6mm (c), and 3.8mm (d) and 4.2mm (e).

Conclusions: We present a 3D CNN based model for segmenting the mitral annulus. Our method uses a novel approach in which a regression model predicts the ten smallest Fourier coefficients of the mitral annulus in each of the three axes. Currently the validation and test performance is similar to existing methods that operate in real-time, although we report a larger error than less-than-real-time methods. However, we believe this approach has the potential for greater accuracy, given the current disparity between training error and test error suggesting an over-fitting issue with our model at present.

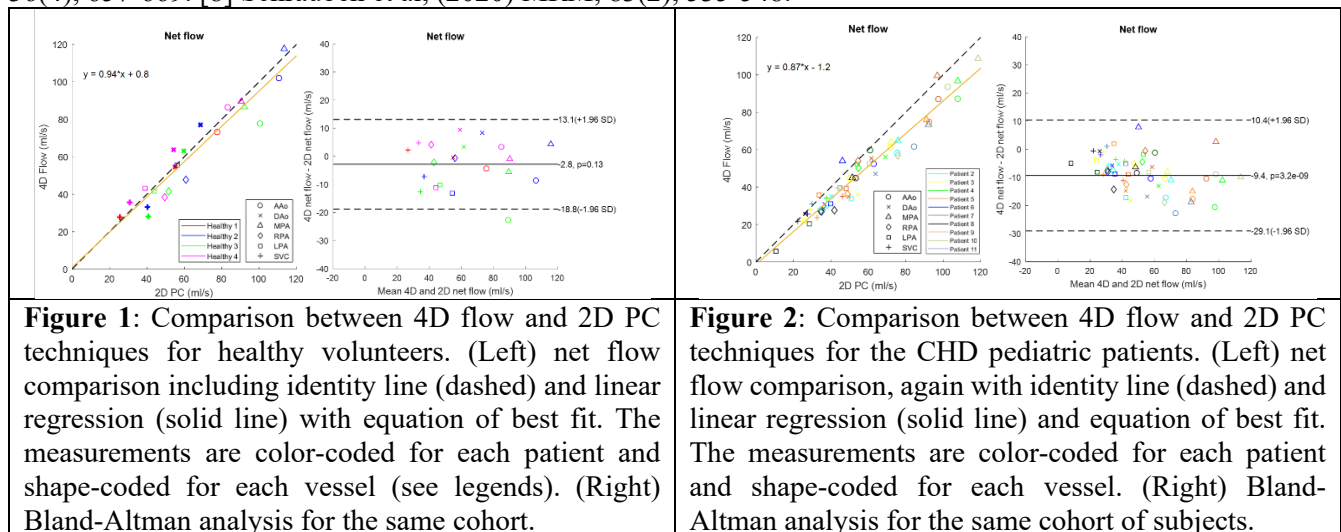
References: 1. Fabricius, A. M., *The Annals of Thoracic Surgery* 78, 575–578 (2004) 2. Li, F. P *et al.*, *Medical Physics* 42, 456–468 (dec 2014). 3. Andreassen, B. S. *et al.*, *IEEE Access* 10, 51472–51486 (2022).

Title: Accelerated 4D flow MRI in pediatric patients with congenital heart disease using an undersampled 3D radial acquisition, double golden angle sampling, and compressed sensing reconstruction

Authors: Fatemeh Rastegar Jooybari^{1,2}, Christopher Huynh², Sharon Portnoy², Jonathan Voutsas³, Diana Balmer-Minnes², Ankavipar Saprungruang⁴, Shi-Joon Yoo⁵, Christopher Z Lam⁴, and Christopher K Macgowan^{1,2}

¹Medical Biophysics, University of Toronto, Toronto, ON, Canada, ²Translational Medicine, Hospital for Sick Children, Toronto, ON, Canada, ³Queen's University, Kingston, ON, Canada, ⁴Department of Diagnostic Imaging, Hospital for Sick Children, Toronto, ON, Canada, ⁵Departments of Medical Imaging and Paediatrics, University of Toronto, Toronto, ON, Canada

Introduction: 4D flow MRI is a MRI technique provides a 3D vector field of blood flow velocities throughout the cardiac cycle.¹ The last decade has seen the development of techniques that have reduced its long scan time (more than 15 minutes) to approximately 5-10 minutes.^{2,3,4} Here we investigate a 5-minute 4D flow technique with undersampled 3D radial acquisition and quantify its accuracy in measuring net flow in healthy volunteers and pediatric patients with congenital heart disease. **Methods:** 11 pediatric CHD patients (12.1 ± 2.9 years, M:F=8:3) scanned on a 1.5T and 4 healthy volunteer (26.7 ± 1.9 years, M:F=3:1) scanned on 3T were recruited. 4D flow data were acquired using an internally developed 3D center-out radial trajectory with golden angle spoke ordering and 4-point flow encoding. A 5-minute free-breathing scan Images were reconstructed using compressed sensing with alternating direction method of multipliers (ADMM) solver⁵. For reference, 2D phase contrast (PC) was also performed in target vessels: ascending aorta (AAo), descending aorta (DAo), main/left/right pulmonary arteries (MPA/LPA/RPA), and superior vena cava (SVC). The spatial resolution for the 4D flow and 2D PC were 1.8 mm isotropic and 1.09-1.33 mm respectively. **Results:** Fig 1 (left panel) shows a comparison of net flow measured by radial 4D flow versus conventional 2D PC in healthy volunteers. Linear regression showed good-excellent agreement between the measurements from healthy subjects ($R^2 = 0.90$, slope = 0.94 ± 0.15). Fig 1 (right panel) shows the Bland-Altman comparison between 4D and 2D measurements, with a difference of 2.3 ± 8.2 ml/s ($p=0.13$). As shown in Fig 2, good correlation was also obtained between 4D vs. 2D net flows from CHD patients ($R^2 = 0.94$, slope = 0.87 ± 0.06). Net flows within a given vessel varied widely between CHD patients because of differences in age and pathology. Bland-Altman analysis shows a difference of 9.4 ± 10.1 ml/s ($p = 3.2e-9$) in the cohort of CHD patients. Previous studies that used respiratory gating or longer scan times have shown similar agreement between 2D and 4D flow measurements in healthy volunteers^{6,7,8}, and in infants with CHD using time-averaged volumetric flow imaging to keep scan times short (~ 3 minutes)⁸. **Conclusion:** The proposed 4D flow method can provide retrospective in-vivo 3D quantification and visualization in 5 minutes in technically challenging clinical population. Future work will evaluate the effect of respiratory motion correction, contrast agent and field strength on flow accuracy. **References:** [1] Markl et al, (2012). JMRI, 36(5), 1015-1036. [2] Pruitt et al, (2021). MRM, 85(3), 1222-1236. [3] Ma et al, (2020). Cardiothoracic Imaging, 2(6). [4] Cheng et al, (2016). JMRI, 43(6), 1355-1368. [5] Wahlberg et al, (2012). IFAC Proceedings Volumes, 45(16), 83-88. [6] Blanken et al, (2022). JMRI, 55(4), 1120-1130. [7] Jacobs et al, (2020). The international journal of cardiovascular imaging, 36(4), 657-669. [8] Schrauben et al, (2020) MRM, 83(2), 535-548.



Progressive Airway Wall Thinning and Loss of Total Airway Count after Three-Years in COPDPaulina V Wyszkievicz,^{1,2} Maksym Sharma,^{1,2} Vedanth Desaiogudar,^{1,2} David G McCormack,³ Miranda Kirby⁴ and Grace Parraga¹⁻³¹Robarts Research Institute, ²Department of Medical Biophysics, ³Division of Respiriology, Department of Medicine, Western University, London, ON, Canada, ⁴Department of Physics, Toronto Metropolitan University, Toronto, ON, Canada

INTRODUCTION: In patients with COPD, chest CT has previously revealed small airway abnormalities,¹ where disease onset and progression are believed to initiate.² The total number of CT-visible airways was previously observed to diminish with increasing disease severity³ and was associated with the number of terminal bronchioles in excised lung specimens measured using micro-CT.⁴ Airway wall thinning was also observed across disease severity,⁵ which was spatially related to missing airways.³ These cross-sectional observations generate hypotheses about the potential for longitudinal airway alterations in ex-smokers, especially those with normal pulmonary function. Based on these previous findings,³⁻⁶ we hypothesized that CT airway measurements would significantly worsen in ex-smokers with and without COPD after three-years, in the absence of pulmonary function worsening.

METHODS: Ninety ex-smokers with (n=50) and without (n=40) COPD provided written informed consent (NCT02279329) to CT, pulmonary function tests, exercise capacity, and quality of life questionnaires at baseline and three-year follow-up.⁷ CT images were analyzed using VIDAvision (VIDA Diagnostics Inc., Coralville, IA) to generate total airway count (TAC), as well as anatomically equivalent segmental, subsegmental and sub-subsegmental airway wall area (WA), lumen area (LA), wall area percent (WA%), and wall thickness percent (WT%). CT emphysema was quantified as the relative area of the lung with attenuation less than -950 Hounsfield units (RA₉₅₀). Paired-samples t-tests were used to evaluate differences between time points.

RESULTS: In 50 ex-smokers with COPD, TAC (baseline, follow-up mean±SD = 241±63, 217±52; p<.001), WA (67.2±1.5mm², 66.9±1.5mm²; p=.04), WA% (83.5±3.0%, 82.3±3.4%; p<.001), and WT% (18.0±0.7%, 17.7±0.8%; p<.001) were significantly decreased after three-years (2.6±0.6, range=1-4years), while RA₉₅₀ (9.2±8.8%, 12.5±9.7%; p<.001) and LA (13.3±2.7mm², 14.5±3.1mm²; p<.001) were significantly increased. In 40 ex-smokers without COPD, WA% (80.4±4.4%, 79.5±3.9%; p=.01) was significantly decreased, while RA₉₅₀ (1.5±1.4%, 2.0±1.5%; p=.02) and LA (16.1±4.0mm², 17.0±3.7mm²; p=.009) were significantly increased. Forced expiratory volume in 1-second (FEV₁) was not significantly different after three-years in ex-smokers with (69±23%, 68±26%; p=.4) or without (103±18%, 104±20%; p=.5) COPD.

CONCLUSIONS: Over a relatively short time period, CT airway wall thinning and luminal dilation were observed in both ex-smokers with and without COPD, whilst decreased total number of CT-visible airways was observed only in ex-smokers with COPD. To our knowledge, this is the first study to show TAC worsening over time in COPD and may suggest airway narrowing, obstruction, and/or obliteration. These longitudinal three-year findings in ex-smokers, in whom there were no significant changes in FEV₁, provide insights into mechanisms of COPD progression, whilst supporting previous cross-sectional evaluations^{3,5} in which diminished TAC and airway wall thinning were observed.

REFERENCES: ¹Nakano, Y. *AJRCCM* (2005); ²Hogg, J.C. *NEJM* (1968); ³Kirby, M. *AJRCCM* (2018); ⁴Kirby, M. *AJRCCM* (2020); ⁵Smith, B.M. *Thorax* (2014); ⁶Kirby, M. *ERJ* (2021); ⁷Kirby, M. *COPD* (2014).

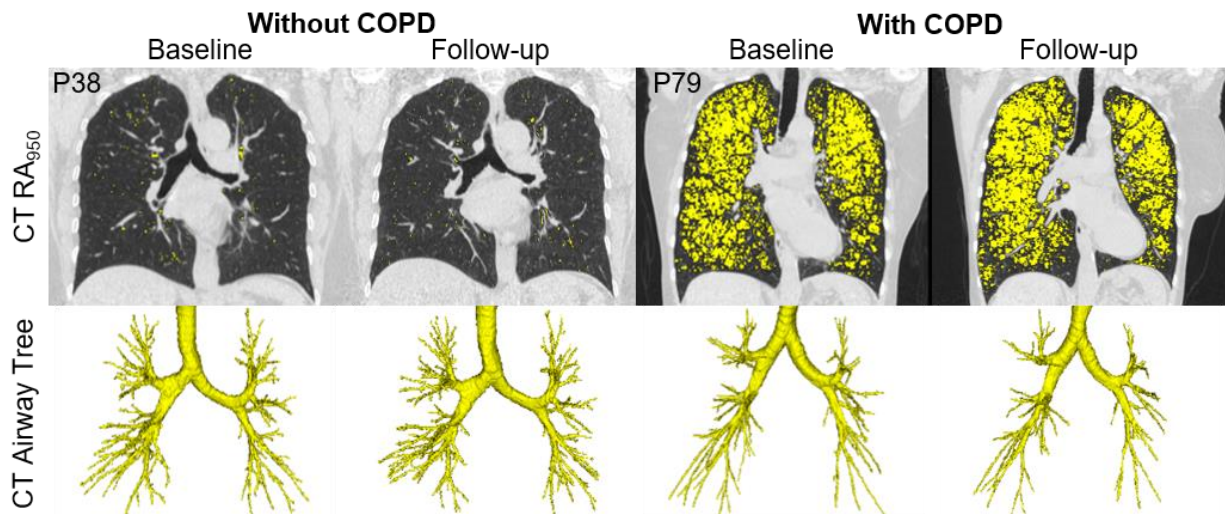


Figure 1. CT images with emphysema maps and segmented airway trees in two participants at baseline and follow-up. P38 is a 70 year old female ex-smoker without COPD, with a follow-up time=31 months, baseline/follow-up FEV₁=93/93 %_{pred}; RA₉₅₀=1/1 %; TAC=306/297. P79 is a 67 year old female ex-smoker with severe COPD, with follow-up time=26 months, baseline/follow-up FEV₁=37/33 %_{pred}; RA₉₅₀=33/37 %; TAC=206/174.

Novel COPD Classification/Staging Technique Using Lung CT Data and Neural Network

Halimah Alsurayhi¹, Abbas Samani^{1,2,3}

^{1,2} Department of Electrical and Computer Engineering, Western University, London, ON, Canada

² Biomedical Engineering School, Western University, London, ON, Canada

³ Departments of Medical Biophysics, Western University, London, ON, Canada

Introduction: Chronic Obstructive Lung Disease (COPD) is a progressive and prevalent lung disease which is associated with airflow obstruction due to inflamed airways and lung parenchyma. The Global Initiative for Chronic Obstructive Lung Disease (GOLD) utilises a combined assessment of COPD using three factors of lung function, symptoms, and exacerbation history to evaluate disease severity and prevent future risk through devising treatment tailored according to the three assessment factors [1]. Utilizing this combined assessment, an Eight COPD Staging System was designed in the COPDGene study [2]. In the Eight COPD Staging System, COPD subjects are classified into eight classes of: A, B, C1, C2, C3, D1, D2, and D3 to provide critical information necessary to guide therapy. Depending on the cause of the disease severity, different kinds of bronchodilators are used for treatment. For example, short-acting bronchodilator is recommended for class A with low symptoms, while a long-acting bronchodilator is required for high symptoms. Patients with high risk of lung function and/or exacerbation require combining two or three kinds of long-acting bronchodilator depending on the risk cause. In this study, we are developing a machine-learning based COPD classification/staging system using an alternative approach. In this approach, we use the patient's thoracic CT images instead of the data pertaining to lung function to assess COPD severity based on the high-resolution 8-stage system.

Methods: A neural network model for COPD classification/staging was developed based on the recent Eight COPD Staging scheme. The model was trained using features extracted from the lung CT data. Two types of features were extracted: lung air volume distribution features and COPD phenotype features. The lung air volume distribution features are 24 features which were extracted based on the air volume variation and distribution in the lung's inhalation and exhalation scans. COPD phenotypes consist of emphysema, air trapping, and functional small airway disease (fSAD). A total of 29 features, including the lung air features, phenotype features and the two features of the exacerbation frequency and symptom level were used. The neural network model was trained using 385 subjects from the NIH COPDGene study. The model was evaluated with StratifiedKfold cross validation to preserve the class distribution in the training and test sets with K =10. The mean of the 10 folds was obtained to present the model overall performance.

Results: The extracted lung air features and the phenotype features have high correlation with PFT measurements. Table 1 shows the correlation coefficients for some of the lung air features and the phenotype features. The model achieved high accuracy result of 0.88 to classify COPD subjects using the novel eight staging scheme. Precision, recall, and F1 score were also used to evaluate the model. A value of 0.9, 0.88, 0.88 were achieved for model precision, recall, and F1 score. This implies effectiveness of the extracted features to build a reliable model for COPD classification/staging.

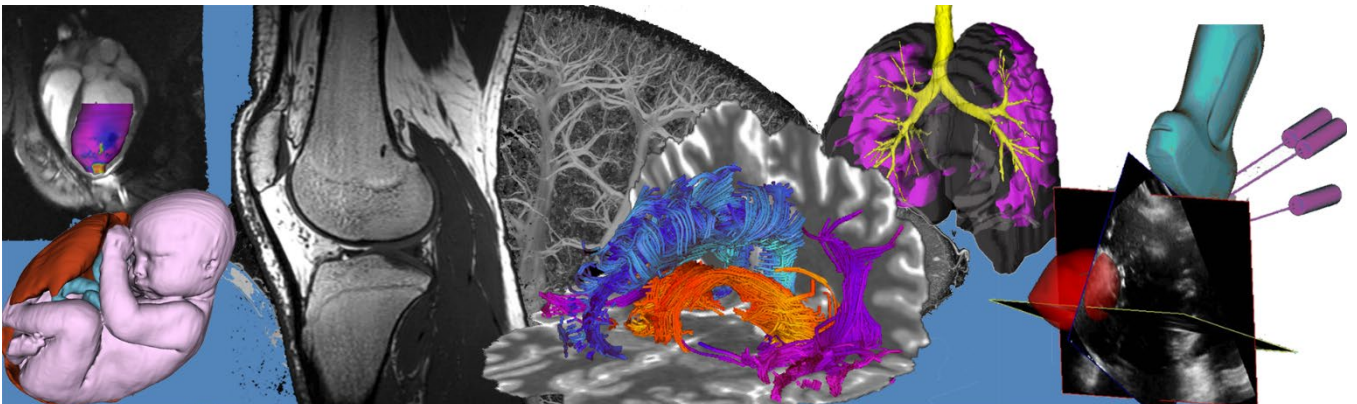
Table 1: Correlation coefficients between the extracted features and the PFT features

Features	Exhalation Air Features				Inhalation Air Features				Phenotype Features		
	V75exh	V70exh	V65exh	MVexh	Vinh	V95inh	V90inh	V85inh	Emph	AirTrap	fSAD
FEV1/FVC	0.81	0.83	0.83	0.81	0.65	0.58	0.64	0.59	0.68	0.70	0.59
FEV1	0.72	0.72	0.71	0.72	0.62	0.54	0.56	0.48	0.62	0.65	0.52

Conclusions: The developed COPD classification/staging system has demonstrated high accuracy in assessing COPD severity using the novel COPD staging scheme, providing highly valuable diagnostic information useful for treatment planning. This indicates a clinical potential for the proposed classification/staging system to be an effective image-based COPD diagnosis technique.

References: [1] "Global Initiative for Chronic Obstructive Lung Disease Global Initiative for Chronic Obstructive Lung Disease pocket guide to copd diagnosis, management, and prevention A Guide for Health Care Professionals," 2017. [2] M. L. K. Han *et al.*, "GOLD 2011 disease severity classification in COPDGene: A prospective cohort study," *Lancet Respir Med*, vol. 1, no. 1, pp. 43–50, Mar. 2013

Pitch/Poster Session 7: Cancer Imaging Abstracts



Radiomics to predict local progression of non-spine bone metastases following stereotactic radiotherapyLauren M. Zelko^{1,2}, Karen Eddy², Jonatan Snir³, Timothy Nguyen³, & Sarah A. Mattonen^{1,2,3}¹*Department of Medical Biophysics, Western University, London, Ontario, Canada*²*Baines Imaging Research Laboratory, London Regional Cancer Program, London, Ontario, Canada*³*Department of Oncology, Western University, London, Ontario, Canada*

Introduction: Stereotactic body radiotherapy (SBRT) is an emerging treatment for patients diagnosed with non-spine bone metastases [1]. Studies have shown that patients benefit from SBRT due to improvements in local control and overall survival, with limited toxicities. However, up to 18% of patients will still develop local progression following treatment [2]. Limited understanding of clinical predictors of risk of progression leads us to believe that the addition of radiomic biomarkers may provide insight into the tumour microenvironment, and thus a deeper understanding of the pathophysiology of different tumours [1]. This study aims to create a machine learning model integrating clinical, dose, and radiomic features to predict which patients will experience local progression following SBRT.

Methods: We analyzed 130 patients diagnosed with 179 non-spine bone metastases treated with SBRT at the London Regional Cancer Program between 2018 and 2021. The gross tumour volumes (GTV) and planning target volumes (PTV) were contoured on the planning computed tomography (CT) scan. The penumbra region was defined as the difference between the GTV and PTV and was created for each lesion. From these regions of interest, 297 radiomic features were extracted using PyRadiomics [3]. The dataset was randomly split on a patient level into independent training (n = 119) and testing (n = 60) sets. Clinical and dose features were collected, and univariate analysis was completed to determine individual association with local progression in the training dataset. Highly correlated features were removed to prevent overfitting and a support vector machine (SVM) model was created to predict local progression. The radiomic features were selected using random forest feature selection then combined with the clinical and dose features in a SVM model. Models were locked and evaluated on the testing dataset. The area under the receiver operator curve (AUC) was calculated to assess the performance of both the clinical and radiomic models and DeLong analysis was used to evaluate differences between the models.

Results: A total of 28 lesions developed local recurrence (15.5%). Seven clinical features, including dose metrics, tumour volume, and age, were included in the clinical model. Radiomic feature selection yielded eight features from the GTV (one shape and two texture), PTV (two texture) and penumbra region (one shape, one first-order and one texture). The clinical SVM model achieved an AUC of 0.61 [95% CI: 0.47-0.74] in the testing dataset. The combined SVM model performance was slightly improved with an AUC of 0.74 [95% CI: 0.61-0.87] in the testing dataset, however this was not statistically significant over the clinical model (p = 0.36).

Conclusions: This preliminary study demonstrates the potential utility for a radiomics-based machine learning model for the prediction of local progression in non-spine bone metastases following SBRT. The combined radiomics and clinical model demonstrated an increase in performance when compared to clinical and dose features alone. Ongoing work includes investigating additional feature selection and classifier algorithms. These models may aid clinicians in identifying patients at a higher risk of local failure to provide more personalized treatment.

References: [1] De la Pinta, C., *Med Oncol*, 2020. 37(12): p. 119. [2] Ito, K., et al., *Radiat Oncol*, 2022. 17(1): p. 156. [3] van Griethuysen, J.J.M., *Cancer Res*, 2017. 77(21): p. e104-e107.

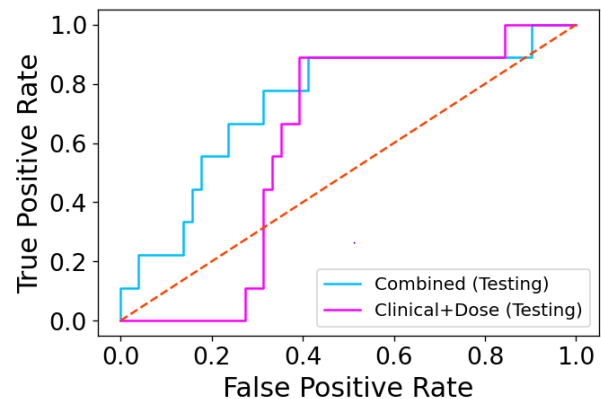


Figure 1: Receiver operating characteristic curves for evaluation of the support vector machine models on the testing dataset (n=60)

Predicting the need for a replan in oropharyngeal cancer: A radiomic, clinical, and dosimetric modelTricia Chinnery¹, Pencilla Lang², Anthony Nichols³, & Sarah Mattonen^{1,2}¹Departments of Medical Biophysics, ²Oncology, ³Otolaryngology, Western University, London, ON

Introduction: Patients with oropharyngeal cancer (OPC) treated with chemoradiation experience weight loss, edema, and tumour shrinkage, which can alter the prescribed radiation treatment.¹ Treatment replanning ensures patients do not receive excessive doses to normal tissue or underdosage to the gross disease. Approximately 25% of patients will require a replan. Currently, there are limited prognostic factors to determine which patients will require a replan, and the process is both time and resource intensive.¹ It takes one to two weeks to acquire a new treatment plan, and during this time, overtreatment of normal tissues could lead to increased toxicities. There remains an unmet need for predictive models to assist in identifying patients who could benefit from the knowledge of a replan prior to treatment. Radiomics aims to extract quantitative image features that can be used to develop predictive models.² The objective of this study is to develop and evaluate a CT-based radiomic model, integrating clinical and dosimetric information, to predict the need for a replan prior to treatment.

Methods: A dataset of patients (n=315) with OPC treated with chemoradiation was used for this study. A total of 78 patients (25%) required a replan during treatment. The dataset was split into independent training (n=220) and testing (n=95) datasets. Tumour volumes and organs at risk (OARs) were contoured on planning CT images prior to treatment (Figure 1). PyRadiomics was used to compute radiomic image features (n=1218) on the original, wavelet, and Laplacian of Gaussian filtered images from each of the primary tumour, nodal volumes, and parotid glands.³ Nine clinical features and nine dosimetric features extracted from the OARs were collected and those found to be significantly ($p < 0.05$) associated with the need for a replan in the training dataset were developed into a baseline logistic regression model. To determine the added value of radiomics, random forest feature selection was applied to select the optimal radiomic features to predict replanning. Logistic regression, Naïve Bayes, support vector machine, and random forest classifiers were built using the non-correlated selected radiomic, clinical, and dosimetric features on the training dataset and performance was assessed in the testing dataset. The area under the curve (AUC) was used to assess the prognostic value.

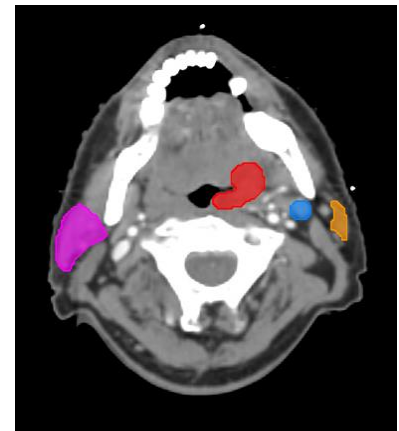


Figure 1: Primary tumour (red), nodal volume (blue), and right (pink) and left (orange) parotid glands contoured on the pre-treatment planning CT.

Results: Smoking status, nodal stage, tumour subsite, and a larynx dose metric were found to be significantly associated with the need for a replan in the training dataset and incorporated into the baseline model, as well as into the combined radiomic, clinical, and dosimetric models. Through feature selection, eight predictive radiomic features were selected (three nodal volume, one primary tumour, and four parotid gland). The baseline model comprised of clinical and dosimetric features alone achieved an AUC of 0.66 [95% CI: 0.51-0.79] in the testing dataset. The Naïve Bayes was the top-performing radiomics model and achieved an AUC of 0.79 [95% CI: 0.72-0.86] in the training dataset and an AUC of 0.80 [95% CI: 0.69-0.90] in the testing dataset, which significantly outperformed the baseline model ($p = 0.005$, testing dataset) (Figure 2).

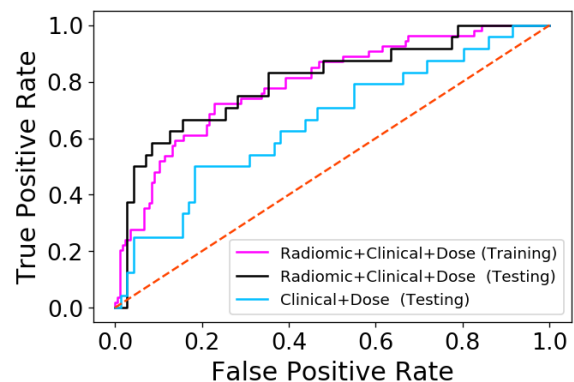


Figure 2: AUCs from evaluation of the Naïve Bayes and baseline models.

Conclusions: To the best of our knowledge, this was the first study to use radiomics from the primary tumor, nodal volumes, and parotid glands for the prediction of replanning for patients with OPC. Radiomic features augmented clinical and dosimetric features for predicting the need for a replan in our testing dataset. Once validated, this model has the potential to assist physicians identifying patients that may benefit from a replan, allowing for better resource allocation, patient management, and reduced toxicities.

References: [1] E. Brown et al., *Radiother. Oncol.* 116, 57–63, 2015. [2] P. Lambin et al., *Eur. J. Cancer* 48, 441–446, 2012. [3] J. J. M. Van Griethuysen et al., *Cancer Res.* 77, e104–e107, 2017.

Title: Prostate Stereotactic Body Radiation Therapy – Using 18 Fluorine Prostate Specific Membrane Antigen-1007 Positron Emission Tomography and Multiparametric Magnetic Resonance Imaging to escalate the dose to Dominant Intraprostatic Lesions – ARGOS-CLIMBER: A phase I/II clinical trial.

Authors: Aneesh Dhar¹, Hatim Fakir¹, Andrew Loblaw², David Laidley¹, Wei Liu³, Lucas C. Mendez¹, Melanie Davidson², Zahra Kassam⁴, Ting-Yim Lee⁵, Aaron Ward⁵, Jonathan Thiessen⁵, Matt Mulligan¹, Linada Berryhill¹, Anders Celinski¹, and Glenn Bauman^{1,5}.

Affiliations: ¹ London Health Sciences Centre, London, ON; ² Sunnybrook Health Sciences Centre, Toronto, ON; ³ BC Cancer Agency, Vancouver, BC; ⁴ St. Joseph's Hospital, London, ON; ⁵ Lawson Health Research Institute, London, ON.

Introduction: Stereotactic body radiation therapy (SBRT) is a high-precision radiation technique that delivers high-dose in a few fractions. Despite the high effectiveness of SBRT for prostate cancer, recurrence is still a significant clinical issue. Most recurrences after radiation originate from larger discrete foci of cancer within the prostate, i.e., the dominant intraprostatic lesions (DILs). Prostate multiparametric Magnetic Resonance Imaging (mpMRI) and 18 Fluorine Prostate Specific Membrane Antigen-1007 (18F PSMA-1007) Positron Emission Tomography (PET) can identify the DILs and offer opportunities for targeted dose escalation.

Methods: ARGOS-CLIMBER is a prospective phase I/II trial enrolling 50 patients in London, Ontario and Toronto, Ontario. Patients with unfavourable intermediate or high-risk disease were included. A hybrid PET/MR imager was used to acquire co-registered 18F PSMA-1007 PET and mpMRI images prior to SBRT. All patients received intra-prostatic fiducial markers and their PET and MR image sets were rigidly fused to their Computed Tomography (CT) Simulation scan. All DILs were delineated on mpMRI and PET images: on mpMRI, DILs were delineated in areas with low T2 signal and restricted diffusion on apparent diffusion coefficient (ADC) maps, and included all lesions noted as scoring 3, 4, or 5 on the Prostate Image Reporting And Data System (PIRADS v2.1); on 18F PSMA-1007 PET, DILs were delineated automatically by using a Standardized Uptake Value (SUV) threshold of 20-40% of the maximum SUV in the prostate, then manually editing this volume to the anatomical contour of the DIL on mpMRI or CT. Planning target doses were as follows: prostate (35Gy/5), elective pelvic lymph nodes and seminal vesicles (25Gy/5), imaging positive lymph nodes (35Gy/5) and DILs (40-50Gy/5); in all cases, organ at risk (OAR) dose constraints took precedence. Patients were treated every other day with cone beam CT guidance and 6-18 months of adjuvant androgen deprivation. Primary outcomes are acute (6 week) and chronic (6 month) genitourinary (GU) and gastrointestinal (GI) toxicity. Secondary outcomes include quality of life metrics and cancer control outcomes including biopsy clearance at 2 years. PET, mpMRI and biologic biomarkers at 6 months and 2 years post treatment are exploratory endpoints.

Results: As of January 2023, 36 MR lesions and 50 PET lesions were detected among the first 18 patients treated, with a median (range) of 2 (1 – 5) MR lesions and 2 (1 – 7) PET lesions per patient. The median (IQR) size of the MR and PET lesions was 11.5 mm (9 – 19 mm) and 10 mm (7 – 15 mm). In SBRT planning, the median (IQR) volume of the DILs delineated using mpMRI was 2.4 mL (0.8 – 13.4 mL), the median (IQR) volume of the DILs delineated using 18F PSMA-1007 PET was 2.9 mL (1.8 – 10.6 mL), and the median (IQR) composite PET/MR volume was 3 mL (1.25 – 7.3 mL). The median (IQR) maximum dose the composite DIL volume received was 46.9 Gy (45.5 – 48.0 Gy), and the median (IQR) dose received by 90% of the composite DIL volume was 43.8 Gy (41.7 – 46.0 Gy). No patients thus far have experienced acute grade 3+ GU or GI toxicity.

Conclusions: Dose escalation to multi-modality imaging defined DILs on ARGOS/CLIMBER has been feasible with acceptable acute toxicity. With 34/50 men enrolled, accrual completion by Q2 2023 is anticipated with the 6-month primary endpoint of GI/GU toxicity available by Q4 2023.

Keywords: phase I/II clinical trial, 18F PSMA-1007 PET, multiparametric MRI, dominant intraprostatic lesions, prostate cancer, stereotactic body radiation therapy

Quantitative nuclear grading to improve risk stratification for patients with noninvasive bladder cancer

Katherine Lindale¹⁻³, Ava Slotman^{2,3}, Minqi Xu², Céline Hardy^{2,3}, Lina Chen², Chelsea L. Jackson^{2,3}, D. Robert Siemens^{6,7}, Robert J. Gooding^{3,4}, Amber L. Simpson^{5,6,8}, David M. Berman^{2,3}

¹ Translational Medicine Graduate Program, Queen's University, Kingston, Canada

² Department of Pathology and Molecular Medicine, Queen's University, Kingston, Canada.

³ Queen's Cancer Research Institute, Kingston, ON, Canada.

⁴ Department of Physics, Engineering Physics, and Astronomy, Queen's University, Kingston, Canada

⁵ School of Computing, Queen's University, Kingston, Ontario, Canada

⁶ Department of Biomedical and Molecular Sciences, Queen's University, Kingston, ON, Canada.

⁷ Department of Urology, Queen's University, Kingston, ON, Canada.

⁸ Centre for Health Innovation, Queen's University, Kingston, ON, Canada.

Introduction: Histopathologic grading in non-muscle invasive bladder cancer (NMIBC) aims to predict how quickly the cancer will grow and spread, guiding disease management through its role in risk scoring. However, the qualitative nature of the current NMIBC grading system limits the ability to optimize its prognostic value (PMIDs: 28457661, 19576682), compromising the potential for data-driven care decision making. Using AI-based image analysis, we have quantified grading features such as the size, shape, and texture of tumour nuclei as well as number of cells undergoing division. We hypothesize that these quantified nuclear features (QNFs) add significant prognostic value during the NMIBC grading and risk stratification process.

Methods: Small (1.0 mm diameter) histopathology images from resected bladder tumours and clinical event timelines were obtained for 163 patients with stage Ta NMIBC, diagnosed and treated at Kingston Health Sciences Centre (KHSC). Over the study period with median follow-up time of 5.9 years, 51.5% of patients experienced a recurrence. Visiopharm image analysis software was used to extract 19 grade-based QNFs from histological images. Cox Proportional Hazards (CPH) and Random Survival Forest (RSF) models are being constructed to determine the added value of these QNFs compared to the standard American Urological Association (AUA) risk scoring algorithm (PMID: 27317986) for the outcome of time to recurrence. Model performance is evaluated using concordance index (C-index) with 5-fold cross-validation on the training set and a holdout test set.

Preliminary and Anticipated Results: Significant likelihood ratio test ($p < 0.05$) between training models indicates added value of quantified histological features to AUA risk score. QNFs mitotic index (cells undergoing division), mean lesser diameter (size, shape) and mean variance HEM (texture) carried the most prognostic value. Upon validation, the CPH model constructed using these QNFs achieved a C-index of 0.68 (CI: 0.51-0.81) comparing to a C-index of 0.63 (CI: 0.46-0.78) using AUA risk score alone. RSF model results will also determine added value of QNFs to standard risk scoring.

Conclusions: QNFs including size, shape, texture, and mitotic index add value and nuance to the standard AUA risk-scoring procedure. These prognostic models will lay the groundwork for proper allocation of treatment and monitoring needed for each individual's level of disease risk, while mitigating the current economic and resource burden on patient quality of life and the healthcare system.

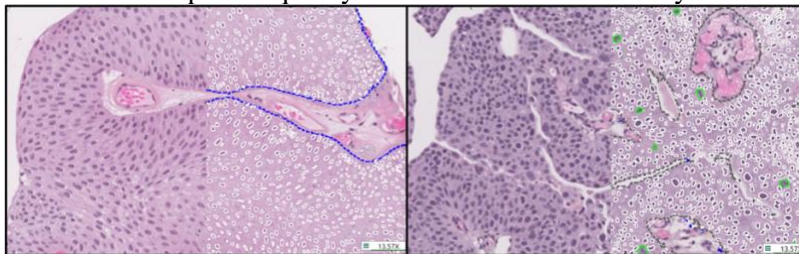


Figure 1. Histological images of stage Ta NMIBC, low-grade (left) and high-grade (right) with overlays of annotations for tumour (blue, grey), nuclei (white), mitotic figures (green).

Prediction Risk of Breast Cancer Development Using Breast Bilateral Asymmetry Analysis within a Machine Learning Framework

Xi Feng¹, Abbas Samani^{1,2,3,4}

¹Department of Electrical and Computer Engineering, University of Western Ontario, London, ON, Canada

²School of Biomedical Engineering, University of Western Ontario, London, ON, Canada

³Department of Medical Biophysics, University of Western Ontario, London, ON, Canada

⁴Imaging Research Laboratories, Robarts Research Institute, London, Ontario, Canada

Introduction: Breast cancer has become the first most prevalent cause of death among women worldwide in 2020, surpassing lung cancer. Significant evidence is available in the literature that women with significantly bilateral asymmetric breasts are more prone to developing breast cancer in their future life than women with normal bilateral symmetry [1]. This has motivated this study of developing a machine learning (ML) classifier capable of predicting the risk of developing breast cancer by analysis of the breast bilateral asymmetry features in MRI images of the breast.

Methods: In this study, a breast T1 MRI dataset pertaining to a longitudinal study, which includes a total of 55 patients with significant bilateral asymmetry, is used in this investigation. The scan intervals were ~3 years on average, with all negative outcomes in first scan and negative/positive (5/50) in the second scan. The number of patients in this study is too low while there is substantial data imbalance between cancer negative (healthy) and positive (confirmed-cancer), rendering the dataset insufficient for developing a ML based classifier. As such, we resorted to physics-based data augmentation using Finite Element simulation where we developed a novel technique based on breast biomechanical modeling. In this technique, we applied mechanically plausible deformation to generate new breast scans pertaining to 45 negative and 109 cases. Image features of the augmented data were extracted using the pyradiomics package (<https://pypi.org/project/pyradiomics>) to evaluate symmetry of shape, image intensity and texture by comparing the Mutual Information of each feature in the two breasts. This was followed by a data clustering technique using the k-means method in conjunction with the Silhouette score. For further validation, a 9-fold cross-validation method was used where the sum of the 50 positive cases and 159 negative cases were randomly divided into 10 exclusive subgroups before using 9 subgroups for training and the remaining subgroup for testing. Furthermore, to verify whether the amount of augmented data is sufficient to train a robust model, we generated an additional 16 cases using the same augmentation method for training a slightly larger dataset. To check convergence, the two datasets were trained using the same process and their clustering results were compared.

Results: The Silhouette score and Elbow Criterion were applied to choose the optimal clustering number. Since our classifier follows an unsupervised learning approach where labels cannot be verified, we considered the associated true negative (TN), true positive (TP), and area under the curve (AUC) to validate the proposed method's effectiveness. The proposed classification technique demonstrates a reasonably high AUC = 0.83 for true-positive rate. The data amount convergence assessment whereby 16 additional breast cases were considered, a difference of only 2% was observed which indicates reasonably sufficient data.

Conclusions: We proposed an end-to-end framework for assessing women's risk of developing breast cancer by analyzing features of their breast bilateral MRI images pertaining to bilateral asymmetry. To address the scarcity of data of breast longitudinal studies, we developed a novel data augmentation technique which provided realistic additional data using a high-fidelity breast biomechanical model. Results indicate that the predictability of the developed is reasonably high as it achieved an AUC of true-positive rate of 0.83. It is anticipated that significant improvement can be achieved through using a dataset of a longitudinal study with a larger number of participants.

Key words: MRI, Bilateral Asymmetry, Breast Cancer, Finite Element Analysis

[1] Kayar R. Cilengiroglu OV: breast volume asymmetry value, ratio, and cancer risk. Breast Cancer: Basic and Clinical Research 2015; 2015: 87–92.

Radiomics-based Approach to Classify Benign and Malignant Solid Renal Masses on MRIRohini Gaikar¹Azar Azad²Nicola Schieda³Eranga Ukwatta¹rgaikar@uoguelph.caazar@aivali.orgnschieda@toh.on.caeukwatta@uoguelph.ca¹School of Engineering, University of Guelph, Guelph, Ontario, Canada; ²A.I. Vali Inc, Toronto, Ontario, Canada; ³Department of Radiology, University of Ottawa, Ottawa, Ontario, Canada.

Introduction: Although computed tomography (CT) is commonly used for imaging solid renal masses (SRMs) in clinical practice, CT is limited in its utility to differentiate benign and malignant SRMs. Due to superior soft tissue contrast in magnetic resonance imaging (MRI), there is a potential to better classify SRMs as benign or malignant. To this end, we developed and validated a machine learning (ML) model using radiomic features to differentiate benign from malignant SRMs.

Methods: In this study, the dataset consisted of 108 patients with histologically confirmed kidney cancers. The malignant cases of SRMs were renal cell carcinoma (RCC) and its subtypes. The benign SRMs were oncocytomas and fat poor renal angiomyolipoma (fpAML). The SRMs were annotated by a fellowship-trained radiologist on axial slices of T2W MRI images. The training cohort (n=86) and test cohort (n=22) were stratified by benign and malignant labels. We tested ML based radiomics feature classification and deep learning-based image classification models for this problem. The radiomics features extracted from SRM masks on T2W images used to train the ML prediction model. Using Pyradiomics library, we extracted 120 radiomic features based on voxel intensities, 3D shapes of original images. The synthetically minority oversampling technique (SMOTE) used to oversample the minority class to mitigate the class imbalance. We selected 22 out of 120 features using dimensionality-reduction principal component analysis (PCA). With the selected feature set, we trained a support vector machine (SVM) with radial basis function (RBF) kernel to classify SRMs as benign and malignant. We evaluated random forest and XG-Boost ML classification models. In the deep learning approach, we designed a convolutional neural network (CNN) to classify SRM as benign or malignant on T2W images. We used same cohort of train and test cases of T2W images. The SRM region of interest (ROI) of size 64 X 64 were prepared from the axial slices to train the CNN model. The CNN model used 2 consecutive convolutional layers of filters 16 and 64 respectively. The flattened vector at the last convolutional layer was input to a hidden layer of 32 neurons followed by one output neuron giving out the classification result. The model was trained with ADAM optimizer and customized focal loss function to minimize false predictions because of imbalanced dataset. The output neuron used sigmoidal activation, where the probability of >0.5 was identified as malignant and the rest was identified as benign. To generate the patient level prediction, we used majority voting strategy SRM classification. The ML and CNN models were evaluated based on accuracy (ACC), precision (PR), recall (RE), specificity (Spec), and area under the curve (AUC) in SRM classification.

Results: The results are summarized in Table 1, where all values are reported as percentage. The proposed SVM-RBF outperformed alternatives (random forest, XG-Boost, and CNN) by generating highest accuracy and AUC values as 85.00% and 75.41%. Our proposed ML model showed similar performances on a limited dataset as compared to previous radiomics and ML algorithms on MRI images.² Oncocytomas decreased the performance of the model because their intensity is like RCC in T2W images. Therefore, it will be exciting to include other pulse sequences of MRI into the prediction model.

Table 1: Comparison of ML and CNN models' results.

Method	ACC	PR	RE	Spec	AUC
SVM-RBF	85.00	86.67	92.85	66.67	75.41
Random Forest	84.61	84.61	78.57	66.67	72.71
XG-Boost	65.00	81.81	64.28	66.67	69.05
CNN	68.18	64.2	81.81	54.54	62.71

Conclusions: The proposed ML model SVC-RBF correctly predicted RCC as malignant SRM on T2W images. In clinical perspective radiomics feature classification model may help in preoperative analysis of SRM to reduce the frequency of benign SRM biopsies or surgical resection.

References:[1] Lin, F. R., Niparko, J. K. and Ferrucci, and L., "Solid Renal Masses: What the Numbers Tell Us," Bone **23**(1),1–7 (2014).

[2] Ngnitewe, R., Stoeckl, E. M., Lubner, M. G., Smith, D., Mao, L., Shapiro, D. D., Abel, E. J. and Wentland, A. L., "Differentiation of benign from malignant solid renal lesions with MRI - based radiomics and machine learning," Abdom. Radiol. **47**(8), 2896–2904 (2022).

Automatic Classification of Endometrial Pathology Slides

Daniel Sherman^{1,2}, Ritesh Ahlawat^{1,2}, Alif Munim^{1,2}, Mara Sobel^{3,4}, Dafna Sussman^{1,2,4}

1. Department of Electrical, Computer, and Biomedical Engineering, Toronto Metropolitan University (formerly Ryerson University), Faculty of Engineering and Architecture Sciences, Toronto, Ontario, Canada; 2. Institute for Biomedical Engineering, Science, and Technology (iBEST), Toronto Metropolitan University (formerly Ryerson University) and St. Michael's Hospital, Toronto, Ontario Canada; 3. Department of Obstetrics and Gynaecology, Mt. Sinai Hospital, Toronto, Ontario, Canada; 4. Department of Obstetrics and Gynecology, Faculty of Medicine, University of Toronto, Toronto, Ontario, Canada.

INTRODUCTION: Endometrial cancer is the 6th most commonly diagnosed cancer in women, with incidence cases rising in recent years [1]. Diagnosing the disease early is critical to maximizing survival rates. Endometrial cancer is typically diagnosed after symptoms arise, making rapid diagnosis important. Furthermore, clinicians spend a majority of their time examining benign tissue, delaying the treatment of patients who have endometrial cancer. An automated tool that can rapidly identify which cases are benign can drastically speed up initial screenings for clinicians, leaving them valuable time to spend identifying cases that may be neoplastic. Our aim is to determine if machine learning could provide a high classification accuracy on a clinical dataset of endometrial cancer whole slide images.

METHODS: The dataset used for this study consists of 1200 digitized endometrial biopsy slides with image-level labels only (404 benign, 380 hyperplastic, 416 neoplastic). They were labeled by clinicians at Mt. Sinai Hospital (Toronto, ON). The images were stained with H&E, fixed in formalin, and after scanning, provided in SVS format with varying dimensions. After reshaping to a consistent image size to minimize distortion, the WSIs (whole slide images) were 51,968 pixels by 37,632 pixels. The images were far too large to use for computer aided diagnosis algorithms. The computational burden of the images was greatly reduced while preserving the low-level features important for classification. Convolutional neural networks aided in reducing the computational burden of the large WSIs. The WSIs were preprocessed and used in an in-house developed machine learning algorithm to classify the compressed representation of the WSI. Following this, attention mechanisms were used to achieve a high accuracy when diagnosing endometrial cancer WSIs as benign, hyperplastic, or neoplastic.

RESULTS: Classification was performed on 10% of the available data (randomly selected) ensuring the class distributions of the subsample and the original dataset were the same. The maximum classification accuracy was found to be 96.39% on the validation set after training for 25 epochs (confusion matrix seen on right).

	Benign	Hyperplasia	Neoplasia
Benign	24	0	4
Hyperplasia	0	26	0
Neoplasia	2	0	27

CONCLUSION: We present an automatic classification algorithm for diagnosing endometrial cancer from WSI with a high and clinically-competitive classification accuracy of 96.39%. The algorithm will aid clinicians by speeding up their workflow allowing them to diagnose endometrial cancer faster. In the future, we aim to add functionality to classify endometrial cancer subclassifications, develop an intuitive user interface for pathologists, and perform a pilot study to test the algorithm on additional data distributions.

ACKNOWLEDGEMENTS

Computations were performed on the SOSCIP Consortium's advanced research computing platforms. SOSCIP is funded by FedDev Ontario, and SOSCIP's Consortium members.

REFERENCES:

- [1] M. Koskas, "Cancer of the corpus uteri: 2021 update - Koskas - 2021 - International Journal of Gynecology & Obstetrics - Wiley Online Library." <https://obgyn.onlinelibrary.wiley.com/doi/10.1002/ijgo.13866> (accessed Jun. 06, 2022).

Horizontal Federated Learning in Kidney Cancer Disease Classification on Histopathology ImagesRohini Gaikar¹Timothy Wong²Kristina Stepanic²Azar Azad²Eranga Ukwatta¹rgaikar@uoguelph.catimothy@aivali.orgkristina@aivali.orgazar@aivali.orgeukwatta@uoguelph.ca¹School of Engineering, University of Guelph, Guelph, ON, Canada; ²A.I. VALI Inc, Toronto, ON, Canada

Introduction: Whole slide images (WSI) of digital histopathology are used in definitive diagnosis of kidney cancer. Although AI-based methods on WSI will be ideal for kidney cancer classification, there are limited availability of WSI in a single center. Horizontal federated learning (HFL)¹ could be a solution to the insufficient data by training and validation through multicenter datasets without explicitly sharing the data across the centers. Here, we present HFL-based method for kidney cancer classification on multi-center kidney WSI.

Methods: This study used urinary tract WSI files from ‘The Cancer Genome Atlas (TCGA)’ repository.² We used data from 4 medical centers (i.e., H0, H1, H2 and H3), where H0, H2, and H3 for training data and H1 was used as testing data. The WSI kidney cancer images

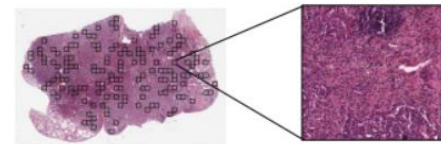
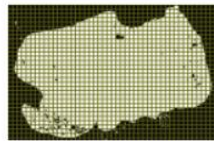


Figure 1: Patches of 224 X 224 extracted from WSI kidney image

were papillary cell carcinoma (Class 0), clear cell carcinoma (Class 1), and chromophobe carcinoma (Class 2). The patches of 224X224 were extracted in 20x magnified WSI as shown in Figure 1.

An architecturally similar convolutional neural network (CNN) model designed for local models H0, H2, and H3 for kidney cancer classification. It used 3 convolutional layers of filters 16,32, 64 with 3x3 kernel and ReLU activation. It followed by 3 dense layers of size 128,128,3. Those local models jointly trained a global model under the coordination of the central server. The global model got trained weights in every iteration from each local models. The global model used federated weighted averaging algorithm to finalize the weights in each training iteration. Those averaged training weights in every iteration were broadcasted back to each local model. This process was repeated for several iterations to improve the global model through the training weights received from local models. In this way, without accessing other medical center datasets each local model received modified training weights through global model. We implemented HFL using Tensorflow Federated Learning library. The local models used Adam optimizer and the global model used stochastic gradient descent (SGD) optimizer. The performances of HFL trained models and individually trained local models were evaluated on similar H1 test data on precision (PR), recall (RE), accuracy (ACC), and ROC-AUC curves in classification of kidney cancers.

Results: The comparison of results in individual and HFL training are summarized in Table 1. The HFL model outperformed individually trained local models by generating the AUC of 79.72% and accuracy of 61.54%. The ROC curves of each class in HFL training are shown in Figure 2. The poor recall and precision in class 0 and 2 respectively was due to the imbalanced dataset in training.

Table 1: Comparison of results

Training Method	ACC	AUC	Class 0		Class 1		Class 2	
			PR	RE	PR	RE	PR	RE
Local-H0	47.59	66.65	8.09	10.20	73.12	52.09	28.83	59.04
Local-H1	57.06	75.57	100	4.10	79.00	66.20	25.20	64.16
Local-H2	46.77	66.88	25.14	89.40	80.45	44.00	27.09	23.21
HFL	61.54	79.72	73.73	35.50	81.63	62.00	32.60	81.23

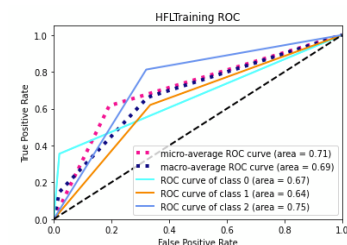


Figure 2: ROC plots in HFL

Conclusion: This study showed that HFL outperformed the local models without sharing actual dataset. This could be a next generation of AI medical solutions for multicenter datasets without compromising the privacy and data protection. In future studies, we can improve HFL model performance by increasing the multi-center involvement.

Acknowledgement: This work was implemented in the Vector Institute of Artificial Intelligence’s summer bootcamp programme “Privacy Enhancing Technologies (PETs)” in August 2022.

[1] Liu, D., Bai, L., Yu, T. and Zhang, A., “Towards Method of Horizontal Federated Learning: A Survey,” 2022 8th Int. Conf. Big Data Inf. Anal., 259–266 (2022).

[2] Riasatian, A., Babaie, M., Maleki, D., Kalra, S. and Valipour, M., “Fine-Tuning and training of densenet for histopathology image representation using TCGA diagnostic slides,” Med. Image Anal. **70**, 102032 (2021).

Deep Learning Method for Detection of Cancerous Lung Nodules from High-Dose and Low-Dose Computed Tomography Images

Jenita Manokaran^a, Richa Mittal^b, Eranga Ukwatta^a,

^aUniversity of Guelph, School of Engineering; ^bGuelph General Hospital.

^a50 Stone Rd E, Guelph, ON, Canada N1G 2W1. ^b115 Delhi Street Guelph ON, Canada N1E 4J4.

Introduction: Lung Cancer is one of the leading causes of mortality among cancers with an estimation of 7.6 million deaths per year worldwide. About Thirty-thousand Canadians die every year from lung cancer with non-small-cell lung carcinoma (NSCLC) accounting for roughly 85% of cases. Most NSCLC patients are diagnosed at late stages of the disease. Algorithms developed using deep learning methods have shown promising results in detection and segmentation of lung nodules. Several lung cancer detection methods have been developed using high-dose computed tomography (HDCT) but few on low-dose CT (LDCT) (commonly used screening tool for lung cancer diagnosis) due to reduced image quality. Comparative study on lung cancer detection using HDCT and LDCT using deep learning method is yet to be explored. The proposed method aims in developing fast, accurate tool for detecting cancerous lung nodules using HDCT and LDCT.

Method: We used National Lung Cancer Screening Trial (NLST) (LDCT) and Lung-PET-CT Dx (HDCT) as our lung cancer datasets. The annotations for the malignant lesions are provided in the form of bounding boxes for both datasets. Our algorithm for lung nodule detection is based on You Look Only Once (YOLOv6) version 6 model, which have shown to outperform recurrent neural networks for object detection in terms of speed. The

Table 1: Data split between the datasets

Dataset	Train	Valid	Test
HDCT	187	21	60
LDCT	133	19	50

nodule sizes $\geq 4\text{mm}$ is considered in this work. An 80-20 (10% for validation) split was considered for training and testing the model's performance. The detailed split between the two datasets is provided in Table 1. The model was trained for 300 epochs using stochastic gradient

descent (SGD) optimizer with a batch size of 32. Data augmentation was performed to artificially increase the data during training. The whole slice containing the cancerous nodules are considered. The image sizes for both HDCT and LDCT were kept the same as 512 x 512. The corresponding bounding box annotations were used as the ground truth for training the model. The bounding box coordinates were provided for HDCT whereas for LDCT, the coordinates were obtained based on the tumor localisation information (weakly labelled data). Evaluation metrics such as precision, recall, Mean Average Precision (mAP) were used.

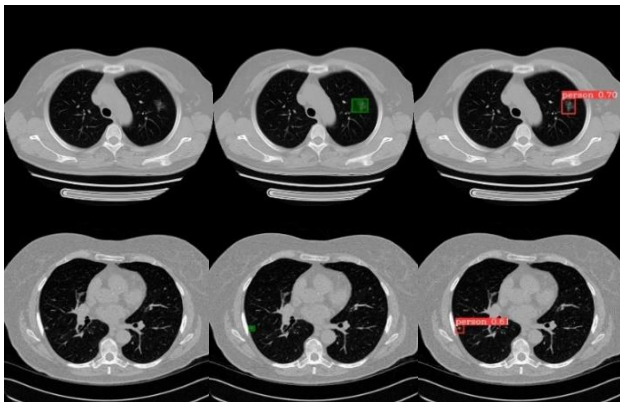


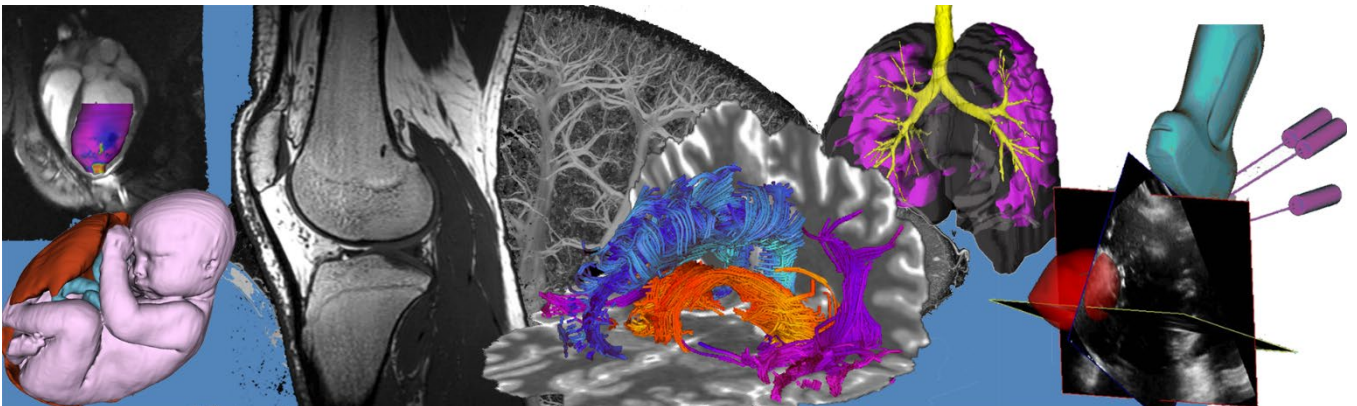
Figure 1: Original image (left), expert annotation (middle), model detection (right). The top row images are based on high-dose and bottom row for low-dose CT images.

Results: An example of the model's prediction and expert annotation results are shown in Figure 1 using HDCT and LDCT images. Though during training only slice with cancerous nodules were used, slices with and without cancerous nodules were included in the test set (un-seen data) to see how well the model performed. Confidence threshold of 0.50 and Intersection Over Union (IoU) of 0.45 was used in both HDCT and LDCT prediction. The model achieved a precision of 0.92, recall of 0.85 and mAP of 0.91 in case of HDCT images. In case of LDCT images, precision of 0.84, recall of 0.79 and mAP of 0.80 were achieved by the proposed model. The model showed high performance in detecting slices without nodules in both the dataset but when false positive detections per slice with

nodules were considered, model showed higher performance with LDCT compared to HDCT.

Conclusion: Timely detection of lung cancer would aid in improving the survival rates of the patients to a greater extent. The result based on the proposed work shows that the model achieved higher performance with HDCT images. Since lung cancer screening using LDCT images reduces high mortality rate, we will be incorporating methods such as transfer learning techniques to improve the performance of the model using LDCT images.

Pitch/Poster Session 8: Musculoskeletal and Vascular Imaging Abstracts



Best Fit Sphere to Determine Femoral Head Centre and Radius from 3D CT DataKenna Bartlett^{1,2}, John Rudan^{1,3}, and Heidi-Lynn Ploeg^{1,2}¹ Centre for Health Innovation, Queen's University, Kingston, ON, Canada² Department of Mechanical and Materials Engineering, Queen's University, Kingston, ON, Canada³ Department of Surgery, Queen's University, Kingston, ON, Canada

Introduction: There is an opportunity for artificial intelligence (AI) and structural analyses to support the diagnosis and treatment planning for hip resurfacing arthroplasty, such as through patient selection [1]. Manual two-dimensional (2D) preoperative planning is more common than three-dimensional (3D), largely due to efficiency concerns with 3D methods. However, the efficacy of AI and structural analyses for preoperative planning may be improved with 3D instead of 2D measures due to the increased accuracy [2], [3]. 3D methods must be streamlined and validated to increase their usage in clinical settings. Many morphological parameters required for preoperative planning and patient selection are dependent on the centre of the femoral head [4], [5], [6]. Therefore, having an efficient and precise method for determining the centre of the femoral head is crucial for the use of 3D preoperative planning. The objective of this study was to investigate the accuracy of a custom MATLAB script to fit a least squares best fit sphere to the femoral head to determine its centre and radius.

Methods: Kingston Health Sciences Centre has a database of 265 computed tomography (CT) scans of proximal femurs of patients prior to receiving hip resurfacing arthroplasty (HRA) (ethics protocol SCOMP-007-11). The CT scans were segmented in Materialise Mimics version 24.0. From this data set, 12 femurs (10 male and 2 female patients, aged 33 to 63 years old) were included in this pilot study to assess the precision of fitting a least squares best fit sphere to the femoral head to determine its centre and radius. Femoral head 3D coordinate datapoints were defined by a sectioning plane through the proximal femur with Materialise Magics version 24.1. A custom MATLAB script was written to fit a sphere to the sectioned femoral head 3D coordinate data.

The centre and radii of 12 femoral heads were determined with the least squares method to fit a sphere to the 3D coordinate data. Radii were determined using the x-y-z-coordinates of the femoral head 3D coordinate data and the equation of a sphere. The root mean squared error (RMSE) assessed the accuracy of the least squares best fit for the sphere: $RMSE = (\sum(R - R_{predict})^2/N)^{1/2}$, where R is the radius of the least squares best fit sphere, and $R_{predict}$ is the radius predicted using the x-y-z-coordinates of the femoral head and the equation of a sphere, and N is the number of radii predicted with the equation of a sphere.

A sensitivity analysis of the location the femoral head sectioning plane was performed. 10 unique 3D coordinate datapoints from one femoral head were selected using 10 unique sectioning planes. Convergence analyses were carried to quantify the impact of the sectioning plane on the least squares best fit sphere.

Results: From the least squares fit the range of radii was 25.29 to 26.66 mm. The average RMSE of the radii was 0.85 mm with a standard deviation of 0.19 mm. The change for each of the data outputs was less than 0.14 mm, with the least change in the y-coordinate of the centre, and the most change in the z-coordinate.

Conclusion: The radius and center of the femoral head could be determined with precision and was not sensitive to the sectioning plane. Efficient and precise determination of the femoral head centre and radius will allow for more accurate 3D measurements of other morphological parameters to improve AI predictions and structural analyses for pre-operative planning of hip arthroplasty. Accurate 3D measurement methodologies will allow future work to compare 2D and 3D approaches.

References:

- [1] Lawrie and Barrack, 2020, *Ann. Jt.*, 10.21037/aoj.2019.12.08
- [2] Huo et al., 2021, *J. Orthop. Surg.*, 10.1186/s13018-021-02294-9
- [3] Chen et al., 2022, *Front Med.*, 10.3389/fmed.2022.841202
- [4] Liang et al., 2020, *BMC Surg.*, 10.1186/s12893-020-00807-7
- [5] Breighner et al., 2019, *AM. J. Sports Med.*, 10.1177/0363546519878170
- [6] Samelis et al., 2021, *Cureus*, 10.7759/cureus.14133

Four-dimensional Computed Tomography and Ultrasonography for Assessing Thumb Biomechanics in Thumb Osteoarthritis Patients

Randa Mudathir^{a,b}, Megan Hutter^{a,b}, Carla du Toit^a, Emily Lalone^b, Aaron Fenster^{a,b}

^aRobarts Research Institute, 100 Perth Drive, London, ON, Canada N6A 5K8

^bWestern University, 1151 Richmond Street, London, ON, Canada N6A 3K7

Introduction: As a saddle joint with a wide range of motion, the thumb joint is critical for performing basic tasks of daily living, and a loss of its function may result in up to 50% of upper limb impairment [1]. Hypermobility, or joint laxity, has been known to increase the risk of thumb osteoarthritis (OA) [1]. Previous studies assessing thumb biomechanics in thumb OA patients have utilized radiography, magnetic resonance imaging, computed tomography imaging, and ultrasound. However, the static nature of these imaging techniques limits their ability to provide information on thumb joint kinematics or joint laxity during motion. Four-dimensional computed tomography (4DCT) is a tool that can be used to investigate joint kinematics of the thumb during motion. In addition, four-dimensional ultrasound (4DUS) can detect joint laxity by visualizing the thumb's stabilizing ligaments during motion. Hence, this work utilizes 4DCT and 4DUS imaging to characterize the biomechanical changes and degrees of joint laxity associated with varying stages of disease progression.

Methods: 4DCT images of primary thumb motions were collected from twelve thumb OA patients. Each 4DCT cine loop contained 25 frames, and every other frame of the 25 frames was segmented using 3D Slicer Software (Version 5.0.2). Custom Python and MATLAB scripts were developed to calculate the transformation matrices of the first metacarpal and trapezium, joint centroid translation, and changes in joint space area. Joint congruency maps were developed by measuring inter-bone distances throughout each motion. A similar analysis was conducted on a set of healthy participants for comparison. A repeated measures analysis of variance test was conducted to detect statistical differences in measured inter-bone distances. A 4DUS imaging system was developed by creating a semi-submerged automated system, where the ultrasound probe was positioned and automatically translated 1-2 cm laterally across the thumb joint during abduction of the thumb. The 4DUS images were exported to 3D Slicer, where the origin and insertion points of the dorsoradial ligament (DRL) of the thumb were detected, and changes in ligament length throughout the motion were measured.

Results: The biomechanical models developed accurately presented joint motion throughout all performed motions. Further anticipated results of this study include assessing changes in the degree of joint centroid translation, as well as changes in joint congruency throughout each motion. The DRL was identified in all frames of the 4DUS images collected, and the origin and insertion points of the ligament were successfully determined. Further results include measuring changes in ligament length throughout each motion, and comparing the values collected from healthy participants to those from thumb OA patients.

Conclusion: This pilot study utilized dynamic imaging techniques to understand the biomechanical factors influencing the onset and progression of thumb OA. The 4DCT images collected provided for a more robust analysis of the joint mechanics associated with thumb OA, while the 4DUS technique developed accurately detected changes in ligament length during thumb motion. Future work includes utilizing both imaging techniques in tandem to categorize the biomechanical changes and degrees of ligament laxity at the thumb joint associated with varying stages of thumb OA.

References: [1] Luker, K. R., Aguinaldo, A., Kenney, D., Cahill-Rowley, K. & Ladd, A. L. Functional Task Kinematics of the Thumb Carpometacarpal Joint. *Clin Orthop Relat Res* 472, 1123–1129 (2014).

The Relationship between Kinematic Joint Loading and Depth-Specific Volumetric Bone Mineral DensityLauren Straatman^{1,2}, Elizabeth Norman², Nikolas Knowles³, David Walton^{1,5}, Nina Suh⁴, Emily Lalone^{1,2}¹Department of Health and Rehabilitation Science, Western University ²Department of Mechanical and Materials Engineering, Western University³Cumming School of Medicine, University of Calgary, ⁴Department of Orthopedics, Emory University, ⁵Department of Physical Therapy, Western University

INTRODUCTION: According to Wolff's law, bone tissue is influenced by its mechanical environment and adapts in response to the mechanical load that acts on it.¹ This law has been supported in studies analyzing bone adaptation in the knee² and hip³, and have also shown that changes to the bone have been found to precede cartilage degeneration in diseases such as osteoarthritis. However, the relationship between bone adaptations and joint loading has not been established in the wrist. Our primary objective is to evaluate the correlation between kinematic joint contact area (JCa) and subchondral volumetric bone mineral density (vBMD), as it relates to depth from the subchondral surface. We hypothesize that a large JCa will be correlated to high vBMD in all layers from the subchondral surface. Our secondary objective is to determine the amount of variance in subchondral vBMD that can be explained by kinematic joint contact.

METHODS: Twenty healthy participants (n = 11 females and n = 9 males) underwent static CT scans of their wrist accompanied by a calibration phantom with known densities, and kinematic CT scans while performing maximum wrist extension to flexion. Average subchondral vBMD was studied at three depths from the surface (0 – 2.5, 2.5 – 5, 5 – 7.5mm) and JCa was studied according to radial articular surface contact (radioscaphoid (RS) and radiolunate (RL)). Pearson product-moment correlations were calculated to determine the relationship between vBMD and JCa, and statistically significant correlations were assessed using a regression model.

RESULTS: Descriptive statistics demonstrated more JCa and higher vBMD in the RS joint for all degrees of motion and all depths from the subchondral surface, when compared to the RL joint. The correlation analysis demonstrated significant positive correlations between vBMD and JCa in the deeper regions from the surface, while the regression analysis demonstrated that 38% and 33% of the variance in vBMD can be explained by degrees of motion in the RS and RL joints, respectively.

Discussion: An increase in vBMD was significantly, positively correlated with an increase in JCa, notably in the deeper regions from the subchondral surface that are primarily composed of trabecular bone; a region that is adaptive to change and metabolically active. This relationship is paramount to better understanding joint remodeling following injury, early osteoarthritic signs in the joint, and the influence of vBMD and JCa adaptations on pain.

REFERENCES: ¹Brand, Richard A. 2010. "Biographical Sketch: Julius Wolff, 1836-1902." *Clinical orthopaedics and related research* 468(4): 1047–49. <https://link.springer.com/article/10.1007/s11999-010-1258-z> (June 22, 2022). ²Sampath, Shameem A., et al., 2015. "Trabecular Orientation in the Human Femur and Tibia and the Relationship with Lower-Limb Alignment for Patients with Osteoarthritis of the Knee." *Journal of Biomechanics* 48(6): 1214–18. ³Zhou, Guang Quan et al. 2014. "Reconstruction of the Biomechanical Transfer Path of Femoral Head Necrosis: A Subject-Specific Finite Element Investigation." *Computers in Biology and Medicine* 52: 96–101.

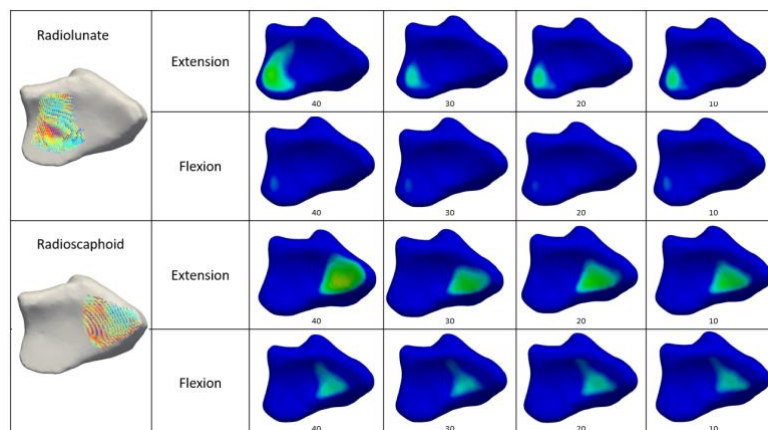


Figure 1. Representative figure of one participant's vBMD scatterplots and respective kinematic JCa maps throughout maximum extension and flexion, in every 10 degrees of motion. The red represents regions of the highest vBMD and JCa, while the green and blue represent regions of low vBMD and small JCa. This figure demonstrates a larger JCa during every degree of extension in comparison to flexion, and serves as a qualitative reference demonstrating the relationship between regions of high vBMD and large JCa.

The Sensitivity of Bony Landmarks and the Scapholunate Interval to Wrist Malrotation in the Posteroanterior Radiograph

Maxwell Campbell^{1,2}, Gregory Garvin³, Nina Suh⁴, Emily Lalone^{1,2}

¹ School of Mechanical and Materials Engineering, Western University, ² Roth McFarlane Hand and Upper Limb Centre, ³ Schulich School of Medicine and Dentistry, ⁴ Emory University School of Medicine

Introduction: Scapholunate ligament instability (SLI) is the most common carpal instability [1]. Left untreated, SLIs contribute to a form of progressive arthritis recognized as scapholunate advanced collapse, responsible for 55% of all wrist osteoarthritis diagnoses [2]. Clinicians use the scapholunate diastasis to diagnose potential SLIs and is measured from the posteroanterior (PA) radiograph of the wrist. It is difficult to get a consistent true PA view due to technologist mal-positioning and patient cooperation, leading to unrecognized error in the measurement of the scapholunate (SL) diastasis, causing misdiagnosis. Previous work has shown that carpal indices are sensitive to rotational mal-positioning in the lateral radiograph, but little work has been done focusing on the PA. Malrotations of 10°-20° regularly occur in the clinical environment, further emphasizing the need for robust indicators of malrotation [3]. This study aims to determine the effect wrist malrotation has on the measured scapholunate diastasis and four proposed bony landmarks in the PA radiograph.

Methods: Eleven healthy fresh-frozen cadaveric wrists (four right, seven left; sex: 10 male, one female) were radiographed in the “expert neutral,” true PA position. Expert neutral in this study was defined as the amount of pronation required to compensate for the wrists thenar eminence, placing the wrist frontal plane perpendicular to the incident x-ray beam. Using a series of custom-built positioning wedges, the cadaveric wrists were rotated to 30° of pronation and supination in 10° intervals and imaged at each interval. The SL diastasis was measured in each radiograph along with the definition of four proposed bony landmarks: (1) the visible perimeter of the base of the hook of the hamate, (2) the radial-ulnar distribution of the dorsal non-articular surface of the distal third-metacarpal head, (3) the radial-ulnar distribution of the pisiform about the longitudinal axis of the ulna, and (4) the overlap of the pisiform and triquetrum. The means of all measurements were graphed against rotation to quantify the relationship, with linear modelling used to determine the rate of SL diastasis change with rotation. A one-way ANOVA was completed to assess statistical significance between landmark measurement means and wrist rotation, and a Tukey post hoc was used to determine inter- and intra-observer reliability of the measures.

Results: The measured SL diastasis was largest within the expert neutral frame and linearly decreased by 34.48% for every 10° of pronation and decreased non-linearly by 86% for the first 10° of supination and a further 6% at 20° of supination, compared to the neutral frame here was no measurable SL diastasis at the 30° extremes of rotation. The distribution of the distal third metacarpal head was shown to be sensitive to both pronation and supination. The perimeter of the hamate, as well as the distribution of the pisiform, were both shown to be sensitive to supination, whereas the overlap of the pisiform was not shown to be sensitive to either direction of rotation.

Conclusions: These results exhibit the sensitivity of the SL diastasis to wrist pronation and supination within the PA radiograph. Using the proposed bony landmarks, clinicians now have a tool to identify malrotated PA radiographs, reducing the unrecognized error in the measurement of carpal indices and, thus, the rate of misdiagnoses. These results motivate the importance of proper wrist positioning during PA radiographs to improve the detection of scapholunate ligament-related injuries.

References:

1. Sikora S, Tham S, Harvey J, et al. The Twist X-Ray: A Novel Test for Dynamic Scapholunate Instability. *J Wrist Surg.* 2019. doi:10.1055/s-0038-1673344
2. Watson HK, Weinzweig J, Zeppieri J. The natural progression of scaphoid instability. *Hand Clin.* 1997. doi:10.1016/s0749-0712(21)00079-2
3. Pennock AT, Phillips CS, Matzon JL, et al. The Effects of Forearm Rotation on Three Wrist Measurements: Radial Inclination, Radial Height and Palmar Tilt. *Hand Surg.* 2005. doi:10.1142/S0218810405002528

Remote Telemetry System for Monitoring Arthritis RehabilitationKyle Wilson^{1,2}, Steven Pollmann², David W. Holdsworth^{2,3,4}

¹Faculty of Engineering, ²Robarts Research Institute, ³Dept. of Medical Biophysics, Schulich School of Medicine and Dentistry, ⁴Dept. of Surgery, Schulich School of Medicine and Dentistry, Western University

Introduction: Arthritis is one of the most common chronic illnesses in North America. The symptoms of arthritis almost always present as painful inflammation and stiffness of the joints [1]. Clinical treatments and therapies can help improve a patient's quality of life by reducing joint pain and increasing range of motion. However, the primary method medical professionals have of evaluating the efficacy of clinical treatments of arthritis is using various self-reporting systems. These methods are subject to inaccuracies in the reported data due to personal bias and a lack of objectivity, thus hindering the abilities of clinicians' to accurately assess the effectiveness of novel treatment methods. Therefore, there is a need for a way to collect quantitative data that measures a patient's daily physical activity, which can then be used to make objective observations regarding the individual's mobility. The overall goal is to develop a remote telemetry system consisting of a single wearable device that performs detailed gait analysis. Our current goal is to establish a method to accurately classify the type of activity that the wearer is engaged in at any point in time based on the recorded motion data.

Methods: Advances in low-cost consumer-grade electronics have made it possible to record continuous motion data with a small battery-powered sensor package. The device will be attached to a single point of the wearer's body to acquire information about the user's gait, such as at the base of the spine. This approach takes advantage of micro-electronic inertial-measurement units (IMUs), which can record motion data directly to local solid-state storage, at rates of up to 500 Hz. The device will utilise a single IMU with 9 degrees of freedom to measure aspects of the wearer's activity and motion, including 3 accelerations (x, y, and z), 3 rotations (around x, y, and z axes) and 3 magnetic field vectors. Five volunteers were asked to wear an early proof-of-concept prototype and instructed to follow a pre-defined course, performing specific activities at designated points. Each of the 5 participants performed 2 separate trials through the course, with 1 participant performing an additional 2 trials, yielding a total of 12 trial datasets.

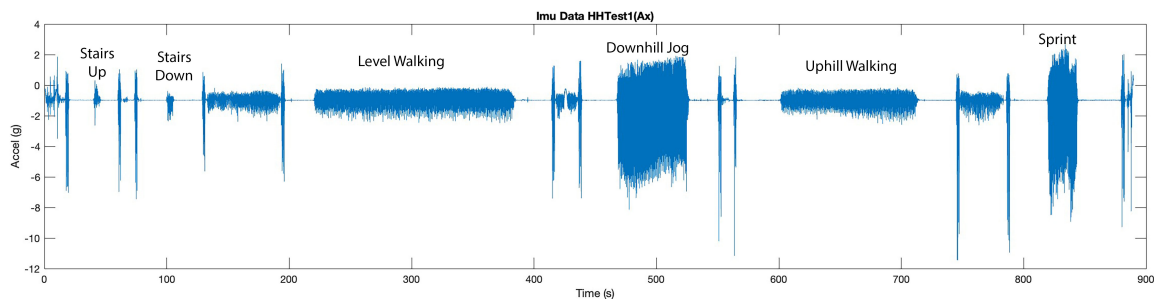


Figure 1: Acceleration data in the direction of the x-axis, collected from one of the volunteers.

Results: The proof-of-concept prototype was successfully built, and an example of one of the measured variables, acceleration in the x-direction, can be seen in the time-series plot shown in Figure 1. Looking at this graph, the sharp spikes represent jumps to signal the beginning and end of an activity. It is possible to visually identify the separate activities and label each section of the data accordingly.

Conclusion: Based on the observed visual patterns in the data, it seems promising to apply machine learning models to classify and label different physical activities based on the measured data. Eventually, a more sophisticated algorithm will be applied to derive much more detailed information about the wearer's movement and gait patterns. This work could lead to a new type of low-cost data acquisition system that will provide objective, detailed data acquired outside of a clinic. With the addition of rapid, automated analysis, this system could significantly improve the assessment of new therapies for musculoskeletal conditions, such as arthritis.

References: 1. Arthritis Society Canada, "The Truth About Arthritis," 2022. [Online].

Synthetic-mask x-ray energy-subtraction angiography for improved cardiac-stent visualization

Lisa M. Garland and Ian A. Cunningham

Robarts Research Institute, Department of Medical Biophysics, Western University

Introduction: Cardiac angioplasty is a standard interventional treatment for arterial stenoses that uses a catheter with balloon or permanent wire stent to open narrowings. Inaccurate stent placement contributes to the high 25% re-stenosis rate, so clear stent visualization during placement and post-operative checkups is very important.¹ Background anatomic structures (lungs, bone, soft-tissue variations) add contrast to these images than can complicate clear visualization. Digital subtraction angiography (DSA) is an effective method for suppressing all background structures but requires a pre- and post-contrast injection image, which can be unsuited for imaging moving structures such as the heart due to the time delay between acquisitions. Energy subtraction angiography (ESA) can be used to selectively suppress or enhance desired structures based on their individual attenuation properties and has a total acquisition time of milliseconds. Yamamoto et al. developed a method to create a mask image for cardiac DSA based on the maximum pixel value of a set of consecutive post-injection images.² The motion of the vessel between these images allows a mask to be created by selecting pixel regions not attenuating the contrasted vessel. This approach proved to be successful but was less effective at soft tissue edges such as the heart and lungs, where severe motion artifacts occurred as a result. We are developing a method to improve stent and contrasted vessel visualization that uses a three-step approach: 1) acquire a set of consecutive ESA images that suppress soft tissue while stent/vessel placement is changing 2) create synthetic mask image using ESA set 3) subtract mask from ESA image to achieve DSA-like result. By eliminating soft tissue from the image set, only motion of the stent is required and the bone must remain stationary, which proved to be reasonable from the previous study.

Methods: Experiments using an anthropomorphic rigid chest phantom and superalloy monofilament wire stent were conducted using a Canon Medical Alphenix angiography system at 60 & 120kV for the low and high energy images, respectively. Using ESA calculations previously developed in our lab, 11 x-ray imaging parameters were optimized computationally for maximum nickel signal to noise ratio³. A set of 4 ESA tissue suppressed images were evaluated with small manual shifts in stent placement on the rigid phantom to simulate heart motion. The maximum pixel value for all ESA images was evaluated to create a synthetic mask image to then be subtracted from a corresponding ESA image to yield a DSA-like image of the stent.

Results: Simulation results showed that, even without sufficient stent motion (i.e., residual stent visible in mask), the subtraction remained effective, and a reduced contrast DSA-like image was achieved (figure 1d). To avoid image artifacts, it is crucial to select the correct ESA image to be subtracted.

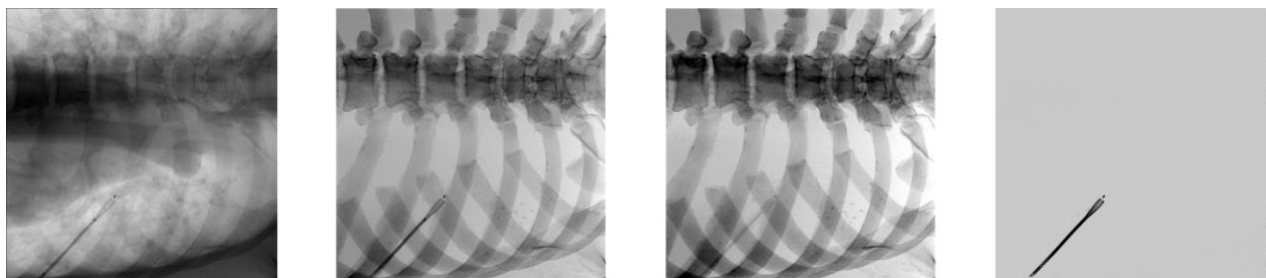


Figure 1: a) Conventional x-ray image of stent b) ESA image of one stent position, c) Resultant mask image d) DSA-like subtraction (image b-c)

Conclusions: When using ESA images as opposed to conventional to create a synthetic mask image, soft tissue edges no longer impact the mask image. By minimizing visibility of background structures obscuring the stent, clinicians may have a greater chance at confirming whether the stent placement and deployment is satisfactory in real time. This technique is also effective for iodinated vasculature as Yamamoto et al. showed, but may prove to be more successful when implementing with ESA images rather than conventional.

1. Cleveland Clinic. (2022). CAD: In-Stent Restenosis. <https://my.clevelandclinic.org/health/diseases/17132-cad-in-stent-restenosis>
2. Yamamoto, M., Okura, Y., Ishihara, M., Kagemoto, M., Harada, K., & Ishida, T. (2009). Development of digital subtraction angiography for coronary artery. *Journal of digital imaging*, 22(3), 319–325.
3. Burton, C.S., Mayo, J.R. and Cunningham, I.A. (2016). Energy subtraction angiography is comparable to digital subtraction angiography in terms of iodine Rose SNR. *Med. Phys.*, 43: 5925-5933.

Dual-energy x-ray angiography with a photon-counting x-ray detector.

Sarah Aubert and Jesse Tanguay | Toronto Metropolitan University

Introduction: Vascular imaging is critical for diagnosis and treatment of cardiovascular disease (CVD). Digital subtraction angiography (DSA) is the reference standard for imaging near-stationary vasculature, such as the peripheral arteries^{1,2}, however, it cannot be used to image the coronary arteries due to its susceptibility to motion artifacts.³⁻⁵ Dual energy (DE) angiography has been investigated as an alternative to DSA, since acquiring x-ray images at different average energies would allow for anatomic noise, such as bone or soft tissue, to be suppressed from angiographic images. However, previous work has reported that DE angiography images have decreased signal-to-noise ratio (SNR) relative to DSA.⁶⁻⁸ In addition, conventional kV-switching DE techniques require a high-energy spectrum that is filtered by up to 2mm of copper, resulting in less than 10% of photons exiting the tube reaching the patient. This places a high demand on the x-ray tube, which limits the number of photons available to produce a DE image in the short exposure times required to minimize motion artifacts.^{7,9,10} In previous work, we optimized single-exposure DE angiography.¹¹ By counting the photons in two energy bins during a single exposure, we eliminate the need for heavy filtration of the x-ray spectrum, potentially overcoming some of the limitations responsible for poor SNR of kV-switching DE angiography. The purpose of this work is to optimize DSA and kV-switching DE imaging approaches implemented with a photon-counting x-ray detector and to compare image quality of optimized conventional kV-switching DE angiography, single-exposure DE angiography and DSA in terms of SNR per root entrance exposure.

Methods: An imaging phantom was developed to investigate the iodine SNR in images produced using a cadmium telluride photon-counting x-ray detector equipped with analog charge summing for charge sharing suppression. The phantom consists of a 30-cm thick water tank with an embedded iodine step wedge (containing 16-48 mg/cm² of iodine). For DSA, we imaged the phantom both pre-injection and post-injection using tube voltages ranging from 70 to 150 kV, which yielded entrance air kerma values from 0.2 to 1.5 mGy. Optimal tube voltage was determined from iodine SNR calculated using the pre-injection and post-injection images. For kV-switching approaches, we fixed the low energy (LE) image at a tube voltage of 70 kV and acquired high energy (HE) images using tube voltages ranging from 120 to 150 kV. Soft tissue suppressed DE images were generated using the gain corrected high and low energy images and a soft tissue suppression parameter that minimized contrast between soft tissue and background. Images were generated for dose allocation factors ranging from 0.25 to 2 for each low and high energy image combination. Optimal dose allocation factor and tube voltage was determined from iodine SNR in the DE image.

Results: It was found that a tube voltage of 100 kV optimized the iodine SNR for DSA and a high-energy tube voltage of 150 kV optimized kV-switching DE imaging. Images acquired using optimal parameters are shown in Fig. 1. Optimized single-exposure DE imaging and kV-switching DE imaging yielded iodine SNR that was 50% and 62% of that of DSA, respectively. The kV-switching approach required a much higher tube load. An air kerma of 1.58 mGy was used for single-exposure DE image acquisition, yielding a tube load of 950 J/mGy at 150 kV. For kV-switching, an air kerma of 1.55 mGy was used at 150 kV for the optimal dose allocation factor of 0.25, this corresponds to a tube load of 3300 J/mGy for the 70kV/150kV low and high energy DE image combination.

Conclusions: Single-exposure DE imaging approaches and kV-switching DE imaging approaches are capable of producing an iodine SNR $\sim 1/2$ and $\sim 2/3$ of that of DSA when implemented with a photon-counting x-ray detector, however kV-switching DE approaches require a greater tube load than single-exposure approaches. Therefore, single-exposure DE imaging of the vasculature may provide an alternative to kV-switching approaches, yielding similar SNR without the limitations imposed by tube loading constraints.

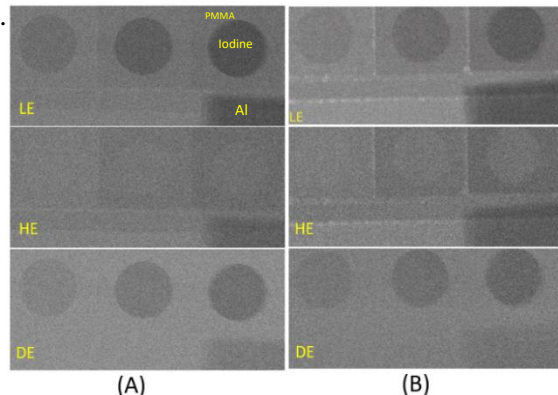


Figure 1. (A) kV-switching DE image generated using LE = 70 kV, HE = 150 kV and an entrance air kerma of 1.55 mGy. (B) Single exposure DE image generated using a tube voltage of 150 kV, an energy bin threshold of 81 keV and an entrance air kerma of 1.58 mGy.

[1] Perrier, L. *Diagn Interv Imaging*. Vol:101(7). 2020.
[2] Wang, A. *Phys Med Imaging*. Vol:7622. 2010.
[3] Brody, W. *IEEE Trans Nucl Sci*. Vol:29(3). 1982.

[4] Meijering, E. *IEEE Trans Med Imaging*. Vol:18(1). 1999.
[5] Turski, P. *AJNR*. Vol:4(3). 1983.
[6] Van Lysel, M. *J Cardiovasc Imaging*. Vol:7. 1991.

[7] Van Lysel, M. *Med Phys*. Vol:21(2). 1994. [10] Ducote, J. *Phys Med Biol*. Vol:52(1). 2006.
[8] Molloi, S. *Med Phys*. Vol:16(2). 1989. [11] Aubert, S. *Med Phys*. 2022.
[9] Xu, T. *Med Phys*. Vol:33(6). 2006.

A Polyacrylamide (PAA) Gel Phantom for Studying Catheter Ablation

Victor A. Chu,^{1,2} David W. Holdsworth,^{1,2} Allan C. Skanes,³ and Maria Drangova^{1,2}

¹Robarts Research Institute, ²Department of Medical Biophysics, ³Department of Medicine, Schulich School of Medicine and Dentistry, Western University

Introduction: Atrial fibrillation (AF) is the most prevalent cardiac arrhythmia and is a leading cause of stroke worldwide [1]. AF is commonly treated by catheter ablation - a procedure in which a catheter-mounted electrode heats localized volumes of cardiac tissue. When heated above 50°C, cardiac muscle cells die, forming a non-conductive volume of scar tissue called a "lesion". Successful procedures electrically isolate sources of AF by forming contiguous patterns of lesions, each through the thickness of the heart wall, to correct the arrhythmia.

Benchtop studies are often performed to evaluate ablation techniques. Many factors, including tissue elasticity, friction, electrical impedance, and perfusion determine lesion depth. While in-vivo studies best replicate these properties, they are expensive to perform and introduce significant variability to results. As such, accurate ex-vivo models are required to study novel techniques. Ex-vivo animal tissues are commonly used as models in ablation studies [1], but they do not consistently replicate the electrical or physical properties of live tissue, and also add variability. In addition, ablations done in any tissues are only analyzable in two-dimensions by optically measuring lesion cross sections, limiting the accuracy of lesion analysis and precluding lesion volume quantification.

The aim of this study was to develop a gel cardiac tissue phantom with reproducible, realistic physical and electrical properties, capable of replicating ablation lesions in-vitro. Based on prior work [2], a polyacrylamide (PAA) gel phantom incorporating bovine serum albumin (BSA) was devised. PAA gels have modifiable elasticity and similar thermal and electrical properties to live human tissues. BSA is a protein that coagulates when heated beyond a pH-dependent temperature. Importantly, when coagulated, BSA clouds optically and creates T2 contrast in MR images [2]. We hypothesize that PAA phantoms can replicate the Young's modulus and frictional properties of live atrial tissue. In addition, we hypothesize that the addition of BSA will enable reproducible characterization of ablation lesions in vitro.

Methods: Gels (n=5) were mixed with acrylamide concentrations of 2%, 8%, 10.5% (n=2), and 12% (g/mL) using 0.2M pH 4.5 buffer in custom molds. Gel Young's moduli and coefficients of friction (μ) were measured by a custom universal tester. Ex-vivo porcine aorta endothelial frictional properties were measured as reference. Gels were ablated in saline solution with 20-40W of power, for 20-40s, with 10-20g of contact force, and imaged with a 3T MRI scanner using a fast-spin echo T2-weighted sequence.

Results: Ablation resulted in visible localized clouding of BSA, creating clear contrast between ablated and un-ablated regions of gel in T2 weighted MR images (Fig. 1). Lesion dimensions obtained from MR images matched values reported in the literature for in-vivo lesions. 12.0% PAA gels had a Young's modulus of 108.0kPa, which matched the reported Young's modulus of contracted skeletal muscle (108.3kPa) [3]. Ex-vivo porcine aortae had μ of 0.058 ± 0.023 , and gel had μ of 0.024 ± 0.0021 (Fig. 2).

Conclusions: Preliminary results demonstrated that PAA/BSA gel phantoms match the elasticity of in-vivo contractile tissue. Ex-vivo porcine aortae showed considerable variability in frictional behavior, dependent on sample age, storage condition, etc. As such, while gel phantoms did not match the mean coefficient of friction of tested tissues, phantoms did replicate the lowest range of observed coefficients (Fig. 2). In addition, these results show that PAA gel phantoms can simulate realistic ablation lesions. Further experiments are required to validate these phantoms.

References: 1) Lippi, G. et al., Int J Str, 2021. 2) Bouchard, L. et al, Med Phys, 2000. 3) Krouskop, T. et al., J Rehab Res Dev, 1987

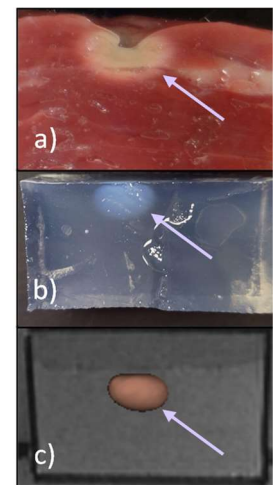


Fig. 1: Ablation lesion in ex-vivo bovine tissue (a). Optical (b) and T2-MR image (c) of lesion in gel.

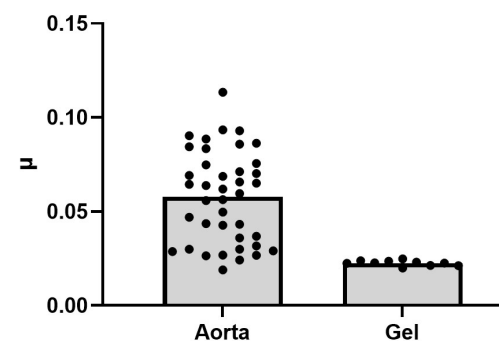


Fig. 2: Friction of ex-vivo porcine aortae and gel.

2D/3D Image Registration for Guidance of Endovascular Interventions in Tibial VesselsMoujan Sadari^{1,2}, Jaykumar Patel^{1,2}, Calder Sheagren^{1,2}, Trisha L. Roy³, Graham A. Wright^{1,2}¹Department of Medical Biophysics, University of Toronto, ²Physical Sciences, Sunnybrook Research Institute,³Department of Vascular Surgery, Houston Methodist DeBakey Heart & Vascular Center

Introduction: Advanced peripheral arterial disease can lead to chronic limb-threatening ischemia, when insufficient blood flow to a limb causes tissue death. Endovascular interventions are a minimally invasive option for revascularization¹. During these procedures, X-Ray Fluoroscopy (XRF) provides image-guidance as clinicians navigate along vessels with guidewires to narrowed regions and deploy devices to restore blood flow. XRF suffers from limitations in visualization, especially in smaller vessels below the knee², as seen in Fig. 1. These limitations could be overcome using overlays from preoperative imaging such as CT (Computed Tomography) Angiography, which produces high resolution 3D vessel maps³. This motivates the development of an image registration technique to align 3D CT datasets with real-time 2D XRF images, to enhance image-guidance of endovascular interventions in tibial vessels. This study aims to show that an existing high-dimensional derivative-free iterative optimizer can reliably determine the spatial parameters defining this registration with acceptable accuracy, provided that initialization errors are sufficiently small.

Methods: XCAT software was used to generate a synthetic CT image of a leg from a numerical phantom⁴, and projections of this 3D dataset produced synthetic X-ray images. An image registration algorithm was developed, which optimizes the 3D position of the CT dataset such that a 2D projection has high correspondence with a target X-ray image. 3D position is characterized by 2 out-of-plane rotations (X_0 : x-ray gantry rotated to head/foot of table, Z_0 : gantry rotated left/right), 1 in-plane rotation, 2 in-plane translations, and 1 magnification parameter. An existing python implementation of BOBYQA⁵ (Bound Optimization BY Quadratic Approximation) was used to maximize Normalized Cross-Correlation, with parameters X_0 , Z_0 and magnification initialized manually within clinically relevant ranges of $\pm 5^\circ$, $\pm 10^\circ$, and ± 0.5 respectively. 21 trials were conducted for each of 4 X-ray images.

Results: For X_0 , errors in initialization correlate with errors in registration (Fig. 2a, Spearman's ρ : 0.73, p-value: 4.5E-15). Z_0 does not show this correlation (Fig. 2b). Magnification errors (Fig. 2c) appear to interact with X_0 errors to compensate, with resulting position shifts improving overall image correspondence. The magnitude of maximum misalignment a point in the image had due to the error in each parameter after registration was: (mean(stdev)) X_0 : 0.32(0.43)mm; Z_0 : 0.13(0.18)mm; Magnification: 7.3(3.3)mm.



Fig. 1. XRF image of knee and leg

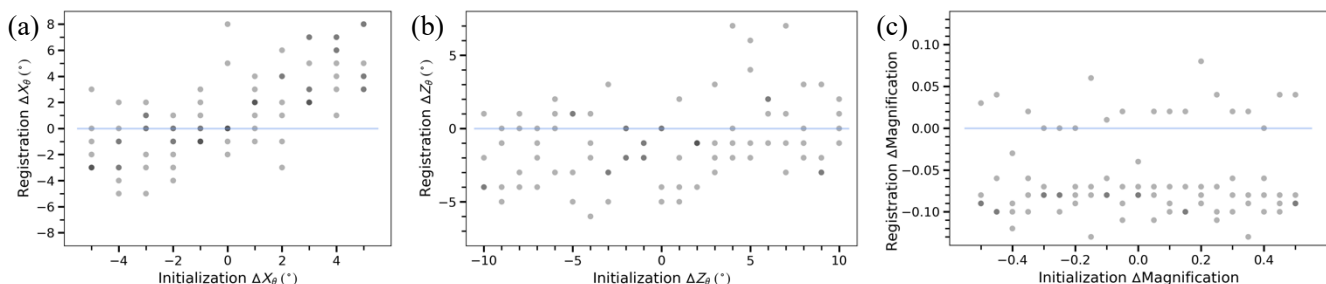
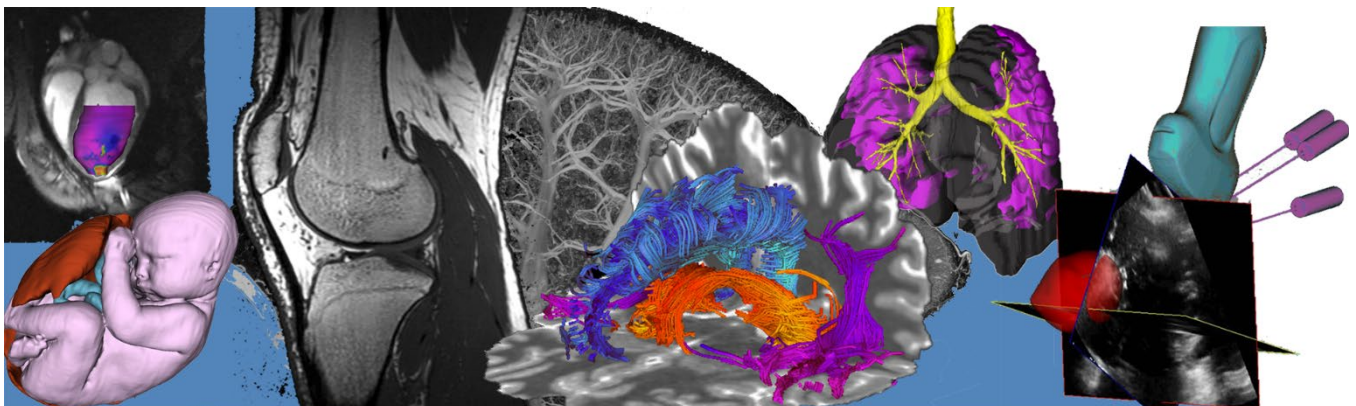


Fig. 2. Resulting registration errors for each parameter, given different initialization errors. (a) Registration error of X_0 has a positive correlation with initial error. (b) Z_0 does not have this correlation. (c) Magnification does not have this correlation.

Conclusions: For a synthetic dataset, initializations of the out-of-plane rotation parameters X_0 and Z_0 within 5° and 10° respectively allow an iterative optimizer to achieve image registration with errors in each parameter causing a maximum offset of less than 1mm. Given that vessels of interest have diameters of around 2-3mm, an image overlay with this spatial accuracy would be sufficient to guide clinical decision making^{6,7}. Notably, the magnification parameter has lower accuracy, likely due to interactions with X_0 errors. Future work will include modification of the algorithm to use only bones as the basis of registration (to avoid misalignment due to shifting soft tissues), and evaluation of performance on an available dataset of real CT and XRF images of limbs of patients with chronic limb-threatening ischemia.

References: 1. L. Uccioli et al., *Vasc. Health Risk Manag.* 14, 63–74 (2018). 2. C. Ward et al., *PanVascular Medicine*, 3195–3203, (Springer, 2015). 3. R. Met et al., *JAMA*. 301, 415–424 (2009). 4. W. P. Segars et al., *Med. Phys.* 37, 4902–4915 (2010). 5. C. Cartis et al., *ACM Trans. Math. Softw.*, 13. 6. R. Lorbeer et al., *PLoS ONE*. 13, e0197559 (2018). 7. Z. Khan et al., *IOSR J. Dent. Med. Sci.* 15, 129–133 (2016).

Oral Session 9: MR and Magnetic Particle Imaging Abstracts



Sodium (^{23}Na) MRI of the prostate using an external butterfly coilJosephine Tan^{1,2,3}, Vibhuti Kalia^{4,5}, Jonathan D Thiessen^{1,2}, Timothy J Scholl^{1,3,6}, Alireza Akbari^{1,3}¹Medical Biophysics, Western University, London, ON, ²Lawson Imaging, Lawson Health Research Institute, London, ON, ³Robarts Research Institute, London, ON, ⁴Medical Imaging, Western University, London, ON, ⁵Medical Imaging, St. Joseph's Health Care, London, ON, ⁶Ontario Institute for Cancer Research, Toronto, ON

Introduction: Sodium (^{23}Na) MRI is a molecular imaging technique that can detect the increased tissue sodium concentration (TSC) exhibited in several tumour types¹. For prostate cancer (PCa) imaging, ^{23}Na MRI is conventionally performed using an endorectal coil to facilitate a higher signal-to-noise ratio (SNR)². However, endorectal coils are associated with a limited field of view, increased scan times, gland deformation, and patient discomfort, which constrain the clinical utility of ^{23}Na MRI for PCa imaging. To address these challenges, we have developed a completely external, non-invasive 'butterfly' coil for ^{23}Na MRI of the prostate. In this abstract, we investigate its imaging performance (resolution and SNR) in a phantom and in healthy male volunteers, and feasibility to detect sodium signal in the prostate of PCa patients.

Methods: All MR images were acquired at 3 T (Siemens Biograph mMR). ^{23}Na MRI was performed with an external, PET-compatible, flexible transmit/receive butterfly coil built in-house (diameter=18cm, tuning=32.6MHz) using a 3D density-adapted radial projection sequence (DA-3DPR)³ (TR=50ms; TE=0.8ms; nominal isotropic resolution=5mm; FOV=36×36×10cm³). To assess image resolution, ^{23}Na MRI was performed in a 3D-printed plastic phantom (68×74×50mm³) consisting of evenly spaced rods of varying diameters (4-9mm). ^{23}Na MRI was then acquired in six male volunteers (age=51.33±16.24 years) to assess SNR in the peripheral (PZ) and transition zones (TZ) of the healthy prostate, and in two patients with biopsy-proven PCa (age=64.0±1.41 years) to visualize the sodium signal in PCa lesions. T₂-weighted images (TR=1700ms, TE=101ms, FOV=360×360mm², resolution=1.13×1.13mm²) were acquired as an anatomical reference.

Results and Discussion: Based on full-width half maximum (FWHM) measurements of the phantom (Figure 1), the actual isotropic resolution using our ^{23}Na MRI system and DA-3DPR sequence is 6mm (FWHM=5.68±0.09), providing a baseline of the minimum lesion size that can be resolved within the prostate. For reference, mean lesion size in PCa as detected by proton (^1H) MRI has been reported to be 15.7mm⁴. Representative volunteer and patient images (Figure 2) show that sodium signal can be detected throughout the whole prostate and pelvic region, in contrast to ^{23}Na images acquired using an endorectal coil¹. Noise appeared uniform across the images. In all volunteers, sodium signal in PZ (SNR=39.7±13.09) was greater than that in TZ (SNR=32.98±8.96), consistent with previous reports^{5,6}. This finding may be attributed to structural

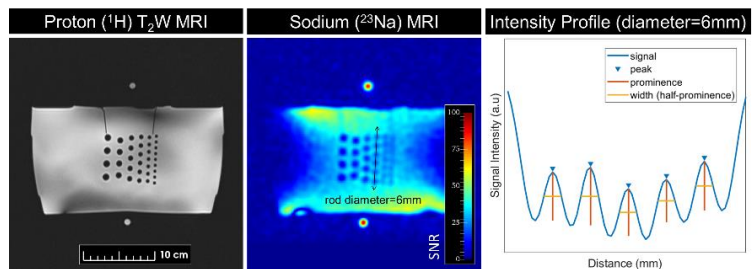


Figure 1: Resolution phantom consisting of solid rods (diameters=4-9mm) across which FWHM was measured on ^{23}Na MRI.

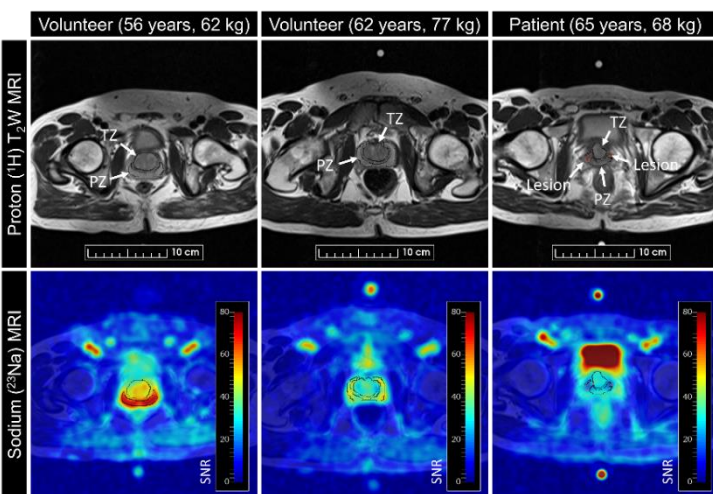


Figure 2: Representative volunteer and patient images exhibiting higher sodium signal in the peripheral zone (PZ) compared to the transitional zone (TZ).

differences in these zones that influence intra- and extracellular volume fraction which, in turn, affect total TSC, such as looser stroma in PZ¹. Patients similarly exhibited a greater sodium signal in PZ relative to TZ, while sodium signal in lesions appeared lower relative to normal PZ and TZ. Future histological work will be needed to validate the sensitivity of this coil for ^{23}Na MRI of PCa.

Conclusion: ^{23}Na MR images acquired with our butterfly coil and DA-3DPR sequence had an actual isotropic resolution of 6mm and high SNR (>30) in the PZ and TZ of the healthy prostate. This work aims to enhance the workflow of ^{23}Na MRI in PCa studies compared to conventional endorectal coils.

References: ¹Poku LO, J Magn Reson Imaging, 2021. ²Broeke N, J Magn Reson Imaging, 2019. ³Nagel AM, Magn Reson Med, 2009. ⁴Pooli A, J Urol, 2021. ⁵Hausmann D, Invest Radiol, 2012. ⁶Barrett T, J Magn Reson Imaging, 2020.

Quantitative Magnetization Transfer Imaging in Glioblastoma Patients using Balanced Steady-state Free Precession on a 1.5 T MR-Linac

Authors: Brandon T.T Tran^{1,2}, Liam S.P. Lawrence^{1,2}, Rachel W. Chan², James Stewart³, Chia-Lin Tseng³, Jay Detsky³, Hany Soliman³, Arjun Sahgal³, Angus Z. Lau^{1,2}

(1) Medical Biophysics, University of Toronto, (2) Physical Sciences Platform, Sunnybrook Research Institute, Toronto, (3) Radiation Oncology, Sunnybrook Health Sciences Centre, Toronto

Introduction: MR-linear accelerators (MR-Linacs) enable daily imaging and could guide radiotherapy in glioblastoma patients. Quantitative magnetization transfer (qMT) imaging can characterize white matter damage thought to be associated with tumor response in glioblastoma patients¹; qMT may be a more specific indicator when compared to standard gadolinium enhanced imaging. Our previous implementation of qMT on an MR-Linac using an off-resonance saturation provided three slices in 15 minutes and lacks the 3D coverage necessary to accurately assess tumor response. In this work, we implemented a fast 3D balanced steady-state free precession (bSSFP) qMT protocol² on an MR-Linac. qMT parameters were derived and repeatability was calculated.

Methods: Six glioblastoma patients received fractionated radiotherapy (60 Gy/30 fx) on a 1.5T Elekta Unity MR-Linac. A 3D bSSFP qMT protocol was acquired during treatment at a weekly interval. A series of 14 bSSFP images were collected; magnetization transfer contrast is modulated by varying the flip angle (α) and the duration of the RF pulse (T_{RF}). bSSFP: ($T_{RF} = 0.672 - 2.221$ ms, $\alpha = 5^\circ - 35^\circ$, TR/TE = 6.2/3.1 ms, voxel size $2.0 \times 2.0 \times 2.0$ mm³, FOV = $192 \times 192 \times 60$ mm³, total scan time = 8 min 24 s). T_1 and B_1 mapping required to derive MT parameters was also performed. Free pool T_2 (T_{2f}) and macromolecular fraction (F) maps were estimated from Bloch equation fitting². The exchange rate was constrained to 4.5 s⁻¹ (mean literature value in white matter²) to account for degeneracies in fitting the F parameter. Four ROIs were analyzed (**Fig. 1A**). Contralateral normal-appearing white matter (cNAWM), contralateral normal-appearing gray matter (cNAGM) and cerebrospinal fluid (CSF) were automatically segmented using FSL FAST³. The gross tumor volume (GTV) was defined at treatment planning by a radiation oncologist. The median F value across voxels within each ROI was calculated. Repeatability in cNAWM and cNAGM was characterized by the within-subject coefficient of variation (wCV).

Results: The median F value in cNAWM, cNAGM and GTV ROIs differ between patients and with time (**Fig. 1B**). Median F values in cNAWM and cNAGM are lower than literature values by 50-60%². The distribution of F values in GTV appears to vary between patients unlike cNAWM, which may suggest characterization of tumor inhomogeneity (**Fig. 1C**). No significant changes to F values with time was found. The scans may be too late in treatment to resolve tumour response, as only the ratio of qMT parameters at week 2 compared to baseline (before treatment) has been shown to differentiate tumour progressors from non-progressors¹. The wCVs were 8.8% in cNAWM and 9.0% in cNAGM. The wCV in cNAWM is higher than literature value (4.7%)⁴, though wCV values may be affected by disease progression and ongoing treatment.

Conclusions: bSSFP qMT was implemented on a 1.5T MR-Linac and provided 3D parameter maps in under 10 minutes. Future analysis will determine if bSSFP qMT parameters are associated with treatment response.

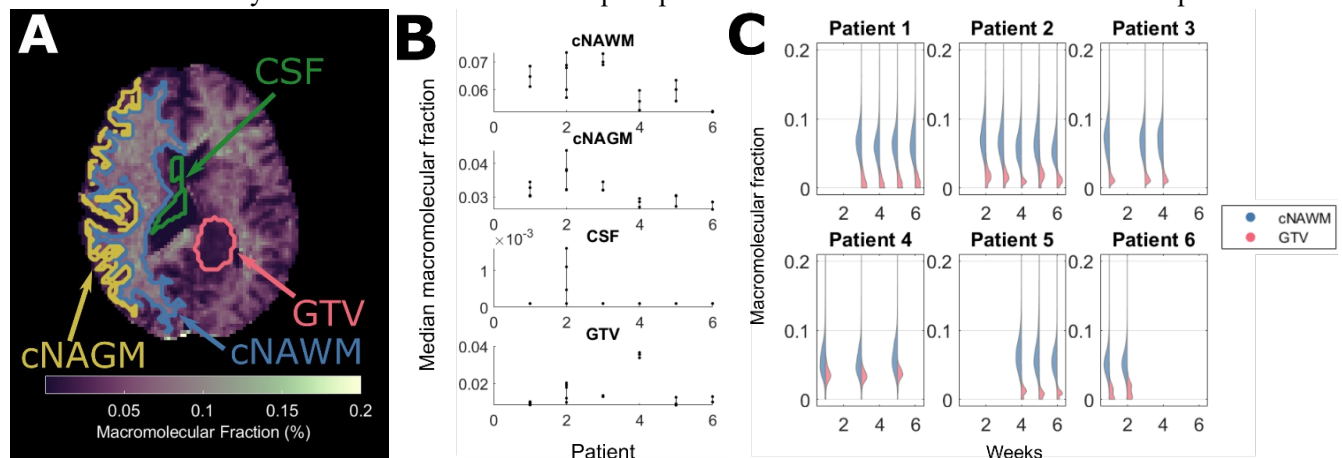


Fig. 1. qMT measurements on the MR-Linac. (A) F map from a single patient. The contours are the ROIs. (B) Median F value in each ROI across all patients. (C) Split violin plot of F value in cNAWM and GTV.

References: 1. Mehrabian et al., *Sci Rep*, 2018. 2. Gloor et al., *Magn Reson Med*, 2008. 3. Zhang et al., *IEEE Trans Med Imag*, 2001. 4. Levesque et al., *Magn Reson Med*, 2010.

Title: Imaging the liver uptake of nanoparticles tailored for magnetic particle imaging

Authors: Nitara E. Fernando, Julia J. Gevaert, Natasha N. Knier, Paula J. Foster

Imaging Research Laboratories, Robarts Research Institute, Canada

Department of Medical Biophysics, University of Western Ontario, Canada

Introduction: In vivo cell tracking can be performed by imaging after the intravenous (iv) administration of superparamagnetic iron oxide (SPIO) nanoparticles. We have used this approach to image tumour associated macrophages (TAMs).¹ Resident macrophages of the reticuloendothelial system (liver, spleen, bone marrow) also take up iv SPIO and this can limit the access of SPIO by TAMs. Polyethylene Glycol (PEG) coating of particles is known to increase blood circulation time and reduce uptake in the liver and spleen by preventing opsonization.² In this study we compare plain and PEG coated SPIO for magnetic particle imaging (MPI). MPI is a new, quantitative imaging modality that directly detects signal from SPIOs. Our short-term goals were to determine if cells can be labeled in vitro with PEG-SPIO and to what extent iv PEG-SPIO is taken up by liver macrophages when compared to a plain coated SPIO. Our long-term goal is to use MPI to measure TAM density in breast cancer to provide a biomarker of tumour aggressiveness.

Methods: Three SPIO preparations were evaluated using MPI relaxometry to assess the particle sensitivity and resolution: (i) Synomag-D (control), (ii) Synomag-D mixed with transfection agents (TAs) (used to enhance in vitro uptake of SPIO) and (iii) Synomag-D-PEG. Next human melanoma cells (A2058) were labeled in vitro by co-incubation. After 24 hours, cells were collected, and magnetic column separation was performed to remove unlabeled cells and to determine labeling efficiency. Perl's Prussian Blue (PPB) was performed to stain cells for iron. MPI was performed on triplicate samples of 5×10^5 labeled cells to determine the iron loading (pg iron/cell). Finally, mice (n=3) were administered SPIOs iv and imaged in vivo at two time points, one day and seven days after injection.

Results: There was no significant difference between particle sensitivity for Synomag-D, Synomag-D (with TAs), or Synomag-D-PEG (A, B). Both the PEGylated and plain Synomag-D produce strong MPI signal. Cells could not be labeled in vitro with plain Synomag-D. Optimal labeling was achieved using Synomag-D and TAs. Cells labeled with Synomag D (with TAs) had ~6 times more iron per cell compared to Synomag D PEG (with TAs) (D). This lower efficiency in vitro (30% lower) was also seen in vivo. MPI of mice showed uptake in the liver for all preparations (E) which decreased over time (F). The liver signal was the lowest after iv Synomag-D-PEG.

Conclusions: In this comparative study, we show preliminary results for PEG coated SPIO having less uptake by liver macrophages. Existing SPIOs for MPI limit in vivo cell tracking utility due to rapid systemic clearance from circulation²; thus, this lower efficiency is important for longer circulation times with the potential to enable quantitative imaging of TAMs.

References:

1. Makela AV, Gaudet JM, Foster PJ. Quantifying tumor associated macrophages in breast cancer: a comparison of iron and fluorine-based MRI cell tracking. *Sci Rep.* 2017 Feb 8;7(1):42109.
2. Jokerst JV, Lobovkina T, Zare RN, Gambhir SS. Nanoparticle PEGylation for imaging and therapy. *Nanomedicine.* 2011 Jun;6(4):715–28

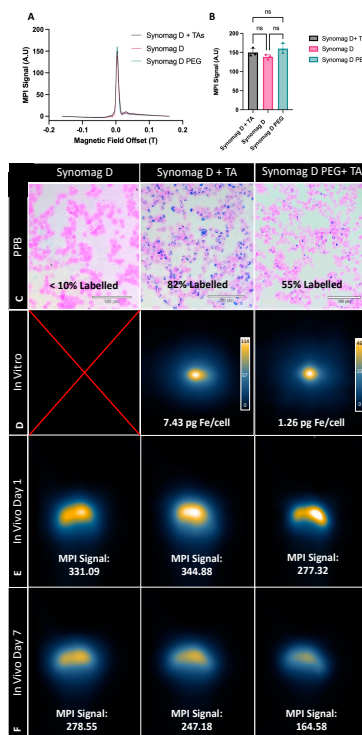


Figure 1. (A) MPI Relaxometry point spread functions of Synomag-D Plain, Synomag-D Plain (with TAs), and Synomag-D PEG. (B) shows that all three conditions have similar sensitivities. A2058 Melanoma cells were labelled with Synomag-D Plain, Synomag-D (with TAs), and Synomag-D PEG (with TAs). (C) shows PPB results before magnetic column where iron in cells is stained blue. In (D), 500 000 labeled cells were imaged using MPI. SPIOs were injected iv in mice and liver signal is seen on day 1(E) and day 7 (F) post injection.

Deep brain stimulation targeting using an open-access anatomical fiducial frameworkAlaa Taha¹, Greydon Gilmore¹, Mohamad Abbass¹, Chris Zajner¹, Abrar Ahmed¹, Ali Hadi¹, Sandy Wong¹,
Ali R. Khan¹, & Jonathan C. Lau¹¹*Robarts Research Institute, Western University, London, Ontario, Canada*

Introduction: Deep brain stimulation (DBS) is a therapeutic procedure that involves the surgical implantation of electrodes at specific regions within the brain to correct aberrant neuronal activity [1]. It is well-established as a treatment for movement and psychiatric disorders [1]. The ability to locate DBS targets in the clinic is not always possible due to: 1) their relatively small size, 2) lack of contrast due to low magnetic resonance imaging (MRI) scanner field strengths (typically 1.5- or 3- Tesla (T) in clinic), and 3) patient motion in the scanner (exacerbated in patients with movement disorders) [2]. A deviation of 2 millimeters (mm) during DBS is enough to create a discrepancy of 60% in clinical improvement [3]. We aim to predict the location of the subthalamic nucleus (STN), one of the most common DBS targets. More specifically, we use machine learning to predict the x, y, and z coordinates of the STN centroid from the coordinates of other salient and reproducible anatomical landmarks which survey the subcortex [4] placed on T1w MRI and highly reproducible even on clinical quality scans [5]. Our ground-truth STN centroid coordinate data was curated from in vivo 7-Tesla (7-T) MRI scans, allowing us to accurately estimate the true anatomical center of the STN [6,7].

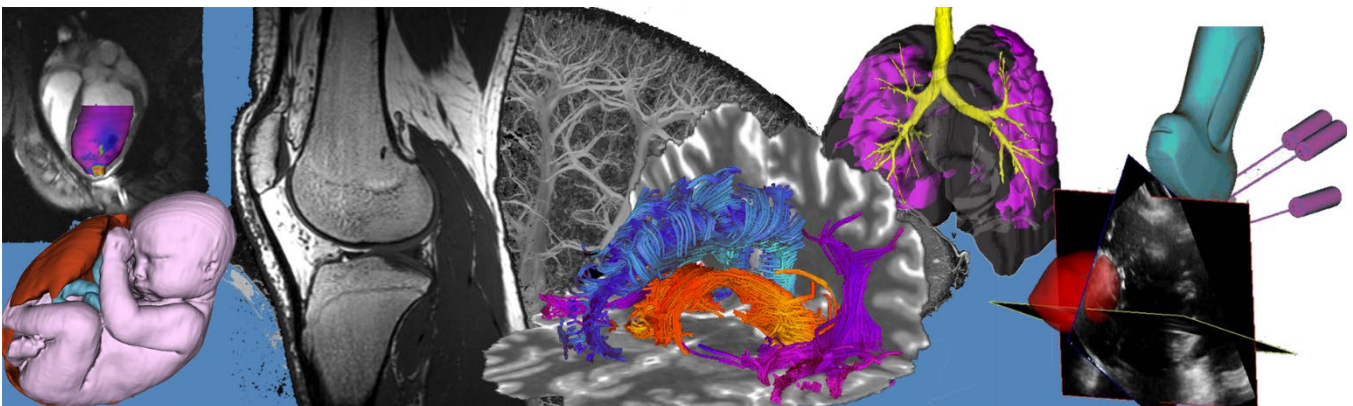
Methods: Thirty-two previously validated anatomical landmarks (also called AFIDs) [4] were applied via 3DSlicer 4.10 on T1w images. These AFIDs were carefully selected salient points in the human brain, shown to have inter-rater localization error of 1-2 mm, even by novice raters across varying MRI field strengths and patients with Parkinson's disease (PD) [5]. Imaging from 32 healthy participants (age: 46.2 ± 13.5 years; 12 female) acquired at Western University on a 7-T head-only scanner (Siemens Magnetom; Germany) was used for training the model. A leave-one-out testing strategy was adopted for assessment of this model. We further validate model results on 7-T imaging acquired from 15 PD patients (age: 60.1 ± 8.2 years; 7 female) and openly release this data. The "ground truth" STN center was computed from the center of mass of segmentations derived from high-resolution (i.e., 7-T MRI) T2w scans in this same dataset. Coordinates of AFIDs were used as features, after principal component analysis (PCA), to predict the anatomical center of STN. Linear and support vector regression (SVR, linear kernel) models were trained. Euclidean distances (EDs) between the ground truth and predicted center on the PD testing dataset (n=15) allowed for clinically relevant assessment of models. Accuracy of our targeting was compared to conventional indirect consensus targeting of STN relative to the mid-commissural point (MCP; $x = \pm 12$, $y = -2$, $z = -4$) via Wilcoxon rank-sum test ($\alpha = 0.05$).

Results: PCA of each of the x, y, and z coordinates yielded a captured variation greater than 90% using top 5 principal components which were selected for subsequent model training. EDs from leave-one-out prediction for left and right STN respectively were: 1) 1.00 ± 0.47 and 1.23 ± 0.59 mm (linear regression) and 2) 1.15 ± 0.55 and 1.03 ± 0.56 mm (SVR). Meanwhile, ED predictions on the PD validation dataset for the left and right STN respectively were: 1) 1.23 ± 0.56 and 1.49 ± 0.76 mm (linear regression) and 2) 1.24 ± 0.60 and 1.46 ± 0.67 mm (SVR). Model predictions are significantly more accurate than indirect consensus coordinate targeting predictions.

Conclusions: This study demonstrates the potential for a novel targeting tool that localizes the STN with millimetric accuracy. This tool 1) can accommodate for inter-patient variability, 2) is agnostic to MRI field strength, 3) uses landmarks on T1w scans (highly reproducible and universal), and 4) is semi-automated. Future directions include further model optimization and prediction of other targets like the zona incerta.

1. Lozano, A. M. *et al.* Deep brain stimulation: current challenges and future directions. *Nat. Rev. Neurol.* 15, 148–160 (2019)
2. Lau, J. C. *et al.* Ultra-High Field Template-Assisted Target Selection for Deep Brain Stimulation Surgery. *World Neurosurg.* 103, 531–537 (2017)
3. Horn, A. *et al.* Lead-DBS v2: Towards a comprehensive pipeline for deep brain stimulation imaging. *Neuroimage* 184, 293–316 (2019)
4. Lau, J. C. *et al.* A framework for evaluating correspondence between brain images using anatomical fiducials. *Hum. Brain Mapp.* 40, 4163–4179 (2019)
5. Abbass, M. *et al.* Application of the anatomical fiducials framework to a clinical dataset of patients with Parkinson's disease. *Brain Struct. Funct.* 227, 393–405 (2022)
6. Keuken, M. C. *et al.* Ultra-high 7T MRI of structural age-related changes of the subthalamic nucleus. *J. Neurosci.* 33, 4896–4900 (2013)

Oral Session 10: Device Development Abstracts



Monitoring Cerebral Oxygenation and Metabolism with Time-Resolved Compressive Sensing Spectroscopy

Natalie C. Li¹, Seva Ioussoufovitch¹, and Mamadou Diop¹⁻³

¹School of Biomedical Engineering, Western University, London, Ontario

²Dept. of Medical Biophysics, Western University, London, Ontario

³Imaging Program, Lawson Health Research Institute, London, Ontario

Introduction: Near-infrared spectroscopy (NIRS) is a safe and portable optical technique that monitors cerebral blood oxygenation and tissue metabolism. Traditional continuous-wave (CW) NIRS can improve real-time detection of cerebral hypoxia in neonates [1]; however, for adults, the more depth-sensitive time-resolved (TR) NIRS is necessary to avoid contamination of the brain signal by thick scalp and skull layers [2]. Unfortunately, there are very few TR-NIRS devices that fulfill the spectral range, resolution, and sampling requirements necessary to accurately quantify changes in blood oxygenation and tissue metabolism simultaneously. Our group recently developed a unique TR-NIRS device that uses compressive sensing to acquire measurements over a wide spectral range with high sampling and resolution while minimizing acquisition time [3]. Here we demonstrate the device's ability to monitor blood oxygenation and metabolism in a homogeneous blood-yeast tissue-mimicking phantom.

Methods: The blood-yeast phantom consisted of an opaque container filled with 0.8% Intralipid (to simulate the scattering properties of tissue), 2 L of phosphate-buffered saline (to mimic physiological pH of 7.4), 2 L of water, and 20 mL of whole blood. The phantom was deoxygenated using 4 g of baker's yeast dissolved in 4 mL of %50 glucose solution and was left for 10 minutes to allow the blood to fully deoxygenate. After 10 minutes, oxygen gas was bubbled into the solution using an air stone to reoxygenate the phantom. Compressive sensing TR-NIRS measurements were acquired every 20 seconds from the surface of the phantom. CW-NIRS measurements were acquired concomitantly using a commercial spectrometer (Maya2000 Pro, Ocean Insight, USA) for comparison. The TR and CW data were analyzed to recover changes in the concentrations of deoxyhemoglobin (Hb) and oxyhemoglobin (HbO), which reflect changes in blood oxygenation, and cytochrome-c-oxidase (oxCCO), which indicates changes in metabolism. TR data was analyzed by fitting late photons [4], while the CW data was analyzed by a fitting routine using the differential form of the modified Beer-Lambert law [5] and its spectral derivatives.

Results: The recovered Hb and HbO changes from the TR data were equal and opposite: Hb increased while HbO decreased when the phantom was deoxygenated, and Hb decreased while HbO increased when the phantom was reoxygenated. The same trend was observed in the CW measurements (Fig. 1). A decrease in oxCCO during deoxygenation and an increase in oxCCO during reoxygenation were observed in both the CW and TR data. Across the plateau, CW measures of hemoglobin and oxCCO changes were on average 24% and 9% higher than the TR measures, respectively.

Conclusions: The observed changes in oxCCO are consistent with changes in yeast metabolism as oxygen availability in the phantom varies. The observed magnitudes of hemoglobin concentration changes are reasonable given the approximate concentration of hemoglobin in the blood. We cannot treat the CW results as the ground truth because CW analysis has its own associated error (mainly due to assumptions made when using the modified Beer-Lambert law [4]), and therefore we do not expect the TR and CW measurements to match perfectly. However, the results are consistent with previous work using multi-wavelength TR-NIRS, which suggests that CW measurements may overestimate TR measurements [6]. In sum, here we demonstrate that we can successfully monitor changes in blood oxygenation and metabolism in a homogeneous phantom. Future work will investigate the sensitivity of the device to changes in the bottom compartment of a 2-layer tissue-mimicking phantom before *in vivo* validation in animal models.

References: [1] Rajaram A., et al. *Biomedical Optics Express* **9**(6), 2588-2603 (2018), [2] Milej D., et al. *Neurophoton* **7**(4), 045002 (2020), [3] Ioussoufovitch S., et al. *Biomedical Optics Express* **12**(10), 6442-6460 (2021), [4] Li, N. and Diop, M. *Biophotonics Congress: Biomedical Optics 2022, Technical Digest Series*, paper JM3A.60 (2022), [5] Kocsis, L., et al. *Phys. Med. Biol.* **51**(5), N61-N98 (2006), [6] Lange, F., et al. *IEEE Journal of Selected Topics in Quantum Electronics* **25**(1), 1-12 (2019)

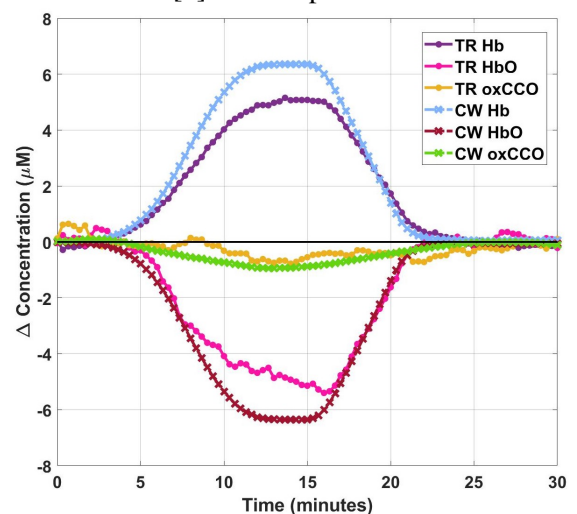


Figure 1: Deoxygenation and reoxygenation began at 3 mins and 13 mins, respectively.

A photothermal therapy guidance platform based on photoacoustic thermometry, diffuse optical tomography, and nanotechnology

Ivan Kosik (University Health Network), **Robert Weersink** (Institute of Biomaterials and Biomedical Engineering, Radiation Oncology, U of Toronto), **Sangeet Ghai** (Princess Margaret Cancer Center), **Andrew Effat** (Institute of Biomaterials and Biomedical Engineering, Radiation Oncology, U of Toronto), **Theodore Husby** (Medical Biophysics, U of Toronto), **Brian Wilson** (Medical Biophysics, U of Toronto)

Introduction: Photothermal therapy (PTT) is a promising minimally invasive cancer treatment alternative where thermal tumor destruction is facilitated by near infrared laser light delivered through thin optical fibers placed inside the target tissue. Our ongoing clinical trial of MRI-guided PTT for prostate cancer shows promise but suffers from complex, indirect and slow imaging guidance, resulting in 30% tumor undertreatment. This is particularly problematic when treatment is near critical structures like the rectal wall where just a few millimeters of overtreatment may lead to serious injury. These drawbacks are contributing to increased recurrence rates due to untreated tumor tissue and as such, are preventing widespread adoption and benefits of PTT.

We are developing a multimodal optical/acoustic-based PTT guidance platform with hand-held capability to specify tumor location, treatment intensity, and treatment response, embodying the 3 main requirements for guiding PTT procedures until now provided only by MRI.

Methods: We constructed a prototype photoacoustic PTT-guidance system as well as a hybrid magnetic resonance-diffuse optical tomography (MR-DOT) prostate-specific probe.

Initial testing of the instrument platform consisted of deep tissue real-time photoacoustic thermal mapping during PTT in tissue mimicking temperature sensitive coagulating phantoms and ex-vivo tissue. Imaging of tumor localizing nanoparticles (Porphysomes) was evaluated in a vascular phantom at clinically relevant depths. Treatment response was assessed with real-time in-patient MR-DOT measurements during PTT for prostate cancer.

Results: The specialized instrument demonstrated real-time (10 Hz) wide-field (5-cm x 5-cm) Porphysome nanoparticle imaging at depths of up to 4 cm. Photoacoustic thermometry during 5-watt and 2-watt PTT in coagulating phantoms and ex-vivo tissue, respectively, was found to be in good agreement with the expected 55 °C coagulation temperature (Figure 1). MR-DOT measurements during in-patient prostate PTT demonstrated >60% coagulation-induced attenuation indicating direct sensitivity to volume of treated tissue.

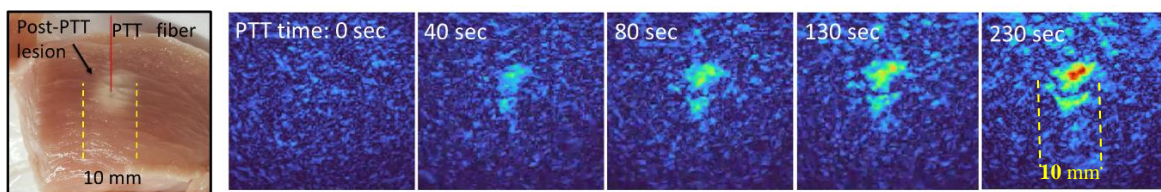


Figure 1. Real-time photoacoustic thermometry in ex-vivo poultry tissue during 2-watt PTT. Photograph shows resulting coagulated tissue lesion after tissue was sectioned at 1.5 cm depth.

Conclusions: This report outlines how the proposed biophotonics-based guidance system uniquely embodies all 3 requirements for PTT, but with direct real-time feedback for efficient functionality and precision. The intuitive precision of real-time hand-held imaging simultaneously specifying tumor location, treatment zone temperature, and volume of treated tissue will spare nearby critical tissues while ensuring complete treatment of the tumor mass. As such, the proposed imaging platform potentially represents both high translational potential as well as very high impact on cancer.

Assessing the Sensitivity of a Full-Head Coverage Near-Infrared Spectroscopy Device (NIRS) to Regional Cerebral Oxygenation Changes

Farah Kamar^{a,b}, Leena Shoemaker^{a,b}, Androu Abdmalak^c, Daniel Milej^{a,b}, Keith St. Lawrence^{a,b}, Mamadou Diop^{a,b}

^a Department of Medical Biophysics, Western University, Canada

^b Imaging Program, Lawson Health Research Institute, Canada

^c Department of Physiology and Pharmacology, Western University, Canada

Presenting Author Email Address: fkamar@uwo.ca

Introduction: Stroke is a serious complication of cardiac surgery, which can lead to long-term cognitive and physical impairments. Cerebral oximetry has become common for neuromonitoring during surgery to detect stroke early and guide subsequent interventions¹. Cerebral oximetry is based on a non-invasive optical imaging technique called near-infrared spectroscopy (NIRS), which is used for monitoring tissue oxygen levels. Commercial cerebral oximeters are equipped with probes that are placed on the forehead; thus, oxygenation decreases in regions supplied by different cerebral arteries go undetected. A potential solution is to use a device with full-head coverage such as the newly developed high-density NIRS system, Kernel Flow². This work aimed to assess Kernel Flow's sensitivity to regional cerebral oxygenation changes using two paradigms: (1) carotid compression (CC), which causes substantial blood flow and oxyhemoglobin (HbO) reductions across the ipsilateral hemisphere, and (2) a finger-tapping exercise that results in localized HbO increases in the contralateral motor cortex.

Methods: Ten healthy volunteers (22-38 years; five females) were recruited for imaging with the Kernel Flow. The Kernel Flow device has 52 sources, and 312 detectors across the whole head, resulting in 2206 potential channels for HbO and deoxyhemoglobin (HbR) measurements of varying source-detector distances (SDD). **Paradigm 1:** CC was performed by applying pressure to the right common carotid artery for 30 s. Channels on the ipsilateral hemisphere at a source-detector distance (SDD) ≥ 25 mm were sorted into four regions (frontal, temporal, occipital, and somatosensory) and differences in the percentage of good quality channels were compared (ANOVA) to assess regional variations in device sensitivity. A group average of HbO and HbR time series was calculated in both the ipsilateral and contralateral hemispheres to compare measured responses. **Paradigm 2:** Righthanded finger tapping was performed in 30-s blocks for a total duration of 6.5 min. A general linear model (GLM) was used to identify significant cortical activation in both HbO and HbR channels ($p < 0.05$ with Bonferroni correction).

Results: **Paradigm 1:** A significantly greater percentage of good-quality channels were found in the ipsilateral frontal region ($p < 0.05$ vs temporal, occipital, and somatosensory). The average times series for the frontal region in both hemispheres are displayed in *Figure 1*. The ipsilateral frontal region displayed expected decreases in HbO and increases in HbR. In the contralateral hemisphere, no HbO or HbR changes were measured during CC. **Paradigm 2:** Five of ten participants had sufficient signal in the somatosensory region for statistical analysis. Of these participants, three showed significant activation in the left primary motor cortex (*Figure 2*).

Conclusion: The expected oxygenation changes for carotid compression was observed best in the frontal region where there is no hair. Expected finger tapping activation was found in subjects with decreased hair density, indicating that hair is a current limitation with the device. In terms of using the system during cardiac surgery, most patients are older and likely have less hair. Future work involves a pilot study using the device in a clinical surgical setting.

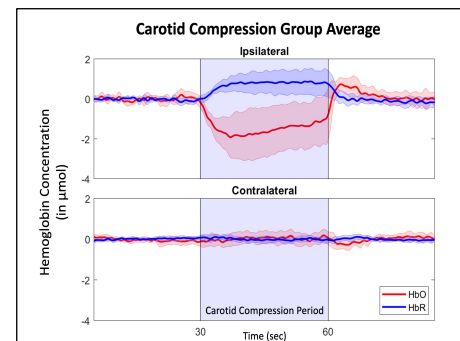


Figure 1: CC group averaged time course from frontal regions of all participants is shown. Shaded region indicates the standard deviation.

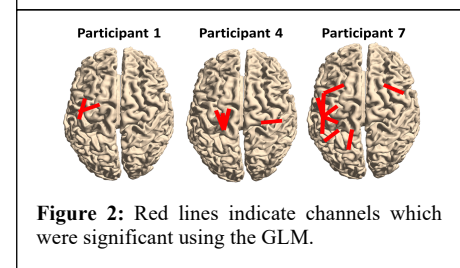


Figure 2: Red lines indicate channels which were significant using the GLM.

1] Murkin, J. M., Adams, S. J., Novick, R. J., Quantz, M., Bainbridge, D., Iglesias, I., Cleland, A., Schaefer, B., Irwin, B., and Fox, S., "Monitoring brain oxygen saturation during coronary bypass surgery: A randomized, prospective study," *Anesthesia and Analgesia* 104, 51–58 (1 2007).

[2] Ban, H. Y., Barrett, G. M., Borisevich, A., Chaturvedi, A., Dahle, J. L., Dehghani, H., Dubois, J., Field, R. M., Gopalakrishnan, V., Gundran, A., Henninger, M., Ho, W. C., Hughes, H. D., Jin, R., Kates-Harbeck, J., Landy, T., Leggiero, M., Lerner, G., Aghajan, Z. M., Moon, M., Olvera, I., Park, S., Patel, M. J., Perdue, K. L., Siepser, B., Sorgenfrei, S., Sun, N., Szczepanski, V., Zhang, M., and Zhu, Z., "Kernel Flow: a high channel count scalable time-domain functional near-infrared spectroscopy system," <https://doi.org/10.1117/1.JBO.27.7.074710>, 074710 (1 2022).

Three-dimensional automated breast ultrasound (ABUS) system toward point-of-care breast cancer screening

Claire K. Park^{1,2}, Tiana Trumppour^{1,2}, Jeffrey Bax², David Tessier², Lori Gardi², Aaron Fenster^{1,2}

¹Department of Medical Biophysics, Schulich School of Medicine and Dentistry, ²Center for Advanced Medical Imaging Technology, Robarts Research Institute, Western University, London, Ontario, Canada

Introduction: Mammography has reduced breast-cancer related mortality through its ability to detect small, early-stage breast cancers. However, the sensitivity of mammography for screening substantially decreases in approximately 40% of all women who have dense breasts. [1] Three-dimensional (3D) automated breast ultrasound (ABUS) is an alternative imaging approach that has been shown to be an effective adjunct for supplemental screening in women with dense breasts. [2] ABUS approaches have enabled multiplanar 3D visualization, improved reproducibility, and overall reduction in operator-dependence. However, most commercially available ABUS systems are relatively costly, and require the installation of a specialized system and workstation, and are not point-of-care, limiting their bedside adoption in clinical practice. This work aims to develop an alternative, cost-effective, dedicated 3D ABUS system with the capability for point-of-care screening. Furthermore, we aim to evaluate its performance with a breast phantom and proof-of-concept healthy female volunteer study.

Methods: We developed a dedicated 3D ABUS system composed of (a) a wearable 3D-printed dam with a replaceable sonolucent membrane to conform to diverse patient sizes and geometries and improve coupling, (b) an adjustable compression assembly to stabilize the breast, and (c) a motorized linear scanner for 3DUS image acquisition, which is adaptable to any conventional linear US transducer [Fig. 1]. [3] 3D ABUS image acquisition involves activating the linear scanner to collect and store 2D US images with a selectable and fixed spatial interval, which are reconstructed in real-time into a 3DUS image. Multi-image registration and fusion of partially overlapping and parallel 3DUS images, acquired with lateral translation of the US transducer, was performed to expand the volumetric field-of-view for whole breast imaging. [4] The 3D ABUS approach was evaluated in a tissue-mimicking breast phantom with visible spherical inclusions (4.76 and 9.53 mm in diameter) to evaluate volumetric reconstruction accuracy. Proof-of-concept dedicated 3D ABUS imaging was performed in a healthy female volunteer and the quality of the 3DUS image was assessed.

Results: In addition to the design and fabrication of the dedicated 3D ABUS system, we demonstrated its ability to acquire high-resolution 3DUS images in tissue-mimicking breast phantoms and a healthy female volunteer. With the breast phantom, absolute and percent volumetric reconstruction errors were $4.40 \pm 4.49 \text{ mm}^3$ and $1.98 \pm 1.34\%$ (N=10) from known volumes, respectively. Dedicated 3D ABUS images were acquired in a healthy female volunteer without the compression assembly, resulting in a high-resolution whole breast 3DUS image with clearly visualized anatomical structures and details, including the skin and glandular tissues [Fig. 2]. The sonolucent membrane stabilized the breast and improved coupling with the skin. Since the 3D ABUS system was affixed directly to the volunteer during image acquisition, minimal artifacts due to free breathing or motion were observed.

Conclusions: The dedicated 3D ABUS device shows potential as an alternative, cost-effective approach for whole breast imaging with the capability for accurate point-of-care imaging. Potential utility exists for widespread adoption for screening breast cancer in increased-risk populations, especially those with dense breasts.

[1] B. L. Sprague et al., *J. Natl. Cancer Inst.*, 106(10) 2014. [2] S. H. Kim, et al. *Korean J. Radiol.*, 21(4) 15–24, 2020. [3] A. Fenster, et al., *US Provisional Patent: 63/335,857*, 2022. [4] C. K. Park, et al. *Med. Phys.* 49(8) 2022.

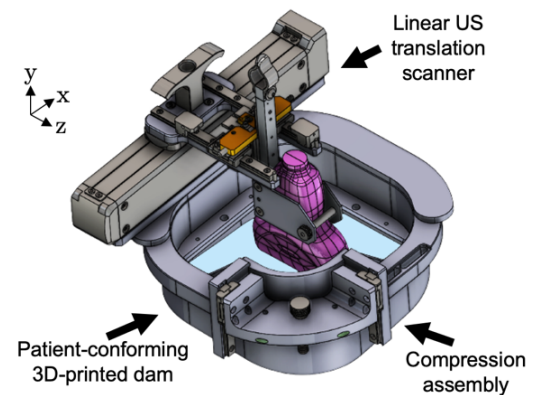


Fig. 1: Computer-aided design (CAD) of the dedicated 3D ABUS system.

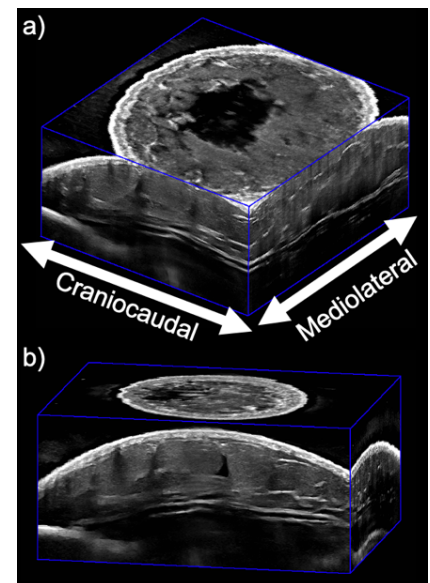
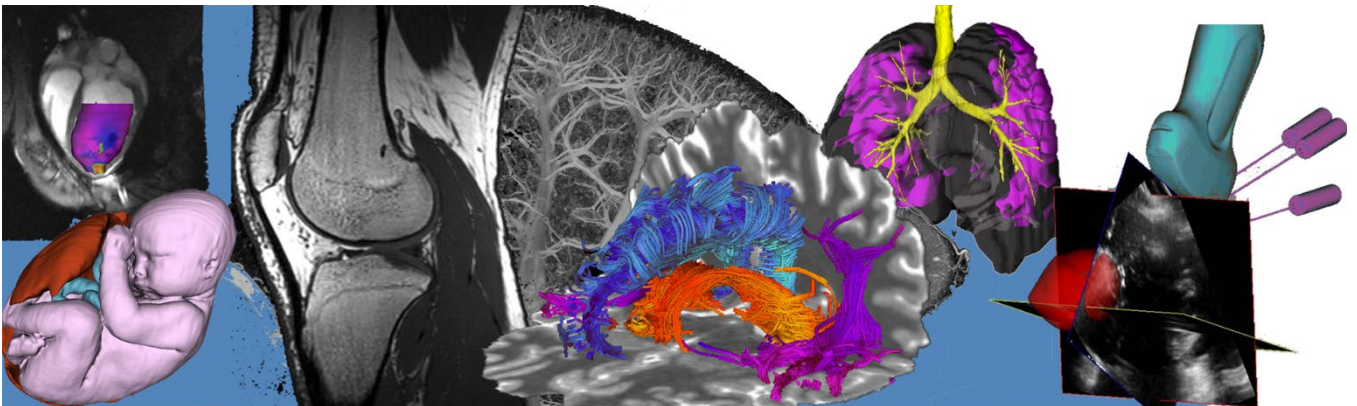


Fig. 2: High-resolution 3D ABUS image of a healthy female volunteer. a) Coronal 3D view showing anatomical directions and b) sagittal view.

Pitch/Poster Session 9: Contrast Agents and Radiopharmaceuticals Abstracts



PET/MRI of microbial therapy in the pig: autoradiography of ⁸⁹Zr-labelled bacteria in the gut¹ Donnelly, SC; ^{1,2,3} Nassar, M; ^{1,4} Rabbath, E; ^{1,5} Fox, MS; ^{1,3,4} Thiessen, J; ^{1,4} Gelman, N; ^{1,6} Jago, H;^{1,6} Sykes, J; ¹ Biernaski, H; ¹ Huston, Y; ^{1,4} Thompson, RT; ^{1,3,4,5} Prato, FS; ^{1,2,7,8} Burton, JP; ^{1,3,4} Goldhawk, DE¹ Imaging Program, Lawson Health Research Institute; ² Microbiology & Immunology, ³ Collaborative Graduate Program in Molecular Imaging, ⁴ Medical Biophysics, ⁵ Department of Physics and Astronomy, Western University; ⁶ Thames Valley Veterinary Services, ⁷ Urology, Surgery, ⁸ Centre for Human Microbiome & Probiotics, St. Joseph's Health Care; London, Canada

Introduction: Microbial therapies such as fecal microbiota transplantation (FMT) have potential in treatment of diseases now associated with perturbations of the intestinal microbiota¹. However, little is known about where these microbes disseminate after their delivery; how long they persist in the body; and what effect these microorganisms have on increased membrane permeability associated with chronic disease. Currently, most microbiota analyses are conducted *ex vivo*, risking potential sample contamination or changes to microbial composition due to collection and storage techniques². To address this, we are using simultaneous positron emission tomography/magnetic resonance imaging (PET/MRI) for *in vivo* assessment of bacterial migration, engraftment, and gut permeability, in real-time. We hypothesize that *ex vivo* tissue autoradiography and staining will validate *in vivo* PET/MRI detection of ⁸⁹Zr-labelled *Lactobacillus crispatus*. Understanding the distribution and retention of ingested microbes is important for more widespread acceptance and implementation of microbial therapies for treatment of disease.

Methods: The commensal *L. crispatus* ATCC33820 was labelled with ⁸⁹Zr-DBN ($t_{1/2} = 78.4$ h; adapting published procedures³); encapsulated in gelatin pills and deposited in the stomach of a healthy pig. Bacterial translocation was monitored 12-14 h post-ingestion by PET/MRI (Siemens Biograph mMR, 3 Tesla), using PET to detect labelled bacteria and MRI for anatomical reference. Post-mortem, tissues were flash-frozen in embedding media and sectioned. To quantify positron or electron emissions by digital autoradiography (Beaquant AI4R), slides were scanned for 4-17 h and analyzed using Beamage 3.3 and ImageJ software. Activity in tissue sections was compared to ⁸⁹Zr standards and corrected for acquisition time and decay.

Results: *In vitro* experiments showed no effect of radiolabelling on bacterial viability with labelling up to 0.005Bq/CFU (data not shown). *In vivo* PET/MRI demonstrates ⁸⁹Zr activity in the pig colon 13 h after administration of capsules (Fig. 1). At 16 h post-ingestion, autoradiography of gastrointestinal tissue sections indicates little or no labelled bacteria in the stomach or small intestines (Fig. 2). However, ⁸⁹Zr activity was noted across areas within the colon, including the cecum (Fig. 2B).

Conclusions: PET/MRI enables *in vivo* tracking of ⁸⁹Zr-labelled bacteria 13h post-ingestion. The absence of PET activity in bone and liver is consistent with chelation of ⁸⁹Zr by DBN covalently bound to bacteria; *in vivo* localization of bacteria in the intestine; and low permeability of the intestinal epithelium in healthy animals. Autoradiography of tissue sections confirms the location of ⁸⁹Zr in the lower gastrointestinal tract. Using electron-capture mode will improve resolution over shorter scans and enable accurate detection of radioactivity. The staining of adjacent tissues sections will also confirm the presence of ⁸⁹Zr-labelled bacteria. *In vivo* imaging will provide longitudinal information on microbial dissemination and persistence following ingestion to aid our understanding of the mechanism behind microbial therapy.

References: ¹Quraishi et al (2017) Aliment Pharmacol Ther, 46, 479. ²Bao et al (2016) Ann Transl Med 5, 33. ³Bansal et al (2015) EJNMMI Res 5:19.

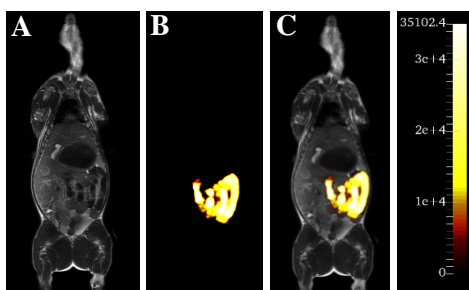


Fig 1. PET/MRI of ingested ⁸⁹Zr-labelled bacteria. Capsules with radiolabelled *L. crispatus* were deposited in the pig stomach and imaged by PET/MRI. Coronal HASTE MRI (A), PET (B), and fused PET/MRI (C) show labelled bacteria in the lower gastrointestinal tract. PET threshold was 5 kBq/cc with scale bar in Bq/cc.

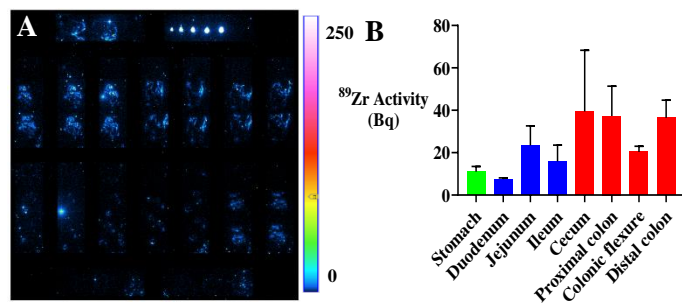


Fig 2. Autoradiography of gut tissues after ingestion of ⁸⁹Zr-labelled *L. crispatus*. Pig tissues were harvested and sectioned for autoradiography. A representative electron-capture 17 h scan (A) indicates standards (top right) and colonic tissue sections. ⁸⁹Zr positron emissions were quantified over 12 h and decay corrected to time of sacrifice (B). Bars are mean activity \pm SEM (green, stomach; blue, small intestines; red, colon; n = 10-18 sections / tissue).

SPAAC Incorporation of Fluorine into FC131 Analogues Towards Discovery of CXCR4 RadiopharmaceuticalsJulia R. Mason¹, Leonard G. Luyt^{1,2}¹Department of Chemistry, University of Western Ontario, London, ON, Canada, ²London Regional Cancer Program, London, ON, Canada**Introduction:**

The CXCR4 receptor could play an important role in cancer imaging and targeted therapy due to its high expression in numerous tumours, including breast, prostate, lung, and colon cancers. The cyclic peptide FC131 binds the CXCR4 receptor with high affinity but has yet been used for the development of a clinical ¹⁸F-PET imaging agent. This peptide provides a targeting entity that we propose to couple to an imaging moiety through strain-promoted alkyne-azide cycloaddition (SPAAC) click chemistry, to develop a ¹⁸F-labelled PET imaging agent. The approach is to incorporate a fluorine-containing azadibenzocyclooctyne imaging moiety (F-ADIBO) onto FC131 at a position which does not interfere with receptor binding.¹ A library of F-ADIBO FC131 analogues were synthesized through modifications to stereochemistry, *N*-methylation, side-chain length, and linker composition. A ¹⁸F-labelled cyclooctyne prosthetic group compatible with SPAAC would provide for translation into peptide PET cancer imaging agents.

Methods:

A non-radioactive fluorine-modified azadibenzocyclooctyne (F-ADIBO) was synthesized and conjugated to peptides through SPAAC.² The library of FC131-based peptides was synthesized using standard Fmoc solid-phase peptide synthesis and were evaluated for binding toward the CXCR4 receptor through a competitive radioligand displacement binding assay using U87 CD4+CXCR4+ cells.

Results:

A library of fluorine-containing FC131-based cyclic peptides was synthesized, purified by preparative HPLC, and characterized by high-resolution mass spectrometry. Binding affinity, including ligand-target interaction influenced by the imaging moiety, was measured through a competitive radioligand binding assay using a U87 cell line transfected to overexpress CXCR4.³ Synthesized analogues in which the side-chain is directly conjugated to F-ADIBO through the triazole, with varying D and L stereochemistry, side-chain length, and *N*-methylation, demonstrated a substantial decrease in affinity compared to FC131. Further analogues extending the space to the F-ADIBO imaging moiety through linker length and composition to incorporate hydrogen-bonding moieties, displayed significantly improved affinity towards the receptor. Successful high-affinity peptide binders are subsequently being translated into PET cancer imaging probes by substituting the non-radioactive ¹⁹F-prosthetic group with its ¹⁸F-analogue.

Conclusions:

A library of fluorine-containing FC131-based peptides was synthesized to target the CXCR4 receptor, a cancer biomarker of interest. Screening of initial analogues provided fundamental information on binding interactions, demonstrating that direct attachment of the imaging moiety results in a loss of receptor affinity. Modifications to increase the space between the peptide and F-ADIBO and incorporation of hydrogen bonding/charges displayed significantly improved binding affinity. Successful high-affinity peptide binders are currently being translated into cancer imaging probes by substituting the non-radioactive ¹⁹F-prosthetic group with its ¹⁸F-analogue for the application of ¹⁸F-PET imaging in a clinical setting. This study demonstrates the straightforward incorporation of the small molecule imaging moiety and its ability to functionalize the FC131 peptide core towards the discovery of PET radiopharmaceuticals for cancer imaging.

References: (1) Demmer, O.; Gourni, E.; Schumacher, U.; Kessler, H.; Wester, H.-J. *ChemMedChem*. **2011**, *6*, 1789–1791. (2) Murrell, E.; Kovacs, M. S.; Luyt, L. G. *ChemMedChem*. **2018**, *13*, 1625–1628. (3) Björndal, Å.; Deng, H.; Jansson, M.; Fiore, J. R.; Colognesi, C.; Karlsson, A.; Albert, J.; Scarlatti, G.; Littman, D. R.; Fenyö, E. M. *J. Virol.* **1997**, *71*, 7478–7487.

A Monte Carlo Voxel Dose Calculation Method for Cancer Radiotheranostics

*Thanh Tai Duong¹, *Danny De Sarno¹, Martin Martinov⁴, Hatim Faker², Kevin Chung^{1,3}; Glenn Bauman^{2,3}, Rowan Thomson⁴, Ting-Yim Lee^{1,2,3}

¹Imaging Group, Robarts Research Institute; ²Oncology & ³Medical Biophysics Departments, University of Western Ontario, London, Ontario; ⁴Physics Department, Carleton University, Ottawa, Ontario

*Contributes equally to this work

Introduction

Radiotheranostics is a new cancer treatment technique wherein a targeting molecule is first labeled with a diagnostic radionuclide (e.g. ¹⁸F, ⁶⁸Ga or ⁸⁹Zr) to check its uptake in the tumor with PET imaging followed by labeling with a therapeutic radionuclide (e.g. ¹⁷⁷Lu or ²²⁵Ac) for treatment. This technique has shown efficacy in treating neuroendocrine and more recently prostate tumor. Despite the success, a significant limitation of radiotheranostics as currently practiced is the lack of treatment planning where every patient is given the same radionuclide dose without regard to the radiation dose delivered to the tumor and organs at risk (OARs). We have developed a Monte Carlo voxel dose calculation program to enable the calculation of the radiation doses based on the time integrated activity (TIA) in the tumor and OARs derived from a diagnostic PET study. The aim of this study was to determine the variations in radiation doses among patients given the same radionuclide dose.

Method

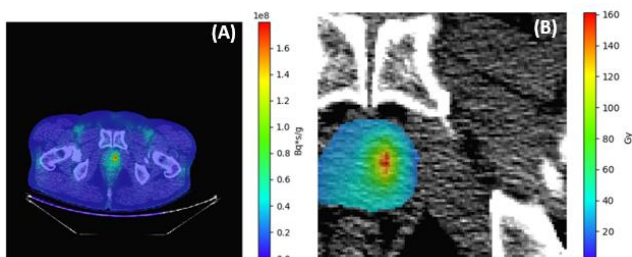
Data from six prostate cancer patients selected from IGPC-02 database were used to demonstrate our technique. Each patient had a PET/CT study with 325MBq ¹⁸F-DCFPyL, a ligand to PSMA receptors on prostate cancer cells. The PET study was acquired as a dynamic study over 22 min from which the Logan distribution volume (LDV) was derived with bespoke graphical analysis method. Under the assumption that the distribution of ¹⁸F-DCFPyL was similar to ¹⁷⁷Lu-PSMA-617, the ¹⁷⁷Lu TIA map was calculated as the LDV map scaled by the AUC of the decayed femoral artery time activity curve extrapolated to 5 half-lives of ¹⁷⁷Lu (33 days). With the ¹⁷⁷Lu TIA map as well as the tissue density and elemental composition maps from the CT scan, a Monte Carlo simulation program based on EGSnrc was developed to score radiation dose imparted to the prostate tumor, overall prostate and OARs, in particular bone marrow in femurs. The tumor was segmented from the ¹⁸F-DCFPyL study with a threshold of 30% SUV_{max}. Physical radiation dose was converted into BED using standard radiobiological linear quadratic model with corrections for DNA repair and clonal repopulation.

Results

Figure (A) shows the TIA map and Figure (B) shows the voxel BED map for a 3.5 mm slice through the prostate tumor of a IGPC-02 patient (#31). Table shows the mean BED in the prostate tumor, overall prostate, and bone marrow in the left and right femur for all six IGPC-02 patients included in this study assuming the 325 MBq of ¹⁸F-DCFPyL administered distributed in the same way as ¹⁷⁷Lu-PSMA-617. The minimum and maximum BED for prostate tumor and overall prostate differed by 3.3 and 1.8 times respectively while that for bone marrow in both left and right femur was 4.3 times.

Discussion

An end-to-end pipeline has been developed for the calculation of patient specific 3D voxel radiation dose distribution from a dynamic PET/CT study. The preliminary results from six prostate cancer patients show that the one size-fit-all radionuclide dosing can result in a large intersubject difference in radiation dose for the tumor and normal tissue and OAR. This difference may lead to under- and/or over-dosing of the tumor and OARs respectively. Both are detrimental to the outcome of cancer radiotheranostics and argue for the patient specific radiation dose calculation as we have developed herein.



IGPC-02 Patient	Mean BED from 0.33 GBq ¹⁷⁷ Lu-PSMA-617 (Gy)			
	Tumor	Prostate	Femur R	Femur L
26	1.84	0.80	0.07	0.07
28	0.78	0.60	0.06	0.06
29	1.24	0.83	0.13	0.13
31	0.96	0.60	0.06	0.06
32	0.60	0.53	0.05	0.05
33	0.55	0.45	0.03	0.03

Radiometallation of Monoclonal Antibodies Relevant to Immune Checkpoint Therapy

Mojmír Suchý^{a,*}, Lara Gerhardt^c, Rene Figueredo^c, Saman Maleki^{c,d}, Ting-Yim Lee^{a,b} and Michael S. Kovacs^{a,b}

^aLawson Health Research Institute, St. Joseph's Hospital, London, ON, Canada ^bFaculty of Medicine & Dentistry, Western University, London, ON, Canada ^cDepartment of Oncology, Western University; London, Ontario, Canada ^dLondon Regional Cancer Program, Lawson Health Research Institute; London, Ontario, Canada. *Presenting author

Introduction: Nivolumab is an immune checkpoint inhibitor (ICI) used in cancer therapy. Nivolumab is a human-specific monoclonal antibody that interacts with PD1 protein expressed on the surface of activated/exhausted T-cells, thus preventing their inactivation by irreversible binding to PD-L1 ligands expressed on the cancer cells surface.¹ While being used to treat different types of solid tumours, ICIs are associated with unpredictable outcomes. The presence of T-cells in the tumor is a predictive biomarker of response to nivolumab in various cancers, therefore, nivolumab was radiolabelled with [⁸⁹Zr]Zr oxalate for PET imaging. Radiolabelling of nivolumab and murine specific PD-L1-targeted antibody with a β -emitter [¹⁷⁷Lu]LuCl₃ was also carried out with the aim to investigate the influence on ICI therapy applicable to murine models of cancer.⁵

Methods: [⁸⁹Zr]Zr oxalate was produced by irradiation of ⁸⁹Y-based solid targets. [¹⁷⁷Lu]LuCl₃ was purchased from a commercial supplier. Conjugation of nivolumab with bifunctional chelators *p*-SCN-Bn-DFO (⁸⁹Zr) or *p*-SCN-Bn-DOTA and *p*-SCN-Bn-CHX-A-DTPA (¹⁷⁷Lu) was carried out using literature protocol.² Purity and identity of the conjugates was verified by SDS-PAGE and HR-ESI-MS. Radiolabelling with both isotopes was performed in acetate buffer at pH ~ 7.0 (⁸⁹Zr) or 5.5 (¹⁷⁷Lu), followed by purification using PD-1 desalting columns. Purity and identity of the radiolabelled conjugates was verified by iTLC and HPLC. An immunoreactivity assay was developed to evaluate the binding ability of the nivolumab conjugates to their target.

Results: Conjugation of nivolumab with bifunctional chelators proceeded smoothly, all conjugates exhibited reasonable purity. Radiolabelling of DFO-nivolumab conjugate with [⁸⁹Zr]Zr oxalate was performed in repetitive manner (*n* = 8) aiming at reproducibility of the methodology. Required specifications,³ radiochemical yield > 55%, specific activity > 37 MBq/mg were achieved in all instances. HPLC and iTLC traces associated with [⁸⁹Zr]Zr-DFO-nivolumab revealed that the presence of unchelated [⁸⁹Zr]Zr oxalate was consistently < 1%. Work is underway to adopt the protocol for nivolumab radiolabelling to meet the criteria for GMP-level production⁴ involving the conjugation of nivolumab with bifunctional chelators and radiolabelling in an air-controlled environment including extensive sterile filtration. Radiolabelling methodology suitable for [¹⁷⁷Lu]LuCl₃ was developed using cheaper and easily accessible nivolumab, the methodology was found applicable to radiolabelling of murine-specific PD-L1-targeted antibody.⁵ DOTA chelator was found to provide superior results, compared to DTPA. A work toward boosting the specific activity of ¹⁷⁷Lu-labelled antibodies to achieve the therapeutic level (~ 185 MBq/mg) was also completed successfully. This is a proof of principle study focused on the development of chemistry suitable for the generation of corresponding radiolabelled antibodies with different radioisotopes. The radiolabelling methodologies providing corresponding modified antibodies in sufficient specific activities suitable for use *in vivo* have been developed successfully; *in vivo* studies are planned to be performed within first half of 2023. If available, preliminary results of these studies will also be presented and discussed.

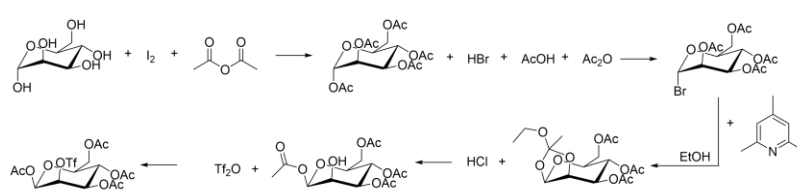
Conclusions: In conclusion we have developed a robust and reliable methodology for the conjugation of nivolumab to various bifunctional chelators suitable for different types of radiometals (⁸⁹Zr, ¹⁷⁷Lu). Consistent high-yielding radiolabelling of DFO-nivolumab conjugate was achieved and the product met some criteria consistent with GMP-level production (radiochemical yield, radiochemical purity, specific activity). Labelling of nivolumab and PD-L1-murine specific antibody with ¹⁷⁷Lu was also developed providing radiolabelled antibodies possessing specific activities compatible with the requirements for their therapeutic application.

References: (1) *Hum. Vaccines Immunother.* **2016**, *12*, 2219-2231. (2) *Nat. Protoc.* **2010**, *5*, 739-743. (3) *Nat. Med.* **2010**, *24*, 1852-1858. (4) *Oncotarget* **2018**, *9*, 17117-17132. (5) *Theranostics* **2021**, *11*, 304-315.

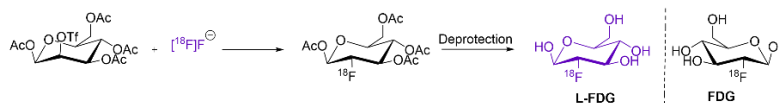
Automated Radiosynthesis of the L-isomer of Fluorodeoxyglucose (FDG)Ghazaleh Takalloobanafshi^{1,4}, Elmer Soto⁴, Michael S. Kovacs^{2,4}, and Justin W. Hicks^{3,4}*Departments of ¹Chemistry, ²Medical Imaging, ³Medical Biophysics, Western University and ⁴Cyclotron and Radiochemistry Facility, Lawson Health Research Institute, London, ON*

Introduction: The most used positron emission tomography (PET) radiopharmaceutical is fluorodeoxyglucose (FDG) radiolabeled with fluorine-18 (¹⁸F; $t_{1/2} = 109.8$ min). Common uses include detecting hypermetabolism in cancer cells and quantifying changes to metabolic rates in neurological disorders (i.e. epilepsy and dementia). The unnatural L-isomer of FDG retains the same chemical properties but is not a substrate for the glucose transporter or hexokinase in healthy tissue. There is some evidence that cancer cells will absorb this L-isomer of glucose to supply their high demand for fuel.[1] Furthermore, a PET tracer for L-glucose could be useful in determining non-specific glucose interactions with tissue *in vivo* as well as changes to tissue permeability. L-[¹⁸F]FDG has been previously synthesized to investigate the non-specific uptake of FDG *in vivo* but has not advanced beyond a preliminary study.[2] Our goal was to reproduce this original study and improve upon the practical radiosynthesis.

Methods: Scheme 1 shows the method to synthesize the precursor for L-[¹⁸F]FDG.[3] The resulting white solid was dissolved in dry acetonitrile and this solution substituted for the D-isomer precursor on a pre-assembled FDG cassette used on a purpose built FDG synthesizer (GE FASTlab) (Scheme 2). Following the preset sequence, L-[¹⁸F]FDG was prepared as an injectable solution in citrate buffered saline. The quality of the radiotracers was assessed according to the FDG product monograph using approved quality assurance procedures at our facility.

**Scheme 1. L-FDG precursor synthesis from L-mannose**

Results: The precursor synthesis gave a white solid with an 5% overall chemical yield (in line with previous reports). All spectroscopic analysis matched reported values. The commercial FASTlab cassette was easily modified to include our in-house precursor and radiolabeling gave enough material (42 GBq; 57% non-decay corrected yield) for multiple human PET scans. From a quality perspective, we obtained results from identical tests used to release D-[¹⁸F]FDG for clinical diagnostics: radiochemical purity (>95%), identity (matched FDG standard on TLC), half-life (109 min), pH (6.0), and appearance (clear, colourless, particulate free). As we are continuously preparing this radiotracer for preclinical studies, up-to-date data will be presented. Two iv injections of L-[¹⁸F]FDG in rats with implanted glioblastoma have been completed, showing remarkably high signal:noise in the tumor compared to the D-isomer (cannot disclose figures at this time).

**Scheme 2. Radiosynthesis of L-[¹⁸F]FDG. Mirror image of [¹⁸F]FDG shown to illustrate chirality**

Conclusions: With no difference chemically, the production of L-[¹⁸F]FDG gave similar yield and quality results to D-FDG, which our site reliably produces every morning. If further imaging studies validate our early proof-of-concept results, clinical translation of L-[¹⁸F]FDG can be readily pursued.

References: [1] K Ono, *Cancer* 2020, 12, 850. [2] J Meng, *Nucl Med Biol* 1994, 21, 633-40. [3] T Toyokuni, *Mol Imaging Biol* 2004, 6, 324-30.

Integrating Tc-99m in small molecules for improving access to Alzheimer's disease imaging

Ghazaleh Takalloobanafshi,^{a,b} Clara Duquette-Evans,^c Leonard Luyt,^{a,c} and Justin W. Hicks^{b,c}
^aDepartment of Chemistry, Western University, London, ON, Canada, ^bCyclotron and Radiochemistry Facility, Lawson Health Research Institute, London, ON, Canada, ^cDepartment of Medical Biophysics, Western University, London, ON, Canada.

Introduction: Alzheimer's disease (AD) and related dementias have a considerable expansion which is concentrated in low- and middle-income regions. These regions have poor access to advanced imaging technology however, barriers likewise exist for rural and remote residents of wealthy nations. Positron emission tomography (PET) is the gold standard for AD imaging and several radiotracers are available if patients have access to a PET scanner. Single photon emission computed tomography (SPECT) is more widely available and cheaper than PET. Additionally, SPECT radiotracers are cheaper to produce (does not require a cyclotron to produce the radionuclides and radiolabeling can occur in nuclear medicine lab). This project objective is to prepare SPECT radiotracers for AD to exploit the lower cost and greater availability. Specifically, we will prepare technetium-99m (^{99m}Tc; E_γ = 141 keV, t_{1/2} = 6.01 h) based radiotracers as this is the most common SPECT radionuclide. Numerous potential ^{99m}Tc agents have been synthesised that meet the in vitro evaluation requirements of an AD imaging probe but none have met the requirement for adequate in vivo brain penetration based on the inability to penetrate the blood-brain barrier (BBB), which is the main bottleneck in the development of all brain therapies and diagnostics.^{1,2} We are using a promising molecular scaffold to overcome the poor BBB permeability.

Methods: For radiolabeling this scaffold with ^{99m}Tc, ferrocene precursors were prepared. Targeting vectors attached to ferrocene were chosen based upon reported high affinity to amyloid-beta aggregates with many forming the backbone of regulator approved, PET radiotracers. As non-radioactive Tc does not exist, in vitro Aβ aggregates binding assays were conducted with Re-congeners. The so-called “standards” are fully characterized spectroscopically and used to identify ^{99m}Tc-labeled radiotracers. Ferrocenes as precursors, are reacted with Mn(CO)₅Br and [^{99m}Tc]NaTcO₄ through a double-ligand transfer reaction to give ^{99m}Tc-labeled radiotracer candidates. Stability of radiolabeled products is determined in saline and rodent plasma at 37°C in addition with transmetalation conditions using cysteine and histidine solutions. Lipophilicity is determined as the partitioning coefficient between n-octanol and phosphate- buffered saline via a shake-flask method. In vitro binding affinity measurements for amyloid fibrils is underway.

Result: Eight Re complexes as standards have been synthesized in moderate yield (25-50%). Re-1 and Re-2 were replicates from the literature² while others are novel. Radiolabeling via the double-ligand transfer gave high radiochemical yield (>90%) and purity after HPLC separation (>95%). We have so far replicated the in vitro binding affinity of Re-1², thus validating the previous results and confirming the CpTc(CO)₃ group is a promising scaffold for imaging amyloid. Work continues to evaluate our novel derivatives and will be reported during the symposium.

Conclusion: By expanding the catalogue of targeted ^{99m}Tc-based radiotracers, we will reduce burdens to access imaging diagnosis and therapy. This will 1) improve diversity in drug trials, 2) increase access to therapies with prerequisite molecular imaging, 3) permit more participation from historically underrepresented groups in clinical imaging studies of disease pathology, and 4) decrease travel from home for diagnosis or treatment.

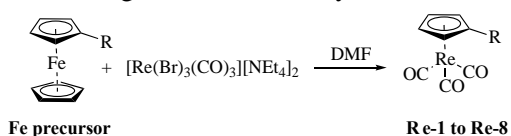


Figure 1. General preparation of Re-congeners. R = amyloid targeting scaffolds

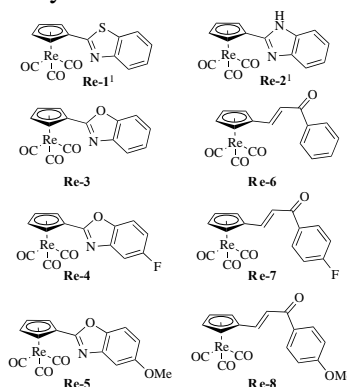


Figure 2. Re-congeners as standards for doing binding assay and to verify ^{99m}Tc labeling.

1. Takalloobanafshi, G., Kukreja, A. & Hicks, J. W. *Front. Nucl. Med.* **2**, 963698 (2022). 2. Sagnou, M. *et al. J. Med. Chem.* **62**, 2638–2650 (2019).

Radiotracer development for imaging the endocannabinoid system with PET

Anna Pees^a and Neil Vasdev^{a,b}

^a Azrieli Centre for Neuro-Radiochemistry, Brain Health Imaging Centre, Centre for Addiction and Mental Health (CAMH), Toronto, ON, Canada

^b Department of Psychiatry, University of Toronto, Toronto, ON, Canada

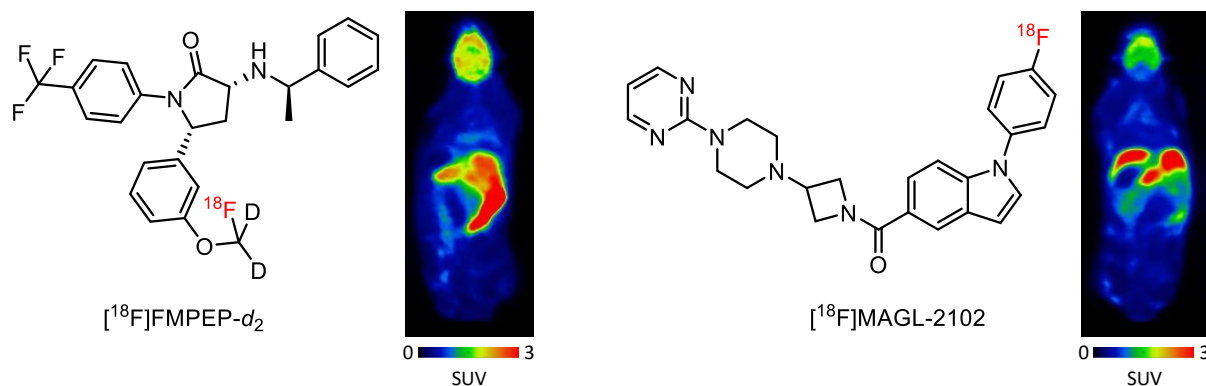
Introduction. Two promising PET radiotracers for imaging the endocannabinoid system (ECS) are [¹⁸F]FMPEP-*d*₂, which targets the cannabinoid receptor type-1 (CB1), and [¹⁸F]MAGL-2102, that targets the enzyme monoacylglycerol lipase (MAGL).^{1,2} [¹⁸F]FMPEP-*d*₂ is currently synthesized via a low-yielding multi-step procedure requiring specialized synthesis apparatus, and no automated synthesis procedure has been reported for [¹⁸F]MAGL-2102, limiting their translation for human use.³⁻⁵ The aim of this project is to explore new synthesis strategies for [¹⁸F]FMPEP-*d*₂ as well as to automate the synthesis of [¹⁸F]MAGL-2102, and to validate both tracers for human use (first-in-Canada ([¹⁸F]FMPEP-*d*₂) and -worldwide ([¹⁸F]MAGL-2102)). Furthermore, we aim to study the involvement of the ECS in Alzheimer's disease (AD) by PET imaging with these radiotracers in a transgenic AD mouse model and autoradiography of murine and human AD brain tissue.

Methods. [¹⁸F]FMPEP-*d*₂ and [¹⁸F]MAGL-2102 were synthesized on an automated radiosynthesis module (GE Tracerlab FX2N). For [¹⁸F]FMPEP-*d*₂, dry [¹⁸F]fluoride was reacted with ditosylmethane-*d*₂ (5 mg) and the precursor PPEP (5 mg) in CH₃CN for 10 min at 80 °C. For [¹⁸F]MAGL-2102, dry [¹⁸F]fluoride was reacted with the boronic acid precursor (3 mg) and Cu(Py)₂(OTf)₂ (7 mg) in n-BuOH/DMAc for 20 min at 110 °C. After quenching, the respective product was purified by reverse phase HPLC and formulated in ethanolic buffered saline. PET-CT images in healthy mice were dynamically acquired over 120 min.

Results. [¹⁸F]FMPEP-*d*₂ was synthesized in a simple and fast one-pot reaction on a commercially available synthesis module with a radiochemical yield (RCY) of 7±2% (decay-corrected, n=10) within 65 min. The synthesis of [¹⁸F]MAGL-2102 was successfully automated with RCYs of 11±3% (n=2). For both tracers, the radiochemical purity was >95%. Preliminary PET imaging in healthy mice showed moderate brain uptake (>1 SUV) and relatively slow tracer kinetics for both tracers, which is consistent with literature findings. Further studies will be performed in AD (APP^{NLGF}) and control mice (m/f) at 4, 8 and 12 months as well as autoradiography experiments in AD mouse (CRND8 and APP^{NLGF}) and human AD tissue.

Conclusions. The syntheses of [¹⁸F]FMPEP-*d*₂ and [¹⁸F]MAGL-2102 were successfully automated and their validations for human use are underway. PET imaging studies with both radiotracers are promising in normal rodents and preclinical studies will guide their application for imaging in AD.

References. [1] Varlow, C. *et al.*, ACS Chem. Neurosci., 2020, 11, 1855-1862; [2] Hou, L. *et al.*, J. Med. Chem., 2021, 64, 123-149; [3] Donohue, S.R. *et al.*, J. Med. Chem., 2008, 51, 5833-5842; [4] Lahdenpohja, S. *et al.*, J. Label. Compd. Radiopharm., 2020, 63, 408-418; [5] Rong, J. *et al.*, J. Med. Chem, 2021, 64, 14283-14298.



Solid-supported preparation of [^{18}F]tetrafluoroborate ([^{18}F]TFB) for Reporter Gene PETJohn Diemert¹, Olujide Oyeniran^{1,3}, Michael S. Kovacs¹⁻³, Justin W. Hicks^{1,3}¹Departments of Medical Biophysics, ²Medical Imaging, Western University and³Cyclotron and Radiochemistry Facility, Lawson Health Research Institute, London ON

Introduction: Reporter gene imaging with positron emission tomography (PET) has long been used to track cells implanted into living organisms to determine their fate. One of the best genes for this purpose is the sodium/iodide symporter (NIS). The gene is normally expressed in human thyroid and stomach tissue, thus does not present an immunological risk.[1] Tetrafluoroborate (TFB) is an iodide mimicking anion. Using a reported production method,[2] we have prepared [^{18}F]TFB for our site, however, the procedure requires harsh and toxic chemicals, highly corrosive boron trifluoride (BF_3) gas, and is difficult to automate on common automated synthesizers. Purchasing premade solutions of BF_3 -tetrahydrofuran avoids the BF_3 gas, but this material is susceptible to deactivation by moisture, leading to poor reproducibility and frequent failed productions.

To address the shortcomings of the reported method, we hypothesized the reaction between [^{18}F]fluoride and BF_3 could be achieved on a solid support. We found a polyvinylpolypyrrolidone- BF_3 (PVPP- BF_3) polymer wherein the BF_3 should remain reactive to fluorination.[3] This non-corrosive material will eliminate the need for unstable and toxic BF_3 reagents. Using this polymer material, we will develop an improved, mild synthesis of [^{18}F]TFB using only aqueous solvents. Once optimized, the process will be automated on widely available commercial synthesizers, ready for human administration.

Methods: PVPP- BF_3 is prepared by stirring PVPP and BF_3 in diethyl ether together for one hour at ambient temperature. After filtering and washing with dichloromethane, the polymer is dried overnight under vacuum to remove any solvents. [^{18}F]fluoride is prepared by $^{18}\text{O}(\text{p},\text{n})^{18}\text{F}$ reaction in our medical cyclotron. The aqueous fluoride is concentrated on an anion exchange cartridge (Waters QMA) and eluted onto the PVPP- BF_3 using a K_2CO_3 solution. The eluent is then neutralized with sodium hydroxide (1 M aqueous) and passed through a neutral alumina bed to capture fluoride, any BF_3 the polymer may have shed, and [^{18}F]TFB. The [^{18}F]TFB is then selectively eluted with sterile saline while BF_3 and fluoride are retained on the alumina. Produced [^{18}F]TFB is tested for radiochemical purity, pH, appearance, endotoxins, and identity according to approved quality assurance procedures at our facility.



Figure 1. Schematic of [^{18}F]TFB production

Results: Somewhat surprisingly, we were able to convert approximately 50% of the fluoride from the cyclotron into [^{18}F]TFB by just washing the target solution over a column of PVPP- BF_3 . After some modification to improve purity, we have produced several batches of [^{18}F]TFB in sufficient yield for clinical administration (0.5 – 1 GBq; 30 – 50% non-corrected yield) with >95% radiochemical purity. We continue to optimize yields and increase the scale of production. An accurate assessment of molar activity is currently under development and will be reported. The total reaction takes less than 10 minutes when conducted by hand and we anticipate the automated procedure will be equally rapid.

Conclusions: The PVPP- BF_3 polymer appears to remain reactive to aqueous fluoride. This important finding will permit the use of a solid-supported precursor with extended shelf-life compared to BF_3 -THF solutions or eliminate the need to dangerous BF_3 gas. In a field often afraid of water in their reactions, our completely aqueous, environmentally friendly procedure stands out. Additionally, the process has been highly reproducible, which is crucial for conducting highly coordinated PET studies. Our next step is to automate this process such that any cyclotron can have a turn-key procedure to producing [^{18}F]TFB, greatly expanding the use of this radiotracer for translation, cell tracking PET.

References: [1] JJ Kelly et al. *Science Advances* 2021, 7, eabc3791. [2] H Jiang et al. *J Nucl Med* 2016, 57, 1454-9. [3] M Mokhartay et al. *Comptes Rendus Chimie* 2012, 15, 530-2.

Comparison of [^{18}F]FEOBV and [^3H]VAT for imaging VACHT in neurodegenerative diseases

Faustine d'Orchymont^a, Andrea Narvaez,^a Roger Raymond,^a Stephen Krause,^b and Neil Vasdev^{a,c}

^a Azrieli Centre for Neuro-Radiochemistry, Brain Health Imaging Centre, Centre for Addiction and Mental Health (CAMH), Toronto, ON.

^b Eisai, Inc., Woodcliff Lake, NJ, USA.

^c Department of Psychiatry, University of Toronto, ON.

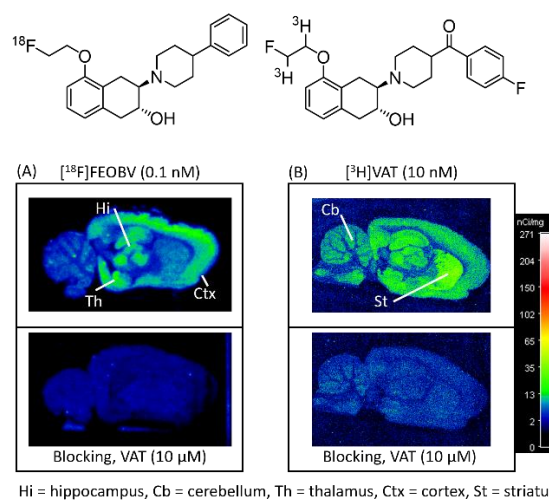
Introduction. Neurodegenerative diseases such as Alzheimer's disease (AD) are characterized by losses of cholinergic neurons and cholinergic neurotransmission deficits.¹ The vesicular acetylcholine transporter (VACHT), a protein located in presynaptic vesicles of cholinergic neurons and responsible for the transport of the neurotransmitter acetylcholine (ACh) into storage vesicles, has been established as a reliable cholinergic marker.² Several PET radiotracers based on (-)-vesamicol have been developed but lack ideal properties for *in vivo* imaging studies.² Recently, two VACHT PET tracers: [^{18}F]FEOBV and [^{18}F]VAT have been translated for human PET imaging studies.³ While both radiotracers appear to be promising and have different kinetics *in vivo*, the goal of the present study is to compare these two radiotracers for measuring the density variability of cholinergic neurons in pathologically diagnosed cases of AD human brains, using *in vitro* radioligand binding assays and autoradiography (ARG). These data will determine which radiotracer to translate for our PET imaging studies of neurodegenerative diseases in humans.

Methods. [^3H]VAT was custom synthesized and [^{18}F]FEOBV was synthesized following a literature procedure.⁴ A preliminary study involving thin section (10 μm) ARG in healthy rat brain was employed to assess tissue section distribution and specific binding for [^{18}F]FEOBV and [^3H]VAT. ARG using homologous equilibrium binding with 10 μm unlabeled "self" was used to show displacability of the radioligands. Region of interest (ROI) analysis was used to quantify radioligand binding density ($\mu\text{Ci/g}$).

Results. The autoradiography images revealed a distribution and retention of [^{18}F]FEOBV and [^3H]VAT consistent with the expected distribution of cholinergic terminals in rat brain, showing high binding in the hippocampus, cerebellum, thalamus, cortex and striatum.⁵⁻⁷ Differences in distribution were observed between [^{18}F]FEOBV and [^3H]VAT, with a higher accumulation of the tritium-labeled compound in the cerebellum and striatum. Treatment with cold VAT significantly reduced the retention of radioactivity in all regions expressing VACHT, confirming the high specific binding of the two tracers towards VACHT. The comparative ARG study will be continued with human AD and control brain tissues in different regions (cerebellum, prefrontal cortex, and hippocampus).

Conclusions. [^{18}F]FEOBV and [^3H]VAT are suitable radiotracers for *ex vivo* ARG in rodent brain, and will be applied to guide the development of PET imaging agents targeting VACHT. Imaging in AD tissues is underway and will also be presented, along with additional radiotracers involved in cholinergic and glutamatergic neurotransmission. As a result, at least one of these tracers will be validated for human translation at our Centre for evaluating cholinergic terminal losses and the state of neurodegenerative diseases.

References. ¹ Whitehouse P. J. *et al. Science* **1982**, 215, 4537, 1237-1239; ² Efanze S. M. N. *FASEB J.* **2000**, 14, 15, 2401-2413; ³ Petrou M. *et al. J. Nucl. Med.* **2014**, 55, 3, 396-404; ⁴ Shao X. *J Labelled Comp Radiopharm.* **2011**, 54, 6, 292-307; ⁵ Parent M. *et al. J. Int. J. Mol. Im.* **2013**, 205045; ⁶ Liang Q. *et al. Eur J. Pharmacol* **2021**, 911, 174556; ⁷ Kilbourn M. R. *et al. Nucl. Med. Biol.* **2009**, 36, 489-493.



Hi = hippocampus, Cb = cerebellum, Th = thalamus, Ctx = cortex, St = striatum

Figure 1. Tissue distribution of (A) [^{18}F]FEOBV, and (B) [^3H]VAT in healthy rat brain by autoradiography.

Pitch/Poster Session 10: Device, Hardware and Software Development Abstracts

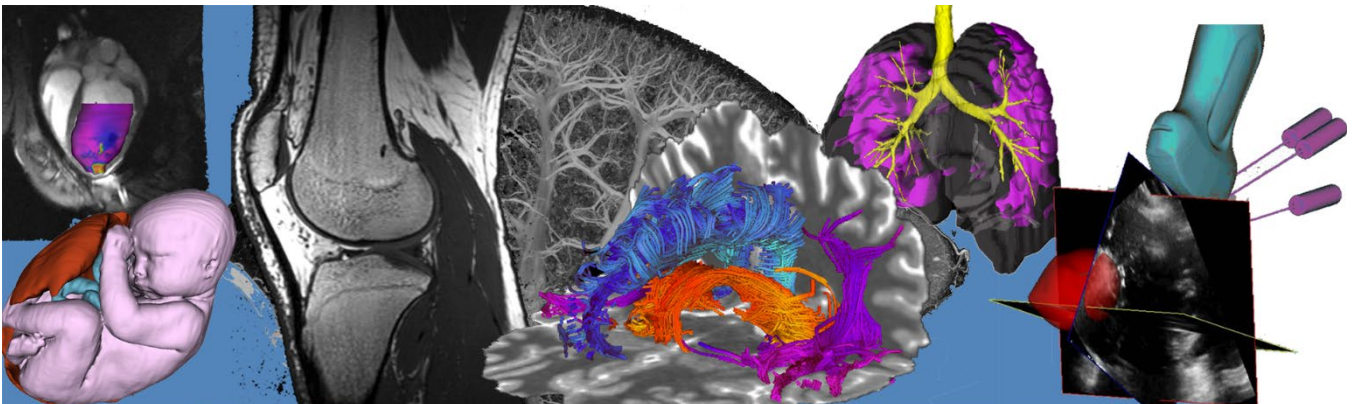


Image Quizzer: A versatile and customizable tool for education and standardized data collection in imaging research

Carol A. Johnson¹, David A. Palma¹⁻³, Aaron D. Ward^{1-3*}

¹Baines Imaging Research Laboratory, London Regional Cancer Program, London, Canada; Department of
²Medical Biophysics, ³Department of Oncology, Western University, London, Canada, *Research Supervisor

Introduction: There is an unmet need for a customizable tool that allows for the easy creation of observer studies or learning aids. Our newly-developed Image Quizzer does this and enables medical image review and contouring/annotation, collection of answers to customizable questions for each image, and captures responses and contours for offline analysis. A study administrator can customize a script defining the appearance and flow of the study using a simple eXtensible Markup Language (XML) editor. No programming skills are required. The tool can be run from any computer, enabling the observer to perform the study at their convenience with no supervision. To date, this module has been used in our lab for two different studies: a pancreatic cancer study comparing observer contours with a gold standard and a brain metastases radiosurgery outcome prediction study.

Workflow and system capabilities: We developed a module (Figure 1) for 3D Slicer (www.slicer.org) that controls the display of questions and images that have been defined in a quiz configuration input file. This input file is created by a study administrator using a simple XML editor (e.g. Notepad). It requires the use of predefined XML elements and attributes but does not require programming skills. The administrator can customize how the questions are presented (check boxes, radio buttons, text or numeric entry) as well as the order, orientation and layout of images (DICOM series or data volumes including PET, label masks, RTStructs, RTDose and time series images) with an annotation/contouring option. The observer navigates from image to image in the quiz using simple Next and Previous buttons, and follows instructions to review images, answer quiz questions, and contour areas of interest on the images. The responses and any annotations are captured automatically for future analysis. For data integrity, the system ensures that all required questions, contours and measurements are completed for a given image before the observer is allowed to proceed to the next image. The system allows for simultaneous viewing and contouring of multimodality image data. Many configuration options are available to activate features (e.g. to control whether the observer is allowed to change responses to questions about previous images in the quiz; or to set up a loop allowing the observer to assess/annotate/contour multiple regions of interest in one image).

Concluding remarks: Taken together, these features enable the Image Quizzer to support observer variability studies in image assessment and contouring, studies of variability in observers' clinical management decisions based on imaging information, and, through *a priori* incorporation of predefined gold-standard assessments, the system can be configured as an educational intervention allowing observers to attempt assessments and contouring tasks and immediately obtain case-by-case performance feedback.

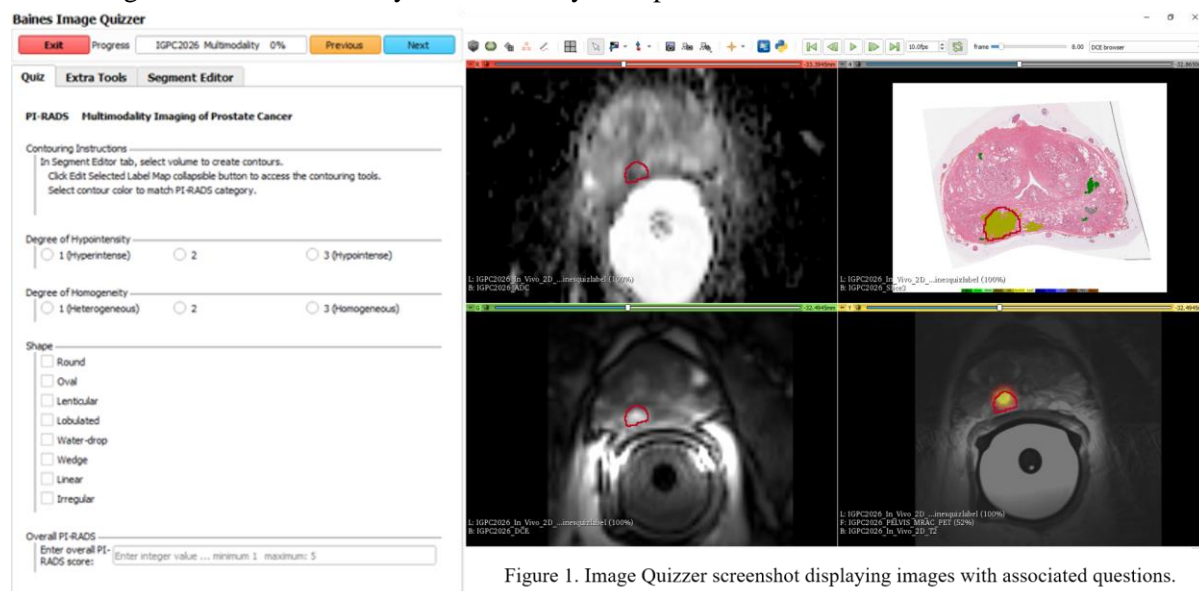


Figure 1. Image Quizzer screenshot displaying images with associated questions.

End-to-end mass spectrometry imaging analysis softwareH Elmi¹, A Jamzad¹, M Sharp¹, JR Rodgers², M Kaufmann³, T Jamaspishvili⁴, R Iseman⁴D.M. Berman⁴, J Rudan³, G Fichtinger¹, P Mousavi¹¹*School of Computing*, ²*Department of Physics and Astronomy University of Manitoba*, ³*Department of Surgery*, ⁴*Department of Pathology and Molecular Medicine Queen's University, Kingston, Canada*

INTRODUCTION: Mass spectrometry imaging (MSI) is a powerful technique that allows imaging of biological molecules with high accuracy [1]. The technique holds potential for identifying specific disease markers in cancer. There is currently no software capable of completing the entire pipeline of preprocessing, visualization, and analysis end-to-end. We propose a software module called “Visualization, Preprocessing, and Registration Environment” (ViPRE), capable of end-to-end analysis of MSI data. ViPRE is implemented in 3D Slicer, a free open-source platform for medical imaging [2]. The platform enables users to perform MSI data analysis, exploration, visualization, and histopathology correspondence in a single environment.

METHODS: ViPRE was developed to provide a single stop platform offering different functionalities required for MSI analysis, which include data import, data visualization, data registration, region-of-interest (ROI) selection, spectral data alignment and data analysis. It also includes various approaches to support thorough analysis of MSI data. The ViPRE pipeline starts with the upload of Mass Spectrometry imaging in .txt format. Next, users can perform single or multi-ion visualization. Principal component analysis (PCA) visualization is also supported, which allows users to visualize and consider the effect of all ions and improve data exploration. The images are then spatially correlated through landmark registration. This allows users to segment ROI based on the histopathology labels and generate a mass spectral dataset. Unlike current industry standards, ViPRE enables users to align and merge mass spectra extracted from separate MSI slides. Finally, using the generated datasets, ViPRE enables users to perform robust data analysis. This includes linear discriminant analysis (LDA), decision tree and lower dimension visualization using scatterplots.

RESULTS: ViPRE was tested using a sample DESI dataset containing a prostate biopsy core. The analysis pipeline was performed using the text file, with multi-ion and PCA imaging generated (Fig 1). Multi-ion visualization helps you define the ions you want to analyze by specifying their m/z value. Each color, in this case, represents a different ion (m/z). On the other hand, PCA imaging enables users to visualize metabolomic differences without defining target ions (m/z). ROI selection can be performed (Fig 1.B) by segmenting our regions of interest. Each highlighted circle in figure B. represents an ROI (Cancer in red, benign in green and background in blue). The resulting segments can then be analyzed using LDA and a scatterplot is generated (Fig 1.C).

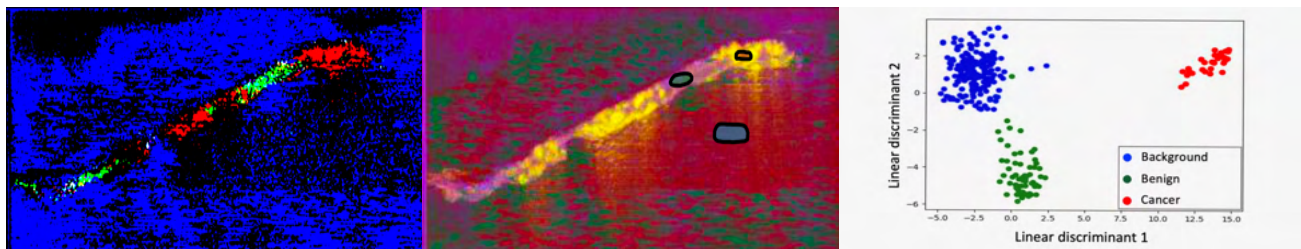


Fig 1 (A-C) – A. multi-ion visualization of the biopsy core, B. PCA visualization with segmented ROI, C. LDA scatterplot of the ROI

CONCLUSIONS: ViPRE allows for preprocessing and analysis of MSI data in one environment whilst introducing new features not offered in current commercial standards. In future work, we aim to provide more functionalities, particularly in visualization, to help MSI analysis. We also intend to compare the results of the platform to current commercial software through a user study.

REFERENCES: [1] Hu H, & Laskin J (2022). Emerging computational methods in mass spectrometry imaging. *Advanced Science*, 2203339. <https://doi.org/10.1002/advs.202203339>

[2] Fedorov A, et al., “3D Slicer as an image computing software implementation for the Quantitative Imaging Network,” *Magnetic Resonance Imaging* 30(9), 1323–1341 (2012)

Comprehensive Review of Biomedical Software Tools for 3D Segmentation and Registration

Ashley Mathialagan, Zaiba Amla, Parminder Singh Khehra, Elodie Lugez

Toronto Metropolitan University

Introduction: The creation of research tools for Computer-Assisted Interventions (CAI) paves the way for numerous innovations in the medical field. Various research software products have been created as a result. Due to the abundance of software that is currently accessible and the vast variety of functionalities they provide, this paper attempts to provide insight into the most frequently utilized tools by the CAI research community. The software tools will compare each tool's standard functionalities, strengths, and weaknesses, as well as its documentation, licensing, extensibility, feature set, and efficiency.

Methods: The reviewed software are 3D Slicer[1], ITK-SNAP[2], MITK[3] and MedINRIA[4]. Each had the basic criteria of being open source. Google Scholar was used to systematically search the relevant literature. Furthermore, we tested each software for the main functionalities they enable, including the following: segmentation and registration as well as additional functionalities the application provided. Segmentation was tested using the threshold function in 3D Slicer, using the seed method in both ITK-Snap and MITK, and MedINRIA using the polygon ROI. To evaluate the registration functionalities, we aligned two magnetic resonance images (MRI) of the same subject manually. Applications were recognized on the user interface, data management, efficiency & effectiveness, stability, resource usage, operating system availability, additional extensions/modules and the abundance of documentation. User-friendliness was established by evaluating the applications' ease of downloading and navigation. The application's database was tested by uploading thousands of MRIs. Efficiency and effectiveness were rated based on the interaction of the functionalities, and any discrepancies were noted. To test the stability of the applications, we stressed the program by inputting multiple commands within a few seconds of each other. When testing the programs' multitasking compatibility, resource utilization was carefully watched to look for spikes in CPU, GPU, and RAM usage. The extensions that each software enabled were explored since they improve the functionality of each software. Based on each software's online presence in terms of forums and community contributors to these forums, community support was evaluated.

Results: Each application was rated from 1-4 on depending on how well they excelled in each category, these results are reported in Table 1. Segmentation was the fastest and easiest using ITK-SNAP, while 3D Slicer was the easiest software for image registration tasks. For first-time users, 3D Slicer and MedINRIA were difficult to use. ITK-SNAP and MITK's interface was laid out neatly and was easier for users to navigate. When compared to the other applications, database testing revealed that 3D Slicer was the most versatile because it had the greatest community and extension support. In contrast to other applications, this one has the drawback of frequently crashing when loaded with several hundreds of files at once. MITK was the application with the most crashes whilst changing settings related to the image viewer, but excelled in resource usage. MedINRIA showed similar issues but they only occur in extreme settings, such as heavy data files. ITK-SNAP is the fastest software among the tested applications, but lacked resource usage accessibility. The literature research showed that 3D Slicer is the most popular and well-known tool and has the greatest community support.

Conclusion: This paper evaluated four free and open-source research tools. 3D Slicer provides an extensive collection of modules and should be used for complex tasks. ITK-SNAP is convenient for performing simple tasks such as segmentation and registration. MITK has excellent resource management, and could be utilized for smaller projects. MedINRIA is not optimized as well as the other applications presented. Our findings provide insight to fellow researchers in selecting the appropriate tool for conducting their CAI projects.

References

- [1] Fedorov A. et al. Magnetic Resonance Imaging. Nov;30(9):1323-41. (2012).
- [2] Paul A et al. Neuroimage. Jul 1;31(3):1116-28. (2006).
- [3] Ivo W et al. Visualization, Image-Guided Procedures, and Display. (2004).
- [4] Nicolas Toussaint et al. Interaction in medical image analysis and visualization. (2007).

Table 1. Rating of software based on proposed criteria

	3D Slicer	ITK-Snap	MITK	MedINRIA
Segmentation	2	4	3	1
Registration	4	3	2	1
User Friendliness	2	4	3	1
Data Management	3	4	1	2
Efficiency & effectiveness	4	3	1	2
Stability	3	4	2	1
Extensibility	4	3	2	1
Resource Usage	1	2	4	3
Documentation	4	3	2	1
Community Support	4	3	1	1

SlicerTrack: an open-source research toolkit for target tracking verification in 3D Slicer

HaPhan Tran, Mubariz Afzal, Elodie Lugez

Toronto Metropolitan University

Introduction: Medical image processing techniques are continuously being developed with increasing demands from the medical field. These global efforts pave the way for the development of tools in areas such as oncology. Several applications and tools have been developed to manipulate, analyze, and process medical images. 3D Slicer is one such tool that is popular and freely distributed to the research community [1]. Indeed, it provides powerful functionality to support medical image informatics. However, 3D Slicer is unable to coherently and dynamically present the results of tracking a region of interest (ROI). We propose to develop an extension in 3D Slicer that replays cine 2D images and overlays the outline of the ROI. The tool is intended to be used for the development, visual verification, and performance comparison of methods for ROI motion tracking.

Methods: 3D Slicer was used to develop the SlicerTrack extension, for visualizing the displacement of a ROI as it moves throughout the images. We chose 3D Slicer due to its popularity within the medical image computing space, the abundance of documentation, and its established culture of open-source extension development. To develop the extension, we utilized 3D Slicer's Python API, supported by its extension development wizard which will generate boiler-plate code. 3D Slicer uses an "Observer MVC" pattern [2], which is represented by the MRML nodes (model), the GUI (view), and the logic (controller). The SlicerTrack extension was tested by visually confirming that the ROI is accurately tracked throughout the images.

Results: The extension accepts three inputs from the user: a 3D segmentation of the ROI, a set of cine 2D MRI images, and transformation data in CSV format. The transformation data includes the registration results of the ROI from each cine 2D image to a 3D reference image. It is used to align the 3D segmentation against the 2D

images. Users can enter a playback speed through the FPS input box. Once the user presses play, the extension will go through the series of 2D images with the 3D segmentation overlaid on the current 2D image. Users can decide to pause at any frame or go to any particular 2D image using the sequence

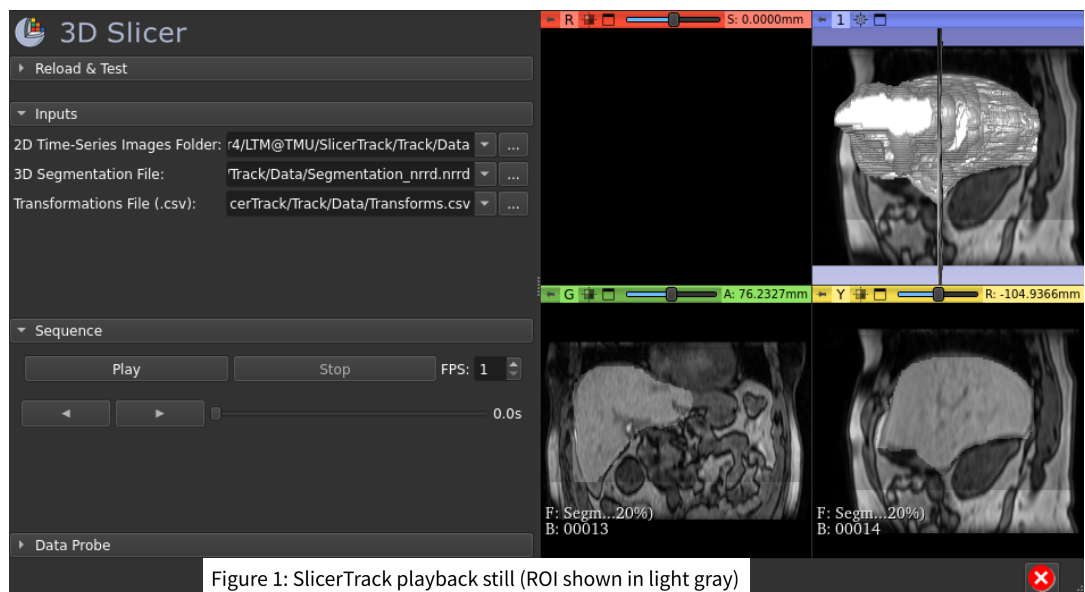


Figure 1: SlicerTrack playback still (ROI shown in light gray)

slider. Prior to the SlicerTrack extension, users would have to inspect each frame and manually verify it in order to validate the tracking algorithm. The extension is currently available on GitHub [3].

Conclusion: An open-source toolkit was developed for visualizing target tracking results. SlicerTrack is a promising extension to 3D Slicer, as it enables researchers to evaluate the performance of tracking methods. Our development of SlicerTrack provides various areas of medicine with a tool for tracking the region of interest (ROI) with ease.

References:

- [1]: Pieper et al. IEEE Cat No. 04EX821 (2004).
- [2]: Pieper, S. National Alliance for Medical Image Computing. (2008).
- [3]: Laboratory for Translational Medicine. <https://github.com/laboratory-for-translational-medicine/SlicerTrack>. (2022).

A “Smart” Brain Retraction System Utilizing Photoplethysmography: Development of a Prototype System to Measure Applied Pressure with Optical Signals

Lee Sikstrom¹, David W Holdsworth^{1,2,3}

¹Dept. of Medical Biophysics and Medical Imaging, ²School of Biomedical Engineering, ³Dept. of Surgery, University of Western Ontario

Introduction: Every year there are approximately 13.8 million neurosurgery cases worldwide, with over 80% of these cases occurring in low- to middle-income regions [1]. When surgical targets are below the surface of the brain, healthy brain tissue must be moved out of the way in a process called retraction. Over 40% of patients who undergo retraction may suffer brain injuries from the pressure applied to the healthy brain tissue during the procedure, no matter how careful the surgeon is [2,3]. There have been tools developed to measure the local pressure applied to the brain during retraction, but they have not been widely adopted by the neurosurgery community due to their size, complexity, or other limitations [4]. Recent advances in optical sensors for photoplethysmography (PPG) have allowed them to be produced in low-cost, ultra-miniaturized self-contained packages. We propose development of a novel, low-cost “smart” retractor system utilizing these new PPG sensors, which will give surgeons real-time continuous monitoring of applied pressure, heart rate, and blood oxygenation of the retracted brain tissue.

Methods: Contact pressure is an established factor in the quality of PPG signals when it is used to monitor vital signs [5]. Recent work has explored the relationship between contact pressure and the properties of the signal [6]. Building on this recent work, we propose to develop a method of determining the contact pressure on the sensor from the generated PPG signal.

We have implemented the MAXM86161 ultra-low-power, optical data-acquisition system to obtain the PPG signals. The package measures 2.9mm x 4.3mm x 1.4mm. It contains three LEDs that produce light at 530 nm, 660 nm, and 880 nm. The package also includes a photodiode and optical readout channel with 19-bit resolution (Fig. 1). The applied pressure is measured simultaneously using a beam load-cell coupled to an HX711 load-cell amplifier. The MAXM86161 and the load cell are controlled by a MAX32630FTHR rapid development platform that uses an ARM Cortex-M4F microprocessor. Tree-based, k^{th} -nearest neighbour, and neural network regression machine-learning models will be used to determine the relationship between the pressure applied to the sensor and the resulting PPG signal.

Results: The test bed for MAXM86161 and load cell was built using 3D printed adapters to accommodate the sensor and the load cell (Fig. 2). The two sensors were connected to the MAX32630FTHR, which was programmed using C++ in Kiel Studio. This provides control over the duration, intensity, and sequence of the LED signals. The data acquisition rate was measured to have a maximum rate of 200 Hz. Serial communication *via* USB was established with the MAX32630FTHR to permit simultaneous logging of the two sensor’s data with the ability for it to be saved a data file for later analysis.

Conclusions: The result of this initial testing demonstrates that the MAXM86161 is an excellent candidate for this novel instrumented retractor system. The data acquisition rate is sufficiently high to capture all the signal components of blood circulation. The data can be recorded and stored in a useable file format for analysis later using machine-learning algorithms. Given the small form factor and high data rate of the sensor, the MAXM86161 shows promise to develop the brain retraction system. Future work will focus on collecting data from a range of participants to account for the biological variability of tissue.

References: 1. M. C. Dewan *et al.*, "Global neurosurgery: the current capacity and deficit in the provision of essential neurosurgical care," *Journal of Neurosurgery*, 2018. 2. B. Konya *et al.*, "Brain retraction injury after elective aneurysm clipping" in *Acta Neurochirurgica* 2022. 3. Z. D. Travis *et al.*, "Surgically-induced brain injury: where are we now?," in *Chinese Neurosurgical Journal*, 2019. 4. R. S. Karmakar *et al.*, "Real-Time Intraoperative Pressure Monitoring to Avoid Surgically Induced Localized Brain Injury Using a Miniaturized Piezoresistive Pressure Sensor," in *ACS Omega*, 2020. 5. D. Castaneda *et al.*, "A review on wearable photoplethysmography sensors and their potential future applications in health care," in *Int J Biosens Bioelectron*, 2018. 6. J. M. May *et al.*, "Effects of Contact Pressure in Reflectance Photoplethysmography in an In Vitro Tissue-Vessel Phantom," in *Sensors*, 2021.



Figure 1: MAXM86161 PPG Sensor

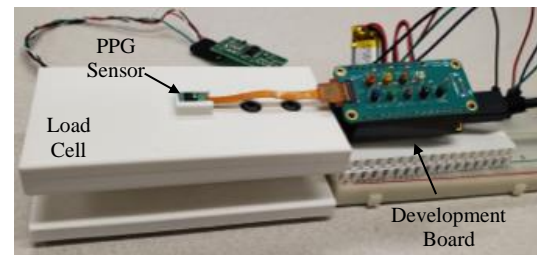


Figure 2: MAXM86161 test bed with load cell and MAX32630FTHR development board.

Adapting electromagnetic tool tracking for ultrasound-guided oral cavity cancer resection

Pavel-Dumitru Cernelev¹, Kristof Moga^{2,3}, Chris Yeung¹, Tamas Haidegger², Gernot Kronreif⁴,
Tamas Ungi¹, Gabor Fichtinger¹

¹Laboratory for Percutaneous Surgery, Queen's University, Kingston, Canada; ²University Research and Innovation Center (EKIK), Obuda University, Budapest, Hungary; ³Doctoral School of Medicine, Semmelweis University, Budapest, Hungary; ⁴ACMIT GmbH, Wiener Neustadt, Austria

INTRODUCTION: The surgical excision of tongue tumors, referred to as glossectomy, is a common treatment for oral tongue cancers. The procedure involves excising the tumor while preserving as much of the surrounding healthy tissue as possible. The excised tongue tumor is sent to a pathologist to analyze the tissue, negative margins indicate that the tumor was sufficiently removed from the patient [1]. The computer-navigation system, *NaviKnife*, uses real-time electromagnetic tracking to determine the location of the surgical tools relative to the patient anatomy, originally developed for breast-conserving surgery. When tested the system resulted in the resection of less healthy tissue as well as increased confidence for the surgeons [2]. In this work, we present the technical challenges and potential solutions when translating previously designed computer navigated systems to glossectomy.

METHODS: The *NaviKnife* system was initially tested for glossectomy by directly applying it to a simulated workspace (Figure 1). However, implementing *NaviKnife* in its current iteration within the glossectomy workspace posed a series of challenges that must be solved. The first challenge comes from the constrained glossectomy workspace. Due to the minimal workspace within the operating room the *NaviKnife* tumor tracking methods must be compact to prevent it from disrupting the surgeon while maintaining a high accuracy. Another issue is the complex anatomy of the tongue, as it has the lingual artery which if breached can cause excessive bleeding. The current standard for tracking tumors within *NaviKnife* is to use ultrasound imaging to generate a 3D visualization in the navigational software, while inserting a tracked needle within the tumor. This could pose challenges for the surgeon if the lingual artery is pierced causing complications for the patient.

RESULTS: The standard electromagnetic tracking elements used for *NaviKnife* while effective for operations with larger workspaces are too large and bulky for use in glossectomies. The tracking methods must be redesigned to prevent disrupting the surgeon and harming the surrounding anatomical structures within the tongue. A potential solution includes implementing a small sensor which can be inserted directly within the tumor to be tracked instead of using a tracked needle (Figure 2). Due to the small nature of the sensor, it will prevent overcrowding in the surgeon's workspace during the procedure.

CONCLUSION: The study captures the complexity of implementing computer navigation within a constrained workspace. Within such a workspace the tracking techniques must be reinvented to allow comfortable non-invasive tracking. Future work includes comparing different tracking elements to determine their performance in a given workspace. Determining new methods for tracking within different surgical contexts that hold unique constraints may allow for the simple translation of existing computer navigation systems to different surgical fields.

REFERENCES:

- [1] Ansarin, M., Bruschini, R., Navach, V., Giugliano, G., Calabrese, L., Chiesa, F., Medina, J. E., Kowalski, L. P., & Shah, J. P. (2019). Classification of glossectomies: Proposal for tongue cancer resections. *Head & Neck*, 41(3), 821–827. <https://doi.org/10.1002/hed.25466>
- [2] Gauvin, G., Yeo, C. T., Ungi, T., Merchant, S., Lasso, A., Jabs, D., Vaughan, T., Rudan, J. F., Walker, R., Fichtinger, G., & Engel, C. J. (2020). Real-time electromagnetic navigation for breast-conserving surgery using NaviKnife technology: A matched case-control study. *The Breast Journal*, 26(3), 399–405. <https://doi.org/10.1111/tbj.13480>



Figure 1: Experimental glossectomy workspace utilizing the *NaviKnife* system.

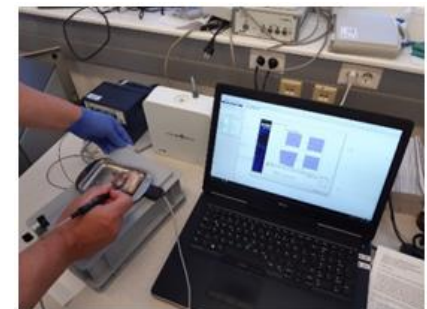


Figure 2: Testing of a sensor where it is inserted in tissue within a simulated working environment.

Optical position tracking fiducial marker for high performance rigid body motion parameter estimationMarina Silic^{1,2}, Aravinthan Jegatheesan^{1,2}, Fred Tam², Simon J. Graham^{1,2}¹ Department of Medical Biophysics, University of Toronto, Toronto, ON² Sunnybrook Research Institute, Toronto, ON

Introduction: Optical position tracking (OPT) using fiducial markers is advantageous for tracking rigid body head motion and for artifact correction in magnetic resonance imaging (MRI), providing high spatiotemporal resolution, MR-compatibility, and precision. For use in prospective or retrospective correction, such tracking should exceed the millimeter spatial resolution typical of most 1.5 and 3 T MRI systems[1]. Although OPT fiducials already have impressive capabilities, opportunities for improvement remain, such as concurrent use of other optical methods and multiple camera views[2], towards increasingly demanding MRI applications. Here we describe promising work assessing the precision of a prototype OPT marker and analysis pathway, prior to validation testing at 3 T.

Methods: A 4.5 x 4.5 cm planar marker (Fig. 1) was fabricated consisting of two laser-printed transparencies adhered to a transparent acrylic plate, for observation by two CCD cameras (WATEC-204CX) with 200mm focal length lenses at 3 m (from the rear wall of the magnet room to the magnet isocenter). A 2.75 x 2.2 cm chessboard pattern was used to track position in six degrees of freedom (DOF) via solving the perspective n-point (PnP) problem with the OpenCV library. The PnP solution was anticipated to provide high quality outputs for in-plane motion (roll, x, y), but insufficient outputs through-plane (pitch, yaw, z). For the latter 3DOF, moiré patterns were used to capture through-plane rotations based on the linear relationship of the pattern phase with rotation, and stereovision was adopted to capture z. Phase was assessed by averaging rows of grayscale values through the moiré pattern and fitting this signal to a sinusoidal function via non-linear least squares to estimate amplitude, frequency, and phase. The phase difference was found by subtracting the fitted parameter from the phase of a reference function. Stereoscopic tracking was performed via the direct linear transformation (DLT) algorithm to estimate through-plane translation (z). Benchtop testing was performed for each DOF separately using positional and rotational stages (Newport Corp. 423 & 481-A). 5DOF were calculated using one 200 mm focal length camera at 3 m. Z translation was assessed in proof-of-concept stereoscopic tracking with two cameras of 50 mm focal length at 1 m, as matching 200 mm lenses were not available at the time of testing. Measurements were taken at stationary positions during 5 s of recording (~150 frames), with individual pose and moiré estimation at each frame. Translations were measured in 0.1 mm increments from 0-1.5 mm; rotations were measured in 0.5° increments from 0-25°. Moiré measurements were in 0.1° increments from 0-2°.

Results: Results are shown in Table 1. As expected, in-plane DOF were well-estimated by PnP whereas through-plane DOF were poorly estimated with high standard deviation. However, moiré results and z measured via DLT performed notably better than their PnP counterparts, indicating their suitability for through-plane tracking.

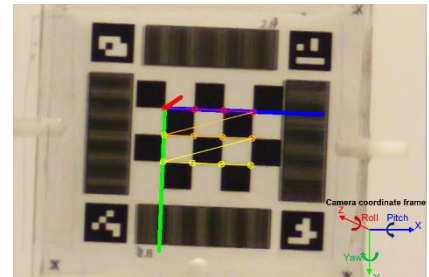


Figure 1. Moiré-enhanced OPT marker

Table 1. Benchtop Testing Results: Translation and Rotation Estimated for Six Degrees of Freedom

Translation DOF	Real Position Increment (mm)	Mean Measured Position Increment (mm)	Standard Deviation (mm)	Rotation DOF	Real Position Increment (degrees)	Mean Position Increment (degrees)	Standard Deviation (degrees)
X (PnP)	0.1	0.09	0.01	Pitch (PnP)	0.5	0.01	1.83
Y (PnP)	0.1	0.10	0.04	Yaw (PnP)	0.5	0.05	2.21
Z (PnP)	0.1	0.13*	1.39	Yaw (Moiré)†	0.1	0.1	0.02
Z (DLT)	0.1	0.11	0.02	Roll (PnP)	0.5	0.49	0.13

* Reported mean was not representative of typical performance, as indicated by the high standard deviation. For comparison, the median PnP z estimate was 0.486 mm.

† Pitch (Moiré) results are excluded as they were comparable to observed yaw (moiré) performance.

Conclusion: A low-cost, high precision OPT tool is proposed here. This tool has the potential to enable research that requires high quality DOF estimates such as characterizing head motion, validating other MR motion correction methods, connecting certain artifacts to types and levels of motion, and more.

References: [1] S. Maknojia et al., *Frontiers in Neuroscience*, 2019. [2] J. Maclaren et al., *PLoS ONE*, 2012.

Low-Cost Fourier Ptychographic Microscope for Malaria DiagnosisJustin H. Yang¹, Aidan Fry¹, Rajan Leung¹, Lisa Garland¹, William Wasswa², Ian A. Cunningham¹¹Imaging Laboratories, Robarts Research Institute, Western University, Canada ²Department of Biomedical Sciences and Engineering, Mbarara University of Science and Technology, Uganda

Introduction. The World Health Organization (WHO) estimated that there were 241 million malaria cases and 627,000 deaths worldwide in 2020. The gold standard for diagnosing malaria involves optical microscopy to determine the fraction of infected red blood cells using a Giemsa-stained blood smear. Treatments are available but are most effective when delivered within a few days of symptoms, requiring rapid point-of-care diagnoses in low-resource rural settings. Fourier ptychographic microscopy (FPM) is a candidate computational optics technology that uses an LED array as the light source to acquire images of the specimen at various illumination angles. Each illumination corresponds to a different band-pass filtered image. The Fourier transforms of all images can be stitched together to create a high-bandwidth composite image having high spatial resolution. This is possible even with low-cost optics are used and maintains the large field of view. Our objective is to develop a prototype low-cost microscope with resolution less than 1 μm using this technology for point-of-care malaria diagnosis in these difficult rural settings.

Methods. Our FPM prototype was assembled using PLA 3D printed components, Raspberry Pi 3B computer, Raspberry Pi V2 NOIR camera (1.12- μm pixel size), and 14x14 LED array (3.3-mm pitch). The default lens in the camera (3.0-mm focal length) was used to achieve magnification of 2.6x. The microscope was programmed in Python 3.10 to capture 196 raw images at each LED illumination angle using green (530 nm) light and reconstructed using Fourier ptychographic algorithm in MATLAB. A United States Air Force (USAF) bar pattern was used to determine spatial resolution, and a Wright's-stained blood smear slide was used to demonstrate image quality.

Results. Our FPM's (Fig. 1a) cost of goods was less than \$200. Resolution in the raw image with the central LED illumination (Fig. 1b) was estimated to be 2.6 μm based on the extent of edge-blurring. This was improved to 0.60 μm in the FPM image (Fig. 1c) using the same optics. The reconstructed blood smear image (Fig. 1d) had less blurring with sharper outlines of red blood cells compared to the raw image (Fig. 1e).

Conclusions. Our prototype improved the resolution from 2.6 to 0.60 μm while costing considerably less than standard laboratory microscopes. We conclude that even with low-cost optics, it is possible to achieve resolution near the wavelength of light.

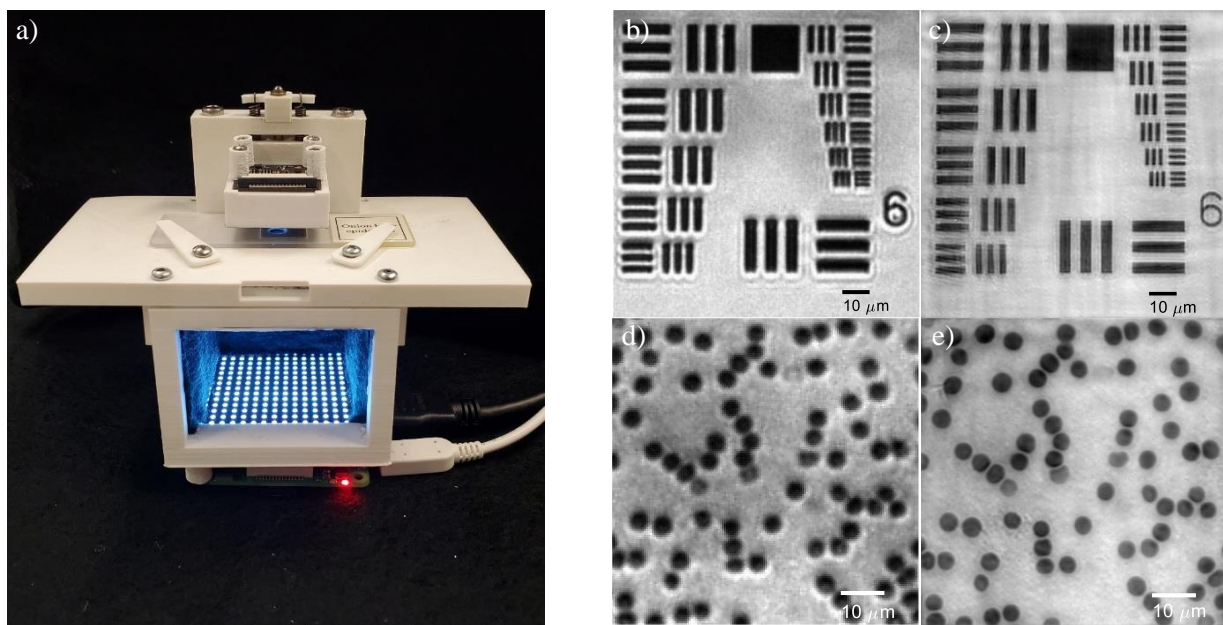


Figure 1: a) Prototype Fourier ptychographic microscope, b) conventional (central LED illumination), c) reconstructed image of United States Air Force bar pattern, d) conventional, e) reconstructed image of a Wright's-stained blood smear.

Inducing cavitation within hollow cylindrical transducers for use in intravascular thrombolysisLi Gong¹, Alex Wright², David Goertz^{1,2}¹Department of Medical Biophysics, Toronto, Canada,²Physics Sciences Platform, Sunnybrook Research Institute, Toronto, Canada,

Introduction: The occlusion of blood vessels with thrombus is a major cause of mortality and morbidity worldwide. Thrombotic occlusions are increasingly treated with catheter based ‘mechanical’ approaches, one of the most important of which is to employ aspiration to extract clot material through a hollow catheter lumen. A central technical challenge for aspiration catheters is to achieve sufficient suction force to overcome the viscous resistance of clot material passing through the catheter lumen. In this study, we examine the feasibility of inducing cavitation within hollow cylindrical transducers with a view to ultimately using them to degrade the mechanical integrity of thrombus entering into the tip of an aspiration catheter. A central challenge with this approach is to achieve very high pressures within these necessarily compact transducers, on the order of those employed in histotripsy. This work demonstrates the feasibility of generating histotripsy-magnitude pressures in an intravascular sized device.

Methods: Hollow cylindrical radially polarized PZT-4d transducers with 3.3/2.5 mm outer/inner diameter were investigated, a spatial scale that will ultimately be relevant for use with pulmonary emboli. Simulations (OnScale™) and hydrophone experiments were used to investigate the pressure field distribution as a function of element length and resonant mode (thickness mode, length mode). For selected lengths, cavitation detection experiments were performed using hydrophone detection, 40 MHz ultrasound imaging as a function of applied pressure (voltage).

Results: The resulting pressure distributions and amplitudes were highly dependent on transducer geometry and resonant mode (see Fig. 1 for selected 2.5 mm length). The highest pressures were produced in thickness mode (5.0 MHz; est. >20 MPa) as indicated with hydrophone and imaging results, in a manner that was dependent on pulse length and interval. Cavitation could be achieved in both degassed and room equilibrated water.

Conclusion: Collectively these results indicate such transducer configurations have potential for use in catheter based thrombectomy procedures.

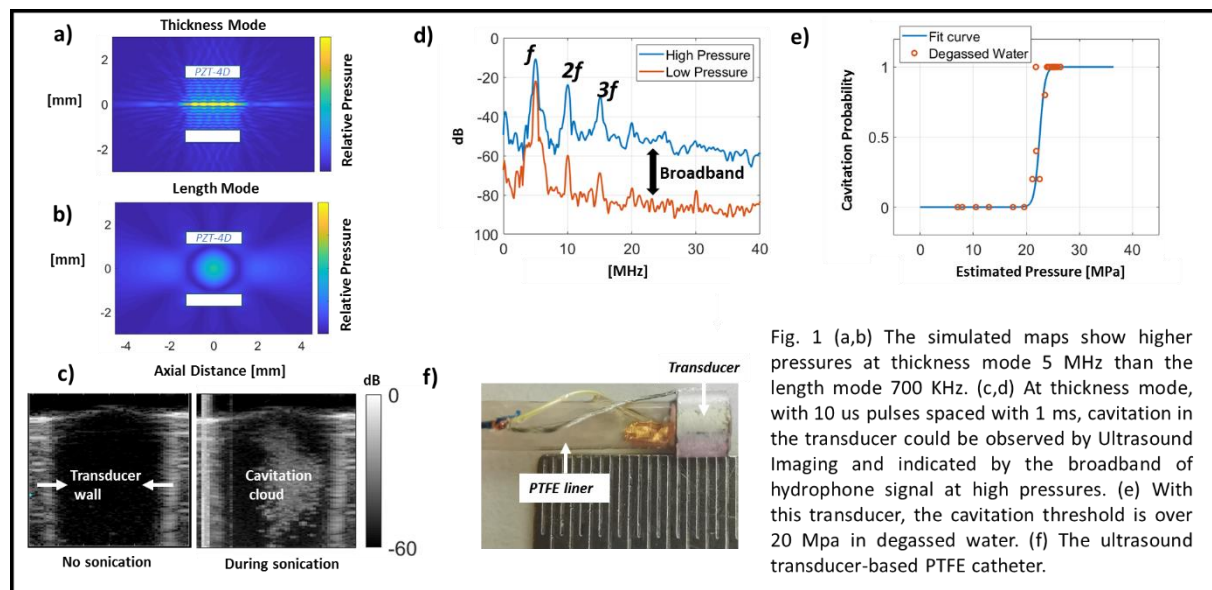
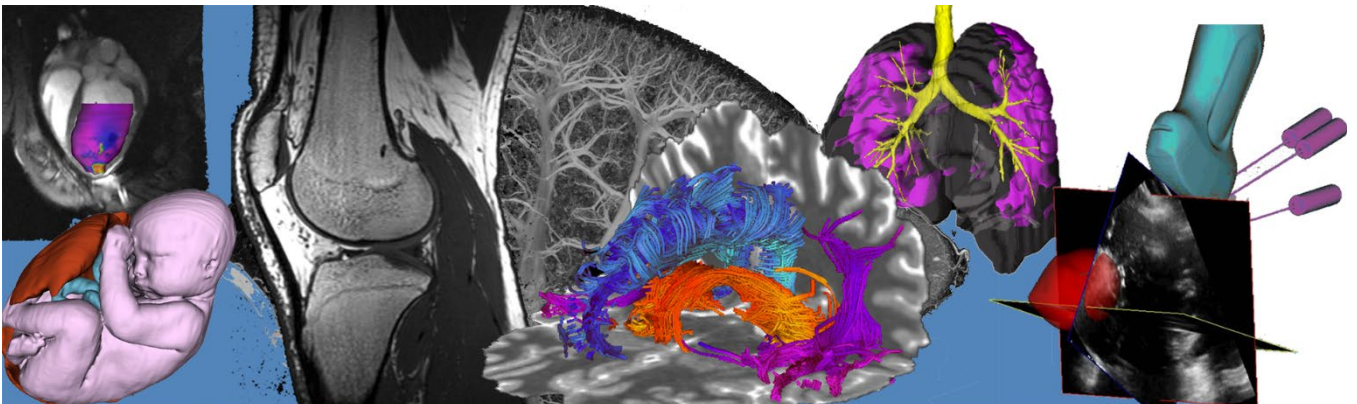


Fig. 1 (a,b) The simulated maps show higher pressures at thickness mode 5 MHz than the length mode 700 KHz. (c,d) At thickness mode, with 10 us pulses spaced with 1 ms, cavitation in the transducer could be observed by Ultrasound Imaging and indicated by the broadband of hydrophone signal at high pressures. (e) With this transducer, the cavitation threshold is over 20 Mpa in degassed water. (f) The ultrasound transducer-based PTFE catheter.

Oral Session 11: Deep Learning Abstracts



Predicting tumour mutational burden from H&E slides of lung squamous cell carcinoma: observers vs a neural network

Salma Dammak^{1,2}, Matthew J. Cecchini^{1,2}, Sherman X.J. Lin¹, Priyadharshini Sivasubramaniam³, Cady Zeman-Pocrnich^{1,2}, Christopher P. Hartley³, Aaron D. Ward^{1,2}

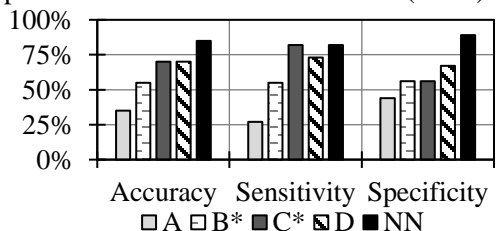
1. Western University, ON, Canada; 2. London Health Sciences Centre, ON, Canada; 3. Mayo Clinic, MN, US

Introduction: Immunotherapy is a novel anti-cancer treatment that has shown significant improvements in outcomes for lung cancer patients. However, this treatment has the potential for substantial side effects in a minority of patients, and many lung cancer patients do not benefit from it. High programmed-death ligand-1 (PD-L1) expression in tumour cells is currently the main biomarker used to identify those who might benefit, but it is not very accurate, with a 45% response rate¹. Tumour mutational burden (TMB) is a biomarker that improves prediction accuracy substantially; lung cancers that have more than 10 mutations/megabase in addition to high PD-L1 have a 75% response rate¹. However, TMB is obtained through extensive genetic sequencing, which is too resource-intensive to be implemented in the clinic in addition to PD-L1 testing. It is more expensive, slower, and requires tissue with high tumour cellularity, which is not always available as part of routine care.

Several studies in digital histopathology have shown that genetic information can be successfully estimated from standard-of-care hematoxylin and eosin (H&E)-stained slides containing the cancer tissue obtained during resections or biopsies². H&E slides are routinely obtained in the clinic and using scanned slides as the only input to a system predicting TMB would enable more straightforward translation to clinical practice. Based on this, we hypothesize that TMB can be predicted in lung squamous cell carcinoma (SqCC) using histopathology slides of tissue from surgically resected specimens prepared and scanned at different centres.

Methods: To test this hypothesis, we obtained digitized histopathology slides of resected lung SqCC of 70 patients from 35 centres through the National Cancer Institute's Genomic Data Commons (GDC) and split them into 50 training and 20 testing slides, with one slide per patient. The slides were all formalin-fixed, paraffin-embedded, and stained using H&E. We obtained the ground truth label of whether TMB was more than 10 mutations/megabase from the GDC. We asked four observers to observe the training slides alongside their TMB status and find features they could use to identify high-TMB slides, and then classify the blinded test set slides. Two observers are pathologists (B, C) and two observers are non-pathologists (A, D). To evaluate observer agreement, we calculated Fleiss' kappa. In parallel with this, we trained and tested a neural network model (NN) using the same sets as the observers: we used VGG16³ pretrained with ImageNet, and replaced the last layer with a single neuron, to match our two-class problem, trained using our training set (learning rate = 0.01, batch size = 100). We then tested the resulting NN on our test set. As the slides we used are much larger than typical available GPU memory sizes, we split them into non-overlapping tiles of 56 μm x 56 μm and only used tiles that were fully within pathologist-contoured cancer tissue. To obtain a per-patient classification, we averaged the per-tile confidences for each patient and used the ideal operating point on the receiver operator characteristic (ROC) curve as a threshold. To evaluate the performance of the observers and the NN, we calculated per-patient test set accuracy, sensitivity, and specificity. We also calculated the NN's per-patient area under the ROC curve (AUC).

Results: Three observers and the NN had an accuracy, sensitivity, and specificity all above chance as shown in the figure. This suggests a relationship between the appearance of a tumour and TMB. However, there was neither agreement between all observers ($K = 0.03$, NS) nor pathologists alone ($K = -0.13$, NS), and both groups had variable performance. In contrast, the NN had the highest performance on all three metrics and an AUC of 0.87.



*Fellowship-trained board-certified pathologists

Conclusions: This study ($n = 70$) shows that predicting TMB from digitized standard-of-care H&E slides of lung SqCC tumour resection tissue is possible on slides from many centres, despite stain variability. While it is possible for humans to detect this relationship, the results were mixed and there was little agreement, suggesting a need for a machine learning model. With further development with a larger dataset, such a system could act as a screening tool to select patients with lung SqCC who are most likely to have high-TMB for traditional genetic sequencing, improving its cost-value ratio and hence its accessibility in the clinic. This will help physicians determine whether patients should be given immunotherapy with more accuracy, which may allow for more effective utilization of immunotherapy and help spare others the toxicities associated with them.

1. Carbone, D. P., *et al.*, *NEJM*, **376**, 2415–2426 (2017).
2. Srinidhi, C. L., *et al.*, *MedIA* **67**, 101813 (2021).
3. Simonyan, K. & Zisserman, A., arXiv:1409.1556 (2014).

Improved surgical margin detection in mass spectrometry data using uncertainty estimation

Ayesha Syeda¹, Fahimeh Fooladgar², Amoon Jamzad¹, Martin Kauffman¹, Kevin Ren¹, Jay Engel¹, Ross Walker¹, Shaila Merchant¹, Doug McKay¹, Sonal Varma¹, Gabor Fichtinger¹, John Rudan¹, Parvin Mousavi¹

¹Queen's University, Kingston, ON ²University of British Columbia, Vancouver, BC

INTRODUCTION: The iKnife uses rapid evaporative ionization mass spectrometry (REIMS) for real-time, intraoperative tissue evaluation, and can reduce the likelihood of incomplete tumor resection in breast cancer patients undergoing breast-conserving surgery. There are some challenges in training a Machine Learning classifier on iKnife data. First, there is significant variability in the biochemical composition of cancer tissue. Second, spectra are coarsely labeled since the presence of cancer at the location of the burn may vary. We propose estimating the uncertainty associated with model predictions to catch errors and improve their reliability.

METHODS: Masksembles [1] layers were used in our convolutional neural network (CNN) model for uncertainty estimation. The CNN contained 5 layers, with each block containing convolutions, batch normalization, max-pool layers and Masksemble layers. Masksembles generate a set of binary masks using hyperparameters such as number of masks and ratio of 1s to 0s. At inference time, one mask is selected and applied to the input; therefore, the result of the forward pass may vary. The outputs of multiple subsequent forward passes were averaged and the entropy of this mean was the corresponding uncertainty estimate. The baseline comprised the same 5-layer CNN structure but without masksemble layers. The prediction confidence was generated by passing model output to a softmax layer to generate a percentage, and was used as an uncertainty measure. For an uncertainty-aware model to be considered reliable, it should be correct about its confident predictions and uncertain when incorrect. Thus, for a noisy mass spectrum, the uncertainty measure associated with the prediction can flag model errors during surgery. The overall reliability of model uncertainty can be measured using the probability metrics $p(\text{accurate}|\text{certain})$ and $p(\text{uncertain}|\text{inaccurate})$ and the accuracy vs. confidence curve. The performance metrics sensitivity, specificity, balanced accuracy and AUC were also reported. The dataset comprised 200 mass spectra (51 cancer, 149 healthy) from 15 patients at Kingston Health Sciences Centre (KHSC), Canada. Our dataset was divided into 5 folds, with burns from every patient staying in the same fold for 5-fold cross validation.

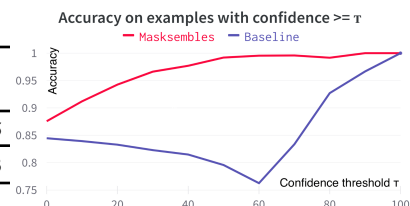
	Sensitivity	Specificity	Accuracy	AUC	$p(\text{accurate} \text{certain})$	$p(\text{uncertain} \text{inaccurate})$
Baseline	74.97 ± 19.98	93.96 ± 5.55	84.47 ± 9.10	96.14 ± 2.88	85.26 ± 17.52	78.30 ± 22.05
Masksembles	80.25 ± 14.04	94.90 ± 5.01	87.57 ± 7.09	96.21 ± 2.91	99.26 ± 2.77	98.61 ± 5.73

Table 1: Performance metrics for the proposed model and the baseline.

RESULTS: The proposed model shows a steady increasing pattern in the accuracy vs. confidence curve, indicating a well-calibrated model, while the baseline shows a decreasing pattern in the 0-60% confidence range, indicating poor calibration. The uncertainty metrics indicate that its predictions are reliable, as seen in Table 1, and the improvements are statistically significant ($p=0.003$ and $p=0.004$ respectively). Sensitivity and specificity indicate the model's effectiveness in classifying cancer and healthy spectra respectively. High specificity values indicate minimal healthy tissue is misclassified as cancer, while the improvements in sensitivity suggest cancer tissue is less likely to be misclassified as healthy. Consequently, we observe improvements in balanced accuracy and AUC over the baseline, indicating the model works well on all tissue types.

CONCLUSIONS: While the performance improvements shown by the proposed model are not statistically significant, the statistically significant improvements in uncertainty metrics indicate improved reliability for clinical use and better performance in practice, resulting in reduced likelihood of incomplete cancer resection and precision in removing minimal healthy tissue. These improvements can assist clinicians in improving outcomes for breast cancer patients. Future work will focus on visualizing confident and uncertain predictions for clinical interpretability.

REFERENCES: [1] Durasov, N. et al. Masksembles for Uncertainty Estimation. CVPR (2021).



Deep Learning for Prostate Cancer Recurrence Prediction on T2W MR Images

Negin Piran
Nanekaran¹

Tony Felefly²

Eranga Ukwatta¹

Nicola
Schieda²

Scott Morgan²

npiranna@uoguelph.ca

tony.felefly@hotmail.com

eukwatta@uoguelph.ca

nschieda@toh.ca

smorgan@toh.ca

¹ School of Engineering, University of Guelph, Guelph, Ontario, Canada; ² Department of Radiology and Surgery (Urology), The University of Ottawa, Ontario, Canada.

Introduction: The occurrence of biochemical recurrence (BCR) after radical radiotherapy (RT) for prostate cancer is a significant concern that affects a high number of patients. This study aims to develop a deep learning (DL) based classifier to predict BCR for intermediate and high-risk prostate cancer, by using pre-treatment T2 weighted (T2W) magnetic resonance (MR) images. The traditional radiomics analysis method is time-consuming and requires significant domain knowledge, but DL techniques can facilitate and automate the process. The proposed DL-based classifier could lead to more personalized treatment options and improved patient outcomes.

Methods: The main objective of this research is to automate the process of prostate segmentation and predict prostate cancer recurrence (PCR). To achieve this, 225 T2W images were obtained from Ottawa Hospital and were pre-processed using resizing, contrast limited adaptive histogram equalization (CLAHE), and curvature driven denoising in T2W MR image slices. These images were then augmented using the Keras library's image augmentation API (ImageDataGenerator) and used to train a U-Net model for prostate gland segmentation [1]. The trained U-Net model was then applied to segment T2W MR images of 189 patients (without prostate masks), provided by the same hospital, which were labeled as recurrent (1) or non-recurrent (0) of prostate cancer by radiologists. These segmented regions of the prostate were then used as input images to 4 different convolutional neural networks (CNNs) to predict PCR. These CNNs contain VGG blocks with batch normalization, dropout, max pooling layers and filters. The performance of the CNN models was evaluated using area under the curve (AUC) metric.

Results: A U-Net model was used for prostate segmentation and the test dataset yielded a Dice score of 78%. An example is shown in Figure 1. The best performing classification models were CNN A and D with AUCs of 0.75 and 0.72 respectively. The main difference between the four CNN models is the use of regularization techniques, Model A does not use any, while Model B uses Dropout, Model C uses both Dropout and multiple convolutional layers, and Model D uses Batch Normalization, Dropout, and multiple convolutional layers. To improve the robustness of the results, cross-validation is proposed to train and test the model on multiple subsets of the data, which will provide a more comprehensive assessment of the model's performance and minimize the risk of overfitting.

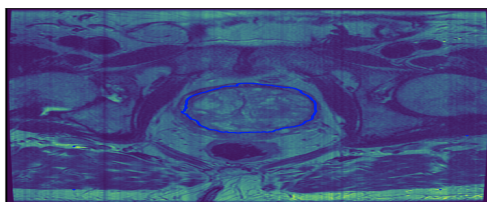


Figure 1: Segmented Prostate

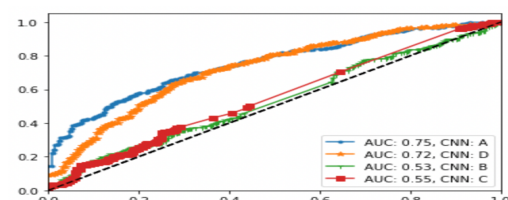


Figure 2: AUC in predicting BCR using DL pipeline

Conclusions: A DL pipeline was developed to segment the prostate gland and predict PCR using T2 weighted MR images. The study showed that the U-Net method effectively prepared the most informative areas of the images for CNN models, resulting in high classification accuracy. This method has the potential to improve patient outcomes by reducing unnecessary treatment and increasing survival rates. Further research using cross-validation and larger patient populations is recommended to validate the classifier.

References: [1] Zabihollahy, Fatemeh, et al. "Automated segmentation of prostate zonal anatomy on T2-weighted (T2W) and apparent diffusion coefficient (ADC) map MR images using U-Nets." *Medical physics* 46.7 (2019): 3078-3090.

Deep Learning-Enabled Fluorescence Imaging for Surgical Guidance: Optical Phantoms from Patient Imaging

Stefanie Markevich,¹ Mandolin Bartling,² Josie La Macchia,¹ Natalie Won,¹ Scott Holtshousen,¹ Esmat Najjar,² Alessandra Ruaro,² Brian C. Wilson,^{1,3} Jonathan C. Irish¹⁻³ and Michael J. Daly¹

¹TECHNA Institute, University Health Network, Toronto ON

²Department of Otolaryngology – Head & Neck Surgery, University of Toronto

³Ontario Cancer Institute, Princess Margaret Cancer Centre, Toronto ON

Introduction: Clinical trials in fluorescence-guided surgery are showing promise in oral cancer patients. Existing fluorescence devices, however, provide only 2D surface visualization that does not help assess the “deep margin” (i.e., maximum infiltration depth of the tumour), which is often the most critical challenge.¹ Our group is developing a 3D fluorescence imaging system for depth quantification based on spatial frequency domain imaging (SFDI) and deep learning (DL) technology; here, we report on evaluation of this system in optical phantoms created based on radiological images of oral cancer patients.

Methods: Magnetic resonance imaging (MRI) images of twenty-one tongue cancer patients were contoured in 3D Slicer software (Fig. a). Tumour segmentations were 3D printed and converted to agar-based optical phantoms (Fig. b) by way of silicone “negative molds”. The agar solution for the tumour and background contained additives for realistic optical absorption (India ink) and scattering (Intralipid), with a fluorescent agent (protoporphyrin IX) in the tumour. SFDI images were acquired at six spatial frequencies ($f_x = 0-0.25 \text{ mm}^{-1}$) in both reflectance and fluorescence imaging mode. Tumour depth and fluorescence concentration maps were estimated using a DL-enabled fluorescence tomography algorithm.²

Results: The tumour segmentations presented a range of surface diameters (~1–3 cm), maximum depths (up to ~1 cm), and shape complexity. The phantom surfaces displayed notable topography, which necessitated illumination compensation based on phase-shift profilometry. After upscaling our DL model to a larger field of view, accuracy in depth and concentration will be assessed in the 21 tumour models.

Conclusion: This study has yielded a set of patient-specific digital tumour models to evaluate a prototype imaging system, with possible future applications in surgical education. The results of this translational research study will characterize 3D fluorescence imaging performance in models mimicking patient cases.

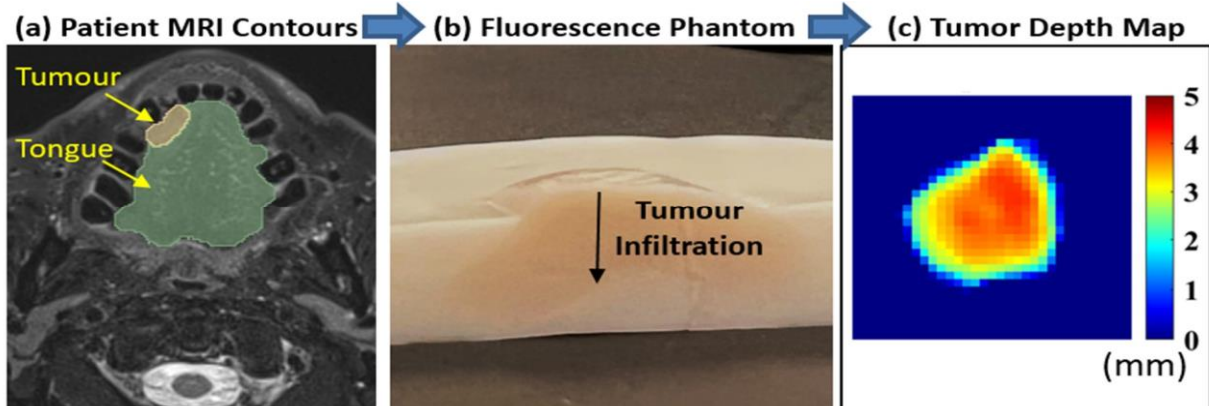


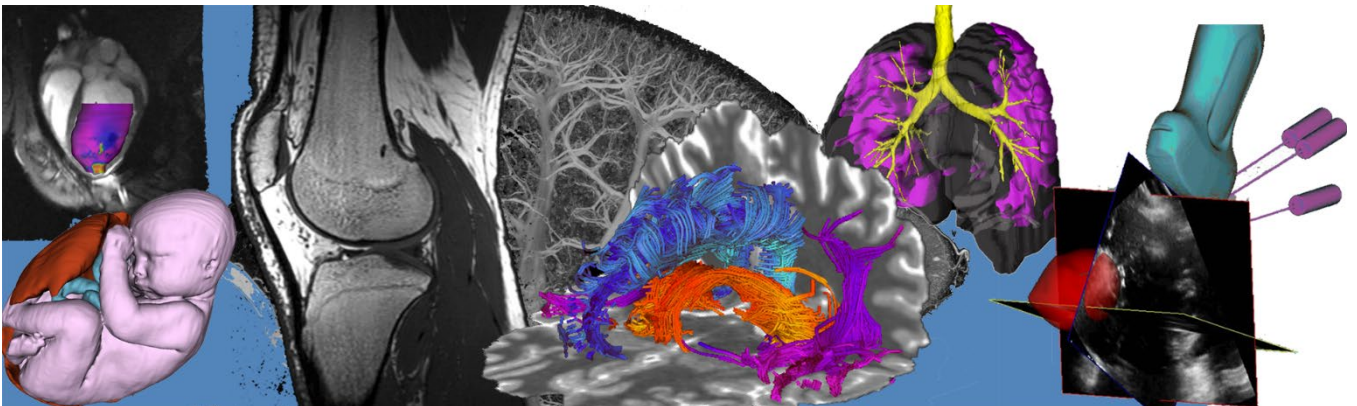
Figure. (a) Representative tongue tumour segmentation. (b) Agar-based optical phantom. (c) Tumour depth map.

References:

1. Brouwer de Koning SG et al., *Eur J Surg Onc.* 2021; 47:2220-2232.
2. Daly MJ et. al., Biophotonics Congress: Biomedical Optics. 2022 OTS-2022 OW4D.4.

Oral Session 12: Neuroimaging II

Abstracts



Development of a brain-penetrating PET radiotracer for imaging 4R-tauopathies

Anton Lindberg,^a Thomas J. Graham,^b Junchao Tong,^a
Robert H. Mach,^b Chester A. Mathis,^c and Neil Vasdev.^{a,d}^aAzrieli Centre for Neuro-Radiochemistry, Brain Health Imaging Centre, Centre for Addiction and Mental Health, Toronto.^bDepartment of Radiology, University of Pennsylvania, USA ^cDepartment of Radiology, University of Pittsburgh, USA.^dDepartment of Psychiatry, University of Toronto.

Introduction. Human tau aggregation is part of the pathophysiology of a class of neurodegenerative diseases called tauopathies. Tauopathies are characterized by their expression of 3R- or 4R-tau isoforms: progressive supranuclear palsy (PSP), and corticobasal degeneration (CBD) are primarily 4R-tau, while Alzheimer's disease (AD) aggregates are comprised of a mixture of both 3R- and 4R-tau. PET imaging of tau aggregates in AD and PSP have been reported using PET tracers optimized for AD, for example, [¹⁸F]Tauvid, [¹⁸F]MK-6240 and [¹⁸F]PI-2620. However, no high-affinity 4R-tau selective PET tracer suitable for neuroimaging exists. Recently, we developed a first-in-class PET radiotracer for imaging 4R-tauopathies ([¹⁸F]CBD-2115) with a novel structural scaffold that unfortunately had low brain uptake in animal PET imaging studies (Lindberg et. al. *ACS Chem. Neurosci.* 2021). Computational predictions to improve brain uptake indicated the need to reduce the number of hydrogen bond donors (HBDs) of the scaffold. The goal of this work was to develop an analog of [¹⁸F]CBD-2115 with fewer HBDs to achieve improved brain uptake. **Methods.** Z-3540 was identified through a fingerprint search using a structure-activity relationship model based on CBD-2115. Two computational methods, central nervous system (CNS)-MPO and BBB score, were used to predict improved brain uptake. [³H]Z-3540 was synthesized and evaluated in binding assays in human CBD, PSP and AD tissue. [¹⁸F]Z-3540 was synthesized using an alcohol-aided copper-mediated transfluorination followed by deprotection (**Figure 1A**). Four healthy Sprague-Dawley rats (2 females, 2 males, 354.3 ± 69.4 g; 10 ± 5 months old) underwent 120 minute dynamic PET imaging following the injection of [¹⁸F]Z-3540 (12.6 ± 4.25 MBq). **Results.** As predicted, Z-3540 had improved CNS-MPO and BBB scores (3.8 and 3.88, resp.) compared to CBD-2115 (3.7 and 3.5, resp.) and is attributed to fewer HBDs. In binding assays using human tissue, [³H]Z-3540 had K_D values of 4.1 nM in CBD, 1.9 nM in AD and 5.1 nM in PSP, and represents a 3-fold improvement compared to [³H]CBD-2115 in AD and 7-fold improvement in CBD. Blocking studies using CBD-2115 revealed that [³H]Z-3540 binds to a different site on tau aggregates than [³H]CBD-2115. [¹⁸F]Z-3540 was produced twice in >0.5 % radiochemical yields, 99% radiochemical purity and molar activities >45 GBq/μmol. The logD_{7.4} of [¹⁸F]Z-3540 measured by the shake flask procedure was 3.36 ± 0.04, and is in the range of brain-penetrating radiotracers (most CNS PET tracers have values between 1.5-3.5). Dynamic PET imaging following bolus intravenous administration of [¹⁸F]Z-3540 in rats revealed that radioactivity reached an initial maximum of 1.7 ± 0.15 standardized uptake value (SUV) within 5 min in whole brain and decreased to below 0.5 SUV by the end of the 120 min PET scan (**Figure 1B & C**), thereby warranting further studies in higher species. **Conclusions.** [¹⁸F]Z-3540 is the first brain-penetrant tau-PET radiotracer based on the CBD-2115 structural scaffold and shows high affinity to tau aggregates in PSP, CBD and AD. While Z-3540 is selective for aggregated tau over other aggregated amyloids, further studies with [¹⁸F]Z-3540 and related derivatives are underway to establish an optimized radiopharmaceutical with selectivity and specificity for aggregated 4R-tau over other tau aggregates.

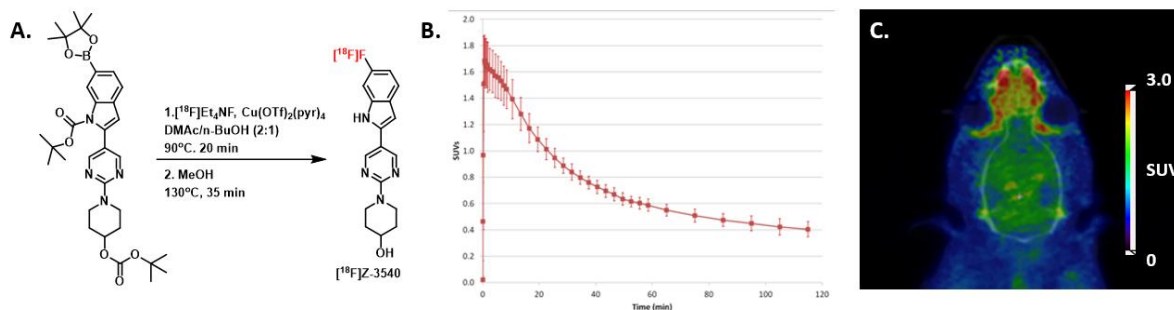


Figure 1. (A) Radiosynthesis of [¹⁸F]Z-3540. (B) Time-activity curves from rat PET imaging of [¹⁸F]Z-3540 (n=4). (C) Summed PET image in rat brain (0-120 min).

Multiphase CT Angiography-based Prediction of Favourable Infarct-Penumbra Mismatch for Acute Ischemic Stroke Treatment Triage

Kevin J. Chung,^{1,4} Sachin K. Pandey,² Alexander V. Khaw,³ Ting-Yim Lee^{1,2,4}

Departments of ¹Medical Biophysics, ²Medical Imaging, and ³Clinical Neurological Sciences, The University of Western Ontario; ⁴Robarts Research Institute and Lawson Health Research Institute, London, Ontario

Introduction: Patients with acute ischemic stroke presenting with a small volume of irreversible brain injury (infarct) relative to a large volume of salvageable tissue (penumbra) are eligible for endovascular stroke treatment. Automated image analysis of high temporal resolution, contrast-enhanced CT perfusion (CTP) imaging can identify patients with this favourable infarct-to-penumbra mismatch profile. However, CTP is often unavailable at resource-limited hospitals due to technical and logistical challenges, preventing its routine acquisition. CTP may also be avoided due to concerns of radiation risk, contrast injections, and delays to treatment. Non-contrast CT and multiphase CT angiography (mCTA) are universally acquired for all stroke patients in Ontario, and together form a low temporal resolution contrast-enhanced dynamic series, which we call mCTA-perfusion (mCTA-P). The objective of this work was to generate perfusion parametric maps and predict mismatch profiles from mCTA-P and compare diagnostic agreement to CTP.

Methods: Sixty-one consecutive patients with acute ischemic stroke who received non-contrast CT, mCTA, and CTP as part of standard of care evaluation at our institution were included in this study. CTP and mCTA-P were independently processed by automated deconvolution software to produce cerebral blood flow (CBF) and Tmax maps. Infarct and penumbra volumes were estimated by thresholding CBF and Tmax maps, respectively, using externally validated thresholds. Concordance in predicting a favourable mismatch profile, defined as infarct < 70 ml, penumbra ≥ 15 ml, and penumbra-to-infarct volume mismatch ratio ≥ 1.8, was determined. Agreement in infarct and penumbra volumes estimated with CTP and mCTA-P were reported as median (interquartile range, IQR) of volume differences (CTP minus mCTA-P).

Results: Forty-six of 61 patients had a target mismatch profile as assessed by CTP. CTP and mCTA-P agreed in determination of mismatch profiles in 82% of patients. Infarct and penumbra volumes tended to be underestimated by mCTA-P compared to CTP as median (IQR) of volume differences were +2.2 (IQR: 0 to 10.8) ml and +14.6 (IQR: -6.8 to 43.0) ml for infarct and penumbra, respectively.

Conclusions: Target mismatch profiles determined with mCTA-P agreed well with those determined by CTP, but infarct and penumbra volumes were underestimated by mCTA-P compared to CTP. mCTA-P may be a pragmatic alternative to CTP-based treatment triage in environments where CTP is unavailable or the risks of CT radiation dose, contrast injections, and delays to treatment outweigh the potential benefit of a separate CTP scan.

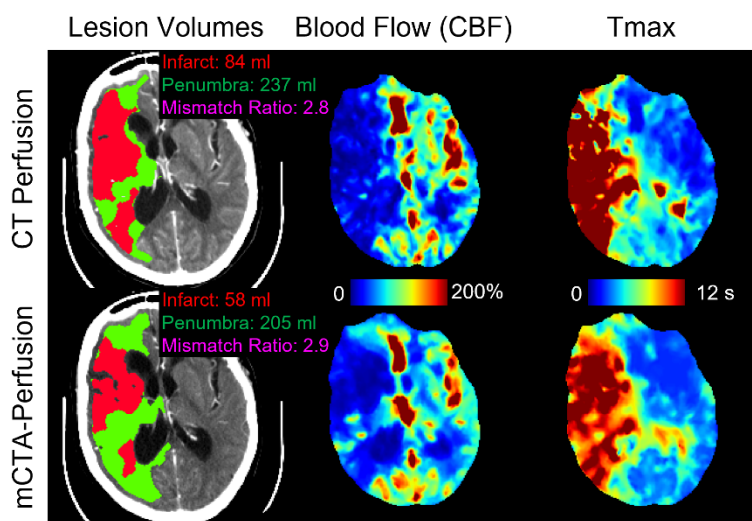


Figure. Example of CT perfusion (top row) and multiphase CT angiography-perfusion (mCTA-P; bottom row) lesion volumes, cerebral blood flow (CBF), and Tmax maps. Despite the similar appearance of perfusion maps and lesion volume segmentations, CTP and mCTA-P disagreed in determined mismatch profiles. CT perfusion predicted an unfavourable mismatch profile due to the infarct volume exceeding the 70 ml threshold. mCTA-P predicted a favourable mismatch due to underestimation of infarct volume. Future work will correct for this underestimation by a calibration procedure.

Choline Changes in the Primary Motor Cortex of People with Mild Cognitive Impairment are Predicted by Dual Task Gait Performance

Jack Elkas¹, Frederico Pieruccini-Faria², Manuel Montero-Odasso², Robert Bartha³

1. Neuroscience Program, Schulich School of Medicine and Dentistry, Western University, London, Ontario, Canada;

2. Gait and Brain Lab, Parkwood Institute and Lawson Health Research Institute, London, Ontario, Canada; 3.

Department of Medical Biophysics and Robarts Research Institute, Schulich School of Medicine and Dentistry, Western University, London, Ontario, Canada

Background: Mild cognitive impairment (MCI) is a transitional state between normal cognition and dementia.¹ Hallmark characteristics of the disease include increased inflammation in the brain, gait impairment and higher risk of falls compared with cognitively preserved older adults. A previous study demonstrated that high levels of choline, a metabolite indicative of inflammation detected using magnetic resonance spectroscopy (MRS) in the primary motor cortex was negatively correlated with walking speed when MCI subjects were asked to simultaneously perform a cognitive task.² Attentional networks may compensate for damage to walking-related brain circuitry that may occur in people with MCI. Thus, overloading the attentional networks during a “dual- task paradigm” (DTP) is recognized as an effective assessment for MCI severity, as the level of gait impairment (dual-task cost) during the task is reflective of the degree of neurodegeneration.³ The aforementioned study² was cross-sectional, and therefore it is unknown whether the degree of gait impairment is associated with a change in choline over time. Thus, the purpose of this study was to better understand the relationship between choline concentration in the motor cortex and DTP gait speed by assessing whether gait impairment detected by a DTP can predict the change in choline over time. We hypothesized that greater dual-task gait cost in speed at baseline would be associated with an increase in primary motor cortex choline concentrations after 6 months.

Methods: 110 participants with MCI were initially recruited through the Synchronized Exercises for Remedies in Gait and Cognition (SYNERGIC) study, a multi-site, longitudinal, randomized clinical trial. Due to attrition, 65 participants' gait data were collected and analyzed at baseline (T0), and MRS data at T0 and after 6 months (T6) [Age: mean = 74, SD = 6 years; Females: N = 33 (50.7%)]. Choline concentration in the primary motor cortex was measured by ¹H magnetic resonance spectroscopy (TE/TR=135 ms/2000 ms, 8 cm³ voxel, 128 acquisitions) collected using 3T MRI and processed to obtain absolute metabolite levels (referenced to 8 unsuppressed water acquisitions) using custom software (fitMAN, BARSTOOL) developed and validated in our laboratory.^{4,5} Participant's gait speeds were recorded during usual or single-task and dual-task conditions at T0 using an electronic mat (Zeno walkway-Protokinetics). For the dual-task condition, participants were asked to ambulate while naming as many animals as possible out loud. The dual-task cost percentage (DTC) or the relative change in gait speed from the single to dual-task condition, was calculated by subtracting the single-task speed from the dual-task speed, and dividing by the single-task speed. A partial Pearson correlation controlling for age, sex, years of education, and MoCA scores was conducted to assess the relationship between T0 DTC in gait speed (%) and the percentage change in choline concentration (%mM) from T0 to T6. ($p \leq .05$). No outliers were detected.

Results: Figure 1 shows a significant positive correlation between the DTC on gait speed at baseline, and the percent change in choline after 6 months in subjects with MCI ($r = .528$, $p < .001$).

Conclusion: Our work supports a relationship between changes in inflammation in the primary motor cortex and dual-task cost in gait speed. Future work should investigate whether these changes in choline measured using MRS persist beyond 6 months and whether changes in the volume of the primary motor cortex are also associated with DTP performance in MCI.

References: [1] 2022 Alzheimer's disease facts and figures. 2022; [2] Annweiler, C. et al. 2013; [3] Montero-Odasso, M. et al. 2018; [4] Bartha R. et al. 1999; [5] Wong D. et al. 2018

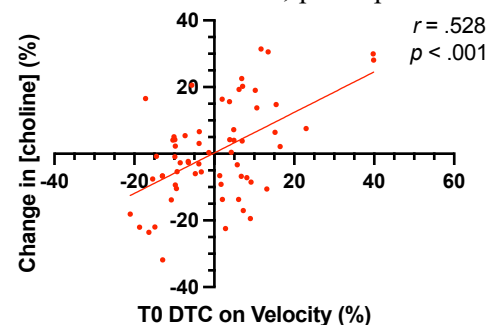


Figure 1: Partial Pearson correlation of DTC on gait speed at T0 with the change in concentration of choline between T0 and T6

Metabolite Abnormalities in Epilepsy Patients with Malformations of Cortical Development Observed with 3T Magnetic Resonance Spectroscopy

Pierre Ibrahim¹, John Adams², Suzan Brown³, Robert Bartha¹, Jorge Burneo³

¹Robarts Research Institute, Schulich School of Medicine and Dentistry, Western University, London, Ontario

²Department of Physics and Astronomy, Western University, London, Ontario

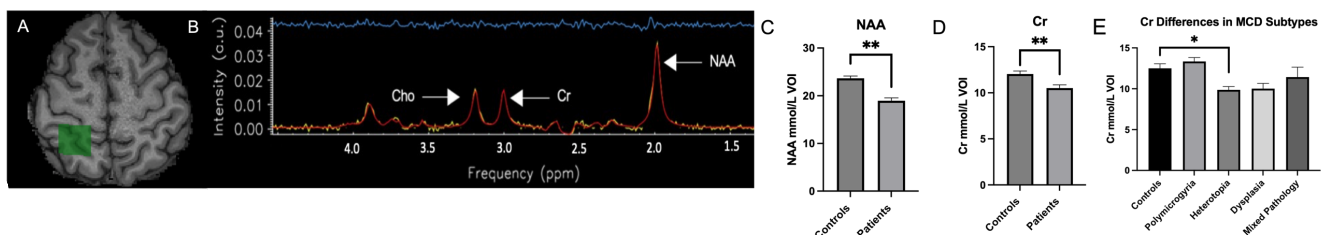
³Epilepsy Program, Department of Clinical Neurological Sciences, Western University, London, Ontario

Introduction: Malformations of cortical development (MCDs) are a major cause of epilepsy that can be categorized into three main types: cortical dysplasia, heterotopia, and polymicrogyria. The metabolic abnormalities associated with MCDs are poorly understood but may result from important pathophysiological changes and could provide useful information to help guide treatment. Single voxel ¹H-magnetic resonance spectroscopy (MRS) is a non-invasive method of quantifying metabolites such as *N*-acetylspartate (NAA), choline (Cho), creatine (Cr), glutamate (Glu), and myo-inositol (Myo) in the brain *in-vivo* and can be integrated into clinical imaging protocols. This study aims to characterize the metabolite profile associated with MCD as well as different MCD subtypes.

Methods: Patients were recruited after being diagnosed with intractable epilepsy caused by MCD. Spectroscopy data were included from 18 patients and 19 healthy participants (control group) matched for age, handedness, and sex. All patients were scanned on a 3T Siemens Prisma Fit MRI system. High resolution T1-weighted anatomical images of the whole brain were acquired, and ¹H spectra were collected from MCD lesions that had been pre-identified in earlier clinical scans. Spectra were also collected from tissue contralateral to the MCD lesions in patients to provide additional control data. In controls, spectra were collected from the motor cortex. Spectra were acquired using a point resolved spectroscopy sequence (PRESS, TR= 2000 ms, TE= 135 ms, number of averages= 192). Spectroscopic data were then processed, corrected, and absolute metabolite levels were quantified using in-lab analysis tools (fitMAN & Barstool). Multivariate analysis of variance (MANOVA) test was used to compare metabolite levels between MCD and control groups, as well as between MCD subtypes. Post hoc tests Tukey test was conducted to determine which MCD subtypes differed. Finally, Pearson correlation was used to correlate metabolites to clinical parameters such as seizure frequency. In all cases $p < 0.05$ was considered significant.

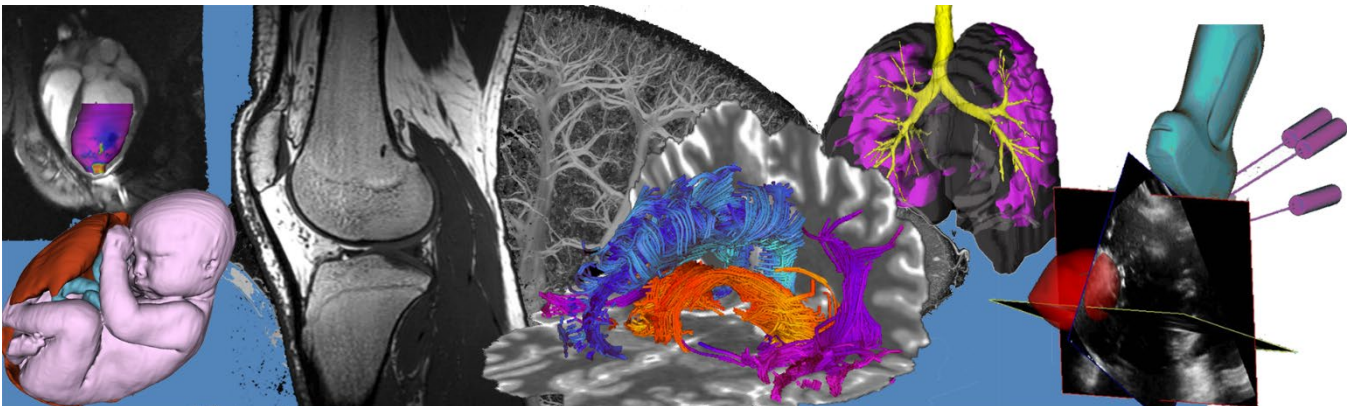
Results: A significant decrease in NAA ($p < 0.001$) (Figure 1C), Cr ($p = 0.002$) (Figure 1D), and Myo ($p = 0.041$) concentrations was observed in MCD patients compared to controls. No other metabolites differences were observed. MANOVA revealed significant between groups differences between the various MCD subtypes for NAA, Cr, Gln, and Myo. Moreover, heterotopia patients had significantly lower NAA levels compared to controls ($p < 0.0001$) and had significantly lower Cr levels compared to controls ($p < 0.01$) (Figure 1E). Pearson's test revealed no significant correlation between Glu levels and seizure frequency.

Conclusions: Observed metabolite differences were consistent with previous findings. Interestingly, we also found a significant difference in Cr levels when comparing MCD patients to controls and between the various subtypes. This result illustrates the potential advantage of absolute metabolite measurements, as these changes may have been obscured by taking metabolite ratios relative to Cr, a common practice in the literature. Future work will also examine differences between lesions and contralateral tissue within MCD subjects.



A) Axial image with voxel (green) location, **B)** MRS spectrum (yellow) with fit (red) and residual (blue), **C)** NAA levels in patients and controls, **D)** Cr levels in patients and controls, **E)** Cr differences between MCD subgroups and controls.

Pitch/Poster Session 11: Deep Learning Abstracts



Federated Learning for Kidney Tumor Segmentation: Preliminary Findings

Prathamesh Samal¹, Pranav Kumar Ayeegoundarvenkatesan², Zachary Szentimrey^{3*}, Rohini Gaikar³, Nicola Schieda⁴, Eranga Ukwatta³

¹Dept. of CSE, Thapar Institute of Engineering and Technology, India; ²Dept. of EEE, National Institute of Technology, Trichy, India; ³School of Engineering, University of Guelph, Guelph, Ontario, Canada;

⁴Department of Radiology, University of Ottawa, Ottawa, Ontario, Canada

First two authors contributed equally to this work. * Indicates presenter.

Introduction: Kidney cancer is one of the most fatal malignancies associated with the urinary system. An early and precise diagnosis can considerably enhance the likelihood of recovery. Artificial intelligence enabled automated detection of kidney tumours in computed tomography (CT) images can aid a radiologist with the clinical workflow. Deep learning models have demonstrated high accuracy in this detection task. These models are generally trained by combining images from various centers into a centralized database, where many images are used for training. However, privacy restrictions concerning medical data may prevent medical institutions from aggregating their data readily. To this end, we propose a U-Net based method using decentralized learning, such as federated learning (FL), for kidney tumor detection from CT images. In FL, only model weights are shared across the institutes instead of imaging data.

Methods: To test FL for kidney tumour detection, we used two different sites for training: KiTS19 (210 images) and a private dataset (65 images) from the Ottawa Hospital. Manual segmentations from expert radiologists were used as ground truth. Different experts segmented the tumors from both the sites, where presence of tumor was confirmed by biopsy. For both sites, the train/test data split was 80/20, and the test images were not used in model training. The 2D U-Net model has an input layer of 512×512 pixels with one channel. Initially, we created multiple U-Net (equal to the number of

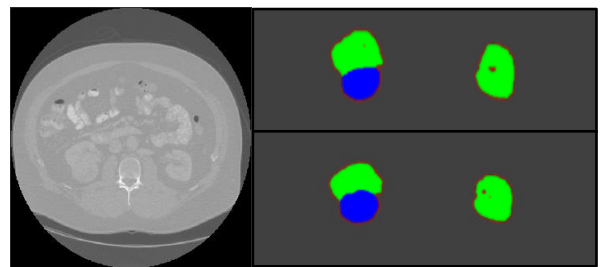


Figure 1: Example segmentation. Top right: Ground truth. Bottom right: 2D U-Net (FL). Left: Patient Slice (2D) from Ottawa Dataset.

datasets+1) models. The training was conducted by repeating two steps (local training and weight aggregation) for t number of iterations ($t=1: T$). First, each model was trained locally using the local dataset at each site. In the second part of the iteration, the weighted average (weights are based on the total number of images in the dataset) of the local model weights were assigned to the global model, and then global model parameters were assigned back to the local models. These iterations in training were conducted until the model converged. This approach of aggregating local model gradients to update a single global model incorporates the accumulated knowledge of both the local models. We used the Dice Similarity Coefficient (DSC) as the metric to evaluate kidney and tumor segmentation using the FL-based model and compared its results to that of individual learning techniques.

Results: From Table 1, it can be inferred that FL yields accuracy comparable to individual model learning, since in FL knowledge of both the dataset is used through weight aggregation. Notably, FL-based model performs within 0.2% and 0.1% DSC difference for kidney of individual learning for KiTS and Ottawa datasets, respectively.

Table 1: DSC results for federated and individual trained model tested.

Dataset	Method	Training Labelled	Test Data	DSC (Kidney)	DSC (Tumour)
KiTS19	Individual	168	42	0.9270	0.8620
Ottawa	Individual	52	13	0.8979	0.9034
KiTS19	Federated (Client 1)	168	42	0.9243	0.8485
Ottawa	Federated (Client 2)	52	13	0.8988	0.8980

Conclusions: We implemented deep learning models (U-Net) to automatically segment kidney tumours from CT images. It was found that FL could provide results similar to on-site machine learning methods. It was also found that FL-based method converged faster than on-site individual learning. By using a collaborative learning approach without sharing any patient data between institutions, FL maintains data privacy while training the models by sharing model weights.

MRI-degad: Conversion of Gadolinium-Enhanced T1w MRIs to Non-Contrast-Enhanced MRIs Using a Convolutional Neural Network

Feyi Ogunsanya^{1,2}, Alaa Taha^{2,3}, Greydon Gilmore^{2,3,4}, Jason Kai^{1,2}, Ali Khan^{1,2,3,5}, Jonathan Lau^{2,3,4,5}

¹Department of Medical Biophysics, University of Western Ontario, London, Canada, ²Imaging Research Laboratories, Robarts Research Institute, University of Western Ontario, London, Canada, ³School of Biomedical Engineering, University of Western Ontario, London, Canada, ⁴Department of Clinical Neurological Sciences, Schulich School of Medicine & Dentistry, London, Canada, ⁵Centre for Functional and Metabolic Mapping, Robarts Research Institute, The University of Western Ontario, London, Canada

Introduction: T1-weighted (T1w) magnetic resonance imaging (MRI) scans with gadolinium (MRI-gad) produce high contrast between vessels and surrounding tissue, allowing for more precise neurosurgical planning. However, the presence of contrast significantly reduces the accuracy of outputs from major neuroimaging workflows such as FreeSurfer's cortical surface reconstruction, which is crucial for subsequent analyses and clinical treatment^{1,2}. Thus, an additional non-contrast MRI (MRI-nogad) is often acquired, but this extends MRI scan time, increasing health care costs, and limits usability of existing MRI-gad datasets without non-enhanced scans. A potential solution is to modify existing workflows to process MRI-gad images with greater precision; however, this would require multiple iterations of training of each software on gadolinium scans.

3D convolutional neural networks (3D-CNN) have been increasingly used for segmentation tasks, with a leading study producing 1-millimeter T1-weighted (T1w) volumes from MRI scans of any orientation, resolution, and contrast³. However, such tools do not tend to generalize to clinically acquired data. To our knowledge, there has not been a study focussed on the reconstruction of MRI-nogad from MRI-gad. Our study aimed to use a 3D CNN-based approach called *MRI-degad* that converts MRI-gad to synthetic scans without gadolinium.

Methods: We retrospectively identified 55 patients who underwent neurological surgery at our center, obtaining MRI-gad and MRI-nogad. We ran the neuroimaging tool fMRIPrep⁴, to assess its performance on both scans by comparing workflow completion time. For *MRI-degad* network training, pre-processing involved isotropic resampling and intra-subject rigid and affine registration of MRI-nogad to MRI-gad scans. Three expert raters quality controlled (QC) the image registrations to ensure sound correspondence. 18 and 7 subjects passed with rigid and affine registrations, respectively. SynthStrip-generated⁵ MRI-gad brain masks were used for the patch sampling space, failing for 2 subjects. Passing subjects (n=23) were randomly split into training (70%; n=16), validation (20%; n=5), and testing (10%; n=2). Convert3D⁶ was used to generate 3D patches (~50,000 patches/patient) to reduce computational load during training and model inference. TensorFlow (version 2.9.0) was used to implement the 3-D U-Net CNN architecture⁷. A loss metric of root mean squared error (RMSE) was used during training.

Results/Conclusions: All 55 of the MRI-nogad images ran to completion with fMRIPrep, while only 37 of the MRI-gad scans completed. Mean completion time of MRI-gad and MRI-nogad for fMRIPrep was respectively 28.33 +/- 17.6 hours (n=37) and 6.873 +/- 1.229 hours (n=55), which was a significant difference ($Z=-5.31$, $p < 0.001$) via a Wilcoxon signed-rank test. Training and validation RMSE error was 216.12 and 321.04. We demonstrate that MRI-gad scans are problematic for a common neuroimaging workflow resulting in failure to complete or extended completion time. Future directions are focused on comparing 3D CNN architecture to a generative adversarial network, incorporating external validation, increasing dataset variation, and the quantitative comparison of FreeSurfer cortex-based and whole-brain measurements of MRI-degad with MRI-gad and MRI-nogad.

1. Reuter et al. (2012). Within-subject template estimation for unbiased longitudinal image analysis. *NeuroImage*, 61(4), 1402–1418. <https://doi.org/10.1016/j.neuroimage.2012.02.084>. 2. Rebsamen et al. (2022). Reliable brain morphometry from contrast-enhanced T1w-MRI in patients with multiple sclerosis. *Human Brain Mapping*, 1–10. <https://doi.org/10.1002/hbm.26117>. 3. Iglesias et al. (2021). Joint super-resolution and synthesis of 1 mm isotropic MP-range volumes from Clinical MRI exams with scans of different orientation, resolution and contrast. *NeuroImage*, 237, 118206. 4. Esteban et al. (2019). fMRIPrep: a robust preprocessing pipeline for functional MRI. *Nature methods*, 16(1), 111–116. <https://doi.org/10.1038/s41592-018-0235-4>. 5. Hoopes et al. (2022). Synthstrip: Skull-stripping for any brain image. *NeuroImage*, 260, 119474. <https://doi.org/10.1016/j.neuroimage.2022.119474>. 6. Yushkevich et al. (2016). IC-P-174: Fast Automatic Segmentation of Hippocampal Subfields and Medial Temporal Lobe Subregions In 3 Tesla and 7 Tesla T2-Weighted MRI. *Alzheimer's & Dementia*, 12: P126-P127. <https://doi.org/10.1016/j.jalz.2016.06.205>. 7. Isensee et al. (2021). nnU-Net: a self-configuring method for deep learning-based biomedical image segmentation. *Nat Methods* 18, 203–211. <https://doi.org/10.1038/s41592-020-01008-z>

Artifact Detection Algorithm Using Deep Learning in Fetal MRI

Adam Lim^{1,2}, Justin Lo^{1,2}, Matthias W. Wagner³, Birgit Ertl-Wagner^{3,5}, Dafna Sussman^{1,2,4}

¹Department of Electrical, Computer and Biomedical Engineering, Toronto Metropolitan University, Faculty of Engineering and Architectural Sciences, Toronto, Ontario, Canada

²Institute for Biomedical Engineering, Science and Technology (iBEST), Toronto Metropolitan University and St. Michael's Hospital, Toronto, Ontario, Canada

³Division of Neuroradiology, The Hospital for Sick Children, Toronto, ON M5G 1X8 Canada.

⁴Department of Obstetrics and Gynecology, Faculty of Medicine, University of Toronto, Toronto, Ontario, Canada

⁵Department of Medical Imaging, Faculty of Medicine, University of Toronto, Toronto, Ontario, Canada

Introduction: Degradation of fetal magnetic resonance images (MRI) are most commonly caused by motion, chemical shift, and radiofrequency artifacts. These artifacts can obscure parts of the fetus, making interpretation challenging for the radiologist. Currently, MRI operators have to manually review each MRI series to determine presence or absence of artifacts. This is a cumbersome and time-consuming process, where errors can have long-term implications, such as inaccurate/missed radiological diagnoses. Automating this process using deep learning methods would improve the workflow and potentially diagnostic outcomes. We propose a novel algorithm that can detect and classify the severity of fetal MRI artifacts into the following 4 different classes: 1) motion, 2) chemical shift, 3) radiofrequency, and 4) no artifacts.

Methods: A total of 31 whole body 3-dimensional (3D) fetal MRI datasets were acquired using either an SSFP (1.5T) or a 3D SSFP sequence with SENSE (3.0T). This produced a total of 2250 2D images that was further divided using an 80:10:10 split representing the training, validation, and testing sets respectively. The ground truth was manually labeled by collaborating subspecialized radiologists into type and severity of artifact using a scale of none, mild, medium, or severe. The proposed algorithm makes use of a convolution neural network (CNN) framework which incorporates skip connections, Inception blocks, and Squeeze and Excitation (SE) blocks that stem from the ResNet-50, Inception, and SE networks respectively. A ResNet-Inception-Squeeze-and-Excitation (RISE) module was used as the main feature extractor to address the vanishing gradient problem, thereby reducing model computational complexity, and placing greater emphasis on significant features. After the feature extraction component, 2 separate classifiers were trained to output the artifact type and the severity. The proposed algorithm was compared to other competitive image classification networks through a 2D analysis. An ablation study was also conducted to ensure all network components were contributing to overall model performance.

Results: Our proposed algorithm, RISE-Net, achieved an average accuracy and F1 score of 90.34% and 90.39% respectively. This surpassed other state-of-the-art networks such as VGG-16, Inception, ResNet-50, ResNet-Inception, SE-ResNet, and SE-Inception. The ablation study consisted of removing network components which resulted in decreased model performance. Notably, the SE element had the most significant impact where accuracy and F1 score decreased by 6.8% and 6% respectively when omitted. Example outputs from the algorithm are shown in Figure 1.

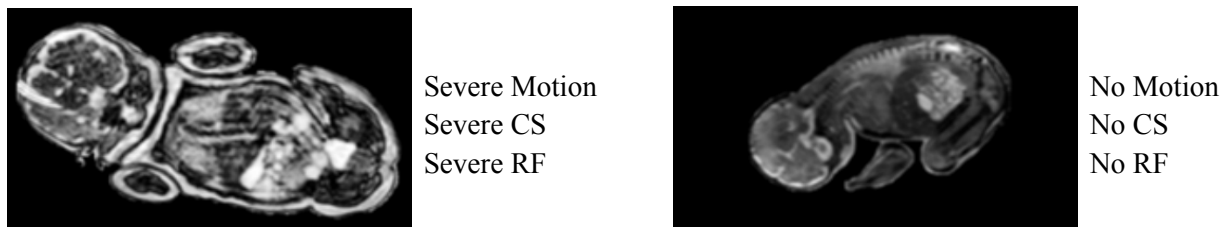


Figure 1: Examples for outputs from RISE-Net. Fetal MRI with severe motion, chemical shift (CS), and radiofrequency (RF) artifacts (left) compared to a fetal MRI with no artifacts (right).

Conclusion: We present a novel deep learning quality assurance algorithm, RISE-Net, that can automatically detect and classify the severity of the most common artifacts in fetal MRI. The promising results indicate that the algorithm can be implemented as a clinical tool to improve MRI acquisition.

Background Parenchymal Enhancement Estimation on DCE Breast MRI using a Siamese NetworkGrey Kuling^a, Belinda Curpen^b, Jennifer Brooks^c, and Anne L. Martel^{a,d}^aMedical Biophysics, University of Toronto, Toronto, ON, Canada^bDept of Medical Imaging, Sunnybrook Health Sciences Centre, Toronto, ON, Canada^cDalla Lana School of Public Health, University of Toronto, Toronto, ON, Canada^dPhysical Sciences, Sunnybrook Research Institute, Toronto, ON, Canada

Introduction: The definition of Background Parenchymal Enhancement (BPE) is the intensity and amount of enhancement of healthy fibroglandular tissue (FGT) on DCE-MRI [1]. Recent research suggests BPE is important as an independent marker for breast cancer and breast cancer treatment outcomes. A radiologist typically records this tissue feature in their imaging report using the Breast Imaging Reporting and Data System (BI-RADS) Lexicon. The BI-RADS lexicon describes BPE with a categorical ranked scale from Minimal to Marked. Past techniques to quantify BPE on a continuous scale have used image segmentation models to identify the FGT in DCE-MRI and calculate the ratio of intense enhancement in the volume of FGT. These methods suffer from the disadvantages of image registration between contrast infusion time points. An alternative is to estimate the level of BPE with a Siamese Network[2] that can take two scan time points of the DCE-MRI as input and estimate a level of BPE. The model shares the same weights on each time point to build a comparable latent space that is combined to regress to BPE level.

Method: We acquired DCE-MRI data from Sunnybrook Health Sciences Institute under REB approval. For training, we used 256 Bilateral DCE breast MRIs. A training example is a single breast from the separated bilateral scan (n=512). Our test set contained 512 Bilateral DCE breast MRIs where between the two breasts, we averaged the BPE estimation (n=512). We took ground truth labels from the radiology reports. We converted the categorical ranked scale to a continuous scale between 0 and 1, where minimal, mild, moderate, and marked categories were labelled as 0.125, 0.375, 0.625, and 0.875, respectively. The Siamese network[2] characteristically uses the same encoding weights for both time point images of the DCE-MRI. Then the latent spaces are concatenated and put through a fully connected regression head to predict BPE. To test the model, we evaluated the Pearson Correlation coefficient (r) between the estimated BPE and BPE categorical ranked scale. We compare the results to a baseline model of a 2D UNet[3], the current state of the art, and take the ratio of FGT that enhances after one infusion time point greater than 40%.

Results: The resulting correlation coefficient for the 2D UNet was 0.430, and the correlation coefficient for the BPE Siamese Network was 0.619. We plot the results on the boxplots provided in Figure 1.

Conclusion: We can see from the Pearson correlation coefficients that the Siamese network adheres to the ground truth of radiologist interpretations better than a segmentation algorithm.

The advantages of using this Siamese network are there is no need to segment the tissues in the scan and no need for image registration between time points. Limitations of this study are the limited dataset sizes, the dataset being from a single institute, and ground truth subjectivity. Future work will focus on longitudinal analysis of the hormone metabolic influences on the estimated BPE. Specifically looking at the effect of menopause, the week of the menstrual cycle in pre-menopausal women, and hormone replacement therapy in postmenopausal women.

We have shown a Siamese Network is more efficient at estimating a BPE quantification than image segmentation.

References:

- [1] Geraldine J. L. et al. Background parenchymal enhancement on breast MRI a co... JMRI, 51(1):43–61, 2020.
- [2] Bertinetto L. et al. Fully-convolutional siamese network ... In Euro. conf on comp. vision, 850–865, 2016.
- [3] Kuling G et al. Domain adapted breast tissue segmentation in ... In 15th IWBI, 11513: 344-351. SPIE, 2020.

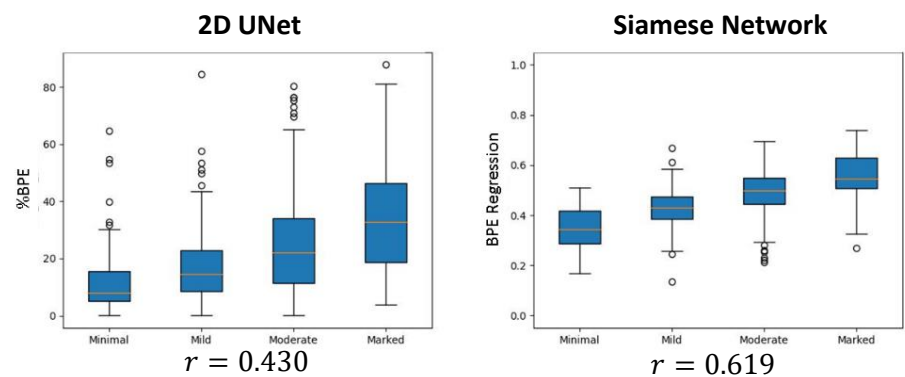


Figure 1: Boxplots of BPE quantification versus the radiologist interpretation of the DCE-MRI

Placental MRI Segmentation Using A Novel Convolutional Neural Network

Alejo Costanzo^{1,2}, Sophie Wagner^{1,3}, Birgit Ertl-Wagner^{4,5}, Dafna Sussman^{1,2,6}

¹Department of Electrical, Computer and Biomedical Engineering, Toronto Metropolitan University (formerly Ryerson University), Faculty of Engineering and Architectural Sciences, Toronto, Ontario, Canada; ²Institute for Biomedical Engineering, Science and Technology (iBEST), Toronto Metropolitan University (formerly Ryerson University) and St. Michael's Hospital, Toronto, Ontario, Canada; ³Faculty of Health Sciences, McMaster University, Hamilton, Ontario, Canada; ⁴Division of Neuroradiology, The Hospital for Sick Children, Toronto, ON, Canada; ⁵Department of Medical Imaging, Faculty of Medicine, University of Toronto, Toronto, ON, Canada; ⁶Department of Obstetrics and Gynecology, Faculty of Medicine, University of Toronto, Toronto, Ontario, Canada

Introduction: During pregnancy, the placental organ serves as the main maternal-fetal interface for fetal development [1]. Placenta accreta spectrum (PAS) includes a range of invasive placentation which can be challenging to diagnose on imaging [2], [3]. PAS is often initially suspected on ultrasound, but MRI may improve diagnostic accuracy [2]. Methods to improve the reliability and accuracy of delineating the placenta in MRI are needed [3]. Current methods of fetal MRI diagnosis can be enhanced through automation with tools such as Convolutional Neural Networks (CNN). We propose a novel CNN architecture (RTNet) for placental organ segmentation from 3D fetal MRI. Through the use of this image segmentation task, segmentation time and cost will dramatically be reduced.

Methods: 28 normal 3D fetal MRIs acquired using a 3D SSFP sequence on a 1.5T or 3.0T MRI scanner were used for this study. Altogether these provided 2,156 2D images which were manually segmented to create the ground truth dataset. This dataset was then validated by expert fetal radiologists and split on a (63/7/30) train, validation and hold-out test sets respectively. For finetuning we used the 63/7 split with 5-fold random sampling cross-validation. Our novel architecture seen in Figure 1., utilizes transformer, attention and atrous pyramid pooling blocks implemented on a ResUNet++ backbone.

Results: The validation set results are seen in Table 1. We achieved a mean DICE similarity score of 93.3% on the training set, with the validation set similarly achieving 93.6%, and the hold-out test set resulting in 86.2%.

Table 1. Tabulated results of RTNet for placental segmentation.

RTNet	Dice
Training	96.3%
Validation	96.7%
Test	86.2%

Conclusion We propose a novel CNN architecture for improving the diagnosis of placental abnormalities through automatic segmentation of the placenta in fetal MRI. Our model is capable of segmenting 2D slices from a 3D dataset and reconstructing its placental volume and surface area, providing important quantitative parameters for fetal diagnosis.

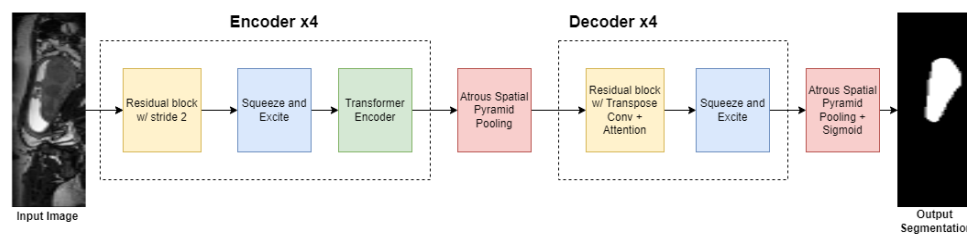


Figure 1. AFNet architecture pipeline for placental fetal MRI segmentation. MRI images are shown in the sagittal plane.

References

- [1] F. G. Cunningham, Ed., "Chapter 5: Implantation and Placental Development," in *Williams obstetrics*, Twenty-Sixth edition., New York: McGraw Hill, 2022.
- [2] C. H. J. R. Jansen *et al.*, "Development of placental abnormalities in location and anatomy," *Acta Obstet. Gynecol. Scand.*, vol. 99, no. 8, pp. 983–993, Aug. 2020, doi: 10.1111/aogs.13834.
- [3] P. Jha *et al.*, "Society of Abdominal Radiology (SAR) and European Society of Urogenital Radiology (ESUR) joint consensus statement for MR imaging of placenta accreta spectrum disorders," *Eur. Radiol.*, vol. 30, no. 5, pp. 2604–2615, May 2020, doi: 10.1007/s00330-019-06617-7.

Intracranial Hemorrhage Detection Using Machine Learning

Navkiran Sohal¹, Emilie Potts², Haojie Mao^{2,3}

[1] Engineering in Medicine, Faculty of Engineering, Western University

[2] School of Biomedical Engineering, Western University

[3] Mechanical and Materials Engineering, Faculty of Engineering, Western University

Introduction: Intracranial hemorrhage (ICH) is a devastating condition that can be produced by a wide range of pathology, including hypertension, underlying vasculitis, trauma, and cerebral arteriovenous malformations. ICH has been linked to numerous deadly repercussions, as 25 out of 100,000 cases annually have related brain tumors with ICH and can account for approximately 16% of strokes [1]. One main challenge with this condition is that it can form in any intracranial compartments, resulting in difficulty for radiologists to accurately determine the cause and minimize hemorrhage expansion, and hence effective and efficient diagnosis is needed. ICH is traditionally diagnosed with unenhanced MRI scans of the brain [2], allowing the different types of ICH (epidural, subdural, subarachnoid, and intraparenchymal) to be differentiated. Our work is based on a computer-aided diagnosis (CAD) system to perform the detection of intraparenchymal hemorrhage and intraventricular hemorrhage.

Methods: The proposed method is comprised of a deep convolutional neural network (CNN) to diagnose ICH using deep learning. This study retrospectively identified unenhanced head MRI examinations that demonstrated ICH, as well as unenhanced MRI scans of the brain that demonstrated no evidence of ICH. A total of 3000 MRI scans were included in the database, 1500 included had hemorrhage present, and 1500 were controls. The dataset was then divided into 2400 images as training and 600 as a validation set. In addition, 60 extra cases were collected to test the developed CNN model. For better performance of the CNN model, all the MRI images were pre-processed. These images were converted into single-channel images, then scaling, flipping, and rotation were applied.

Results: The CNN architecture was composed of blocks and operated on 2D slices. Each block contains $k=2$ convolutional layers and a rectified linear unit (ReLU). Based on 3000 MRI scans, our CNN model achieved a training accuracy of 98.9%. The trained classifier was a further success when evaluating 60 different cases (30 control cases and 30 ICH cases), resulting in 59 out of 60 being successfully diagnosed by our CNN model. Examples of successful predictions are below in Figure 1.

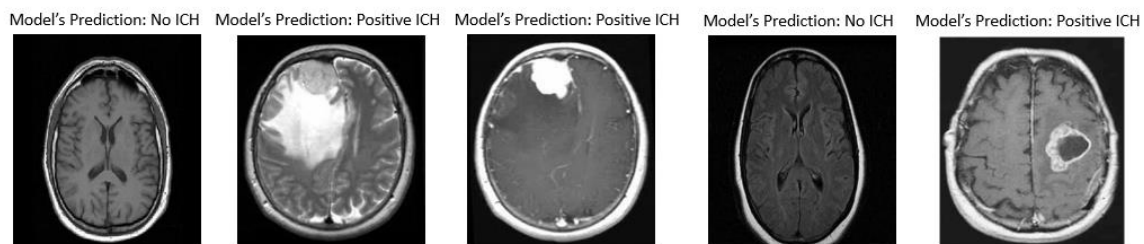


Figure 1. CNN-predicted ICH.

Conclusions: The focus of this research was to use machine learning to detect hemorrhages. The goal of our CNN model developed was to improve medical imaging diagnosis. It is important these days to assess the effectiveness of a CAD system with radiologists as ICH can be detected by standardized examinations at its earlier stage. Our approach towards the diagnosis using deep learning is a promising technique in medical imaging. The proposed model comprises preprocessing, thresholding, extraction, and classification. The input MRI images in the initial phase were converted into a compatible format. To evaluate the performance of the presented CNN model, a testing set was used. The CNN model showcased outstanding results with an accuracy of 98.9% and an accurate prediction of 59 cases out of 60. Future work includes detecting more subtle ICH and incorporating demographics into the analysis. Data and codes of this study are available on request.

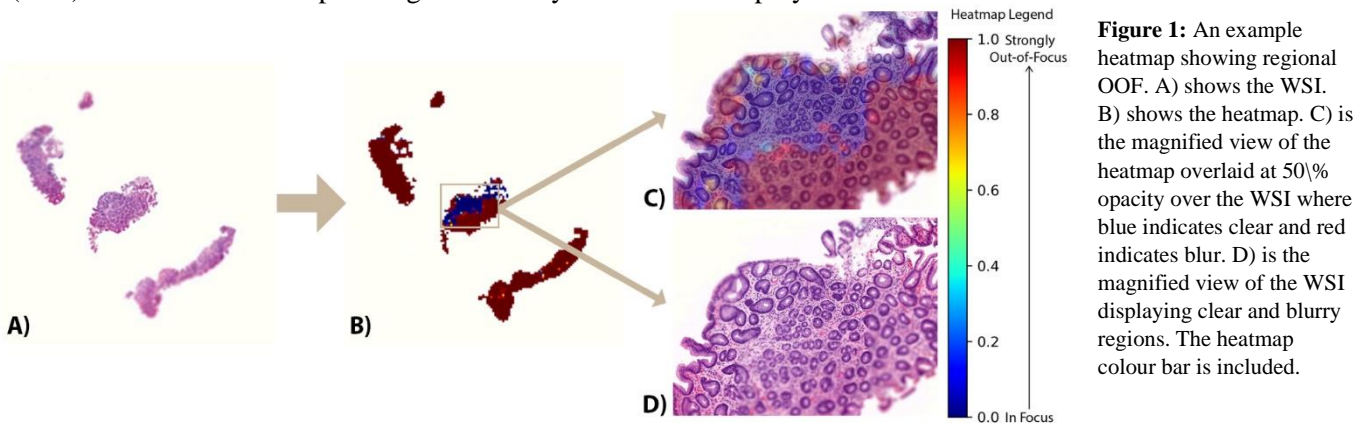
References:

[1]: Jeremy J. Heit, *et al.*, Journal of Stroke, 2017 [2]: Phong, *et al.*, International Conference on Machine Learning and soft computing - ICMLSC'17, 2017.

Creating better whole slide image datasets:**Quality control detection of out-of-focus patches in digital pathology**Phoenix Wilkie^{1,2}, Lukasz Itert², Dina Bassiouny Abousheishaa², Anne Martel^{1,2}¹Department of Medical Biophysics, University of Toronto; ²Sunnybrook Research Institute

Introduction: The digitization of histopathological slides is advancing clinical workflows and presents an opportunity for large-scale machine learning. One of the bottlenecks of high-throughput scanning for computational pathology remains quality control. Out-of-focus (OOF) blur occurs during the scanning process. This can be due to dirty glass, dust and dirt, pen markings, or tissue thickness irregularities. Currently, to detect OOF regions, a pathologist must inspect each whole slide image (WSI) manually. This process can take 8-16 hours per slide [1]. While this works well for large patches of blur, it is difficult to find smaller OOF areas. The goal is to create a convolutional neural network model that achieves high accuracy in finding OOF regions on commercially available computer hardware in a short amount of time. This model would have a user-friendly interface and could be incorporated into the scanner's software. This would enable the scanner to automatically rescan OOF slides during batch scans.

Methods: We have trained an accurate OOF model using WSI patches derived from 52 different tissue areas and stained with a variety of stains. To augment publicly available curated datasets with manually annotated OOF patches, we developed a method of generating realistic synthetic OOF patches using Gaussian and Bokeh blur filters to mimic existing levels of OOF. In total, the training dataset contained 171,436 patches with a breakdown of 41,851 synthetically blurred patches, 52,800 real OOF patches, and 76,785 clear patches. The patches were stained with different stains and taken with a variety of scanners at different resolutions. A graphical user interface (GUI) was created for the pathologists to easily interact and employ the model.



Results: Our model was verified using a publicly available, labelled, dataset called FocusPath [2]. Out of 138,240 patches of 256 x 256 pixels, our model achieved 99.99% ($\pm 1.73\%$) accuracy on average. The model generalizes well and achieved 92.86% ($\pm 3.17\%$) accuracy on average when tested with a never-before-seen Masson's Trichrome stain. A WSI can be evaluated for OOF regions in under one minute on a seven-year-old NVIDIA GeForce GTX TITAN X 12GB GM200 graphics processing unit. Model output is available as a CSV file with prediction values as well as heatmaps that can be overlaid on the original WSIs (see Figure 1).

Conclusion: This paper proposes a supervised OOF detection model packaged in a user-friendly format to improve the focus quality control pipeline for pathologists. The OOF detection model achieves high accuracy and generalizes well. The GUI is currently in beta testing and is being used by a pathology research fellow. Ongoing feedback confirms the accuracy and the pathology fellow reports that it greatly reduces the time they spend checking the focus quality of slides before doing any rescans. This project has the potential to be integrated into built-in scanner software. Our future work will consist of maintaining this for deployment in research institutions and adding more features that pathologists may request.

References: [1] Timo Kohlberger, et al. Whole-slide image focus quality: Automatic assessment and impact on AI cancer detection. *Journal of Pathology Informatics*, 10, 2019. [2] Zhongling Wang, et al. FocusLiteNN: High efficiency focus quality assessment for digital pathology. 1, 2020.

Classifying points of interest in FAST ultrasound videos using neural networks

Ilan Gofman^{a,b}, Matthew Holden^b

^aDepartment of Computer Science, University of Toronto, Toronto, Canada

^bSchool of Computer Science, Carleton University, Ottawa, Canada

Introduction: The Focused Assessment with Sonography in Trauma (FAST) is a Point-of-Care Ultrasound procedure used to identify possible trauma by examining areas for lacerations and free fluid. The assessment covers four regions of the body: left upper quadrant, right upper quadrant, cardiac, and pelvic. Each region has various points of interest (POIs) that are important for ultrasound operators to examine comprehensively to ensure an accurate diagnosis. Our goal is to develop an objective system that can identify which POIs have been scanned and provide feedback to the ultrasound operators regarding their scans. To accomplish this, we propose several Convolutional Neural Network (CNN) architectures for classifying POIs that have been scanned across regions. A POI classifier can be integrated within a real-time information system for the assessment that will notify the operator which POIs require further scanning to ensure that each patient is fully scanned.

Methods: The dataset contains 17 videos of scans completed of the 4 regions, where each region contains between 8 to 12 POIs. As multiple POIs can occur in the same video frame we use multi-label classification to predict the list of POIs that are present. We propose 2 architectures for this task, a single-frame architecture and an architecture for classifying video fragments. For the video classification, we split the original video into short snippets consisting of 5 to 20 frames, and classify all the POIs observed in the snippet. The single frame classification is done using the InceptionV3 model architecture proposed by Szegedy et al [1]. While the video classification model architecture is a modified Inflated 3D ConvNet (I3D) [2] that can be seen in Figure 1. It is a two-stream version of the InceptionV1 model architecture but with another dimension added to the convolutional layers to capture the temporal information. One stream uses the original ultrasound images to train, while the other stream uses the optical flow of the video frames. They are trained independently, and the predictions are then averaged. The test set consists of 3 videos, while the remaining 14 were used to train and tune the model through cross-validation.

Results: The performance of the model was measured using the full-label accuracy which measures the portion of predictions where all POIs are predicted correctly in a single label, as well as the micro F1-score. The best performing model was the InceptionV3 model that predicts POIs using single frames, having achieved a full-label accuracy of 88.1% with a micro F1-score of 0.63. The video classification achieved a full label accuracy of 63% with a micro F1-score of 0.34 when using 10 frames per video fragment. Although the results are worse when training using the I3D model, we have found that additional data augmentation improves the performance. By using techniques such as translations, mirroring, and temporal flipping, the micro F1-score improves by 0.07.

Conclusions: The single frame classification model using the InceptionV3 architecture performed the best. Given the small size of the dataset, applying data augmentation was critical to the performance of the model. To conclude, this work has shown CNNs can be used effectively to classify the POIs scanned during a FAST exam. By using a POI classifier, the models trained can provide objective feedback to the ultrasound operator on which areas have not been scanned in a particular region. This work can be expanded to provide real-time feedback as part of the FAST examination to ensure each patient is assessed comprehensively and all POIs have been scanned.

References

- [1] C. Szegedy, V. Vanhoucke, S. Ioffe, J. Shlens, and Z. Wojna, "Rethinking the inception architecture for computer vision," Dec. 2015.
- [2] J. Carreira and A. Zisserman, "Quo vadis, action recognition? a new model and the kinetics dataset," May 2017.

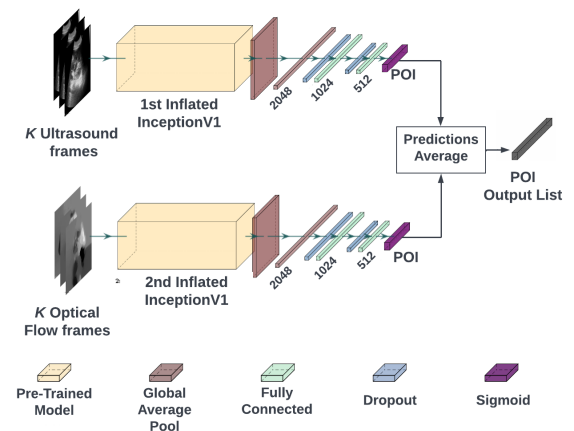


Figure 1: The modified I3D model architecture used for predicting POIs.

Improving the reliability of video-based skill assessment metrics with uncertainty quantification

Catherine Austin, Rebecca Hisey, Olivia O'Driscoll, Tamas Ungi, Gabor Fichtinger

Laboratory for Percutaneous Surgery, School of Computing, Queen's University, Kingston, Canada

Introduction: The creation of video-based skill assessment platforms that use object detection for tool tracking are becoming more common. This is due to the increased level of convenience and cost effectiveness object detection offers in comparison to traditional tracking systems. However, object detection is typically less reliable than traditional tracking approaches. Object detection networks will often falsely predict the presence of a tool which can lead to artificial inflation of metrics that are frequently used to evaluate surgical skill such as path length. The artificial inflation of these metrics leads to an over-estimate user skill, which can have serious consequences to patient safety. Typically, methods to minimize false predictions center around acquiring larger datasets to create better performing object detection networks. Due to the low availability of participant data, this is not always a feasible solution. We aim to create an alternative approach to this method by identifying and removing instances where an object detection network falsely predicts the location of a tool. This approach was tested on Central Line Tutor, a video-based skill assessment platform for central venous catheterization (CVC) [1].

Methods: To identify false predictions made by the object detection network, the level of uncertainty of each prediction had to be calculated. The uncertainty was calculated using the network's second last layer of output for each prediction and the Shannon entropy equation shown in Equation 1 [2]. Then, a threshold of uncertainty, defined as the optimal point of a Receiver Operating Characteristic curve, was established. Any false predictions generated by the object detection network were identified and removed if its uncertainty exceeded this threshold. The effectiveness of our method was tested by obtaining 50 video recordings of 5 expert and 5 novice participants practicing CVC. Each of the frames from those videos were annotated with bounding box locations for syringe and the phantom. A You Only Look Once (YOLO) object detection network was trained using the ground truth data. Metrics for path length were calculated using both the ground truth labels and the predictions for each video. The two sets of metrics were used to establish a baseline comparison between ground truth boxes and predictive results. The predictive bounding boxes generated by YOLO were then evaluated using the previously described entropy equation, and the results identified as false predictions were removed. Metrics were then calculated for the modified set of predicted bounding boxes. The metrics for this set were compared to the baseline performance established for the ground truth and predicted bounding boxes using a Pearson Correlation.

$$H(X)_{\text{discr}} = -\sum_{x \in \Omega} p(x) \cdot \log_2(p(x)) \quad (1)$$

Results: The syringe and ultrasound path lengths for both the baseline results and results with false predictions removed are shown in Figure 1. The initial Pearson correlations for the baseline comparisons were 0.922 for syringe path length and 0.753 for ultrasound path length. When false predictions made by the object detection network were removed, the Pearson correlations between those results and the ground truths were 0.816 for syringe path length and 0.510 for ultrasound path length.

Conclusions: The path lengths calculated from the results that had false predictions removed were consistently reduced, bringing the path length computed using object detection closer to that of the ground truth. This shows that this method was able to successfully reduce metric inflation without requiring a more highly performing object detection network. In future work, we will explore ways to ensure that this method reduces metric inflation without compromising the trends shown by the difference in path length from trial to trial.

References: [1] Hisey R, Camire D, Erb J, Howes, Fichtinger G, Ungi T. System for central venous catheterization training using computer vision-based workflow feedback. *IEEE Transactions on Biomedical Eng.* 2021 Nov. 2

[2] Namdari, A., Li, Z., "A review of entropy measures for uncertainty quantification of stochastic processes," *Advances in Mechanical Engineering* 11(6) (2019).

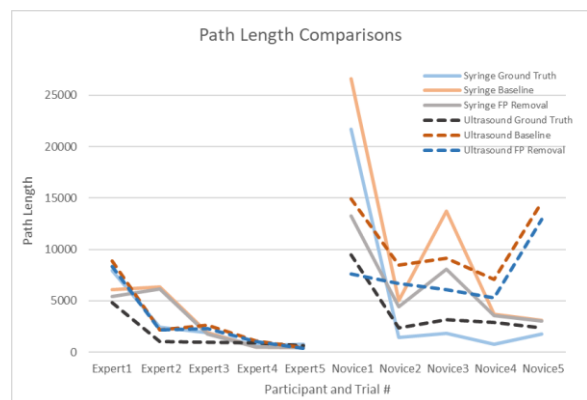
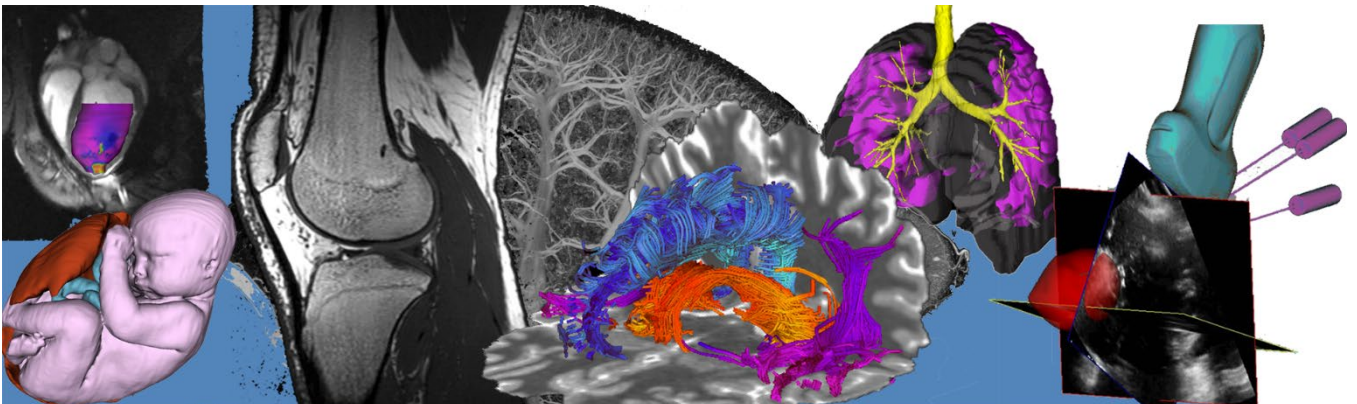


Fig 1: A comparison of path lengths.

Pitch/Poster Session 12: Cellular and Molecular/Image Guidance Abstracts



Tracking ^{89}Zr -labelled *Escherichia coli* Nissle 1917 post-ingestion using PET/MRI

M Nassar^{1,2,3,4}, S Donnelly⁴, J Hadway⁴, L Morrison⁴, J Butler⁴, H Biernaski⁴, Y Huston⁴, H Jago^{4,5}, J Sykes^{4,5}, N Cockburn^{4,6}, M Kovacs^{4,6,7}, Prato FS^{2,4,7}, J Thiessen^{2,4,7}, JP Burton^{1,3,8} and D Goldhawk^{2,4,7}

¹Department of Microbiology and Immunology, ²Graduate Program in Molecular Imaging, Western University; ³Centre for Human Microbiome and Probiotics, ⁴Imaging program, Lawson Health Research Institute; ⁵Thames Valley Veterinary Services; ⁶Cyclotron Facility, Lawson Health Research Institute; ⁷Department of Medical Biophysics, ⁸Department of Surgery, Western University, London, Canada.

Introduction: The microbiome is an integral part of the human body and is important in health and disease. Microbiota have been extensively studied using *ex vivo* techniques that provided data on the bi-directional association of microbiota composition and disease evolution. However, there is a lack of information on causal relationships between microbiota and health status, such as spatial and temporal information on the distribution of microorganisms. Our study aims to assess post-ingestion gastrointestinal transit, persistence, and potential dissemination of ^{89}Zr -labelled *Escherichia coli* Nissle (EcN) in the healthy pig using hybrid positron emission tomography/magnetic resonance imaging (PET/MRI).

Methods: *Escherichia coli* Nissle 1917 were radiolabeled with ^{89}Zr -p-isothiocyanato-benzyl-desferrioxamine (^{89}Zr -DBN) by adapting published procedures [1]. ^{89}Zr -labelled bacteria were then double encapsulated in gelatin pills and delivered to the stomach of a pig using a feeding tube. Following administration, PET/MRI was performed at 4 bed positions for whole body coverage at 6h or 12h post-ingestion, and again at 4 and 7 days post ingestion (n = 2 pigs). Another pig was imaged only at 12h post ingestion. Quantification of radioactivity in individual organs (mean, maximum, and total activity) was determined by manual segmentation of whole-body T2 HASTE images integrated with PET using 3D slicer (Version 4.11).

Results: Bacterial labelling efficiency was approximately 80%. Specific activity was approximately 0.00002, 0.007, and 0.001 Bq/colony forming unit (CFU; live bacterium) for pigs 1, 2 and 3, respectively. Most ^{89}Zr -labelled bacteria were localized in the stomach at 6h post-ingestion, confirming the feeding tube position, and in the large intestines by 12h (Figure 1). Less than 1% of ingested bacteria were detected on subsequent imaging days, consistent with little or no unchelated ^{89}Zr in liver or bone. In this small sample, variation in the mean radioactivity present in the large intestines (85 versus ~2 Bq/cc) was noted at day 4, post-ingestion. However, by day 7, imaging revealed diffuse activity that was close to background (mean ~1-2 Bq/cc).

Conclusion: Tracking microbiota with PET/MRI using a long-lived isotope (^{89}Zr , 3.3-day half-life) is a powerful tool for real-time visualization and quantitative assessment of the biodistribution of ingested bacteria.

References: 1. A. Bansal et al., 2015, *EJNMMI Res*, **5**, 19.

Cumulative Biodistribution of single dose transplanted ^{89}Zr -radiolabelled EcN
[Three pigs at different timepoints]

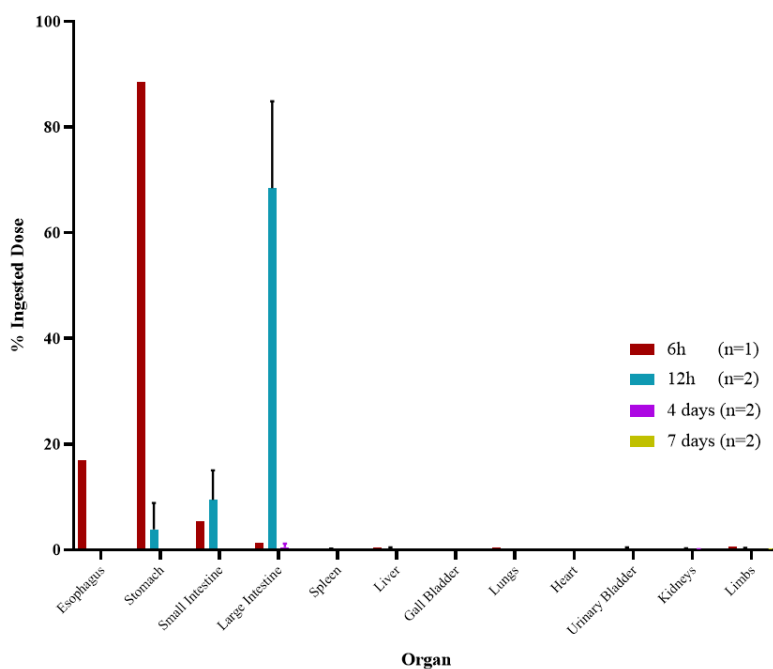


Figure 1. Whole body activity after PET/MRI in a pig model of probiotic ingestion.

Biodistribution of ^{89}Zr -labeled EcN in the pig is represented as percent of ingested dose for each organ at each timepoint.

Activatable Reporter Imaging Systems for Visualization of New Genomic Medicines Called Adenine Base Editors

Shirley Liu^{1,2}, Melissa M Evans^{1,2}, Joshua ST Krautner^{1,2}, Timothy J Scholl^{1,2}, John A Ronald^{1,2,3}

¹Robarts Research Institute; ²Dept. of Medical Biophysics, University of Western Ontario; ³Lawson Health Research Institute, London, ON, Canada

Introduction: Single base pair changes in DNA, called point mutations, are associated with over 30 000 genetic diseases including sickle cell anemia, muscular dystrophy, and numerous types of cancers^{1,2}. Base editors (BEs) are recently developed genome editing tools for the targeted conversion of a single base. Adenine base editors (ABEs) specifically convert an adenine (A) to a guanine (G) nucleotide and can correct ~48% of disease-causing point mutations³. Currently, *in vivo* base editing is limited by poor editing efficiency and delivery into tissues of interest. To non-invasively evaluate new BEs and BE delivery vectors, we aim to develop activatable imaging reporter systems for the tracking of *in vivo* ABE activity. A secondary objective is to compare base editing efficiency of two ABE delivery vectors: 1) ABE-expressing plasmids, which are circular DNA vectors; and 2) ABE-expressing minicircles⁴, which are smaller DNA vectors derived from plasmids and lacking a bacterial backbone, which we hypothesize will improve delivery and editing.

Methods: We built activatable “Gene On” (GO) systems for two imaging reporter genes: green fluorescent protein (GFP) for *in vitro* fluorescence imaging and Akaluc for *in vitro* and eventual *in vivo* bioluminescence imaging (BLI). These reporter genes were mutated to contain a premature TAG stop codon which will stop proper protein production, and should only produce imaging protein and imaging signal when TAG is edited to TGG by an ABE. HEK293T or HeLa cells were transduced via lentivirus to express GFPGO or AkalucGO, respectively. Plasmids were cloned to express ABE (PP-ABE) or Cas9 as a control (PP-Cas9). From these plasmids, minicircles (MC-ABE and MC-Cas9) were produced. To measure reporter gene activation, cells were transfected with PP-Cas9, MC-Cas9, PP-ABE, or MC-ABE. After 48 h, GFPGO cells were analyzed by flow cytometry and AkalucGO cells were analyzed by BLI.

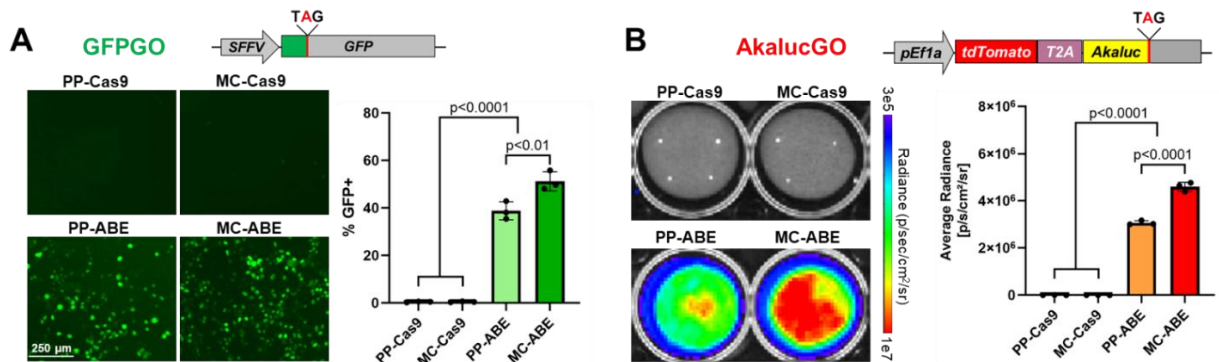


Figure 1. (A) GFPGO reporter for visualization of ABE activity by fluorescence imaging. (B) AkalucGO reporter for visualization of ABE activity by BLI.

Results: For both systems, a significant increase in reporter expression was observed when cells were transfected with ABE compared to Cas9 (Fig. 1). Additionally, MC-ABE resulted in enhanced editing over PP-ABE.

Conclusions: We have developed highly sensitive and specific activatable imaging reporter systems for the visualization of ABE activity. Additionally, we showed for the first time that minicircle delivery of ABE leads to higher *in vitro* base editing compared to plasmids, which is likely due to their smaller size. We are currently testing these systems *in vivo* in preclinical cancer models with BLI. These systems will then be used to evaluate new ABEs being rapidly developed and new ABE delivery platforms for the treatment of genetic diseases.

References: [1] Mahdih et al., Iran J Pediatr, 2013, 23: 375-388. [2] Stephens et al., Nature, 2012, 486: 400-404. [3] Gaudelli et al., Nature, 2017, 551: 464-471. [4] Munye et al., Sci Rep, 2016, 6:23125.

Detecting *in vivo* cell-cell communication using an inducible antigen-dependent synthetic blood biomarkerYangHao Fu^{1,2}, TianDuo Wang^{1,2}, John. A. Ronald^{1,2,3}

1. Robarts Research Institute – Imaging; 2. Department of Medical Biophysics, University of Western Ontario;

3. Lawson Health Research Institute, London, ON, Canada.

INTRODUCTION: The field of cellular immunotherapy has made major improvements to cancer treatment over recent years. For instance, chimeric antigen receptor (CAR) T-cell therapy has been proven to be the paradigm for engineered T-cell therapies due to its efficacy in treating blood-based cancers such as leukemia and lymphoma.¹ Although the state-of-the-art CAR T-cell therapies have shown high success in most patients, it is difficult to understand why they have minimal effect in others. Clinically, blood tests are often used to monitor immunotherapies to detect circulating immune cells, which doesn't accurately capture treatment efficacy. This study aims to build a new activatable system that secretes a unique blood biomarker when engineered therapeutic immune cells interact with target cancer cells within tumors. The Synthetic Notch (SynNotch) receptor is one of the most mechanistically versatile systems that signal cell-cell contact via transcriptional modulation of desired genes in response to SynNotch receptor-antigen binding (Fig. 1A).² Our approach is to engineer immune cells with a SynNotch receptor that, upon cancer antigen binding, activates the expression of secreted embryonic alkaline phosphatase (SEAP) – a safe and sensitive human-derived blood-based reporter³, allowing for blood-based detection of *in vivo* cell-cell communication.

METHODS: We engineered Jurkat cells, a human T cell line, via sequential lentiviral transduction of two components: (1) a SynNotch receptor directed against the B cell leukemia antigen CD19, and (2) a reporter response element encoding SEAP. The B-cell surface antigen CD19 was chosen as it is the most successful target of CAR-T immunotherapy in humans currently.⁴ Successfully dual-engineered T cells were isolated using fluorescence-activated cell sorting and expanded. To validate this activatable system *in vitro*, 10⁵ T cells were co-cultured in well plates with CD19+ Nalm6 B-cell leukemia cells at a 1:1 ratio. As a negative control, we used CRISPR-knockout to generate CD19- Nalm6 cells. In media, SEAP concentration was assessed every 24 hours for 2 days using the Great EscAPe SEAP Chemiluminescence Assay kit 2.0. Translating this system *in vivo*, Nod-scid-gamma (NSG) mice were implanted with either CD19+ or CD19- Nalm6 cells subcutaneously. Once tumours reached ~100mm³, mice received an intratumoural injection of engineered Jurkat cells (1x10⁷), and blood samples were taken from the left flank for SEAP assays.

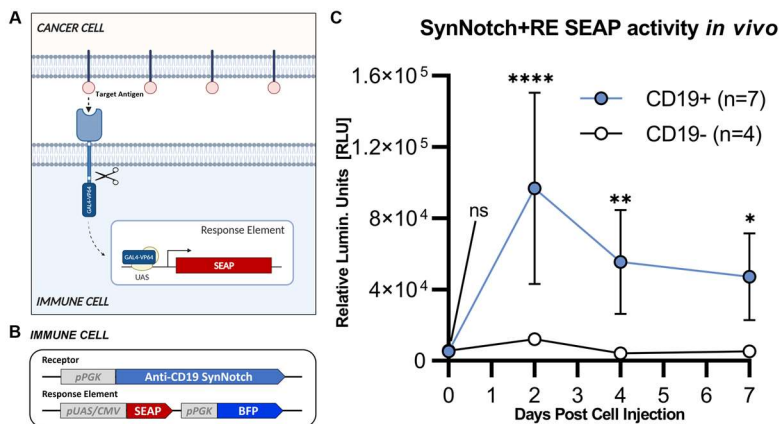


Figure 1. (A) Schematic of SynNotch system. CD19 binding by the CD19-targeted SynNotch receptor induces intracellular cleavage of a GAL4-VP64 transactivator, which binds to an upstream activating sequence (UAS) to initiate transcription of genes of interest encoded in the response element. **(B)** Jurkat cells were engineered with CD19-targeted SynNotch driven by the phosphoglycerate kinase 1 promoter (pPGK), and a response element containing reporter genes as well as a pPGK-driven blue fluorescence protein (BFP) for sorting. **(C)** Average blood SEAP activity measured from mouse carrying CD19+ or CD19- tumor cells before and after the delivery of SynNotch+RE T cells.

RESULTS: *In vitro* Co-culturing of dual-engineered T cells with CD19+ cells resulted in significantly higher SEAP activity on all days ($p < 0.001$, not shown here). In contrast, reporter expression was minimal when T cells engineered with the reporter gene only or naïve T cells when co-cultured with CD19+ cells. Co-culturing with CD19- cells resulted in no detectable SEAP levels above the background. *In vivo*, no SEAP activity was also observed prior to engineered cell injection in tumor-bearing mice (Fig. 1C). Importantly, significantly elevated SEAP activity was observed post-T cell injection in mice bearing CD19+ tumors, but not CD19- tumors (Fig. 1C).

DISCUSSION: We have established a synthetic biology reporter system that activates upon antigen binding, which allows for the detection of immune-cancer cell interactions through a simple and convenient blood test. Future work includes transferring this system into primary T-cells as well as expanding the potential target antigen. The development of this system would allow for a specific monitoring tool for many cell-based cancer immunotherapies, ultimately improving our understanding of the treatment dynamics as well as the presence of side effects in individual patients.

REFERENCES: [1] June et al., Science, 2018, 359(6382):1361-1365. [2] Maude et al., NEJM, 2014, 371: 1507-1517. [3] Berger et al., Gene, 1988, 66(1):1-10. [4] Sadelain et al., J Clin Invest, 2015, 125(9): 3392-3400.

Visualizing Cytosine Base Editor Activity following Minicircle Delivery using an Activatable Reporter Gene System

Melissa M Evans^{1,2}, Shirley Liu^{1,2}, Timothy J Scholl^{1,2}, John A Ronald^{1,2,3}

¹Robarts Research Institute; ²Dept. of Medical Biophysics, University of Western Ontario; ³Lawson Health Research Institute, London, ON, Canada

Introduction: Thousands of diseases could be cured if we had the ability to alter the DNA at precise locations within the genome and body. Genome editing is a rapidly growing field, revolutionized by CRISPR associated nuclease 9 (Cas9) being able to target a specific DNA site using a complementary guide RNA (gRNA). There are several limitations of Cas9 editing, chiefly that it creates double stranded breaks of the DNA potentially causing severe unintended consequences such as chromosome translocations or oncogenesis [1]. It is also difficult to efficiently deliver Cas9 materials to some tissues for clinical applications, so new delivery vehicles are needed [2]. Cytosine base editors (CBEs) are a Cas9 based technology that can edit DNA sequences without double strand breaks. This results in the conversion of a cytosine (C) base to a thymidine (T) [3]. To balance efficient in vivo delivery with limiting unwanted off-target effects that may come from persistent CBE expression we have tested non-viral minicircles (MCs) to deliver CBEs. MCs are a derivative of parental plasmids (PP) with the prokaryotic backbone removed to shorten the size, resulting in improved delivery, safety, and translation potential.

Methods: To visualize base edited cells, we acquired previously developed CBE Gene On (GO) system containing green fluorescent protein (GFP^{GO}) or the bioluminescence imaging (BLI) reporter firefly luciferase (LUC2^{GO}) [4]. In this system, cells that are transfected with our MCs will express a CBE and targeted guide RNA that will correct a mutant start codon (ACG) into a functional start codon (ATG) and initiate protein translation of our reporter genes [4]. This allows us to visualize/detect which cells were correctly base edited. HeLa cells were transduced with either GFP^{GO} or LUC2^{GO} lentiviral vectors to produce stable cells. Next, we produced plasmids and MCs containing CBE or Cas9 (as a control) plus our targeted gRNA (PP-CBE, MC-CBE, PP-Cas9, MC-Cas9). HeLa cells were transfected with these 4 vectors. For GFP^{GO}, the fluorescent expression of GFP was measured continually for 72 hours. For LUC2^{GO}, luciferase activity was assessed 48 hours after transfection using BLI.

Results: Significantly higher GFP^{GO} cells expressed GFP after transfection with MC-CBE (10.5%) compared to PP-CBE (3%) after 72 hours (Fig 1B). Importantly, all controls showed minimal GFP expression. LUC2^{GO} cells transfected with MC-CBE had significantly higher signal than either PP-CBE (p<0.01) or the MC-Cas9 and PP-Cas9 controls (p<0.001, 2-way ANOVA) (Fig 1D). Some minimal background signal was noted for control cells, which is likely due to unwanted translation using a cryptic start codon.

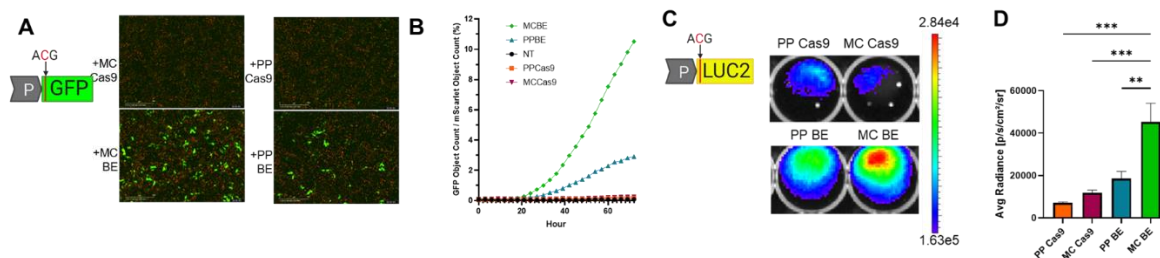


Figure 1: (A) Fluorescence imaging of GFP^{GO} reporter activation over time by CBE correction of start codon mutation. (B) GFP object count over 72 hours. (C-D) LUC2^{GO} transduced with PP and Cas9, CBE and Cas9 fluorescence imaging and activation over time.

Conclusions: The GO system allows for visualization of CBE activity through activated imaging reporter gene expression. This system can be used to evaluate new CBE designs and delivery strategies such as plasmids/minicircles, viruses, mRNA and protein across many different cell types. We have shown that MCs can be used as novel delivery vehicles for CBEs and our initial results support an advantage of MCs over traditional plasmids. We are currently evaluating the ability to noninvasively image CBE activity in vivo by implanting our LUC2^{GO} cancer cells in mice, delivering our MCs to these tumours, and performing in vivo BLI over time.

References: [1] Kosicki et al., Nat. Biotechnol. 36(8):765-771 (2018). [2] Newby, GA., Liu, DR., Mol. Therapy 29(11):3107-3124 (2021) [3] Komor et al., Nature, 533(7603):420-424 (2016).[4] Katti et al., Nuc. Acids Res. 48(6):2841-2852 (2020).

Magnetic resonance relaxation rates of bacteria:***Magnetospirillum magneticum* AMB-1 versus *Lactobacillus crispatus* ATCC33820**

¹Yohans, J, ¹Hassan, S, ¹Donnelly, SC, ¹Rabbath, E, ^{1,2}Thompson, RT, ^{1,2,3}Prato, FS,
^{1,2}Gelman, N, ^{1,2,3}Goldhawk, DE

¹Imaging Program, Lawson Health Research Institute, London, ON; ²Medical Biophysics and

³Graduate Program in Molecular Imaging, Western University, London, ON

Introduction: With superb spatial and temporal resolution, magnetic resonance imaging (MRI) has demonstrated utility for mammalian cell tracking, including the development of reporter gene expression modeled on the bacterial magnetosome¹. To better understand the nature of bacterial signals and develop methods for imaging the magnetosome and microbial therapies using MRI, we examined relaxation rates in magnetotactic and commensal bacteria using species that depend on either iron (*Magnetospirillum magneticum* AMB-1) or manganese (*Lactobacillus crispatus* ATCC33820), respectively. By characterizing these bacterial strains, we show that ultrashort echo times are needed to capture rapid changes in the relaxation of select species.

Methods: Cultures of AMB-1 were grown for 7 days in liquid medium with 10 μM ferric quinate². Lactobacilli were cultured overnight anaerobically in MRS medium³. At harvest, cells were centrifuged, washed with phosphate buffered saline pH 7.4 (PBS), and serially diluted prior to mounting in a 4% gelatin/PBS cell phantom^{3,4}. MRI relaxation rates were measured at 3 Tesla using inversion-recovery (IR) spin-echo (SE) for R1 (1/T1); single-echo SE for R2 (1/T2); and multi-echo gradient echo (GRE) for R2* (1/T2*)^{3,4}. To measure T2* at the shortest echo time (~ 1 ms), GRE IR from VIBE sequences were employed. Images were evaluated using custom MATLAB software. Bar graphs and statistics were generated using GraphPad Prism 8.0.1.

Results: Figure 1 compares the magnitude of R2* obtained from *L. crispatus* and AMB-1. Extrapolation of serially diluted *L. crispatus* predicted an R2* of approximately 400 S^{-1} for undiluted cells (100%; shortest TE ~ 10 ms). This was validated by incorporating short TE of ~ 1 ms. By comparison, the rapid decay of AMB-1 could not be measured in undiluted samples. At 1/100 dilutions of AMB-1 (1% cells/gelatin/PBS), R2* was approximately 700 S^{-1} . In both species, R2* was dominated by the R2 component. Unlike the transverse relaxation rates, R1 measures in AMB-1 were $0.987 \pm 0.329 \text{ S}^{-1}$ (n=3) regardless of sample dilution. However, for manganese-dependent *L. crispatus* R1 increased as dilution of bacteria decreased.

Conclusions: Comparison of transverse and longitudinal relaxation rates between *L. crispatus* and AMB-1 indicates that, depending on cell type, relatively few magnetosomes or bacteria (*i.e.*, partially filled volumes) may provide detectable MR measures *in vivo*. Moreover, to characterize the rapid decay of transverse relaxation in undiluted samples of select bacterial species (*e.g.*, dysbiosis or infection), MR sequences with (ultra) short TE may be required.

References: ¹Goldhawk et al (2017) In: Design and Applications of Nanoparticles in Biomedical Imaging. p. 187; ²Le Nagard et al (2018) J Vis Exp JoVE 140, 58536; ³Donnelly et al (2022) BIORXIV/2022/490857; ⁴Sengupta et al (2014) Front Microbiol 5, 29

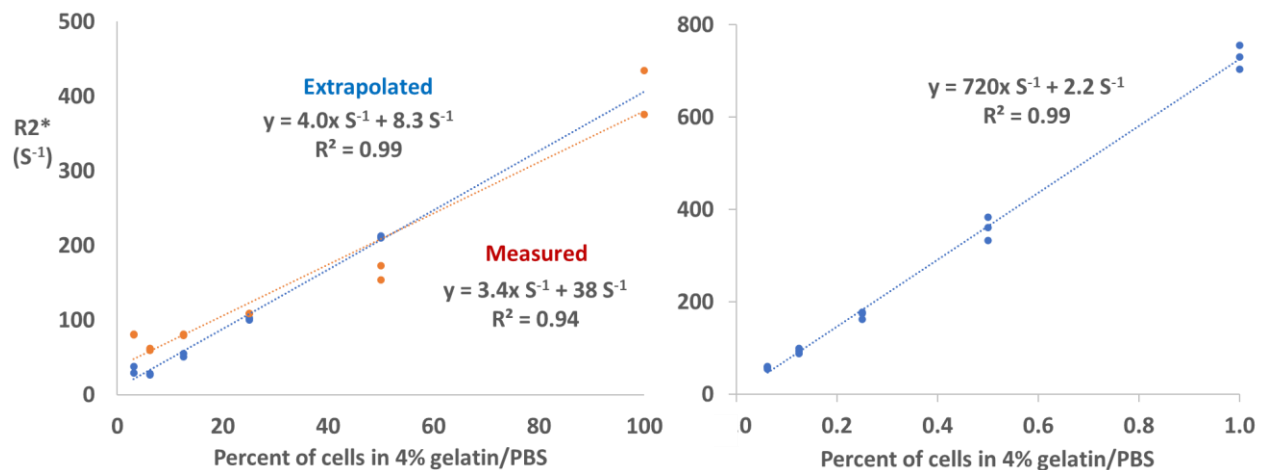


Figure 1. Correlating amount of bacteria with R2*. Using a gelatin cell phantom, transverse relaxation rates were measured at various concentrations of *L. crispatus* (left) and AMB-1 (right). Scatter plots show a strong positive linear correlation between R2* and serial dilutions of each bacterium (n = 2-3).

Elucidating factors that contribute to changes in magnetic particle imaging (MPI) signal for the longitudinal tracking of iron-labeled therapeutic cells

Samantha N. Flood^{1,2}, Olivia C. Sehl^{1,2}, Paula J. Foster^{1,2}

¹Imaging Research Laboratories, Robarts Research Institute, Canada

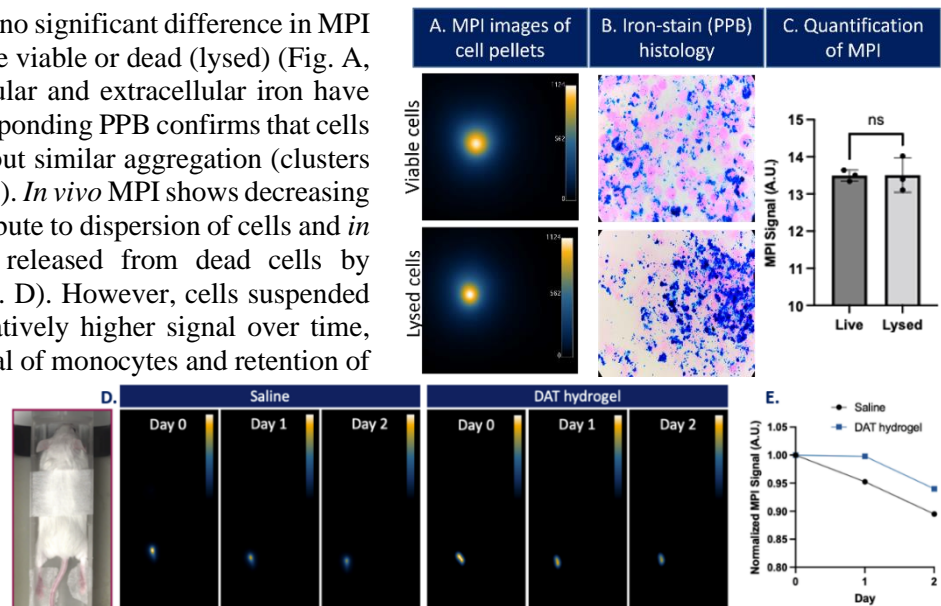
²Department of Medical Biophysics, University of Western Ontario, Canada

Introduction: Stem cells (SCs) have shown promising results as a cellular therapeutic, however their potential is limited by SC death and immune rejection. Cell-instructive delivery platforms (*i.e.*, cell scaffolds) can augment the retention and support the functioning of SCs by establishing a supportive microenvironment. The development of a technique to quantitatively monitor SC engraftment and survival over time would be invaluable for evaluating these platforms. Magnetic particle imaging (MPI) is an emerging imaging technique that can be used to image cells labeled with superparamagnetic iron oxide nanoparticles (SPIO). We have previously used MPI to track mesenchymal SC transplanted intramuscularly in mice and showed a reduction in the MPI signal over time. However, it is not clear whether the reduced MPI signal is due to cell death and clearance, dispersion of SPIO or changes in magnetization due to internalization of SPIO. In this study we evaluate MPI signals from (1) live vs. dead (lysed cells) and (2) cells implanted in mice with and without decellularized adipose tissue (DAT) scaffolds.

In vitro methods: Mouse mesenchymal SC were labeled *in vitro* by overnight cocubation with Vivotrax⁺ and transfection agents. Cells were collected and magnetic column enrichment was performed to eliminate unlabeled cells. Pellets of 2×10^6 labeled SC were imaged with MPI (MomentumTM, Magnetic Insight Inc.) using 5.7 T/m selection gradients and excitation fields of 20 mT at 45kHz ($n = 3$). Cells were lysed to mimic apoptosis/necrosis using freeze (-80deg)/thaw(37deg) cycles and then re-imaged. Perl's Prussian blue (PPB) was performed on cells before and after lysis to visualize the iron distribution relative to cells. **In vivo methods:** THP-1 monocytes were labeled *in vitro* by overnight cocubation with Synomag-D and transfection agents. 1×10^6 THP-1 cells were administered to the left hind muscle of NOD/SCID mice suspended in 17.5 mg/mL DAT gel or saline ($n = 2$ each). 2D imaging was performed on the day of injection (Day 0), and after 24 hours (Day 1), and 48 hours (Day2).

Results/Discussion: There was no significant difference in MPI signal produced when cells were viable or dead (lysed) (Fig. A, C). This conveys that intracellular and extracellular iron have the same MPI signal. The corresponding PPB confirms that cells were lysed and released SPIO but similar aggregation (clusters of blue, iron) is observed (Fig. B). *In vivo* MPI shows decreasing signal over time, which we attribute to dispersion of cells and *in vivo* clearance of free SPIO released from dead cells by phagocytic macrophages^[1] (Fig. D). However, cells suspended in the DAT hydrogel have relatively higher signal over time, demonstrating improved survival of monocytes and retention of SPIO, compared to saline controls (Fig. E). Faster SPIO clearance (and decrease in signal) is a sign of cell death^[2].

Conclusion: In this study we aim to elucidate the reasons why MPI signals from SPIO-labeled SC transplants decrease over time. *In vitro*, we see that cell death and release of SPIO does not change MPI signal, thus we do not anticipate SPIO internalization and aggregation to significantly contribute to MPI signal changes *in vivo*. Excitingly, we see that more MPI signal is detected from cells transplanted in DAT hydrogels (which support cell function and growth). This may be because a higher percentage of cells in saline were apoptotic, leading to release of SPIO and clearance by macrophages and faster loss of MPI signal. Secondly, it is possible that cells administered in saline are more likely to disperse and reduce MPI signal intensities. In future work, we will include Bioluminescence imaging (BLI) to provide a measure of cell survival.



[1] Theruvath, AJ et al. *Radiology* (2019). [2] Daldrup-Link, HE, and Nejadnik, H. *J Stem Cell Res Ther* (2014).

Margin detection in skin cancer surgery via 2D representation of mass spectrometry data

Laura Connolly¹, Fahimeh Fooladgar², Amoon Jamzad¹, Ayesha Syeda¹, Martin Kaufmann¹, Kevin Ren¹, Purang Abolmaesumi², John F. Rudan¹, Doug McKay¹, Gabor Fichtinger¹ and Parvin Mousavi¹

1. Queen's University, Canada – 2. University of British Columbia, Canada

INTRODUCTION: Basal cell carcinoma (BCC) is a highly prevalent form of skin cancer that is often treated with surgical resection. In these procedures, the surgeon will resect the visible lesion from the tissue with an electrocautery device. In some cases, BCC lesions will extend deep into the tissue (beyond the visible borders) which makes it challenging to achieve complete resection. The intelligent knife (iKnife) is a device that uses rapid evaporative ionization mass spectrometry (REIMS) to help mitigate this challenge. This technology enables the intraoperative deployment of mass spectrometry by evacuating the smoke that is released during tissue cauterization directly into a mass spectrometer. Previous work has demonstrated that deep learning techniques can be used to separate tissue according to its pathology (as either cancer or benign) based on these mass spectrometry signatures [1]. Currently it is difficult to assign labels to intraoperative iKnife data because of the continuous and destructive nature of data collection. Therefore, we hypothesize that self-supervised learning, a deep learning technique that does not require labelled data, can be used to leverage unlabelled intraoperative data, and improve tissue characterization with the iKnife. In this study, we investigate this hypothesis and explore the potential benefit of converting iKnife signature to images to leverage more general DL infrastructures.

METHODS: The dataset for this study consists of 10407 intraoperative burns and 693 ex vivo tissue burns collected with the iKnife during BCC lesion excisions. The intraoperative data was collected continuously during the procedure and is unlabelled whereas the ex vivo data was collected and labelled after the surgery and under the supervision of a trained pathologist (Fig 1). The ex vivo burns are augmented such the final training set consists

of 948 cancer burns and 831 benign burns. We also reserve a validation set with 37 cancer and 57 benign burns for fine-tuning, and a test set with 57 cancer and 107 benign burns for evaluation. The metabolomic signatures from this data are converted to images using a Gramian angular difference field. All of our intraoperative and ex vivo training data are fed to a self-supervised learning approach called VicReg [2] which is used to pretrain a ResNet-18 encoder. The pretrained backbone is then combined with a linear classifier (multiple dense layers) to perform binary classification.

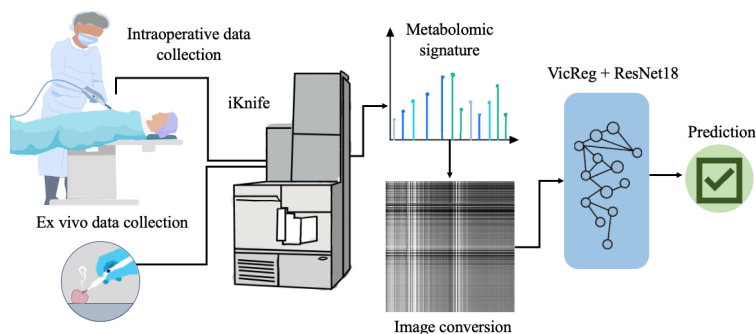


Figure 1: Method overview - intraoperative and ex vivo iKnife data is collected, the signatures are converted to 2D images, these images are used to pretrain a ResNet-18 backbone with VicReg, the backbone is then fine-tuned with ex vivo data and used to perform tissue classification.

RESULTS: Self-supervised learning with both intraoperative and ex vivo iKnife data resulted in a statistically significant improvement on balanced accuracy (72.1 ± 1.7) when compared to classification with no self-supervision (62.0 ± 2.3). There is also an improved sensitivity with this approach (62.3 ± 5.6 vs. 33.1 ± 5.6). This is also the first study to our knowledge that uses 2D representations of iKnife data to perform tissue classification.

CONCLUSIONS: These preliminary results demonstrate the advantage of using unlabelled, intraoperative iKnife data and self-supervision for tissue characterization with the iKnife. The conversion of mass spectrometry signatures to 2D images also enables the use of a broader category of classification infrastructure such as ResNet.

ACKNOWLEDGEMENTS: L. Connolly is supported by NSERC CGS-D and the Walter C. Sumner Memorial Fellowship. G. Fichtinger is supported by NSERC Canada Research Chair. P Mousavi is supported by CIFAR AI Chair and the Vector Institute.

REFERENCES:

- [1] Santilli et al. Perioperative margin detection in basal cell carcinoma using a deep learning framework: a feasibility study. *Int Journal of Computer Assisted Radiology and Surgery* 15(5), 887–896 (2020)
- [2] Bardes, A., Ponce, J., LeCun, Y.: Vicreg: Variance-invariance- covariance regularization for self-supervised learning. arXiv preprint arXiv:2105.04906 (2021).

OPEN SOURCE VIDEO-BASED HAND-EYE CALIBRATION

Tara N. Kemper^{a,d}, Daniel R. Allen^{a,b}, Adam Rankin^a,
Terry M. Peters^a, Elvis C. S. Chen^{a,b,c}

^aRobarts Research Institute, Canada, ^bSchool of Biomedical Engineering, Western University, Canada, ^cDepartment of Medical Biophysics, Western University, Canada, ^dDepartment of Physics and Astronomy, Western University, Canada

INTRODUCTION Surgical cameras have become a regular fixture of modern operating rooms, creating opportunities to further image-guided surgery techniques by using augmented reality (AR) to allow preoperative images (such as CT or MRI) to be overlaid onto live surgical video feeds from these cameras. However, a highly accurate hand-eye calibration must be achieved to prevent misalignment between the real and virtual objects of interest. Many methods of intrinsic and hand-eye calibration already exist but their current implementations are all quasi-static, meaning the image and spatial data for each individual phantom location must be manually captured. This poses a problem when any significant amount of data is required, causing large-scale analyses of overall precision and accuracy for a given algorithm to be limited in scope due to the time required for data collection. To address these issues, we present an open-source 3D Slicer¹ module to perform video-based hand-eye calibrations by implementing the preexisting calibration method of *Morgan et al.*[1] on individual frames of a recorded video of the tracked ball-tipped stylus. The main benefit of our video-based implementation is its ability to quickly collect vast amounts of data with relative ease. This offers many possibilities for applying previously impractical methods into real-time interventional settings. The source code can be cloned or downloaded from the corresponding GitHub repository².

METHODS Throughout both the development and testing phases of the module, a Logitech C920 Pro HD Webcam with an image resolution of 640 x 480 was used to capture the 2D video feed, and an NDI Polaris optical tracker was used to collect the 3D spatial data of both the ball tipped stylus and camera. A planar chessboard phantom was first used for the intrinsic calibration, then a video of the ball-tipped stylus being moved throughout the camera's field of view could be captured and processed by the 3D Slicer module which produces the hand-eye calibration matrix. For analysis of the module's overall precision and accuracy, a Monte Carlo simulation was used which randomly chose points from within predetermined sections of the camera's optical field to produce calibrations with between 6 and 16 data points

(aka. registration fiducial points) as input. This simulation was run 5000 times per n number of data points, and the mean pixel errors of all the runs for each n were then calculated and displayed in box and whisker plots along with the max, min and outliers for each n .

RESULTS The preliminary results show that for a range of 6 - 16 data points per calibration, the average projective target registration errors (TRE) in pixels (aka. pixel error) fall below 3 and roughly take on the shape of an exponentially decreasing curve as the number of data points per calibration increases, as seen in Fig. 1. The average pixel error is defined by the Euclidean distance between the 2D centroid and reprojected pixels. Therefore, the decreasing curve is expected as generally the more data points included in a calibration, the more accurate that calibration should be, provided all those data points are accurate

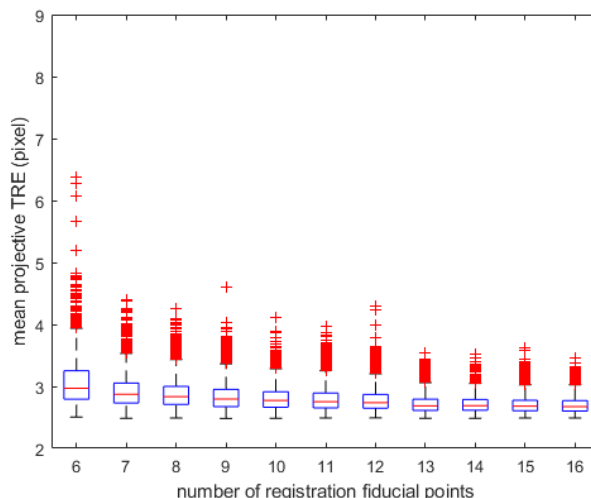


Figure 1: Box and whisker plot resulting from Monte Carlo analyses of a single data collection from a 30 second video sequence containing approximately 300 tracked image frames

CONCLUSION In this work, we present a framework for performing hand-eye calibration with improved efficiency, enabling greater data analysis capabilities. This video-based approach can be applied to various calibration methods and equipment setups due to its use of 3D Slicer and open-source nature. Its ability to produce accurate and precise results while significantly reducing data collection time opens many doors to further understanding hand-eye calibration and increased implementation in real-time surgical scenarios.

REFERENCES

- [1] Isabella Morgan, Uditha Jayarathne, Adam Rankin, Terry M. Peters, and Elvis C.S. Chen. Hand-eye calibration for surgical cameras: a procrustean perspective-n-point solution. *International Journal of Computer Assisted Radiology and Surgery*, 12:1141–1149, 2017.

¹<https://www.slicer.org/>

²<https://github.com/TaraKemper/VideoBasedHandEye>

Comparing methods of identifying tissues for workflow recognition of simulated open hernia repairElizabeth Klosa^a, Rebecca Hisey^a, Kian Hashtrudi-Zaad^a, Boris Zevin^b, Tamas Ungi^a, Gabor Fichtinger^a^aLaboratory for Percutaneous Surgery, School of Computing, Queen's University, Kingston, Canada^bDepartment of Surgery, Queen's University, Kingston, Ontario, Canada

INTRODUCTION: Surgical training can be enhanced through the use of computer-assisted training systems. In a simulated environment, trainees can gain hands-on experience while receiving instruction and feedback without requiring an expert observer [1]. We look to develop a computer-assisted training system for open inguinal hernia repairs (OIHR) by providing instruction and assessment through workflow recognition [2]. Using video-based analysis, we identify workflow tasks of an OIHR based on tool-tissue interactions. To identify interactions between the tools and tissues, we must first recognize them separately. Previously, we trained a u-net in tissue recognition. We now aim to increase tissue recognition performance though integrating a colour-based predictor into our u-net. Since we can run multiple predictors on the images and fine-tune specific predictors for each tissue, the proper incorporation of a colour-based predictor to our existing u-net should improve, but at the very least maintain, performance. Before combining these methods, our new work in progress compares their separate performance on each individual tissue to inform on how we will combine them.

METHODS: We recorded surgeons and residents performing an OIHR on a phantom. Throughout the videos, the visible tissues in each frame were manually segmented, assigning each pixel to a class label representing one of the tissues. A u-net was then trained using leave-one-user-out cross validation to predict the tissues and was found to sufficiently identify the skin. This was useful for our colour-based approach, in which we found the bounding region around the u-net's skin prediction to provide an estimated region of the phantom. We then performed colour-based recognition of the tissues within this smaller region. This eliminated any false predictions in the



Figure 1: (a) original image (b) ground truth segmentation (c) u-net prediction (d) colour-based prediction

background, one of the main issues that occurred when doing colour-based recognition on the whole image. Using the ground truth segmentations from one video, we computed the HSV colour range of each tissue as the average hue, saturation, and value plus

and minus one standard deviation. A different video was used for the predictions. For each image throughout the prediction video, each pixel was predicted based on which colour range it fell into. If a pixel fell into multiple ranges, priority was given to classes based on the order in which they are visible throughout the repair. We then computed the F-Score of each tissue to evaluate the performance of both methods.

RESULTS: Table 1 shows the F-Scores of the u-net and colour-based methods. Figure 1 compares the ground truth segmentation, u-net prediction, and colour-based prediction.

Table 1: F-Score for each tissue type

Tissue	F-Score u-net	F-Score colour-based
Skin	0.93	0.75
Subcutaneous tissue	0.27	0.17
Superficial epigastric vessels	0.23	0.28
Scarpa's fascia	0.23	0.16
External oblique aponeurosis	0.39	0.25
Spermatic cord	0.65	0.36
Hernia sac	0.97	0.21
Nerve	0.98	0.005

CONCLUSION: To effectively recognize the tissues, we are looking for an ensemble of predictors rather than a single method. The colour-based predictor has potential as a helpful adjunct, as it can partially recognize some tissues. However, it is not sufficient or robust enough on its own due to limitations in varying lighting conditions leading to colour saturation. However, when combined with other predictors, it may help to improve recognition of certain tissues and structures and reduce incorrect predictions. Through further refinement of the colour predictor and utilizing a combination of the u-net and colour-based predictor, we hope to improve robustness of out tissue recognition as we work toward developing a functional system to provide computer-assisted skill assessment in OIHR training.

REFERENCES:

- [1] Lin, H.C., et al., "Towards automatic skill evaluation: Detection and segmentation of robot-assisted surgical motions," *Computer Aided Surgery*, 11(5), 220-230 (2010).
 [2] Goldbraikh, A., et al., "Video-based fully automatic assessment of open surgery suturing skills," *Int J CARS*, 17, 437-448 (2022).

Author Index

Name	Presentation	Page
Aalto, Hannah	O3-1	60
Abbass, Mohamad	O9-4	153
Abdalmalak, Androu	O10-3	157
Abdelrazek, Mohamed	P3-8	77
Abolmaesumi, Purang	O7-4	123
	P12-7	206
Abousheishaa, Dina Bassiouny	P11-7	196
Abrahao, Agessandro	O5-4	93
	P6-8	117
Adams, John	O12-4	188
Adewale, Anjola	P1-2	42
Afzal, Mubariz	P10-4	173
Agrawal, Sumit	P5-7	106
	P5-9	108
Ahlawat, Ritesh	P7-7	136
Ahmed, Abrar	O9-4	153
Akbari, Alireza	O9-1	150
Akbari, Atena	P2-6	55
Akbulatov, Arthur	O4-4	68
Akinyemi, Rufus	O2-3	38
Alawneh, Yara M	O5-2	91
Albert, Mitchell S.	O3-1	60
Allen, Daniel	P4-4	83
	P12-8	207
Alsurayhi, Halimah	O8-4	128
Amla, Zaiba	P10-3	172
Anazodo, Udunna	O2-3	38
	P2-1	50
	P2-3	52
Andrade, Andrea	O2-1	36
	P6-7	116
Antonyshyn, Oleh	P5-8	107
Appleby, Ryan	P5-5	104
Aragaki, Masato	O1-1	31
Arezza, Nico J. J.	O6-2	96
Arianpouya, Maryam	P6-2	111
Armstrong, Mark	O6-4	98
Arnott, Stephen	P6-8	117
Aubert, Sarah	P8-7	146
Austin, Catherine	P11-9	198

Name	Presentation	Page
Ayeegoundarvenkatesan, Pranav Kumar	P11-1	190
Azad, Azar	P7-6	135
	P7-8	137
Azarpazhooh, Reza	P4-6	85
Babaeipour, Ramtin	P3-3	72
Bailey, Colleen	P6-5	114
Bainbridge, Daniel	O8-1	125
Balmer-minnes, Diana	O8-2	126
Baron, Corey A.	O2-2	37
	O6-2	96
Barr, Colton A	O1-3	33
Bartha, Robert	O6-1	95
	P6-8	117
	O12-3	187
	O12-4	188
Bartlett, Kenna	P8-1	140
Bartling, Mandolin	O4-2	66
	O11-4	183
Batarchuk, Viktoriia	O3-1	60
Bauman, Glenn	P7-3	132
	P9-3	162
Bax, Jeffrey	P1-8	48
	O10-4	158
Bellyou, Miranda	O5-3	92
Benkert, Thomas	P3-9	78
Berman, David	P7-4	133
	P10-2	171
Bernard, Timothy	P6-7	116
Bernards, Nicholas	O1-1	31
Bernstein, Hannah	P6-7	116
Berryhill, Linada	P7-3	132
Bhalla, Anurag	O3-2	61
	O3-3	62
	P3-2	71
Bharucha, Apurva	O8-1	125
Biancaniello, Alexander	P3-2	71
Biernaski, Heather	P9-1	160
	P12-1	200
Bilgic, Berkin	O6-3	97
Binns, Malcolm	P6-8	117

Name	Presentation	Page
Bjornson, Bruce	P6-7	116
Borrie, Michael	P6-8	117
Bouch, Sheena	P3-6	75
Bourbeau, Jean	P3-5	74
Brackstone, Muriel	P1-1	41
Brooks, Jennifer	P11-4	193
Brown, Arthur	O2-2	37
Brown, Suzan	O12-4	188
Burneo, Jorge	O12-4	188
Burton, Jeremy	P9-1	160
	P12-1	200
Butler, John	P12-1	200
Camara, Mamadou	P4-9	88
Cambranis-Romero, Joeana N	O4-1	65
	P4-8	87
	P5-1	100
Campbell, Maxwell	P8-4	143
Carlson, Helen	P6-7	116
Carnahan, Patrick	O8-1	125
Carson, Jeffrey	P1-1	41
	P1-3	43
Cecchini, Matthew	O11-1	180
Celinski, Anders	P7-3	132
Cernelev, Pavel-Dumitru	P10-6	175
Chakraborty, Sudesna	P6-6	115
Chan, Harley	P1-2	42
Chan, Rachel	P2-7	56
	O9-2	151
Chasse, Melissa	P2-9	58
Chen, Elvis C. S.	O4-1	65
	P4-4	83
	P4-6	85
	P4-8	87
	P5-1	100
	O8-1	125
	P12-8	207
Chen, Lina	P7-4	133
Chinnery, Tricia	P7-2	131
Choi, Michellie	P4-6	85
Chong, Jaron	P1-7	47
	O7-2	121

Name	Presentation	Page
Christie, Jaryd R	P5-6	105
Chu, Victor A	P8-8	147
Chung, Kevin J	P2-4	53
	P9-3	162
	O12-2	186
Clarke, Collin	P4-4	83
Cockburn, Neil	P12-1	200
Connolly, Laura P	P4-3	82
	P4-7	86
	P12-7	206
Cool, Derek	O4-1	65
	P5-1	100
Correa, Rohann	O7-3	122
Costanzo, Alejo	P11-5	194
Cronin, Alicia	O6-1	95
Cunningham, Ian	P8-6	145
	P10-8	177
Curpen, Belinda	P11-4	193
Czarnota, Gregory	O1-2	32
Daly, Michael J	P1-2	42
	O4-2	66
	O11-4	183
Dammak, Salma	O11-1	180
Das, Sunit	P2-7	56
Dassanayake, Praveen Sankajith B	P2-3	52
Davidson, Melanie	P7-3	132
De Sarno, Danny	P9-3	162
Desaigoudar, Vedanth	P3-7	76
	O8-3	127
Deschamps, Joseph	O3-1	60
Desjardins, Lise	P2-4	53
Desmond, Kimberly	O2-4	39
Detombe, Sarah	O6-1	95
Detsky, Jay	P2-7	56
	O9-2	151
deVeber, Gabrielle	P6-7	116
Dhaliwal, Inderdeep	P3-8	77
Dhar, Aneesh	P7-3	132
Diao, Babacar	P4-9	88
DiCenzo, Daniel	O1-2	32
Diemert, John	P9-8	167

Name	Presentation	Page
Dilliot, Allison Ann	P6-8	117
Diop, Mamadou	P1-3	43
	P1-4	44
	P2-8	57
	O10-1	155
	O10-3	157
Dlamini, Nomazulu	P6-7	116
Domi, Trish	P6-7	116
Donnelly, Sarah C	P9-1	160
	P12-1	200
	P12-5	204
d'Orchymont, Faustine	P9-9	168
Doyle, Thomas	P2-2	51
Drake, James	O4-4	68
Drangova, Maria	P6-3	112
	P8-8	147
D'Souza, David	O7-3	122
du Toit, Carla	O1-4	34
	P8-2	141
Dueck, Andrew	P4-2	81
Duggal, Neil	O6-1	95
Duong, Thanh-Tai	P9-3	162
Duquette-Evans, Clara	P9-6	165
Eddy, Karen	P7-1	130
Eddy, Rachel	P3-2	71
Edirisinghe, Chandima	O7-3	122
Edwards, Glenn	P5-8	107
Eed, Amr	O5-3	92
Effat, Andrew	O10-2	156
Ehrlich, Josh H	P4-1	80
Elkas, Jack TE	O12-3	187
Elmi, Hanad B	P10-2	171
Engel, Jay	P4-1	80
	O11-2	181
Ertl-Wagner, Brigit	P11-3	192
	P11-5	194
Eskandari, Rasa	P1-4	44
Evans, Melissa M	P12-2	201
	P12-4	203
Fakir, Hatim	P7-3	132
	P9-3	162

Name	Presentation	Page
Faran, Muhammad	P3-8	77
Felefly, Tony	O11-3	182
Feng, Xi	P7-5	134
Fenster, Aaron	O1-4	34
	P1-5	45
	P1-7	47
	P1-8	48
	O4-1	65
	P5-1	100
	O7-3	122
Fenster, Aaron	P8-2	141
	O10-4	158
Fernando, Nitara	O9-3	152
Fichtinger, Gabor	O1-3	33
	O4-3	67
	P4-1	80
	P4-3	82
	P4-5	84
	P4-7	86
	P4-9	88
	P5-3	102
	O7-1	120
	P10-2	171
	P10-6	175
	O11-2	181
	P11-9	198
	P12-7	206
	P12-9	208
Figueredo, Rene	P9-4	163
Finger, Elizabeth	P6-8	117
Fischer, Corinne	P6-8	117
Fishman, Zachary	P5-8	107
Flammino, Marcus	P2-4	53
Flood, Samantha N	P12-6	205
Fooladgar, Fahimeh	O7-4	123
	O11-2	181
	P12-7	206
Foster, Paula	O9-3	152
	P12-6	205
Fox, Matthew	O3-4	63
	P3-3	72

Name	Presentation	Page
	P3-4	73
	P9-1	160
Frank, Andrew	P6-8	117
Freedman, Morris	P6-8	117
Freund, Sabrina	O2-1	36
Fry, Aidan	P10-8	177
Fu, Yanghao	P12-3	202
Gaikar, Rohini P	P7-6	135
	P7-8	137
	P11-1	190
Gardi, Lori	P1-8	48
	O10-4	158
Garland, Lisa	P8-6	145
	P10-8	177
Garvin, Gregory	P8-4	143
Gati, Joseph	P2-6	55
Gelman, Neil	P9-1	160
	P12-5	204
Genkin, Daniel	P3-9	78
Gerhardt, Lara	P9-4	163
Gevaert, Julia	O9-3	152
Ghai, Sangeet	O10-2	156
Gilany, Mahdi	O7-4	123
Gilbert, Kyle	O5-3	92
Gillies, Derek J	O7-3	122
Gilmore, Greydon	O9-4	153
	P11-2	191
Goertz, David	P1-6	46
	P10-9	178
Gofman, Ilan	P11-8	197
Goldhawk, Donna	P9-1	160
	P12-1	200
	P12-5	204
Gong, Li	P10-9	178
Gooding, Robert	P7-4	133
Gou, Shuiping	P1-7	47
Graham, Simon	P6-2	111
Graham, Simon J	P10-7	176
Graham, Thomas	O12-1	185
Gregor, Alexander	O1-1	31
Gross, Robert	P2-5	54

Name	Presentation	Page
Groves, Leah	P4-7	86
	P4-9	88
Grynko, Vira	O3-1	60
Gyackov, Igor	P1-8	48
Haast, Roy AM	O2-1	36
	P6-6	115
Hadi, Ali	O9-4	153
Hadway, Jennifer	P2-4	53
	P12-1	200
Haidegger, Tamas	P10-6	175
Haidegger, Tamás	O1-3	33
Haile, Denait	O2-1	36
Hamilton, Jake	O2-2	37
Hampole, Prakash	O7-3	122
Harding, Thomas	O7-3	122
Hardisty, Michael	P5-4	103
	P5-8	107
Hardy, Céline	P7-4	133
Hartley, Christopher	O11-1	180
Hashtrudi-Zaad, Kian	P4-5	84
	P12-9	208
Hassan, Salvan	P12-5	204
Hatolkar, Ved	P6-5	114
Headrick, Andrew	O4-4	68
Hegele, Rob	P6-8	117
Helpard, Luke	P5-7	106
Hewlett, Miriam	P6-3	112
Hicks, Justin	P2-1	50
	P3-4	73
	P9-5	164
	P9-6	165
	P9-8	167
Hisey, Rebecca	P4-5	84
	P4-9	88
	P5-3	102
	P11-9	198
	P12-9	208
Hobson, Sebastian	P5-2	101
Hocking, David	P5-1	100
Holden, Matthew	P11-8	197
Holdsworth, David W	O5-1	90

Name	Presentation	Page
	P8-5	144
	P8-8	147
	P10-5	174
Holtshousen, Scott	O4-2	66
	O11-4	183
Hoover, Douglas	O7-3	122
Husby, Theodore	O10-2	156
Huston, Yvonne	P9-1	160
	P12-1	200
Hutter, Megan	O1-4	34
	P8-2	141
Huynh, Chris	O8-2	126
Ibrahim, Pierre	O12-4	188
Incze, Roland	O1-3	33
Ioussoufovitch, Seva	O10-1	155
Irish, Jonathan	P1-2	42
	O4-2	66
	O11-4	183
Isbaine, Faisal	P2-5	54
Iseman, Rachael	P10-2	171
Itert, Lukasz	P11-7	196
Jackson, Chelsea	P7-4	133
Jago, Hannah	P9-1	160
	P12-1	200
Jagota, Arjun	O4-2	66
Jamaspishvili, Tamara	P10-2	171
James, James	P3-5	74
Jamzad, Amoon	P4-1	80
	P4-7	86
	P5-3	102
	O7-1	120
	O7-4	123
	P10-2	171
	O11-2	181
	P12-7	206
Jegatheesan, Aravinthan	P10-7	176
Johnson, Carol A	P10-1	170
Joshi, Chandra	O4-3	67
Jurkiewicz, Michael	O2-1	36
Kadem, Mason	P2-2	51

Name	Presentation	Page
Kadota, Brenden T	P6-4	113
Kai, Jason	O2-1	36
	P11-2	191
Kajal, Dilkash	P5-2	101
Kalia, Vibhuti	O9-1	150
Kamar, Farah	O10-3	157
Karagulleoglu-Kunduraci, Sule	P2-8	57
Kassam, Zahra	P7-3	132
Kassner, Andrea	P6-7	116
Kaufmann, Martin	P4-1	80
	P5-3	102
	O7-1	120
	P10-2	171
	O11-2	181
	P12-7	206
Kazemian, Pedram	O5-2	91
Keenlside, Lynn	P2-4	53
Kemper, Tara N	P12-8	207
Keshavarz, Mohammadmahdi	P4-2	81
Khan, Ali R.	O2-1	36
	O6-2	96
	P6-6	115
	P6-9	118
	O9-4	153
	P11-2	191
Khaw, Alexander	O12-2	186
Kim, Danny	P6-7	116
Kim, Janny	P3-6	75
Kirby, Miranda	P3-5	74
	P3-9	78
	O8-3	127
Kirton, Adam	P6-7	116
Kitner, Nicole	O4-3	67
Klosa, Elizabeth H	P4-5	84
	P12-9	208
Knier, Natasha	O9-3	152
Knowles, Nikolas	P8-3	142
Koga, Takamasa	O1-1	31
Koletar, Margaret	P6-5	114
Kolios, Christopher	O1-2	32
Komeili, Amin	P5-5	104

Name	Presentation	Page
Kooner, Harkiran K	O3-2	61
	P3-1	70
	P3-2	71
	P3-7	76
	P3-8	77
Korzeniowski, Martin	O4-3	67
Kosik, Ivan	O10-2	156
Kovacs, Michael	P2-1	50
	P9-4	163
	P9-5	164
	P9-8	167
	P12-1	200
Krause, Stephen	P9-9	168
Krautner, Joshua	P12-2	201
Krishnan, Pradeep	P6-7	116
Kronreif, Gernot	P10-6	175
Kuling, Grey C	P11-4	193
Kwan, Donna	P6-8	117
La Macchia, Josephine	P1-2	42
	O4-2	66
La Macchia, Josephine	O11-4	183
Ladak, Hanif M	P5-7	106
	P5-9	108
Laidley, David	P7-3	132
Lalone, Emily	O1-4	34
	P8-2	141
	P8-3	142
	P8-4	143
Lam, Chris	O8-2	126
Lam, Wilfred	P6-1	110
Lang, Anthony	P6-8	117
Lang, Pencilla	O7-2	121
	P7-2	131
Lau, Angus	P2-7	56
	O9-2	151
Lau, Jonathan C	P2-5	54
	O9-4	153
	P11-2	191
Lawrence, Liam SP	P2-7	56
	O9-2	151
Laxer, Sam	O5-3	92

Name	Presentation	Page
Lee, Ting-Yim	P2-4	53
	P7-3	132
	P9-3	162
	P9-4	163
	O12-2	186
Leung, Rajan	P10-8	177
Levine, Brian	P6-8	117
Li, Daniel	P3-6	75
Li, Natalie	O10-1	155
Liebig, Patrick	O6-1	95
Liem, Brett	P2-6	55
Lim, Adam	P11-3	192
Lim, Heeseung	P3-4	73
Lim-Fat, Mary Jane	P2-7	56
Lin, Sherman	O11-1	180
Lindale, Katherine	P7-4	133
Lindberg, Anton	O12-1	185
Litvack, Michael	P3-6	75
Liu, Junmin	P6-3	112
Liu, Linshan	P2-3	52
Liu, Ningtao	P1-7	47
Liu, Shirley	P12-2	201
	P12-4	203
Liu, Wei	P7-3	132
Lo, Justin	P11-3	192
Lo, Wei-Ching	O6-3	97
Loblaw, Andrew	P7-3	132
Lugez, Elodie	P10-3	172
	P10-4	173
Luk, Ethan J	P6-7	116
Luyt, Leonard	P9-2	161
	P9-6	165
Macgowan, Chris	O8-2	126
Mach, Robert	O12-1	185
MacNeil, Jonathan	O6-4	98
Macsemchuk, Craig	O4-4	68
Mainprize, James	P5-8	107
Makimoto, Kalysta M	P3-5	74
Maleki, Saman	P9-4	163
Mao, Haojie	P11-6	195

Name	Presentation	Page
Maralani, Pejman	P2-7	56
March, Lucas D	P5-3	102
Markevich, Stefanie	O4-2	66
	O11-4	183
Marras, Connie	P6-8	117
Martel, Anne L	P11-4	193
	P11-7	196
Martinov, Martin	P9-3	162
Masellis, Mario	P6-8	117
Mason, Julia R	P9-2	161
Matheson, Alexander M	O3-3	62
	P3-1	70
	P3-7	76
	P3-8	77
Mathialagan, Ashley	P10-3	172
Mathis, Chester	O12-1	185
Matsuura, Naomi	O1-1	31
Mattonen, Sarah	P5-6	105
	O7-2	121
	P7-1	130
	P7-2	131
McCormack, David	P3-1	70
	P3-7	76
	O8-3	127
McGrath, Sean F	O1-1	31
McIntosh, Marrassa	O3-2	61
	O3-3	62
	P3-1	70
	P3-2	71
	P3-7	76
McKay, Doug	P3-8	77
	P5-3	102
	O11-2	181
	P12-7	206
McLachlin, Stewart	P5-4	103
McLaurin, JoAnne	P6-5	114
Mendez, Lucas	P1-5	45
	O7-3	122
	P7-3	132
Menon, Ravi	P2-6	55
	O5-3	92

Name	Presentation	Page
	O6-3	97
Merchant, Shaila	O11-2	181
Micuda, Ashley	P5-7	106
Mihele, Maria	P3-3	72
Milej, Daniel	O10-3	157
Miller, Jacob	O5-2	91
Mittal, Richa	P7-9	138
Moga, Kristof	P10-6	175
Montero-Odasso, Manuel	P6-8	117
	O12-3	187
Morgan, Scott	O11-3	182
Morrison, Laura	P2-4	53
	P12-1	200
Morton, David	P4-7	86
Motooka, Yamato	O1-1	31
Mousavi, Parvin	O4-3	67
	P4-1	80
	P4-3	82
	P4-7	86
	P4-9	88
	P5-3	102
	O7-1	120
	O7-4	123
	P10-2	171
	O11-2	181
	P12-7	206
Mudathir, Randa	O1-4	34
	P8-2	141
Mulligan, Matt	P7-3	132
Munoz, Douglas	P6-8	117
Munum, Alif	P7-7	136
Mushtaha, Farah N	O6-2	96
Muthusami, Prakash	P6-7	116
Myrehaug, Sten	P2-7	56
Najjar, Esmat	P1-2	42
	O11-4	183
Narciso, Lucas D L	P2-3	52
Narvaez, Andrea	P9-9	168
Nassar, Moayyad N	P9-1	160
	P12-1	200
Naxpati, Nealen	P2-5	54

Name	Presentation	Page
Near, Jamie	O5-4	93
	P6-4	113
	P6-5	114
Neto, Pedro-Rosa	O2-3	38
Nguyen, Timothy	P7-1	130
Nichols, Anthony	P7-2	131
Nicholson, J Michael	P3-8	77
Norman, Elizabeth	P8-3	142
Noseworthy, Michael	P2-2	51
Nouri, Maryam	O2-1	36
Oakden, Wendy	P6-5	114
O'Driscoll, Olivia	P11-9	198
Ogunsanya, Feyifoluwa W.M.	P11-2	191
Okonkwo, Ozioma	O2-3	38
Olding, Tim	O4-3	67
Omidi, Parsa	P1-1	41
Oran, Omer	O6-3	97
Orange, JB	P6-8	117
Orlando, Nathan	O7-3	122
Orosz, Gábor	O1-3	33
Orunmuyi, Akintunde	O2-3	38
Ouriadov, Alexei V	O3-4	63
	P3-3	72
	P3-4	73
Oyeniran, Olujide	O2-3	38
	P2-1	50
	P9-8	167
Ozzoude, Miracle	P6-8	117
Palaniyappan, Lena	P6-9	118
Palma, David	P10-1	170
Parasram, Tristhal	O6-4	98
Park, Claire K	P1-5	45
	P1-8	48
	O10-4	158
Parraga, Grace	O3-2	61
	O3-3	62
	P3-1	70
	P3-2	71
	P3-4	73
	P3-7	76
	P3-8	77

Name	Presentation	Page
	O8-3	127
Patel, Jaykumar	P8-9	148
Paul, Narinder	O3-3	62
Pees, Anna L	P9-7	166
Pejovic-Milic, Ana	O1-2	32
Pellow, Carly	P1-6	46
Perera-Ortega, Andrea	O7-4	123
Perron, Samuel	O3-4	63
Peters, Terry	O4-1	65
	P4-4	83
	P4-6	85
	P4-8	87
	P5-1	100
	O8-1	125
	P12-8	207
Pieruccini-Faria, Frederico	O12-3	187
Pinto, Samara	P2-3	52
Piran Nanekaran, Negin	O11-3	182
Ploeg, Heidi-Lynn	P8-1	140
Pollmann, Steven	P8-5	144
Portnoy, Sharon	O8-2	126
Posiewko, Melanie	P3-6	75
Post, Martin	P3-6	75
Potts, Emilie	P11-6	195
Prato, Frank	P9-1	160
	P12-1	200
	P12-5	204
Purzner, Jaime	O7-1	120
Purzner, Teresa	O7-1	120
Rabbath, Enzo	P9-1	160
	P12-5	204
Radcliffe, Olivia	P4-3	82
Rafay, Mubeen	P6-7	116
Raguram, Keeirah	P3-3	72
Manokaran, Jenita	P7-9	138
Ramirez, Joel	P6-8	117
Rankin, Adam	P12-8	207
Rascevaska, Elina	P1-1	41
Rastegar Jooybari, Fatemeh	O8-2	126
Ratjen, Felix	P3-9	78

Name	Presentation	Page
Raymond, Roger	P9-9	168
Ren, Kevin Yi Mi	P5-3	102
	O11-2	181
	P12-7	206
Rezazada, Jeffrey	O5-2	91
Roberts, Angela	P6-8	117
Robertson, Amanda	P6-7	116
Rodgers, Jessica R	P1-5	45
	O4-3	67
	P5-3	102
	P10-2	171
Rogaeva, Ekaterina	P6-8	117
Rohani, Seyed Alireza	P5-7	106
	P5-9	108
Ronald, John	P12-2	201
	P12-3	202
	P12-4	203
Roy, Priyanka	O4-1	65
Roy, Trisha	P8-9	148
Ruaro, Alessandra	P1-2	42
	O11-4	183
Rudan, John	P4-1	80
	P4-3	82
	P4-7	86
	P5-3	102
	O7-1	120
	P8-1	140
	P10-2	171
	O11-2	181
	P12-7	206
Ruschin, Mark	P2-7	56
Ruset, Iulian Constantin	O3-1	60
Sachin, Pandey	O12-2	186
Sadanand, Siddharth	P6-1	110
Saderi, Moujan	P8-9	148
Safakish, Aryan	O1-2	32
Sahgal, Arjun	P2-7	56
	O9-2	151
Samal, Prathamesh	P11-1	190
Samani, Abbas	O8-4	128
	P7-5	134

Name	Presentation	Page
Sannachi, Lakshmanan	O1-2	32
Santilli, Alice	P5-3	102
Santyr, Giles	P3-6	75
	P3-9	78
Saprungruang, Ankavipar	O8-2	126
Schieda, Nicola	P7-6	135
	O11-3	182
	P11-1	190
Schmitz, Taylor	P6-6	115
Scholl, Timothy J.	O9-1	150
	P12-2	201
	P12-4	203
Seck, Idrissa	P4-9	88
Sehl, Olivia C	P12-6	205
Sembhi, Ramanpreet K	P3-4	73
Senthil, Sneha Vaishali	P6-4	113
Serajeddini, Hana	O3-2	61
	P3-2	71
Sewani, Alykhan	O5-2	91
Sharma, Maksym	O3-2	61
	P3-1	70
	P3-7	76
	O8-3	127
Sharp, Mackenzie	P10-2	171
Sheagren, Calder D	P8-9	148
Shen, Yu-Jack	O1-1	31
Shepelytskyi, Yurii	O3-1	60
Sherman, Daniel	P7-7	136
Shoemaker, Leena	O10-3	157
Shroff, Manohar	P6-7	116
Siemens, Robert	P7-4	133
Sikstrom, Lee	P10-5	174
Silic, Marina	P10-7	176
Simpson, Amber	P7-4	133
Singh Khehra, Parminder	P10-3	172
Sivan, Vignesh	P5-4	103
Sivasubramaniam, Priyadharshini	O11-1	180
Skanes, Allan	P8-8	147
Slotman, Ava	P7-4	133
Smart, Kelly	O2-4	39
Snir, Jonatan	O7-2	121

Name	Presentation	Page
	P7-1	130
Sobel, Mara	P7-7	136
Soddu, Andrea	P2-3	52
Sohal, Navkiran	P11-6	195
Soliman, Hany	P2-7	56
	O9-2	151
Sorzano, Rochelle	O2-1	36
Soto, Elmer	P9-5	164
Spinelli, Egidio	O2-1	36
Srikanthan, Dilakshan	O7-1	120
St. Lawrence, Keith	P2-3	52
	O10-3	157
Stanisz, Greg	P2-7	56
	P6-1	110
Stark, Helmut	O5-4	93
Stence, Nicholas	P6-7	116
Stepanic, Kristina	P7-8	137
Stewart, James	P2-7	56
	O9-2	151
Straatman, Lauren	P8-3	142
Strafella, Antonio	O2-4	39
Strong, Michael	P6-8	117
Suchy, Mojmir	P9-4	163
Suh, Nina	P8-3	142
	P8-4	143
Sumra, Vishaal	P6-8	117
Sunderland, Kelly	P6-8	117
Sunderland, Kyle	P4-7	86
	P4-9	88
Surry, Kathleen	P1-5	45
Sussman, Dafna	P5-2	101
	P6-1	110
	P7-7	136
	P11-3	192
	P11-5	194
Swartz, Rick	P6-8	117
Syeda, Ayesha	O11-2	181
	P12-7	206
Sykes, Jane	P9-1	160
	P12-1	200
Szabó, Róbert	O1-3	33

Name	Presentation	Page
Szentimrey, Zachary	P11-1	190
Taha, Alaa	O9-4	153
	P11-2	191
Tahghighi, Peyman	P5-5	104
Takalloobanafshi, Ghazaleh	P9-5	164
	P9-6	165
Tam, Fred	P10-7	176
Tan, Brian	P6-8	117
Tan, Josephine L	O9-1	150
Tan, Wan-Cheng	P3-5	74
Tanguay, Jesse	P8-7	146
Tang-Wai, David	P6-8	117
Tartaglia, Carmela	P6-8	117
Tavallaei, Ali	P4-2	81
	O5-2	91
Taylor, Mary G	O2-1	36
Terricabras, Maria	O5-2	91
Tessier, David	P1-7	47
	P1-8	48
	O4-1	65
	O10-4	158
Therriault, Aimee	P2-7	56
Thiessen, Jonathan	P3-4	73
	P7-3	132
	O9-1	150
	P9-1	160
	P12-1	200
Thompson, Caleb	P5-9	108
Thompson, R. Terry	P9-1	160
	P12-5	204
Thomson, Rowan	P9-3	162
To, Minh Nguyen Nhat	O7-4	123
Tong, Junchao	O12-1	185
Tong, Olivia	P2-4	53
Townson, Jason	P1-2	42
Tran, Brandon	O9-2	151
Tran, Ha Phan	P10-4	173
Troyer, Angela	P6-8	117
Trumpour, Tiana	P1-5	45
	P1-8	48
	O10-4	158

Name	Presentation	Page
Truong, Peter	O5-4	93
	P6-4	113
Tseng, Chia-Lin	P2-7	56
	O9-2	151
Tseu, Irene	P3-6	75
Tyler, Susan	P2-4	53
Tzelnick, Sharon	P1-2	42
Ukwatta, Eranga	P5-5	104
	P7-6	135
	P7-8	137
	P7-9	138
	O11-3	182
	P11-1	190
Ungi, Tamas	O1-3	33
	O4-3	67
	P4-1	80
	P4-3	82
	P4-5	84
	P4-7	86
	P4-9	88
	P10-6	175
	P11-9	198
	P12-9	208
Uribe, Carme	O2-4	39
Van Dyken, Peter	P6-9	118
Varela-Mattatall, Gabriel	O6-3	97
Varma, Sonal	O11-2	181
Vasdev, Neil	O2-4	39
	P2-9	58
	P9-7	166
	P9-9	168
	O12-1	185
Velker, Vikram	O7-3	122
Voutsas, Jonathan	O8-2	126
Vujovic, Teodora	P5-4	103
Wagner, Matt	P11-3	192
Wagner, Sophie	P11-5	194
Walker, Kirstin A	P6-7	116
Walker, Ross	O11-2	181
Walton, Dave	P8-3	142
Wang, Edward	O7-2	121

Name	Presentation	Page
Wang, Hui	P1-3	43
Wang, TianDuo	P12-3	202
Ward, Aaron	P7-3	132
	P10-1	170
	O11-1	180
Waspe, Adam	O4-4	68
Weersink, Robert	O10-2	156
Whitehead, Shawn	P3-4	73
Whyne, Cari	P5-8	107
Wilkie, Phoenix Y	P11-7	196
william, wasswa	P10-8	177
Wilson, Brian	P1-2	42
	O4-2	66
	O10-2	156
	O11-4	183
Wilson, Kyle	P8-5	144
Wilson, Paul F R	O7-4	123
Wilson, Sydney	O5-1	90
Wintermark, Max	P6-7	116
Wodlinger, Brian	O7-4	123
Won, Natalie J	O4-2	66
	O11-4	183
Wong, Sandy	O9-4	153
Wong, Suzanne	O4-4	68
Wong, Timothy	P7-8	137
Wright, Alex	P1-6	46
	P10-9	178
Wright, Graham	P4-2	81
	O5-2	91
	P8-9	148
Wyszkiewicz, Paulina V	P3-1	70
	P3-7	76
	P3-8	77
	O8-3	127
Xiao, Dan	O6-4	98
Xing, Shuwei	O4-1	65
	P4-6	85
	P5-1	100
Xu, Kathy	O2-2	37
Xu, Minqi	P7-4	133

Name	Presentation	Page
Yamashita, Cory	O3-2	61
	O3-3	62
	P3-2	71
Yang, Justin	P10-8	177
Yasufuku, Kazuhiro	O1-1	31
Yeo, Caitlin	P4-3	82
Yeung, Chris	O1-3	33
	P4-1	80
	P10-6	175
Yip, Lawrence	P1-1	41
Yohans, Jonathan	P12-5	204
Yoo, Shi-Joon	O8-2	126
Young, Dylan	P5-2	101
Zajner, Chris	P2-5	54
	O9-4	153
Zanette, Brandon	P3-9	78
Zelko, Lauren M	P7-1	130
Zeman, Peter	P2-6	55
	O5-3	92
Zeman-Pocrnich, Cady	O11-1	180
Zevin, Boris	P4-5	84
	P12-9	208
Zhao, Xiaoxiao	P1-6	46
Zinman, Lorne	O5-4	93
	P6-8	117

The Organizing Committee for the ImNO 2023 Annual Symposium would like to thank you for attending and acknowledge our supporting consortia and sponsors.

We invite you to attend the 22nd ImNO Symposium in March 2024 in Toronto, Ontario.



**Machine Learning in
Medical Imaging Consortium
(MaLMIC)**

Scintica:

